TTI: 0-7040

Texas A&M Transportation Institute

Evaluation of Corrosion Prevention and Mitigation Approaches Used on Texas Bridges—Volume 2: Reinforced Concrete Bridges

Technical Report 0-7040-R1-Vol2

Cooperative Research Program

TEXAS A&M TRANSPORTATION INSTITUTE
COLLEGE STATION, TEXAS

sponsored by the
Federal Highway Administration and the
Texas Department of Transportation
https://tti.tamu.edu/documents/0-7040-R1-Vol2.pdf

Technical Report Documentation Page

1. Report No. FHWA/TX-24/0-7040-R1-Vol2	2. Government Accession No.	3. Recipient's Catalog No.
4. Title and Subtitle EVALUATION OF CORROSION PREVENTION AND MITIGATION APPROACHES USED ON TEXAS BRIDGES—VOLUME 2: REINFORCED CONCRETE BRIDGES		5. Report Date Published: July 2024 6. Performing Organization Code
7. Author(s) Stefan Hurlebaus, Anna Birely, Matthew Yarnold, Arash Noshadravan, Arash Rockey, Pushkar Shivechchhu, Seung Hyun Yoon, and Zhen Zhang		8. Performing Organization Report No. Report 0-7040-R1-Vol2
9. Performing Organization Name and Address Texas A&M Transportation Institute The Texas A&M University System College Station, Texas 77843-3135		10. Work Unit No. (TRAIS) 11. Contract or Grant No. Project 0-7040
12. Sponsoring Agency Name and Address Texas Department of Transportation Research and Technology Implementation Office 125 E. 11th Street Austin, Texas 78701-2483		13. Type of Report and Period Covered Technical Report: January 2019–November 2023 14. Sponsoring Agency Code

15. Supplementary Notes
Project sponsored by the Texas Department of Transportation and the Federal Highway Administration.
Project Title: Evaluation of Corrosion Prevention and Mitigation Approaches Used on Texas Bridges
URL: https://tti.tamu.edu/documents/0-7040-R1-Vol2.pdf

16. Abstract
Corrosion in reinforced concrete is a self-accelerating process. As rust forms on steel, it enlarges in size and exerts tension on concrete, causing cracks and further corrosion in steel. The Texas Department of Transportation spends millions of dollars every year for repair and maintenance of concrete bridges; thus, a comprehensive study is essential to evaluate the corrosion resistance of concrete bridges across the state. In Texas, corrosion prevention and mitigation strategies for concrete decks involve the use of epoxy-coated rebar in addition to high-performance concrete. A calcium nitrite inhibitor, which increases the chloride threshold of concrete, is common in northern counties where a concrete accelerator is essential to achieve concrete strength during the early stages of winter. Additionally, surface treatments are also applied on concrete decks to reduce permeability of concrete. Findings of this research suggest that employing epoxy-coated rebar enhances the durability and corrosion resistance of reinforced concrete decks, while the use of uncoated black rebars can be still suitable for low corrosive environments. In the event that structures are located in highly corrosive regions such as marine environments and areas that heavily use deicing salt, the use of epoxy-coated rebar in addition to other mitigation strategies—like high-performance concrete—is recommended. Researchers also concluded that corrosion is inevitable in locations with surface cracking. In that case, corrosive agents can contact steel and initiate corrosion on reinforcing bars. Carbonation was determined to not be significant in inspected concrete decks unless cracks and concrete spalling happened. In general, most concrete decks inspected in this research were in acceptable condition except for a few cases that are documented within this report.

17. Key Words	18. Distribution Statement
Reinforced Concrete, Corrosion, Epoxy-Coated Rebar, High-Performance Concrete, Surface Treatment, Calcium Nitrite Inhibitor, Potentiometric Titration, Acid-Soluble Chloride Content, Carbonation, Bulk and Surface Resistivity, Sorptivity, EIS	No restrictions. This document is available to the public through NTIS: National Technical Information Service Alexandria, Virginia https://www.ntis.gov

19. Security Classif. (of this report)	20. Security Classif. (of this page)	21. No. of Pages	22. Price
Unclassified	Unclassified	784	

EVALUATION OF CORROSION PREVENTION AND MITIGATION APPROACHES USED ON TEXAS BRIDGES—VOLUME 2: REINFORCED CONCRETE BRIDGES

by

Stefan Hurlebaus, Ph.D.
Research Scientist
Texas A&M Transportation Institute

Anna C. Birely, Ph.D.
Research Scientist
Texas A&M Transportation Institute

Matthew Yarnold, Ph.D.
Research Scientist
Texas A&M Transportation Institute

Arash Noshadravan, Ph.D.
Assistant Research Scientist
Texas A&M Transportation Institute

Arash Rockey, Ph.D.
Postdoctoral Research Associate
Texas A&M Transportation Institute

Pushkar Shivechchhu
Graduate Assistant Researcher
Texas A&M Transportation Institute

Seung Hyun Yoon
Graduate Assistant Researcher
Texas A&M Transportation Institute

Zhen Zhang
Graduate Assistant Researcher
Texas A&M Transportation Institute

Report 0-7040-R1-Vol2
Project 0-7040
Project Title: Evaluation of Corrosion Prevention and Mitigation Approaches Used on Texas Bridges

Sponsored by the
Texas Department of Transportation
and the
Federal Highway Administration

Published: July 2024

TEXAS A&M TRANSPORTATION INSTITUTE
College Station, Texas 77843-3135

DISCLAIMER

This research was sponsored by the Texas Department of Transportation (TxDOT) and the Federal Highway Administration (FHWA). The contents of this report reflect the views of the authors, who are responsible for the facts and the accuracy of the data presented herein. The contents do not necessarily reflect the official view or policies of FHWA or TxDOT. This report does not constitute a standard, specification, or regulation.

This report is not intended for construction, bidding, or permit purposes. The engineer (researcher) in charge of the project was Stefan Hurlebaus. The United States Government and the State of Texas do not endorse products or manufacturers. Trade or manufacturers' names appear herein solely because they are considered essential to the object of this report.

ACKNOWLEDGMENTS

This project was conducted at Texas A&M University and was supported by TxDOT and FHWA through the Texas A&M Transportation Institute as part of Project 0-7040, Evaluation of Corrosion Prevention and Mitigation Approaches Used on Texas Bridges. The authors thank the individuals who were involved with this project and provided invaluable assistance, including Tom Schwerdt (TxDOT, project manager) and the TxDOT Project Monitoring Committee: Johnnie Miller, Steven Austin, Rachel Cano, Robert Owens, Sydney Newman, Teresa Michalk, Niyi Arowojolu, Kevin Pruski.

TABLE OF CONTENTS

LIST OF FIGURES

Page

LIST OF TABLES

Page

1 INTRODUCTION

1.1 BACKGROUND AND SIGNIFICANCE

Reinforced concrete bridges exhibit greater resilience to corrosion problems than steel girder bridges, and they are preferred in the construction of these superstructures. The Texas Department of Transportation (TxDOT), in particular, is willing to use concrete in the construction of bridges and overpasses because the overall effect is that concrete enhances the corrosion resistance of reinforcing steel bars, making the structure more durable. However, concrete is classified as ceramics (from a material point of view), and it exhibits brittleness properties. Hence, cracks can form on the top layers of concrete and grow on top of steel, introducing a path for corrosive agents to contact reinforcing bars. In addition to cracks, defects such as macro-size voids and damage, like concrete spalling and delamination, can increase the volume of moisture and pollutants in concrete, thus initiating corrosion on steel reinforcement.

Corrosion is a self-accelerating process. As electrochemical reactions proceed, not only does metal loss happen in oxidized locations, but corrosion products also accumulate on reduction sites, which causes more cracks and spalling in the concrete. Identifying corrosion problems in concrete is a cumbersome task and requires destructive testing in many instances, therefore making repair and maintenance expensive.

Several types of corrosion prevention and mitigation methods have been applied on concrete decks in Texas, including coating the steel bars with epoxy, applying a surface treatment on the concrete deck, employing high-performance concrete (HPC), and adding calcium nitrite-based inhibitors to the concrete mixed design. Although these mitigation methods have been in service for decades, there is no comprehensive assessment of the performance of these systems in enhancing corrosion resistance of reinforced concrete structures. Studies focused on corrosion prevention techniques rarely consider the effect of combined mitigation methods in improving corrosion resistance of reinforced concrete structures. The evaluation of the protection system was limited to specimens made in the laboratories and subjected to accelerated corrosion testing. However, the current study evaluates the long-term performance of these systems on in-service concrete bridges in Texas.

The researchers evaluated the performance of corrosion prevention and mitigation methods employed in TxDOT concrete decks to help the state agency and affiliated departments select a

proper mitigation method for bridge superstructures by considering the corrosivity of the environment. Based on the results of field inspections and laboratory testing, researchers investigated whether the combination of corrosion prevention techniques mitigate the adverse effects of corrosion on concrete decks in different corrosive environments. Researchers also provide guidelines for laboratory examinations that can aid in determining corrosion issues in concrete specimens.

1.2 OBJECTIVES AND SCOPE

The major objectives of this research were as follows:

- Review the existing studies and document the relevant literature on the performance of corrosion prevention and mitigation techniques employed in concrete bridges to enhance the corrosion resistance of the structure.
- Perform comprehensive field investigations of several concrete decks across Texas and develop surface crack and corrosion mapping for inspected structures.
- Conduct laboratory examinations to accurately assess the quality of concrete cores obtained from inspected concrete decks and investigate the extent of corrosion on steel bars.
- Evaluate the volume of moisture in concrete specimens and the potential amount of pollutant that has penetrated the concrete decks.
- Develop a decision support tool by considering a multidimensional, multi-criterion ranking and scoring process to assess the performance of corrosion prevention and mitigation methods for new and existing structures. This tool will aid the state agency and affiliated departments in selecting proper mitigation methods for enhancing the corrosion resistance of concrete structures in different corrosive environments.

1.3 RESEARCH PLAN

To accomplish the outcomes of this research study, the following tasks were conducted:

- Task 1—Project Management and Research Coordination.
- Task 2—Review State-of-the-Art and State-of-the-Practice.
- Task 3—Field Evaluation to Investigate Effectiveness of Corrosion Mitigation.

- Task 4—Perform Laboratory Tests.
- Task 5—Develop Decision Tool for Effective Corrosion Prevention and Mitigation.

This document is Volume 2 of a two-volume report that provides comprehensive findings of field inspections and laboratory testing in addition to recommendations on corrosion prevention and mitigation strategies applied to concrete superstructures.

1.4 REPORT OUTLINE

The report is divided into six chapters. Chapter 1 discusses the motivation, significance, and objectives of this research. It outlines tasks conducted during this study to evaluate long-term performance of corrosion prevention and mitigation approaches applied in TxDOT concrete bridges. Chapter 2 contains a comprehensive literature review and previous studies to identify corrosion-related problems in concrete through both field investigation and laboratory examinations.

Chapter 3 discusses the selection of reinforced concrete bridges in addition to field inspection and evaluation of the results. A total of 61 concrete bridges were selected across Texas representing different environmental conditions. Conditions considered in a corrosion risk assessment map developed for Texas and reported in Volume 1 of this report were considered in the selection of the reinforced concrete decks.

Chapter 4 summarizes the results of laboratory testing performed on concrete core specimens obtained from inspected concrete decks. The laboratory examinations conducted in this research work include surface resistivity, bulk resistivity, ultrasonic pulse velocity, water absorption test, chloride content measurement, carbonation depth measurement, coating adhesion testing, and electrochemical impedance spectroscopy. The procedure was taken for each individual test and a comprehensive analysis on the results were also reported in this chapter.

Chapter 5 describes the development of a decision support tool based on the results of field evaluation and laboratory testing. This decision tool offers proper corrosion prevention and mitigation methods depending on corrosivity of the environment.

Finally, Chapter 6 presents the summary and conclusions derived from the current research. According to the findings obtained from this research project, recommendations are outlined in this chapter for a proper selection of corrosion prevention and mitigation methods employed in reinforced concrete bridge decks.

2 LITERATURE REVIEW

In 2002, the Federal Highway Administration published a study that estimated the cost of metallic corrosion and provided suitable preventive methods to minimize the impact of corrosion in concrete bridges (Koch et al., 2002). The annual estimated direct cost of corrosion in the United States at that time was $276 billion, equivalent to 3.1 percent of the gross domestic product, and the annual average direct cost of corrosion on highway infrastructure was $8.26 billion. The direct cost of corrosion was estimated by using a combination of the cost for structurally damaged bridges (approximately 46 percent) as well as the cost of maintenance of concrete bridge decks (approximately 24 percent) and concrete substructures (approximately 24 percent).

The long-term performance and structural integrity of bridges are important to ensure efficient transportation and economic growth. According to the Texas bridge inventory database (TxDOT, 2023), Texas has 54,432 bridges (roughly 9 percent of the total bridges in the United States). Among these bridges, 29,421 are reinforced concrete bridges, and the majority of them were constructed between 1940 and 2000. The rate of corrosion for different types of bridges is different and significantly relies on the surrounding micro- and macroenvironmental conditions. Thus, routine maintenance and repair is required to keep the reinforced concrete sub- and superstructures in structural function.

A good quality and dense concrete provide protection to the reinforcing steel unless cracks appear on the concrete surface. If corrosive agents contact reinforcing bars for any reason, a corrosion product can form on the steel substrate causing concrete cracks and spalling. There are two types of corrosion prevention and mitigation techniques that can be implemented in concrete structures. These techniques either increase corrosion resistance of concrete or are alternative reinforcing bars with greater corrosion resistance. In Texas, the use of HPC is sometimes implemented to reduce the permeability of concrete, while air entrainment is also common to relieve pore pressures and enhance the freeze-thaw resistance of concrete. Alternative reinforcing bars, such as epoxy-coated reinforcement, hot-dip galvanized reinforcement, fiber-reinforced polymer (FRP), and stainless-steel bars, are also used in TxDOT bridge concrete structures.

This chapter is divided into three sections. It explains the corrosion mechanism and important factors in reinforced concrete bridges, then it discusses the corrosion mitigation techniques employed on the decks of reinforced concrete bridges in Texas. Finally, it describes a

few instances of concrete bridge deteriorations reported in the literature and reviews the previous studies conducted on the effectiveness of corrosion prevention and mitigation methods.

2.1 MECHANISM OF CORROSION AND CRITICAL PARAMETERS

Corrosion is an electrochemical process that involves chemical reactions and electron exchanges between metal and reactive agents. Corrosion activity happening in a concrete bridge structure can vary depending on local environmental conditions and the implemented protection system. Reinforced concrete can generally provide greater protection against corrosion because concrete acts as a barrier against corrosive agents.

Corrosion of reinforcement in concrete is an electrochemical process as shown in Figure 2.1. For steel in concrete, electron transfer between two half-cell reactions at the steel-concrete interface occurs as follows:

Anodic reaction: $$2Fe \rightarrow 2Fe^{2+} + 4e^{-} \quad (2.1)$$

Cathodic reaction: $$O_2 + 2H_2O + 4e^{-} \rightarrow 4OH^{-} \quad (2.2)$$

Total reaction: $$2Fe + 2H_2O + O_2 \rightarrow 2Fe(OH)_2 \quad (2.3)$$

Ferrous ions (Fe^{2+}) can react further with oxygen and water, leading to the formation of oxides and hydroxides. Hydrated ferrous oxide (rust) is a porous material that enlarges in size over time, causing cracking and spalling in concrete. After concrete cracking and spalling, a new and shallower interface is created that intensifies the corrosion rate of the steel rebar.

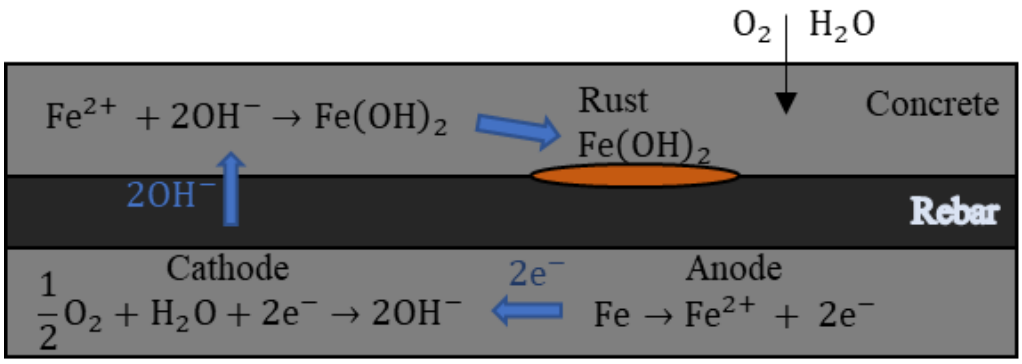

Figure 2.1. Corrosion of Steel Bar Embedded in Concrete (ACI 228.2R-13, 2013)

In an alkaline environment, a passive film of ferric oxyhydroxide (FeOOH) forms on the surface of steel rebars because the electrode potential shifts in a more anodic direction and increases the concentration of ferrous ions at the rebar surface. Therefore, these ions react with surrounding moisture and form a protective layer, as the following formula indicates:

$$Fe^{2+} + 2H_2O \rightarrow FeOOH.H_2O + 3H^+ + e^- \quad (2.4)$$

Chloride-induced corrosion is one of the main corrosion mechanisms in reinforced concrete structures. It typically occurs when the structure is exposed to a high chloride concentration environment. When the chloride penetrates concrete, it reduces the alkalinity near reinforcement, and electrochemical reactions need to take place for the environment to reach equilibrium. Therefore, chloride ions diffused within the passive layer maintain electroneutrality and displace the protective layer with chloride hydroxides, as described in the following:

$$FeOOH + Cl^- \rightarrow FeOCl + OH^- \quad (2.5)$$

$$FeOCl + H_2O \rightarrow Fe^{3+} + Cl^- + 2(OH)^- \quad (2.6)$$

When the protective oxide film is damaged by chloride, it causes small cavities in the passive layer. These cavities have an anodic nature, while aerated areas outside the cavity have a cathodic nature. Developed imbalanced sites result in extremely localized and widespread galvanic corrosion. Additional chloride ions that were not participants in the reactions act as a catalyst and make the corrosion process highly localized, which often cause section loss and pitting corrosion rather than uniform corrosion. The overall process further results in self-propagating pitting corrosion. In addition to chloride, steel can be subjected to high concentrations of oxygen and moisture in confined areas composed of multiple layers of steel and concrete. These stagnant locations attract aggressive ions, which leads to more corrosive activity.

For typical corrosion potential, the critical total chloride varies between 0.4 and 1 percent by the weight of cement (Angst et al., 2009). However, Figueira et al. (2017) suggested that the ratio of chloride concentration to hydroxide concentration can be a better representation of the chloride limit in concrete.

Carbonation is another corrosion mechanism that may occur in a reinforced concrete structure; it is defined as elevated pH in concrete voids near to steel reinforcement. When carbon

dioxide (CO_2) penetrates concrete, it neutralizes the alkalis in pore water. The reactions lead to the formation of carbonic acid (H_2CO_3) and makes the surrounding environment acidic, as described in the following (Goyal et al., 2018):

$$C0_2 + H_2O \rightarrow H_2CO_3 \quad (2.7)$$

$$H_2CO_3 + Ca(OH)_2 \rightarrow CaCO_3 + 2H_2O \quad (2.8)$$

Carbonation does not cause damage to concrete directly. Indeed, it can even reduce the porosity and result in an increase in strength. However, when the pH value of pore solution decreases due to the carbonation process, the passive layer is not more stable, and pitting corrosion is initiated on the rebar surface. In extreme cases, the passive layer can be completely dissolved due to the acidic nature of the environment (Aperador et al., 2015).

The volume of water content in concrete pores is essential for the carbonation process in concrete. Ahmad (2003) reported that the greatest rate of carbonation in concrete specimens happens at 50–70 percent relative humidity (RH). However, in high RH conditions (above 80 percent), the water filling in the pores can inhibit the diffusion of both carbon dioxide and oxygen and thus reduce the carbonation rate.

Uniform corrosion, *pitting corrosion, crevice corrosion*, and *corrosion cracking* are typical forms of corrosion that can occur in reinforced concrete. Among all these kinds of corrosion, uniform corrosion is known as the prevalent form that has a less detrimental effect than the other types (Fontana & Greene, 1986). Uniform corrosion occurs when the exposure conditions, such as corrosive agents and environmental factors, are uniform across the surface of the metal. Thus, the corrosion process proceeds evenly across the entire surface, resulting in uniform corrosion (Hurlebaus et al., 2016). Uniform corrosion in a concrete deck can occur on uncoated black rebar that can affect reinforcing bars over time. Corrosion prevention and mitigation methods to prevent uniform corrosion in reinforced concrete include the use of coating or other corrosion-resistant materials.

Pitting corrosion is an extremely localized attack that results in holes in the metal. This process is one of the most destructive forms of corrosion because a small cavity develops in the depth of the steel. It is difficult to detect pitting corrosion on reinforcing steel bars embedded in concrete, and failure as a result of this type of corrosion is unexpected and carries severe

consequences (Fontana & Greene, 1986). This form of corrosion occurs when a localized anodic or cathodic site creates a small corrosion cell on the metal surface (Hurlebaus et al., 2016).

Localized chemical and mechanical damage to the protective oxide film can cause pitting corrosion, which can occur in both black rebar and ECR. In the case of uncoated rebar, the absence of any protective coating makes it more susceptible to pitting corrosion when exposed to corrosive environments. The coating provides protection against uniform corrosion for ECR, but the reinforcing bar may still experience pitting corrosion through localized breaches or damage to the coating. Any defects within the epoxy layers can cause localized corrosion on the steel substrate. Proper installation, inspection, and maintenance of the coating are essential to prevent pitting corrosion. Additionally, corrosion-resistant materials can also be adopted to prevent pitting corrosion.

Crevice corrosion is another form of localized corrosion frequently occurring within crevices and shielded areas on metal surfaces exposed to corrosive environments. Crevice corrosion usually happens in areas with a different concentration of ions (Fontana & Greene, 1986). It also frequently occurs in enclosed regions that have a limited oxygen presence. Corrosive agents can enter these regions, but the limited circulation of oxygen prevents re-passivation of the metal surface. Consequently, the developed stagnant solution reduces the pH level from neutral conditions. This imbalance between the crevice and the external surface accelerates the corrosion process (Fontana & Greene, 1986). Like pitting corrosion, proper installation, inspection, and maintenance of the coating are essential to prevent crevice corrosion.

Corrosion cracking can be generally classified as *stress corrosion cracking* (SCC), *corrosion fatigue* (CF), and *hydrogen-induced cracking*. SCC can occur when a crack grows on a strand due to simultaneous occurrences of both tensile stresses and a corrosive environment. Hydrogen embrittlement may occur when the steel absorbs the hydrogen gas produced by a cathodic reaction in some areas where oxygen is not available. This event causes the loss of ductility and brittle fracture. CF is defined as the cracking of a metal under the combined action of a corrosive environment and repetitive stresses. Pitting corrosion is known as the main cause of fatigue cracking in metals (Bastidas-Arteaga et al., 2009). Corrosion cracking is not common in reinforced concrete bridges; however, it is still considered one of the higher-risk, critical factors that can cause the failure of reinforced concrete bridges (Martin et al., 2020).

2.2 CORROSION IN REINFORCED CONCRETE BRIDGES

Corrosion is a major challenge in reinforced concrete bridges, and it causes substantial financial loss in Texas every year. Bridge structures consist of three primary components—the *deck*, *superstructure*, and *substructure*—all of which are commonly constructed using materials such as reinforced concrete, steel, and prestressed concrete that are susceptible to corrosion. Concrete desks, particularly, are susceptible to rapid initiation of corrosion because they are directly exposed to corrosive agents. If the corrosion rate of reinforcing bars in concrete increases, it indicates the gradual deterioration of structural elements. An elevated rate of corrosion in concrete can eventually result in the complete collapse of the whole system. Such incidents not only endanger lives but also impact the economy.

Reinforced concrete is a dominant material widely used in the construction of bridge structures. In Texas, prestressed concrete bridges have also been constructed because they can increase the structural capacity and the lifespan of the system as well as decrease the construction time. However, special consideration must be given to the risk of corrosion in reinforced and prestressed concrete bridges because of the high cost of repair and maintenance. Generally, the ideal service life of a concrete bridge is over 50 years; however, aggressive ion attack from products of chloride or carbonation reduces the lifespan (K. Ann et al., 2009; Luca Bertolini et al., 2013).

Reinforcing bars embedded in concrete are protected by an oxide passivation layer developed in an alkaline environment. The pH of ordinary concrete generally ranges between 12 and 13. This level of pH helps steel remain passivated (Ahmad, 2003; Deschner et al., 2012). A factor that can directly impact the properties of the protective layer is concrete permeability. A low permeable concrete protects reinforcing bars from corrosion attacks because it forms a barrier around the steel, preventing the penetration of a corrosive agent such as chloride, carbon dioxide, or water. However, concrete is not protective in corrosive environments, such as when the structure is located in marine environments or exposed to the routine use of deicing salts (Tuutti, 1982).

Concrete cracks can impair the protective properties of concrete by providing a pathway for corrosion-inducing agents such as water, carbon dioxide, and chloride (Ahmad, 2003). The corrosion-inducing agents will lower the pH of concrete, resulting in the degradation of the protective layer. This process can accelerate the initiation and propagation of corrosion on reinforcing bars and reduce the overall service life of the bridge structures (Otieno et al., 2010).

For example, Manafpour et al. (2016) conducted field investigations on reinforced concrete bridges and showed that surface cracking developed on bridge decks significantly impacts the corrosion rate and long-term performance of the structures. Arya and Ofori-Darko (1996) and Bentur et al. (1997) studied the distribution of surface cracking on concrete decks and concluded that the depth and width of cracks—in addition to their orientations relative to the steel reinforcement—causes corrosion-related problems in concrete structures.

Corrosion causes metal loss, thus reducing the capacity of structural resistance. Meanwhile, the volume of corrosion product (rust) is three to six times greater than that of the original steel. As rust forms on reinforcing bars, it exerts significant tensile forces on concrete, leading to cracking, delamination, and spalling of the concrete cover (Vu & Stewart, 2000). For example, in Canada, Dickson Bridge was replaced in 1994 after 39 years in service because the bridge was showing rust stains, spalling of the concrete cover, exposure of the reinforcing bars, and loss of the steel cross-sectional area in several locations. In addition, severe delamination was found in the bridge deck, with chloride ion contents significantly above the permissible limits (Fazio, 1999). Figure 2.2 also shows some examples of bridges experiencing concrete spalling and corrosion on rebar due to concrete spalling.

(a) Spalling at Rail Due to Corrosion (b) Spalling at Girder End Due to Corrosion

Figure 2.2. Deterioration of Reinforced Concrete Structures Caused by Steel Corrosion.

Several research projects have focused on investigating corrosion mitigation methods. Pyc et al. (2000) and Pincheira et al. (2015) conducted a study to evaluate the effectiveness of ECR and its performance in corrosion protection. Howell et al. (2015), sponsored by the Kentucky Transportation Center, examined deterioration mechanisms and proposed mitigation measures for chloride intrusion in Kentucky bridges. These studies provide insights into the challenges of

corrosion and offer recommendations for improving corrosion resistance and preserving bridge infrastructure.

Pincheira et al. (2015) conducted a study with the Minnesota Department of Transportation on the corrosion performance of epoxy-coated bars in four bridge decks built in the 1970s. The study involved two separate investigations, 10 years apart. Field inspections included visual assessment, chain drag surveys, and half-cell potential measurements. The laboratory testing included measurement of chloride ion content, carbonation depth, and coating adherence. The overall condition of the bridge decks was found to be very good, with minimal delamination. However, evidence of corrosion activity was observed at expansion joints, cracks, and delaminated or spalled areas. Corrosion was detected even in low chloride ion concentrations in the surrounding concrete, but uniform corrosion on steel reinforcement was only found in higher chloride ion concentrations. Regardless of corrosion, the loss of coating adherence was observed in both corroded and noncorroded reinforcing bars. The study recommended proper sealing of cracks and expansion joints to prevent chloride ion ingress and a minimum bar cover of 3.0 in.

Pyc et al. (2000) evaluated the capability of ECR to mitigate corrosion. In this study, the authors examined concrete cores obtained from 18 reinforced concrete bridges from 2 to 20 years old in Virginia. Field inspections involved a survey of cracks and measurements of cover depth, while laboratory experiments included measurements of carbonation depth, moisture content, absorption, and chloride ion content. The study concluded that the average loss of epoxy bonds happened in 4 years, even prior to chloride ions reaching the reinforcing bars. Based on these findings, alternative protection systems such as calcium nitrate and low-permeability concrete combined with calcium nitrite were recommended as cost-effective options for increasing corrosion resistance of the structure.

Lastly, Howell et al. (2015) conducted a comprehensive study to understand deterioration mechanisms and develop effective mitigation strategies for bridges in Kentucky. The primary focus of their investigation was on the volume of chloride ingress in concrete, resulting from the penetration of de-icing salts. The researchers conducted visual inspections of 24 bridges and performed laboratory tests on concrete cores. Significant deterioration and high levels of chloride contamination were observed from the laboratory examinations, and it was concluded that the chloride concentration in many cases surpassed the chloride threshold for reinforcing steel. This study suggested a range of potential solutions to mitigate corrosion in concrete, including the use

of admixtures to reduce porosity, sealants, cleaning procedures, electrochemical chloride extraction, cathodic protection, crack and joint repair, and concrete resurfacing. It also shows some examples of concrete spalling due to corrosion.

2.3 CORROSION MITIGATION METHODS

Adopting cost-effective materials and regular maintenance in addition to implementing effective strategies are essential to delay the onset of corrosion and extend the service life of reinforced concrete bridges. This section focuses on the corrosion prevention and protection systems used in reinforced concrete decks in Texas. Note that the performance of the protective systems cab be influenced by both micro- and macroenvironmental conditions.

Macroenvironments can be categorized as mild or rural (with minimal exposure to airborne or deicing salts), moderate or industrial (with some exposure to airborne or deicing salts), and severe or marine (characterized by high salt concentration due to proximity to the coast or deicing salts, as well as high humidity and moisture). However, the microenvironment depends on factors such as material composition, configuration, orientation relative to runoff, and exposure to direct sunlight. In this study, the Texas environment was divided into six corrosive risk environments (Region 1 to Region 6). Using environmental parameters explained in Chapter 3 of Volume 1 of this report, Region 1 and Region 2 were characterized as low corrosive environments. Region 3 and Region 4 fall under the category of medium corrosive environments, and Region 5 and Region 6 were classified as highly corrosive environments.

Corrosion protection systems for concrete bridges can be divided into different classes. For example, supplementary cementitious materials, water-repellent sealers, ECR, metallic rebar coatings, and cathodic protection.

2.3.1 Concrete Admixtures

To delay the onset of corrosion, supplementary cementitious materials are added to create HPC. HPC is made of cement and mineral components such as blast furnace slag, silica fume, fly ash, and fillers such as limestone powder (Gowripalan et al., 1998). The permeability of HPC is lower than Portland cement concrete, which allows concrete to restrain the flow of chloride ions. Several studies (Dhir & Jones, 1999; Noumowe et al., 2009; Rupnow, 2012) described different concrete mixtures that enhance the durability and decrease the porosity of HPC and can indeed

limit chloride ingress in the structure. Furthermore, using cementitious materials not only reduces permeability, it also improves the workability of concrete and produces a higher ultimate strength than normal concrete while maintaining the equivalent freeze-thaw resistance, higher modulus of elasticity, and resistance to deicing salts (Rupnow, 2012).

In addition to supplementary cementitious materials, adding corrosion inhibitors to concrete mixtures to improve the corrosion resistance of concrete is also common. Corrosion inhibitors are chemical compounds that reduce the corrosion rate by affecting the anodic and cathodic reactions. Hansson et al. (2007) studied the impact of concrete admixtures on increasing the corrosion resistance of the structures and concluded that anodic inhibitors reduce the corrosion rate by blocking the anodic reaction in concrete, which can increase the resistance of the passive film on steel and limit the access of water and oxygen. Atkinson and Nickerson (1984), and later Söylev and Richardson (2008), suggested calcium nitrite, the most widely used anodic inhibitor, restrains the anodic corrosion reaction and reduces the corrosion rate. Moreover, sodium hydroxide and sodium carbonate, the most common cathodic inhibitors, increase the pH near steel and reduce the oxygen transport by protecting the steel surface (Bentur et al., 1997; Söylev & Richardson, 2008).

Mixed inhibitors act on both anodic and cathodic sites. They form a thin protective layer that reduces the corrosion rate of steel reinforcing bars without a significant change in the corrosion potential of steel. Nitrogen, sulfur, and hydroxide ions with hydrophobic properties are the most effective mixed inhibitors (Söylev & Richardson, 2008). However, even though corrosion inhibitors have been used successfully in other structures, such as steel pipelines and tanks, a lack of understanding on their environmental and safety aspects still exists (Söylev & Richardson, 2008). Furthermore, inhibitors that are common in concrete mixtures are costly and toxic in nature; therefore, different cost-effective and environmentally friendly inhibitors have to be developed (Bavarian & Reiner, 2002).

A calcium nitrite inhibitor (CNI) of corrosion is often used in the northern part of Texas to mitigate corrosion because it can accelerate the hardening period of concrete in low-temperature casting environments. Incorporating calcium nitrite into concrete enhances the steel's resistance to corrosion damage by reinforcing the passive layer of steel reinforcement. Additionally, calcium nitrite's tendency to react with both free and bonded chloride ions contributes to this enhanced resistance (Neville, 1995). Calcium nitrite is identified as an anodic inhibitor because it functions

at the anode, oxidizing ferrous ions (which is the first product of corrosion) to form a protective film of Fe_2O_3 around the anode, thereby precluding further corrosion. Evidence from numerous studies demonstrates the application of CNI increases the corrosion resistance of concrete and rebar and thus reduces the corrosion risk to the reinforcement (Al-Amoudi et al., 2003; K.-Y. Ann et al., 2006; K. Y. Ann & Buenfeld, 2007; Kessler et al., 2007; Söylev & Richardson, 2008).

2.3.2 Surface Treatments

Concrete sealants are applied to the surface of the concrete or cracks within the concrete in order to slow the ingress of water and chloride ions (Deschner et al., 2012; Hansson et al., 1998). Sealants can be organic or inorganic. Although organic sealants are most frequently used, their service life is limited. They have poor fire resistance and easily crack and detach from the underlying concrete. Inorganic treatments such as sodium silicate, potassium silicate, lithium silicate, and fluosilicates have greater durability; however, their performance and long-term results have not been as thoroughly investigated (Pan et al., 2017a).

Sealants can be grouped into four main classes based on their mode of operation. These classes are as follows: (a) surface coating that can form a continuous polymer film on the surfaces of concrete (Medeiros & Helene, 2008); (b) sealers that penetrate the pores of concrete substrate (Giannini et al., 2015), resulting in a stronger molecular attraction between the water and concrete, thereby inhibiting water penetration (de Vries & Polder, 1997); (c) pore-blocking surface treatments that block capillary pores and reduce the porosity of the concrete surface (Pan et al., 2017a); and (d) multifunctional surface treatments that have at least two functions, such as ethyl silicate (Franzoni et al., 2013). Among these surface treatments, the performance of penetrating sealers is dependent on the depth of penetration, and the most commonly used ones are silane (SI) and siloxane. In addition, pore-blocking treatments may not perform well in concrete made with supplementary cementitious materials and may not penetrate the concrete with exposed cracking (Freitag & Bruce, 2010). In general, the performance of sealants relies on factors such as the environment, condition of concrete structures, and traffic volume. Sealants have to be reapplied because their performance decreases after years of exposure to the environment (Pritzl et al., 2015).

Two widely used concrete surface treatments (CST) are SI and linseed oil (LO). Of these, SIs are a highly recommended choice, with numerous laboratory and field studies demonstrating their efficacy (Li et al., 2023; Pan et al., 2017a, 2017b). Remarkably, SIs can maintain their

hydrophobic effect for nearly 20 years, while oil-based treatments fade in as little as 5 years. LO falls short due to insufficient hardening, making it insufficiently resistant to vehicle abrasion. SI can reduce water permeability by 80 percent compared to concrete samples with the same mix design (Pan et al., 2017b).

Regarding freeze-thaw resistance, although surface treatments cannot replace air-entraining agents to combat freeze-thaw cycles, they can provide supplemental protection. Surface treatments can delay the ingress of moisture under freeze-thaw conditions, thereby prolonging the time to reach critical moisture thresholds (Dang et al., 2014).

In the corrosion protection of steel bars, the surface treatment exhibited a general ability to inhibit the ingress of chlorides, thereby delaying the initial time of steel corrosion. It is generally accepted that polymer coatings are superior to other treatments in resisting chloride ingress. However, their protective ability is limited. Notably, the effect of SI on corrosion exhibits complexity in that it accelerates the corrosion of reinforcement embedded in cracked concrete while reducing the corrosion rate of uncracked concrete. This phenomenon is attributed to different oxygen diffusion rates (Tittarelli & Moriconi, 2010). For degraded coatings, the diffusion rate of chloride ions in treated concrete can exceed that of untreated concrete. This result may be attributed to two factors: (a) the accumulation of surface chloride ion concentration, and (b) the continuous wetting of the concrete due to the treatment, which makes it easier for chloride ion ingress (Pan et al., 2017b).

2.3.3 Alternative Reinforcement

In highly corrosive environments, alternative reinforcing bars such as stainless steel, epoxy-coated reinforcing (ECR) bars, hot-dip galvanized reinforcing bars, and FRP bars are used to prevent corrosion of reinforcement in concrete. These materials are often grouped into the following categories: coated reinforcement, high chromium steel bars, and FRP bars (Lute et al., 2021).

2.3.3.1 Coated Reinforcement

The first category includes alternative reinforcement that is a coating around the steel to prevent chlorides from reaching the steel substrate. Such coated reinforcements are epoxy-coated steel (ECR), dual-coated steel, galvanized steel, and stainless steel-clad steel. ECR, introduced in

the 1970s, are manufactured according to the following standards: ASTM A775/A775M (2022), ASTM A934/A934M (2022), and ASTM D3963/D3963M (2021). The latter provides instructions on how to handle manufactured bars.

Epoxy coating shows a relatively good corrosion resistance and is the most commonly used corrosion prevention and mitigation method in concrete bridges (Van Dyke et al., 2017). Lawler et al. (2011) inspected 33 bridge decks in West Virginia, which included 14 decks with ECR and 19 decks with uncoated reinforcing bars, to analyze the long-term performance of ECR on bridge decks in corrosive environments. Significant applications of deicing salts applied on roads and the impact of repeated freeze-thaw cycles factored in this study. The result showed that only three of the decks with ECR had deteriorated, while all 19 decks reinforced with uncoated reinforcing bars displayed corrosion and metal loss. However, Smith and Virmani (2000) noted that the adhesive strength between epoxy and rebar can decrease over time, and ECR only provides effective protection when paired with sufficiently thick concrete cover. Moreover, Ramniceanu et al. (2008) reported that ECR samples assessed by the researchers had defects introduced during the manufacturing process, and the coatings had not been allowed to fully cure. They argued that such cases are problematic because corrosion can proceed severely.

Hot-dip galvanized reinforcing bars with a zinc coating are another effective method to provide good corrosion resistance to reinforcing steel embedded in concrete. Zinc-coated steel bars are manufactured according to ASTM A767/A767M (2019). Zinc coating improves the corrosion resistance of rebar because the zinc layer behaves as a sacrificial anode and protects underlying steel (Dallin et al., 2015). Although unprotected carbon steel embedded in concrete depassivates when the pH falls below 11.5, zinc-coated steel stays passivated until the pH is lower than 9.5, thus providing a larger threshold at which corrosion initiates (Yeomans, 2004). In addition, less defects are made during the manufacturing process of zinc-coated rebar than with ECR. However, zinc-coated rebar may be more vulnerable to the effects of chloride ions (Pianca et al., 2005).

Stainless steel cladding is another metallic protective system (Ryan et al., 2012). Even though stainless steel is effective at resisting corrosion, the cost of using stainless steel is very expensive. To obtain the advantages of stainless steel yet keep the cost down, stainless clad rebar was developed. Many studies have demonstrated its effectiveness in protecting against corrosion. Rasheeduzzafar et al. (1992) showed that stainless clad rebar performed better than ECR at high

chloride levels. However, Cross et al. (2001) showed that flaws or imperfection on the coating can reduce the service life of stainless clad rebar.

2.3.3.2 High Chromium Steel

The second group includes stainless steel and low-carbon chromium steel reinforcement. Stainless steel has a passive film that is rich in chromium and is self-healing in an oxygen-rich environment (Van Dyke et al., 2017). Therefore, the corrosion resistance of stainless steel is significantly higher than that of regular reinforcing bars. However, it is well established that the steel is susceptible to pitting corrosion (Luca Bertolini et al., 2013). Pitting corrosion can also be prevented by using austenitic and duplex stainless steel having content of at least 18 percent Cr (Chromium) and 8 percent Ni (Nickel) (Presuel-Moreno et al., 2010). Ferritic stainless steel was suggested for mild environments where the aggressive agent is carbonation only (Hartt et al., 2004; Scully et al., 2007). ASTM A240/A240M (2023), ASTM A995/A995M (2020), and ASTM A1035/A1035M (2020) are followed during the manufacture of stainless steel. Because stainless steel is relatively expensive, it is only used in highly corrosive environments.

2.3.3.3 FRP Steel

FRP is a composite material consisting of a polymer matrix imbedded with high-strength fibers, such as glass, aramid, and carbon (Groover, 2020). Glass FRP (GFRP) is typically the least expensive method (Benmokrane et al., 2002). FRPs display high strength-to-weight ratios, high stiffness-to-weight ratios, good ductility, and are lightweight. In addition, FRPs have lower lifecycle costs than conventional reinforcement steel and higher corrosion and fatigue resistance (Keller & Materials, 2001). ACI specifications for using carbon FRP and GFRP are ACI 440.5-08 (2008) and ACI 440.6-08 (2008), respectively.

In recent years, concerns have been raised regarding the use of FRP bars. Researchers such as Böer et al. (2013) have observed that FRPs are not immune to deterioration when exposed to harsh environmental conditions. Additionally, since FRPs are relatively new in civil engineering applications, engineers have limited experience with their long-term performance, and a lack of extensive data exists (Alampalli & Ettouney, 2006). Furthermore, it should be acknowledged that utilizing FRPs as a reinforcing material in concrete bridges tends to be more expensive than traditional steel reinforcement. The higher cost associated with FRPs can be a limiting factor for

their widespread adoption in bridge construction projects. When considering these factors, engineers need to carefully evaluate the specific requirements and conditions of each project when considering the use of FRPs as a corrosion-resistant reinforcement option. Cost effectiveness, long-term performance, and durability considerations should be carefully weighed against the benefits that FRPs can offer in terms of corrosion resistance and extended service life.

2.4 NONDESTRUCTIVE EVALUATION (NDE)

Concrete is a nonconductive and non-homogeneous material; hence, it is difficult to use NDE techniques to identify corrosion in concrete. However, destructive testing can also cause damage to the concrete structure. Therefore, it was decided to conduct common NDE techniques to investigate the effectiveness of these methods in detecting defects such as corrosion in concrete.

2.4.1 Infrared Thermography (IRT)

IRT is a nondestructive evaluation (NDE) method that converts thermal energy emission from the surface into a temperature map (Figure 2.3). This method is especially useful for detecting delamination, cracks, and voids in concrete (Hurlebaus et al., 2016). However, performing IRT can be difficult because it is highly dependent on ambient temperature conditions. IRT has continued to develop over the past few decades, becoming a highly useful device well known for its capability of detecting superficial flaws in concrete structures. Note that IRT technologies only provide images of surface energy emission; they do not provide any information regarding the depth of defects.

IRT devices can be categorized as either active or passive systems. While an external source of heat or excitation is introduced to the medium in an active system, passive infrared systems are contactless technologies that rely on the heat of the sun and different times of the day to provide temperature gradients for thermal inspection (Hurlebaus et al., 2016). Many researchers have utilized this technique to inspect delamination in reinforced concrete bridge decks. Ichi and Dorafshan (2022) and Omar and Nehdi (2017) used IRT in in-service bridges to detect surface and subsurface delamination.

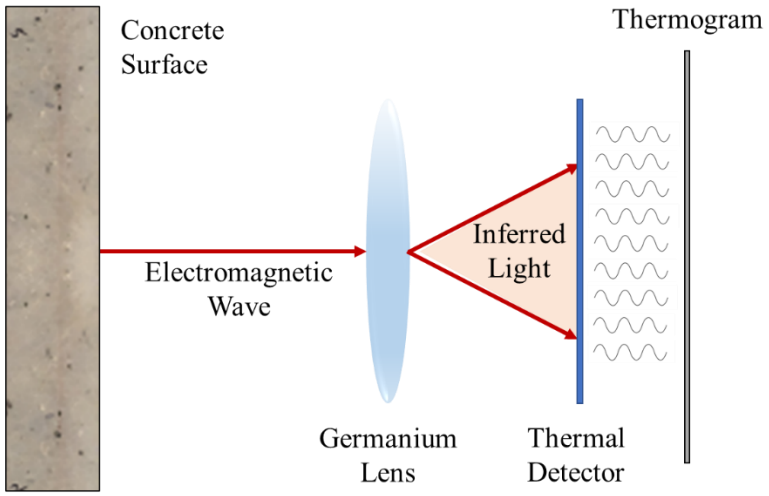

Figure 2.3. Schematic View of IRT.

Figure 2.4 shows the FLIR T640 used for IRT inspection in the field. The FLIR T640 is a thermal imaging, 5-megapixel visual camera with an accuracy calibrated within ±3.6°F or ±2 percent of reading a 77°F nominal.

Figure 2.4. FLIR T640 Infrared Camera for IRT Inspection.

2.4.2 Ground Penetrating Radar (GPR)

GPR is the most successful and well-known NDE for the investigation of bridge decks and pavements (ACI 228.2R-13, 2013). Yehia et al. (2007) reported that GPR is a rapid method for

assessing in-depth characteristics of subsurface layers and is known for its capability to detect damage, delamination, and voids.

GPR uses electromagnetic (EM) waves to evaluate the condition of the concrete and reinforcements. It emits EM waves and receives reflection at interfaces between different material with different dielectric constants and electrical conductivity. EM waves penetrate concrete and get reflected from rebars, cracks, and the bottom surface of bridge decks (Sun et al., 2018). Hong et al. (2014) used GPR on bridge decks to identify concrete deterioration and detect corroded rebars. In addition, Kofman et al. (2006) and Hoegh et al. (2015) evaluated voids in concrete using GPR, while Benedetto (2013) located cracks and delamination. However, for the comprehensive evaluation of concrete bridge decks in reference to corrosion, several studies (Gucunski et al., 2005; Sun et al., 2018; Yehia et al., 2007) suggested that multiple NDE techniques should be conducted in addition to GPR. Figure 2.5 shows a StructureScan MINI HR GPR with a 2,600 GHz antenna. The survey wheels on the device rotate and record the data as the unit is moving.

Figure 2.5. StructureScan Mini HR for GPR Inspection.

2.4.3 Ultrasonic Tomography (UST)

Ultrasonic examination is the use of acoustic waves over 18 kHz to detect defects in concrete structures (Blitz & Simpson, 1995). A group of sensors emits a stress wave, such as a P-wave, S-wave, or R-wave, into a specimen. The wave propagates until it is reflected by the change of impedance caused by defects or any discontinuities (Im & Hurlebaus, 2012). Many studies utilized ultrasonic techniques and detected internal defects in concrete structures. Krause et al. (1995) used ultrasonic techniques to identify concrete thickness. Schickert (1995) detected

deterioration such as cracks and voids. Iyer et al. (2003) detected voids in concrete specimens by evaluating the ultrasonic images.

Figure 2.6 shows ultrasonic shear wave tomography with multiple arrays of probes (MIRA A1040) used for UST inspection. MIRA is a low frequency (20–100 kHz), multifunctional phased array ultrasonic system to detect objects, interfaces, and anomalies in concrete structures. The process involves generating shear waves by exciting a piezoelectric material with a high-amplitude, short-burst pulse containing high voltage and current. The MIRA testing principle relies on the ultrasonic pulse-echo method, which utilizes transmitting and receiving transducers. One transducer emits a stress wave pulse while another receives the reflected pulse. The time elapsed between the pulse initiation and the echo reception is measured, allowing for computation of the wave speed and estimation of the reflected depth of the interface. If the wave speed C_s is known, the depth of the reflecting interface can be calculated as follows:

$$d = C_s \frac{\Delta t}{2} \tag{2.9}$$

where C_s is shear wave speed, and Δt is travel time.

By analyzing the arrival times of pulses and the positions of the transmitter-receiver pairs, the depth of the reflecting interface can be determined. Unlike conventional ultrasonic testing, the MIRA's ultrasonic probes do not require a coupling gel for wave transmission, thereby allowing easy movement from one position to another with minimal surface preparation. The MIRA antenna consists of a 4 × 12 array of point transducers that act as transmitters and receivers in a sequential manner. When each channel acts as either a transmitter or a receiver, a total of 132 transmitting and receiving pairs are utilized, as shown in Figure 2.7. MIRA can provide a three-dimensional (3D) representation of the concrete condition, enabling engineers to assess the integrity of the concrete structures (Figure 2.7).

Figure 2.6. MIRA A1040 for UST Inspection.

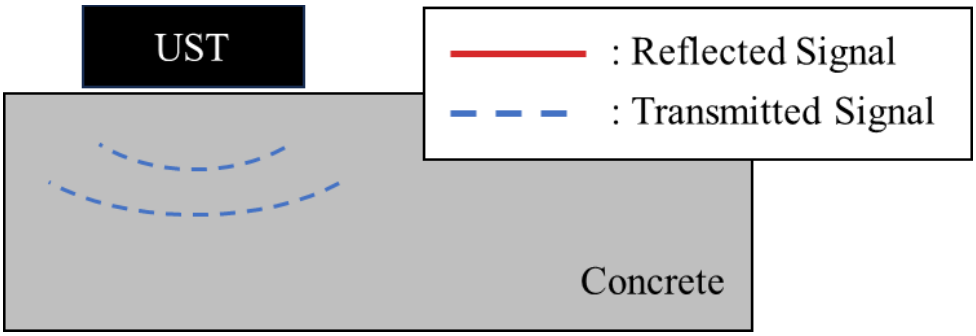

Figure 2.7. Illustration of Ultrasonic Imaging Test Using MIRA A 1040.

2.4.4 Half-Cell Potential Method

The half-cell potential (HCP) method is a quick and cost-effective in-situ testing technique utilized to detect active corrosion by assessing the electrochemical behavior of corrosion in the rebar. The HCP method is effective for monitoring rebar corrosion in concrete bridge decks and other structures as long as the temperature exceeds +2°C and the rebar is not epoxy coated. ASTM C876 (2015) provides guidelines for interpreting half-cell measurements, and Table 2-1 presents the relationship between potential measurements and the probability of corrosion presence.

Table 2-1. Interpretation of Half-Cell Measurements (ASTM C876, 2015).

HCP Measurements (Mv)	Probability of Rebar Corrosion Activity
> −200	Less than 10%
−200 to −350	Uncertain
< −350	More than 90%

Elsener et al. (2003) suggested the HCP method for multiple purposes, such as locating corroding reinforcing bars to assess their condition; identifying positions for further destructive analysis (like chloride analysis and visual inspection of rebars); evaluating the corrosion condition

of rebar after repair procedures to assess the efficiency and durability of repairs; and designing anode layouts for cathodic protection systems. HCP measurements are generally suitable for structures exposed to the atmosphere regardless of concrete cover depth and rebar size.

Pradhan and Bhattacharjee (2009) used HPC to detect chloride-induced corrosion in reinforced concrete structures. Analyzing the top surface of the beam specimens with embedded rebar subjected to 3 percent NaCl—in wet and dry cycles—Pradhan and Bhattacharjee (2009)concluded that HCP is a suitable method for determining the parameter indicating rebar corrosion initiation in chloride-contaminate concrete structures.

In several studies, HCP measurements were found to be affected by factors like temperature, humidity, fly ash content, and chloride concentration. For example, Zou et al. (2016) observed that HCP recordings were a lower voltage when an increase in temperature and chloride concentration occurred, while an increase in fly ash content led to higher voltage measurements. Yodsudjai and Pattarakittam (2017) also reported a shift in HCP measurements with an increase in chloride content.

The HCP method has certain limitations and has become less useful in detecting corrosion within epoxy-coated layers of ECR. This technique does not provide details regarding the probability of corrosion activity within the range of −200 to −350 mV. Frølund et al. (2003) reported that this method can lead to erroneous conclusions when applied in situations where the concrete is water-saturated, carbonated, and exposed to very low temperature.

2.4.5 Corrosion Rate Mapping

Corrosion rate mapping can be developed using iCOR, the device shown in Figure 2.8. The main technology used in iCOR is the connection-less electrical pulse response analysis (CEPRA). The impedance of the interface between rebar and concrete can characterize the state of corrosion in reinforcing steel. The response of noncorroding rebar decreases greatly with higher frequency, while corroding rebar does not, as shown in Figure 2.9.

Figure 2.8. Giatec iCOR Used for Corrosion Rate Mapping Inspection (Giatec, 2019).

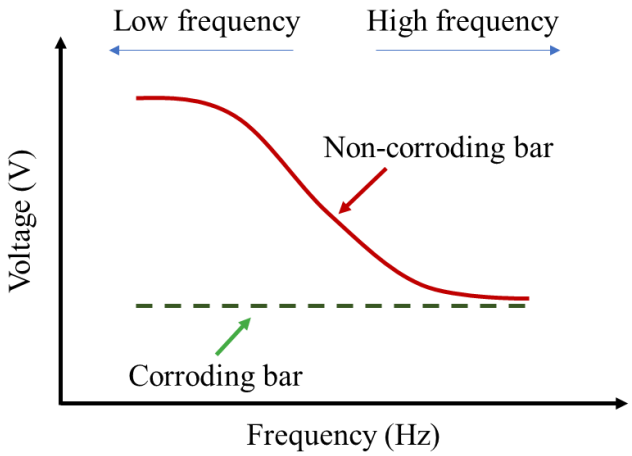

Figure 2.9. Schematic Illustration of the Voltage-Frequency Response (Giatec, 2019).

In a study conducted by Zhang (2001), the researcher utilized a Wenner array probe (Figure 2.10[a]) to polarize reinforced concrete and measure the interface impedance change with frequency. Although promising results were documented, some discrepancies were also observed that were attributed to a portion of the current flowing through the concrete, while another portion polarized the reinforcement (Zhang, 2001).

To address this issue, Fahim et al. (2019) made improvements to Wenner probe's arrangement (Figure 2.10[b]). The modified method included two outer probes parallel to the rebar direction and another two outer probes perpendicular to the rebar direction. Additionally, two inner probes were introduced for current measurement. This modified setup allowed for the measurement of concrete resistivity through the normally placed outer probes at high frequency ranges, and at lower frequency ranges, it enabled the measurement of the sum of polarization

resistivity and concrete resistivity. The modified arrangement by Fahim et al. (2019) has been implemented in iCOR.

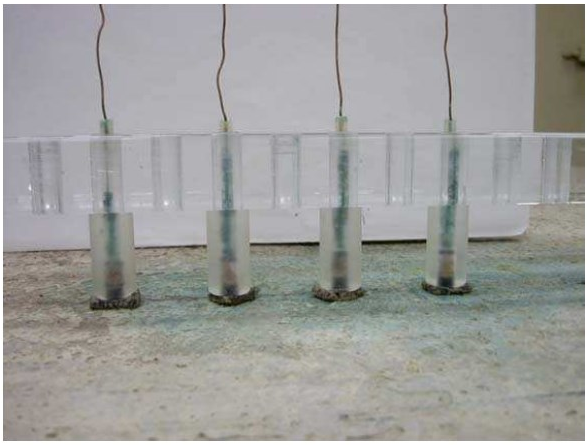

(a) Wenner Probe Array: Parallel to Rebar (Zhang, 2001)

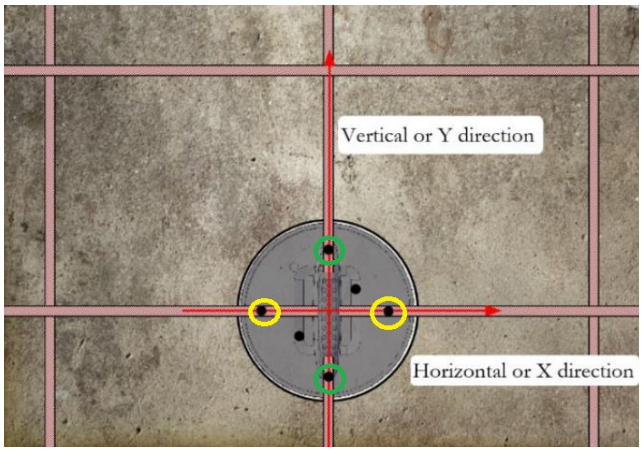

(b) Wenner Probe Array: Two Parallel to Rebar; Another Perpendicular to Rebar (Fahim et al., 2019)

Figure 2.10. Comparison of Linear and Circular Wenner Probe Array.

The Connectionless Electrical Pulse Response Analysis (CEPRA) system used in corrosion rate mapping is illustrated in Figure 2.11. R_{c1} refers to the probe's contact resistance; R_{c2} represents the resistivity in one current path that does not polarize the rebar; R_{c3} denotes the resistivity in another current flow path that polarizes the rebar or charges the double-layer capacitance; and R_{c4} is the charge transfer resistance of rebar. Additionally, C_{dl} represents the double-layer capacitance.

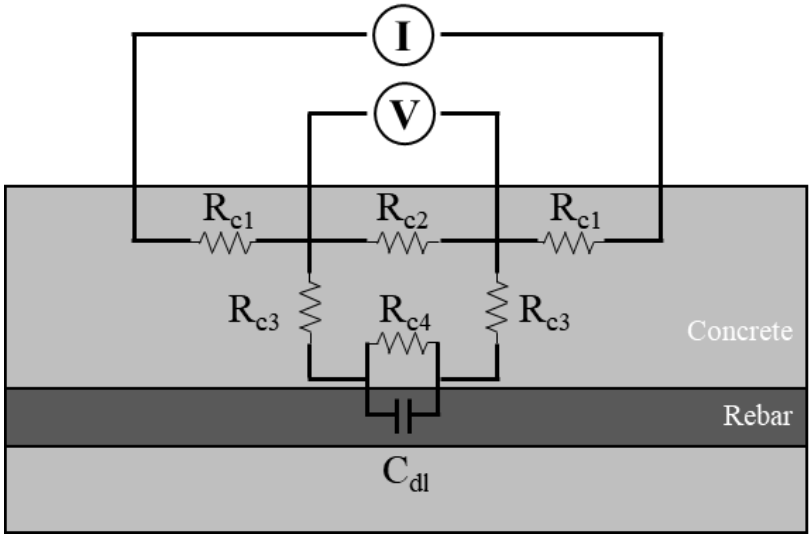

Figure 2.11. Schematic Equivalent Circuit of CEPRA Technique.

The corrosion current density in iCOR is similar to the liner polarization method:

$$R_p = A_p \, R_{c4} \tag{2.10}$$

$$i_{\text{corr}} = \frac{K}{R_p} \tag{2.11}$$

where A_p is the polarized area of rebar, the constant K is roughly 0.026, which represents the anodic and cathodic Tafel slopes, which are the slope of the polarization curve, and R_p is the polarization resistance. The electrical resistivity of concrete is:

$$\rho = 2\pi a \, R \tag{2.12}$$

where a is a constant parameter depending on the geometry of probe, and R is the equivalent resistance of concrete calculated from R_{c2}, R_{c3}, and R_{c4}.

Fahim et al. (2019) performed multiple laboratory tests to assess the effectiveness of the iCOR method. One of the tests involved an accelerated corrosion test in which the average corrosion rates measured by the CEPRA monitor were compared to gravimetric (mass loss) measurements. It was observed that although the CEPRA monitor could overestimate the passive corrosion rate, it provided a reliable range of corrosion rate for actively corroding reinforcements. These rates varied from 0.5 to 2 times the actual average corrosion rate.

2.5 SYNTHESIS OF RESEARCH

Studying the literature indicates that reinforced concrete bridges in highly corrosive environments are susceptible to severe corrosion that can lead to costly repairs and a reduction in service life. To address the issue, early detection of corrosion is critical, but current inspection procedures rely on qualitative visual assessments. To enhance field evaluations, more objective field testing—such as IRT, GPR, UST, and corrosion rate mapping—is needed. This study provides a detailed explanation of the objective testing procedures employed, and the obtained results are analyzed and studied.

TxDOT has implemented various corrosion mitigation methods in concrete bridges, such as ECR, FRP, surface treatment, calcium nitrite, and HPC. To establish optimal guidelines for corrosion mitigation techniques in both new and existing reinforced concrete bridges, a comparative analysis of the existing corrosion mitigation methods utilized in different regions of

Texas is essential. In addition, since multiple mitigation methods can be applied to bridges, understanding the combined effect of these methods is crucial. This research offers a systematic approach to selecting the most suitable corrosion mitigation methods for various regions in Texas.

3 FIELD EVALUATION TO INVESTIGATE EFFECTIVENESS OF CORROSION MITIGATION

Field inspections are essential to assess the current condition of concrete bridge structures because they provide insights into the effectiveness of corrosion prevention and mitigation methods used in reinforced concrete decks. In the current study, 60 concrete decks were inspected across the state, and cores obtained from these structures were examined in a laboratory. This chapter—structured in four sections—outlines the procedure for selecting concrete bridges to evaluate to effectively represent different corrosion risk regions. It also elaborates on the corrosion prevention and mitigation methods utilized in the selected concrete bridges and provides an overview of the specific methods implemented to prevent corrosion and enhance the durability of the bridge decks. The subsequent section explains the overall procedure and methods employed during the field inspection. Finally, it presents the results obtained from the field inspection and highlights the findings, observations, and evaluations made during the inspection process, thereby shedding light on the current condition of the bridges and the performance of the corrosion prevention and mitigation methods.

3.1 SELECTION OF BRIDGES

The initial consideration for this study involved the assessment of reinforced concrete bridges in Texas based on factors such as the year of construction, condition ratings of the deck and superstructure, presence of overlays, and the corrosion mitigation methods employed on the bridge decks. The main objective was to evaluate the current condition and effectiveness of corrosion mitigation methods for bridges that were in service over 20 years. To facilitate comparisons across different bridge ages, bridges below 20 years were also included in the field inspection (Figure 3.1). Concrete decks with overlays were excluded from the selection due to the asphalt overlay because it is not effective in preventing or mitigating corrosion. Additionally, care was taken to select structures located in different corrosive environments. Figure 3.2 and Figure 3.3 show the locations in Texas of the bridge structures inspected in this research.

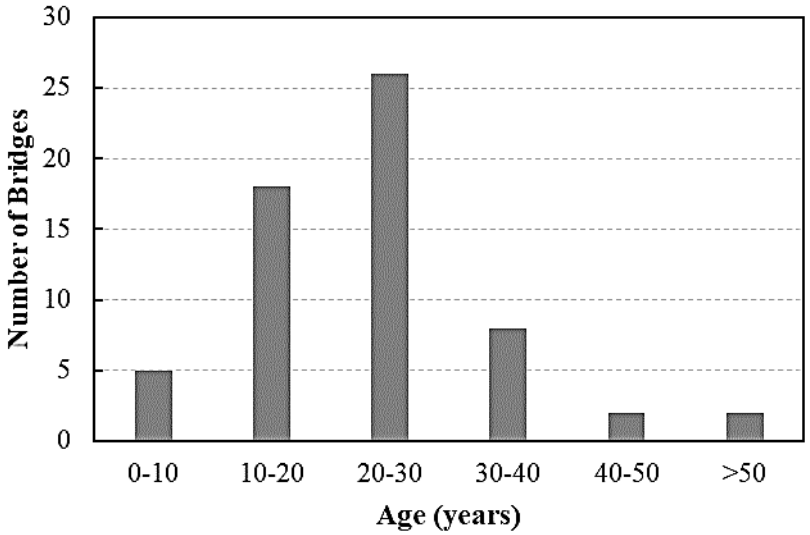

Figure 3.1. Age Distribution of RC Bridges.

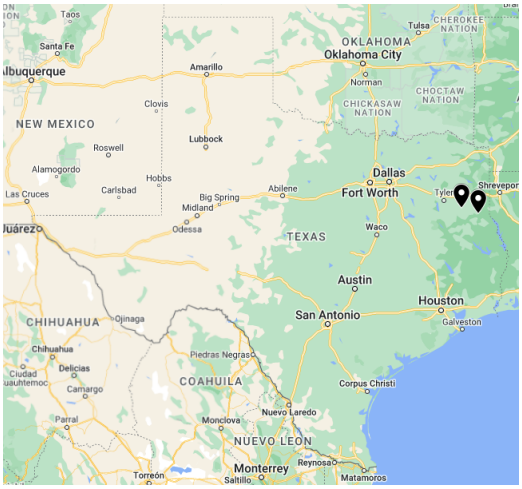

(a) Region 1 and Region 2

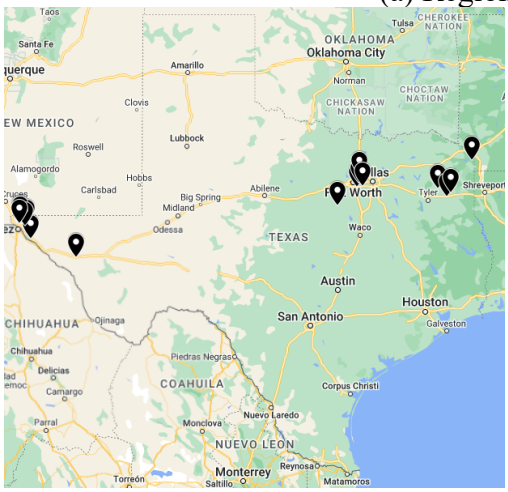

(b) Region 3

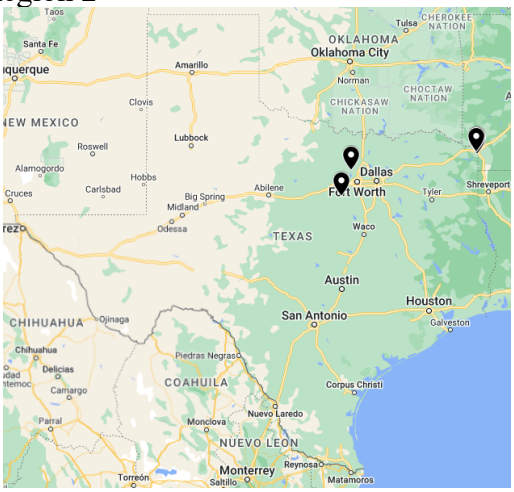

(c) Region 4

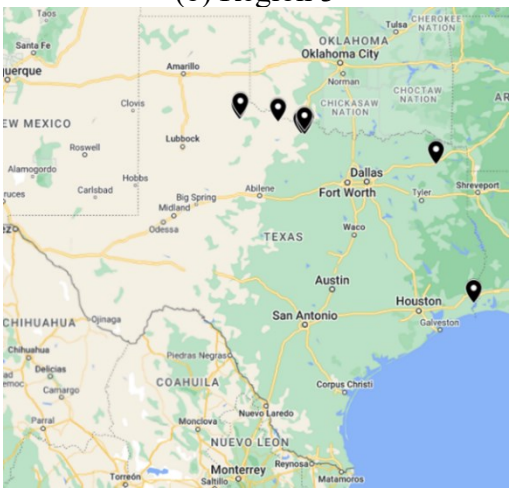

(d) Region 5

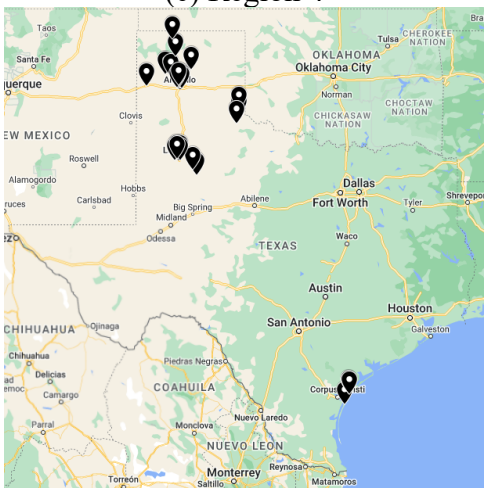

(e) Region 6

Figure 3.2. Location of Bridges in Regions.

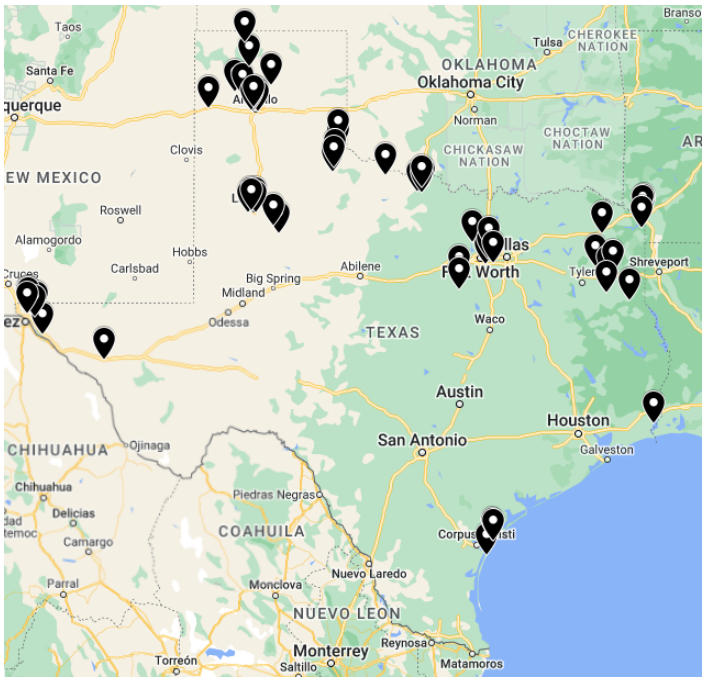

Figure 3.3. Location of All Reinforced Concrete Bridges.

The selected concrete decks were distributed across five out of the six corrosive risk regions containing different levels of corrosion risk. This selection aimed to consider diverse environmental factors such as temperature, humidity, areas with high airborne chloride concentration, use of deicing salt, and variations between rural and urban conditions. Because Region 1 has minimal to no threat of corrosion, concrete bridges located in this region were excluded from the current study. By including concrete decks from Region 2 to Region 6, the study aimed to conduct a comprehensive inspection of the performance of all prevention and mitigation methods in different risk environments.

Region 5 and Region 6 were found to have specific environmental conditions characterized by low average annual temperatures, a high number of freeze days, frequent use of deicing salts, and more airborne sulfate concentration. The Texas Panhandle (Amarillo and Lubbock), which is part of Region 6, receives the state's greatest snowfall and has the longest length of time in which the temperature is at or below freezing (Jackson et al., 2017). These environments are highly corrosive due to regular use of deicing salts. In addition, marine environments such as Corpus Christi, which also falls in Region 6, have a high level of airborne sea salts. Therefore, the decision was made to inspect more concrete decks from these regions, so a total of 26 concrete bridges were inspected in Region 6, and 11 bridges were inspected in Region 5.

On the other hand, Region 3 and Region 4 experience moderate to high average annual temperatures accompanied by high RH levels. These regions also have a lower number of freeze days and use less deicing salts than Region 5 and Region 6. Consequently, it was decided to inspect 17 concrete decks in Region 3 and 5 bridges in Region 4. In the low corrosive environment (Region 2), it was decided to inspect only two concrete decks. Figure 3.3 shows the location of concrete decks selected in this study to evaluate the performance of corrosion prevention and mitigation methods in each corrosive region. Figure 3.4 shows region distribution of selected bridges based on corrosive risk environments presented in Volume 1, Chapter 3 of this report.

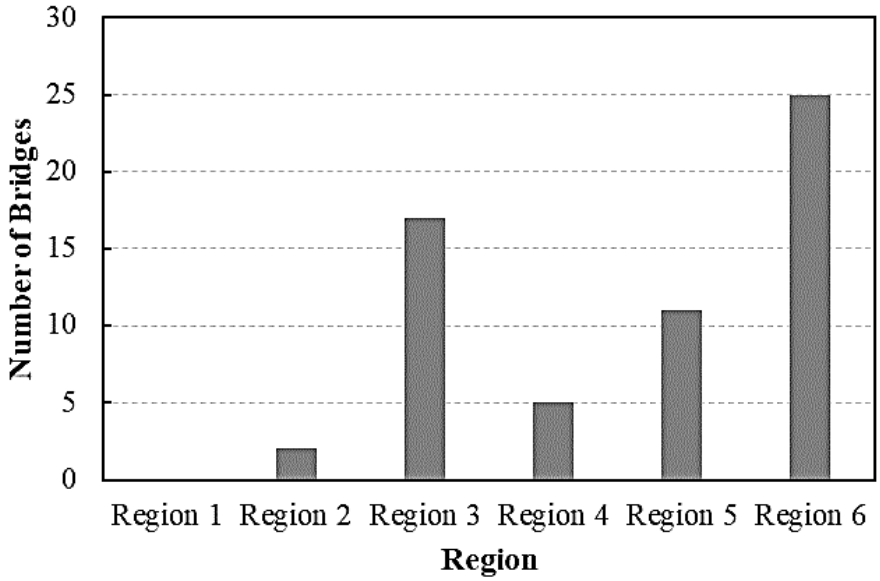

Figure 3.4. Region Distribution of RC Bridges.

3.2 SELECTED MITIGATION METHODS

After selecting the concrete bridges based on environmental conditions, corrosion prevention and mitigation methods implemented in structures were extracted from as-built documentations. Table 3-1 and Table 3-2 show the recommended corrosion mitigation methods used in concrete decks by TxDOT. Table 3-1 provides concrete durability recommendations for different districts in Texas and outlines the recommended approaches for enhancing the durability of concrete elements in reinforced concrete bridges. These recommendations are aimed at improving the resistance of concrete to corrosion-related deterioration. As shown in Table 3-1, TxDOT suggests using HPC for the bridge rail, employing HPC for the bridge deck, utilizing corrosion-inhibiting admixture for prestressed concrete girders, and employing a combination of HPC, corrosion-inhibiting admixture, and surface protective coating for elements in the substructure.

Table 3-2 presents the recommended options for corrosion-resistant reinforcement. It highlights the different reinforcement materials and techniques suggested for mitigating corrosion in concrete structures. These options offer alternatives to conventional steel reinforcement and are intended to improve the durability and longevity of the reinforced concrete elements. For the bridge rail, TxDOT suggests using continuously galvanized reinforcing steel (CGR), ECR, and hot-dipped galvanized reinforcing steel (HDG). On the bridge deck, TxDOT recommends employing ECR, CGR, GFRP, and HDG. In the substructure, the recommended options for reinforcing steel are ECR, HDG, and low-carbon, chromium-reinforcing steel (LCCR).

In this study, the decision was made to only investigate the durability and performance of corrosion prevention and mitigation methods implemented in concrete bridge decks. These methods include HPC, HPC with microfibers (HPCF), corrosion-inhibiting admixtures such as CNIs, and concrete surface protective coatings such as LO and SI. HPC is a dense concrete with supplementary cementing materials (SCMs) such as fly ash, slag, and silica fume at varying minimum replacement percentages. SCMs significantly lower the permeability of HPC, making it an alternative to ordinary concrete. Lower permeability concrete reduces the ability of chlorides to attack the reinforcing steel and cause corrosion. CNI is a chemical compound that limits the access of water and oxygen and delays the onset of corrosion by blocking the anodic reaction in concrete to increase the resistance of the passive film on the surface of the steel.

Concrete surface protective treatments are applied to the surface of the concrete deck or crack within the concrete to slow the ingress of water and chloride ions. TxDOT uses LO and SI on the surface of bridge deck. SI is a type of sealer that penetrates the pores of the concrete substrate (Giannini et al., 2015) and strengthens a molecular attraction between water and concrete, thereby inhibiting water penetration (de Vries & Polder, 1997). The performance of penetrating sealers depends on the depth of penetration. On the other hand, LO is a pore-blocking surface treatment. Pore-blocking surface treatments block capillary pores in the concrete surface to reduce the porosity of the concrete surface (Pan et al., 2017a). ECR are often used in Texas as alternative reinforcing bars in highly corrosive environments such as Texas Panhandle districts (Amarillo and Lubbock) and northeast Texas districts (Atlanta and Tyler).

Table 3-1. Concrete Durability Recommendations for Structures (Farris, 2018).

Districts	Bridge Rail	Bridge Deck		P/S Beams	Bridge Substructure		
	HPC	HPC	Poly Fibers	Corrosion-Inhibiting Admixture	HPC	Corrosion-Inhibiting Admixture	Surface Protective Coatings' Substructure
ABL	Y	Y	Y	Y	Y	Y	Y
AMA	Y	Y	Y	Y	Y	Y	Y
ATL	Y	Y	N	Y	Y	Y	Y
AUS	N	N	N	N	N	N	N
BMT	N	N	N	N	N	N	N
BRY	N	N	N	N	N	N	N
BWD	Y	Y	Y	Y	Y	Y	Y
CHS	Y	Y	Y	Y	Y	Y	Y
CRP	N	N	N	N	N	N	N
DAL	Y	Y	N	Y	Y	Y	Y
ELP	Y	Y	Y	Y	Y	Y	Y
FTW	Y	Y	N	Y	Y	Y	Y
HOU	N	N	N	N	N	N	N
LBB	Y	Y	Y	Y	Y	Y	Y
LFK	N	N	N	N	N	N	N
LRD	N	N	N	N	N	N	N
ODA	Y	Y	Y	Y	N	Y	Y
PAR	Y	Y	N	Y	Y	Y	Y
PHR	N	N	N	N	N	N	N
SAT	N	N	N	N	N	N	N
SJT	N	N	Y	N	N	Y	Y
TYL	N	N	N	N	Y	Y	Y
WAC	N	N	N	N	Y	N	Y
WFS	Y	Y	Y	Y	Y	Y	Y
YKM	N	N	N	N	N	N	N

Note: Y indicates districtwide application of the specific recommendation.

Table 3-2. Recommended Options for Corrosion-Resistant Reinforcement for Structures (Farris, 2018).

Districts	Bridge Rail	Bridge Deck	Substructure Reinforcing	
	CGR, ECR, HDG	ECR, CGR, GFRP, HDG	ECR	HDG, LCCR
ABL	Y	Y	Y	Y
AMA	Y	Y	Y	Y
ATL	Y	Y	N	N
AUS	N	N	N	N
BMT	N	N	N	N
BRY	N	N	N	N
BWD	Y	Y	Y	Y
CHS	Y	Y	Y	Y
CRP	N	N	N	N
DAL	Y	Y	Y	Y
ELP	Y	Y	Y	Y
FTW	Y	Y	Y	Y
HOU	N	N	N	N
LBB	Y	Y	Y	Y
LFK	N	N	N	N
LRD	N	N	N	N
ODA	Y	Y	Y	Y
PAR	Y	Y	N	N
PHR	N	N	N	N
SAT	N	N	N	N
SJT	Y	Y	Y	Y
TYL	N	N	N	N
WAC	Y	Y	Y	Y
WFS	Y	Y	Y	Y
YKM	N	N	N	N

Note: Y indicates districtwide application of the specific recommendation.

Corrosion protection systems investigated in this study can be divided into three categories. The first category includes concrete admixtures added in mixed design to improve water permeability of the concrete, including concrete admixtures and corrosion inhibitors, as well as HPC. The second category contains the ones applied to the concrete surface, known as surface treatments, including LO and SI. The third includes alternative reinforcement such as ECR.

In general, multiple corrosion mitigation methods are applied in concrete decks to increase the durability of the structure against corrosion deterioration. Therefore, a combination of the mentioned mitigation methods implemented on bridge structures was considered in the analysis rather than a single method. Table 3-3 shows the mitigation methods utilized in TxDOT concrete

decks, with the associated corrosion risk region specified. It is important to note that microfibers are added to HPC to reduce the plastic shrinkage cracking of concrete rather than to mitigate corrosion. Although HPCF could be considered as the same mitigation method in terms of corrosion resistance, the term HPCF was used to differentiate between HPC and HPC with microfibers and to evaluate the effect of reduced cracking caused by microfibers.

Note that both SI and LO are evaluated as concrete surface treatments. The results of these surface treatments were examined to assess their impact on concrete in relation to other corrosion mitigation methods. Furthermore, an analysis and comparison between LO and SI was also conducted through chloride concentration measurements to provide insights into their effectiveness in mitigating chloride ingress.

Table 3-3. Combination of Mitigation Methods Used in Each Bridge.

Bridge ID	Corrosion Risk Region	Mitigation Methods
AMA–RC–01	6	LO, ECR
AMA–RC–02	6	HPC, ECR
AMA–RC–03	6	HPC, CNI, LO, ECR
AMA–RC–04	6	CNI, LO, ECR
AMA–RC–05	6	CNI, SI, ECR
AMA–RC–06	6	HPC, CNI, ECR
AMA–RC–07	6	HPC, CNI, ECR
AMA–RC–08	6	HPC, CNI, LO, ECR
AMA–RC–09	6	CNI, SI, ECR
AMA–RC–10	6	HPC, CNI, LO, ECR
AMA–RC–11	6	ECR
AMA–RC–12	6	ECR
ATL–RC–01	4	None
ATL–RC–02	4	None
ATL–RC–03	4	ECR
ATL–RC–04	3	HPC, ECR
ATL–RC–05	2	ECR
ATL–RC–06	5	HPC, ECR
ATL–RC–07	3	ECR
BMT–RC–01	5	HPC
CHS–RC–01	6	ECR
CHS–RC–02	6	CNI, SI, ECR
CHS–RC–03	6	HPC, ECR
CHS–RC–04	6	HPC, ECR
CHS–RC–05	5	ECR
CHS–RC–06	5	ECR
CRP–RC–01	6	None
CRP–RC–02	6	None

Bridge ID	Corrosion Risk Region	Mitigation Methods
CRP–RC–03	6	None
ELP–RC–01	3	HPC, LO
ELP–RC–02	3	HPC, LO
ELP–RC–03	3	HPC, ECR
ELP–RC–04	3	HPC, SI
ELP–RC–05	3	HPC, SI
ELP–RC–06	3	None
ELP–RC–07	3	LO, ECR
ELP–RC–08	3	LO, ECR
FTW–RC–01	4	LO, ECR
FTW–RC–02	3	SI, ECR
FTW–RC–03	3	LO, ECR
FTW–RC–04	3	LO, ECR
FTW–RC–05	3	LO, ECR
FTW–RC–06	3	SI, ECR
FTW–RC–07	4	SI, ECR
LBB–RC–01	6	LO, ECR
LBB–RC–02	6	HPC, LO, ECR
LBB–RC–03	6	LO, ECR
LBB–RC–04	6	LO, ECR
LBB–RC–05	6	HPCF, ECR
LBB–RC–06	6	HPCF, ECR
LBB–RC–07	6	HPCF, LO, ECR
TYL–RC–01	3	ECR
TYL–RC–02	3	None
TYL–RC–03	2	LO, ECR
WFS–RC–01	5	HPC, CNI, LO
WFS–RC–02	5	HPC, CNI, LO
WFS–RC–03	5	ECR
WFS–RC–04	5	HPC, ECR
WFS–RC–05	5	ECR
WFS–RC–06	5	ECR
WFS–RC–07	5	None

3.3 FIELD EVALUATION

A field inspection was conducted to evaluate the effectiveness of corrosion mitigation methods used in reinforced concrete decks; the inspection involved both a visual inspection and NDT to assess the condition of the concrete. The NDT methods included in this study were IRT, GPR, UST, and iCOR corrosion rate measurement. Following the completion of NDEs, core specimens were also extracted from bridge decks for further analysis in the laboratory to gain a

deeper understanding of the structure conditions. The locations of coring were selected inside of grids where NDE was performed.

A visual inspection was conducted on the bridge deck, superstructure, and substructure to document any damage and identify areas requiring more detailed assessment. Infrared pictures were taken to detect surface defects in specific areas showing signs of deterioration. In limited areas of the deck, GPR was employed to locate reinforcing steel inside concrete, while UST was utilized to detect voids and delamination. Finally, corrosion rate mapping was developed to measure the corrosion rate of the reinforcing rebars.

3.3.1 Visual Inspection

Surface cracking and concrete spalling were documented during the visual inspection of concrete structures, and any exposed rebars were carefully noted, as detailed in the appendix. Figure 3.5 illustrates a few examples of damages detected on concrete bridge structures. Note that the inspection of bridge decks was always limited to a single lane and the shoulder due to traffic control requirements. The selected lanes may not always correspond to the areas with the most severe damage on the deck because the lane selection was determined beforehand in coordination with traffic control.

(a) Cracks at Deck Joint

(b) Exposed Rebar on Deck due to Delamination

(c) Exposed Rebar on Concrete Rail

(d) Spalling at a Girder End

Figure 3.5. Types of Deterioration.

Deck inspection involved identifying and documenting the location, direction (transverse or longitudinal), pattern, and size of surface cracking. The inspection also aimed to document areas with concrete spalling and exposed rebars. Additionally, conditions affecting the bridge drainage, such as standing water or debris accumulation on the shoulders, were recorded and reported in the appendix. Assessment of surface cracking included documentation of transverse and longitudinal cracks attributed to precast panel joints, longitudinal cracks that were developed to girders, and cracks in continuous deck regions (poor boy joint).

Based on findings of the surface cracking assessment, the locations speculated to have the potential for the highest chloride ingress were identified for the purpose of NDT and coring. On most concrete decks, one grid was placed on the drive lane and another one on the shoulder lane. The location of grids was selected according to cracking patterns—transverse cracks at panel joints and longitudinal cracks at girder locations. In cases where certain areas of the deck exhibited more severe cracking in terms of quantity or size, grids were positioned in those areas. The grids had

dimensions of 2 ft × 4 ft and were marked by 2 in^2 (Figure 3.6). Crack widths greater than 0.005 in. were marked and recorded, while cracks narrower than 0.005 in. were considered hairline cracks, and only the locations were documented.

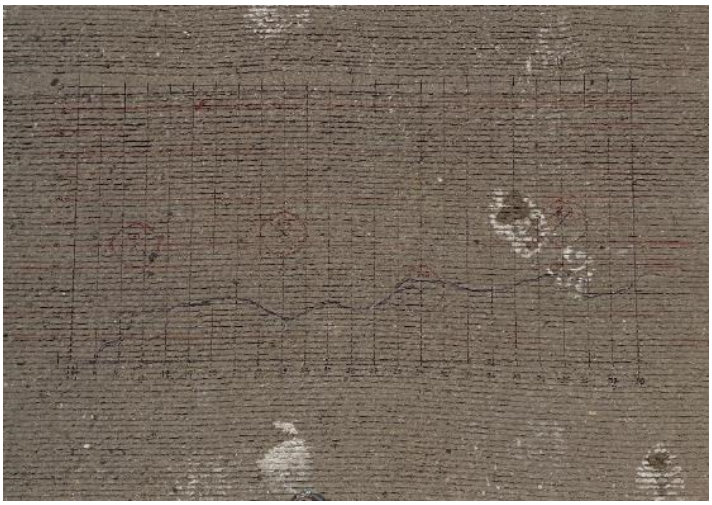

Figure 3.6. Grid on Concrete Deck.

While inspecting superstructure and substructure, researchers identified some differences in the types of damage that can occur. Flexural and shear cracks were commonly found to develop on bent caps. However, the bottom of the deck, with precast concrete panels (PCP), exhibited fewer cracks but often displayed efflorescence caused by absorbed water. The end sections of girders frequently exhibited exposed rebars due to concrete spalling.

3.3.2 Infrared Thermography

IRT was used for detecting any surface damage on concrete structures. During and after the visual inspection, infrared pictures were taken at the grids and at places where severe deteriorations were visible. Figure 3.7 shows longitudinal surface cracking that was visible in thermal imaging. The thermal imaging results are documented in the appendix.

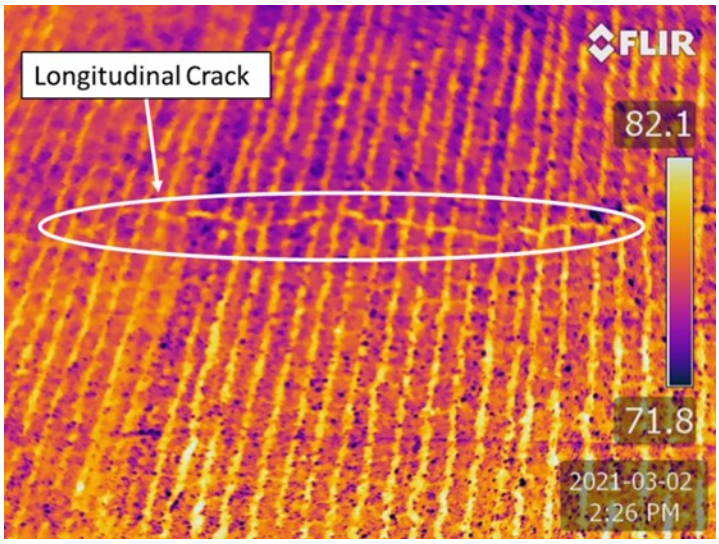

Figure 3.7. Infrared Picture of a Deck Showing a Transverse Crack.

3.3.3 Ground Penetrating Radar

GPR is a common method for detecting the location of rebars in concrete bridge decks and identifying any damages in concrete. GPR operates by transmitting EM waves into the probed material and receiving the reflected pulses as they encounter discontinuities—like an interface between materials with different dielectrics. A GSSI StructureScan MINI HR was used in the field inspection.

GPR was conducted for all NDE grids identified during the visual inspection. 3-D scanning was conducted to locate the rebars embedded in concrete. The depth of the scan was set to 12 in. to capture the entire deck thickness, which is 8 in. thick in general. An example of GPR scanning is shown in Figure 3.8. Preliminary evaluation of GPR results was used to locate longitudinal and transverse rebars and their intersects for the purpose of developing the corrosion rate mapping and extracting cores.

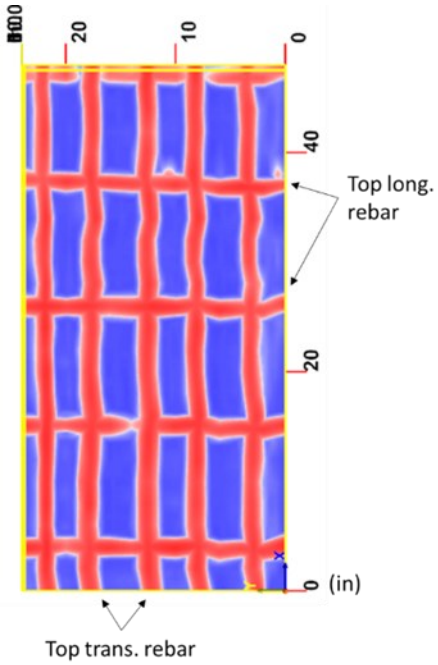

Figure 3.8. Results of a GPR Scanning.

3.3.4 Ultrasonic Tomography

UST was conducted with A1040 MIRA. The principle of UST is that the equipment emits stress waves (P-wave, S-wave, or R-wave) from its transducers into the specimen and captures any reflected wave caused by changes in impedance. Impedance change occurs where discontinuities such as a change of material and voids exist. The defect in concrete can be measured by recording the time of reflection and frequency and amplitude of sound waves.

Figure 3.9 shows an example of the UST results conducted on concrete decks. As shown in this figure, large reflection occurs at the rebar locations because of impedance differences. Through further analysis of the results, smaller reflections were identified, and it was possible to identify some deterioration such as cracks and voids in concrete.

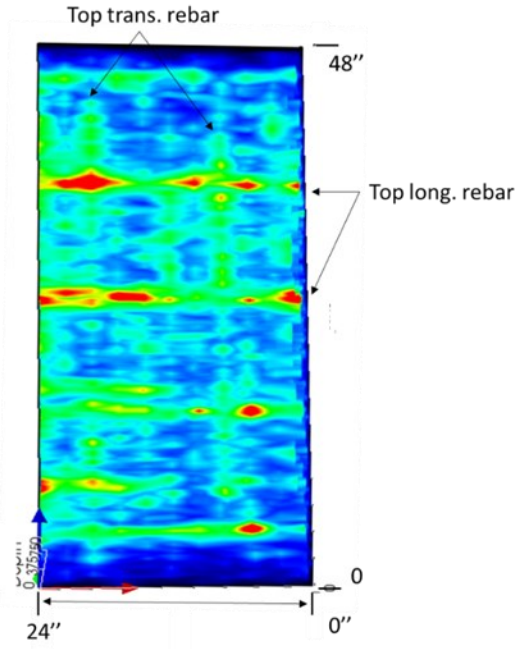

Figure 3.9. Results of UST.

3.3.5 Corrosion Rate Mapping

iCOR was used to measure the instantaneous corrosion rate of the rebar and in-situ resistivity. The device measured the corrosion rate without making a direct connection with the rebar, which made this process an advantage during scanning of the concrete decks. The iCOR readings from intersections of rebars identified from the GPR scanning were documented for further analysis and to develop corrosion rate mapping and evaluate the in-situ resistivity of concrete. Figure 3.10 shows a typical corrosion rate mapping developed for AMA–RC–10.

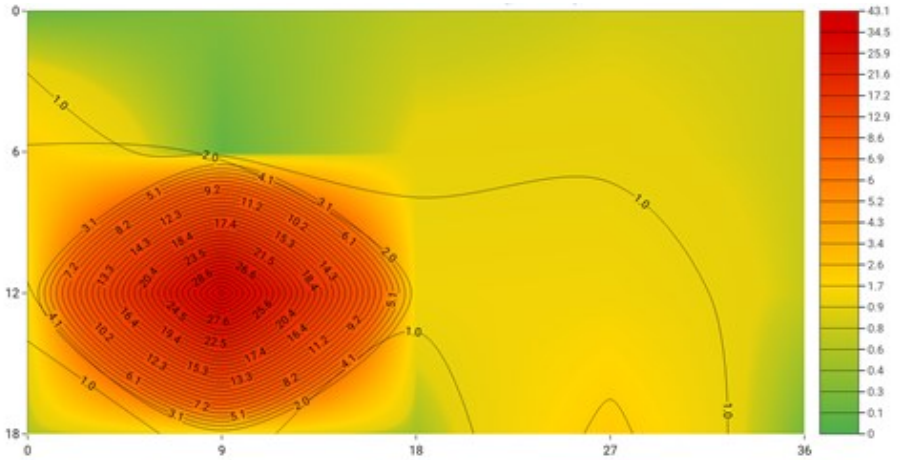

Figure 3.10. Result of AMA–RC–10 Bridge Corrosion Rate Mapping, Corrosion Current Density (µA/cm^2).

A description of the process to estimate the service life of reinforced concrete structures and identify the severity of corrosion based on in-situ measured current density is summarized in Table 3-4 and Table 3-5 (John P Broomfield, 2023; Clear, 1989; Giatec, 2019). In Table 3-5, relationship between current density and corrosion rate in mills penetration per year (mpy) is described as well. When corrosion's current density is higher than 0.2 μA/cm^2, the service life of structures must be expected to be less than 15 years. If the corrosion current density is recorded as 1 μA/cm^2 or greater, the service life of the concrete structure must be considered to be less than 10 years. The surface resistivity measurement can indicate an area with low quality, rapid chloride ingress, and high corrosion risk.

Table 3-4. Corrosion Rates and Remaining Service Life (John P Broomfield, 2023; Giatec, 2019).

Corrosion Current Density (μA/cm^2)	Remaining Service Life
$i_{corr} < 0.2$	No corrosion damage
$0.2 < i_{corr} < 1.0$	Corrosion damage in the range of 10 to 15 years
$1.0 < i_{corr} < 10$	Corrosion damage in the range of 2 to 10 years
$i_{corr} > 10$	Corrosion damage less than 2 years

Table 3-5. Corrosion Rate Mapping Explanation (John P Broomfield, 2023; Giatec, 2019).

Color Code	Current Density	Corrosion Rate	Classification
	μA/cm^2	mpy	
Green	< 0.1	< 0.05	Passive/Low
Yellow	0.1–0.5	0.05–0.25	Moderate
Orange	0.5–1	0.25–0.50	High
Red	> 1	> 0.50	Severe

3.3.6 Coring

Following NDEs, concrete cores were obtained from the designated locations inside the grids. The cores extracted from the concrete deck were placed in bags and sealed for further analysis. These core specimens were later used to develop chloride profiles, measure carbonation depth, and obtain the general quality of concrete. Cores with embedded rebar were also examined to determine the bond between the epoxy coat and steel substrate and to estimate the corrosion rate of the steel reinforcement.

The selection of coring locations within a grid was based on the presence of cracks and rebars. At each grid, four cores were extracted from the concrete decks—two containing rebar and two without rebar. Whenever possible, one core was taken at a cracked location and another from

an uncracked area. Most of the cores had a diameter of 4 in., while the target length ranged from 5 to 6 in, depending on the deck thickness.

If it was feasible, the cores were drilled deep enough to extract a portion of the precast panel. Figure 3.11 provides an example of a core sample with rebar, and Figure 3.12 illustrates the distribution of core locations within a grid. Following the extraction of core samples, the holes were patched using Quikrete Fastset DOT Mix Cement and gravel, following the guidelines outlined in the *Concrete Repair Manual* (TxDOT, 2021).

(a) Top View (b) Side View

Figure 3.11. Pictures of an Extracted Core.

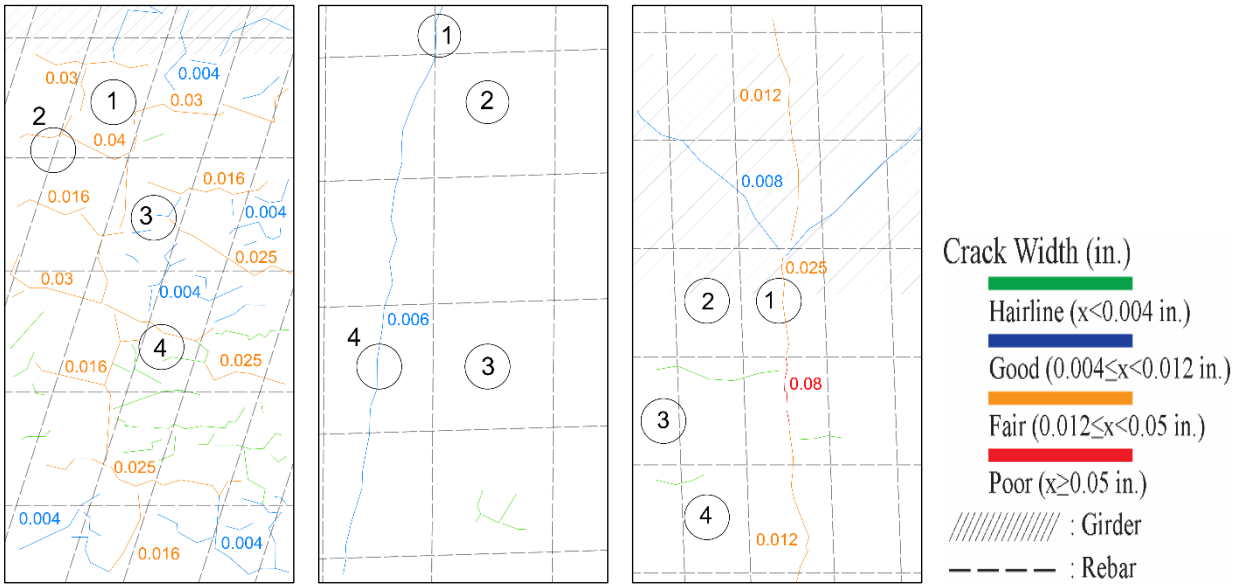

(a) AMA–RC–01, G1 (b) ATL–RC–01, G1 (c) FTW–RC–01, G1

Figure 3.12. Locations of Obtained Cores, Cracks, Rebar, and Girder in Grids.

3.3.7 Crack Mapping

Concrete acts as a barrier against corrosive agents and protects reinforcement steel from making direct contact with corrosive elements, such as moisture and chloride ions. However, when a crack forms, it can have a significant impact on the corrosion of reinforcement steel. Surface cracking allows a higher volume of moisture and other corrosive agents in concrete and provides a pathway for the corrosive elements to reach the steel reinforcement. In addition, concrete bridge decks often have protective coatings or sealants, to provide an additional barrier. However, cracks can diminish the integrity of the protective coatings and the effectiveness of the protections and increase the rate of corrosion.

Association of State Highway and Transportation Officials (AASHTO (2011)) recommends that a concrete specimen with surface cracking be considered in poor condition if the crack width exceeds 0.05 in. The standard also suggests a concrete specimen with surface cracking be considered in fair condition if the crack width ranges between 0.05 in. and 0.012 in. The concrete must be designated in good condition if the crack width is narrower than 0.012 in. Table 3-6 provides the condition of concrete with surface cracking for different crack widths. Note that cracks wider than 0.005 in. were marked and measured during the field evaluation, while cracks narrower than 0.005 in. were considered hairline cracks, and their locations were documented, as shown in Figure 3.12.

Crack density is a measurement introduced by Darwin et al. (2007) that was utilized—in addition to crack width—to ensure consistent and unbiased assessments across different inspectors. According to Darwin et al. (2007), crack density is defined as the length of cracks in inches per square inches of the bridge deck. However, in this study, crack density was determined based on measurements taken from the grids, and the crack density represents the length of cracks within the grids in inches per square inches of the grids. It should be noted that hairline cracks were neglected in the analysis.

Table 3-6. Surface Condition (AASHTO, 2011).

Crack Width (in.)	Crack Condition
Severe/Impacted	Severe
> 0.05	Poor
0.012–0.05	Fair
< 0.012	Good
No Crack/Minor	Perfect

3.4 RESULTS AND DISCUSSION

This section presents the results documented from the field inspection for reinforced concrete bridges. For each bridge, a detailed summary, including NDE results, is provided in the appendix. An overview of common findings and details of unique damages found in some bridges are discussed in this section.

3.4.1 Visual Inspection

Cracks were visible on all concrete decks. The types of visible cracks were transverse cracks, longitudinal cracks, diagonal cracks, and map cracks. In general, the most prominent transverse cracks (excluding the intentionally formed cracks at poor boy joints) were located at the panel joints. Longitudinal cracks were typically present along the girder lines. Figure 3.13(a) shows transverse and longitudinal cracks created due to panel joints. Diagonal cracks were commonly found at the joints of skewed bridges. Map cracks were found on many bridge decks. Map cracks are fine in width, shallow in depth, and are often attributed to improper curing rather than structure movement and loading (Safiuddin et al., 2018).

Apart from cracking, the extent of damage to the decks was generally minimal. On some bridges, minor spalling was observed along the cracks at poor boy joints or at the edges of sealed expansion joints. Occasionally, there were small areas of spalling on some bridges. Exposed steel reinforcement was found on one bridge deck (LBB–RC–04). This specific region, measuring approximately 8 in^2 in the main lane, is depicted in Figure 3.13(b) and indicated a lack of sufficient overlay cover.

Visible damage on the underside of the decks was generally limited to specific areas such as deck joints, overhangs, and thickened end slabs. Staining in the panel joints was observed in several bridges. Continuous decks exhibited varying degrees of cracking, staining, and efflorescence. In the thickened end regions near abutments, some bridges displayed longitudinal hairline cracks, although not all thickened end regions were closely examined to determine the presence of these cracks due to accessibility constraints. In the full-depth, cast-in-place overhangs, transverse cracks spaced at regular intervals typically aligning with the panel joints were observed on most bridges. However, the visibility of transverse cracks varied in some bridges.

Abutment damage was documented in many bridges and typically consisted of horizontal and vertical cracks on the backwalls on the outside of the girders. These cracks were measurable

widths for most bridges. The horizontal cracks often extended between the girders, as shown in Figure 3.13(c). Damage was observed in the backwall, where girder expansion led to the ends bearing against the backwall, as shown in Figure 3.13(c).

Cracks that appeared on the girders of the most inspected bridges were limited to hairline cracks. In addition, horizontal cracks were frequently observed to form at the interface of girder webs and flanges. Spalling was also observed at the ends of girders in some bridges, which caused corrosion damage to mild steel and prestressing strands. One potential reason for the concrete spalling was because of thermal expansion and settlement of the abutment, which resulted in bearing of the girder against the backwall, as shown in Figure 3.13(d). Concrete spalling of the girders was observed in the Amarillo and Lubbock Districts.

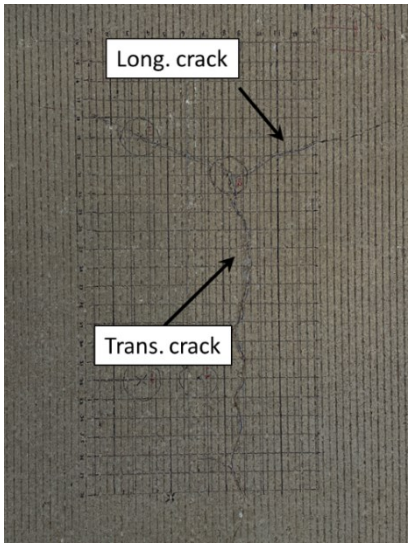

(a) Transverse and Longitudinal Cracks at PCP Joints (ATL–RC–05)

(b) Exposed Rebar on Deck (LBB–RC–04)

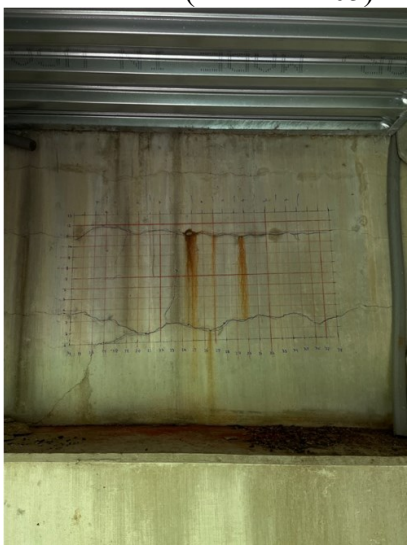

(c) Cracks and Efflorescence on Abutment (LBB–RC–06)

(d) Exposed Rebar on the Girder (LBB–RC–06)

Figure 3.13. Common Damages in Concrete Bridges.

Inspection of defects and corroded members in bent caps and columns was limited for most bridges because a close inspection was difficult to perform. On several bridges, columns had isolated regions of spalling or measurable cracks, but most columns had no damage, or the cracks were limited to map cracking. The most significant column damage was found on WFS–RC–04 on the north face of the exterior columns. It was not possible to access most bent caps to assess if hairline cracking was present; thus, documentation of damage areas was limited to what could be seen from the ground. Any visible cracks were typically diagonal cracks in the overhangs, negative

flexure cracks at the columns, or positive flexure cracks between the columns. Spalling was observed on the end faces of some bridges in the Amarillo District. Damage other than cracking along the interior faces of the bent cap was observed on two bridges, AMA–RC–04 and ATL–RC–01. In both cases, there were regions of exposed rebar, and the bent caps were located below expansion joints that were fully or partially open and allowed significant water to hit the bent caps. On AMA–RC–04, longitudinal cracks were visible near the top layer of reinforcement.

Similar types of deterioration were present on all concrete bridges. Types of deterioration included cracks, spalling, efflorescence, and steel reinforcement corrosion; however, the severity of the deterioration was different. Visual inspection results and a description of damages on the bridges are documented in detail in the appendix. Figure 3.14 illustrates deterioration of concrete bridge structures in Region 2. Figure 3.14(a) shows spalling at the abutment wall, and Figure 3.14(b) illustrates cracks and a sign of corrosion at the abutment wall of TYL–RC–03. Figure 3.15 displays deterioration of bridges in Region 3. Figure 3.15(a) shows map cracks propagating from a joint, and Figure 3.15(b) displays water leakage from a crack at an abutment on ELP–RC–01. Although rust was not visible, moisture on the concrete surface that might cause corrosion inside the concrete was observed. Figure 3.15(c) shows corrosion having already formed on the metal deck form near the abutment joint on ELP–RC–06. This deterioration is common in bridges with a metal deck form. Water penetrates through joints, and the metal deck forms near joints corrode due to the presence of corrosive agents. This action may weaken the metal deck form and affect the integrity of concrete bridges.

Figure 3.15(d) shows corrosion near the bearing pad on FTW–RC–03. Figure 3.15(e) illustrates the corroded metal deck form near the abutment joint on FTW–RC–04. Figure 3.15(f) displays cracks and efflorescence on the abutment backwall on FTW–RC–05, and Figure 3.15(g) shows exposed and corroded rebar on the abutment due to spalling of concrete on TYL–RC–02. Spalling of concrete frequently leads to exposure of rebar, which is prone to corrosion. Consequently, it is necessary to address spalling, implement appropriate maintenance, and repair strategies to prevent corrosion. Figure 3.16 shows exposed and corroded rebar on the concrete rail on ATL–RC–01 in Region 4. The rebar corroded due to concrete spalling, as well.

(a) Spalling at abutment wall (TYL–RC–03)

(b) Crack at abutment wall (TYL–RC–03)

Figure 3.14. Deterioration of Bridges in Region 2.

(a) Map cracks propagating from a joint (ELP–RC–01)

(b) Water leakage from crack at abutment (ELP–RC–01)

Figure 3.15. Deterioration of Bridges in Region 3.

(c) Corrosion at metal deck from an abutment (ELP–RC–06)

(d) Corrosion near bearing pad (FTW–RC–03)

(e) Corrosion detected at deck (FTW–RC–04)

(f) Crack and efflorescence at abutment backwall (FTW–RC–05)

(g) Exposed and corroded rebar at abutment (TYL–RC–02)

Figure 3.15. Deterioration of Bridges in Region 3 (Cont.).

Figure 3.16. Exposed and Corroded Rebar at Concrete Rail at ATL–RC–01 in Region 4.

Figure 3.17 illustrates the deterioration of bridges in Region 5. Figure 3.17(a) shows cracks and delamination of the asphalt overlay. Cracks and delamination allow moisture to penetrate the asphalt overlay and reach the concrete underneath, which can cause further corrosion of reinforcement steel in bridge decks. Figure 3.17(b) depicts cracks on the bottom surface of the deck. Figure 3.17(c) shows cracks and rust on the abutment backwall on CHS–RC–06. This type of cracking was probably caused by settlement of the abutment and often leads to corrosion of rebar. Figure 3.17(d) shows exposed and corroded rebar at the concrete rail in the WFS–RC–03 bridge, which may be due to spalling of concrete from corrosion formation on the rebar surface. Figure 3.17(e) also shows a similar crack to the one in Figure 3.17(c), but it perhaps developed as a result of water leakage on the abutment backwall on WFS–RC–03. Cracks on the abutment wall are common types of concrete cracking due to settlement. Figure 3.17(f) displays a corroded metal deck form near a joint on WFS–RC–04 that was generally visible on bridges with a permanent metal deck form (PMDF) at joints due to water leakage from the joints. Figure 3.17(g) illustrates horizontal cracks and efflorescence on the abutment backwall on WFS–RC–05, while Figure 3.17(h) shows a hole that formed within the pavement and extended into the deck. Severe pitting corrosion and metal loss of the reinforcement steel as a result of the hole are evident in Figure 3.17(i).

(a) Cracks and delamination of asphalt overlay (CHS–RC–05)

(b) Moderate cracks on bottom surface of deck (CHS–RC–05)

(c) Cracks at abutment backwall (CHS–RC–06)

(d) Exposed and corroded rebar at concrete rail (WFS–RC–03)

(e) Crack at abutment backwall (WFS–RC–03)

(f) Corroded metal deck form near joint (WFS–RC–04)

Figure 3.17. Deterioration of Bridges in Region 5.

(g) Horizontal cracks and efflorescence at abutment backwall (WFS–RC–05)

(h) Development of a hole on deck (WFS–RC–07)

(i) Pitting corrosion where the hole was (WFS–RC–07)

Figure 3.17. Deterioration of Bridges in Region 5 (Cont.).

Figure 3.18 shows deterioration of bridges in Region 6. Figure 3.18(a) shows exposed and corroded ECR due to settlement on AMA–RC–02. As the abutment wall fell off, the ECR was exposed to air, thus damaging the coating and potentially causing corrosion of the rebar. Rust propagated and caused further spalling on the abutment wall. Figure 3.18(b) displays rust on the concrete rail on AMA–RC–04. Rebar was not exposed to air, but water penetration within cracked spaces still remains possible. Figure 3.18(c) shows typical corrosion on the PMDF near a joint on AMA–RC–04 that was also observed on WFS–RC–04.

Figure 3.18(d) shows the condition of exposed rebar due to impact damage on the rail on AMA–RC–06 where corrosion of the rebars were detected. Figure 3.18(e) displays cracks and

efflorescence on the bottom surface of the deck on AMA–RC–08 that can potentially lead to the corrosion of either black rebar or ECR, particularly if the coating has been damaged.

On AMA–RC–05, widespread cracks were detected on the concrete deck, and efflorescence was visible on the bottom surface of the girders. During inspection, a core sample was extracted from an area near the cracks and efflorescence, revealing severe corrosion of the ECR within the core specimen. The presence of extensive efflorescence on the bottom surface of the deck indicates a high rate of water penetration into the concrete and an increased likelihood of rebar corrosion.

Figure 3.18(f) to Figure 3.18(k) display various issues on CHS–RC–01, including spalling at a joint, exposed and corroded rebar at the girder end due to spalling, sealed cracks on a bent cap, corroded uncoated black rebar at the bottom rebar mesh near the overhang, and concrete fall-off at the intersection of the replaced overhang. Note that CHS–RC–01 was in poor condition at the time of inspection, and rehabilitation was in progress. In Region 6, the use of ECR in both the top and bottom mesh of reinforcement (in addition to other mitigations such as HPC) is recommended to prevent corrosion initiation and propagation within concrete decks. Figure 3.18(l) shows transverse and longitudinal cracks on the deck surface. In general, longitudinal cracks located above girders are caused by girders, while transverse cracks are caused by concrete precast panels. Figure 3.18(m) shows hairline cracks on the abutment back wall on CHS–RC–04.

Based on the observed deteriorations during the field investigation, it is evident that appropriate maintenance and repair are essential, particularly in areas where severe cracks or spalling have occurred. One conclusion that can be drawn from the observations depicted in Figure 3.14 to Figure 3.18 is that the types of deterioration detected on superstructures of bridges primarily involved cracking and spalling on the deck and girders. However, a trace of corrosion was also evident in addition to cracking and spalling on the substructures of the bridges, particularly the abutments and bent caps.

(a) Exposed and corroded ECR due to spalling at abutment (AMA–RC–02)

(b) Rust at rail bottom (AMA–RC–04)

(c) Corrosion on the metal deck form near a joint (AMA–RC–04)

(d) Exposed rebar due to impact damage on a rail (AMA–RC–06)

(e) Cracks and efflorescence on bottom surface of deck (AMA–RC–08)

(f) Spalling of overlay at joint (CHS–RC–01)

Figure 3.18. Deterioration of Bridges in Region 6.

(g) Spalling and exposed rebar at girder ends (CHS–RC–01)

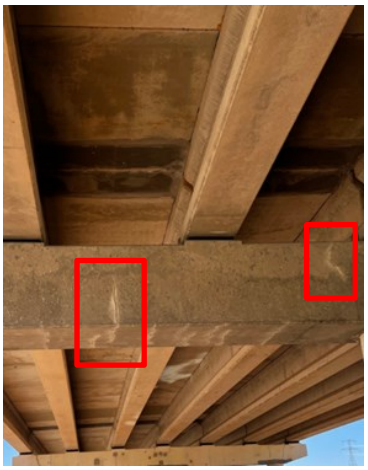

(h) sealed cracks on a bent cap (CHS–RC–01)

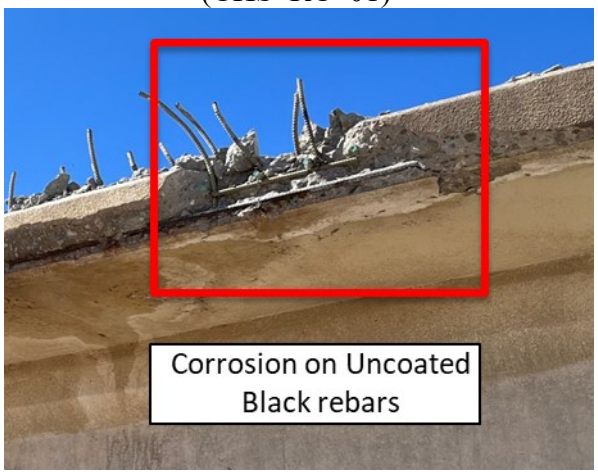

(i) Location of the corroded uncoated black rebar (CHS–RC–01)

(j) Corrosion on uncoated black rebar at the bottom mesh near overhang (CHS–RC–01)

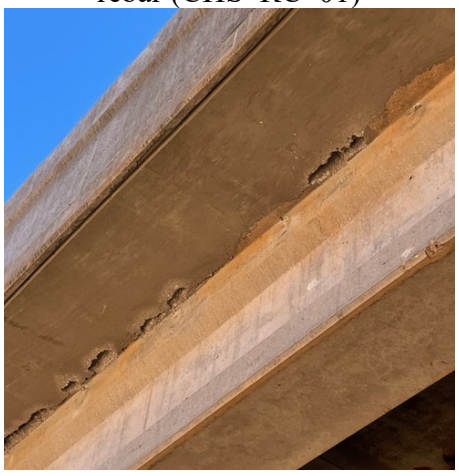

(k) Concrete fall-off at intersection of replaced overhang (CHS–RC–01)

(l) Transverse and longitudinal cracks on deck surface (CHS–RC–02)

Figure 3.18. Deterioration of Bridges in Region 6 (Cont.).

(m) Hairline cracks at abutment back wall
(CHS–RC–04)

Figure 3.18. Deterioration of Bridges in Region 6 (Cont.).

3.4.2 Infrared Thermography

Thermal images taken from bridge structures were used to analyze surface cracking on concrete elements. Figure 3.19 shows longitudinal cracks that are visible from the IRT photos. As shown in Figure 3.19, thermal imaging enables quick and efficient assessment of cracks. It can detect superficial defects on the bridge decks, including cracks that may not be easily visible to the unaided eye. IRT detects temperature differences caused by cracks, enabling precise identification and mapping of surface cracking.

Due to the presence of grooves on the bridge deck, cracks that run along the grooves can be challenging to identify. However, cracks that are perpendicular to the grooves can be easily detected using IRT. IRT relies on the detection of temperature variations on the surface of the bridge deck. Cracks that run perpendicular to the grooves can interrupt the heat flow and create temperature differences that are easily detectable with IRT. As the camera scans the surface, it detects variations in thermal patterns associated with cracks, which allows for the identification and mapping of cracks that may not be easily visible to the unaided eye.

IRT can be integrated with other NDT methods, such as GPR or ultrasonic testing, to obtain a more comprehensive understanding of the condition of the bridge deck and the underlying causes of crack formation.

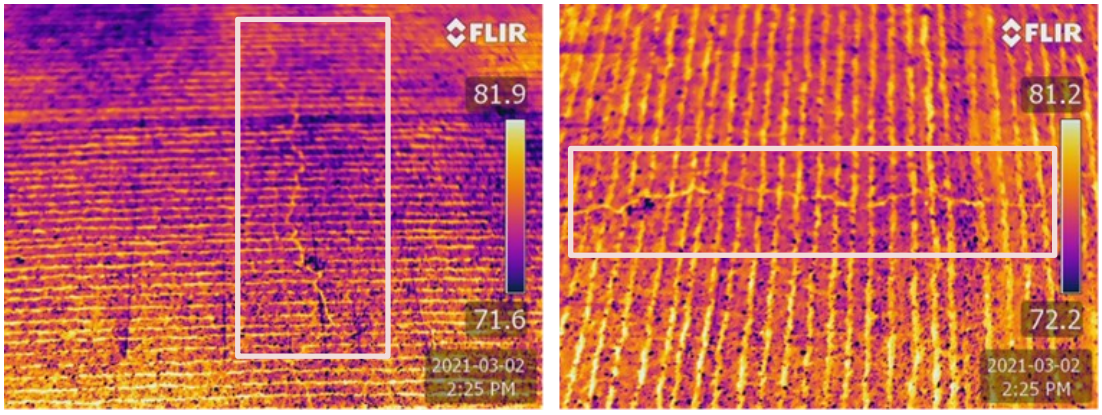

Figure 3.19. Thermal Imaging of CRP–RC–02 Showing Cracks.

3.4.3 Ground Penetrating Radar

GPR was conducted on all NDE grids. Figure 3.20 shows GPR results, providing a clear visualization of the rebar location inside the concrete deck. The grids were typically oriented perpendicular to the vehicle lane; therefore, rebar from the top to bottom are transverse rebar, and rebar going from left to right are longitudinal rebars. Since concrete cores were mainly extracted from the top portion of the deck, the GPR results focused on identifying the location of the top longitudinal and transverse rebars. Figure 3.21 shows post-processed results of GPR. During the field inspection, based on the GPR results, coring locations and measurement locations for corrosion rate mapping were selected.

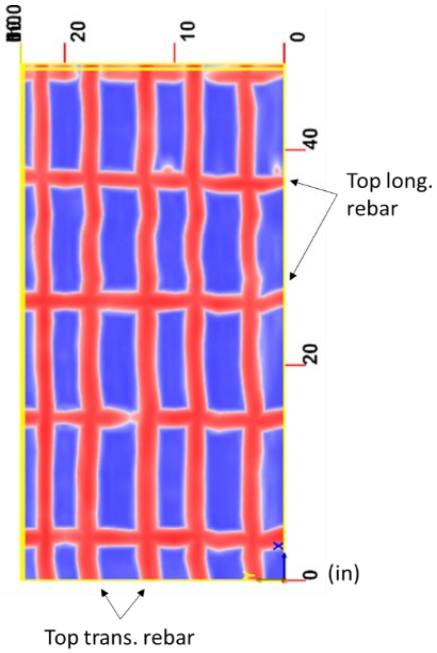

Figure 3.20. 2D Results of GPR Scanning.

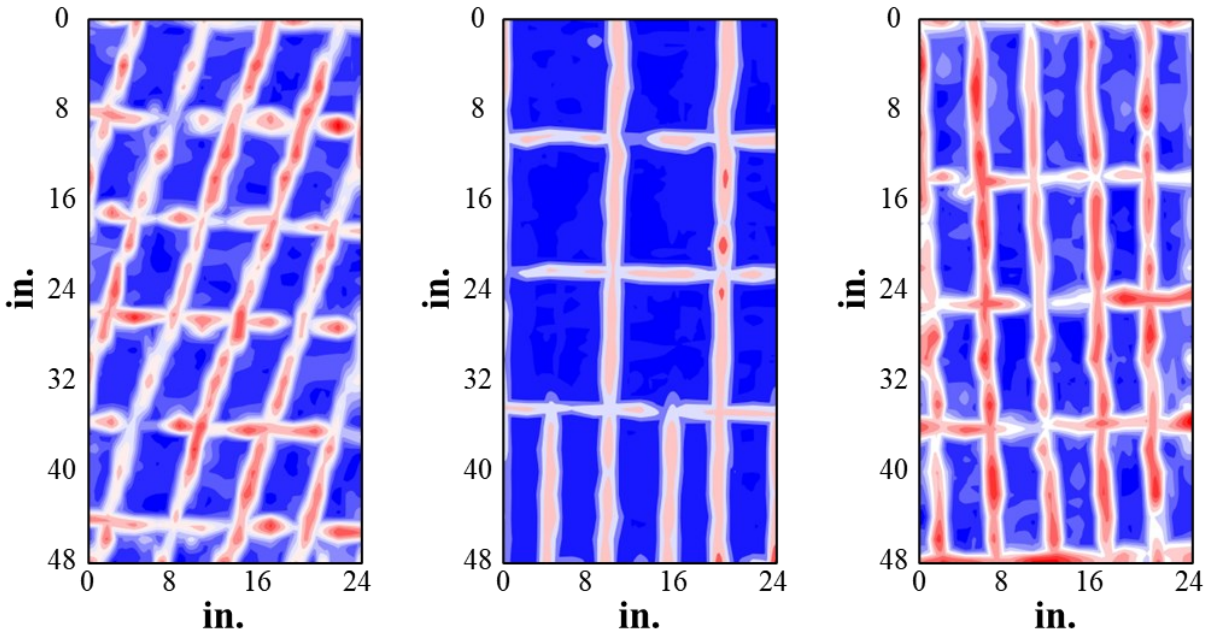

(a) AMA–RC–01, G1 (b) ATL–RC–01, G1 (c) CHS–RC–01, G1

Figure 3.21. Results of GPR.

3.4.4 Ultrasonic Tomography

Figure 3.22 shows UST results that can be used to locate the rebar inside and on the bottom of the concrete deck. Note that any defects that were smaller than rebar were difficult to find due to reflections. It is hard to determine whether the reflection is due to a defect or is just noise. If there were overlays such as asphalt, then it would be even more difficult to find the rebars because of noises around the asphalt surface (Figure 3.23[a]). However, if a bridge does not have an overlay, UST scanning can be useful to locate rebar and identify potential areas of deterioration (Figure 3.23[b]). To reduce the noise, the results needed to be normalized and validated by comparing the UST results with the actual cores. After normalization and validation, deteriorations such as voids and corrosion could be found by analyzing the UST results. The appendix contains all the UST scanning results, while Figure 3.24 supplies examples of a few concrete decks.

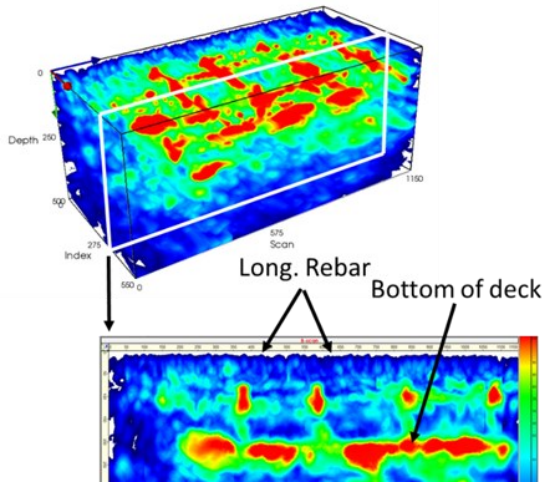

Figure 3.22. Result of UST Showing Rebar Location and Bottom of Deck (LBB–RC–02).

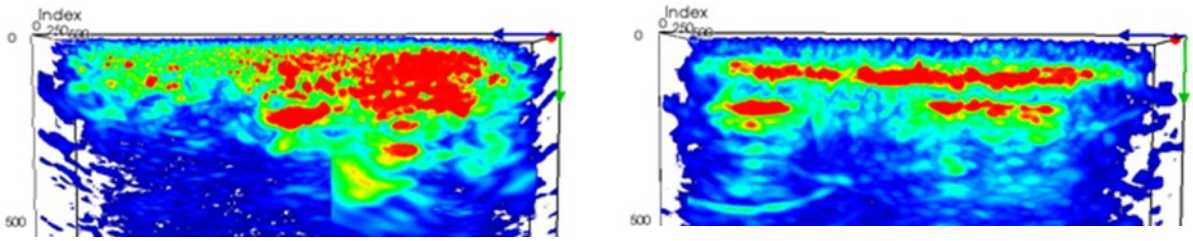

(a) UST Results with Overlay (b) UST Results without Overlay

Figure 3.23. UST Results with and without Overlay.

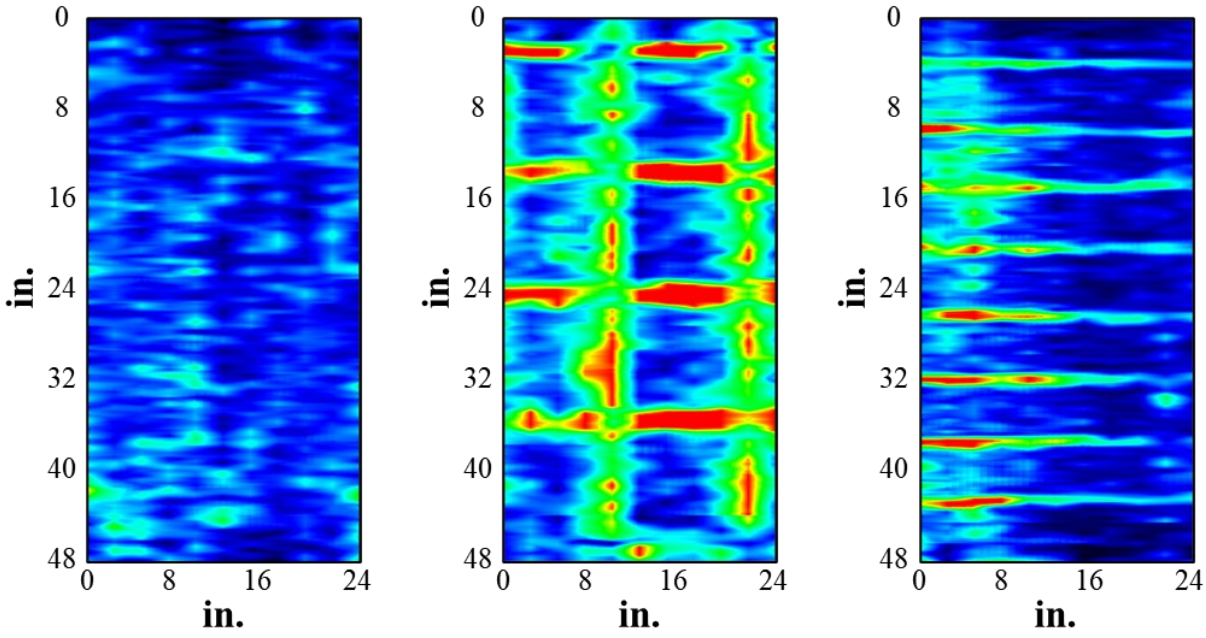

(a) AMA–RC–01, G1 (b) ATL–RC–01, G1 (c) CHS–RC–01, G1

Figure 3.24. Results of UST.

The resolution of the results obtained from UST was sometimes poor. A possible reason is that UST was only performed in one direction, mainly due to time constraints during the field investigation. As a result, the propagated wave in the concrete was polarized, making it difficult and challenging to interpret the resulting data and accurately match rebar to produce an image of rebar. Additionally, the presence of grooves on the concrete surface may have also caused dispersion of sound waves. Therefore, some of the results provided by UST did not lead to desirable outcomes.

3.4.5 Corrosion Rate Mapping

The results of the corrosion rate mapping of concrete bridges indicate that most of the inspected bridge decks are in good condition, though with some exceptions. Note that the corrosion rate mapping was exclusively conducted on bridges located in Amarillo, El Paso, and Lubbock.

Figure 3.25 shows results of corrosion rate mapping of bridges in Region 3, including ELP–RC–03, ELP–RC–05, ELP–RC–07, and ELP–RC–08. Among the bridges, ELP–RC–03 G2, ELP–RC–07, and ELP–RC–08 were classified as being in moderate condition in terms of corrosion rate. These bridges exhibited corrosion damage within the range of 10 to 15 years according to the corrosion rate mapping. On the other hand, ELP–RC–03 G1 and ELP–RC–05 had a high corrosion rate and were expected to have some corrosion damage within the range of 2 to 10 years; particularly, ELP–RC–08 and ELP–RC–05 had corrosion rates of 7 and 10 $\mu A/cm^2$, respectively, which is close to the moderate range. Additionally, it is worth mentioning that ELP–RC–03 exhibited a high corrosion rate only in a limited area, while all other locations exhibited low to no corrosion rates.

Figure 3.26 illustrates the corrosion rate mapping developed for concrete decks in Region 6, including AMA–RC–10, LBB–RC–01, LBB–RC–02, LBB–RC–03, LBB–RC–04, LBB–RC–05, LBB–RC–06, and LBB–RC–07. Among these bridges, LBB–RC–01, LBB–RC–02, LBB–RC–04, LBB–RC–05, and LBB–RC–07 were determined to be in a moderate condition in terms of corrosion rate. These concrete structures exhibited corrosion damage within the range of 10 to 15 years. On the other hand, AMA–RC–10, LBB–RC–03, and LBB–RC–06 had high corrosion rates and were expected to have corrosion damage within the range of 2 to 10 years. Only limited areas of LBB–RC–03 and LBB–RC–06 showed corrosion rates of 18 and 15 $\mu A/cm^2$, respectively. AMA–RC–10 G1 exhibited a corrosion rate of 30 $\mu A/cm^2$ in a very limited area.

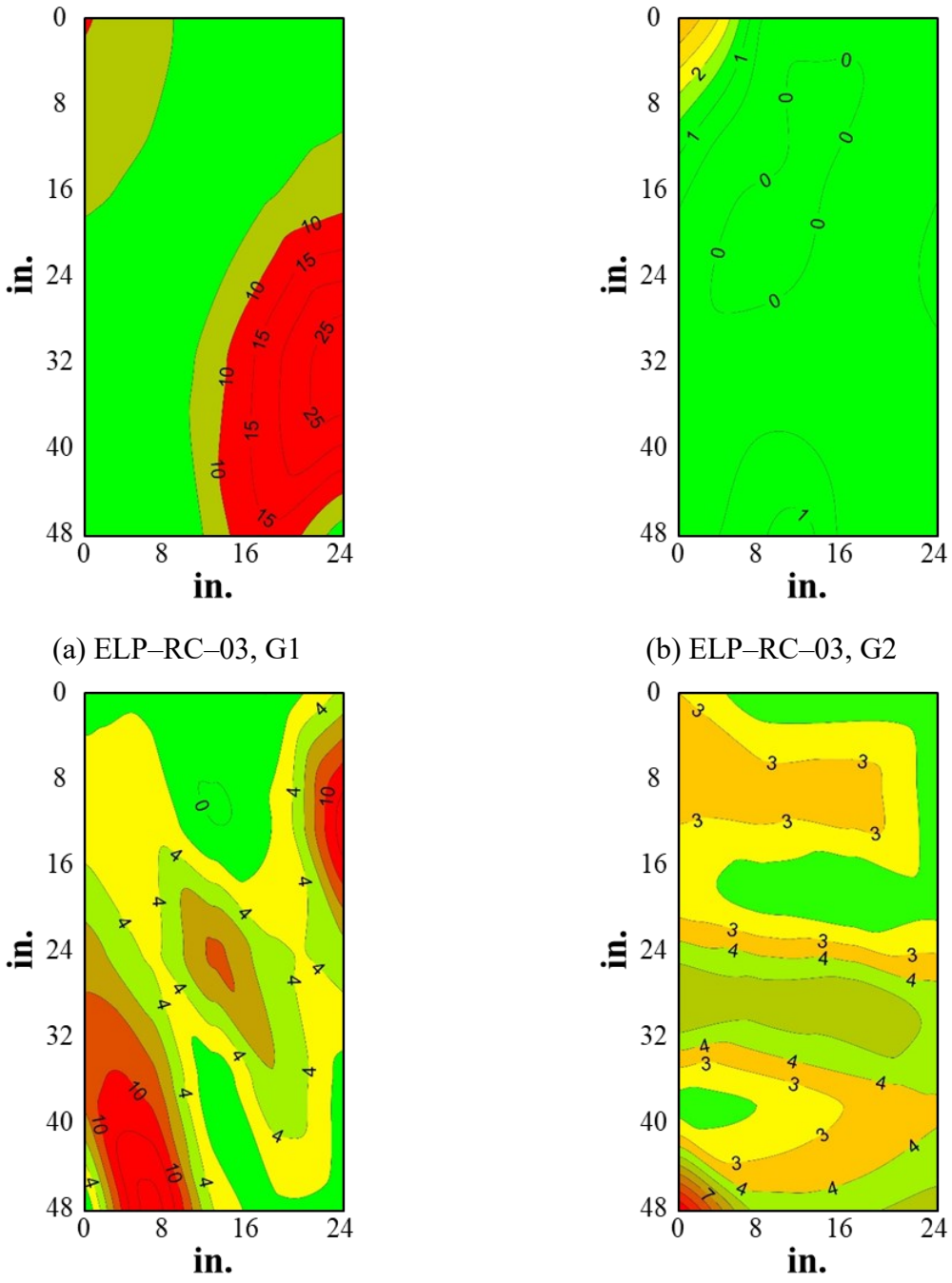

(a) ELP–RC–03, G1

(b) ELP–RC–03, G2

(c) ELP–RC–05, G2

(d) ELP–RC–07, G1

Figure 3.25. Corrosion Rate Mapping Results of Bridges in Region 3, Corrosion Current Density (μA/cm^2).

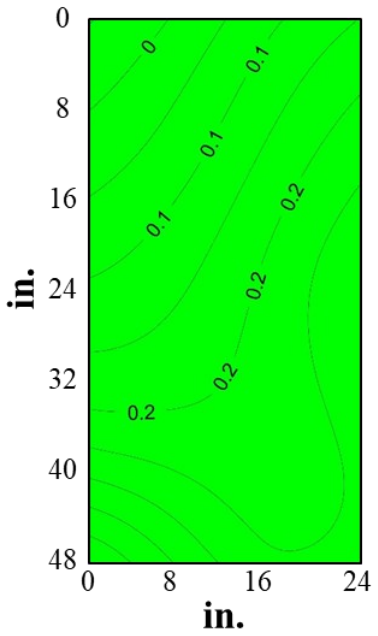

(e) ELP–RC–07, G2

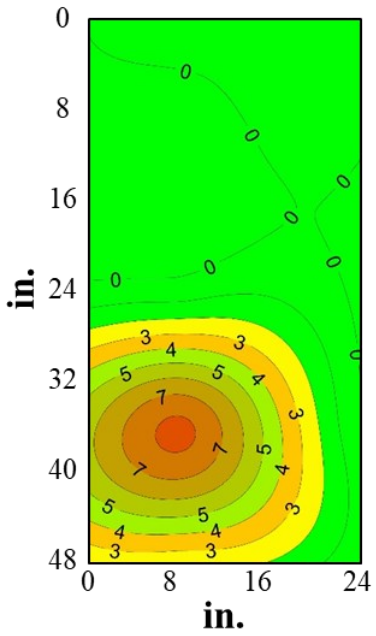

(f) ELP–RC–08, G1

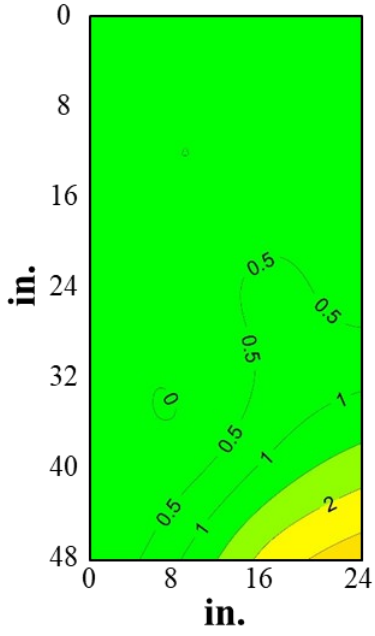

(g) ELP–RC–08, G2

Figure 3.25. Corrosion Rate Mapping Results of Bridges in Region 3, Corrosion Current Density (µA/cm^2) (Cont.).

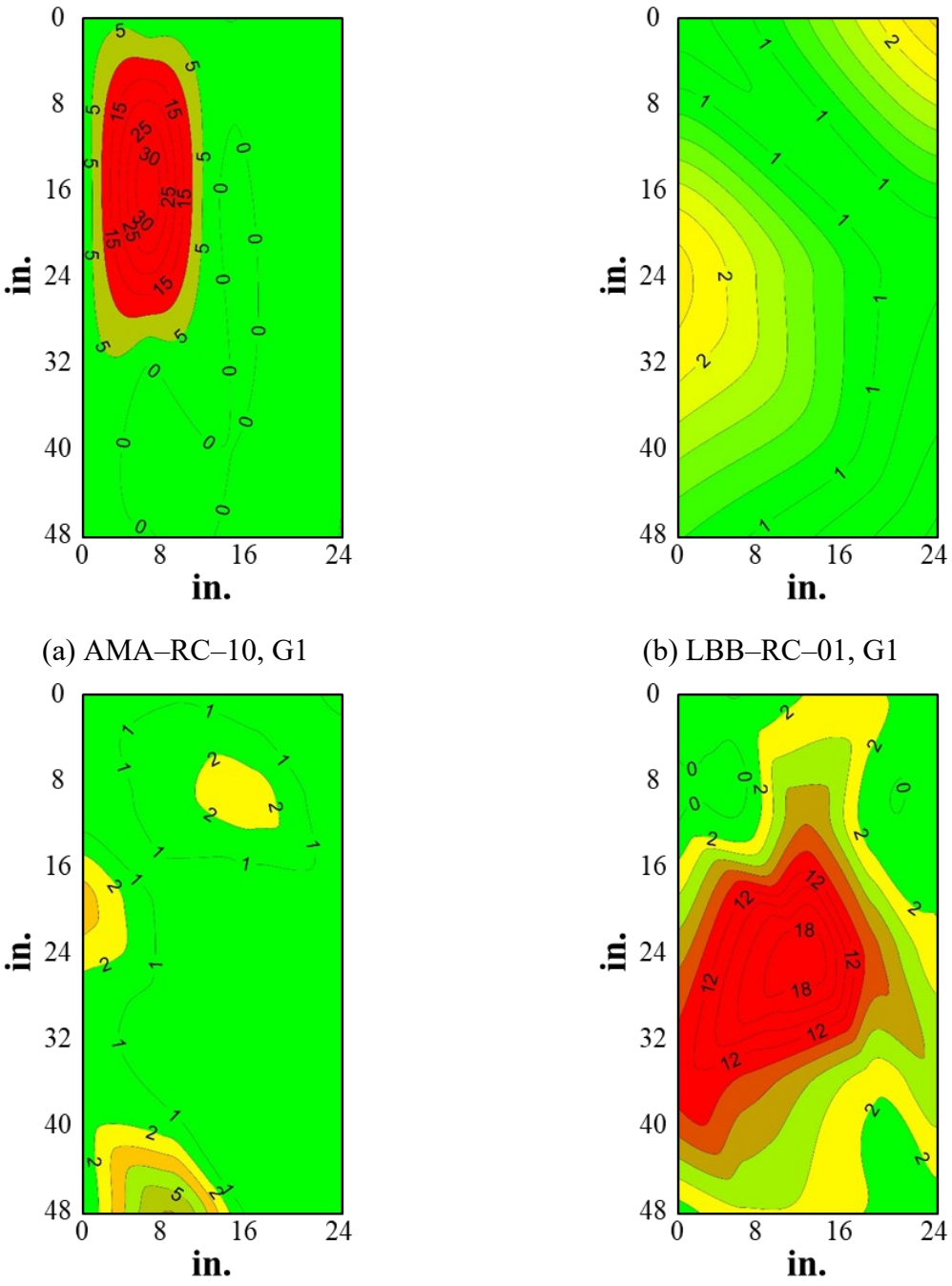

(a) AMA–RC–10, G1

(b) LBB–RC–01, G1

(c) LBB–RC–02, G1

(d) LBB–RC–03, G1

Figure 3.26. Corrosion Rate Mapping Results of Bridges in Region 6, Corrosion Current Density (μA/cm^2).

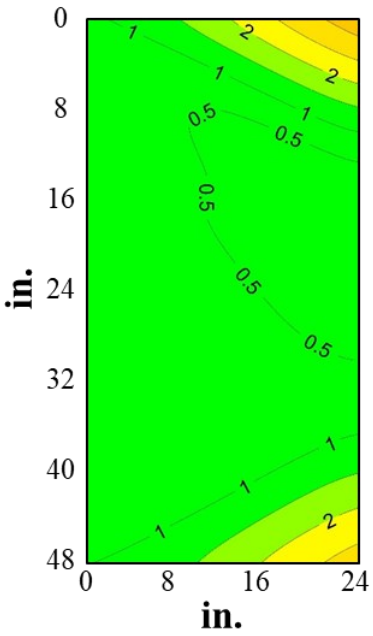

(e) LBB–RC–04, G1

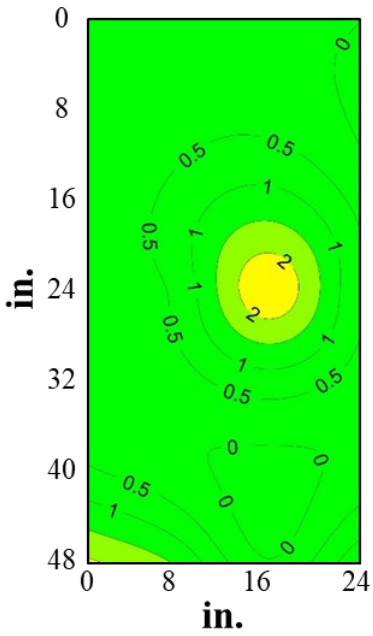

(f) LBB–RC–05, G1

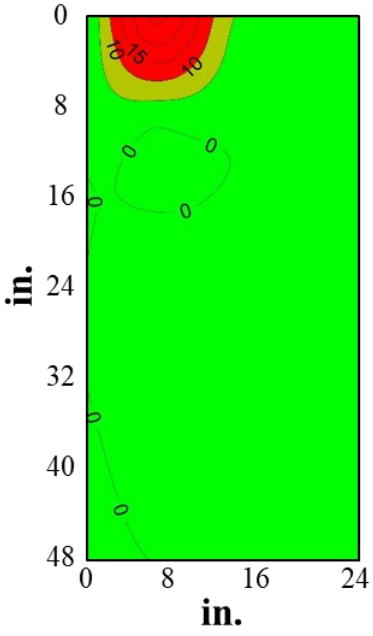

(g) LBB–RC–06, G1

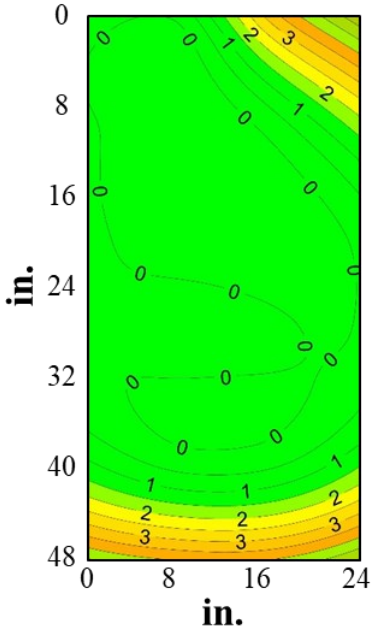

(h) LBB–RC–07, G1

Figure 3.26. Corrosion Rate Mapping Results of Bridges in Region 6, Corrosion Current Density (µA/cm^2) (Cont.).

3.4.6 Coring

Overall, the rebar and cores were found to be in good condition and showed no sign of corrosion. However, laboratory examinations were also conducted to determine the corrosion condition of core specimens, and the results will be reported in Chapter 4. Figure 3.27 shows a core from its side, top, and bottom. The core, labeled 1-1, is a core from Grid 1 of LBB–RC–03, and it represents an example of a core in good condition. Upon examination, there were no visible cracks on its top surface, no delamination on the bottom surface, and no visible voids or cracks on the side surface.

Figure 3.28 illustrates cores with visible deterioration, each showing different forms of damage and degradation. The core labeled 2-3 from AMA–RC–03 (Figure 3.28[a]) exhibited a crack along the intersection of aggregates, which can be attributed to plastic shrinkage. This process is a form of drying shrinkage that occurs while the cement is unhardened. This type of cracking, known as settlement or subsidence cracking, is influenced by drying atmospheric conditions and can lead to segregation of coarse aggregate from the paste (ACI 224 R). Figure 3.28(b) shows a small void 1.5 in. from the top surface of a core taken from the concrete deck of AMA–RC–04. As shown in Figure 3.28(c), a core extracted from AMA–RC–05 exhibited traces of corrosion on the bottom surface and a crack propagating from or to the reinforcing bar. This occurrence suggests that the crack may have facilitated the corrosion process on steel reinforcements. Although corrosion from the rebar could potentially lead to delamination of the concrete, it is challenging to draw a definitive conclusion because concrete typically breaks during coring rather than from delamination. Figure 3.28(d) shows a similar deterioration, but the steel bar at the end of the crack remained uncorroded, indicating that the epoxy coating effectively prevented corrosion. Figure 3.28(e) illustrates a core from ATL–RC–04 split due to a plastic crack. No corrosion was observed in this specimen despite the crack passing through the reinforcing bar. The core in Figure 3.28(f) was collected from a construction joint in BMT–RC–01; it showed no signs of corrosion on the reinforcement. Figure 3.28(g) displays a core from CHS–RC–02 with a crack propagating from or to steel, accompanied by corrosion on the reinforcement. In Figure 3.28(h), a core from CHS–RC–06 exhibited several plastic cracks on the side surface; however, the top surface displayed no cracks. Figure 3.28(i) depicts a core from WFS–RC–01 that reveals a crack propagating from a joint of PCPs through a steel bar. However, no corrosion was observed on the steel.

The appendix contains comprehensive details about the extracted cores, including dimensions, rebar details, and information about cracks. Additionally, the appendix presents images such as in Figure 3.27, showing the top and bottom surfaces, as well as the side surface of each core. These images will aid in visualizing the condition and characteristics of the cores.

(a) LBB–RC–03, Core 1-1			

Figure 3.27. Pictures of Core 1-1 of LBB–RC–03 in Good Condition.

(a) AMA–RC–03, Core 2-3			
(b) AMA–RC–04, Core 1-1			
(c) AMA–RC–05, Core 2-3	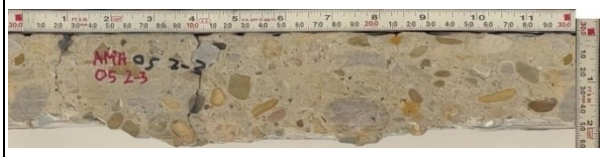		
(d) AMA–RC–10, Core 2-4	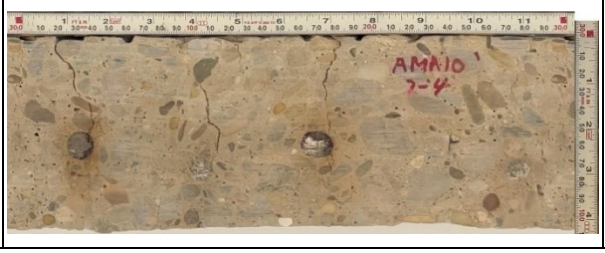		

Figure 3.28. Pictures of Cores with Deterioration.

(e) ATL–RC–04, Core 2-3			
(f) BMT–RC–01, Core 1-2	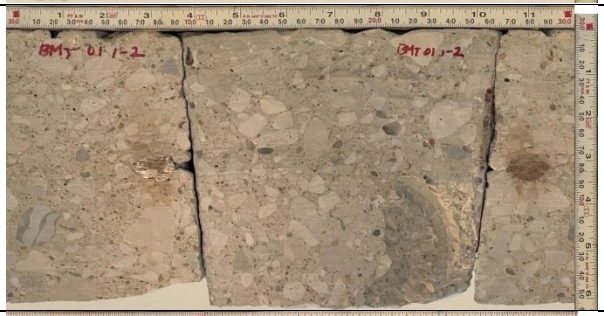		
(g) CHS–RC–02, Core 1-2			
(h) CHS–RC–06, Core 2-1			
(i) WFS–RC–01, Core 2-3			

Figure 3.28. Pictures of Cores with Deterioration (Cont.).

3.4.7 Crack Mapping

A summary of measured crack width and calculated crack density for inspected bridge decks are provided in Table 3-7 and Table 3-8. The crack width and crack densities were measured from the grids that were placed in areas of the deck with the most extensive cracking. The crack width recorded may not fully reflect the overall condition of the entire deck. However, this measurement can be correlated with the results obtained from NDT and laboratory experiments.

Table 3-7 provides the crack width for each concrete deck inspected in this research, ranging from 0.001 to 0.08 in. In some cases, no crack width was recorded due to an overlay on the bridge deck. Based on findings given in Table 3-7, the crack width occurred on concrete decks located in Region 6 (particularly Amarillo and Lubbock), and it was relatively greater than other regions. The crack width recorded for the concrete deck in Amarillo ranged from 0.008 to 0.05 in., while it ranged from 0.004 to 0.025 in. for the structure in El Paso. Although the bridges in Lubbock are located in Region 6, the crack width of most bridges ranged from 0.004 to 0.008 in.; the one exception was LBB–RC–05, which had a crack width of 0.024 in.

Table 3-8 provides the crack density of each concrete deck inspected in this work and its associated corrosion risk region. As shown in Table 3-8, a similar trend was also observed for the crack density. The bridges in Region 6 have greater crack densities, except for the bridges in Lubbock, while bridges in Region 2 and Region 3 have relatively smaller crack densities. The differences in crack densities between regions were found to be small.

Table 3-7. Corrosion Risk Regions and Maximum Crack Width on Concrete Bridge Decks.

Bridge ID	Corrosion Risk Region	Maximum Crack Width (in.)
AMA–RC–01	6	0.040
AMA–RC–02	6	—
AMA–RC–03	6	0.008
AMA–RC–04	6	0.030
AMA–RC–05	6	0.020
AMA–RC–06	6	0.001
AMA–RC–07	6	—
AMA–RC–08	6	0.050
AMA–RC–09	6	0.012
AMA–RC–10	6	0.010
AMA–RC–11	6	—
AMA–RC–12	6	—
ATL–RC–01	4	0.008
ATL–RC–02	4	0.004
ATL–RC–03	4	0.030
ATL–RC–04	3	0.030
ATL–RC–05	2	0.012
ATL–RC–06	5	0.012
ATL–RC–07	3	0.010
BMT–RC–01	5	0.004
CHS–RC–01	6	—
CHS–RC–02	6	0.020
CHS–RC–03	6	0.004
CHS–RC–04	6	0.008
CHS–RC–05	5	0.001
CHS–RC–06	5	0.030
CRP–RC–01	6	—
CRP–RC–02	6	—
CRP–RC–03	6	—
ELP–RC–01	3	0.025
ELP–RC–02	3	0.010
ELP–RC–03	3	0.004
ELP–RC–04	3	0.004
ELP–RC–05	3	0.025
ELP–RC–06	3	0.008
ELP–RC–07	3	0.014
ELP–RC–08	3	0.012
FTW–RC–01	4	0.080
FTW–RC–02	3	0.025
FTW–RC–03	3	0.012
FTW–RC–04	3	0.008
FTW–RC–05	3	0.004

Bridge ID	Corrosion Risk Region	Maximum Crack Width (in.)
FTW–RC–06	3	0.004
FTW–RC–07	4	0.004
LBB–RC–01	6	0.004
LBB–RC–02	6	0.004
LBB–RC–03	6	0.008
LBB–RC–04	6	0.006
LBB–RC–05	6	0.024
LBB–RC–06	6	0.008
LBB–RC–07	6	0.004
TYL–RC–01	3	—
TYL–RC–02	3	0.010
TYL–RC–03	2	0.007
WFS–RC–01	5	0.018
WFS–RC–02	5	0.004
WFS–RC–03	5	0.001
WFS–RC–04	5	0.008
WFS–RC–05	5	0.004
WFS–RC–06	5	0.012
WFS–RC–07	5	0.004

Note: "–" indicates bridges with an overlay; therefore, no cracks were measured.

Table 3-8. Corrosion Risk Regions and Crack Densities on Concrete Bridge Decks.

Bridge ID	Corrosion Risk Region	Crack Density (in./in^2)
AMA–RC–01	6	0.24
AMA–RC–02	6	—
AMA–RC–03	6	0.04
AMA–RC–04	6	0.06
AMA–RC–05	6	0.05
AMA–RC–06	6	0.00
AMA–RC–07	6	—
AMA–RC–08	6	0.05
AMA–RC–09	6	0.14
AMA–RC–10	6	0.09
AMA–RC–11	6	—
AMA–RC–12	6	—
ATL–RC–01	4	0.04
ATL–RC–02	4	0.06
ATL–RC–03	4	0.05
ATL–RC–04	3	0.08
ATL–RC–05	2	0.05
ATL–RC–06	5	0.11
ATL–RC–07	3	0.04
BMT–RC–01	5	0.00
CHS–RC–01	6	—
CHS–RC–02	6	0.10
CHS–RC–03	6	0.04
CHS–RC–04	6	0.05
CHS–RC–05	5	0.00
CHS–RC–06	5	0.05
CRP–RC–01	6	—
CRP–RC–02	6	—
CRP–RC–03	6	—
ELP–RC–01	3	0.23
ELP–RC–02	3	0.09
ELP–RC–03	3	0.04
ELP–RC–04	3	0.04
ELP–RC–05	3	0.12
ELP–RC–06	3	0.10
ELP–RC–07	3	0.04
ELP–RC–08	3	0.05
FTW–RC–01	4	0.07
FTW–RC–02	3	0.03
FTW–RC–03	3	0.06
FTW–RC–04	3	0.05
FTW–RC–05	3	0.03
FTW–RC–06	3	0.06

Bridge ID	Corrosion Risk Region	Crack Density (in./in^2)
FTW–RC–07	4	0.04
LBB–RC–01	6	0.03
LBB–RC–02	6	0.04
LBB–RC–03	6	0.05
LBB–RC–04	6	0.07
LBB–RC–05	6	0.05
LBB–RC–06	6	0.15
LBB–RC–07	6	0.02
TYL–RC–01	3	—
TYL–RC–02	3	0.05
TYL–RC–03	2	0.02
WFS–RC–01	5	0.08
WFS–RC–02	5	0.12
WFS–RC–03	5	0.00
WFS–RC–04	5	0.04
WFS–RC–05	5	0.06
WFS–RC–06	5	0.14
WFS–RC–07	5	0.17

Note: "–" indicates bridges with an overlay; therefore, no cracks were measured.

Figure 3.29 to Figure 3.33 show crack maps of inspected bridges in Region 2 to Region 6, respectively. Crack widths were categorized in different color codes to indicate their severity. A crack width larger than 0.05 in. is considered poor and marked with red. Cracks with widths ranging from 0.012 to 0.05 in. are categorized as orange. A blue color indicates cracks with widths between 0.004 in. and 0.012 in. Cracks narrower than 0.004 in. are classified as hairline cracks and marked green. The color codes provide a visual representation of the severity of cracks on the bridge decks.

Figure 3.29 provides surface crack mapping of the concrete decks in Region 3, highlighting the variations in crack conditions. As shown in this figure, the crack mapping of Grid 2 in ATL–RC–05 illustrates a 0.006-in.-wide transverse crack as well as a hairline crack. Although surface cracking was detected in Grid 2, the crack mapping represented in Figure 3.29 shows the absence of any kind of surface cracking developed in Grid 1 of TYL–RC–03. The transverse cracking observed in ATL–RC–05 is a common type of crack that can develop at the joint of PCPs. This variation in crack conditions among bridges in the same region suggests the influence of different factors such as construction methods or environmental conditions, which may contribute to the varying levels of cracking observed on the bridge decks. Cracking can occur either during construction or as a result of stress concentration after installation. If the interior diagram of

concrete panels is not properly positioned to support the concrete deck, it can result in increased rates of transverse crack development due to the production of negative longitudinal bending moments. Additionally, factors like thermal and shrinkage effects can also contribute to development of transverse cracking (Buth et al., 1972).

Figure 3.30 provides insights into the condition of bridge decks in Region 3. Figure 3.30(a) shows crack distribution on the deck of ELP–RC–01, which is classified in bad condition despite not having wide enough cracks to be considered a poor-quality concrete. However, the crack density of ELP–RC–01 was found to be significantly high, indicating a high fraction of surface cracking on the deck. In contrast, in Grid 1 of ATL–RC–04 (Figure 3.30[c]), a wider crack was observed, but the associated crack density was calculated as low. The cracks in this case are seen to propagate from a poor boy joint (PBJ). Figure 3.30(b) shows Grid 2 of ELP–RC–04, wherein the concrete deck is in a very good condition with only a few cracks, thereby justifying a good rating.

Figure 3.31 shows crack mapping of bridges in Region 4. Figure 3.31(a) shows an example of a moderate crack condition from Grid 1 of ATL–RC–01, while Figure 3.31(b) depicts a similar crack mapping from ATL–RC–02 with additional hairline cracking. ATL–RC–02 was found to be in good condition in terms of crack width; however, many hairline cracks were visible inside the grid.

Figure 3.32 includes crack mapping of bridges in Region 5, which contains concrete bridges such as CHS–RC–05, WFS–RC–06, and WFS–RC–07. Although Figure 3.32(a) shows a grid with only few hairline cracks, Figure 3.32(b) and (c) illustrate grids with several cracks ranging between 0.004 in. and 0.012 in. width. Figure 3.33 displays surface crack mapping of concrete decks located in Region 6. AMA–RC–01, AMA–RC–02, and AMA–RC–08 exemplify such concrete structures. Figure 3.33(a) and (b) show bridges in Amarillo in moderate and severe conditions, and Figure 3.33(c) illustrates a concrete deck in Lubbock with several hairline cracking. As noted previously, these observations suggest that the condition of bridge decks can vary within the same region since they were captured from a limited area of the bridge deck.

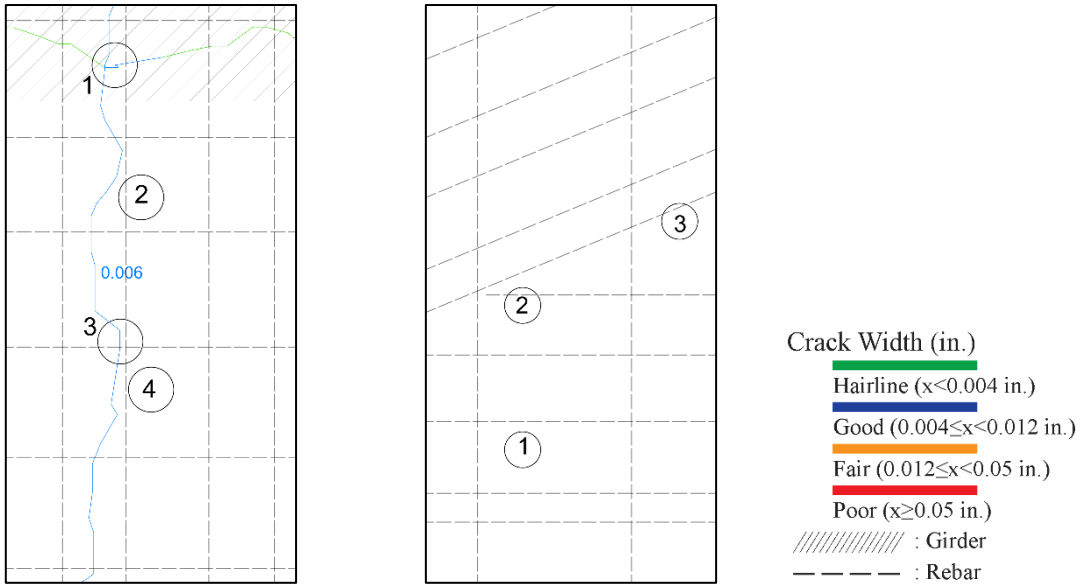

(a) ATL–RC–05, G2 (b) TYL–RC–03, G1 (NO CRACK)

Figure 3.29. Crack Mapping of Concrete Decks in Region 2.

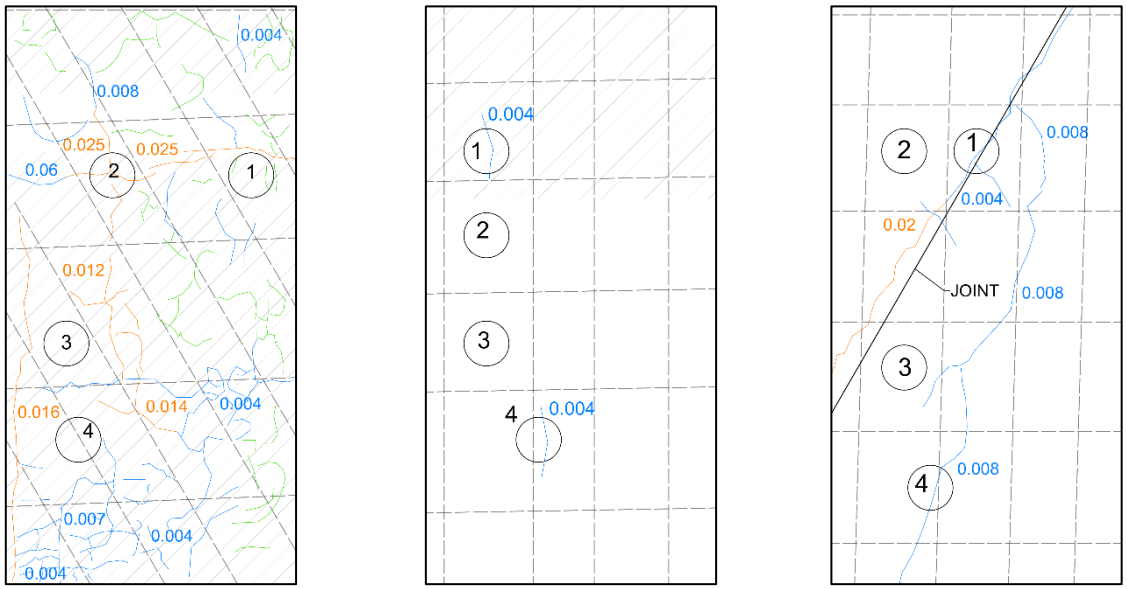

(a) ELP–RC–01, G1 (b) ELP–RC–04, G2 (c) ATL–RC–04, G1

Figure 3.30. Crack Mapping of Concrete Decks in Region 3.

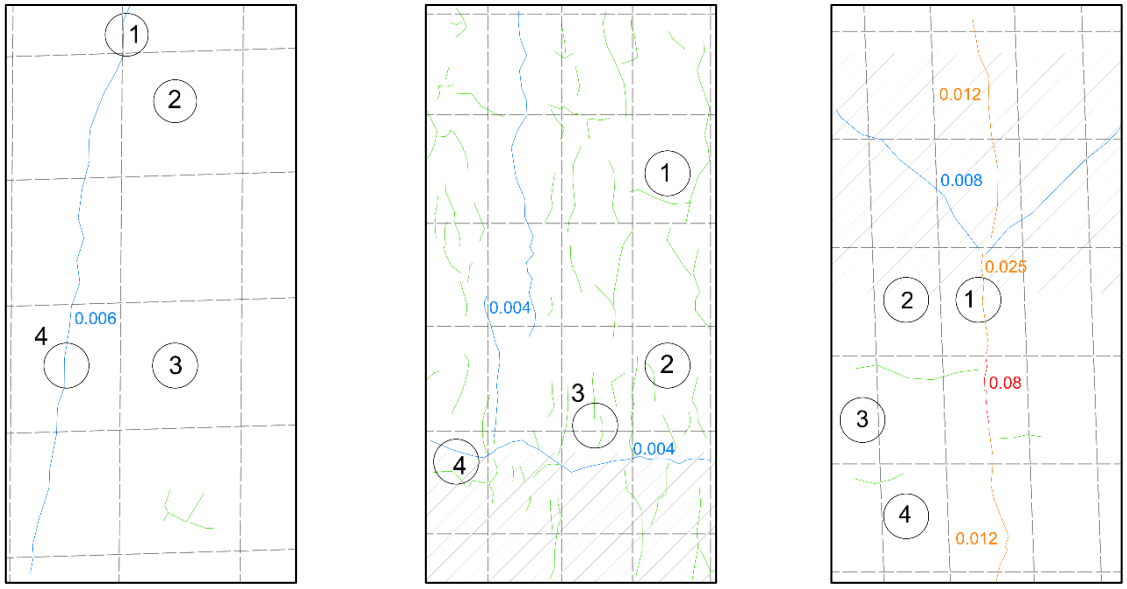

(a) ATL–RC–01, G1 (b) ATL–RC–02, G1 (c) FTW–RC–01, G1

Figure 3.31. Crack Mapping of Concrete Decks in Region 4.

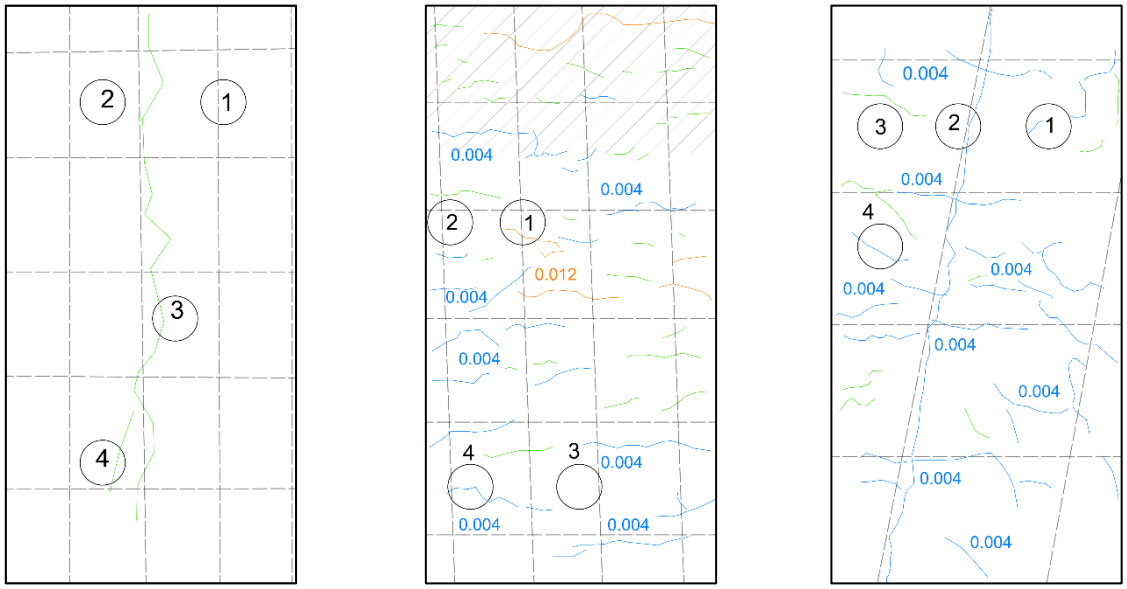

(a) CHS–RC–05, G2 (b) WFS–RC–06, G1 (c) WFS–RC–07, G1

Figure 3.32. Crack Mapping of Concrete Decks in Region 5.

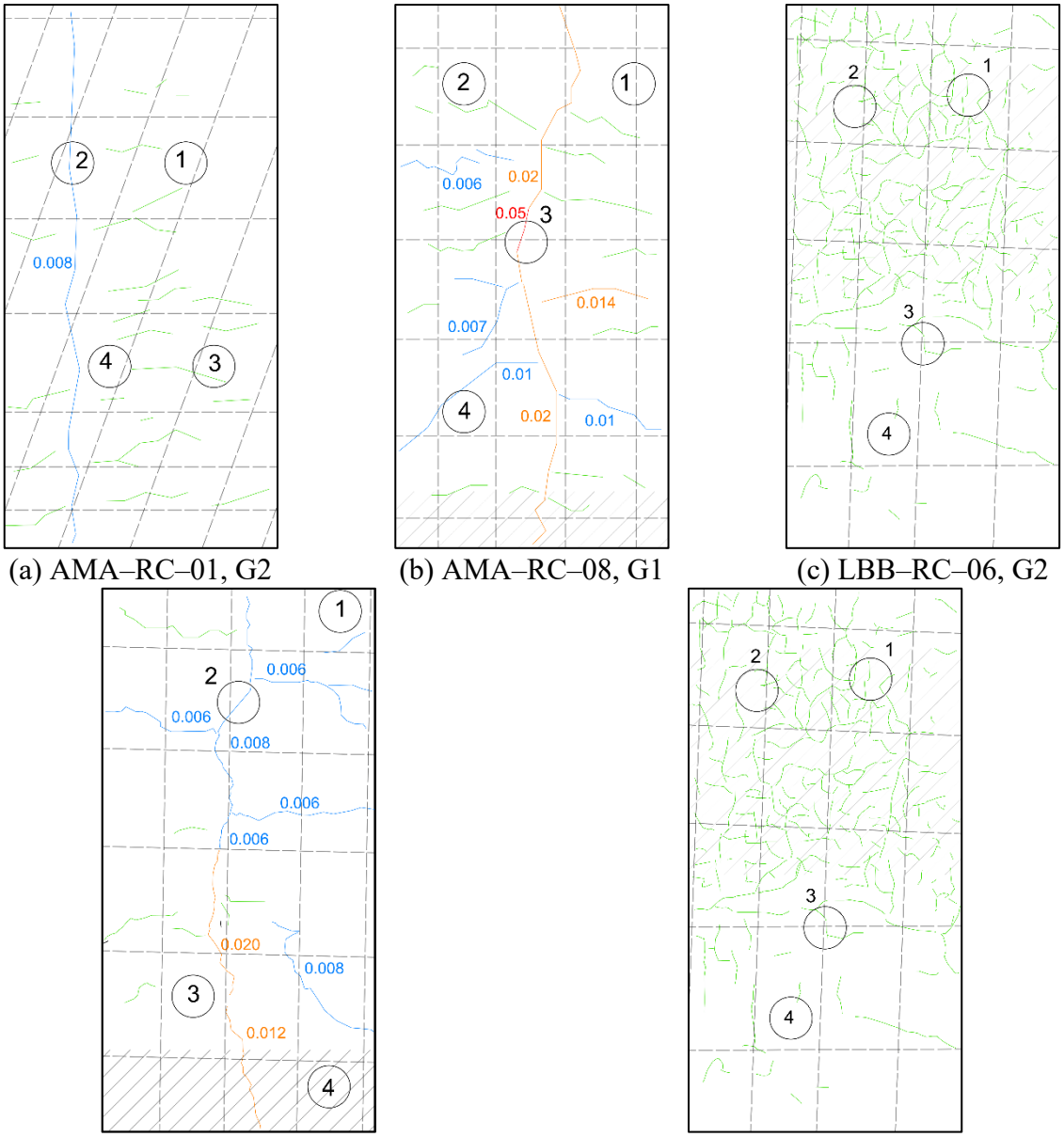

Figure 3.33. Crack Mapping of Concrete Decks in Region 6.

3.5 SUMMARY

Visible cracks, including transverse, longitudinal, diagonal, and map cracks were detected during inspection of concrete bridges. Minimal damage was observed on the decks, with minor spalling and exposed reinforcement in some areas. It was also documented limited damage in specific locations underside of the decks. However, measurable cracks and spalling was detected in abutments and girders, while bent caps and columns had limited damage in the form of spalling or map cracking. Similar deterioration was present in all bridges but varied in severity.

Thermal imaging showed the locations of surface cracking on concrete decks. Thermal imaging can be used as a quick assessment of surface cracks and detection of defects that were not easily visible to the unaided eye. The imaging helped to identify cracks through temperature differences of concrete surface and cracking area.

GPR was conducted on reinforced concrete decks to detect the location of reinforcing steel bars. The results were evaluated in the field to develop corrosion rate mapping at the intersections of longitudinal and transverse rebars. The results of GPR were also used to select the location of coring. In addition to GPR, UST was also conducted to detect defects in concrete decks. The UST scanning was used to estimate the thickness of the deck and locate rebar within concrete. In general, it was difficult to detect small defects in concrete primarily because of noise reflections.

The corrosion rate mapping indicates that most of the inspected bridge decks in Amarillo, El Paso, and Lubbock were in good condition, with some exceptions. In Region 3, bridges such as ELP–RC–03, ELP–RC–07, ELP–RC–07, and ELP–RC–08 were classified as being in moderate condition in terms of corrosion rate, with expected corrosion damage within 10 to 15 years. However, ELP–RC–03, ELP–RC–05, and ELP–RC–08 had a high corrosion rate and are expected to exhibit corrosion damage within 2 to 10 years. Similar assessments made in Region 6, bridges like LBB–RC–01, LBB–RC–02, LBB–RC–04, LBB–RC–05, and LBB–RC–07 were found to be in moderate condition, while AMA–RC–10, LBB–RC–03, and LBB–RC–06 had high corrosion rates. A routine maintenance and monitoring are recommended for these concrete decks to ensure the structural integrity of the bridges.

The crack width and crack density of the bridge decks were documented during the field inspections. The crack width ranged from 0.001 to 0.08 in., with bridges in Amarillo and Lubbock generally exhibiting greater crack widths. It was determined that bridges in Region 6 having higher crack densities. The surface crack mapping illustrates the distribution and severity of cracks in different regions.

4 LABORATORY TESTS

This chapter describes laboratory examinations and analysis conducted on reinforced concrete specimens that were obtained from TxDOT concrete decks. The aim of the experiments reported in this chapter was to assess the current condition of the concrete decks across the state and evaluate the effectiveness of corrosion mitigation techniques in protecting steel reinforcement from corrosive environment. The examinations carried out in this research were divided into three distinct categories. The initial set of experiments aimed to evaluate the quality of the concrete, including the pore distribution and calculation of the concrete strength. These tests included surface and bulk resistivity measurements, ultrasonic pulse velocity (UPV) analyses, and water absorption tests. The secondary set of testing focused on determining the diffusion of aggressive ions in the concrete, such as recording chloride concentration and measuring the level of carbonation at different depths of the concrete core specimens. The examinations performed for this purpose were potentiometric titrations and carbonation depth measurements. The final set of experiments carried out in this study aimed to evaluate the condition of the concrete reinforcing bars—both black rebar and epoxy-coated steel reinforcement. The tests conducted for the analysis of rebar were coating adhesion tests, and electrochemical impedance spectroscopies (EISs) were done to assess the durability of the steel reinforcement in concrete decks.

4.1 REINFORCED CONCRETE BRIDGE DECKS

For the given experiment, a specific procedure was followed to select core specimens extracted from concrete decks. Figure 4.1 shows flowcharts and procedures taken during the specimen selection. Concrete cores without any embedded rebar were selected for concrete resistivity measurements because steel is electrically conductive and can influence the applied voltage and current of the device. Therefore, reinforcing rebars affect the resistivity recordings and can cause erroneous interpretation of the quality of the concrete. AASHTO T358 (2015) and ASTM C1876 (2019) state that cores without any cracks or voids should be used for resistivity measurements. Therefore, core samples selected to use in surface and bulk resistivity examinations were without steel bars and visible defects. Note that the height of the core samples needed to be longer than 5.2 in. for surface resistivity measurements due to the size of the testing equipment, and it had to be longer than 3.75 in. for bulk resistivity recordings, according to ASTM C1876 (2019). Apart from the specimen height, the requirements for UPV testing were similar to those

for resistivity measurements; the cores should not have steel bars and visible defects. No specific requirements were provided for potentiometric titration, and the sample used in the experiment was concrete dust collected directly from the core specimens. The same concrete cores were used for carbonation depth measurements. However, the samples were required to be broken to measure the carbonation depth. From these specimens, the embedded reinforcing bars were also extracted for the purpose of conducting coating adhesion tests. Concrete cores containing rebar were preserved for EIS examination, while the remaining concrete specimens were used for the sorptivity test.

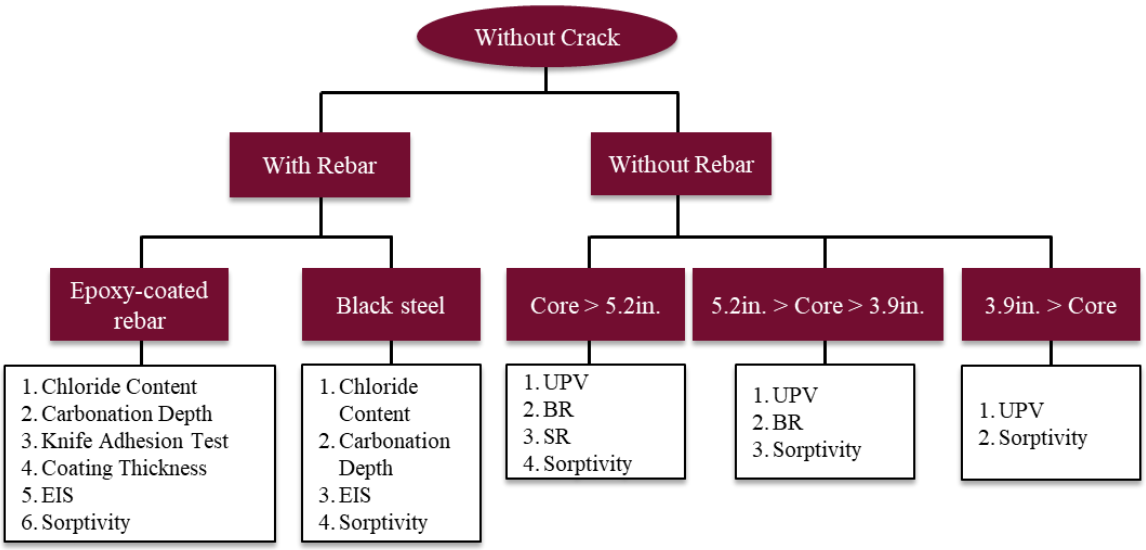

(a) Cores without Cracks

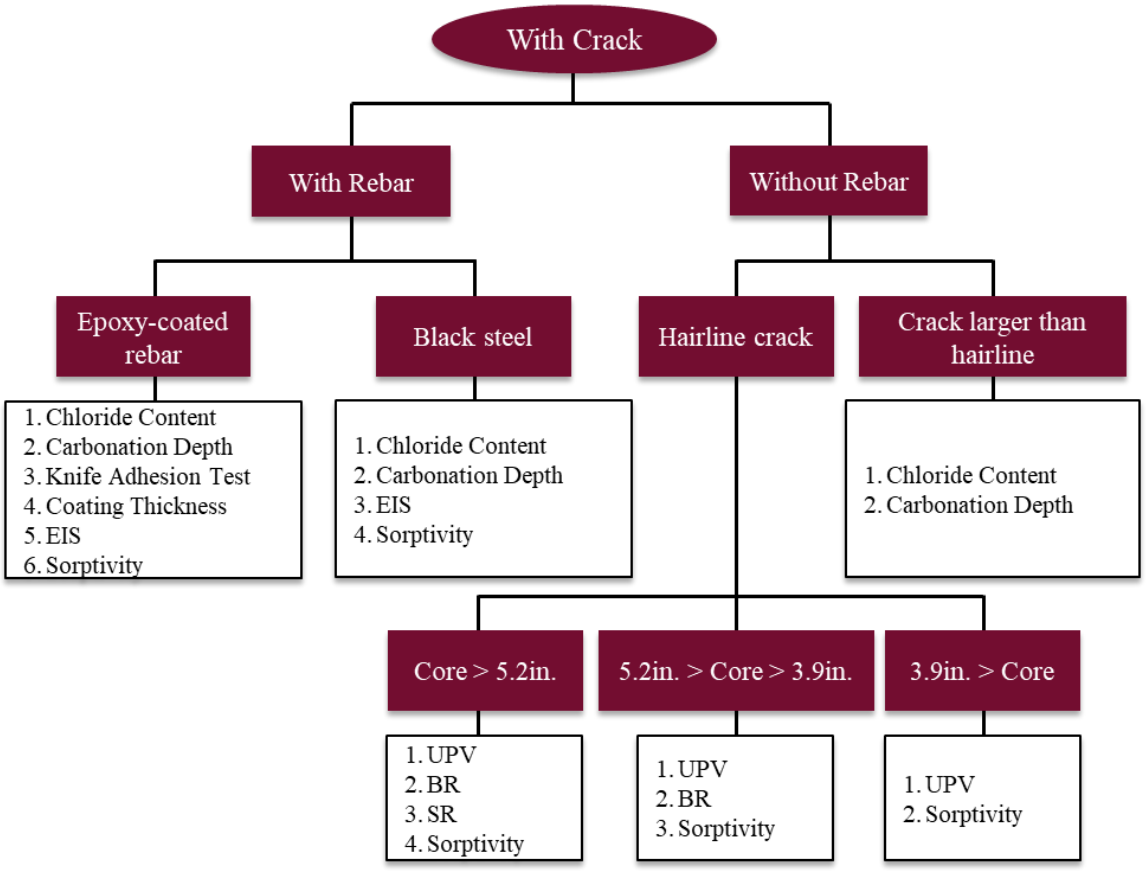

(b) Cores with Cracks

Figure 4.1. Selection of Laboratory Examinations Based on the Core Specimen Condition.

4.1.1 Surface Resistivity

Electrical resistivity of a core specimen indicates the resistance of the concrete to environmental loads, such as water permeability and chloride ion diffusivity. A higher resistivity indicates a greater capacity to resist environmental loads. In this study, it signified that concrete is more resistant to chloride ion penetration. In this research, surface resistivity and bulk resistivity were measured for core specimens taken from TxDOT concrete decks. The documented results are presented in this section and in more detail in the appendix.

Factors impact the electrical resistivity of a concrete sample, including the composition of the concrete admixture, the accumulation of chloride ions, and moisture content stored in vicinities and voids within concrete sample. The volume of water in concrete, which has a great relationship with resistivity, is directly influenced by the microstructure of the concrete, including the degree of void interconnection within cement products and the distribution of capillary pore sizes in cement paste.

The type of cement and the water/cement ratio (W/C) impact the size and pore structure in concrete. A finer pore network reduces the permeability of water, resulting in an increase in electrical resistivity (Layssi et al., 2015). Furthermore, an increase in RH causes a higher degree of saturation in concrete, leading to a larger volume of pore water and subsequently lower electrical resistivity. However, under constant RH, an increase in temperature can also contribute to a decrease in resistivity due to the change in mobility of ions in concrete. Using slag or fly ash in mixed designs results in finer pores and improves specimen resistivity. As the hydration process in cement process progresses, concrete becomes denser, leading to an increase in the electrical resistance of the material. This outcome is more evident for aged and air-dried concrete specimens. In addition, the incorporation of CNI, while elevating the chloride threshold level, might result in a reduction of concrete resistivity due to the higher diffusivity of chloride ions (K.-Y. Ann et al., 2006; K. Y. Ann & Buenfeld, 2007; Keller & Materials, 2001). Nevertheless, research by Abushanab and Alnahhal (2021) indicated that the addition of fly ash can enhance the resistivity of concrete with CNI. For a corrosion inhibitor to be fully effective, it has been recommended to add silica fume or fly ash to the concrete mix, which allows the concrete pore structure to be denser and more resistant to chloride penetration. Nonetheless, limited information is available regarding the impact of calcium nitrite on chloride transport.

Table 4-1 shows some major parameters influencing the electrical resistivity of concrete (Luca Bertolini et al., 2013; Beushausen & Luco, 2015).

Table 4-1. Factors Affecting Resistivity of Concrete.

Factors	Parameters	Relationship with resistivity
Environmental condition	RH	Inverse
	Temperature	Inverse
Chemical attack	Chloride	Inverse
	Carbonation	Direct
	Sulfate	Inverse
Concrete composition	Slag or fly ash	Direct
	W/C	Inverse
	Aggregate content	Direct
	CNI	Inverse
Time	Exposure time	Direct

4.1.1.1 Experimental Setup

As in AASHTO T358 (2015), a 4-point Wenner array probe was employed to measure surface resistivity of concrete specimens (Figure 4.2). The device consisted of four probes: two outer probes that applied an alternating current ranging from 50 μA to 200 μA to the concrete sample, and two inner probes that recorded the corresponding electrical potential. After recording the electrical potential, the surface resistivity of a semi-infinite region was calculated as follows:

$$\rho = 2\pi a \frac{V}{I} = 2\pi a R \tag{4.1}$$

where ρ is the resistivity of the concrete in Ω m; a is the distance between the electrodes; V is the applied voltage between two potential measurement electrodes; R is the specimen impedance (Ω); and I is the applied current. Note that because the diameter of the concrete core was much greater than the probe distance, a geometry correction factor had to be applied to the results recorded for surface resistivity.

Figure 4.2. Measurement of Surface Resistivity Using 4-point Wenner Array Probe.

Cheytani and Chan (2021) monitored surface resistivity of concrete cores immersed in water in different time periods. The authors observed that surface resistivity of specimens remains almost constant after 48 hours of saturation, and minimal change was recorded for the electrical resistivity of the specimens. Thus, researchers in this study made the decision to immerse the concrete samples in water at room temperature for 2 days.

Surface resistivity was measured on cores with both cast-in-place (CIP) and PCP concrete. The testing equipment had 5.2 in. between outer probes, while the CIP portion of concrete was sometimes shorter than that. Thus, specimens lower than that height could not be used for surface resistivity examinations.

The procedure taken for the surface resistivity test is as follows:

1. Mark the top and circumference of the sample at 0, 90, 180, 270 degrees (Figure 4.3).
2. Submerge the concrete samples in water for a period of 48 hours.
3. Ensure that the temperature of the solution (water) remained within the range of 68 to 77°F.
4. After removing the specimen from the water, wipe the surface of the sample while also ensuring that the surface remains in a wet condition.
5. Place 4-point Wenner array probe on the longitudinal side of the sample, aligning it with the zero-degree-mark.

6. Ensure that the center mark on the specimen is positioned at the center of two inner probes, and monitor concrete resistivity until the reading becomes stable.
7. Rotate the sample and repeat Steps 4 and 5 at 90, 180, 270 degrees.
8. Repeat Steps 3 to 7 for each sample and calculate the average surface resistivity according AASHTO T358.

Figure 4.3. Concrete Core Specimen with Marks at 0 and 90 Degrees.

4.1.1.2 Experimental Results

Figure 4.4 shows the recorded results of surface resistivity categorized based on similar or different corrosion mitigation methods implemented in concrete decks as well as similar or different corrosion risk environments. It was observed that the surface resistivity of core specimens decreased for the aging concrete deck. This result indicates an increase in the electrical connectivity of the concrete structures, which can be attributed to factors such as the volume of moisture and chloride content over time. The experimental results of surface resistivity were adjusted using a geometry correction factor, k_n, as recommended by AASHTO T358 (2015). This correction accounts for the dimensional variations of the concrete cores extracted from the structures and can be expressed as the following:

$$\rho_s = k_n R \tag{4.2}$$

where R is measured resistance, and k_n is the geometry correction factor. When both diameter and length of the specimen are smaller than six times the probe spacing ($d/a < 6$ and $L/a < 6$) or the cores are shorter than 9 in., correction factor k_1 should be used, as determined by the following equation:

$$k_1 = 1.10 - \frac{0.730}{\frac{d}{a}} + \frac{7.34}{\left(\frac{d}{a}\right)^2} \tag{4.3}$$

where d is the diameter of the core, and a is the probe spacing. Another correction factor (k_2) should be considered when the height of a core is larger than five times the probe spacing or greater than 9 in. It can be determined as follows:

$$k_2 \cong \frac{2\pi}{1.09 - \frac{0.527}{\frac{d}{a}} + \frac{7.34}{\left(\frac{d}{a}\right)^2}} \tag{4.4}$$

Figure 4.4 has also been classified based on the corrosion mitigation methods applied on concrete decks. The mitigation methods used in TxDOT bridges include CNI, concrete surface treatments (LO, SI, and CST[LO/SI]), ECR, HPC, and HPCF. Note that it is common practice to implement a combination of these mitigation methods on the concrete deck to minimize the risk of corrosion. Therefore, 12 classes of mitigation methods were identified and studied to evaluate the effectiveness of these methods in preventing corrosion.

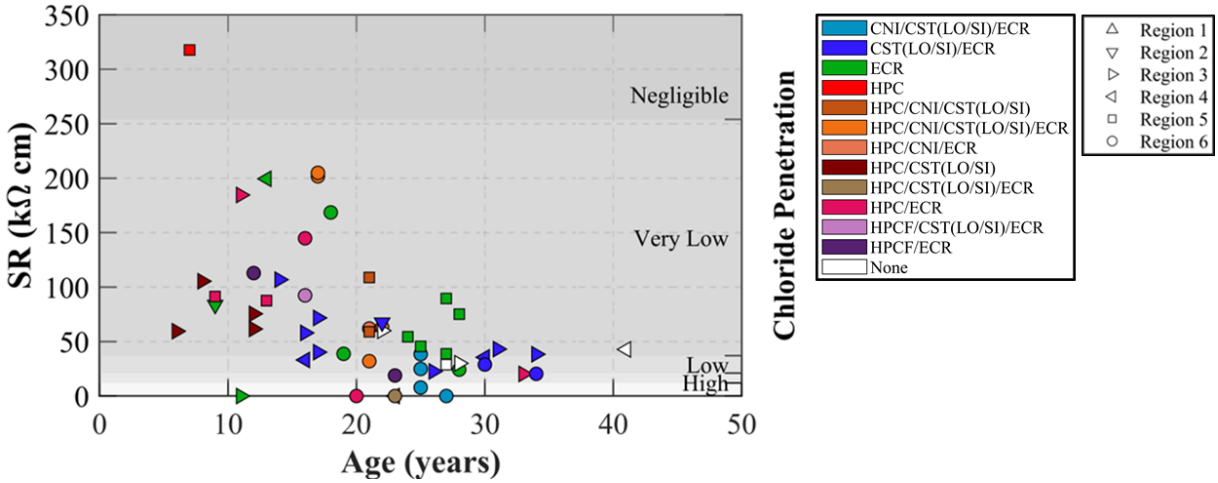

Figure 4.4. Surface Resistivity Recorded for Concrete Core Specimens.

The results shown in Figure 4.4 are further categorized based on the corrosivity level of the environmental risk, which ranges from low-risk environments to high-risk environments. As shown in Figure 4.4, the surface resistivity decreases over time from Region 1 to Region 6.

Another classification used in Figure 4.4 is based on chloride ion penetration, as recommended by AASHTO T358 (2015) (Table 4-2). According to this classification, if the surface resistivity of a concrete specimen measures lower than 12 kΩ cm, it indicates a relatively high concentration of chloride ions in the sample. When the resistivity falls between 12 kΩ cm to 21 kΩ cm, the level of chloride penetration in the concrete specimen is considered moderate. If the resistivity is 21 kΩ cm or greater, it suggests a low concentration of chloride ions in concrete specimens.

Table 4-2. Penetration of Chloride Ions in Concrete (AASHTO T358, 2015).

Chloride Ion Penetration	Surface Resistivity Results (kΩ cm)
High	<12
Moderate	12–21
Low	21–37
Very Low	37–254
Negligible	>254

Figure 4.5 illustrates the surface resistivity of concrete core specimens extracted from TxDOT concrete decks with varying ages of construction. In low corrosion risk environments such as Region 1 and Region 2, the surface resistivity of the concrete samples (ATL–RC–05 and TYL-EC-03) was greater than 50 kΩ cm, indicating a low concentration of chloride ions in the specimens. However, as the environment became more corrosive, the surface resistivity gradually decreased below 37 kΩ cm over time, which suggests that the volume of moisture absorbed in concrete decks was higher for older bridges.

In Region 6, which represents a severe corrosion risk environment, the surface resistivity of samples aged over 25 years fell into the moderate and high categories of chloride ion penetration. This finding indicates that corrosion issues might have emerged in the bridge decks located in this region (AMA–RC–05, LBB–RC–04 and LBB–RC–06), and further investigation is needed to assess the extent of corrosion and its impact on the concrete structures.

The moisture and chloride content of the specimens taken from bridges aged less than 25 years for concrete decks located in Region 3, Region 4, and Region 5 and aged less than 20 years for concrete decks located in Region 6 were estimated to be low; surface resistivity was recorded above 37 kΩ cm for most of these specimens except for FWT–RC–07 in Region 4, which had a lower surface resistivity reading.

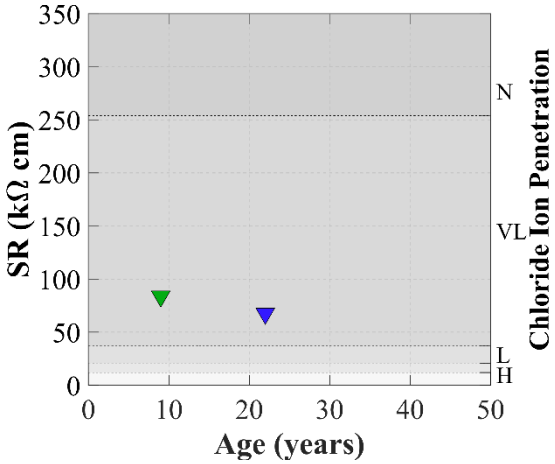

(a) Region 1 and Region 2

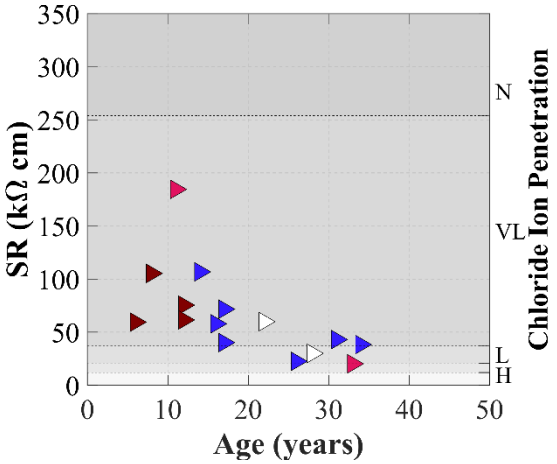

(b) Region 3

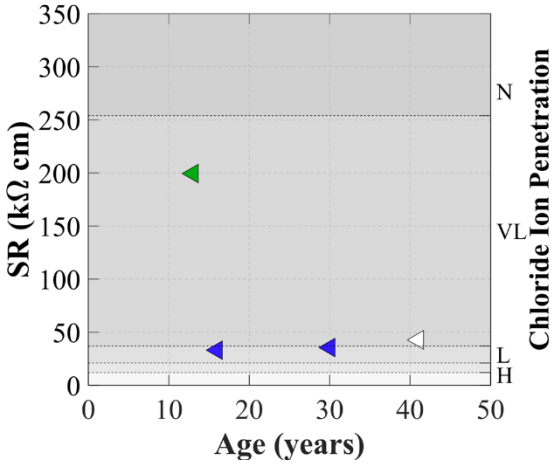

(c) Region 4

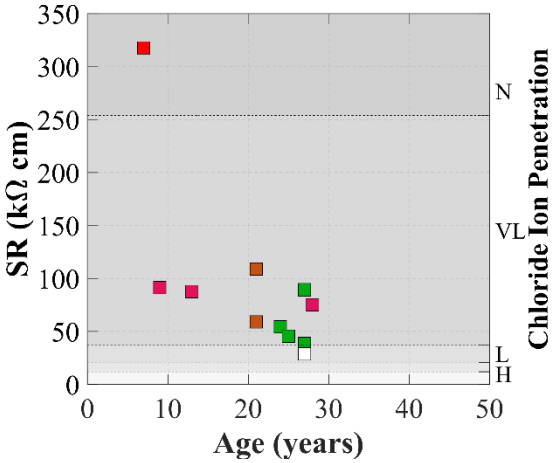

(d) Region 5

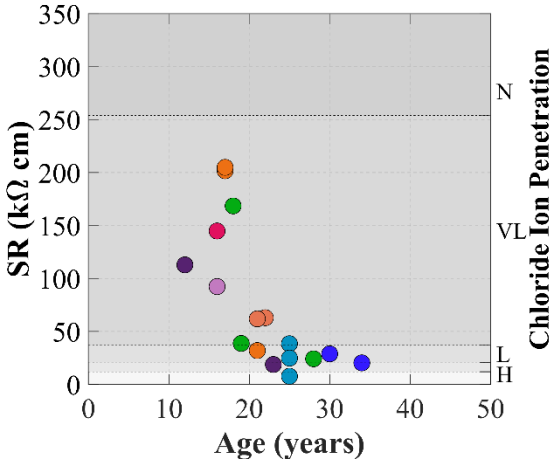

(e) Region 6

Figure 4.5. Surface Resistivity Measured for Aged Concrete Specimens Based on Different Corrosion Risk Environments.

Figure 4.6 shows the surface resistivity measurements obtained from concrete specimens taken from each individual bridge inspected in this study. The surface resistivity could not be recorded on the core specimens obtained from ATL–RC–02 and ATL–RC–07 because of their shorter length or because of the presence of embedded steel bars.

In Region 3, the surface resistivity recorded for specimens from the El Paso District indicates that, except for ELP–RC–03 and ELP–RC–06, the concrete decks of other bridges were in good condition. FTW–RC–05, in the Fort Worth District, showed low resistivity. The remaining samples exhibited high resistance, with ATL–RC–04 recording a surface resistivity higher than 150 kΩ cm, indicating a very good condition for that concrete deck and low moisture and chloride contents.

In Region 4, the resistivity of the specimen taken from ATL–RC–03 was relatively high, exceeding 150 kΩ cm. However, the resistivity of the other specimens taken from different Atlanta and Fort Worth concrete decks averaged below 50 kΩ cm, but the measured resistivity was still higher than 20 kΩ cm. The surface resistivity recorded from BMT–RC–01, located in Region 5, was relatively high, exceeding 200 kΩ cm, implying that concrete deck was in very good condition. Except for WFS–RC–07, which falls into moderate territory, the moisture content and chloride content in the concrete decks of most bridges in this region are expected to be low. In Region 6, the surface resistivity of the sample from AMA–RC–05 measured lower than 12 kΩ cm, indicating a high concentration of moisture and chloride ions in the concrete deck. Similar behavior was observed in resistivity results recorded for specimens taken from LBB–RC–04 and LBB–RC–06.

The corrosion mitigation methods employed in the bridge decks did not appear to have a significant effect on the surface resistivity results. For example, surface resistivity measured from CHS–RC–01, CHS–RC–05, and CHS–RC–06, which did not have a CNI in the concrete admixture, was similar to CHS–RC–02 having a CNI in the concrete deck. Similarly, CST(LO/SI) was applied to some bridges in Fort Worth, but apart from FTW–RC–02, the surface resistivity of concrete decks for these bridges was similar. Therefore, it cannot be concluded that the mitigation methods effectively altered long-term surface resistivity of the concrete deck.

Surface resistivity is a useful indicator of the resistance of bridge decks to moisture and water permeability in concrete structures. However, studying the surface resistivity alone may not provide a complete understanding of the overall condition or performance of concrete decks, and

additional tests and assessments are required. Therefore, surface resistivity, though a valuable parameter, should be considered alongside other relevant factors when evaluating the overall performance of bridge decks.

More details on the surface resistivity and the potential for moisture and chloride penetration in each concrete core specimen are provided in the appendix.

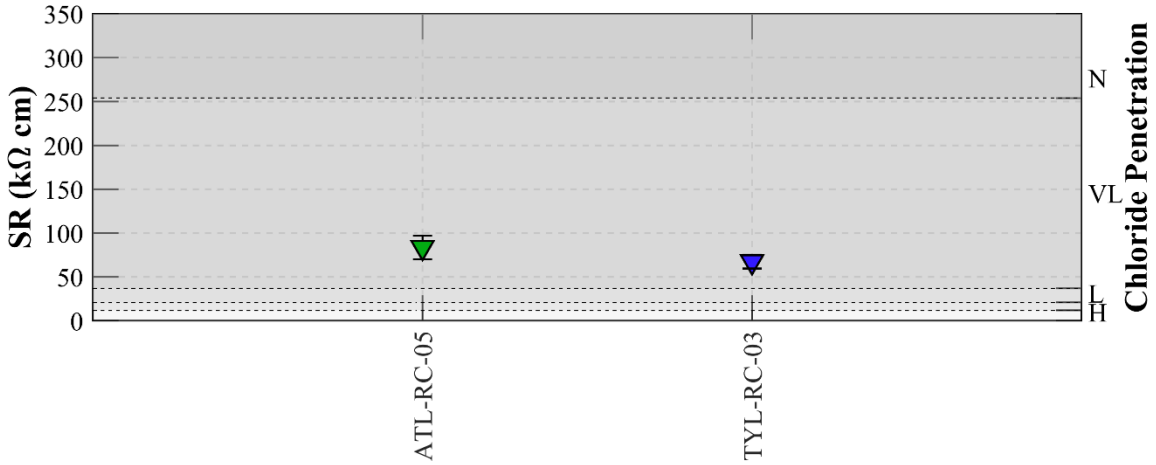

(a) Region 2

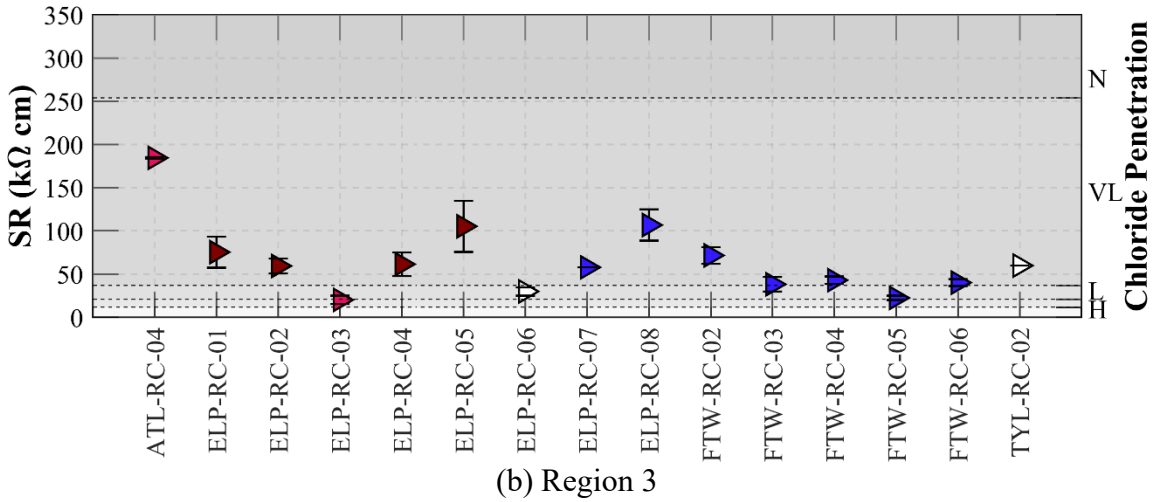

(b) Region 3

Figure 4.6. Surface Resistivity Measured for Concrete Bridges.

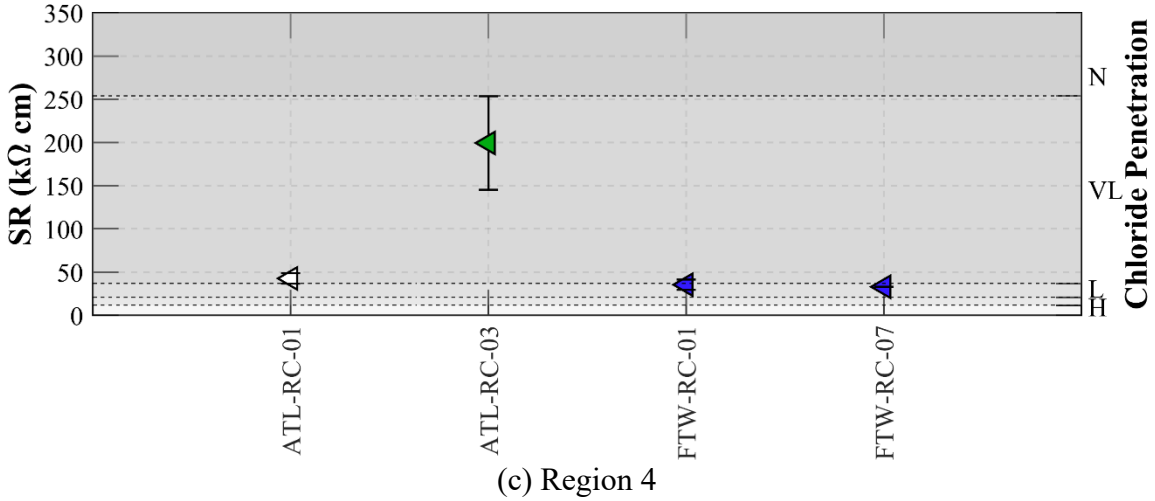

(c) Region 4

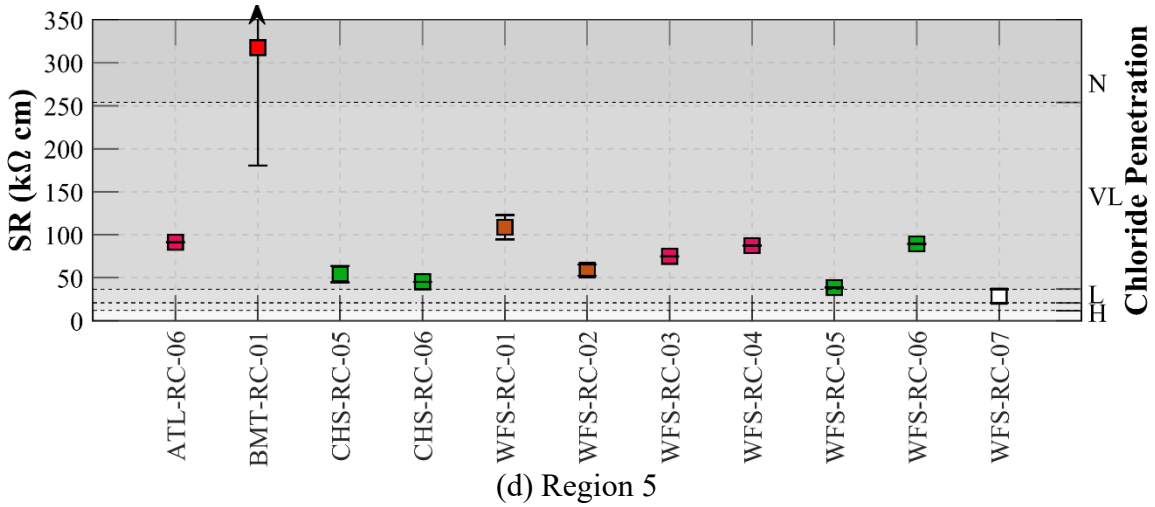

(d) Region 5

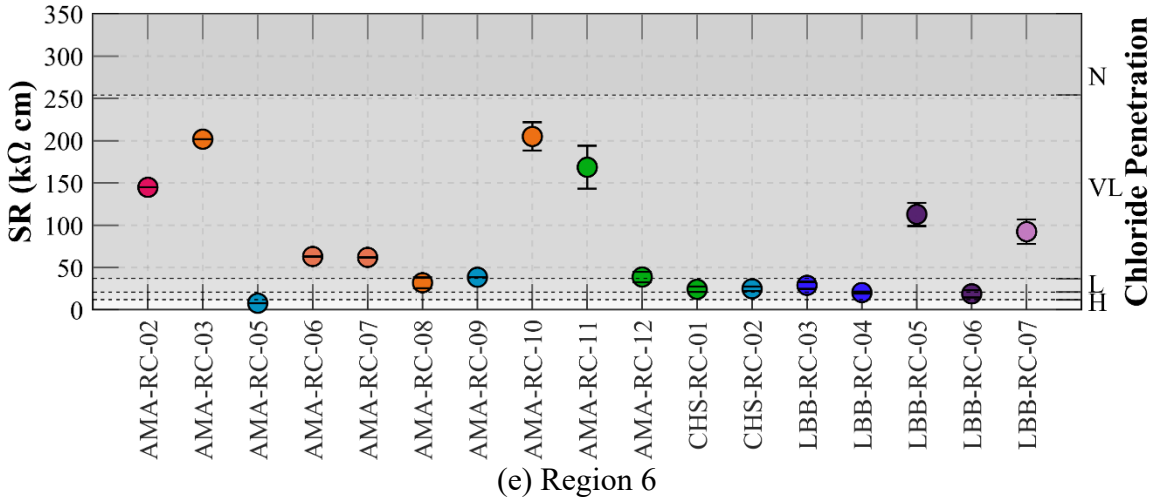

(e) Region 6

Figure 4.6. Surface Resistivity Measured for Concrete Bridges (Cont.).

4.1.2 Bulk Resistivity

Another commonly used resistivity examination method is bulk resistivity measurements. This method can be utilized to evaluate concrete durability, permeability, and chloride diffusivity. Bulk resistivity measurements involve using plate electrodes positioned on the top and bottom ends of the sample and measuring the electrical resistance of the core specimen. Similar to the surface resistivity measurements, the experimental results must be adjusted for the geometry of the sample after recording the electrical resistivity of the sample. Note that a uniformly distributed current is applied throughout the concrete bulk during this examination, whereas surface resistivity testing involves taking measurements on the side surface of the specimen.

4.1.2.1 Experimental Setup

The examination began by sawing cores at the intersection of CIP and PCP. The length-to-diameter ratio of the core specimens should be at least 1:1, as specified in ASTM C1876 (2019). Additionally, some of the core specimens extracted from the concrete decks had grooves on the top and unevenness on the bottom surface. Consequently, the core samples were processed using an electrical saw, which involved sawing and grinding the concrete top and bottom faces to obtain flat and even surfaces.

The apparatus shown in Figure 4.7 was utilized to measure the bulk resistivity of the concrete cores, as depicted in ASTM C1876 (2019). The examination was carried out by employing a Giatec RCON™ device to apply a voltage between two electrodes positioned at the top and bottom faces of the sample and subsequently recording the resistance of the core. Bulk resistivity, ρ, represents the resistivity of a concrete sample to the flow of electric current:

$$\rho_b = R\frac{A}{L} \tag{4.5}$$

where L is average specimen length (m); A is the specimen cross-sectional area (cm^2); and R is specimen impedance (Ω).

Figure 4.7. Apparatus Used in Bulk Resistivity Measurements.

Spragg et al. (2013) reported that electrical resistivity can be affected by several factors, including specimen geometry, degree of saturation, testing temperature, and age of the specimen. To ensure reliable results, all parameters were kept constant except for the age of the specimens.

The procedure taken to determine the bulk resistivity of concrete specimens is as follows:

1. Record the cross-sectional areas and heights of specimens.
2. Submerge the samples in a twenty-liter bucket with simulated pore solution (lime water) for at least 6 days. Note that the temperature of the solution is kept at 23.0 ± 2.0°C.
3. Remove specimens from container, remove excess liquid, and place them in device.
4. Saturate conductive sponges and place them between the specimen and the top and bottom electrodes.
5. Document the resistivity of the sample.

4.1.2.2 Experimental Results

Figure 4.8 illustrates the recorded bulk resistivity measurements of concrete cores extracted from TxDOT concrete decks; they show a similar trend to surface resistivity, with a general reduction in resistivity over time. This decrease indicates a surge in the electrical connectivity of the concrete structures that can be attributed to factors such as an increase in volume of moisture and chloride content over time. The bulk resistivity recordings in Figure 4.8 are organized based on different corrosion risk environments and corrosion mitigation methods.

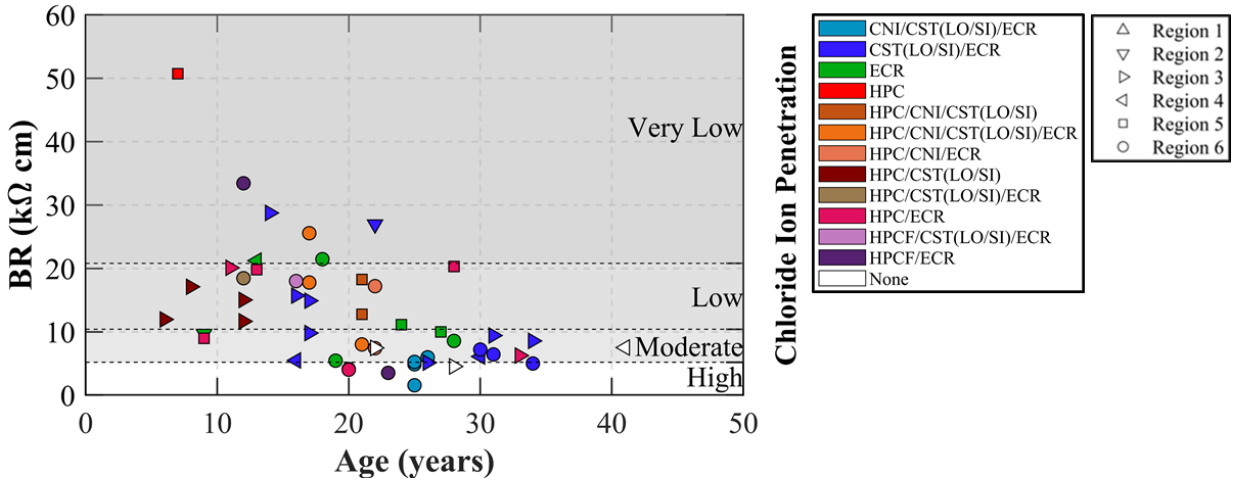

Figure 4.8. Bulk Resistivity Recorded for Concrete Core Specimens.

Because the dimensions of the core specimens were not similar, the recorded bulk resistivity of specimens (ρ_b (kΩ cm)) was adjusted using the modification factor that follows:

$$\rho_b = k \cdot Z_c \tag{4.6}$$

where k (cm) is the geometry factor, and Z_c (kΩ) is the measured impedance of the concrete. The geometry factor of a cylindrical core can be expressed in terms of A, which is the cross-sectional area (cm^2), and L, which is the height of concrete cores (cm):

$$k = \frac{A}{L} \tag{4.7}$$

Table 4-3 provides a classification of the chloride ion penetration in concrete based on the study by Spragg et al. (2013). The range of resistivity measurements can be used as an indication of the chloride content in concrete specimens. Higher resistivity values generally indicate lower chloride content, while lower resistivity values suggest a higher presence of chloride ions in the specimen. According to Neville (1995), it is widely accepted that a resistivity higher than 10 kΩ cm indicates a lower amount of water in a moist concrete specimen and particularly indicates a lower W/C. This element aligns with the classification provided in Table 4-3, wherein chloride ion penetration in concrete above 10.4 kΩ cm is considered to be low.

Table 4-3. Penetration of Chloride Ions in Concrete (Spragg et al., 2013).

Chloride Ion Penetration	Bulk Resistivity Results (kΩ cm)
High	<5.2
Moderate	5.2–10.4
Low	10.4–20.8
Very Low	20.8–207
Negligible	>207

Figure 4.9 illustrates the recorded bulk resistivity with respect to different corrosive risk environments. Generally, a declining trend of bulk resistivity over time was observed for the samples used in this study. In a low corrosion risk environment, such as Region 1 and Region 2, a sample taken from a relatively new concrete deck in the Atlanta District exhibited a low bulk resistivity, with an average resistivity level measured below 10 kΩ cm. However, other specimens extracted from concrete decks in the Tyler District that were in service for over 30 years displayed a relatively high bulk resistivity, exceeding 20 kΩ cm.

New concrete decks constructed in Region 3 within the last 2 decades exhibited a bulk resistivity higher than 10 kΩ cm, indicating the use of higher-quality concrete during bridge construction. However, decks constructed prior to that period displayed resistivity levels lower than 10 kΩ cm. It was concluded that the application of surface treatments on the top surface of the concrete deck did not show any improvement in bulk resistivity, indicating that the resistivity is primarily influenced by factors such as the concrete mix design and W/C used during construction. With the exception of ATL–RC–03, the average bulk resistivity of concrete specimens taken from structures in Region 4 was generally less than 10 kΩ cm.

A declining trend in bulk resistivity was observed for samples extracted from concrete decks in both Region 5 and Region 6. The bulk resistivity dropped to 5 kΩ cm regardless of the mitigation method employed for bridges in Region 6 for structures over 20 years old. However, as previously discussed, this result can be attributed to factors such as the concrete admixture and mixed design. The concrete used in TxDOT bridge decks has become denser in the past 2 decades, resulting in higher resistivity values.

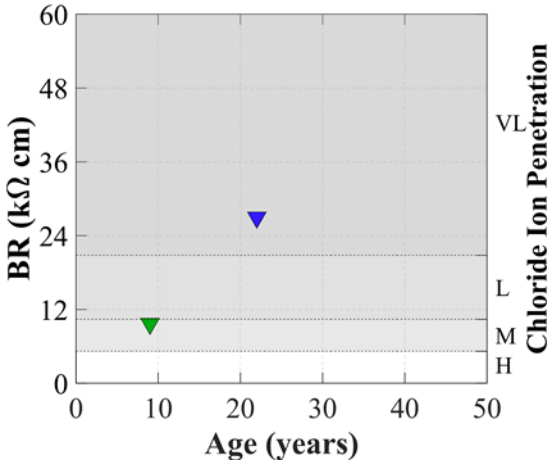

(a) Region 1 and Region 2

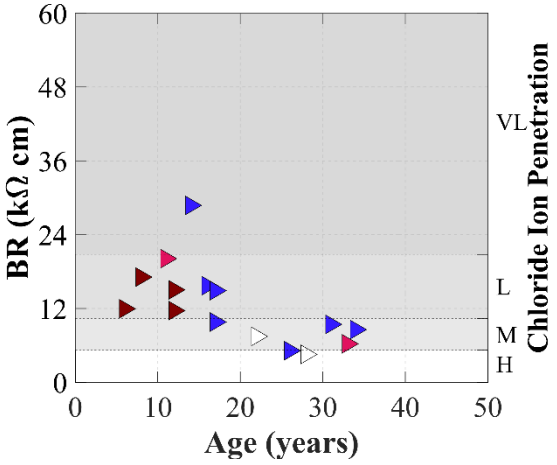

(b) Region 3

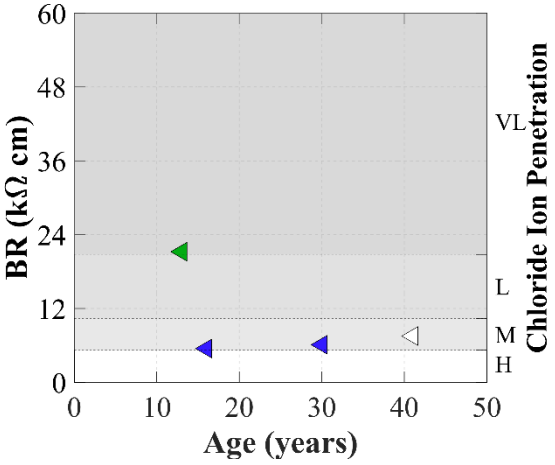

(c) Region 4

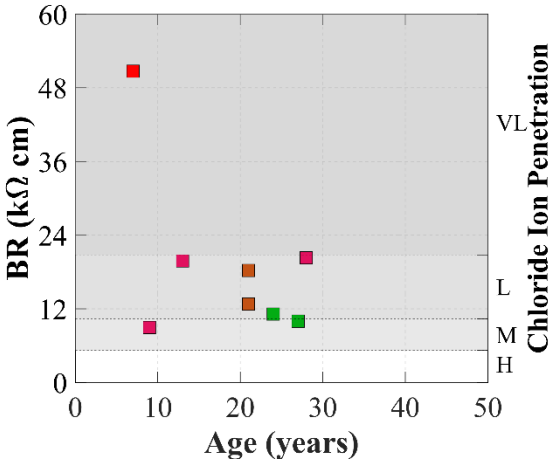

(d) Region 5

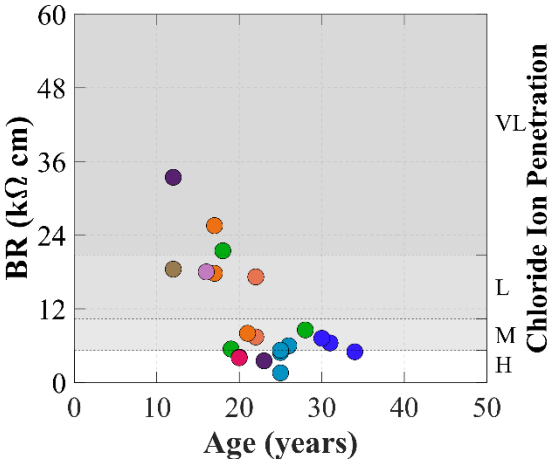

(e) Region 6

Figure 4.9. Bulk Resistivity Measured for Aged Concrete Specimens Based on Different Corrosion Risk Environments.

The recorded bulk resistivity of concrete core specimens provides a valuable insight into the quality of concrete decks when compared to the results recorded for surface resistivity. This finding is due to the longer time duration of saturation required for the bulk resistivity examination. It was concluded that aged concrete typically requires more time to reach full saturation, and therefore the time duration specified in the standards must be increased for the aged specimens.

Figure 4.10 depicts the bulk resistivity recorded for each core specimen. ELP–RC–03, ELP–RC–06, and FTW–RC–05 exhibited low bulk resistivity, even lower than 5 kΩ cm, indicating poor concrete quality. These bridges are located in Region 3, which is classified as a moderate corrosion environment. Thus, further investigation is recommended into the concrete decks of these bridges. The recorded bulk resistivity of FTW–RC–03, FTW–RC–04, and FTW–RC–06 was higher than 5 kΩ cm but lower than 10 kΩ cm, suggesting a poor-quality concrete used in the decks. The estimated chloride content in those concrete decks is considered moderate. In Region 4, the average bulk resistivity of ATL–RC–05 was higher than 20 kΩ cm, indicating good concrete quality. However, the average bulk resistivity was relatively low for ATL–RC–01, FTW–RC–01, and FTW–RC–07, measuring around 5 kΩ cm.

In highly corrosive environments such as Region 5 and Region 6, the bulk resistivity generally appeared to be low due to factors such as the extensive use of deicing salt during winter or airborne chloride deposition. In Region 5, the resistivity of the newly constructed bridge structure (BMT–RC–01) was found to be relatively high, indicating the use of concrete with a low W/C. In contrast, the average bulk resistivity of the newly built bridge (ATL–RC–06) was less than 10 kΩ cm. Additionally, WFS–RC–05 and WFS–RC–07, also located in Region 5, showed resistivity lower than 10 kΩ cm. Most specimens extracted from the concrete decks of bridges in the Amarillo District exhibited a low bulk resistivity except for AMA–RC–03, AMA–RC–07, AMA–RC–10, and AMA–RC–11. The electrical resistivity of all concrete specimens obtained from concrete decks in Childress was lower than 10 kΩ cm, and the same was observed for samples taken from structures in Lubbock except for LBB–RC–02, LBB–RC–05, and LBB–RC–07. Among all the specimens examined in this study, the bulk resistivity of AMA–RC–05 was particularly low, indicating a very poor condition of the concrete deck.

Note that similar to the surface resistivity examination, it was not possible to conduct the experiment on all core samples due to limitations in measuring electrical resistivity. Bulk resistivity can only be accurately measured on core samples that meet specific criteria, such as

limited surface defects and lack of embedded steel reinforcement. As a result, the decision was made to exclude certain core specimens from the electrical resistivity measurements if the sample did not meet the standard requirements. Examples of these specimens include AMA–RC–01 and ATL–RC–02. For detailed information on resistivity measurements, the reader is referred to the appendix.

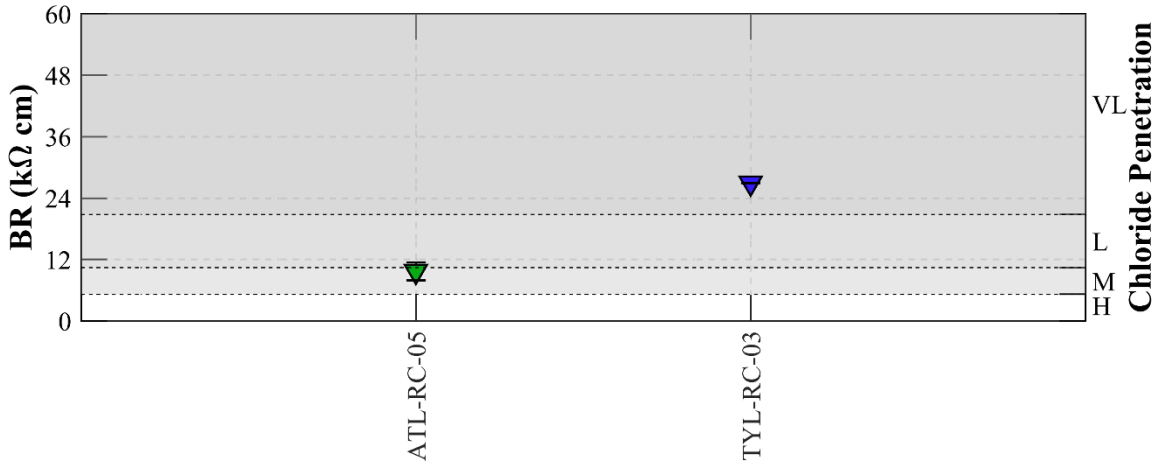

(a) Region 2

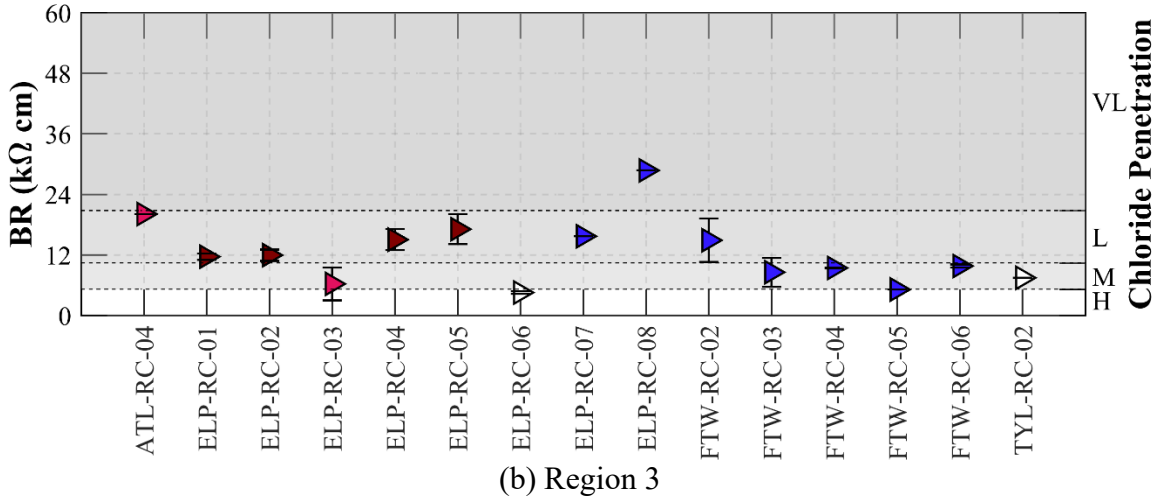

(b) Region 3

Figure 4.10. Bulk Resistivity Measured for Concrete Bridges.

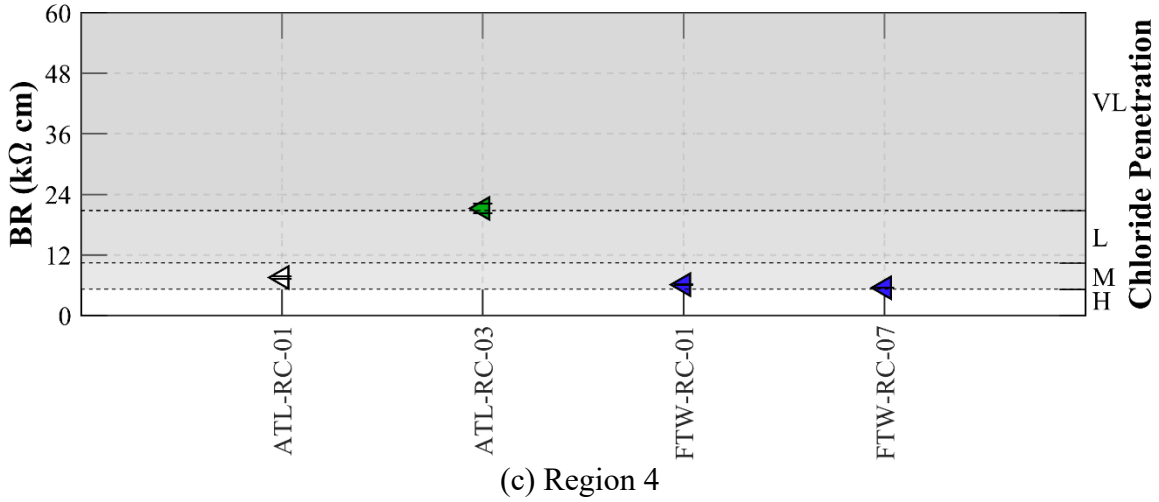

(c) Region 4

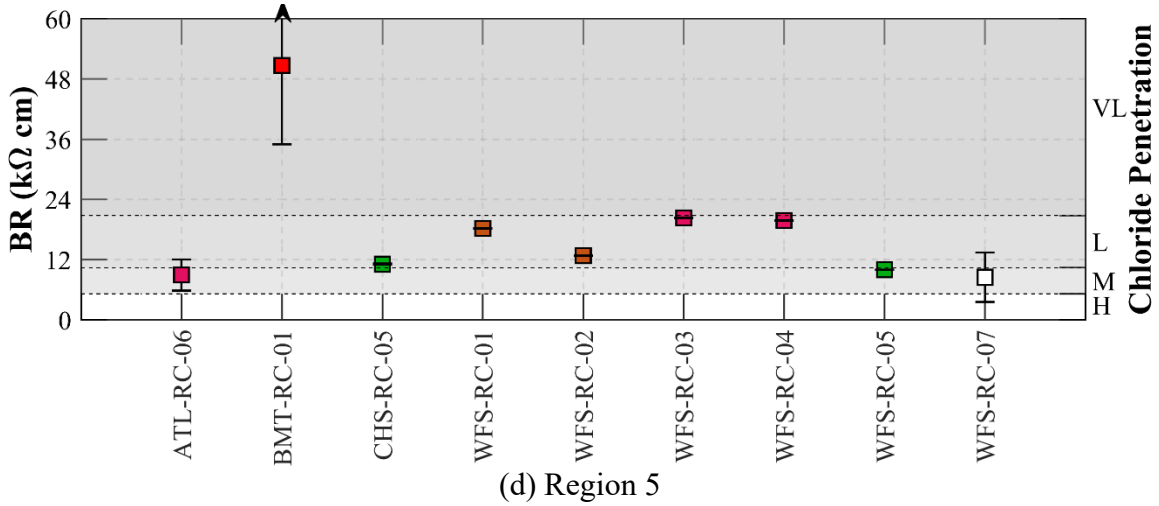

(d) Region 5

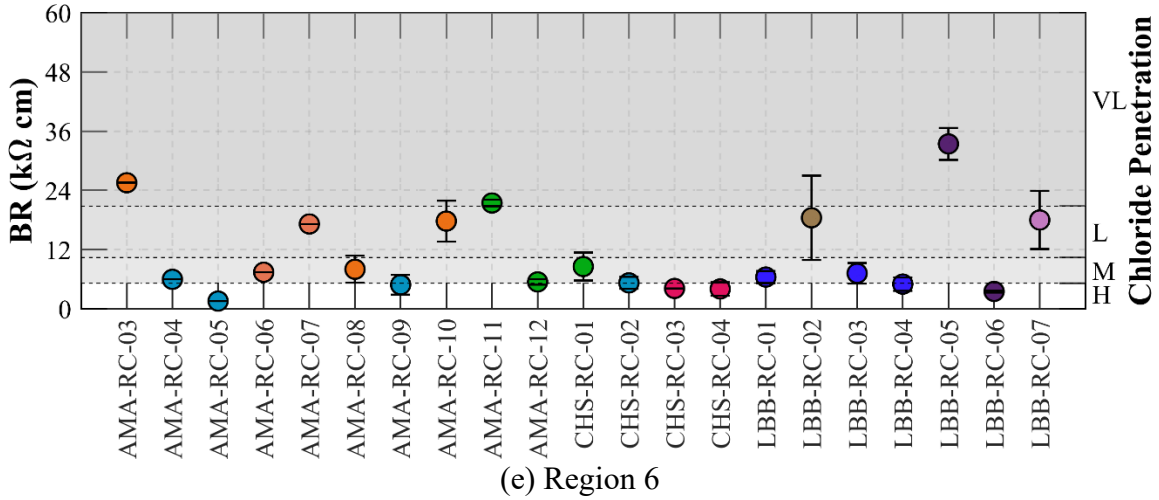

(e) Region 6

Figure 4.10. Bulk Resistivity Measured for Concrete Bridges (Cont.).

Figure 4.11 shows the correlation between surface resistivity and bulk resistivity. Although surface resistivity recordings were generally higher than bulk resistivity recordings, a positive correlation of 0.92 was observed between the two sets of measurements. As discussed earlier, a sufficient time duration of saturation for aged concrete is essential so that a fully saturated condition is maintained during the test. Therefore, further studies are recommended to refine the procedure outlined in AASHTO T 358 for the surface resistivity examination.

The analysis of electrical resistivity data from both surface and bulk resistivity examinations revealed a consistent trend of decreasing resistivity in the core specimens over time. The newly constructed bridge BMT–RC–01 in the Beaumont area exhibited high electrical resistivity despite the fact that the bridge deck is located in a highly corrosive coastal region of Texas. In addition, based on the results of both examinations, it can be concluded that the bridge decks in the Amarillo, Childress, and Lubbock Districts are expected to have higher moisture content and potentially increased chloride ion ingress. Particularly, the concrete deck of AMA–RC–05 was found to be in poor condition based on the experimental results.

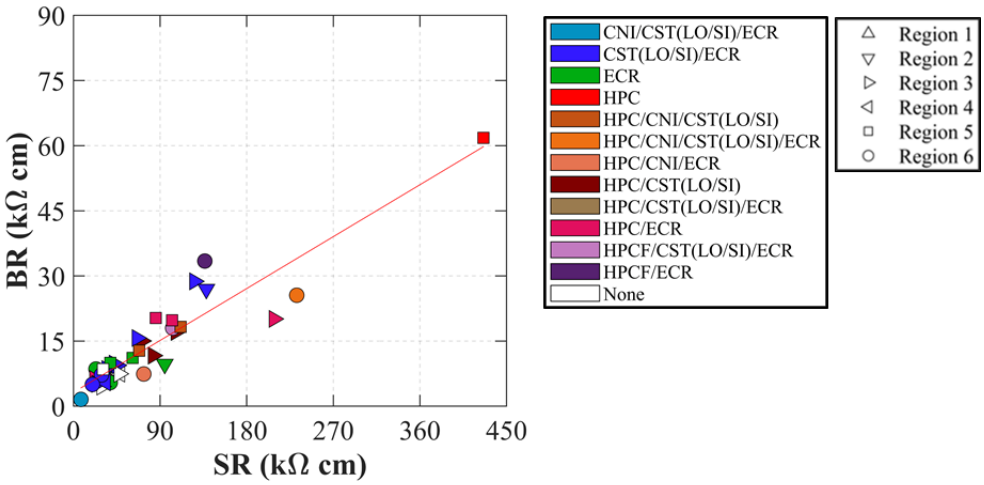

Figure 4.11. Correlation between Bulk Resistivity and Surface Resistivity.

4.1.3 Ultrasonic Pulse Velocity Test (ASTM C 597)

A nondestructive technique that can be used for quality control of concrete specimens is a UPV test. In this approach, a pulse wave is sent through the core sample, and the elapsed time taken for the sound waves to travel from the transmitting probe to the receiving probe is recorded. The speed of the traveling wave in the concrete specimen then can be studied to identify defects

such as voids and deep cracks. The speed of a longitudinal wave (V) in concrete is influenced by material properties such as density (ρ) and modulus of elasticity E, as follows:

$$V = \sqrt{\frac{E(1-v)}{\rho(1+v)(1-2v)}} \tag{4.8}$$

Neville (1995) stated that Poisson's ratio (v) of a concrete specimen is not a known value, and it can introduce an error of about 11 percent in the calculations of Young's modulus. Additionally, there is no physical relation between the strength of concrete specimens and UPV; particularly for aged concrete samples, there is no widely accepted experimental equation to estimate compressive strength from Young's modulus. Therefore, the decision was made to not calculate the modulus of elasticity for specimens taken from concrete decks.

4.1.3.1 Experimental Setup

As depicted in ASTM C597 (2016), UPV testing was performed on core specimens taken from TxDOT concrete decks. The apparatus needed for UPV examination is shown in Figure 4.12. To transmit and receive signals, Pulser/Receiver Panametrics 5072PR was utilized in transmission mode, in addition to a damping resistor of 200 Ω and a pulse repetition frequency (PRF) of 500 Hz. The cutoff points for the low pass filter were set at 10 MHz, while the cutoff points for the high pass filter were set at 1 MHz. A Tektronix-TDS 3034 digital storage oscilloscope was used to visualize the time-variant signals. The height of the core specimens varied between 1.6 in. and 9.8 in.

The procedure taken for UPV examination is as follows:

1. Saw and grind the surfaces of the specimens to obtain a flat surface.
2. Document the height and cross-sectional area of the core samples.
3. Apply couplant (ultrasonic gel) to both faces of the testing specimen.
4. Position transducers and initiate the measurements.
5. Record the traveling time of sound waves to the nearest 0.1 ns.
6. Repeat Step 5 at least two more times.
7. Calculate the average velocity of the sound wave in concrete.

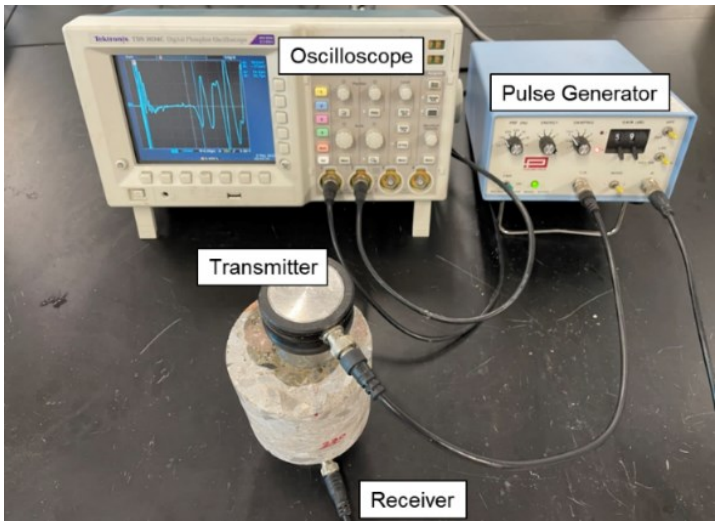

Figure 4.12. UPV Experimental Setup.

4.1.3.2 Experimental Results

The UPV examination is a suitable method for evaluating the condition and quality of concrete. It can be used to estimate the amount of water content in the sample and identify the presence of voids and deep cracks in concrete. In this examination, the velocity of the sound wave in concrete can be estimated by dividing the traveling distance (L) of the transmitting wave by the traveling time (T):

$$V = \frac{L}{T} \tag{4.9}$$

Cheesman (1949) proposed criteria for evaluating the quality of concrete based on the velocity of the sound wave. According to the author, if the velocity of the sound wave in concrete is higher than 11.8×10^3 ft/s, it indicates a good quality concrete with low water content, but if the velocity is less than 9.8×10^3 ft/s, it raises concerns about the condition of the concrete, suggesting higher water content or even the presence of cracks and voids in the concrete. Table 4-4 provides the mentioned criteria to estimate the quality of concrete samples based on the speed of a sound wave traveling in the specimen.

Table 4-4. Concrete Conditions Rating through UPV Values (Cheesman, 1949).

Condition	UPV (m/s)	UPV (ft/s)
Perfect	> 4500	> 14800
Good	3600–4500	11800–14800
Fair	3000–3600	9800–11800
Poor	< 2500	< 9800

Figure 4.13 shows the recorded velocities of sound waves in concrete specimens extracted from concrete decks in Texas. The UPV testing results were analyzed and classified according to different corrosion risk environments and corrosion mitigation methods. In general, the quality of concrete used in bridge decks was found to be in good or perfect condition, regardless of the bridge construction year. However, there were some exceptions to this trend. For example, three decks in Region 6 that utilized CNI in the mixed design were classified as being in fair condition.

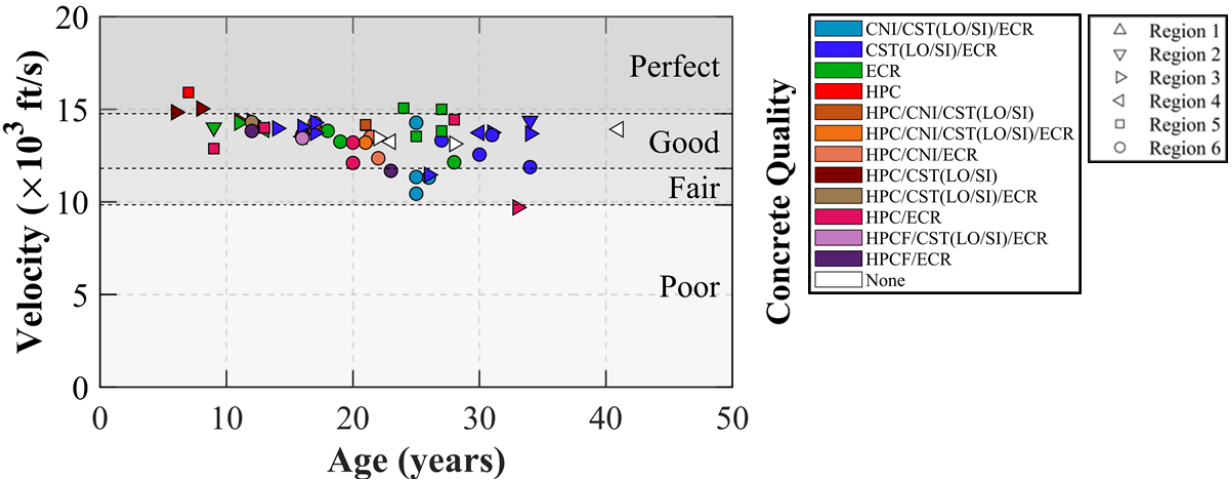

Figure 4.13. Velocity of Sound Wave in Concrete Specimens.

Figure 4.14 and Figure 4.15 show speed of sound waves measured in concrete specimens per region. Two bridges in Region 3 were identified as having poor-quality concrete. ELP–RC–03, which utilized HPC in its mixed design, was found to be in poor condition. This result highlights the need for additional investigation of the concrete deck, particularly considering that the bridge was constructed over 30 years ago. Similarly, FTW–RC–05, despite being relatively new compared to the El Paso bridge, was classified as being in fair condition.

In a low corrosive environment, UPV examination was carried out only on one core sample from the Atlanta area (ATL–RC–05). The lack of additional cores for testing in this environment was due to the limitations mentioned earlier, such as the presence of embedded steel bars in core specimens or the allocation of samples for other test measurements. ATL–RC–05 was constructed recently and made of regular reinforced concrete with embedded ECR. The quality of the concrete was estimated to be in good condition based on the velocity of the sound wave, which was measured to be approximately 14×10^3 ft/s.

In Region 3, except for ELP–RC–03 and FTW–RC–05, the quality of concrete in other samples was generally estimated to be in good or perfect condition. Particularly, the newly constructed HPC bridges exhibited perfect concrete quality. However, an older bridge constructed with HPC with embedded epoxy rebar showed poor concrete condition (ELP–RC–03). For bridges older than 15 years, bridge structures were mostly made of ordinary reinforced concrete with CST(LO/SI) applied on top of the bridge deck. Overall, most of these bridges were in good condition, with the exception of FTW–RC–05. In addition, all concrete decks located in Region 4 were found to be in relatively good condition. These structures were constructed with ordinary concrete reinforcement, and in some cases, CST(LO/SI) was applied to the deck of these bridges.

The quality of the concrete was estimated to be in good condition for the majority of concrete decks located in the highly corrosive environments of Region 5 and Region 6. In Region 5, most bridges were constructed using regular concrete, while some of them utilized embedded ECR. ATL–RC–06, a newly constructed concrete deck, was made of HPC with embedded epoxy. However, the UPV measurements for ATL–RC–06 showed that although the quality of the concrete was good, the velocity of the sound wave was slightly lower than other specimens obtained from different concrete decks in the region, which suggests that there may be some moisture diffusion in Atlanta's bridge structure.

The quality of concrete decks was generally identified to be in good condition in Region 6. However, there were a few exceptions. One of the concrete decks, LBB–RC–06, located in Lubbock, was classified as in fair condition. Another concrete deck, CHS–RC–04, located in Childress, was also classified as fair condition. The deck was constructed using HPC. Both structures have embedded ECR in their concrete decks. In Amarillo, three concrete decks were found to be in fair to poor condition—AMA–RC–07, AMA–RC–09, and AMA–RC–05—that were constructed using regular concrete with the addition of CNI in the concrete admixture. However, it was observed that the application of HPC and CST(LO/SI) in addition to the CNI resulted in increased resistance to moisture penetration in bridge structures located in the Amarillo District. Examples of such bridges are AMA–RC–03 and AMA–RC–07.

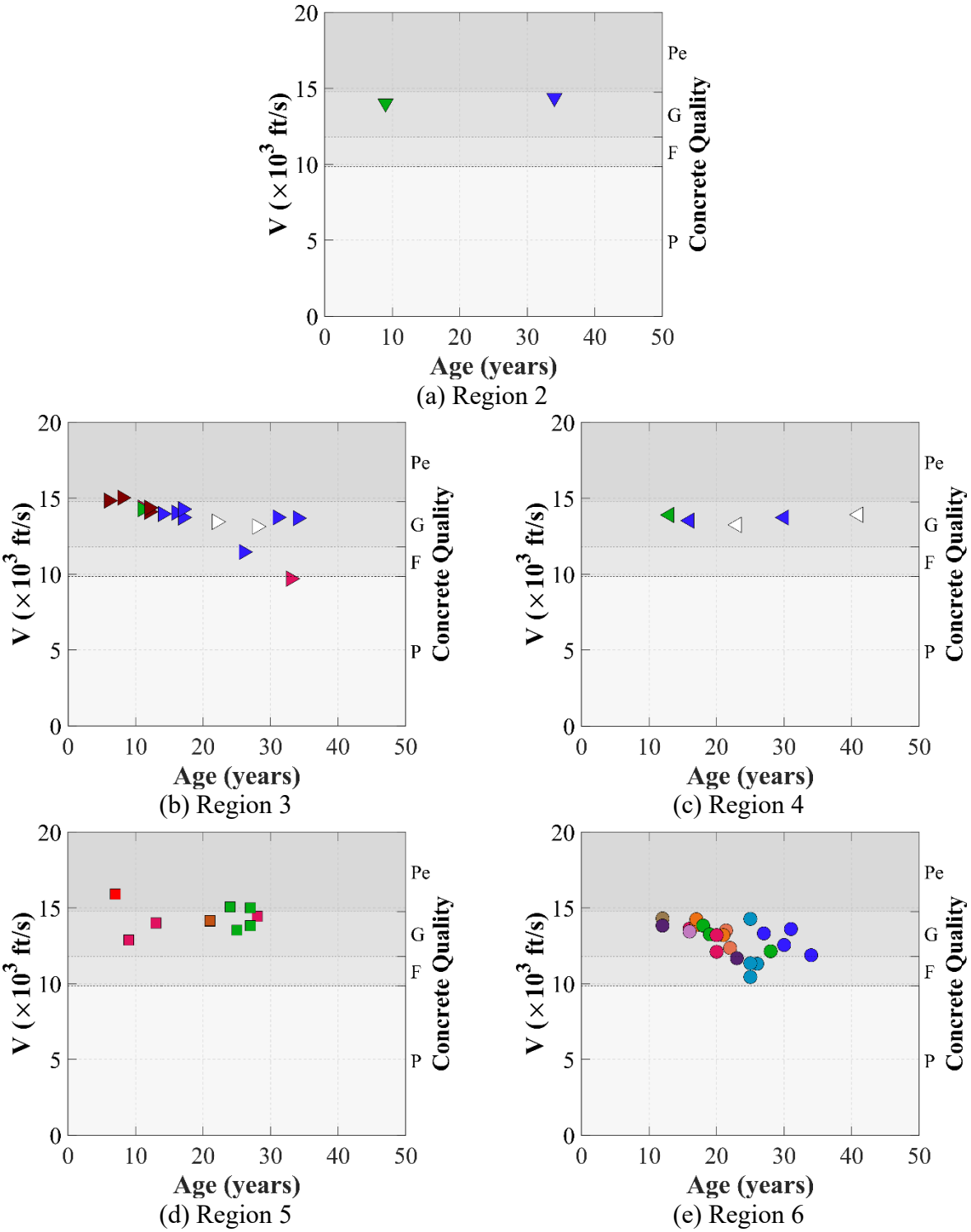

Figure 4.14. Recorded Sound Wave Velocity in Aged Concrete Specimens Based on Different Corrosion Risk Environments.

A comparison between resistivity testing results and UPV measurements reveals some similarity of findings between to tests (Figure 4.15). For example, if the velocity of the sound wave in the specimen extracted from the concrete deck was recorded as approximately lower than 10×10^3 ft/s, then the bulk resistivity was also recorded to be less than 10 kΩ cm on average, indicating poor quality of the concrete. In a medium corrosive environment, the bulk resistivity values of ELP–RC–03, ELP–RC–06, and FTW–RC–05 were very low, which aligns with the poor quality of the concrete, as indicated by UPV testing. Particularly, ELP–RC–03 failed both resistivity and UPV tests, confirming its poor quality.

In highly corrosive environments, the bulk resistivity of core specimens extracted from ATL–RC–06 and WFS–RC–05 was relatively low. These specimens were classified as being in fair and good condition based on the UPV measurements. For BMT–RC–01, both the bulk resistivity and UPV results indicate a very high-quality concrete. The relatively high value of bulk resistivity suggests excellent corrosion resistance, which is supported by the UPV measurements classifying the concrete as perfect. In Region 6, bridges such as AMA–RC–04, AMA–RC–05, and AMA–RC–09 showed low bulk resistivity values, which raises concerns regarding the quality of the concrete. The UPV measurements also indicated low velocities for sound waves in the concrete, confirming the lower quality of the concrete. Similarly, CSH–RC–01 and CHS–RC–04 exhibited low bulk resistivity values and low UPV measurements, indicating potential issues with the quality of the concrete in these bridges, as well.

In Region 4, the recorded bulk resistivity from ATL–RC–01, FTW–RC–01, and FTW–RC–05 were very low. However, the UPV measurements showed good concrete quality for all samples taken from the deck of these bridges. Similar observations were made for the specimens from FTW–RC–03, FTW–RC–04, and TYL–RC–02 in Region 3, as well as the samples tested from CHS–RC–02, CHS–RC–03, and LBB–RC–01 in Region 6. Overall, the analysis led to the conclusion that when the UPV results indicated a low value and poor concrete quality, the bulk resistivity measurements also showed a low electrical resistivity. However, the opposite is not valid since there were cases where the bulk resistivity was relatively low but the UPV measurements indicated good concrete quality.

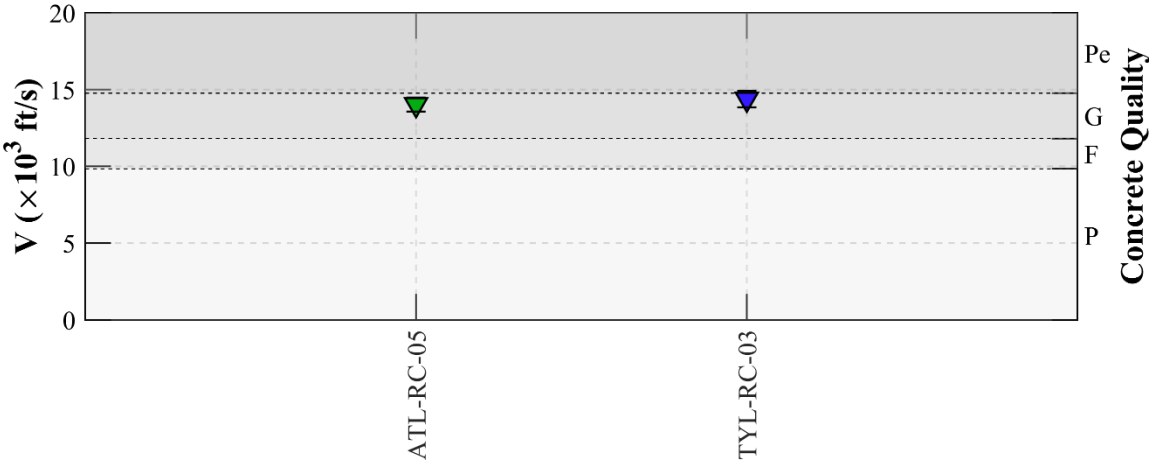

(a) Region 2

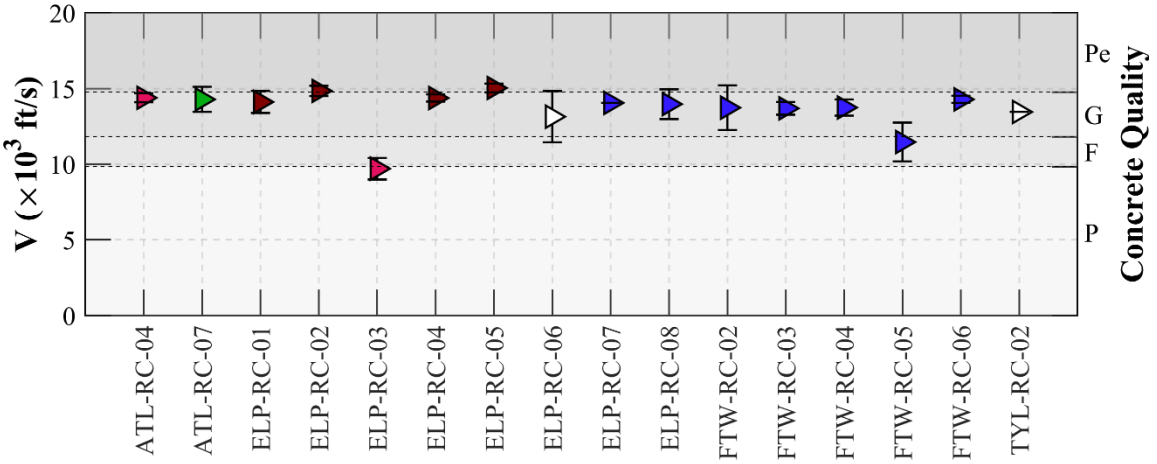

(b) Region 3

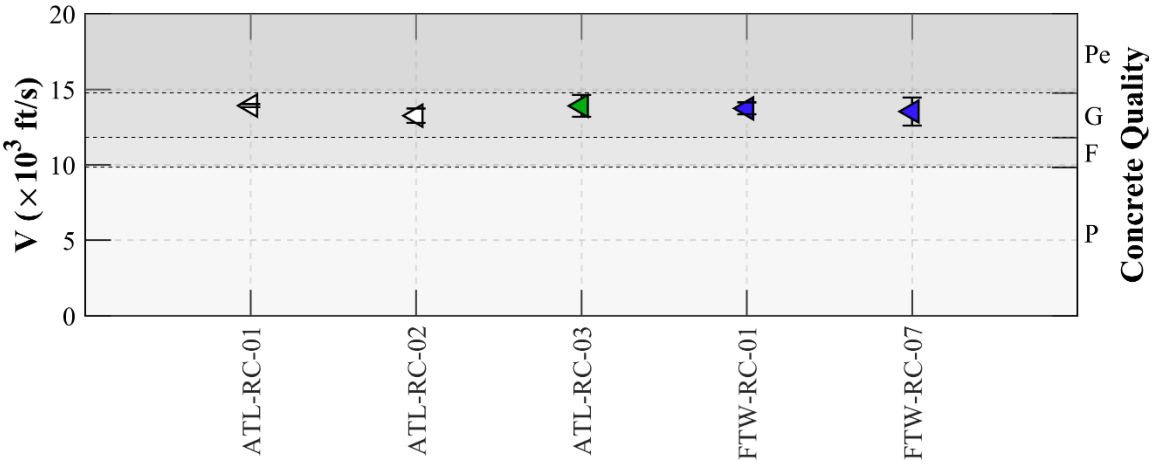

(c) Region 4

Figure 4.15. Recorded Sound Wave Velocity for Concrete Bridges.

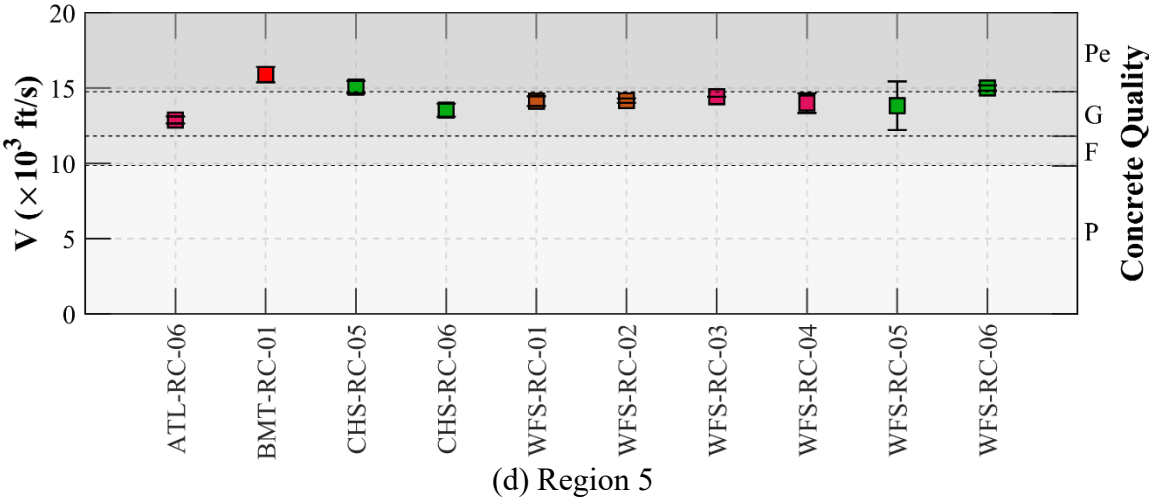

(d) Region 5

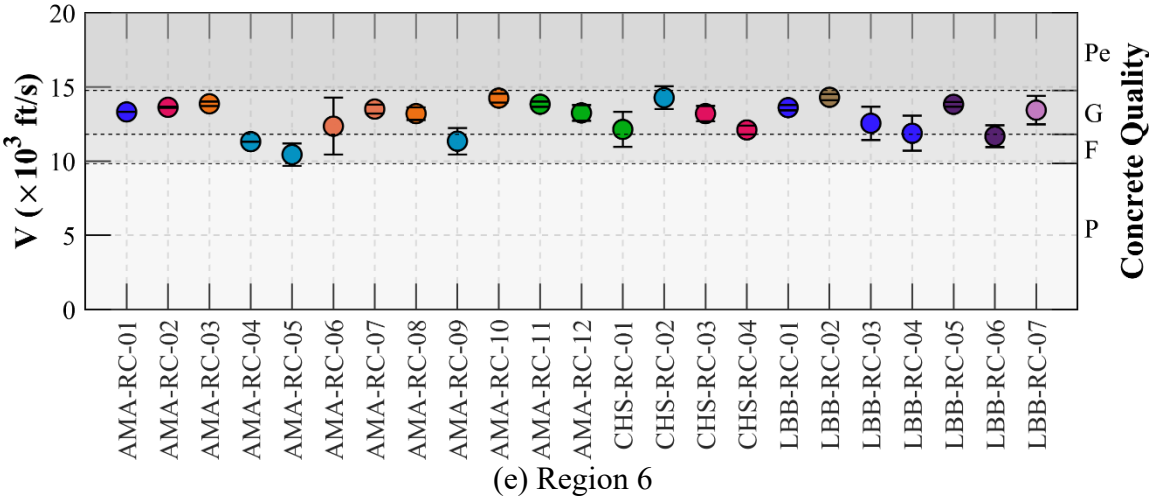

(e) Region 6

Figure 4.15. Recorded Sound Wave Velocity for Concrete Bridges (Cont.).

A nonlinear correlation between bulk resistivity and the velocity of a sound wave in concrete was observed for the experimental data documented in this work (Figure 4.16). Equation (4.10) represents a relationship between UPV recordings and bulk resistivity results, with the regression error (R^2) computed to 0.5:

$$V = 10^3(10.6 + 3\log\rho_b) \tag{4.10}$$

where V is velocity of sound wave, and ρ_b is bulk resistivity of the concrete specimen.

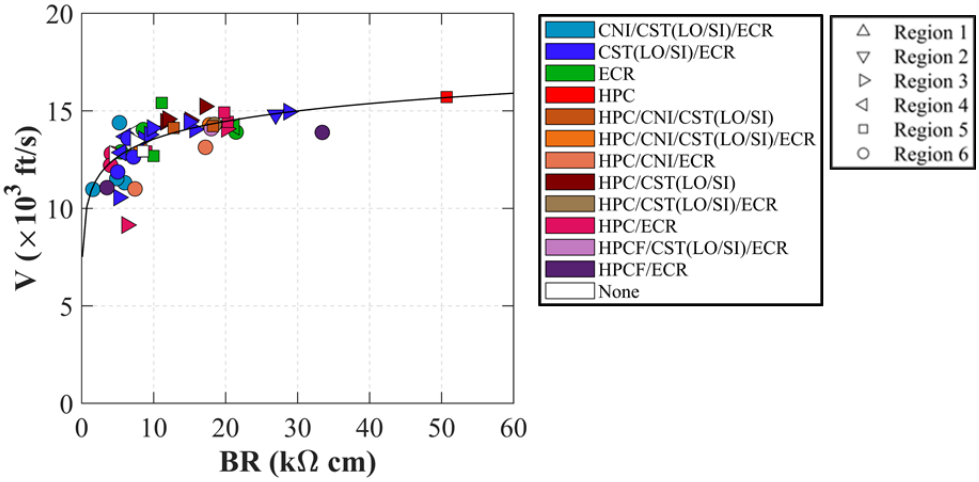

Figure 4.16. Correlation between Bulk Resistivity and Velocity of Sound Wave in Concrete.

4.1.4 Water Absorption Test

A porous medium like normal concrete generally tends to absorb water. The process in which water is transported through the pores and small voids of concrete is known as *capillary action*. The absorption rate at which water or other liquids enter unsaturated concrete due to capillary action can be defined by *sorptivity* (ASTM C1585, 2020; Hall, 1989). Factors such as the penetrability of the pore system, surface tension, viscosity, and density of water can affect the absorption rate of a concrete specimen (L. Bertolini et al., 2014).

In this study, the water absorption test was carried out to measure the capacity of concrete specimens to absorb capillary water. To this end, two absorption rates calculated from the experimental results include initial and secondary sorptivity.

The initial sorptivity was calculated based on the measurements taken during the first 6 hours, while the secondary sorptivity was determined from water absorption recordings after the 1st day of examination. The initial absorption rate reflects the rate at which water occupies the larger pores and cracks within the concrete (Marchand et al., 1996; Martys & Ferraris, 1997). Generally, the short-term sorptivity of a concrete specimen is higher than the secondary absorption rate. The secondary rate indicates the rate that water fills the air voids within the concrete (Yang, 2004) and can be used to estimate the time it takes for a sample to reach a critical degree of saturation, which is associated with the onset of freeze and thaw deterioration.

4.1.4.1 Experimental Setup

As in ASTM C1585 (2020), the concrete cores were placed in an environmental chamber with a controlled temperature of 50°C and RH of 80 percent for a period of 3 days (Figure 4.17). Next, the cores were air dried for a minimum of 15 days to maintain a uniform moisture state. Then, the circumference and top face of the concrete cores were sealed with epoxy to ensure that moisture exchange would occur through the bottom face of the specimen.

The following describes the procedure for conducting the water absorption test:

1. Cut samples in 4 in. diameter and in lengths of 2 in.
2. Place each sample in a sealable container with a free flow of air.
3. Store the container at 23 ± 2°C for 15 days.
4. Remove the samples from the container.
5. Measure the cross-sectional area and height of the specimens.
6. Seal the circumference and top face of the sample with epoxy.
7. Measure the weight of the sealed samples to the nearest 0.01g.
8. Place the specimens on the support device, ensuring that the surface without the sealer is in direct contact with water.
9. Maintain the water level at approximately 0.1 in. to 0.2 in. above the top of the support device.
10. Wipe the sample's bottom face with dampened papers at the time of measurements.
11. Place the specimens on the support device and repeat the measurements for every 30 minutes for 6 hours, then repeat the measurements every day for 9 days.

Figure 4.18 shows the schematic view of the sealed specimen placed in the container and water diffused from the bottom face of the sample.

Figure 4.17. Concrete Samples inside Environment Chamber.

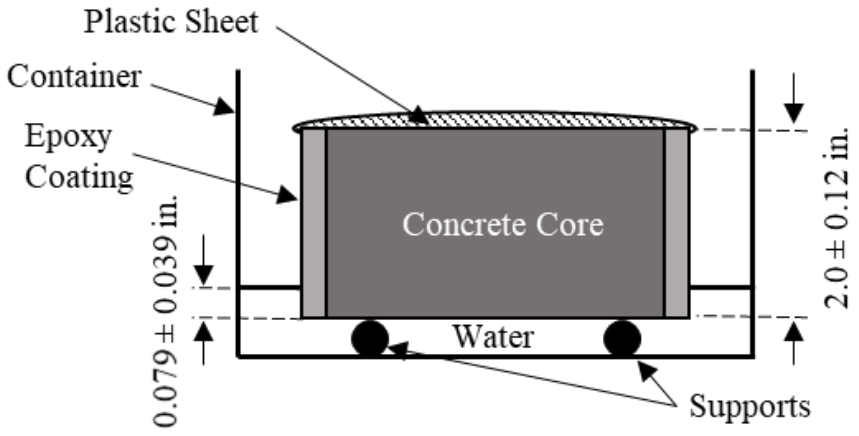

Figure 4.18. Schematic of the Absorption Test.

4.1.4.2 Experimental Results

Water absorption, I (mm), can be calculated by dividing the mass change of the sealed sample, m_t (g), at time t over the exposed area of the specimen, a (mm^2), and density of water, d (g/mm^2):

$$I = \frac{m_t}{a \times d} \tag{4.11}$$

The rate of absorption, or sorptivity (S), in concrete is described by the square root law (Martys & Ferraris, 1997):

$$I = S \cdot t^{0.5} + c \tag{4.12}$$

Here, the initial disturbance constant (c) represents the surface condition of concrete.

Figure 4.19 shows the recorded data of capillary water absorption for a period of 9 days for the specimens extracted from AMA–RC–05, AMA–RC–07, and AMA–RC–11. Using this figure, the initial sorptivity (S_i) and secondary sorptivity (S_s) were determined by analyzing the slope of the line fitted to the water absorption data plotted against the square root of time. Note that a comprehensive report of water absorption recordings for the concrete core specimens from TxDOT bridge decks is provided in the appendix.

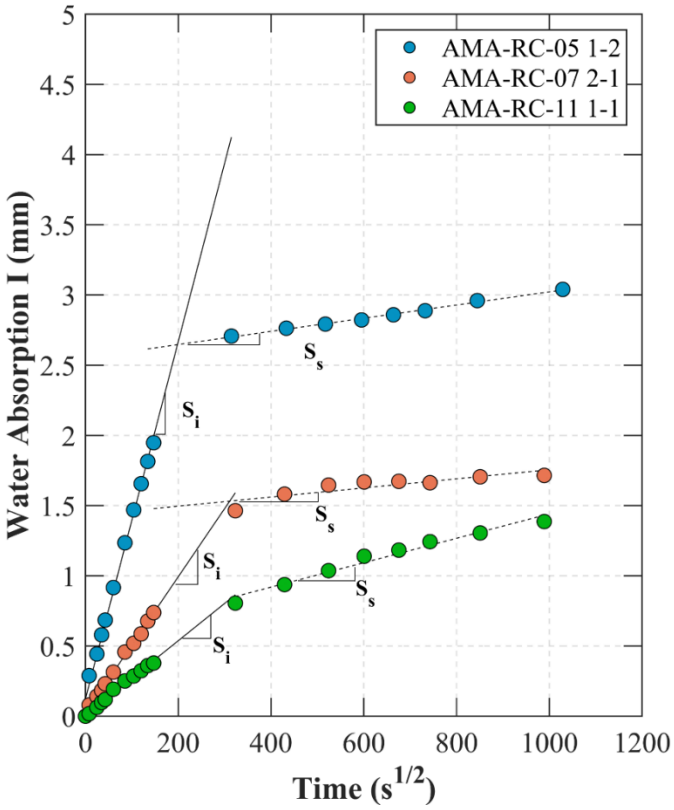

Figure 4.19. Water Absorption over 9-Day Period of Measurements.

Figure 4.19 also depicts a comparison of water absorption for three specimens taken from different concrete decks located in the Amarillo District. The results indicate that the initial absorption rate of AMA–RC–05, which has been in service for 26 years, was significantly higher

than the other two specimens. CNI was used in the mixed design of AMA–RC–05 and AMA–RC–07, but the results of the absorption test indicate a significantly lower initial sorptivity for AMA–RC–07 than for AMA–RC–05. AMA–RC–11, constructed with ordinary reinforced concrete and in service for 19 years, exhibited a lower initial absorption rate than the other specimens, suggesting a higher quality of concrete in terms of resistance to water penetration.

Figure 4.20 illustrates an upward trend in the initial sorptivity of core specimens when the samples are obtained from older concrete decks. Concrete decks in service are typically unsaturated structures (Castro et al., 2011); thus, the capillary action plays a significant role in the transport of chloride and sulfur ions within the concrete. As concrete ages, a larger portion of the capillary gel within the concrete dries out or reacts with the surrounding environment. This drying process leads to the formation of pores and microcracks in the paste and at the interface between the aggregate and the dried paste. In addition, since the initial sorptivity reflects the rate at which water occupies the larger pores and cracks within the concrete, the initial sorptivity increases with the age of concrete because cracks may develop over years. On the other hand, Figure 4.21 shows the opposite trend for the secondary sorptivity. This result can be attributed to the fact that the aged specimens have already filled large voids and microcracks with water during the initial period of 6 hours of testing, resulting in reduced water absorption.

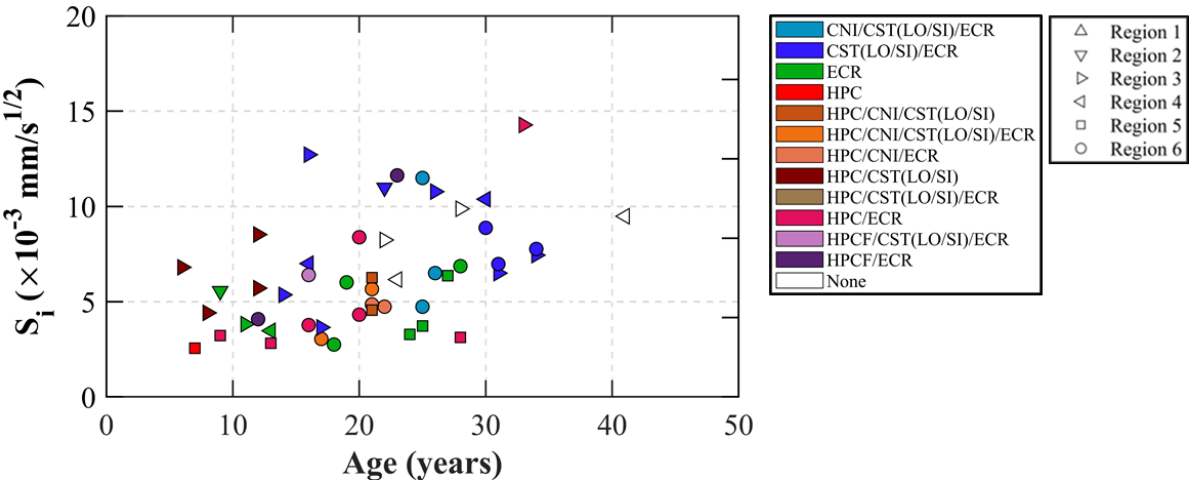

Figure 4.20. Initial Sorptivity Calculated for Core Specimens.

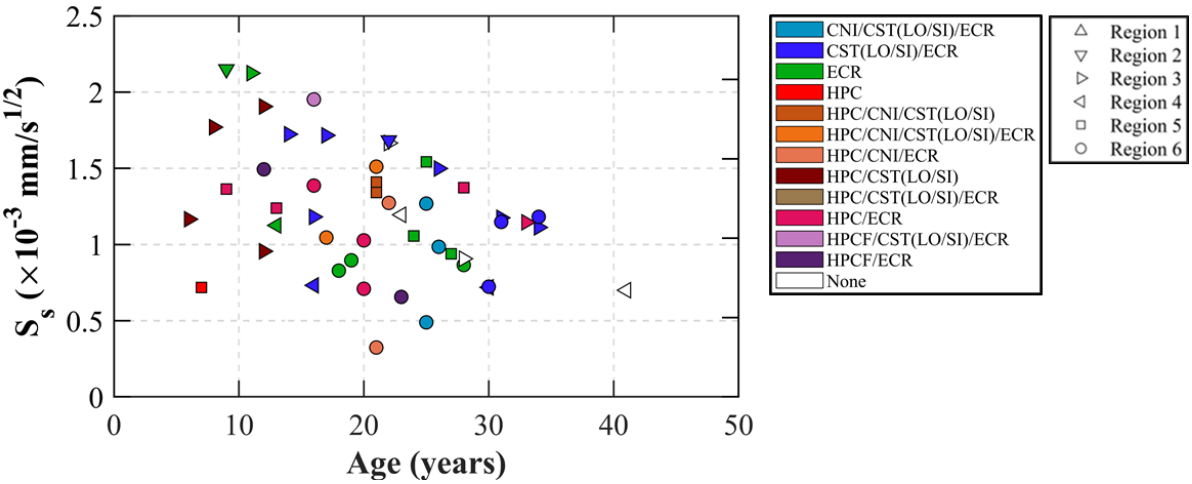

Figure 4.21. Secondary Sorptivity Calculated for Core Specimens.

Another observation derived from Figure 4.19 through Figure 4.21 is that the current mitigation methods used in concrete decks are not effective in reducing capillary water absorption. No consistent pattern of initial or secondary sorptivity was seen for concrete decks that were the same age and employed the same mitigation methods. The location of the bridges or the level of corrosivity of the environment does not significantly affect the sorptivity values either.

Researchers observed that in a medium corrosive environment such as Region 3 and Region 4, specimens with a bulk resistivity lower than 10 kΩ cm exhibited a high initial sorptivity (Figure 4.21), indicating poor concrete quality. This outcome, as supported by the results from UPV testing, could be attributed to a higher volume of defects, like microvoids and microcracks, within the concrete specimens, resulting in increased water content over time. It can also imply a higher W/C employed in the concrete mixed design. For instance, Region 3 (ELP–RC–03, ELP–RC–05, and ELP–RC–06) as well as Region 4 (FTW–RC–01 and FTW–RC–07) exhibited bulk resistivity values lower than 5.2 kΩ cm. These specimens also demonstrated a relatively high initial sorptivity (over 10×10^{-3} mm/s$^{1/2}$). It was determined that when the bulk resistivity is relatively high, the corresponding initial sorptivity should be lower than 6×10^{-3} mm/s$^{1/2}$. However, it should be noted that there are a few exceptions, such as ELP–RC–04 and ELP–RC–07. Though having a bulk resistivity of over 10 kΩ cm, the initial sorptivity of specimens extracted from these bridges was relatively high, suggesting that porosity of concrete near the surface is high. This finding agrees with the findings from potentiometric titration examinations and carbonation depth measurements.

In Region 5, the calculated initial sorptivity for the specimens was found to be lower than 6×10^{-3} mm/s$^{1/2}$. For example, BMT–RC–01 exhibited a higher bulk resistivity of over 36 kΩ cm, and its initial sorptivity was very small. In the highly corrosive environment of Region 6, the calculated initial sorptivity for AMA–RC–05 and LBB–RC–06 averaged 12×10^{-3} mm/s$^{1/2}$, indicating poor-quality concrete. This finding agrees with the results obtained from resistivity testing and UPV measurements. Except for CHS–RC–02 and CHS–RC–03, which exhibited extremely low bulk resistivity and low initial sorptivity, a general observed trend was that if the initial sorptivity was higher than 6×10^{-3} mm/s1/2, then the bulk resistivity was recorded low.

As discussed previously, the initial water absorption rate increases with concrete age, while the secondary absorption rate of concrete decreases. Studying the results presented in Figure 4.22 and Figure 4.23 provide further insight into this observation. If the secondary sorptivity is lower than 1×10^{-3} mm/s$^{1/2}$ and the initial sorptivity is lower than 6×10^{-3} mm/s$^{1/2}$, then the concrete can be considered dense. However, if the initial sorptivity is higher than 6×10^{-3} mm/s$^{1/2}$, it indicates a higher fraction of pores in the concrete. For example, specimens taken from ELP–RC–03, AMA–RC–05 and LBB–RC–06 showed low electrical resistivity, with an average initial sorptivity of about or greater than 12×10^{-3} mm/s$^{1/2}$ and a secondary sorptivity lower than 1×10^{-3} mm/s$^{1/2}$, which indicates poor-quality concrete. On the other hand, concrete cores extracted from BMT–RC–01, AMA–RC–03, and AMA–RC–11 exhibited a high electrical resistivity, averaging about or higher than 24 kΩ cm. The initial sorptivity of these samples was lower than 6×10^{-3} mm/s$^{1/2}$, and the secondary sorptivity was also less than 1×10^{-3} mm/s$^{1/2}$, indicating a dense concrete. For moderate quality concrete, the secondary absorption rate is approximately or slightly greater 1×10^{-3} mm/s$^{1/2}$. Improving the microstructure of the concrete, such as by improving the capillary pore size distribution and reducing void interconnection, can increase the electrical resistivity of the concrete. A finer pore structure with less connectivity results in lower permeability, higher electrical resistivity, and a slower absorption rate.

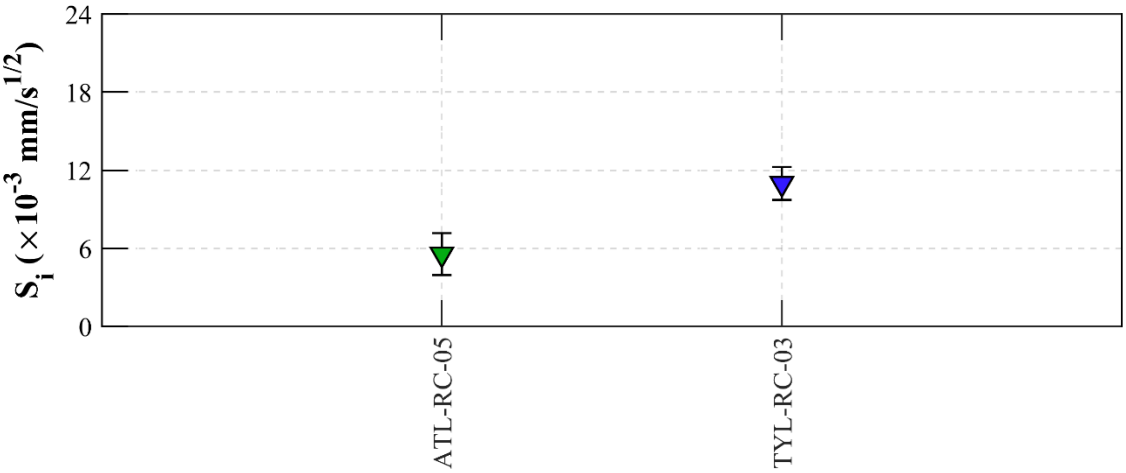

(a) Region 2

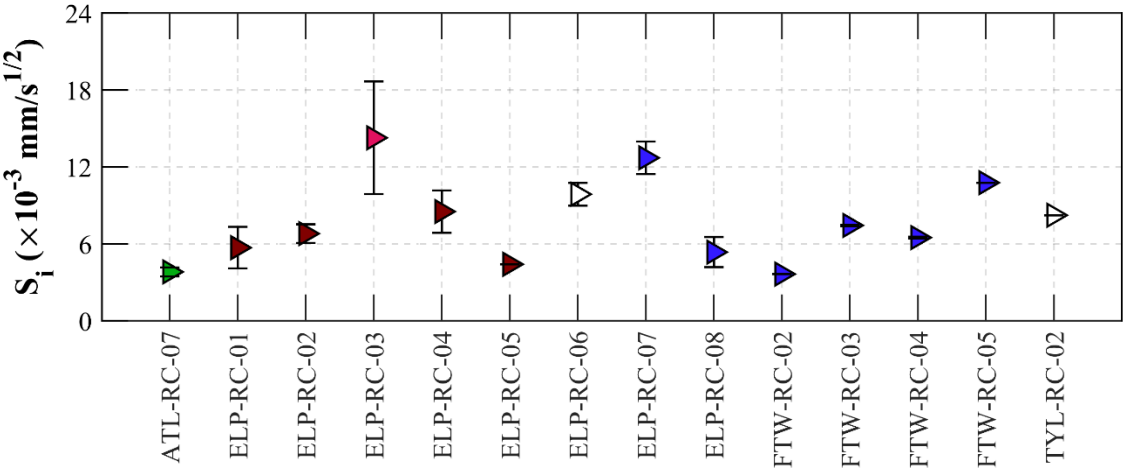

(b) Region 3

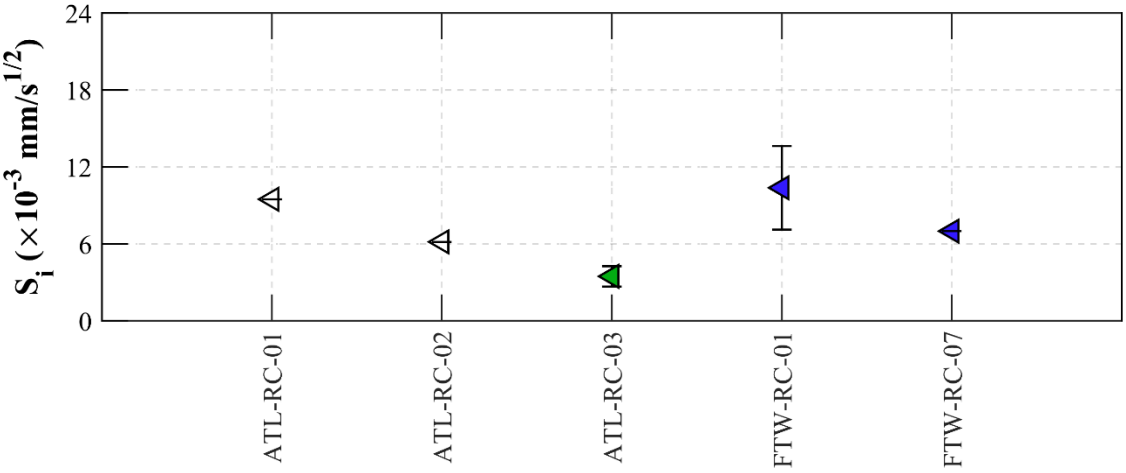

(c) Region 4

Figure 4.22. Initial Sorptivity Calculated for Concrete Bridges.

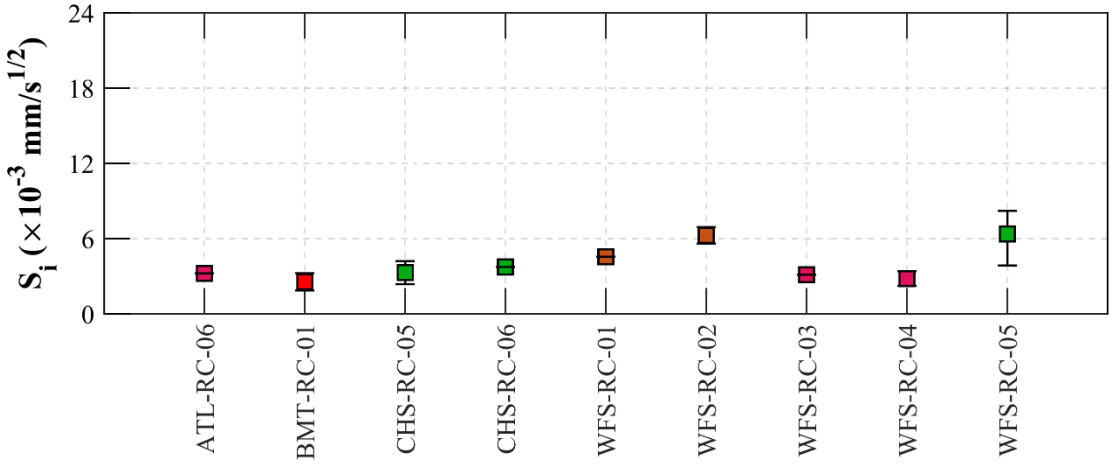

(d) Region 5

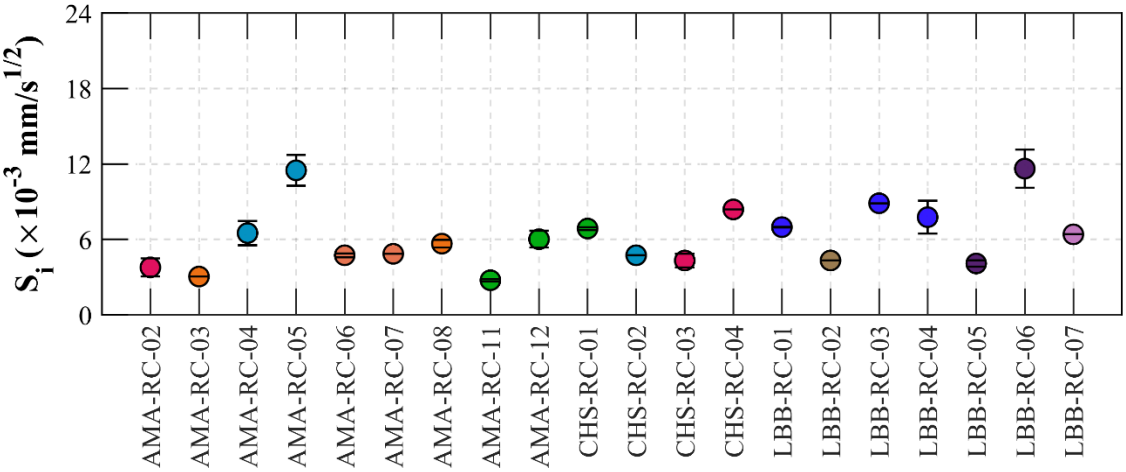

(e) Region 6

Figure 4.22. Initial Sorptivity Calculated for Concrete Bridges (Cont.).

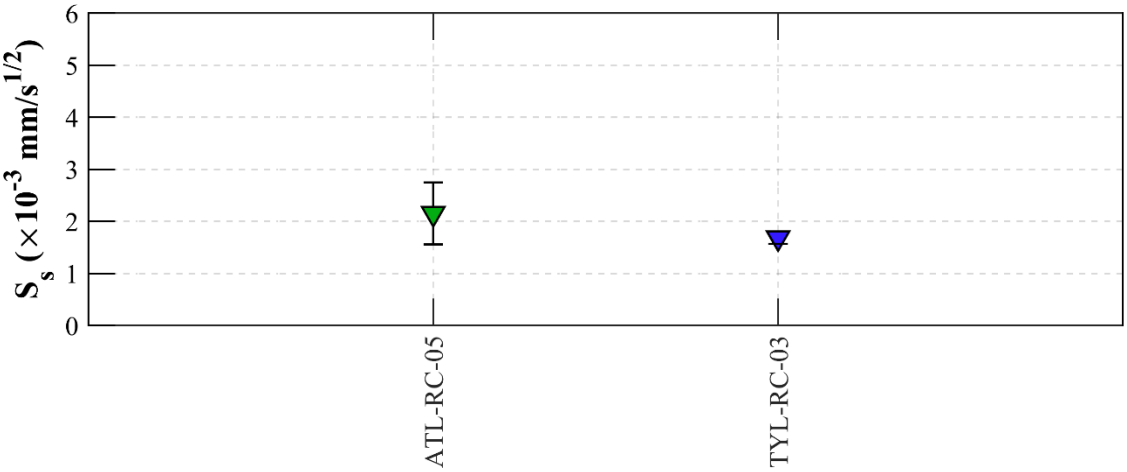

(a) Region 2

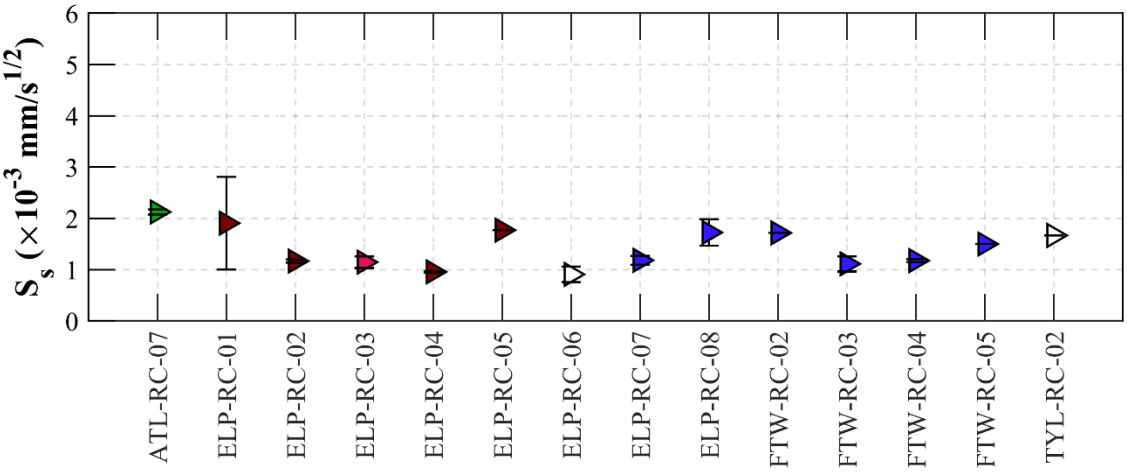

(b) Region 3

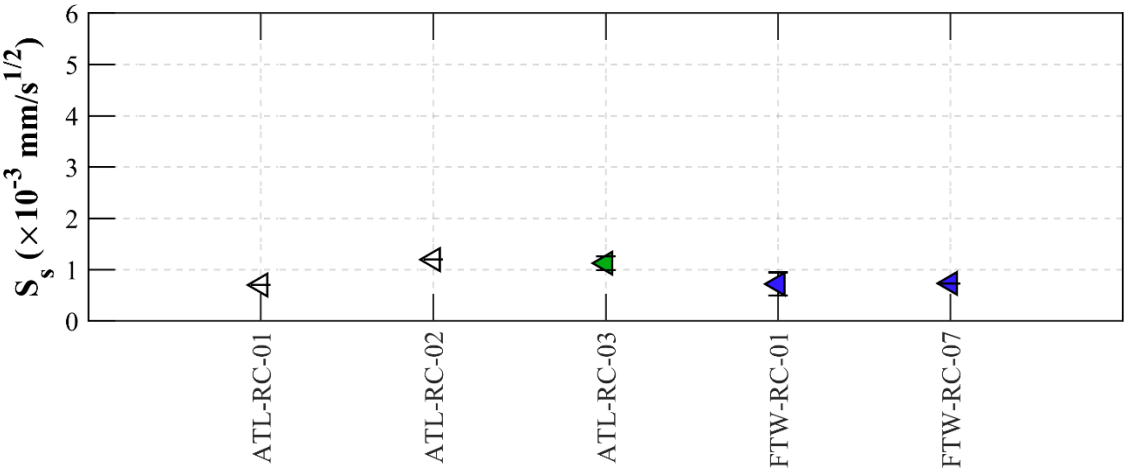

(c) Region 4

Figure 4.23. Secondary Sorptivity Calculated for Concrete Bridges.

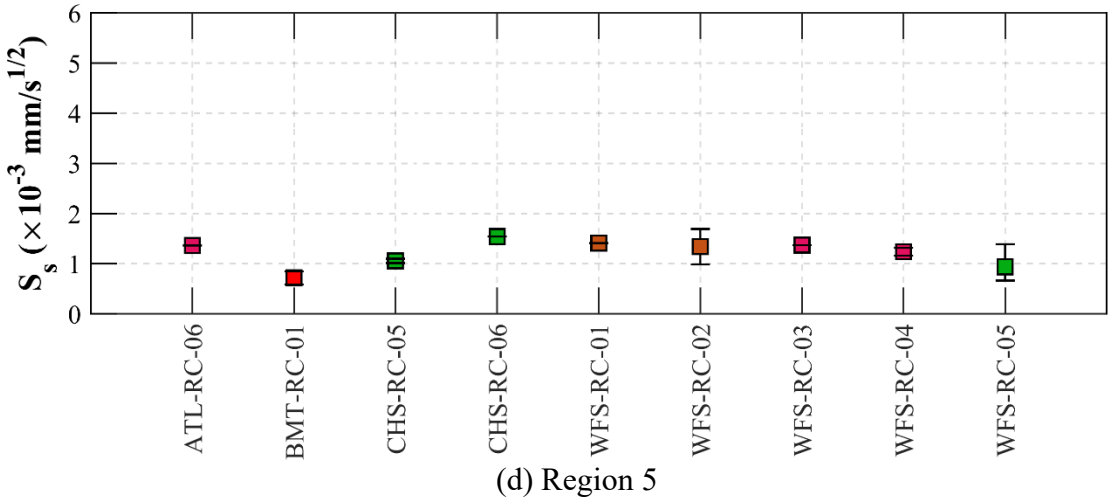

(d) Region 5

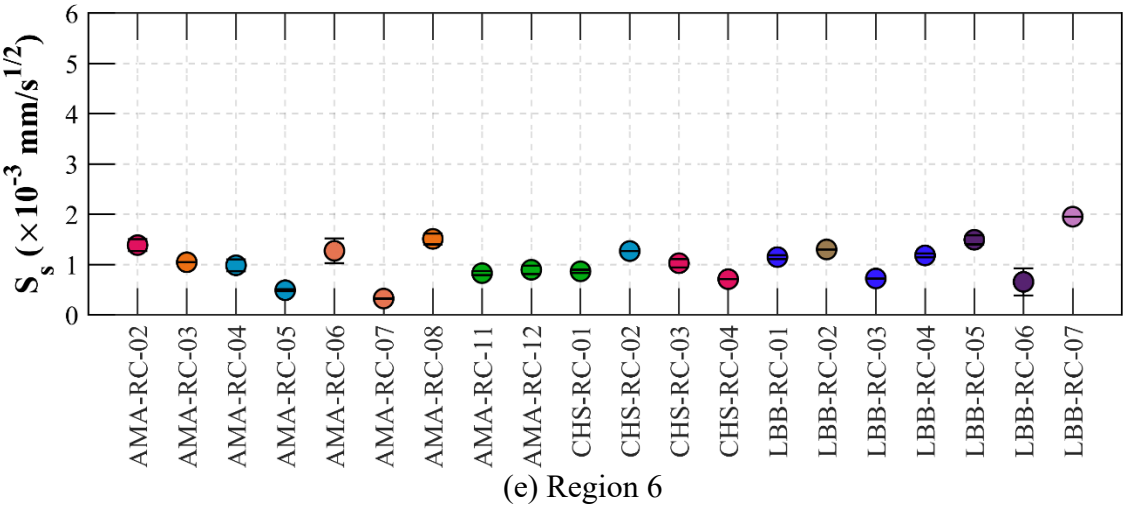

(e) Region 6

Figure 4.23. Secondary Sorptivity Calculated for Concrete Bridges (Cont.).

4.1.5 Chloride Content Measurement

Chloride ingress is a major contributor to the degradation of steel rebar in reinforced concrete bridges. Chloride ions can exist in concrete in the form of free ions mixed in pore water or bonded with aggregates or cementitious components. Two common methods employed to determine the chloride concentration in concrete are the acid-soluble method, per ASTM C1152 (2004), and the water-soluble method, per ASTM C1218 (2012). The acid-soluble method is particularly useful because it can measure both free and bonded chloride ions (Angst et al., 2009; National Academics of Sciences & Medicine, 2020), and it was adopted in this research to measure the chloride content in concrete cores.

The chloride content at the surface of steel bars can initiate corrosion when it exceeds a certain threshold. This threshold represents the concentration of chloride in concrete required to break down the passive layer of the steel reinforcement. For black rebar, the critical chloride concentration is 0.05 weight percent relative to concrete (or 0.4 weight percent relative to cement) (ACI 365.1R-17, 2017; Angst et al., 2009). For ECR, the chloride threshold that has been reported in literatures (Fanous & Wu, 2000; Keßler et al., 2015; Lute et al., 2021) ranges from 0.05 weight percent of concrete to 0.14 weight percent of concrete. Note that the corrosion performance of ECR can be affected by several factors, such as coating defects, coating adhesion loss, and time of wetness. When the quality of both epoxy coating and concrete is poor, it should not be expected that ECR will provide additional protection against chloride-induced corrosion. On the other hand, if the quality of epoxy coating is in great condition (no damage on coating or no disbonding of the coating and steel substrate), it is expected that ECR will provide significant protection against chloride ions. In this study, the chloride threshold value of uncoated black rebar was used for ECR.

CNIs are commonly added in the mix design, not only to increase the chloride threshold of concrete but also to accelerate the hardening period of concrete, especially in low-temperature casting environments such as the Amarillo, Lubbock, and Childress Districts. The addition of calcium nitrite in concrete enhances the resistance of steel to corrosion damage by strengthening the passive layer of steel reinforcement and by its tendency to react with both free and bonded chloride ions (Neville, 1995). Table 4-5 provides the level of chloride concentration allowed in percent by weight of concrete (% wt. conc.) at the surface of reinforcement in concrete where CNI is added in the concrete mixed design.

Table 4-5. Chloride Threshold for Different Doses of CNI in Concrete (ACI 365.1R-17, 2017).

CNI Dose		Threshold (% wt. conc.)
liters/m^3	gal/CY	
0	0	0.05
10	2	0.15
15	3	0.24
20	4	0.32
25	5	0.37
30	6	0.40

4.1.5.1 Experimental Setup

Potentiometric titration was conducted on powders collected from concrete core specimens, as in ASTM C 1152. To that end, 10 grams of concrete powder were extracted from individual cores at every 0.4 in. increment using a rotary impact drill, as shown in Figure 4.24. Then, the samples had to be pulverized using a pestle and mortar so that all the material passed through a No. 20 (0.0331 in.) sieve. Before beginning the experiment, samples were prepared by adding 25 mL of diluted nitric acid to the paste-like powder and heating the solution to the recommendation level found in ASTM C 1152. The chloride concentration of the concrete powders was measured through the potentiometric titrator. Figure 4.25 shows the equipment used in this study.

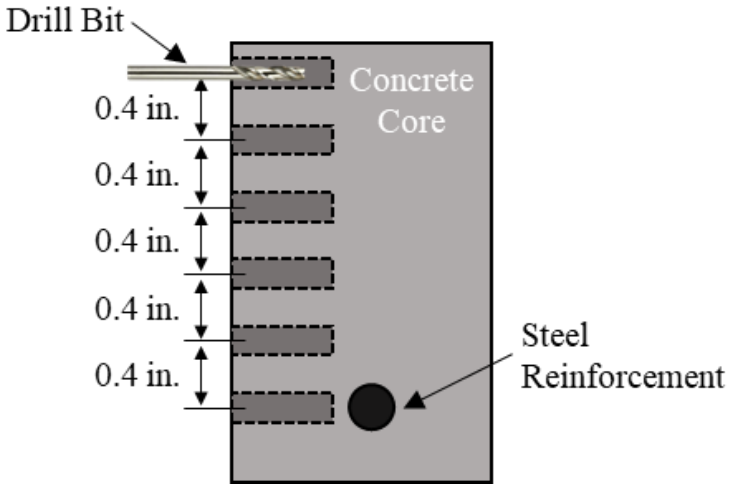

Figure 4.24. Collection of Concrete Dust at Different Depths.

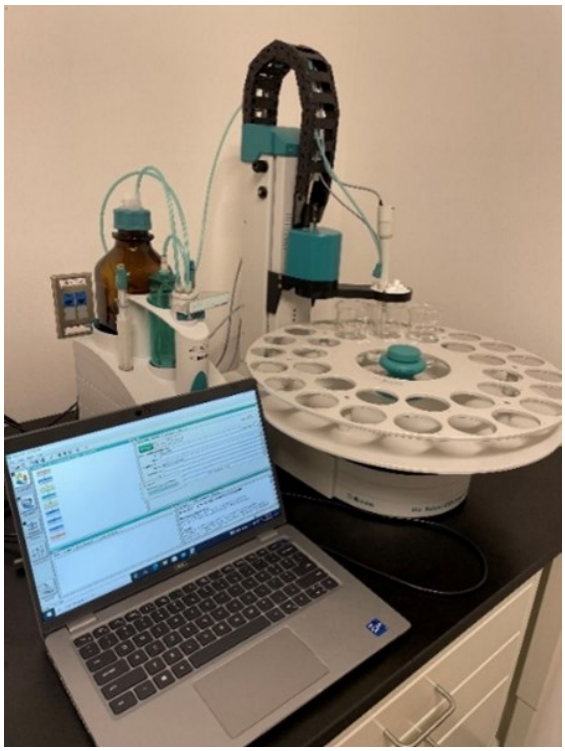

Figure 4.25. Metrohm-Brinkmann Auto-Titrator.

The procedure for potentiometric titration is as follows:

1. Drill core specimens using a rotary impact drill at every 0.4 in. increments.
2. Retrieve 10 grams of concrete powder for each level of drilling.
3. Prepare samples according to ASTM C 1152
4. Place samples in beaker and conduct Metrohm-Brinkmann Auto-Titrator.
5. Document the results for further analysis.

4.1.5.2 Experimental Results

The main process during the acid-soluble chloride concentration test is the following silver chloride reaction:

$$Ag^+ + Cl^- \rightarrow AgCl \tag{4.13}$$

Silver chloride is not soluble in the aqueous solution, and it is common to use the Nernst Equation to calculate the concentration of silver chloride:

$$E_{AgCl/Ag^+} = E^o_{AgCl/Ag^+} - \frac{0.059}{n}\log\frac{1}{Cl^-} \tag{4.14}$$

As chloride ions are consumed during the chemical reactions, the addition of silver nitrate causes a sudden change in electric potential that indicates the end of the titration process. This ending is also known as the equivalence point—or end point—and it can be determined by locating the inflection point of the titration curve. The chloride concentration consumed in the reactions can be estimated from the volume of 0.05 N $AgNO_3$ solution used during titration (V_1) and used for blank titration for 35.453 g/mol of chloride (V_2):

$$Cl\ (\%) = \frac{3.545(V_1 - V_2)N}{W} \tag{4.15}$$

where N is the exact normality of 0.05 percent $AgNO_3$ solution, and W refers to the mass of the sample in grams.

If the chloride concentration at the rebar level, around 2.5 in. depth, exceeds the chloride threshold, the aggressive ions diffused in concrete can break the passive film developed on the steel surface over time and initiate corrosion. The main objective of the potentiometric titration examination is to compare the chloride concentration in concrete decks constructed in different risk environments.

Figure 4.26(a) shows chloride profiles generated for some concrete specimens examined in this work. As illustrated in this figure, the concentration of chloride generally decreased for the samples extracted from deeper concrete layers, and it was negligible at the rebar level. The diffusion of chloride was low (lower than 0.1 % wt. concrete) for different depths of the specimens taken from ELP–RC–03, while the bulk resistivity for this bridge was recorded on average lower than 5.2 kΩ cm, and the initial sorptivity was calculated on average higher than 12×10^{-3} mm/s1/2. The results obtained from resistivity and water absorption examinations indicate that the concrete used in ELP–RC–03 and ELP–RC–06 is not in good condition. However, it can be concluded that the amount of salt applied on the bridge deck over the years was not significant; otherwise, the concentration of chloride should be higher than the measured values. Similarly, samples taken from ATL–RC–01 exhibited the same chloride diffusion pattern, even though the resistivity of the concrete was relatively low and the initial sorptivity was calculated relatively high.

Figure 4.26(b) also shows results obtained for ATL–RC–06 and AMA–RC–03, both constructed with good quality concrete. These structures can resist the diffusion of chloride ions

as long as cracks do not appear on the concrete surface. For example, the chloride concentrations in specimens extracted from the concrete decks were relatively high near the surface but significantly reduced as the depth of the concrete increased. The bulk resistivity measured for ATL–RC–06 was on average 10 kΩ cm and for AMA–RC–03 was 24 kΩ cm. The initial sorptivity calculated for these structures was lower than 6×10^{-3} mm/s$^{1/2}$, indicating the presence of dense concrete. A comprehensive report containing the chloride profiles tested in this study is included in the appendix.

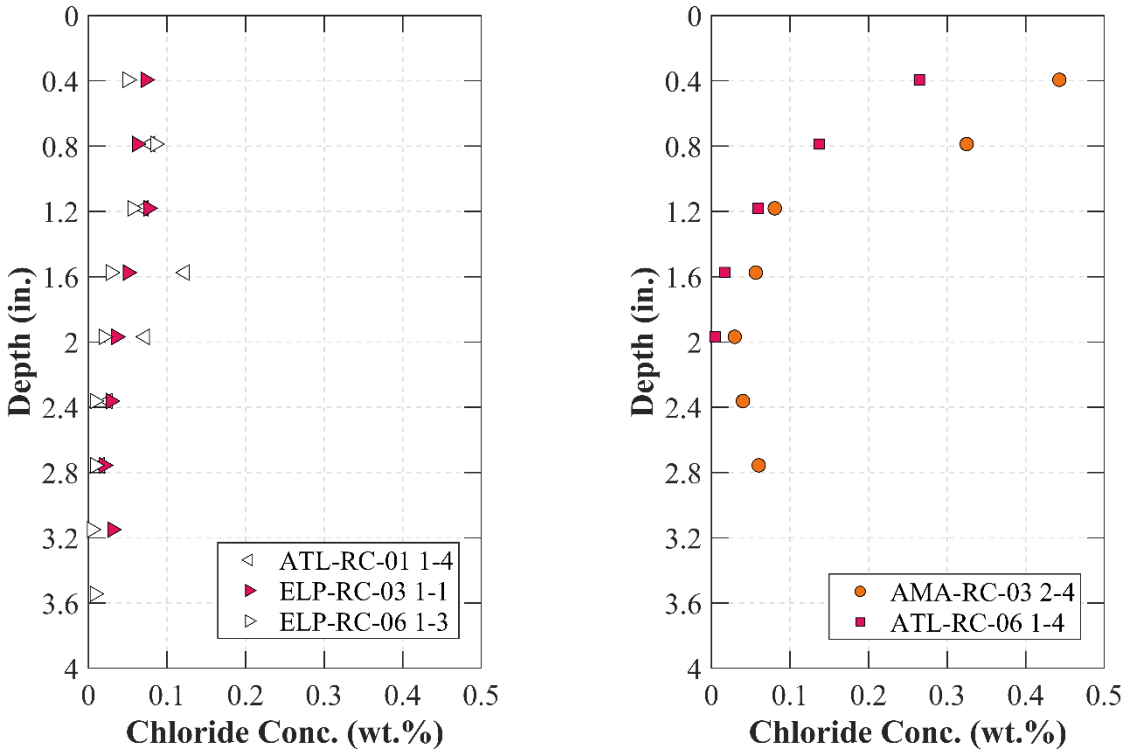

(a) Medium Corrosion Risk Environment (b) High Corrosion Risk Environment

Figure 4.26. Chloride Profiles for Concrete Specimens.

Figure 4.27 shows the concentration of chloride ions at the concrete and steel reinforcement interface. The chloride threshold was lower than 0.05 % wt. conc. for most of the specimens examined in this study. However, in a highly corrosive environment such as Region 6, chloride ions diffused deep into the concrete, regardless of the employed mitigation method. Chloride concentration at the rebar level was determined to be on average greater than 0.05 % wt. conc. for most concrete decks in Region 6, two bridge decks in Region 4 (ATL–RC–03 and FTW–RC–01), and one deck located in Region 5 (WFS–RC–06). However, the concentration was still less than 0.1 % wt. conc. for the structures in Region 4 and Region 5.

The distribution of chloride ions in concrete can be heavily affected by several parameters such as environment, concrete composition, and the presence of cracks on the surface. In areas with high deicing salt exposure, such as Amarillo and Childress, concrete samples can have higher surface chloride concentration due to the heavy application of deicing salt. In addition, the chloride concentration on a bridge deck can vary in different areas of the structure. Chloride-laden water can flow down and accumulate on the shoulder lane due to the slope of the concrete deck. Thus, the surface chloride concentration in the shoulder lane of some bridges can be larger than that of the driving lane, leading to a higher risk of corrosion of the steel reinforcement within the concrete, particularly if the shoulder lane is not properly sloped or drained.

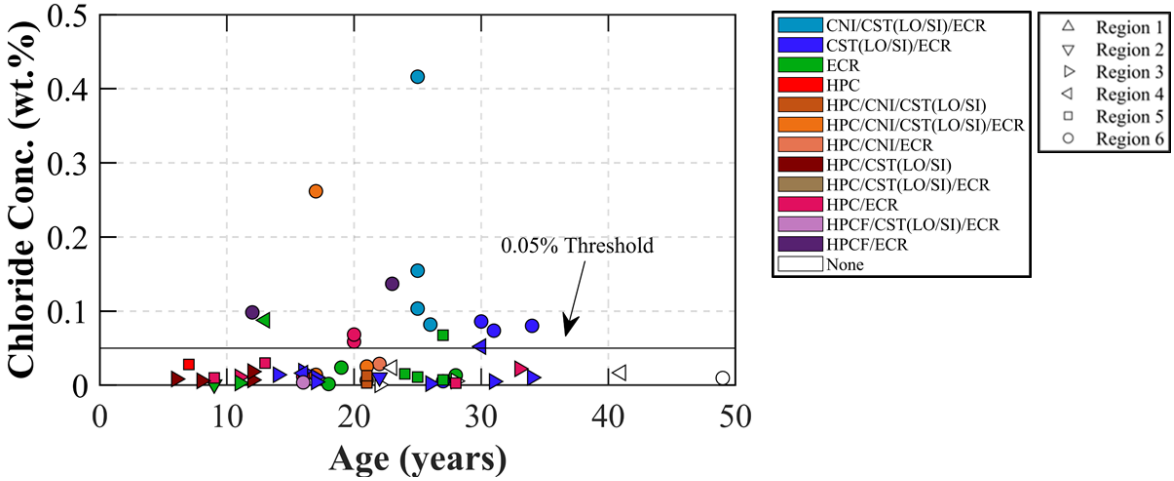

Figure 4.27. Chloride Concentration at the Concrete and Steel Reinforcement Interface.

Figure 4.28 shows the range of chloride concentration at the rebar level of every individual bridge. The diffusion of chloride ions in concrete was negligible at the interface of steel and concrete for most of the concrete decks across Texas, except those located in Region 6 (as discussed). The concentration of chloride in concrete cores extracted from AMA–RC–05 and LBB–RC–04 measured significantly high, particularly for specimens taken from the concrete shoulders (as referred to in the appendix). The recorded bulk resistivity for these specimens was remarkably low, whereas the calculated initial sorptivity was high. A similar pattern was observed for AMA–RC–09; the level of chloride ions was considerably high for the specimen extracted from the concrete shoulders. Bulk resistivity measured for this concrete deck was also low, but the initial sorptivity of this structure is not known because no specimen from this structure was examined during the water absorption test.

Although the chloride level increased to 0.4 % wt. conc. at the surface, the chloride concentration at the HPCF concrete and steel rebar interface was negligible for core specimens obtained from LBB–RC–07, which implies resistance of the concrete deck to chloride diffusion, even though salt accumulates at the top layers of the concrete cover. The average of bulk resistivity measured for specimens taken from LBB–RC–07 was about 20 kΩ cm, and the initial sorptivity was measured at 6×10^{-3} mm/s$^{1/2}$. It was concluded that the concrete deck of LBB–RC–07 is in good condition. A similar pattern was observed for LBB–RC–02. The average of chloride concentration at the rebar level for other specimens extracted from concrete decks in the Lubbock District exceeded the chloride threshold of 0.05 % wt. conc. recommended by Angst et al. (Angst et al., 2009).

Chloride content at the rebar level measured higher than the chloride threshold for specimens taken from concrete decks in the Childress District, with the exception of CHS–RC–01. Note that the results obtained from potentiometric titration for specimens examined in this district agree with the measurements obtained from the resistivity, UPV, and water absorption examinations.

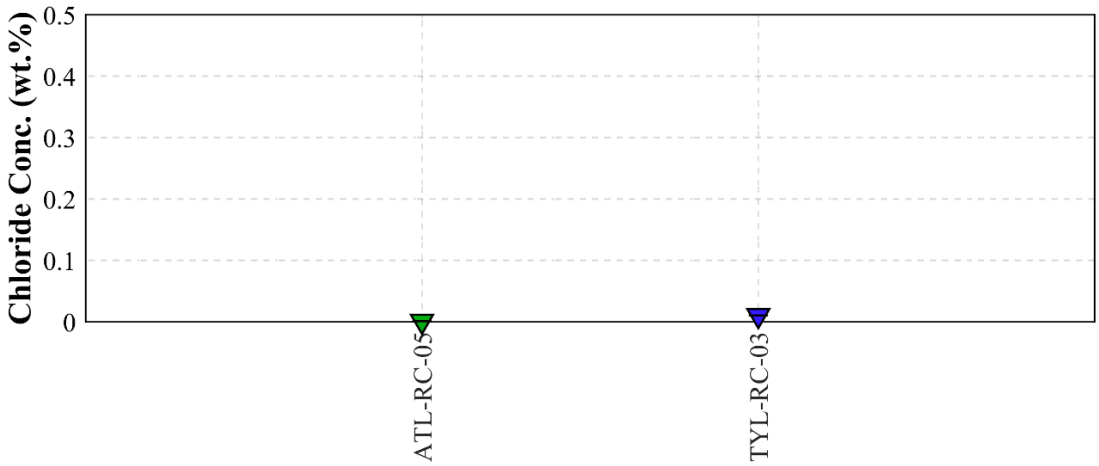

(a) Region 2

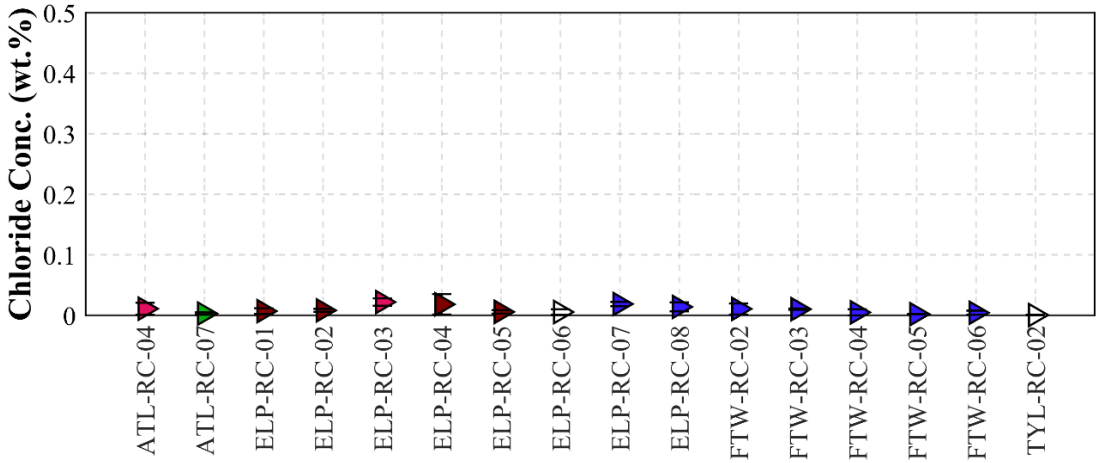

(b) Region 3

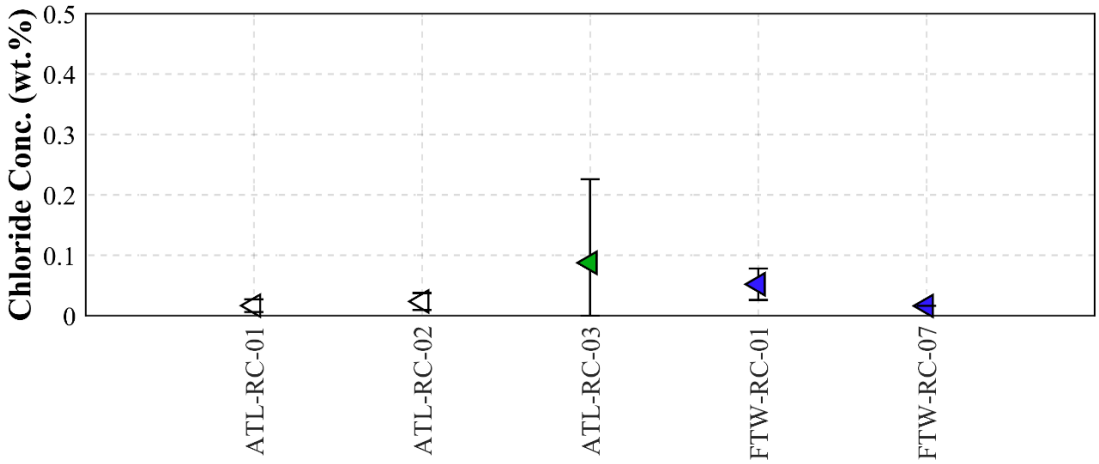

(c) Region 4

Figure 4.28. Chloride Concentration at Rebar Level for Concrete Bridges.

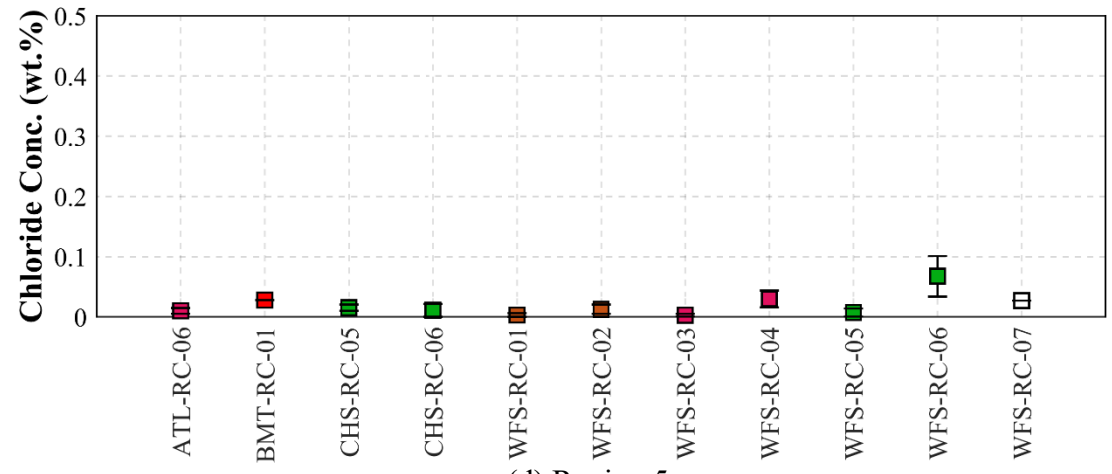

(d) Region 5

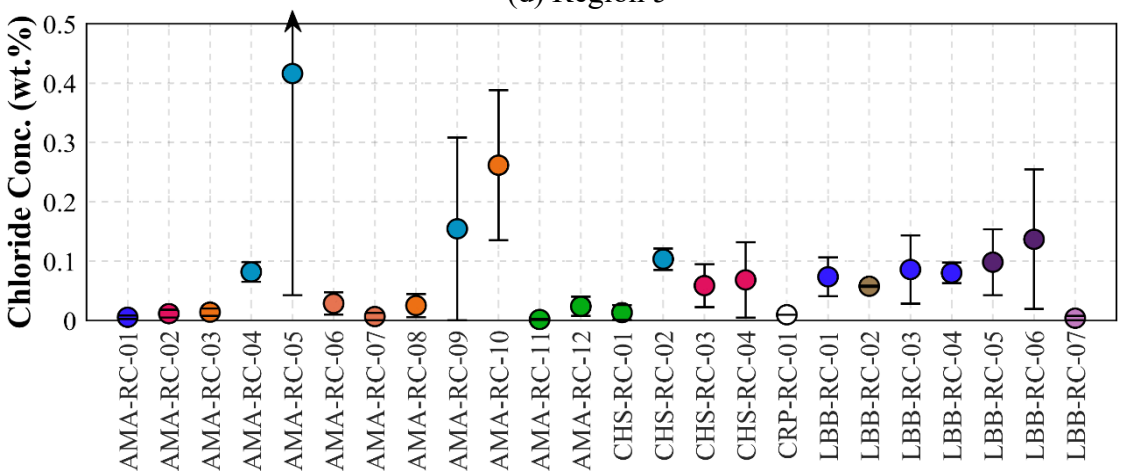

(e) Region 6

Figure 4.28. Chloride Concentration at Rebar Level for Concrete Bridges (Cont.).

Regardless of the quality of concrete, the acid-soluble chloride concentration test provides the level of chloride content at the depth of a core specimen. For example, in Region 6, the recorded values obtained from the resistivity, UPV, and sorptivity testing imply that the quality of HPCF concrete employed in LBB–RC–05 is in good condition and is a dense concrete with a relatively high bulk resistivity (35 kΩ cm) and low initial sorptivity (4×10^{-3} mm/s$^{1/2}$). However, the concentration of chloride at the rebar level of the specimen obtained from LBB–RC–05 was on average 0.1 % wt. conc. A similar pattern was observed for AMA–RC–10; despite having a bulk resistivity of on average 20 kΩ cm, the level of chloride at the concrete and steel bar interface measured high—0.27 % wt. conc. ATL–RC–03, in Region 3, had a bulk resistivity of 24 kΩ cm

and an initial sorptivity lower than (6×10^{-3} mm/s$^{1/2}$). However, the average chloride level at the rebar level measured 0.1 % wt. conc.

The accumulation of chloride ions at the concrete and steel interface (at least for the three concrete decks shown in Figure 4.29) was due to crack formation on the top surface of the concrete. These cracks propagated within the concrete, reaching the level of the rebar. Chloride ions can transport through these cracks and subsequently aggregate near the steel reinforcement. Particularly in the Amarillo and Lubbock Districts, where the application of deicing salt on bridge roads is substantial, the average chloride content at the steel rebar was high. In fact, corrosion rust and peeling of the epoxy coating were detected for core specimens taken in Region 6.

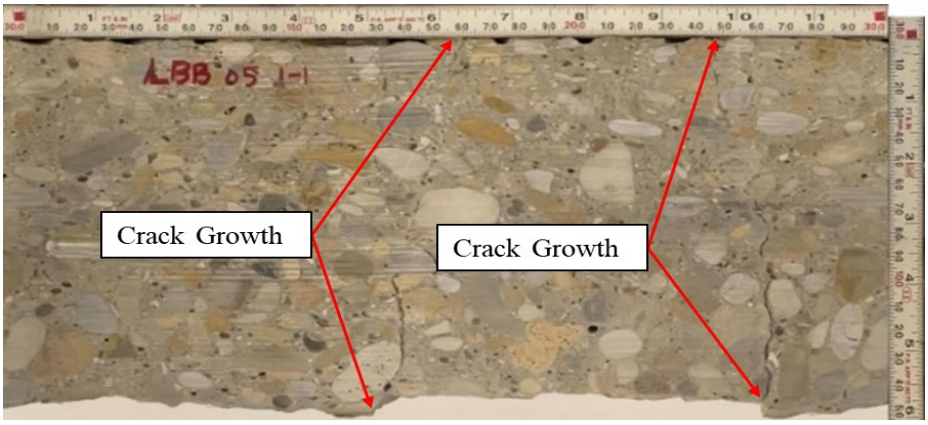

(a) Core Specimen Obtained from LBB–RC–05

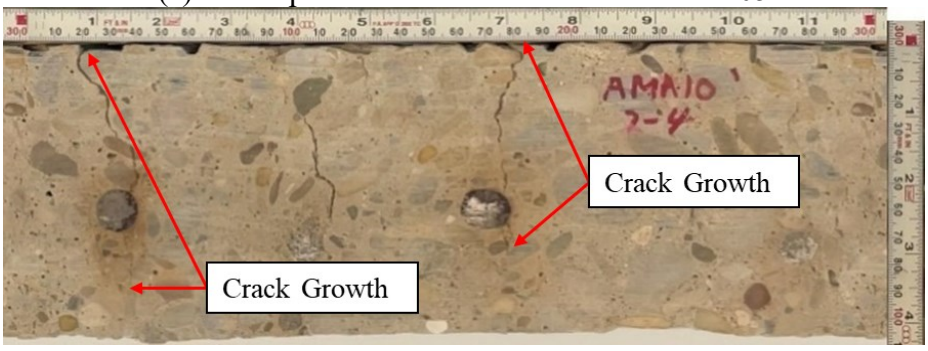

(b) Core Specimen Obtained from AMA–RC–10

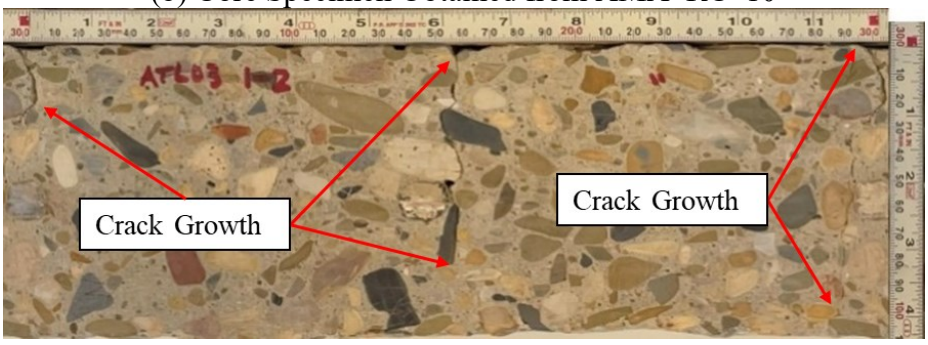

(c) Core Specimen Obtained from ATL–RC–03

Figure 4.29. Propagation of Cracks in Concrete Specimens.

4.1.5.2.1 Comparison between LO and SI

Chloride concentration test results on a limited selection of coring samples from mildly corrosive environments were compared, as shown in Figure 4.30, in an effort to present the effect of surface treatment on mitigating chloride ingress. The investigation focused on samples with a uniform mitigation strategy in addition to those with the absence of cracks.

The results showed that none of the samples, whether treated with SI or LO, exhibited chloride concentrations above critical thresholds at the rebar level. However, there is little difference in the top surface chloride concentration. The combination of HPC and SI has less surface chloride concentration than the HPC and LO combination. The utilization of ECR and SI together resulted in a lower surface chloride concentration than when ECR was combined with LO. Samples treated with SI showed a slight advantage over samples treated with LO, consistent with previous indications of the enhanced performance of SI in reducing surface chloride ingress. This observation, consistent with the better protection of SI, aligns with the conclusions in the existing literature on the comparative effectiveness of these treatments. However, given the limited coring samples, varying bridge age, and intricate combination of different corrosion mitigation methods, it is not easy to draw a valid and convincing conclusion regarding the efficiency of LO and SI.

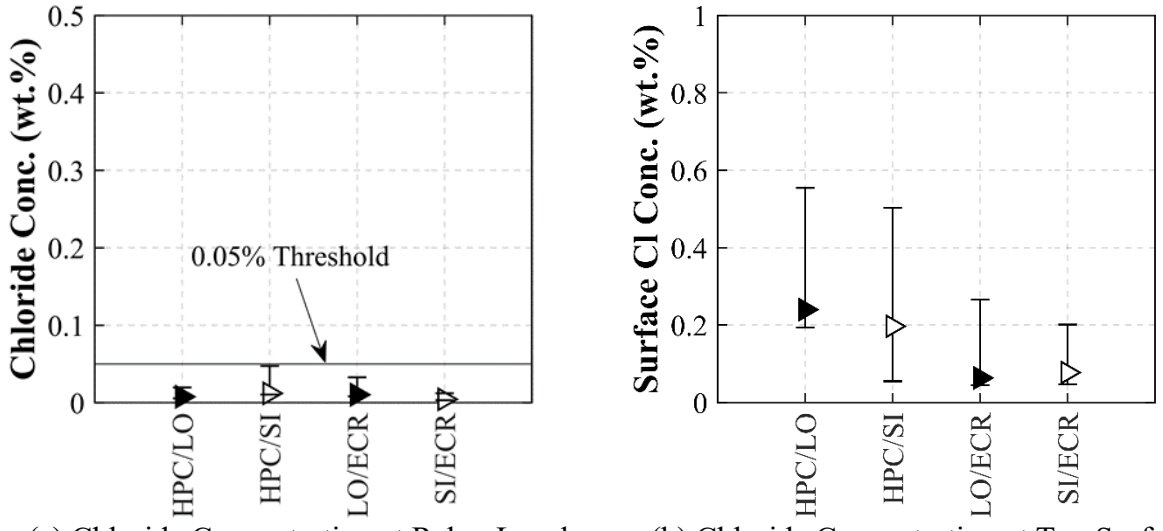

(a) Chloride Concentration at Rebar Level (b) Chloride Concentration at Top Surface

Figure 4.30. Comparison of LO and SI in Region 3.

4.1.6 Carbonation Depth Measurement (RILEM CPC-18)

Carbonation of concrete occurs when carbon dioxide penetrates concrete and reacts with cement products. If carbon dioxide dissolves in pore water, carbonic acid will form that can react with calcium hydroxide and produce calcium carbonate, thereby causing a corrosive environment (L. Bertolini et al., 2014; J.P. Broomfield, 2006; Neville, 1995). Concrete is alkaline and has a pH level of around 12 to 13. This high alkalinity environment causes an oxide film to develop on steel reinforcement that protects the substrate from corrosion. The passivation layer becomes unstable when the pH of the pore solution drops, and consequently corrosion may initiate on steel reinforcement (Aperador et al., 2015).

Carbonation damage is not common in modern structures with dense concrete and a low W/C. However, if adequate concrete cover is not provided for a structure, carbonation can initiate corrosion in the steel reinforcement. When concrete dries, the cement products on the surface rapidly react with free carbon dioxide in the air, leading to the early-stage carbonation of the exposed concrete surface. Moreover, if cracks appear on the surface, the concrete layers at the crack face will also become carbonated due to exposure to air. In this study, the decision was made to differentiate between carbonation resulting from exposure to air and carbonation resulting from the diffusion of carbon dioxide in concrete pores. The former was considered as the depth of the cracks, while the latter was recorded as the depth of carbonation.

It is common to measure carbonation depth by using a phenolphthalein solution (J.P. Broomfield, 2006). A concrete surface sprayed with the phenolphthalein solution will either retain its original color or turn pink. If the color of the exposed surface remains colorless, then the pH of the concrete is less than 9.5, which indicates a low occurrence of carbonation. However, if the color of the exposed surface turns pink, the pH of the concrete must be greater than 9.5, indicating the presence of an excessive amount of free $Ca(OH)_2$ on the concrete surface. A strong shade of pink color that appears on the surface indicates a pH higher than 9.5, while a softer shade of pink implies a pH closer to 9.5.

4.1.6.1 Experimental Setup

As in RILEM CPC-18 (1988), concrete specimens were fractured by using a chisel, and a solution of 1 percent phenolphthalein in 70 percent ethyl alcohol was immediately applied on the fresh surface. Then, the results were carefully documented for reference and further analysis. For

example, Figure 4.31 illustrates the procedure taken for measuring the carbonation depth of a concrete specimen extracted from AMA–RC–05. As shown in this figure, the top layers of the core sample remained colorless after applying the phenolphthalein solution, but the rest turned pink, indicating an alkaline environment. After a day, researchers measured the length of the colorless sections at four different locations to the nearest 0.04 in., and the average of the measurements was recorded as the crack depth or carbonation depth. In this example, the colorless surface turned into a blackish color after a while because the location was a crack face exposed to air for long time. Therefore, the testing area was documented as crack depth rather than carbonation depth.

Figure 4.31. Measurement of Carbonation Depth for Concrete Specimens.

4.1.6.2 Experimental Results

Figure 4.32 depicts the carbonation of concrete specimens obtained from AMA–RC–03 after applying the phenolphthalein solution on the fresh broken face. If the tested surface was colorless after applying the solution, as shown in Figure 4.32(a), the depth of the colorless area was considered as carbonation due to diffusion of carbon dioxide in concrete. When the concrete surface was exposed to air for a long period, carbonation might already have happened, and the tested area turned to a dullish color, as shown in Figure 4.32(b). Therefore, it was concluded that the area with the dullish color had been exposed to air because of cracks on the top surface and had been carbonated over a period of time. The carbonation depth was then only measured from the locations without any cracks to only consider carbonation depth due to diffusion of carbon dioxide in concrete.

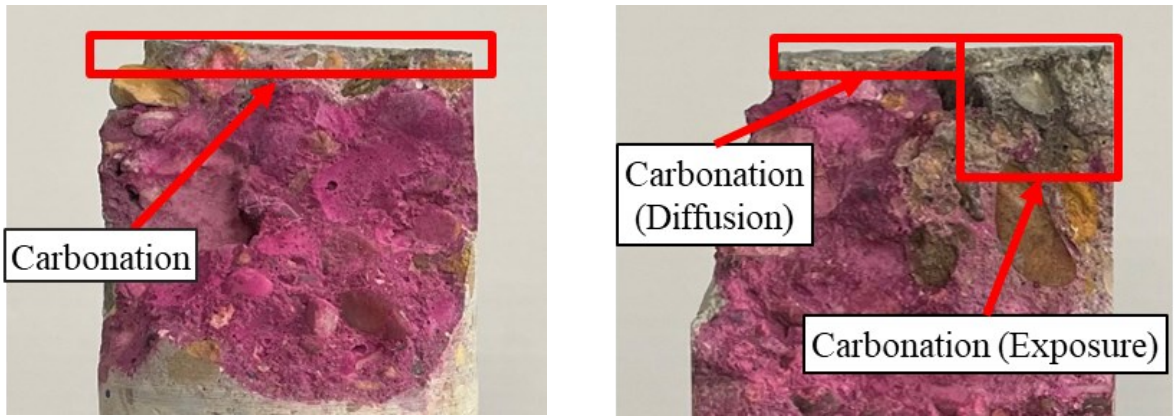

(a) Carbonation Due to Diffusion (b) Carbonation Due to Air Exposure

Figure 4.32. Carbonation Depth Measurement—AMA–RC–03; Core Sample 1–4.

Figure 4.33 represents the carbonation depths measured for core specimens taken from concrete decks across Texas. Although carbonation was generally expected to be low in low-risk environments—Region 1 and Region 2—the depth of carbonation was on average approximately 1 in. for the specimens extracted from ATL–RC–05 and TYL–RC–03. The Tyler bridge is located 15 miles away from Martin Lake Coal Plant and 16 miles away from Tenaska Gateway Generating Station Gas Plant. Similarly, the Atlanta bridge is also located 20 miles away from Martin Lake Coal Plant and 15 miles away from Tenaska Gateway Generating Station Gas Plant. The fact that the bridges are located in industrial environments can explain the higher depth of carbonation measured for the core specimens. The initial sorptivity was calculated on average as 12×10^{-3} mm/s$^{1/2}$ for TYL–RC–03, while it was on average lower than 6×10^{-3} mm/s$^{1/2}$ for ATL–RC–05.

In Region 3, carbonation was detected for specimens taken from structures located in the El Paso District, a medium corrosive environment. The level of carbon monoxide released into the air was reported to be as high as 10.9 ppmv (parts per million by volume), with an average of 2.9 ppmv, for the El Paso area from 2006 to 2022 (TCEQ, 2023). That fact may explain the development of carbonation in concrete decks located in this district. For example, carbonation depth was measured on average as approximately 0.2 in. for specimens taken from ELP–RC–04 and 0.5 in. for the samples taken from ELP–RC–07. Both bridges are located in industrial environments. ELP–RC–08 is also located in the industrial environment, and the depth of carbonation was measured on average as approximately 0.2 in. The initial sorptivity calculated for

ELP–RC–04 and ELP–RC–07 was relatively high, more than 12×10^{-3} mm/s$^{1/2}$, indicating a porous concrete, while the recorded bulk resistivity for these specimens implies that water content of these specimens must be low (bulk resistivity was measured to be over 10 kΩ cm). No signs of carbonation were observed for the specimens taken from concrete decks located in Region 4.

In Region 5, the average carbonation depth measured for the core sample extracted from WFS–RC–02 was approximately 0.2 in. The recorded bulk resistivity was on average 10 kΩ cm, and the initial sorptivity was calculated to be on average 6×10^{-3} mm/s$^{1/2}$, indicating a good quality concrete. However, the bridge was located 6 miles away from a natural gas plant at Allendale, Texas. In Region 6, carbonation was observed for core samples obtained from the Lubbock District. Of the concrete decks inspected in this district, LBB–RC–01, LBB–RC–02, LBB–RC–03, LBB–RC–04 exhibited high resistivity and low initial sorptivity. The depth of carbonation for those older concrete decks is acceptable (all constructed before 2000). The carbonation depth was on average 0.2 in. for newly built structures LBB–RC–05 and LBB–RC–06. This reading was even higher (approximately 0.4 in.) for the specimen extracted from LBB–RC–07.

The bulk resistivity recorded for LBB–RC–05 and LBB–RC–07 was over 10 kΩ cm, and the initial sorptivity was measured lower or close to 6×10^{-3} mm/s$^{1/2}$. However, both bridges are constructed in the industrial zone, and both are located 3 miles away from Lubbock Central Heating and Cooling plant and 12 miles away from Jones Station gas plant at Ransom Canyon, Texas. The bulk resistivity recorded for the core specimen obtained from LBB–RC–06, located 8 miles away from Lubbock Central Heating and Cooling plant and 15 miles away from Jones Station gas plant, was lower than 5.2 kΩ cm. The initial sorptivity was also found to be on average 12×10^{-3} mm/s$^{1/2}$. Hence, the quality of the inspected concrete deck is reported to be poor.

In general, it was concluded that carbonation is not a major cause of corrosion initiation in TxDOT concrete decks if an adequate concrete cover is provided over the steel reinforcement. A depth of 0.5 in. was measured for carbon dioxide penetration within concrete specimens taken from concrete decks across Texas. Note that in the event that cracks appear in the concrete, carbonation aligns with other pollutant such as chloride and sulfur ingress can be expected to cause deterioration of steel rebar. However, the carbonation of concrete surface should not be considered as a result of carbon dioxide diffusion within concrete.

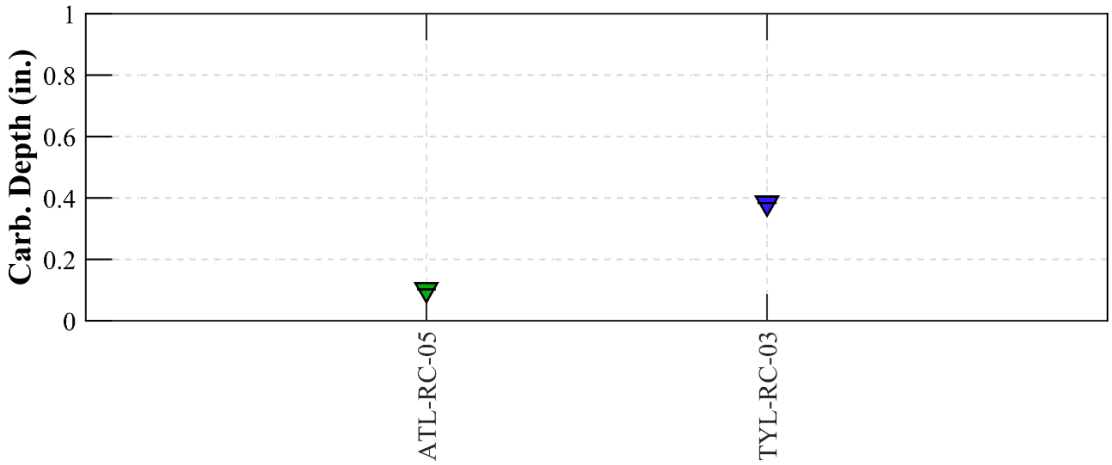

(a) Region 2

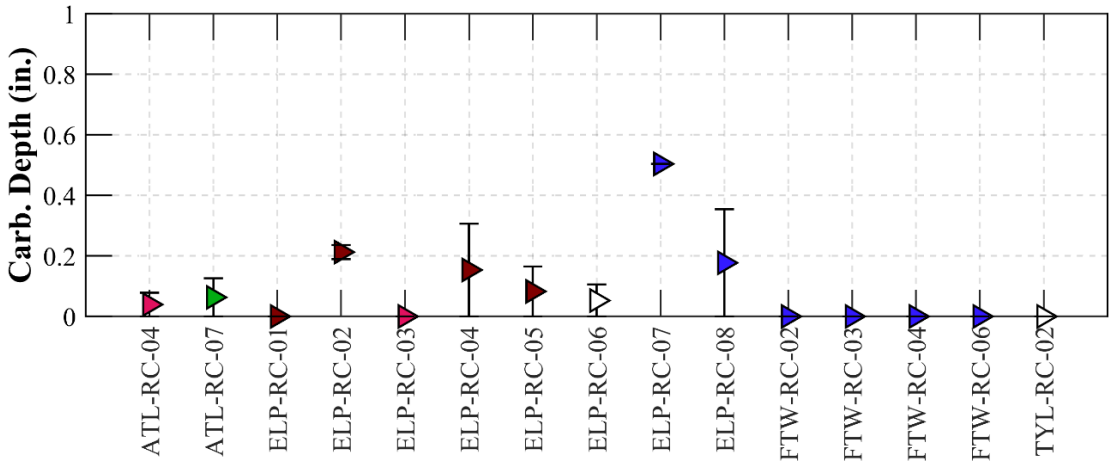

(b) Region 3

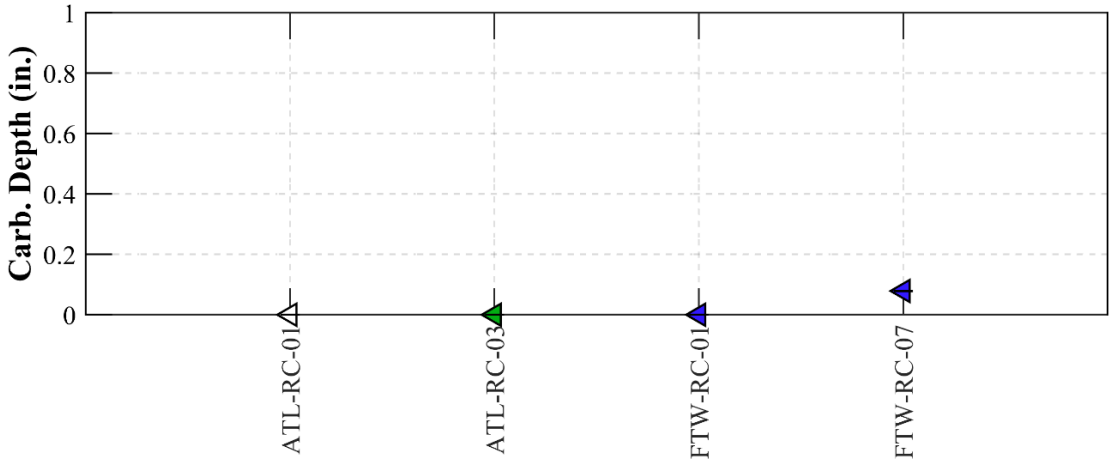

(c) Region 4

Figure 4.33. Carbonation Depth Measured for Concrete Specimens.

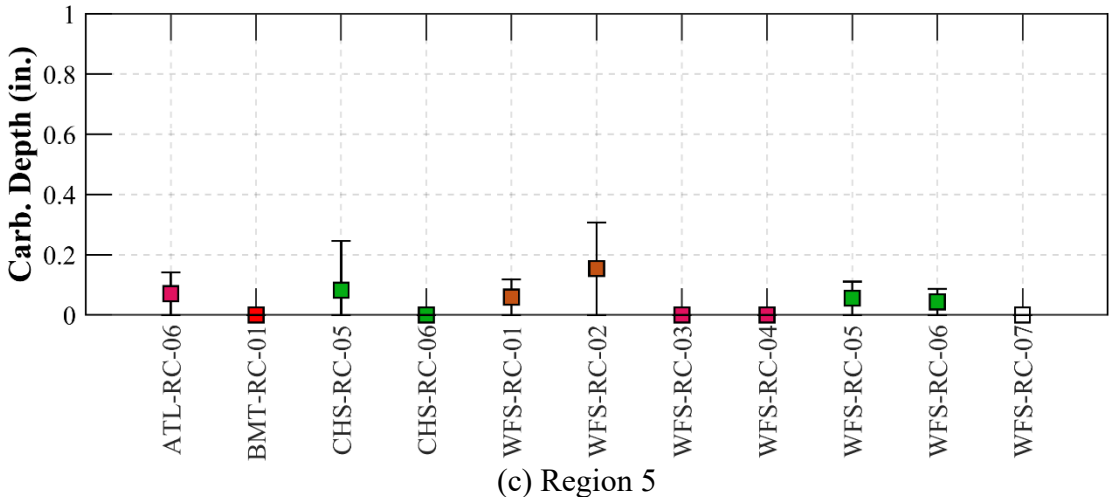

(c) Region 5

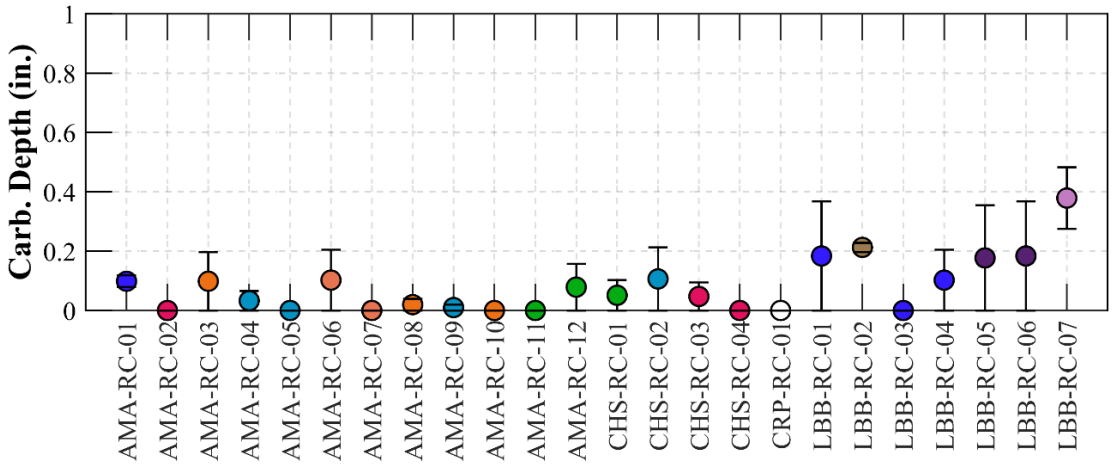

(d) Region 6

Figure 4.33. Carbonation Depth Measured for Concrete Specimens (Cont.).

4.1.7 Coating Adhesion Testing

Coating adhesion testing was conducted to determine if an adequate bond exists between the substrate and epoxy coating. Adhesion testing can give valuable insight into the quality of the epoxy coating in reinforcement concrete structures. Chloride or sulfur ions dissolved in pore water can degrade the coating, leading to disbonding of the epoxy-coated layer. These substances can reach the steel surface, either by permeating through the coating or by contacting the steel surface through coating damage. Thus, continuous exposure of the steel to aggressive solutions (such as chloride-laden water) significantly affects the adhesion bond between the epoxy coating and the steel (Pincheira et al., 2015). Because the steel surface is no longer protected by the coating, any damage to the epoxy-coated layer can readily result in the corrosion of the reinforcing steel.

Additionally, the formation of corrosion products at the defect sites can weaken the bond between the epoxy coating and steel substrate, leading to further disbonding.

Vaca-Cortés et al. (1998) suggested conducting the coating adhesion test (also known as peel or knife test) by using a sharp knife. The author recommended that the knife test be performed after an accelerated corrosion process, such as solution immersion, hot water immersion, cathodic disbondment, a bend test, or accelerated corrosion inside concrete (Vaca-Cortés et al., 1998). However, an accelerated process is required when the aim is to replicate the service environment more quickly. In this study, there was no requirement to conduct the accelerated corrosion process because the steel ECR were obtained from aged structures. As a result, no accelerated tests were performed prior to the knife testing to evaluate the quality of the existing coatings already exposed to the environment.

4.1.7.1 Experimental Setup

Following ASTM D6677 (2018), the procedure taken during a knife test is as follows:

1. Select an area free of blemishes and imperfections.
2. Cut the coating at a 30° to 45° angle to the base metal using a hobby knife blade. Note that the cuts should extend down to the substrate and intersect to form an "X." Each leg of the angle should be at least 1 ½ in. (38.1 mm) in length.
3. Use the point of the knife and, starting at the vertex of the angle, attempt to lift up the coating from the substrate.
4. Evaluate the results using a 4-level rating system, as shown in Table 4-6.
5. Repeat the examination in two other locations of the coating.
6. Examine the cutting edge and document the result of qualitative evaluation.

ASTM D6677 (2018) proposed a ranking criteria to assess the quality of epoxy layers coated on steel rebars that is summarized in Table 4-6.

Table 4-6. Epoxy Coating Quality Ranking (ASTM D6677, 2018).

Rating	Description
10	Coating is extremely difficult to remove; fragments no larger than approximately 1/32 in. by 1/32 in. (0.8 mm by 0.8 mm) removed with great difficulty.
8	Coating is difficult to remove; chips ranging from approximately 1/16 in. by 1/16 in. (1.6 mm by 1.6 mm) to 1⁄8 in. by 1⁄8 in. (3.2 mm by 3.2 mm) can be removed with difficulty.
6	Coating is somewhat difficult to remove; chips ranging from approximately 1⁄8 in. by 1⁄8 in. (3.2 mm by 3.2 mm) to 1⁄4 in. by 1⁄4 in. (6.3 mm by 6.3 mm) can be removed with slight difficulty.
4	Coating is somewhat difficult to remove; chips more than 1⁄4 in. by 1⁄4 in. (6.3 mm by 6.3 mm) can be removed by exerting light pressure with the knife blade.
2	Coating is easily removed; once started with the knife blade, the coating can be grasped with one's fingers and easily peeled to a length of at least 1⁄4 in. (6.3 mm).
0	Coating can be easily peeled from the substrate to a length greater than 1⁄4 in. (6.3 mm).

4.1.7.2 Experimental Results

An adequate bond between the substrate (reinforcement steel) and epoxy coating was observed for most of the examined rebar. However, severe deterioration of the coating was also detected for ECR when the coating was easily peeled from the substrate. As seen in Table 4-6, the rebars with intact coating were ranked 10, while those with a severely deteriorated coating were scored 0. Figure 4.34 shows the adhesion rating of all ECR samples tested in this study with the corresponding year of bridge construction.

As shown in Figure 4.34, the adhesion rating of some of the ECR extracted from core specimens from Region 6 was low, and pitting corrosion was also detected on those specimens. A low adhesion rating was also documented for some specimens taken from concrete decks in Region 3. However, no trace of corrosion was observed for these particular samples.

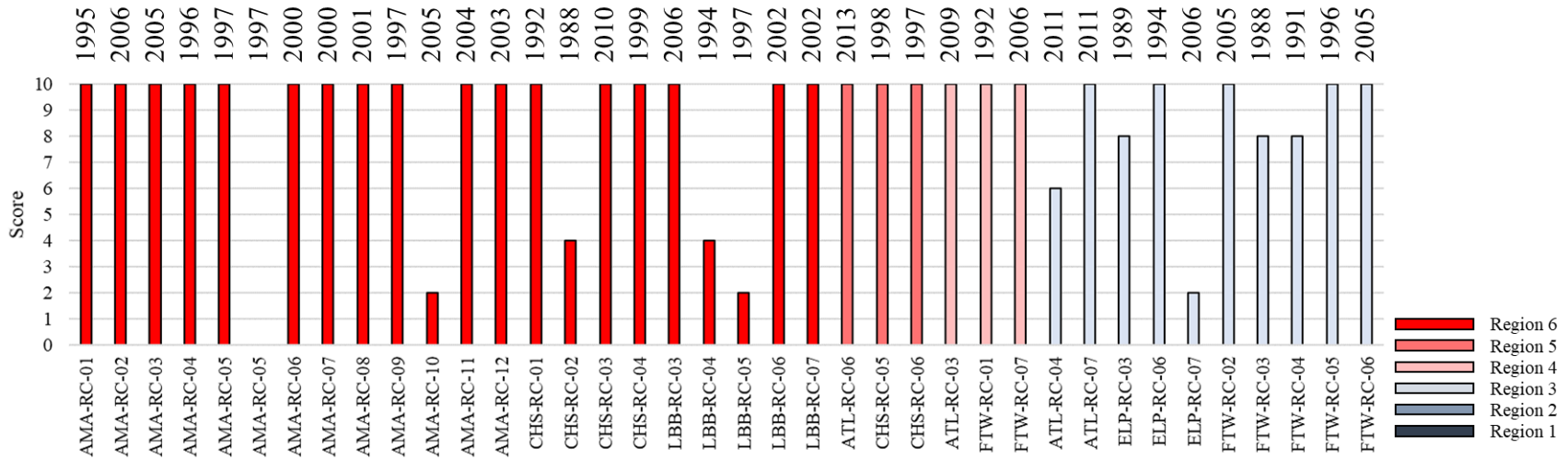

Figure 4.34. Adhesion Rating of Bridges and Built Year of Bridges.

Figure 4.35 depicts rebars with severe corrosion extracted from concrete decks located in highly corrosive environments such as Amarillo, Lubbock, and Childress. Figure 4.36 shows some moderately deteriorated coatings that were ranked between 2 and 6, depending on the quality of coating adhesion. These coatings that were susceptible to chipping when subjected to light pressure were identified as "ease of removal." Among these coatings, traces of corrosion were sometimes observed on steel substrate. For example, light corrosion was detected for the samples taken from ELP–RC–07 and LBB–RC–05 as the coat was peeled off.

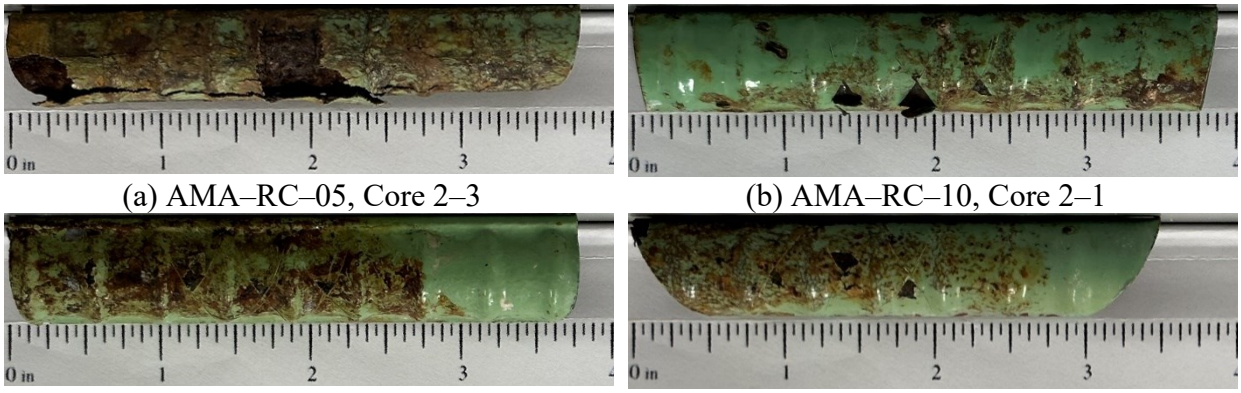

(a) AMA–RC–05, Core 2–3 (b) AMA–RC–10, Core 2–1

(c) LBB–RC–04, Core 2–3 (d) CHS–RC–02, Core 1–2

Figure 4.35. Severely Deteriorated Coating Samples.

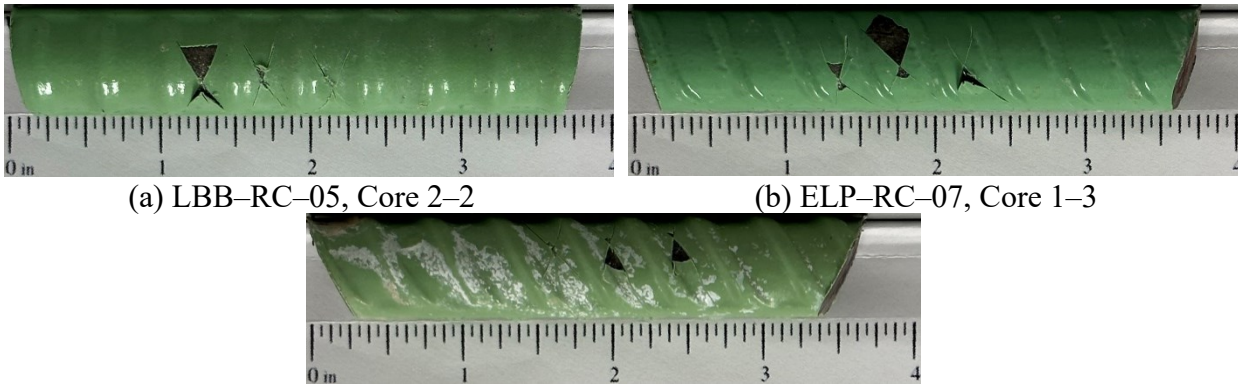

(a) LBB–RC–05, Core 2–2 (b) ELP–RC–07, Core 1–3

(c) ATL–RC–04, Core 2–3

Figure 4.36. Moderately Deteriorated Coating Samples.

The crack condition of the cores sampled with moderately and severely deteriorated coatings are shown in Figure 4.37. Core samples from AMA–RC–05, AMA–RC–10, LBB–RC–04, and CHS–RC–02 show deep cracks, suggesting that these cracks could have led to corrosion on the coating and a loss of adhesion between the coating and the steel. In contrast, no cracks were found on the core samples from LBB–RC–05 and ELP–RC–07, indicating that other factors such

as poor quality control of the coating or handling of the ECR could have contributed to a loss of bond between the coating and the steel.

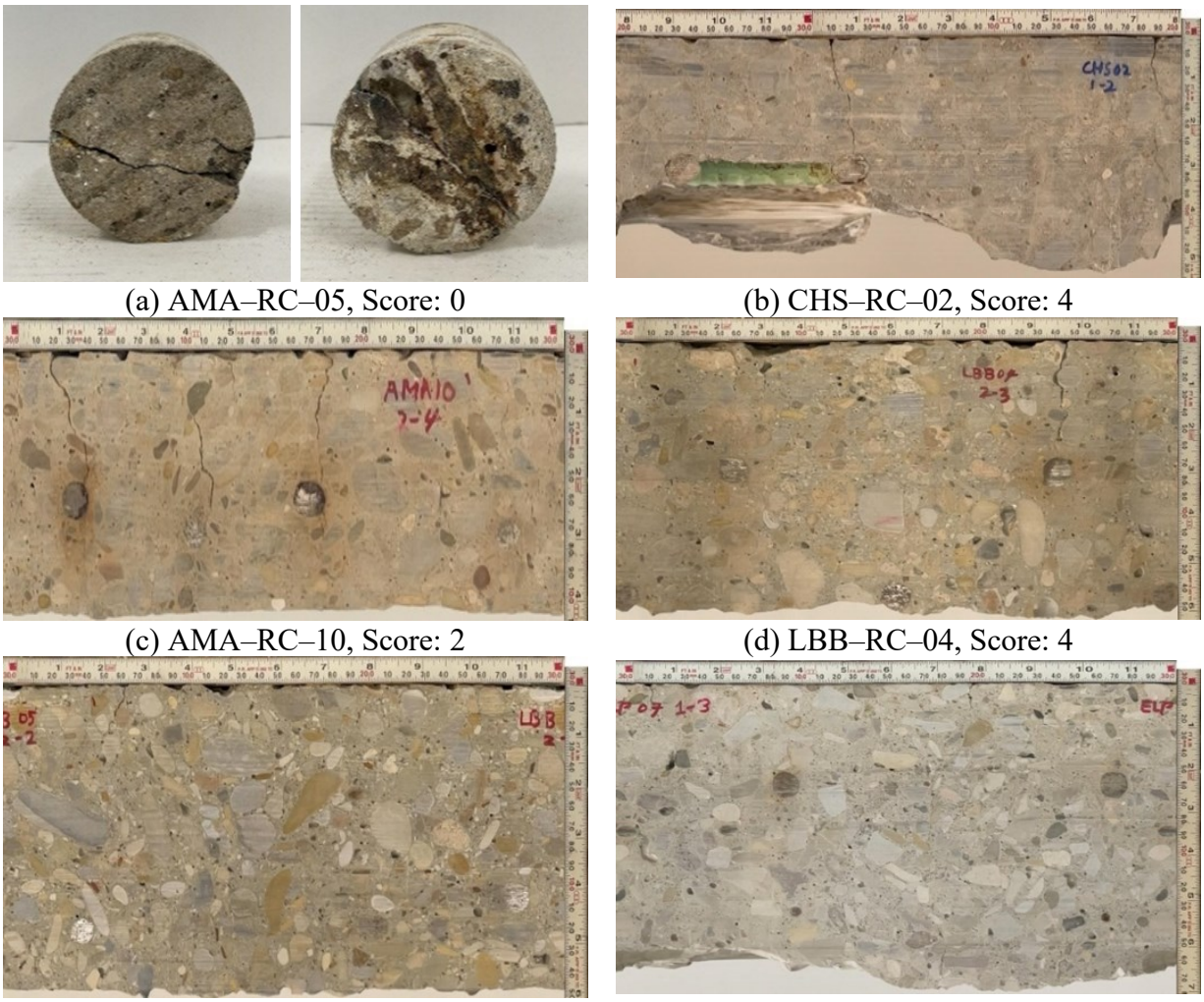

(a) AMA–RC–05, Score: 0

(b) CHS–RC–02, Score: 4

(c) AMA–RC–10, Score: 2

(d) LBB–RC–04, Score: 4

(e) LBB–RC–05, Score: 2

(f) ELP–RC–07, Score: 2

Figure 4.37. Condition of Cores of Low Adhesion Rating Bridges.

In general, researchers concluded that the bond between the steel reinforcement and epoxy coating was in good condition. However, some samples exhibited weak bonding to the steel substrate because of corrosion initiation (Figure 4.38). As shown in Figure 4.38, age of the rebar did not correlate with the condition of the coating and adhesion rating.

The initial sorptivity of the concrete specimen was high for the deteriorated coating specimens. For example, the sample obtained from ELP–RC–03 was scored on average 6, and the specimen taken from ELP–RC–07 was ranked on average 2. The average initial sorptivity of the concrete specimens were over 12×10^{-3} mm/s$^{1/2}$. The coated samples extracted from FTW–RC–

03 and FTW–RC–04 were ranked on average 8. The average initial sorptivity calculated for these cores was computed to be slightly more than 6×10^{-3} mm/s$^{1/2}$. However, the opposite of this conclusion is not always supported. For example, the initial sorptivity of the concrete specimens obtained from ELP–RC–06 and FTW–RC–01 was high (approximately 10×10^{-3} mm/s$^{1/2}$), but the coatings remained intact when they were ranked on average 10. This finding indicates that factors such as porous concrete, elevated water content in concrete, chloride ingress, and deep cracks can cause corrosion problems if the epoxy-coated layer is damaged for any reason, such as mishandling during construction or the manufacturing process. If so, the corrosion can propagate in the interface between the coating and steel substrate, causing deterioration of the coated layer and acceleration of the corrosion process in steel reinforcement.

In Region 6, the bulk resistivity for the concrete cores obtained from AMA–RC–05 was recorded as lower than 5.2 kΩ cm, and the average initial sorptivity was calculated as 12×10^{-3} mm/s$^{1/2}$. The adhesion quality of the epoxy coating was ranked on average 5 for the specimens obtained from that concrete deck. Similarly, the sample taken from CHS–RC–02 was scored on average 4. The concrete specimen had a bulk resistivity on average lower than 5.2 kΩ cm but an initial sorptivity lower than 12×10^{-3} mm/s$^{1/2}$, indicating a dense concrete with high water content. Note that the chloride concentration measured at the rebar level was high for both cases, particularly for AMA–RC–05, which was on average 0.4 % wt. conc. A similar pattern was observed for the sample extracted from LBB–RC–04.

The epoxy-coated layer was not sufficiently adhering to the steel substrate for the specimen obtained from LBB–RC–05, suggesting poor surface preparation during the manufacturing of the epoxy-coated reinforcement. This issue can result in the loss of the adhesion bond and the initiation of corrosion in the future. Particularly, the chloride content at the rebar level was measured on average 0.1 % wt. conc. for the specimens extracted from LBB–RC–05 despite the good quality concrete evidenced by the result obtained during resistivity and water absorption tests.

The coating of the sample taken from AMA–RC–10 deteriorated and was ranked 2. As discussed previously, the concentration of chloride at the concrete and rebar interface was recorded as being high for the specimen obtained from this concrete deck—on average 0.14 % wt. conc.

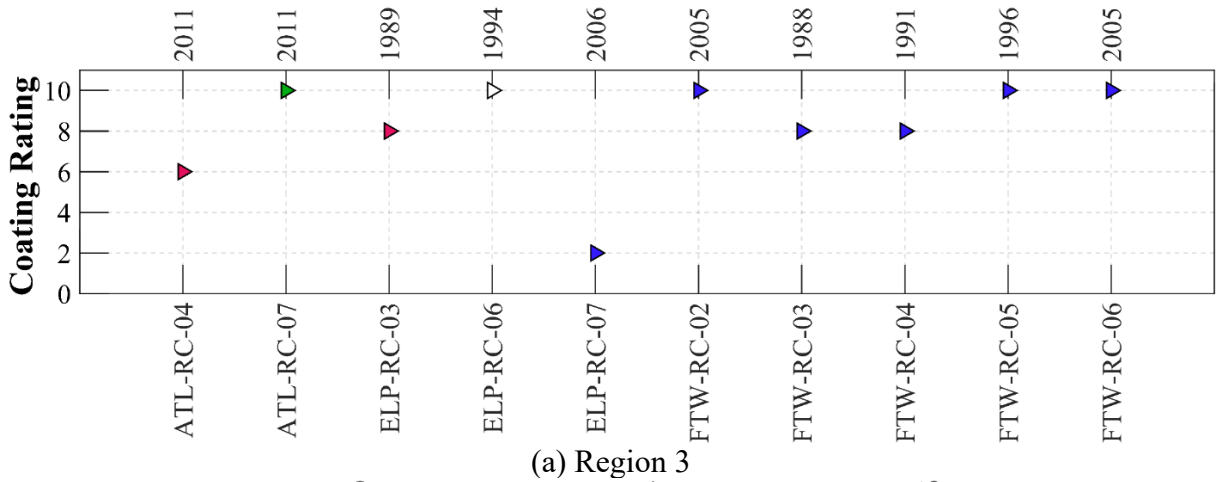

(a) Region 3

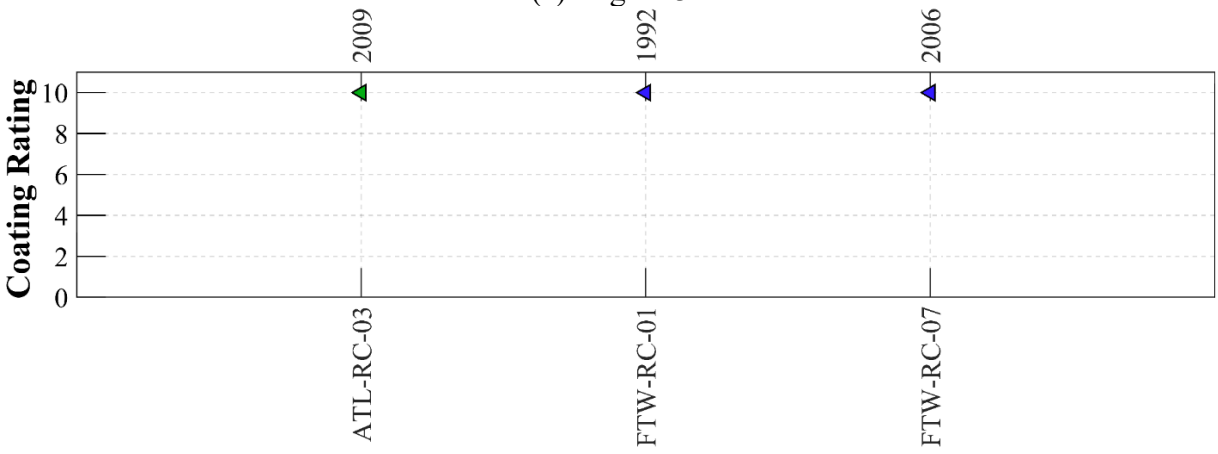

(b) Region 4

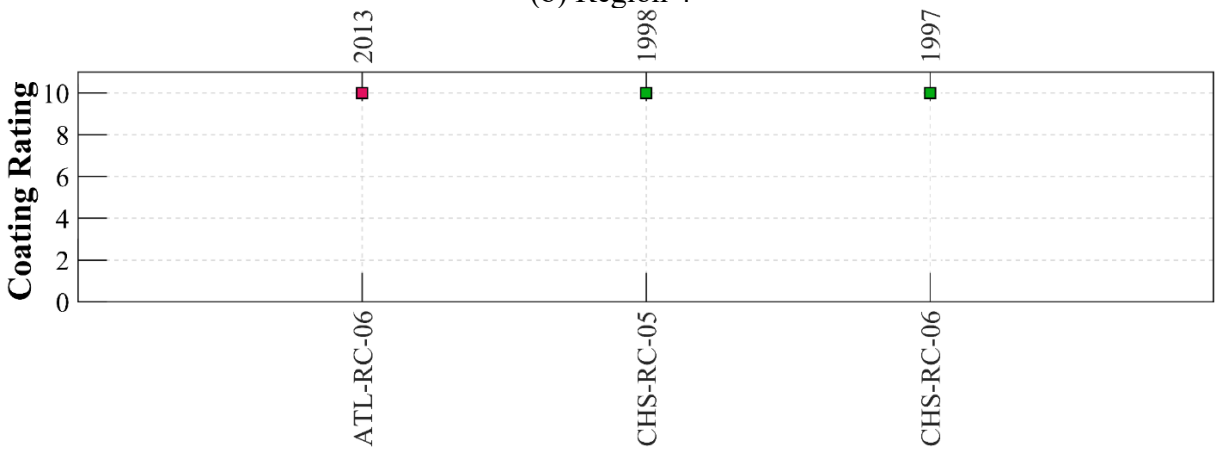

(c) Region 5

Figure 4.38. Rankings Obtained for Adhesion of Epoxy Coating.

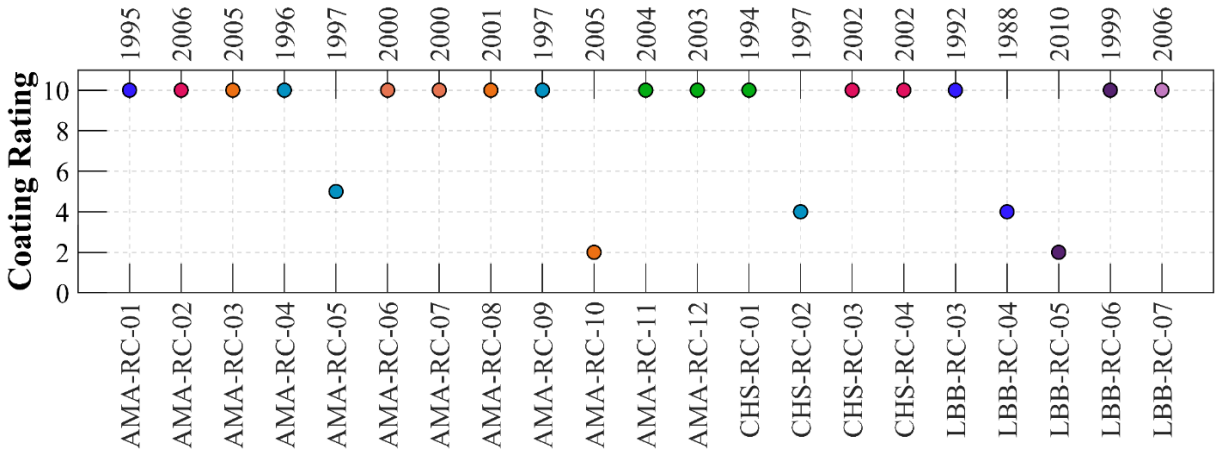

(d) Region 6

Figure 4.38. Rankings Obtained for Adhesion of Epoxy Coating (Cont.).

4.1.8 Electrochemical Impedance Spectroscopy

Impedance analysis is an effective method that can be utilized to assess the durability of steel reinforcement in concrete. This technique is widely used to estimate the corrosion rate of metals and evaluate the performance of barrier coatings and the durability of the passivation layer in metals (Popov, 2015; Rockey, 2022). During EIS examination, the specimen is subjected to a low amplitude alternating current over a wide range of frequencies, and the impedance response of the system is calculated accordingly.

TxDOT (2022b) recommends the use of a fusion-bonded coating on the steel reinforcing bar (specified by ASTM A775/A775M (2022), particularly in the areas prone to corrosion. Kamde and Pillai (2021) studied the performance of fusion-bonded epoxy rebars due to corrosive environments and concluded that the epoxy coating protects steel from corrosion as long as no defects occur on the coated layer. Moreover, the authors also reported the use of impedance measurements to monitor the initiation of corrosion and detect any damage on ECR embedded in concrete. In the current research, EIS was employed to determine the corrosion state of black rebar in concrete cores and evaluate the quality of epoxy coating layers that have been in service for years.

4.1.8.1 Experimental Setup

Schematic representation of the experimental setup and apparatus required for conducting EIS examination is depicted in Figure 4.39. A Gamry Interface 1010E instrument was employed

to apply alternating current and analyze the impedance response of the system. The working electrode (WE) was connected to the Gamry potentiostat using copper foil tape. The WE was carefully covered with conductive tape to prevent any contact with the titanium mesh that was used as the counter electrode (CE). A wet sponge was positioned between the concrete core and the titanium mesh to ensure optimal electrical contact. The responding signals were recorded with the aid of a copper/copper sulfate reference electrode (RE). Figure 4.40 represents the actual test setup used during the EIS examination.

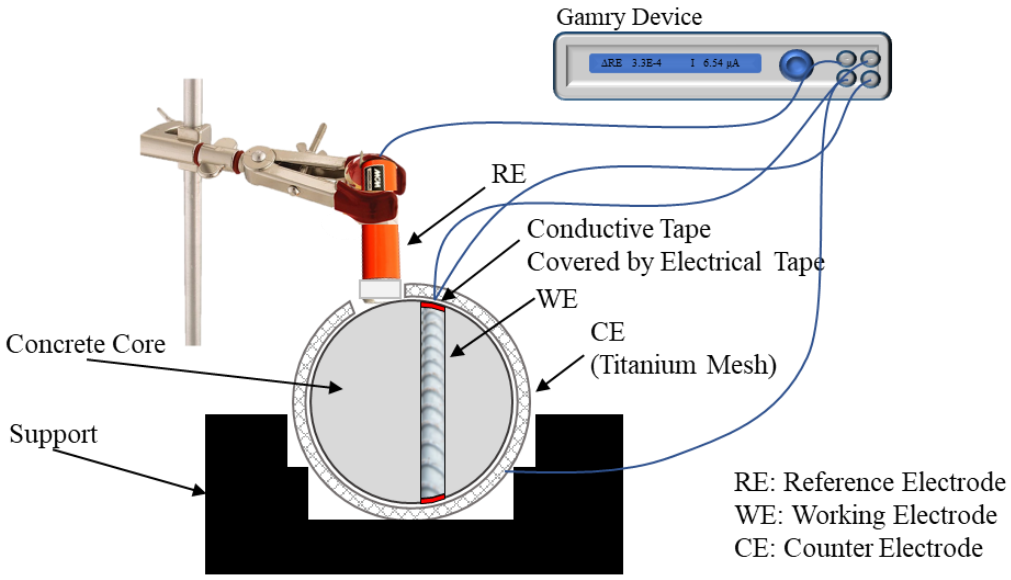

Figure 4.39. Schematic View of EIS Experiment.

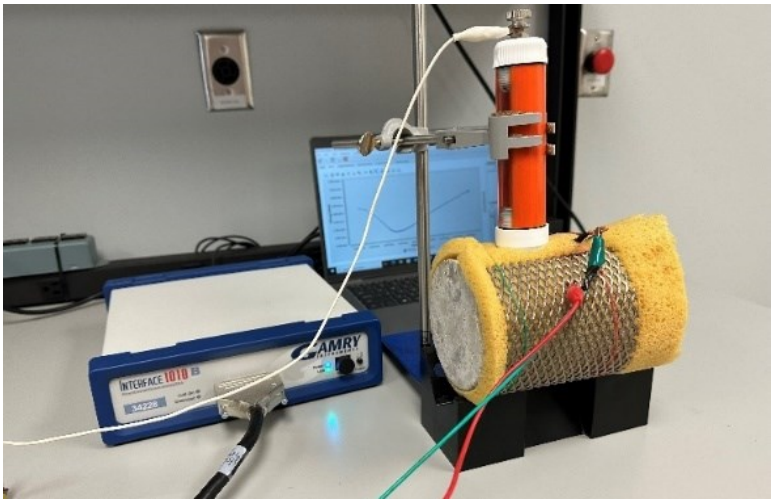

Figure 4.40. Experimental Setup of EIS.

The procedure to perform EIS is as follows:

1. Sand off the rebar surface and connect steel rebar to potentiostat using wire and conductive tape.
2. Mask the steel rebar, wire, and conductive tape with nonconductive tape.
3. Wrap the concrete specimen with wet sponge and secure the titanium mesh over the wet sponge.
4. Place the sample on support and adjust the lab stand to ensure that the RE is in close contact with the sample.
5. Connect reference electrode and CE with Gamry Interface 1010E instrument.
6. Monitor open circuit potential until the stability in voltage recordings is achieved.
7. Set the scan rate to 0.167 mV/s and record impedance responses for the frequency decreasing from 100 kHz to 10 mHz in a logarithmic decay.
8. Break the specimen and measure the rebar length to the nearest 0.001 m.

4.1.8.2 Experimental Results

Polarization resistance of black rebar is significantly smaller than that of epoxy-coated steel because the protective layer acts as an electrical barrier and also preserves the steel from corrosion. Therefore, electrochemical reactions do not proceed evenly in a highly corrosive environment because ferrous and ferric ions cannot interact with corrosive agents—that remains unchanged until damage to the epoxy layer occurs. Defects on the protected layers may also happen during the transportation of steel rebars and construction of concrete decks. If the water content in the concrete and around the steel rebars is high, it can penetrate the epoxy-coated layers through these defects, causing the initiation of corrosion and debonding of the coating.

Figure 4.41 illustrates equivalent circuits considered to analyze the impedance measurements of the core specimens extracted from concrete decks. Ribeiro and Abrantes (2016) proposed a modified Randles cell for concrete structures, which is a network consisting of three circuits connected in a series, with a constant phase element (CPE) connected in parallel to a resistor (Figure 4.41[a]). This model represents the concrete (R_C), the steel reinforcement (R_p), and the interface of concrete and steel (R_f). It is common to use a dummy resistor (R_O) in the equivalent circuit that will add to R_C to estimate the concrete resistance, while polarization resistance (R_p) is used to determine the corrosion rate of steel reinforcement. Rodrigues et al. (2021) suggested a

different equivalent circuit, shown in Figure 4.41(b), to model an ECR with existing defects. This model represents concrete with a single resistor that is in series with a network of two CPEs and two resistors, indicating the polarization resistance as well as the resistance associated with defects (R_{pore}). The capacitive behavior of the system is modeled by using a CPE_{dl} in both networks. Note that the Simplex method was implemented to obtain the best equivalent network for the EIS recordings.

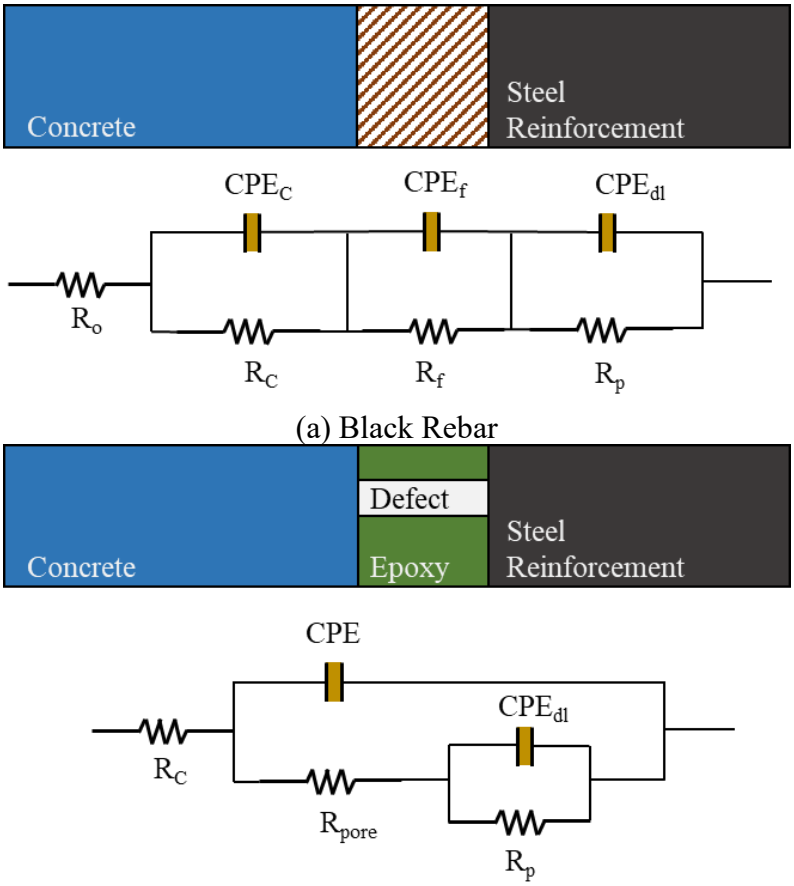

Figure 4.41. Schematic Representation and Idealized Equivalent Circuit of Steel Reinforcement in Concrete.

The impedance responses of the core specimens examined in this study (Nyquist plots and Bode diagrams) are included in the appendix. The readers are referred to the appendix for detailed results. However, a study on the polarization resistance and corrosion rate of the specimens tested in this research is presented in this section. The corrosion rate of systems with black rebar was calculated by using the Stern-Geary equation, which can be reduced to the following:

$$i_{\text{corr}} = \frac{0.026}{R_{\text{p}}} \tag{4.16}$$

where Tafel slopes are in the range of 120 mV (Popov, 2015). Table 4-7 gives criteria proposed by Fontana and Greene (1986) (later modified by J.P. Broomfield (2006)) to assess the extent of corrosion on steel based on exchange current density (i_{corr}).

Table 4-7. Assessment Criteria of Uncoated Steel Corrosion Condition (J.P. Broomfield, 2006; Fontana & Greene, 1986).

Corrosion Rate (mpy)	Steel Condition
< 0.05	Passive condition
0.05 to 0.25	Low to moderate corrosion
0.25 to 0.5	Moderate to high corrosion
> 0.5	High corrosion rate

When the exchange current density of steel is below 0.05 mpy, it implies that electrochemical reactions are not taking place, or if they are, they proceed at a negligible rate, resulting in a so-called passive state. When exchange current density is between 0.05 and 0.25 mpy, it indicates low to moderate corrosion rate. As exchange current density increases within the range of 0.25 and 0.5 mpy, it suggests a moderate to high corrosion rate. When the exchange current density exceeds 0.5 mpy, then corrosion rate of the steel section should be expected to be high (Figure 4.42).

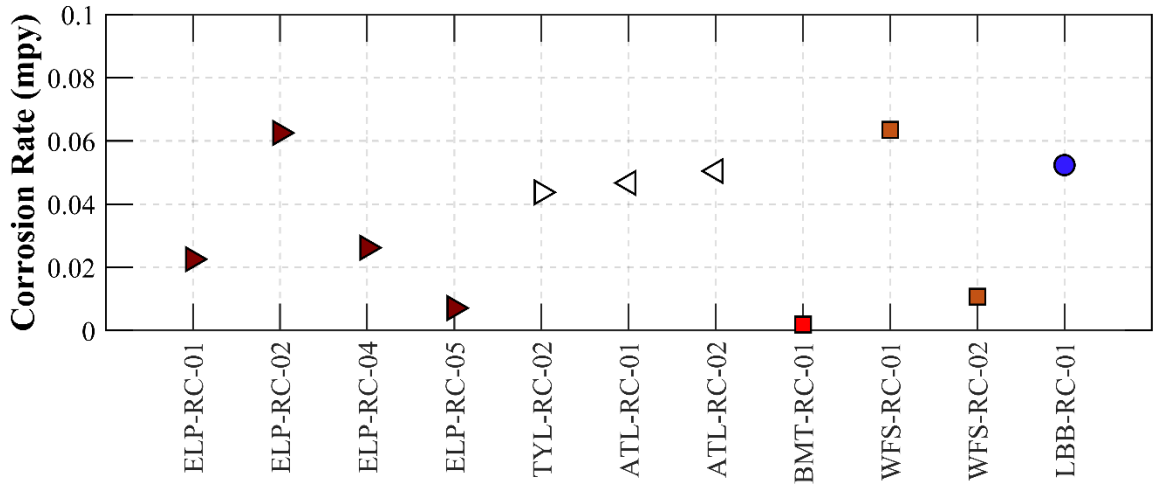

Figure 4.42. Corrosion Rate Calculated for Black Rebars Obtained from Core Specimens.

Using Faraday's Law, Figure 4.42 shows calculated corrosion rates for the concrete core specimens with black rebars. More details, including polarization resistance and exchange current

density of black rebars, are also provided in Table 4-8. The state of corrosion was obtained to be negligible or low to moderate for all the specimens. However, it is worth noting that corrosion is a localized problem, and the results shown in Figure 4.42 represent the general condition of the reinforced concrete structure.

Table 4-8. Evaluation of Corrosion for Concrete Cores with Black Rebars.

Bridge Name	R_p (kΩ cm^2)	i_{corr} (µA/cm^2)	Corrosion Rate (mpy)
ELP–RC–01	527	0.05	0.023
ELP–RC–02	190	0.14	0.063
ELP–RC–04	454	0.06	0.026
ELP–RC–05	1,666	0.02	0.007
TYL–RC–02	272	0.10	0.044
ATL–RC–01	255	0.10	0.047
ATL–RC–02	336	0.11	0.050
BMT–RC–01	6,346	0.00	0.002
WFS–RC–01	187	0.14	0.064
WFS–RC–02	1,110	0.02	0.011
LBB–RC–01	227	0.11	0.052

After studying the calculated corrosion rate for steel rebar embedded in the core samples, researchers concluded that the concrete condition contributes to the extent of corrosion in deck structures. For a dense and good quality concrete, it is expected that electrochemical reactions will not proceed. As the initial sorptivity of the concrete specimen increased—along with a decrease in bulk resistivity—the rate of corrosion also increased.

In Region 3, the corrosion rate of the specimens was generally low since HPC was used in the construction of concrete decks. However, the specimen extracted from ELP–RC–02 exhibited a corrosion rate over 0.05 mpy, indicating a moderate rate of corrosion. The chloride concentration at the rebar level was negligible for concrete decks located in Region 3, while the initial sorptivity was calculated as being high for ELP–RC–02 and ELP–RC–04. The bulk resistivity of the specimens extracted from ELP–RC–04 was higher than ELP–RC–02, and the corrosion rate was lower. ELP–RC–01 had an average bulk resistivity of 10 kΩ cm, which is within the ELP–RC–02 range, but despite the initial sorptivity recorded for ELP–RC–02, it was lower than 6×10^{-3} mm/s$^{1/2}$ for the specimens taken from ELP–RC–01. This conclusion is also valid for TYL–RC–02; the corrosion rate was higher than for ELP–RC–01 and ELP–RC–04, while the initial sorptivity computed for this specimen was higher than 6×10^{-3} mm/s$^{1/2}$ (within the ELP–RC–02 range), and the average bulk resistivity was lower than 10 kΩ cm.

In Region 4, the corrosion rate of ATL–RC–01 was almost 0.05 mpy, indicating a moderate rate of corrosion. The initial sorptivity calculated for this specimen was generally greater than 6×10^{-3} mm/s$^{1/2}$, and the bulk resistivity was lower than 10 kΩ cm. The corrosion rate of the black rebar in the core sample extracted from ATL–RC–02 was 0.05 mpy. The average initial sorptivity of the specimen was 6×10^{-3} mm/s$^{1/2}$, but the bulk resistivity is not known for this specimen. The average velocity of the sound wave in the specimens taken from ATL–RC–02 was measured at 13×10^{3} ft/s, which was lower than what was measured for ATL–RC–01.

In Region 5, the average bulk resistivity of the specimens taken from BMT–RC–01 was 48 kΩ cm, and the initial sorptivity was lower than 6×10^{-3} mm/s$^{1/2}$. As shown in Figure 4.42, the rate of electrochemical reactions happening on the steel surface was found to be negligible. Note that other factors can contribute to increasing the corrosion rate on steel reinforcements. For example, similar to the concrete deck in Beaumont area, HPC was utilized in the construction of the structures in Wichita Falls District. The bulk resistivity recorded for the specimen extracted from WFS–RC–01 and WFS–RC–02 was over 10 kΩ cm, and the initial sorptivity of these specimens was at or lower than 6×10^{-3} mm/s$^{1/2}$. The corrosion rate calculated for the steel rebar in the core specimen extracted from WFS–RC–01 was low, yet the rate was significantly greater for the black rebar in the core taken from WFS–RC–01. After reviewing the documentation provided in the appendix, it was concluded that a deep crack originating on the concrete surface and developing over the steel reinforcing bar caused the initiation of corrosion on one side of the steel member. In Region 6, the corrosion rate of steel in LBB–RC–01 was also calculated over 0.05 mpy. The initial sorptivity obtained for the core specimen was higher than 6×10^{-3} mm/s$^{1/2}$, and the average bulk resistivity was lower than 10 kΩ cm. In addition, the average chloride concentration at the rebar level was measured at 0.08 % wt. conc. for the core samples obtained from this bridge deck. In fact, the chloride content at the rebar level was over 0.05 % wt. conc. of the threshold recommended by ACI 365.1R-17 (2017). Figure 4.43 shows the logarithmic polarization resistance calculated for core specimens with embedded ECR. The results shown in this figure were ordered with respect to the age of the concrete decks from which the core specimens were extracted. As shown in this figure, the logarithmic polarization resistance of ECR samples varies and is not correlated with the age of the specimens.

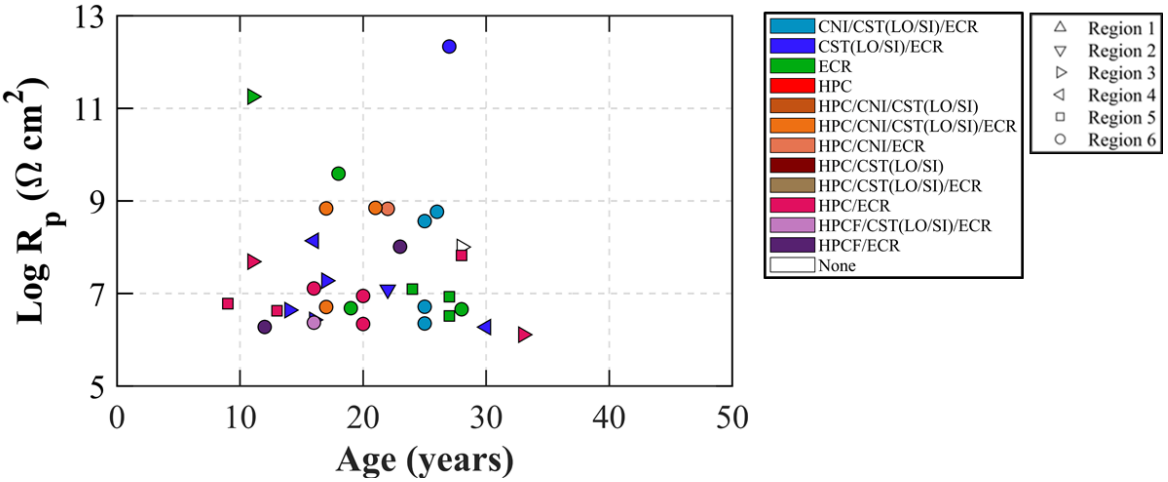

Figure 4.43. Polarization Resistance Recorded for ECR.

Figure 4.44 shows the electrical resistance or redox reactions occurring at the steel-coating interface in logarithmic order. The corrosion rate of the specimens embedded in concrete cores was determined to be negligible because the polarization resistance of the samples was relatively high at the metal-coating interface. For epoxy-coated steel, smaller polarization resistance indicates a higher possibility of corrosion. As the coating resistance decreases, it is indicative of an increase in corrosive agents within the concrete and the formation of corrosion products (Lau & Sabbir, 2015). Kamde and Pillai (2021) suggested that the coating resistance of an intact fusion-bonded epoxy is greater than 1×10^3 kΩ cm^2, which agrees with our findings from the EIS measurements conducted on the core samples taken from concrete decks. In general, the logarithmic R_p values of all the specimens was measured at or over 6 Ω cm^2, except AMA–RC–10 and FTW–RC–04, whose resistances were measured at 5.75 Ω cm^2 and 5.88 Ω cm^2, respectively. No sign or trace of corrosion was detected during the visual inspection of all the ECR after removing them from concrete. It was found from the EIS results documented for black rebar that electrochemical reactions proceed steadily when the logarithmic R_p value is less than 5.4 Ω cm^2. This feature is equivalent to a polarization resistance of 240 kΩ cm^2 and a corrosion rate of 0.05 mpy.

The color of the epoxy coating of specimens extracted from ELP–RC–03, FTW–RC–04, and CHS–RC–01 was found to be dark green; in comparison, other samples were bright green. The logarithmic resistance of these specimens measured low—6 Ω cm^2 or lower. The average initial sorptivity of cores obtained from ELP–RC–03 was calculated as 12×10^{-3} mm/s$^{1/2}$, and the bulk resistivity was lower than 5.2 kΩ cm, both findings indicating a poor-quality concrete.

However, the core of the other specimens had the initial sorptivity higher than 6×10^{-3} mm/s$^{1/2}$, and the resistivity lower than 10 kΩ cm. Although analyzing the EIS results revealed that the quality of epoxy coating of the specimens tested in the impedance examination was generally good, damage on some coatings with severe corrosion and deterioration of the steel substrate was detected on specimens obtained from AMA–RC–05, AMA–RC–10, LBB–RC–04, and CHS–RC–02 (Figure 4.35). These specimens were not tested in the EIS examination, and they were obtained from a different location of the concrete decks. In all four cases, a deep crack was discovered that had been initiated on the top surface of the concrete and propagated over the steel reinforcing rebar.

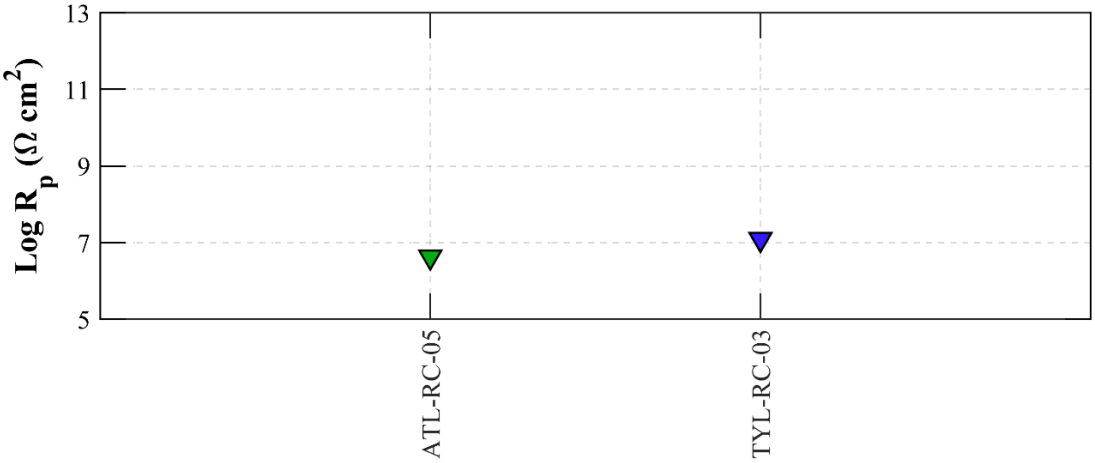

(a) Region 2

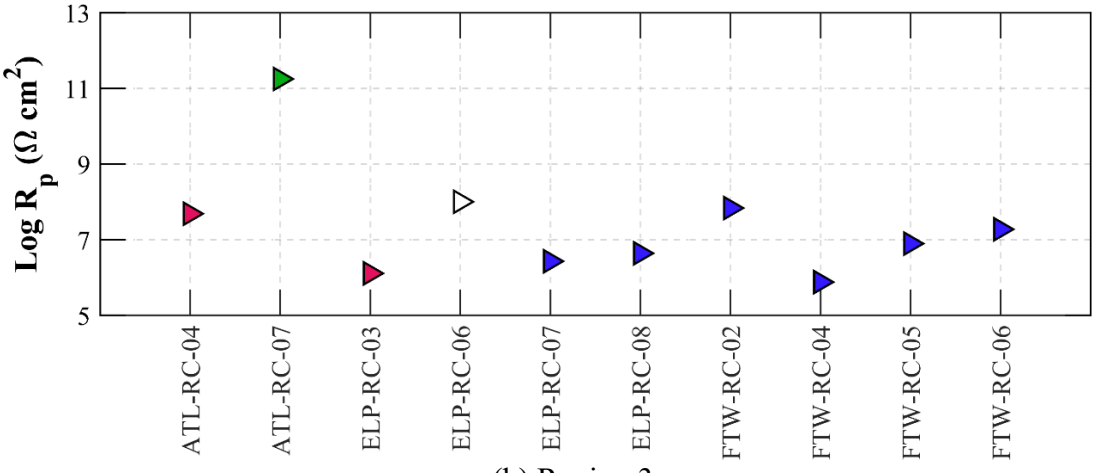

(b) Region 3

Figure 4.44. Coating Resistance (R_p) Calculated for ECR.

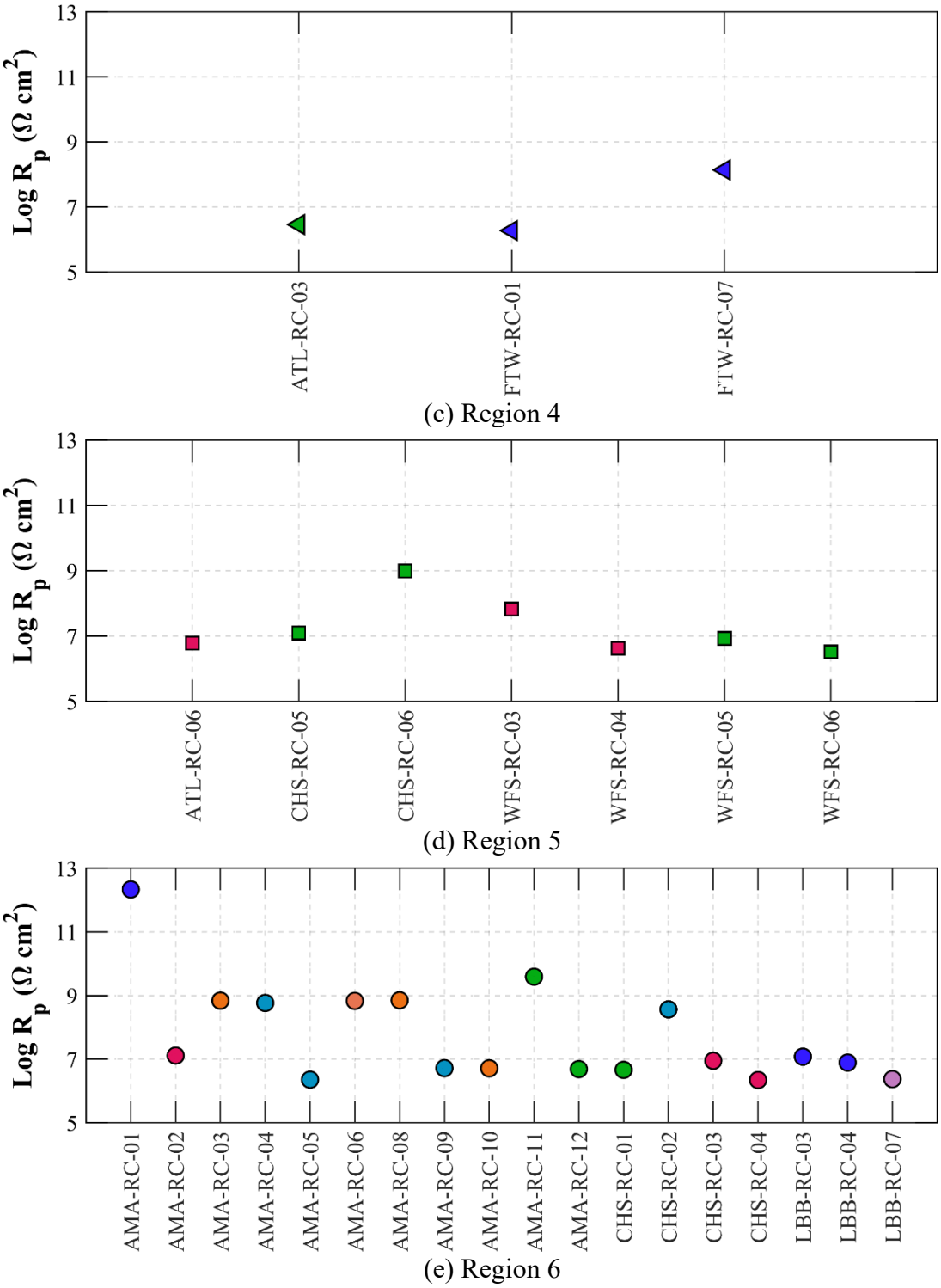

Figure 4.44. Coating Resistance (R_p) Calculated for ECR (Cont.).

Figure 4.45 shows the extent of corrosion on the black rebar extracted from core specimens. The polarization resistance and corrosion rate of these steel bars are given in Table 4-8. For the specimen obtained from ELP–RC–02, uniform corrosion was observed where the corrosion

propagated around the surface surrounding the rebar. Severe corrosion was also detected on the top of the rebar taken from WFS–RC–01, and pitting corrosion was detected in several locations on the specimen obtained from LBB–RC–01. This pitting corrosion was more evident at crevices near the transverse and longitudinal ribs. Uniform corrosion happened on transverse and longitudinal ribs of the specimen extracted from ATL–RC–01, and uniform corrosion was detected on one side of the steel taken from ATL–RC–02. This flaw was also apparent at the crevices of the longitudinal ribs of TYL–RC–02 and ELP–RC–04. No sign of corrosion was seen on samples extracted from ELP–RC–01 and ELP–RC–05. Similarly, a minor trace of corrosion was observed on samples taken from WFS–RC–02 and BMT–RC–01 (just over the cross-sectional area). It is speculated that minor volume rust occurred on these samples after the cores were obtained.

(a) ELP–RC–01

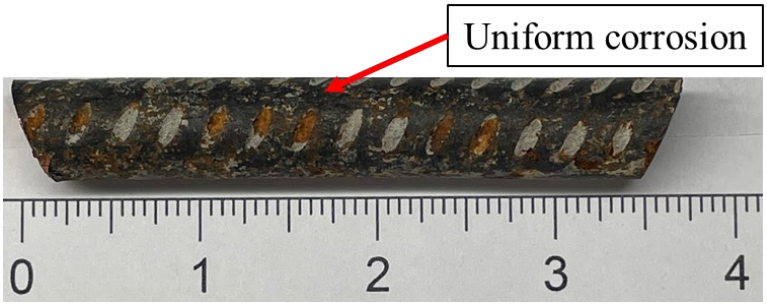

(b) ELP–RC–02

Figure 4.45. Extracted Black Rebar from Concrete Core Specimens.

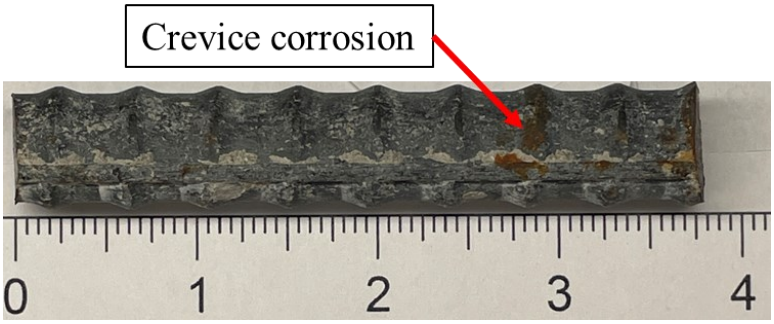

(c) ELP–RC–04

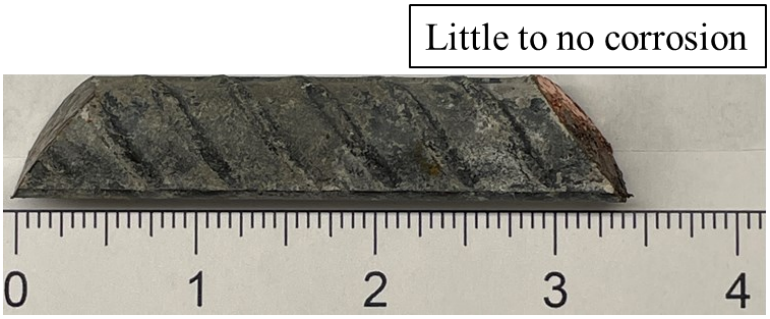

(d) ELP–RC–05

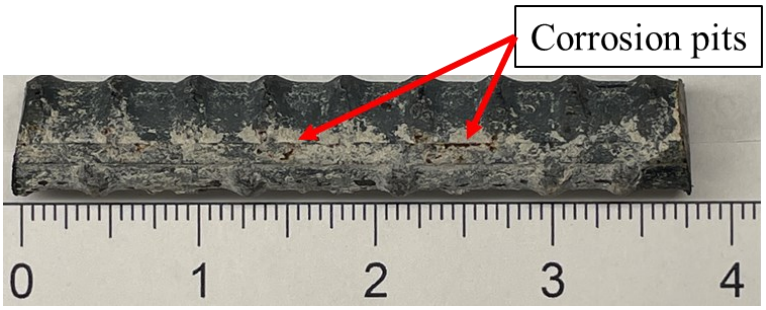

(e) TYL–RC–02

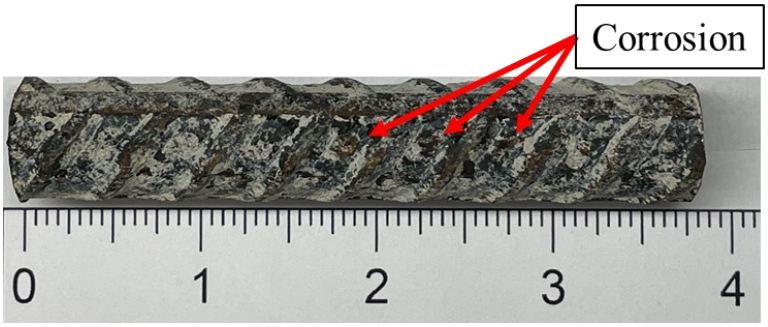

(f) ATL–RC–01

Figure 4.45. Extracted Black Rebar from Concrete Core Specimens (Cont.).

(g) ATL–RC–02

(h) BMT–RC–01

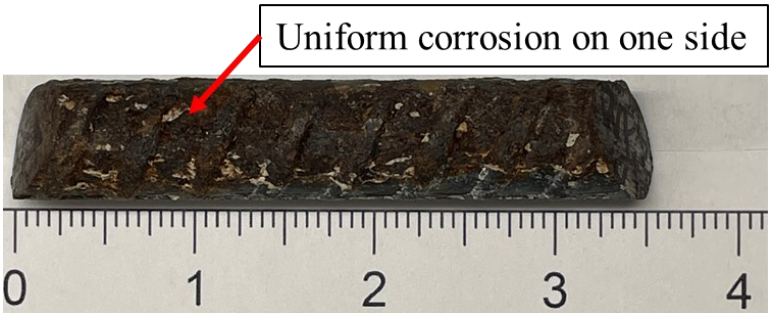

(i) WFS–RC–01

(j) WFS–RC–02

Figure 4.45. Extracted Black Rebar from Concrete Core Specimens (Cont.).

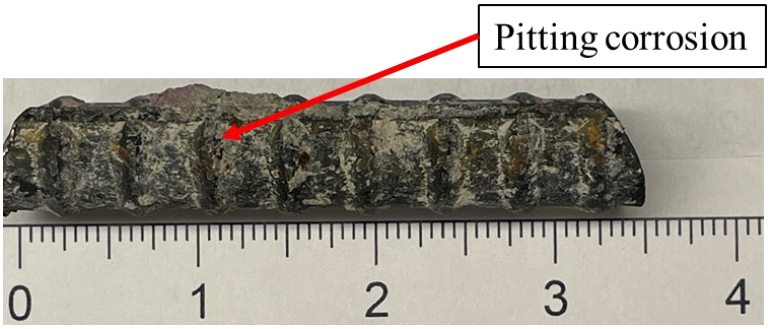

(k) LBB–RC–01

Figure 4.45. Extracted Black Rebar from Concrete Core Specimens (Cont.).

4.2 CORROSION RATE MAPPING

Since the field examination conducted using iCor was limited to a few concrete decks, it is difficult to draw a general conclusion on the corrosion rate mapping presented in this report. iCor is not suitable for detecting corrosion products that may initiate between the steel substrate and epoxy coating. Electrical resistance of epoxy coatings is relatively high, making it difficult to detect corrosion beneath epoxy coatings, and if the coating is in perfect condition and the bond between the coating and the steel substrate is strong, corrosion is not expected to initiate on the steel substrate. However, if the coating was damaged during construction, or corrosion products and pitting nucleation cause damage to the coating, then the application of iCor becomes more suitable.

The results from corrosion rate mapping in Figure 3.25(a) indicate that the maximum corrosion current density (i_{corr}) for the concrete deck of ELP−RC−03, examined during the field inspection, was estimated to be 25 μ/cm^2. This value is equivalent to a corrosion rate of 11.4 mpy. The logarithmic polarization resistance of the core specimen taken from ELP−RC−03 measured slightly higher than 6 Ω cm^2. The ECR received a ranking of 8 during the knife test, indicating that the coating has degraded to some extent. Although chloride concentration at the rebar level was found to be low, the average initial sorptivity of the core from this concrete deck was recorded as 10×10^{-3} mm/s$^{1/2}$, and the average bulk resistivity measured from the core specimens taken from ELP−RC−03 was documented as 6.3 kΩ cm. These results indicate that the quality of the concrete deck is not in good condition because of relatively high initial sorptivity and low electrical resistivity.

The maximum corrosion current density measured for the concrete deck of AMA−RC−10 was 30 μ/cm^2, which is equivalent to 13.7 mpy (Figure 3.26[a]). Although the quality of concrete used in AMA–RC–10 was determined to be of good quality based on the average bulk resistivity of the specimens extracted from this deck (measured at 20 kΩ cm), the chloride concentration at the rebar level was relatively high (0.27 wt.% concrete), indicating potential corrosion risk. Corroded rebar with damage to the epoxy coating were found in the cores tested during laboratory examinations. The quality of this epoxy coating was ranked 2 during the knife test, yet the quality of the epoxy coating in other areas of the concrete deck was found to be good. For the specimens taken from a different location and subjected to EIS examination, the logarithmic polarization resistance was measured at 6.7 Ω cm^2, indicating a high-quality epoxy coating. Surface cracking was also observed on the deck during the field inspection. It was concluded that aggressive ions from deicing salt can penetrate the concrete and reach the rebar level, leading to the deterioration of ECR over time. In locations where cracking is not present, significant damage and corrosion products are less likely to occur.

The results of corrosion rate mapping for LBB− RC− 03, as shown in Figure 3.26(d), revealed a maximum corrosion current density of 18 μ/cm^2, which is equivalent to 8.23 mpy. For the core obtained from this concrete deck, the average initial sorptivity was greater than 12×10^{-3} mm/s$^{1/2}$ and the bulk resistivity was 6 kΩ cm, which indicated a porous and poor-quality concrete. However, the quality of the epoxy coating was in good condition, as evidenced by the results from EIS, where a logarithmic polarization value exceeded 7 Ω cm^2, and the outcome of the knife test was a 10.

The corrosion rate mapping results for LBB−RC−06, as shown in Figure 3.26(g), indicate a maximum corrosion current density of 17 μ/cm^2, which is equivalent to 7.78 mpy. The concrete deck exhibited a relatively low bulk resistivity, measuring at about 3.5 kΩ cm, and a high initial sorptivity, reaching 11.6×10^{-3} mm/s$^{1/2}$, which suggested a porous and poor-quality concrete. The results from EIS and the knife test indicated that the epoxy coating remains in excellent condition. However, the chloride concentration at the rebar level was as high as 0.18 wt.% in the concrete.

The maximum corrosion current density observed on the concrete deck of ELP−RC−05 was 10 μ/cm^2, which is equivalent to 4.57 mpy, indicating significant corrosion in the rebar (Figure 3.25[c]). The concrete deck of this specific bridge utilized black rebar for reinforcement. The

average initial sorptivity recorded for the specimen taken from this concrete deck was lower than 6×10^{-3} mm/s$^{1/2}$, and the average bulk resistivity was 17 kΩ cm, indicating the concrete deck was of decent quality. However, surface cracking was detected in areas displaying high corrosion current density, with a crack width of 0.025 in. During the EIS examination, the corrosion rate of the rebar embedded in the core specimen measured very low, 0.01 mpy, thus suggesting no significant signs or traces of corrosion. The visual inspection of the rebar specimen extracted from the core further confirmed the findings of EIS (Figure 4.45[d]).

Note that corrosion products are expected to appear on the steel surface if the corrosion rate exceeds 0.05 mpy (Table 4-7), and a severe corrosion attack on steel rebar is anticipated when the corrosion rate is greater than 0.5 mpy. The corrosion rate mapping results indicate a higher corrosion rate on some of the mentioned concrete decks, which is further supported by the laboratory and field examinations conducted in this study. However, the concrete deck of ELP–RC–05 is in excellent condition, and the chloride concentration at the rebar level is also low. The results of laboratory experiments do not suggest any deterioration of the reinforcing steel due to corrosion. The core subjected to EIS examination was taken from areas with a high corrosion rate, as indicated by corrosion rate mapping, and the results showed a low corrosion rate on steel. Therefore, the results of iCor should not be construed as being able to determine with high certainty the locations with extended corrosion; instead, they can be used as a probable indicator of locations at risk of corrosion.

4.3 SUMMARY

Surface resistivity and bulk resistivity were calculated for concrete specimens extracted from TxDOT projects. A declining trend in resistivity was observed over time as concrete decks aged. Most bridges in Texas were classified as having high resistivity, which indicates a low volume of moisture and chloride. It was discovered that concrete decks located in the Amarillo, Childress, and Lubbock Districts are more susceptible to corrosion issues because the electrical resistivity of core samples taken from the superstructures was generally low.

After analyzing UPV results, researchers concluded that concrete decks with the addition of CNI admixture generally showed fair quality conditions. In Region 3 and Region 6, several concrete decks—particularly, ELP–RC–03 in Region 3 as well as AMA–RC–04, AMA–RC–05, and AMA–RC–09 in Region 6—were found to have a low transmitting sound wave velocity,

thereby suggesting poor concrete quality. It was also concluded that when the speed of sound waves in concrete is low, the bulk resistivity of the specimen is also low, indicating an increased volume of water content in concrete. Although a positive correlation was found between wave velocity and bulk resistivity, the trend is not linear between resistivity and UPV measurements when the quality of the concrete specimen is perfect, suggesting that the use of UPV examinations focus on identifying poor-quality and moist concrete.

A clear trend was found between absorption rate and the age of concrete structures. The initial sorptivity of the concrete cores increased with age, while the secondary sorptivity decreased in specimens taken from older concrete bridges. This rate describes the void distribution and possible defects in concrete samples, and it can provide general conditions of a concrete specimen. A high initial sorptivity was calculated for ELP–RC–03 and ELP–RC–07 in Region 3, as well as AMA–RC–05 and LBB–RC–06 in Region 6, indicating poor-quality concrete was used in these concrete decks. A correlation was observed between the electrical resistivity and rate of water absorption, wherein lower absorption rates indicated higher resistance. It was concluded that the quality of concrete specimens must be considered perfect if the initial absorption rate is lower than 6×10^{-3} mm/s$^{1/2}$ and the secondary absorption rate is lower than 1×10^{-3} mm/s$^{1/2}$.

The ingress of chloride into concrete structures can result from several factors, including environmental conditions, concrete composition, and surface cracks. The study revealed that bridges in regions with high exposure to deicing salt, such as the Amarillo, Lubbock, and Childress Districts, exhibited higher surface chloride concentrations due to frequent application of deicing salt. The surface chloride concentration in the shoulder lane was discovered to be higher than that in the driving lane, which can be attributed to the deck slope causing water to flow down and accumulate on the shoulder lane, thus leading to a higher concentration of chloride ions.

The chloride concentration at the rebar level can be used to evaluate the potential occurrence of chloride-induced corrosion. This study found that bridges in Region 6 had an average chloride concentration of 0.072 % wt. conc. at the rebar level, while bridges in Region 2 and Region 3 maintained low chloride concentration levels. Samples with chloride levels around the rebar exceeding 0.07 % wt. conc. exhibited clear signs of corrosion rust and peeling of the epoxy coating. The application of CNI was found to prevent corrosion in concrete specimens with high chloride levels.

Carbonation can lead to the degradation of the rebar, making it susceptible to corrosion attack if the carbonation depth exceeds the clear cover of the concrete deck. However, this study found that the carbonation depth in the examined concrete samples was less than 1 in., which is below the cover depth. Therefore, carbonation is not considered a primary threat in the inspected bridges.

The results of the coating adhesion test revealed a generally strong bond between the steel reinforcement and epoxy coating. However, some samples, such as AMA–RC–05, AMA–RC–10, LBB–RC–04, CHS–RC–02, LBB–RC–05, ELP–RC–07, and ATL–RC–04, showed lower scores, indicating weaker adhesion. This result could be attributed to the excessive use of deicing salt in the northern region of Texas and the deposition of airborne chloride in the coastal region in the south. Region 6 had the highest number of severely corroded epoxy coatings, likely due to the extensive use of deicing agents in that area.

When analyzing the impedance results documented in EIS examination, the polarization resistance of uncoated black rebars was found to be lower than that of epoxy-coated steel. No trace of corrosion was seen on ECR. However, corrosion products were observed in some black rebar extracted from core specimens. For these samples, a deep crack was found in concrete specimens that had developed on top of the steel bars. It was determined that if the average logarithmic polarization resistance of a specimen is 5.4 Ω cm^2, then the corrosion rate of steel rebar is 0.05 mpy, implying a low to moderate corrosion rate. Corrosion problems should be expected to occur in concrete specimens if the recorded logarithmic resistance is lower than 5.4 Ω cm^2. In the case of epoxy-coated samples, the polarization resistance was relatively high, suggesting a greater protective ability of the coating. The inherent electrical resistance of epoxy coating contributes to the higher resistance value, further highlighting the superior quality of the epoxy coating.

Table 4-9 provides a summary table of the results of all the laboratory experiments conducted in this research.

Table 4-9. Summary Table of Experiment Results.

Bridge ID	Built Year	Age of Rebar	Surface Resistivity (kΩ cm)	Bulk Resistivity (kΩ cm)	UPV ($\times 10^3$ ft/s)	Initial Sorptivity (mm/s$^{1/2}$)	Secondary Sorptivity (mm/s$^{1/2}$)	Chloride Content (wt.% concrete)	Carbonation Depth (in.)	Coating Adhesion	EIS (ECR)	EIS (Uncoated Rebar)
											Log R_p (Ω cm^2)	Corrosion Rate (mpy)
AMA–RC–01	1995	28	—	—	13.3	—	—	0.005	0.098	10	12.33	—
AMA–RC–02	2006	17	145	—	13.6	3.78	1.39	0.012	0.000	10	7.11	—
AMA–RC–03	2005	18	203	25.6	13.9	3.05	1.05	0.014	0.098	10	8.84	—
AMA–RC–04	1996	27	—	6.0	11.3	6.50	0.98	0.082	0.033	10	8.77	—
AMA–RC–05	1997	26	7.80	1.6	10.4	11.49	0.49	0.416	0.000	5	6.35	—
AMA–RC–06	2000	23	63.0	7.4	12.4	4.74	1.27	0.029	0.102	10	8.83	—
AMA–RC–07	2001	22	62.0	17.2	13.5	4.86	0.32	0.007	0.000	10	—	—
AMA–RC–08	2001	22	32.0	8.0	13.2	5.66	1.51	0.025	0.020	10	8.85	—
AMA–RC–09	1997	26	38.5	4.9	11.3	—	—	0.155	0.010	10	6.72	—
AMA–RC–10	2005	18	205	17.8	14.3	—	—	0.262	0.000	2	6.71	—
AMA–RC–11	2004	19	169	21.5	13.8	2.75	0.83	0.002	0.000	10	9.59	—
AMA–RC–12	2003	20	38.7	5.4	13.3	6.02	0.90	0.024	0.079	10	6.68	—
ATL–RC–01	1981	42	42.8	7.5	13.9	9.48	0.70	0.017	0.000	—	—	0.047
ATL–RC–02	1999	24	—	—	13.2	6.16	1.20	0.024	—	—	—	0.050
ATL–RC–03	2009	14	200	21.2	13.9	3.48	1.13	0.088	0.000	10	6.46	—
ATL–RC–04	2011	12	185	20.1	14.4	—	—	0.011	0.039	6	7.69	—
ATL–RC–05	2013	10	83.7	9.7	14.0	5.56	2.15	0.001	0.102	–	6.63	—
ATL–RC–06	2013	10	91.4	9.0	12.9	3.23	1.36	0.010	0.071	10	6.78	—
ATL–RC–07	2011	12	—	—	14.3	3.82	2.12	0.003	0.063	10	11.25	—
BMT–RC–01	2015	8	318	50.7	15.9	2.56	0.72	0.028	0.000	—	—	0.002
CHS–RC–01	1994	29	24.2	8.6	12.1	6.87	0.87	0.013	0.051	10	6.66	—
CHS–RC–02	1997	26	24.9	5.3	14.3	4.74	1.27	0.103	0.106	4	8.56	—
CHS–RC–03	2002	21	—	4.1	13.2	4.32	1.03	0.059	0.047	10	6.95	—

Table 4-9. Summary Table of Experiment Results (Cont.).

Bridge ID	Built Year	Age of Rebar	Surface Resistivity (kΩ cm)	Bulk Resistivity (kΩ cm)	UPV ($\times 10^3$ ft/s)	Initial Sorptivity (mm/s$^{1/2}$)	Secondary Sorptivity (mm/s$^{1/2}$)	Chloride Content (wt.% concrete)	Carbonation Depth (in.)	Coating Adhesion	EIS (ECR)	EIS (Uncoated Rebar)
											Log R_p (Ω cm^2)	Corrosion Rate (mpy)
CHS–RC–04	2002	21	—	4.0	12.1	8.38	0.71	0.068	0.000	10	6.34	—
CHS–RC–05	1998	25	54.4	11.1	15.1	3.29	1.06	0.015	0.082	10	7.10	—
CHS–RC–06	1997	26	45.6	—	13.5	3.73	1.54	0.011	0.000	10	9.00	—
CRP–RC–01	1973	19	—	—	—	—	—	0.010	0.000	—	—	—
ELP–RC–01	2010	13	75.5	11.7	14.1	5.71	1.91	0.007	0.000	—	—	0.023
ELP–RC–02	2016	7	59.5	12.0	14.8	6.81	1.17	0.008	0.213	—	—	0.063
ELP–RC–03	1989	34	20.3	6.30	9.70	14.3	1.15	0.022	0.000	8	6.11	—
ELP–RC–04	2010	13	61.6	15.0	14.4	8.53	0.96	0.018	0.154	—	—	0.026
ELP–RC–05	2014	9	105	17.1	15.0	4.42	1.77	0.006	0.083	—	—	0.007
ELP–RC–06	1994	29	30.1	4.50	13.1	9.88	0.91	0.006	0.052	10	8.00	—
ELP–RC–07	2006	17	58.0	15.7	14.0	12.7	1.18	0.019	0.504	2	6.43	—
ELP–RC–08	2008	15	107	28.8	14.0	5.36	1.72	0.014	0.177	–	6.64	—
FTW–RC–01	1992	31	35.6	6.10	13.7	10.4	0.72	0.052	0.000	10	6.28	—
FTW–RC–02	2005	18	71.7	14.9	13.7	3.65	1.72	0.011	0.000	10	7.84	—
FTW–RC–03	1988	35	38.4	8.60	13.7	7.45	1.11	0.010	0.000	8	—	—
FTW–RC–04	1991	32	43.1	9.40	13.7	6.50	1.18	0.005	0.000	8	5.88	—
FTW–RC–05	1996	27	22.6	5.10	11.5	10.8	1.50	0.002	—	10	6.90	—
FTW–RC–06	2005	18	40.3	9.80	14.3	—	—	0.004	0.000	10	7.28	—
FTW–RC–07	2006	17	33.1	5.50	13.5	7.00	0.73	0.016	0.079	10	8.14	—
LBB–RC–01	1991	32	—	6.40	13.6	6.98	1.15	0.074	0.184	—	—	0.052
LBB–RC–02	1962	13	—	18.5	14.3	4.32	1.30	0.058	0.213	—	6.26	—
LBB–RC–03	1992	31	28.9	7.20	12.6	8.88	0.72	0.086	0.000	10	7.08	—
LBB–RC–04	1988	35	20.4	5.00	11.9	7.77	1.18	0.080	0.102	4	6.89	—

Table 4-9. Summary Table of Experiment Results (Cont.).

Bridge ID	Built Year	Age of Rebar	Surface Resistivity (kΩ cm)	Bulk Resistivity (kΩ cm)	UPV ($\times 10^3$ ft/s)	Initial Sorptivity (mm/s$^{1/2}$)	Secondary Sorptivity (mm/s$^{1/2}$)	Chloride Content (wt.% concrete)	Carbonation Depth (in.)	Coating Adhesion	EIS (ECR)	EIS (Uncoated Rebar)
											Log R_p (Ω cm^2)	Corrosion Rate (mpy)
LBB–RC–05	2010	13	113	33.4	13.8	4.09	1.49	0.098	0.177	2	6.28	—
LBB–RC–06	1999	24	18.9	3.50	11.7	11.6	0.66	0.137	0.184	10	8.01	—
LBB–RC–07	2006	17	92.4	18.0	13.4	6.40	1.95	0.004	0.379	10	6.37	—
TYL–RC–02	2000	23	60.0	7.50	13.4	8.24	1.67	0.001	0.000	—	—	—
TYL–RC–03	2000	23	67.5	27.0	14.4	11.0	1.68	0.011	0.384	—	7.09	0.044
WFS–RC–01	2001	22	109	18.3	14.1	4.55	1.41	0.003	0.059	—	—	0.064
WFS–RC–02	2001	22	59.0	12.8	14.2	6.26	1.34	0.013	0.154	—	—	0.011
WFS–RC–03	1994	29	75.2	20.3	14.4	3.13	1.37	0.003	0.000	—	7.82	—
WFS–RC–04	2009	14	87.7	19.8	14.0	2.82	1.24	0.030	0.000	—	6.63	—
WFS–RC–05	1995	28	38.7	10.0	13.8	6.37	0.94	0.007	0.055	—	6.93	—
WFS–RC–06	1995	28	89.5	—	15.0	—	—	0.068	0.043	—	6.52	—
WFS–RC–07	1961	62	28.8	8.50	—	—	—	0.027	0.000	—	—	—

Note: "—" indicates bridges with missing data due to restraints such as number of concrete cores or condition of concrete cores

5 DECISION TOOL

5.1 INTRODUCTION

This chapter describes a set of metrics designed in this research to evaluate corrosion prevention and mitigation methods applied to the reinforced concrete decks. The primary objective of the metrics is to provide an approach for selecting proper mitigation methods for the use in TxDOT concrete structures. To this end, a weighted sum model (WSM) was implemented to assign a final score to each individual mitigation technique, as the result enabling a ranking system across various categories.

This chapter is divided into three primary sections. The first section discusses the background and details of the WSM method, emphasizing its advantages compared to other decision analysis methods. The subsequent section elaborates on the criteria developed in the decision matrix, providing a detailed explanation of how mitigation methods are scored and ranked. Finally, the last section focuses on the development of the decision matrix, describes the selection of weighted categories, and demonstrates the application of the decision matrix to rank the corrosion prevention and mitigation methods employed in a concrete deck.

5.2 DECISION ANALYSIS METHOD

In this research, a decision support tool was developed to effectively evaluate the performance of corrosion prevention and mitigation methods for reinforced concrete bridge decks. The tool utilizes a multidimensional, multi-criterion ranking and scoring process to incorporate the outcomes of field inspection and laboratory experiments.

5.2.1 The Weighted Sum Model

The WSM is a well-known multicriteria decision-making tool used in decision analysis, as reported on in several studies. Triantaphyllou and Mann (1989) compared it to different decision-making tools such as the weighted product model, the analytic hierarchy process, and the revised analytic hierarchy process. According to their study, the WSM is a simple and effective tool for normalized multidimensional problems (Hurlebaus et al., 2016). Fishburn (1967) used the WSM to estimate the overall score (A) in terms of the available options (M) and criteria (N). According

to the author, the overall score of a particular option is calculated by summing the weights (w_j) applied to each possible option (a) across all criteria:

$$A_j = \sum_{i=1}^{N} a_j w_i\,, \quad j = 1,2,3,\ldots,M \tag{5.1}$$

Available options (*M*) are mitigation methods, criteria (*N*) are durability and cost, and parameter a represents testing evaluation results, respectively. After scores were calculated, they should be normalized in the final step to prevent the inconsistency of units. Note that the range of scores used in this research were from 0 to10, where 0 represents the lowest score possible (least desirable), and 10 represents the highest score (most desirable).

5.2.2 Description of Criteria

The selection of mitigation methods relies on two key categories: durability and cost. In the subsequent sections, each category will be thoroughly described to provide a comprehensive understanding of their significance in the evaluation process.

5.2.2.1 Durability

Durability refers to the ability of a mitigation method to resist degradation of steel components caused by corrosive elements over an extended period of time. Environmental factors were considered to develop a ranking system to evaluate the corrosion prevention and mitigation methods. The factors considered are moisture and chloride from deicing salts during winter storms, chloride airborne deposition in marine environments, and carbon dioxide and sulfur dioxide in industrial areas. Therefore, a scaling system based on laboratory experiments was developed to evaluate the effectiveness of each mitigation method used in TxDOT bridges. The scores obtained were scaled from 0 to 10, where a score of 10 represents the highest effectiveness and a score of 0 indicates the poorest performance. Note that since multiple corrosion prevention and mitigation methods were applied to the bridge decks inspected in this work, the study focused on assessing the durability of the combination of these methods rather than evaluating the durability of a single corrosion prevention and mitigation method.

5.2.2.1.1 Resistivity

Electrical resistivity of concrete samples can show the durability and permeability of concrete to chloride-laden water. Table 5-1 provides scores used to evaluate concrete resistivity. Spragg et al. (2013) suggested moderate, low, very low, and negligible categories to estimate chloride ion penetration in concrete based on the electrical resistivity of a core sample. If the bulk resistivity is between 5.2 kΩ cm to 10.4 kΩ cm, the chloride penetration is considered moderate; if it is between 10.4 kΩ cm to 20.8 kΩ cm, the chloride penetration is considered low; and if the resistivity is greater than 20.8 kΩ cm, the chloride penetration is considered very low. Therefore, concrete samples with resistivity lower than 5 kΩ cm were assigned a score of 0, while concrete samples with resistivity higher than 200 kΩ cm were given a score of 10. Concrete cores with resistivity between 5 kΩ cm and 10 kΩ cm had a score of 2; cores between 10 kΩ cm to 20 kΩ cm had a score of 5; and cores between 20 kΩ cm to 200 kΩ cm had a score of 8.

Table 5-1. Score Values for Resistivity.

Resistivity (kΩ cm)	Score
< 5	0 (Worst)
5 – 10	1
	2
	3
10 – 20	4
	5
	6
20 – 200	7
	8
	9
> 200	10 (Best)

5.2.2.1.2 Ultrasonic Pulse Velocity

The assessment of concrete quality involved analyzing the propagation of longitudinal wave pulses through the concrete specimens. Based on UPV results, Table 5-2 gives a ranking system for evaluating the quality of concrete specimens that was proposed by Cheesman (1949). According to this ranking system, concrete specimens with a sound wave velocity less than 8200 ft/s were assigned a score of 0. Specimens with velocities between 8200 ft/s and 9800 ft/s were assigned scores between 1 and 3. Cores with velocities between 9800 ft/s and 11800 ft/s were assigned scores from 4 to 6. Similarly, samples with velocities between 11800 ft/s and 14800 ft/s

were assigned scores ranging from 7 to 9. Finally, cores with velocities exceeding 14800 ft/s were assigned a score of 10. To determine the score of a particular specimen with a specific sound wave velocity, linear interpolation was conducted based on the values provided in Table 5-2.

Table 5-2. Score Values for UPV.

UPV (ft/s)	Score
Severe: < 8200	0 (Worst)
Poor: 8200–9800	1
	2
	3
Fair: 9800–11800	4
	5
	6
Good: 11800–14800	7
	8
	9
Perfect: > 14800	10 (Best)

5.2.2.1.3 Chloride Concentration

A factor that can influence the performance of concrete reinforcing rebar is the level of chloride concentration of aggregates that penetrates the cement paste. Thus, sample cores collected at different depths were used to calculate the chloride diffusion rate in concrete specimens. Exceeding the chloride threshold in concrete can break the passive layer of reinforcement, leading to corrosion initiation. The chloride threshold, in the case of black rebar, is suggested (ACI 365.1R-17, 2017; Angst et al., 2009) to be at 0.05 % wt. conc. at rebar depth. Table 5-3 provides scores assigned to different chloride concentrations. Concrete samples with chloride concentrations exceeding 0.05 percent at the rebar level were assigned a score of 0. However, the scores were determined based on the data distribution and statistical analysis for concrete samples with chloride concentrations below 0.05 percent.

Table 5-3. Score Values for Chloride Concentration.

Chloride Concentration (% Weight Concrete)	Score
≥ 0.05	0 (Worst)
0.023–0.05	1
0.014–0.023	2
0.0093–0.014	3
0.0062–0.0093	4
0.0041–0.0062	5
0.0025–0.004	6
0.0014–0.0025	7
0.0006–0.0014	8
0.0002–0.0006	9
0–0.0002	10 (Best)

As shown in Figure 5.1, the quantile-quantile plot (Q-Q plot) illustrates a close alignment of the data points along a straight line, indicating that the dataset closely resembles a gamma distribution.

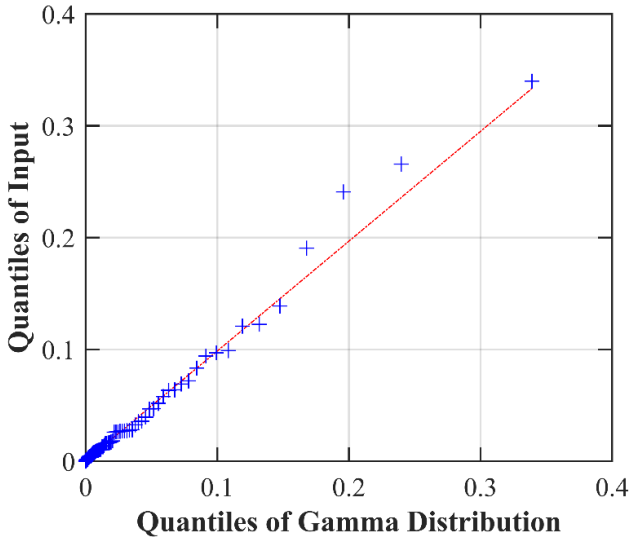

Figure 5.1. Q-Q Plot of Chloride Concentration Results.

5.2.2.1.4 Carbonation Depth

Carbonation of concrete occurs when carbon dioxide penetrates concrete and reacts with calcium hydroxide. This reaction leads to a decrease in the pH of the environment that it subsequently causes the initiation of corrosion on the reinforcement. In this study, the carbonation depth of core specimens was measured to assess the extent of carbonation and determine if carbon dioxide reached the level of steel bars or not. Table 5-4 provides scores based on the carbonation

depth of the concrete specimens. If the carbonation depth reached the clear cover depth of the deck, which is typically 2.5 in., the concrete sample was considered poor and was ranked 0. However, if the carbonation depths were measured between the concrete surface and the clear cover depth, the scores were linearly interpolated with the depth of the concrete.

Table 5-4. Score Values for Carbonation Depth.

Carbonation Depth (in.)	Score
> 2.50	0 (Worst)
2.25–2.50	1
2.00–2.25	2
1.75–2.00	3
1.50–1.75	4
1.25–1.50	5
1.00–1.25	6
0.75–1.00	7
0.50–0.75	8
0.00–0.50	9
0.00	10 (Best)

5.2.2.1.5 Electrochemical Impedance Spectroscopy

Polarization resistance obtained from EIS can provide valuable information about the corrosion rate of reinforcements and, consequently, the quality of the concrete. Table 5-5 provides scores assigned for polarization resistance computed from EIS. The condition of the epoxy coating was considered to be perfect when the polarization resistance was higher. However, it should be noted that no standardized criterion was currently adapted for analyzing the condition of the epoxy coating based on polarization resistance. Therefore, a relative scoring approach was developed in this research to evaluate the quality of ECR using polarization resistance of the samples. Table 5-5 gives the scoring system according to the logarithm of the measured resistance of the specimens.

Table 5-5. Score Values for Polarization Resistance.

Log Polarization Resistance (MΩ cm^2)	Score
< 1	0 (Worst)
1–2	1
2–3	2
3–4	3
4–5	4
5–6	5
6–7	6
7–8	7
8–9	8
9–10	9
> 10	10 (Best)

5.2.2.1.6 Cracks on Concrete Deck

Cracks developed on the surface of concrete deck can significantly reduce corrosion resistance of the reinforced concrete structures. As a crack forms in the concrete, it accelerate the corrosion process because it provides a pathway for corrosive agents to reach the reinforcing steel directly. It is common to apply protective coatings or sealants on concrete bridge decks as an additional barrier. If cracks appear on the concrete surface, they can deteriorate the integrity of the protective layers. This result will further affect the durability of the concrete and increase the risk of corrosion.

Crack width and crack density were two parameters considered in developing a ranking system in this study. if crack width exceeded 0.05 in., the concrete deck was considered to be in poor condition. If the width ranged between 0.05 in. and 0.012 in., the concrete was classified in fair condition. Finally, the concrete deck was marked as good if the crack width was measured narrower than 0.012 in. Table 5-6 provides scores for crack width based on AASHTO (2011).

Darwin et al. (2007) introduced the concept of crack density, which is determined by the ratio of crack length to the square inch of the bridge deck (in./in^2). Table 5-6 provides the assigned score values for crack density.

Table 5-6. Score Values for Surface Condition.

Surface Condition		Score
Crack Width	**Crack Density**	
Severe/Impacted	> 0.170	0 (Worst)
Poor: > 0.05	0.130–0.170	1
	0.092–0.130	2
	0.069–0.092	3
Fair: 0.012–0.05	0.052–0.069	4
	0.039–0.052	5
	0.029–0.039	6
Good: < 0.012	0.020–0.029	7
	0.013–0.021	8
	0.006–0.013	9
No Cracks/Minor	> 0	10 (Best)

In this study, crack density was measured by analyzing the grids used during NDT. The scoring for crack density was based on the distribution of the data. Figure 5.2 demonstrates a close alignment of the data points with a straight line on the Q-Q plot, indicating that the dataset closely follows the characteristics of an exponential distribution.

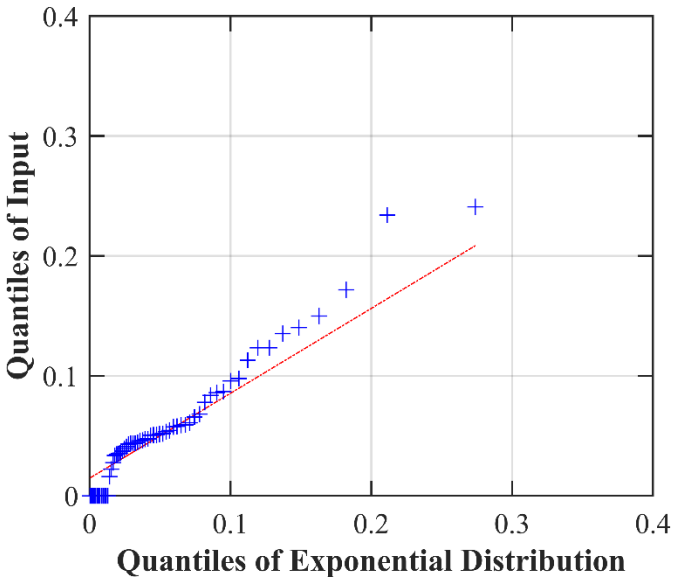

Figure 5.2. Q-Q Plot of Crack Density Results.

5.2.2.2 Cost

This section discusses the cost associated with the corrosion prevention and mitigation methods implemented on TxDOT concrete decks, estimated in U.S. dollars per square foot of concrete deck. Cost is a significant consideration when assessing the performance of mitigation

methods employed on the concrete bridges. In this study, only the cost of materials was considered for the purpose of decision-making; it was assumed that the process of deck construction (including labor, machinery, and engineering and design) remains the same regardless of the chosen mitigation methods. Table 5-7 provides the cost of each mitigation method per square foot of concrete deck, which is also reported in TxDOT (2022a).

According to the report, the cost of an HPC slab was estimated to be $22.10 per square foot, while a regular concrete slab was estimated to be $18.20 per square foot. The price difference between HPC and regular concrete, which amounts to $3.88 per square foot, was considered the price of HPC for determining the score. Other costs associated with mitigation methods include the latex-modified concrete overlay, which costs $9.44 per square foot when converted from $85 per square yard. Similarly, the CST(LO/SI) costs $0.91 per square foot when converted from $8.21 per square yard. The cost of incorporating polypropylene fibers into the concrete mix was estimated to be $3.90 per pound (Nycon, 2023). On average, 0.033 pounds of fiber (polypropylene fibrillated fiber) per cubic foot was assumed to be added to the HPC. Assuming a CIP concrete thickness of 4.5 in., the cost of HPCF was estimated to be $4.45 per square foot. The cost of the CNI was estimated to be $9 per gallon. Approximately, 3 gallons of CNI per cubic yard were assumed to be added to the concrete mixed design. Assuming a CIP concrete deck thickness of 4.5 in., the cost of CNI was calculated to be $1.13 per square foot. Note that this cost may vary depending on the specific product and manufacturer. Additionally, additional cementitious materials in the concrete mix may contribute to an increase in the overall cost.

As reported by Lute et al. (2021), the cost of ECR was estimated to be $0.63 per pound, while black rebar (ASTM A615 Grade 60) cost $0.42 per pound. On average, 6.5 pounds of ECR per square foot were used in the concrete deck. Therefore, the cost of ECR amounted to $4.10 per square foot. Similar to HPC, the price difference between ECR and black steel was considered the price of ECR for the purpose of cost evaluation.

Table 5-7. Cost of Each Mitigation Method.

Mitigation Methods	Cost ($/SF)
HPCF	4.45
HPC	3.88
ECR	1.40
CNI	1.13
CST(SI/LO)	0.91
None	0.00

As was mentioned when discussing durability, a combination of corrosion prevention and mitigation methods has often been employed in TxDOT bridges. Consequently, it was necessary to determine scores for the combined mitigation methods. Although the cost of each method was determined individually, the overall cost was determined by adding up the individual costs of each mitigation method.

Table 5-8 shows the total cost of combined mitigation methods employed in the inspected concrete decks. To incorporate cost into the decision-making tool, it needed to be assigned a score ranging from 0 to 10. The scores for the cost were normalized based on the highest cost scenario.

Table 5-8. Cost and Score Values of Combination of Mitigation Methods.

Mitigation Methods Used in Bridges	Cost ($/SF)	Score
None	0	10
CNI/CST(LO/SI)/ECR	3.4	8.3
CST(LO/SI)/ECR	2.3	8.8
ECR	1.4	9.3
HPC	3.9	8.1
HPC/CNI/CST(LO/SI)	5.9	7.0
HPC/CNI/CST(LO/SI)/ECR	7.3	6.3
HPC/CNI/ECR	6.4	6.8
HPC/CST(LO/SI)	4.8	7.6
HPC/CST(LO/SI)/ECR	6.2	6.9
HPC/ECR	5.3	7.4
HPCF/CST(LO/SI)/ECR	6.8	6.6
HPCF/ECR	5.9	7.1

The utilization of ECR and CST(LO/SI) as mitigation methods appears to be more affordable than other techniques since they receive higher scores. On the other hand, constructing a concrete deck with HPCF as a corrosion prevention and mitigation method would reduce the scores. The combination of CNI, HPC, CST(LO/SI), and ECR results in a higher cost due to the increased number of mitigation methods. In particular, HPC contributes significantly to the overall cost.

5.3 DEVELOPMENT OF DECISION MATRIX

A scoring scheme utilizing a decision matrix was developed in this research to rank the performance of corrosion prevention and mitigation methods implemented in TxDOT concrete decks for a given risk environment. This tool effectively implements the defined metrics discussed

in the previous sections and establishes benchmarks for scoring the corrosion prevention and mitigation methods based on a 3D decision matrix (Figure 5.3).

5.3.1 Rating of Mitigation Methods for Durability and Cost

The decision matrix in Figure 5.3 illustrates the practical implementation of a 3D WSM to rank the corrosion prevention and mitigation methods employed in TxDOT concrete decks. The matrix considers the definitions for durability and cost as the criteria for decision-making, thus enabling the assessment and comparison of different mitigation options in a 3D framework. The matrix outlines the process of assigning an overall score (S_{ik}) to each corrosion mitigation method based on its individual scores (a_{ijk}) calculated for durability and cost. These scores are evaluated for each of the six-corrosion risk environments mentioned earlier.

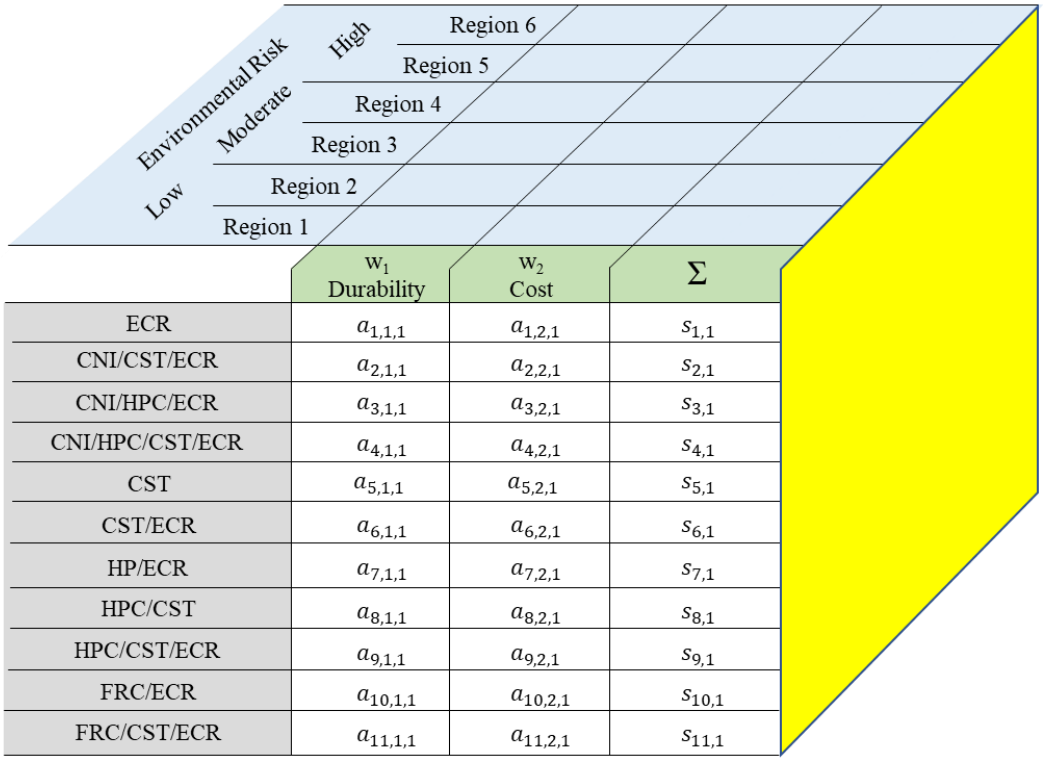

	w_1 Durability	w_2 Cost	Σ
ECR	$a_{1,1,1}$	$a_{1,2,1}$	$s_{1,1}$
CNI/CST/ECR	$a_{2,1,1}$	$a_{2,2,1}$	$s_{2,1}$
CNI/HPC/ECR	$a_{3,1,1}$	$a_{3,2,1}$	$s_{3,1}$
CNI/HPC/CST/ECR	$a_{4,1,1}$	$a_{4,2,1}$	$s_{4,1}$
CST	$a_{5,1,1}$	$a_{5,2,1}$	$s_{5,1}$
CST/ECR	$a_{6,1,1}$	$a_{6,2,1}$	$s_{6,1}$
HP/ECR	$a_{7,1,1}$	$a_{7,2,1}$	$s_{7,1}$
HPC/CST	$a_{8,1,1}$	$a_{8,2,1}$	$s_{8,1}$
HPC/CST/ECR	$a_{9,1,1}$	$a_{9,2,1}$	$s_{9,1}$
FRC/ECR	$a_{10,1,1}$	$a_{10,2,1}$	$s_{10,1}$
FRC/CST/ECR	$a_{11,1,1}$	$a_{11,2,1}$	$s_{11,1}$

Figure 5.3. 3D Decision Matrix to Assess Quality of Corrosion Mitigation Methods.

The overall score of each individual method for a considered deterioration condition is determined as follows:

$$S_{ik} = \sum_{j=1}^{2} a_{ijk} w_j \tag{5.2}$$

where index i denotes 11 combined corrosion mitigation methods; index j stands for the criteria that changes from 1 to 2 for two categories, durability and cost; and index k stands for six regions. The weight factors w_1 and w_2 are the weight factors for durability and cost, respectively.

Due to the variation in mitigation methods used on TxDOT bridges and their specific application in certain regions, the durability score of some mitigation methods in certain regions could not be measured. Therefore, the durability of such methods was calculated using scores of other similar mitigation methods. For example, no bridges consisting of HPCF were inspected in Region 5; thus, because the concrete quality of HPC and HPCF is the same, except for only reduced plastic shrinkage cracks, the decision was made to assign the durability scores obtained for bridges with HPC in Region 5 as the scores for HPCF as well. Similarly, in Region 4, the score of CST(LO/SI)/ECR was used to calculate the durability score of CNI/CST(LO/SI)/ECR since the bridges with CNI/CST(LO/SI)/ECR were not inspected. CNI would increase the chloride threshold of ECR, resulting in a better score of epoxy rebar. Accordingly, the score of CNI/CST(LO/SI)/ECR was calculated by assuming the score of CNI/CST(LO/SI)/ECR would be equal to or greater than the score of CST(LO/SI)/ECR.

The overall scores of each mitigation method applied to TxDOT bridges are depicted in stacked bar charts from Figure 5.4 to Figure 5.8. These charts consider the environmental corrosion risk associated with the location of the inspected concrete bridges. Additionally, a durability-driven approach is employed wherein durability is assigned a weight of 80 percent and cost is assigned a weight of 20 percent, as specified in Table 5-9. This weighting scheme implies the greater importance of durability in the decision-making process for selecting corrosion mitigation methods due to consideration of safety concerns. Although cost variations among the methods are considered, they are not as significant a factor in the decision-making process as durability.

Table 5-9. Categories and Weight Factors for Durability-Driven Scenario.

Weighted Category	**Durability-Driven Scenario**	
Durability	W_1	80%
Cost	W_2	20%

5.3.2 Result of Scoring and Discussion

Figure 5.4 illustrates the overall scores of each mitigation technique in a low corrosive risk environment—namely, Region 1 and Region 2. This figure indicates that the application of mitigation methods on the concrete deck is not particularly effective for concrete bridges in these regions because corrosion is not a significant factor to consider. In low-risk corrosive environments, the overall scores for durability are similar across all mitigation techniques, while cost becomes the determining factor. It was observed that the highest overall scores were associated with not using any mitigation technique or with the application of CST(LO/SI) with ECR, which suggests that cost plays a primary role in decision-making for these regions and influences the overall scores.

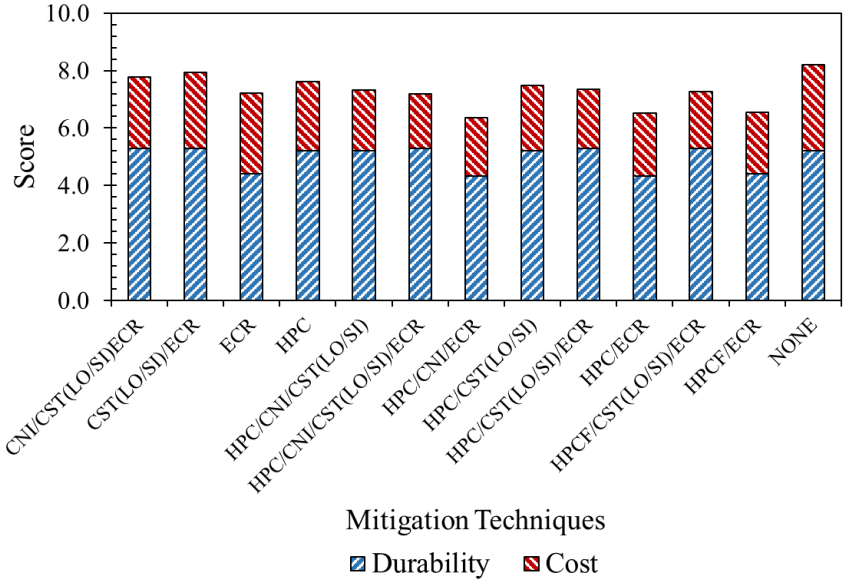

Figure 5.4. Total Score of Mitigation Methods in Region 1 and Region 2.

The total scores of each mitigation method in a medium corrosive environment are depicted in Figure 5.5 and Figure 5.6. These scores highlight the effectiveness of employing ECR in concrete bridge decks in Region 3 because it achieved higher scores, indicating greater durability than other techniques. Not utilizing any mitigation methods was also a reasonable choice since the durability of most mitigation methods in Region 3 was similar, except in cases involving ECR, while the cost associated with not using any mitigation methods was higher than other alternatives. The combination of CST(LO/SI) and ECR, as well as the combination of CNI and CST(LO/SI) with ECR, also received high scores, positioning them as the third and fourth most durable

mitigation approaches in Region 3. As the risk of corrosion increases in Region 4, not using any mitigation methods is not a good option. However, similar durability scores were observed for the mitigation methods. The use of ECR in concrete received significantly higher scores, suggesting that ECR are highly recommended for bridges in regions with a medium to slightly high corrosive environment. Following ECR, CST(LO/SI)/ECR and CNI/CST(LO/SI)/ECR are also effective mitigation methods in Region 3 since they ranked second and third, respectively.

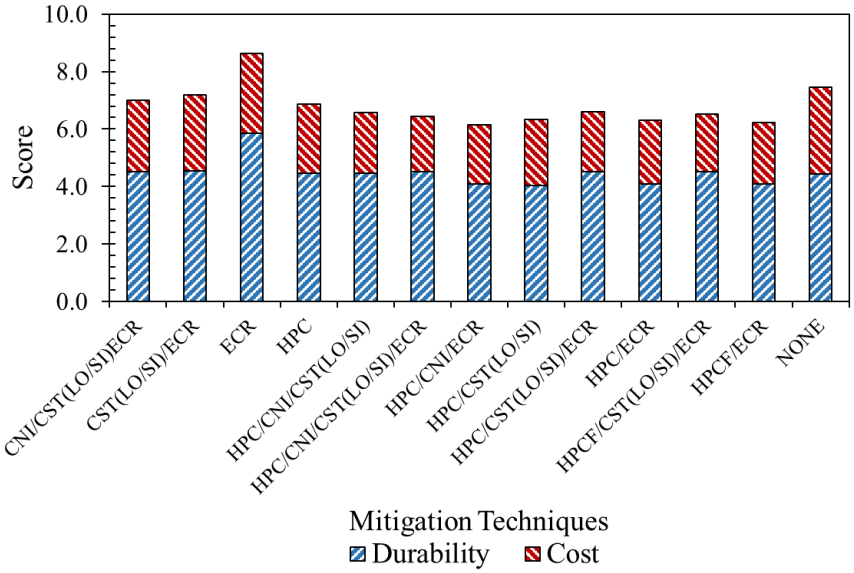

Figure 5.5. Total Score of Mitigation Methods in Region 3.

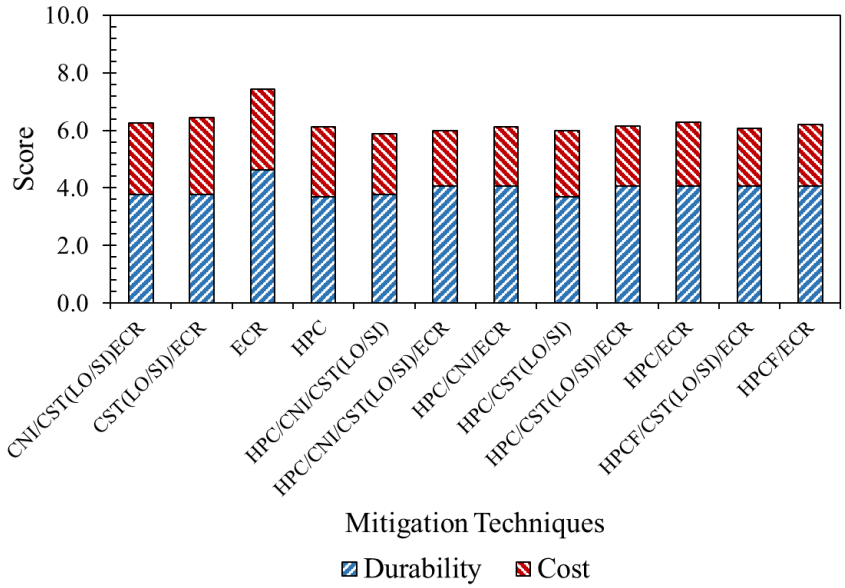

Figure 5.6. Total Score of Mitigation Methods in Region 4.

The application of ECR and HPC, particularly when combined with other mitigation techniques such as CNI, is recommended for bridges located in high-risk corrosive environments such as Region 5. However, the use of CNI is not advised in environments with normal to high temperatures. The primary reason for adding CNI in concrete mix designs is to accelerate the concrete set, thus it is normally recommended to use in areas with low temperatures. As shown in Figure 5.7, if no mitigation method used in concrete deck, it leads to a significant decrease in the score, highlighting the importance of the corrosion attack in this region. ECR proves to be a highly effective approach since it consistently received higher scores in the WSM evaluation.

If cost is not a primary consideration, the application of HPCF can greatly enhance the corrosion resistance of concrete decks. In contrast, while CST(LO/SI) is a cost-effective mitigation technique, its ability to improve durability of the system is limited and may only provide short-term benefits. CST(LO/SI) is ineffective in increasing the corrosion resistance of concrete bridges in high-risk environments, as indicated by the results shown in Figure 5.8. In Region 6, ECR is strongly recommended, and all inspected bridges in this region used ECR. Therefore, mitigation methods without ECR do not have any scores and are not recommended in Region 6.

As the risk of corrosivity increases, the use of ECR in HPC concrete combined with CNI (for the concrete casts in low-temperature environments) proves to be a more effective mitigation technique. Additionally, the application of HPCF is highly recommended. In severe corrosive environments, it was concluded that the application of ECR with an additional mitigation strategy such as HPC or HPCF can be particularly effective in enhancing the corrosion resistance of concrete decks.

Figure 5.9 provides a summary of the previous discussion by presenting the overall scores of all mitigation methods in a single bar chart. This depiction allows the reader to quickly grasp the performance of the mitigation techniques across different environmental regions in terms of corrosivity. In addition, Figure 5.10 also illustrates the effectiveness of the mitigation methods by aggregating their scores for each corrosion risk region. These figures provide a comprehensive visual representation of how the mitigation techniques perform in different regions and their overall effectiveness in mitigating corrosion.

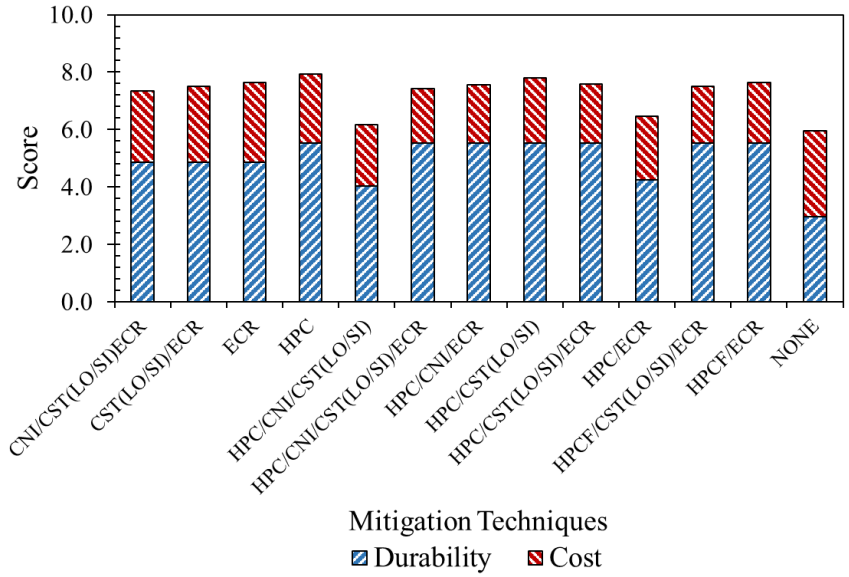

Figure 5.7. Total Score of Mitigation Methods in Region 5.

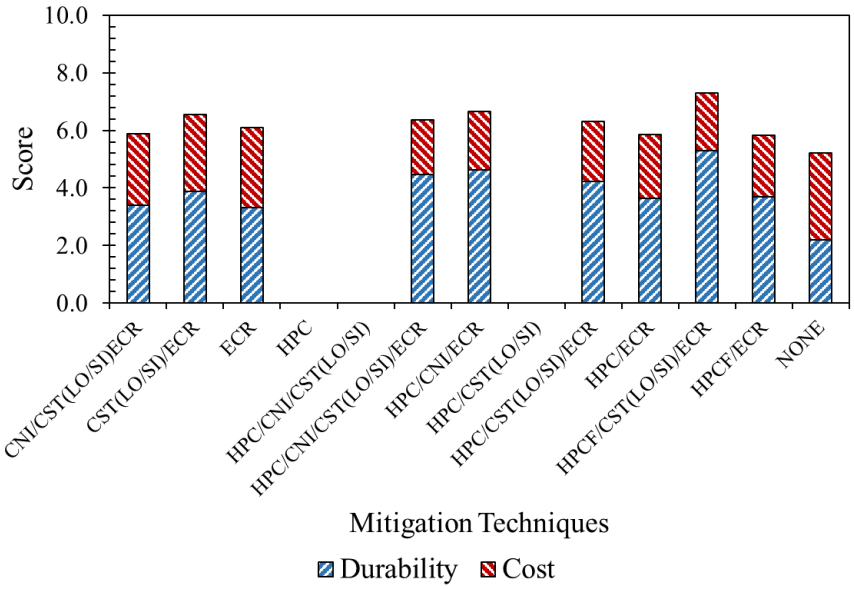

Figure 5.8. Total Score of Mitigation Methods in Region 6.

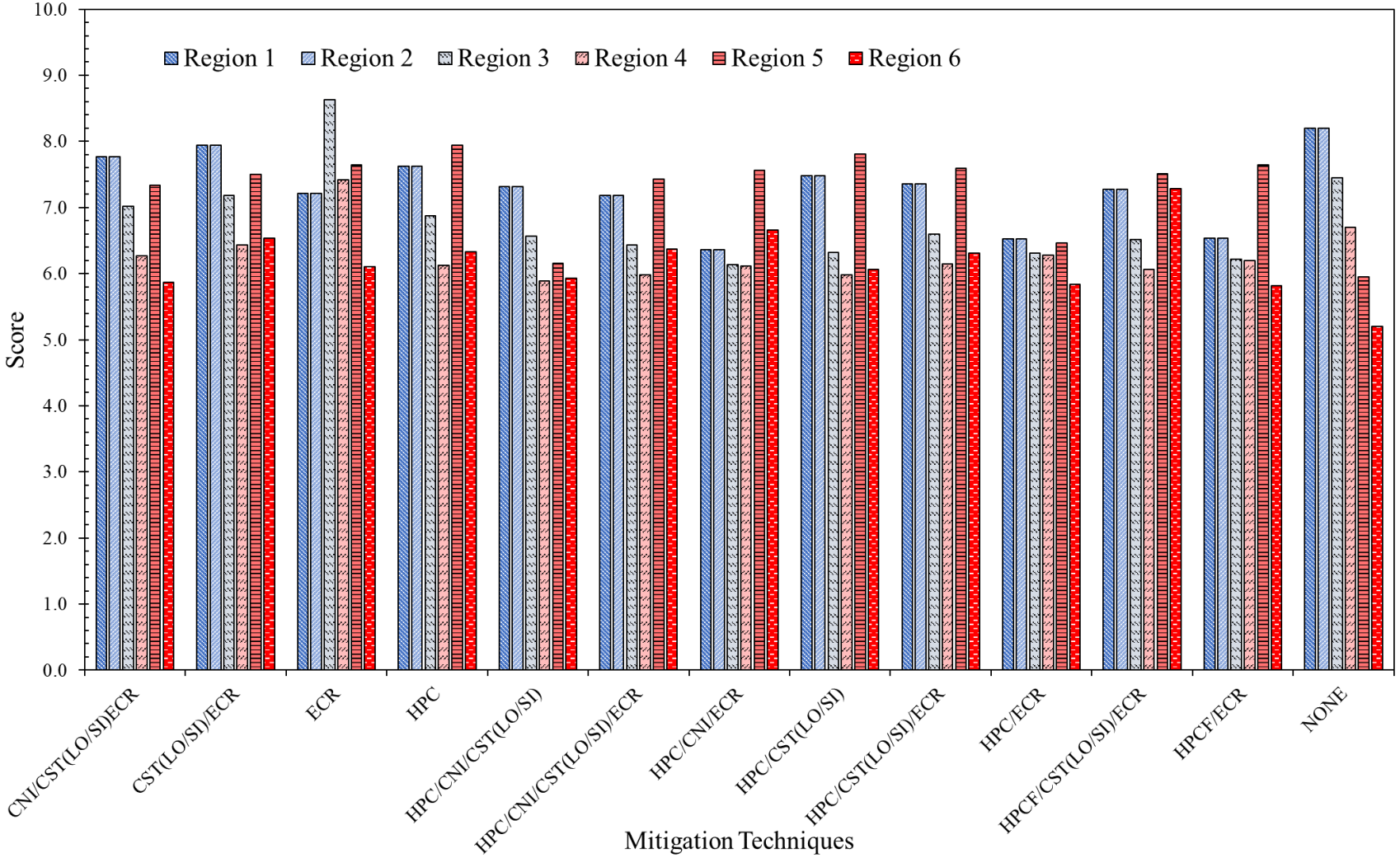

Figure 5.9. Score of Mitigation Methods in Different Regions.

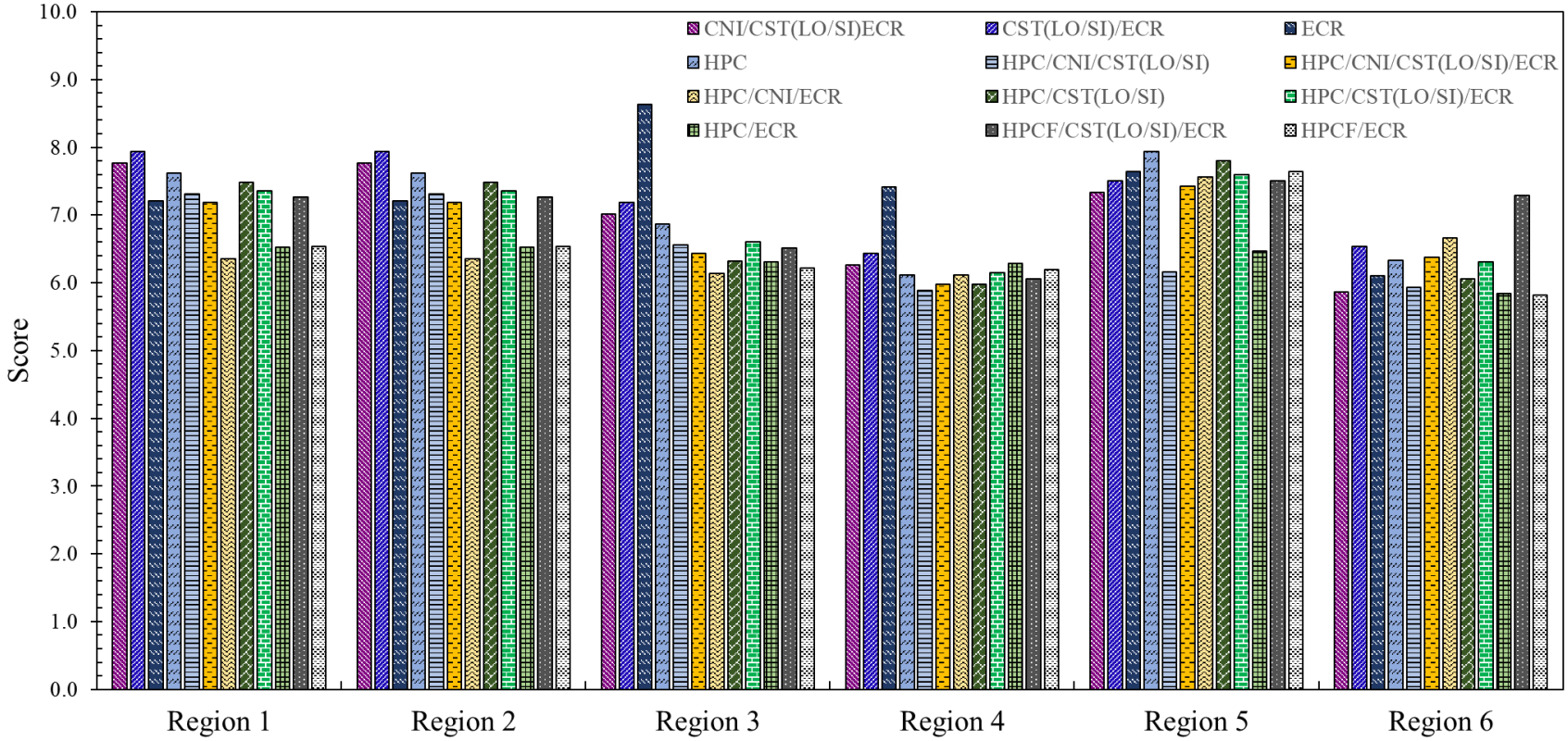

Figure 5.10. Score of All Mitigation Methods in Each Region.

5.4 APPLICATION OF DEVELOPED TOOL

For convenience, a program was developed using Microsoft Excel spreadsheet software to aid in visualizing scores of each corrosion prevention and mitigation method employed in concrete structures. This program, attached to this document, enables users to easily navigate different aspects of the decision framework developed in this study. Figure 5.11 to Figure 5.13 provide a screenshot of the program interface, highlighting its features and capabilities. Users can select specific corrosive risk regions and analyze the effectiveness of mitigation techniques employed in TxDOT concrete bridges. The program develops diagrams that gives an overview of overall scores as well as ranks the performance of different methods in different corrosive risk regions. The program provides users to customize the weights for durability and cost based on their preferences. To use the program, the user selects Reinforced Concrete Bridge and specifies the county. Then, the user should assign weights to durability and cost, as shown in Figure 5.11. These parameters are used to generate several outputs, including the corrosion risk region, a priority rating table and plotting (Figure 5.12 and Figure 5.13).

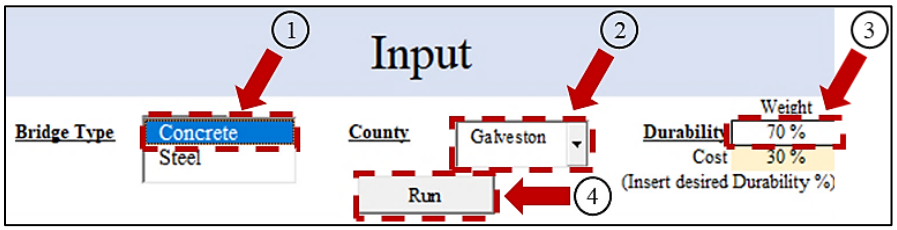

Figure 5.11. Procedure of Decision Tool Implementation.

Corrosion Risk Region	6		
Mitigation	Weighted Durability	Weighted Cost	Total Score
FRC/CST/ECR	4.8	2.0	6.8
CNI/HPC/ECR	4.6	2.0	6.7
CST/ECR	3.9	2.7	6.5
CNI/HPC/CST/ECR	4.5	1.9	6.4
HPC/CST/ECR	4.2	2.1	6.3
HPC/ECR	4.0	2.2	6.2
ECR	3.3	2.8	6.1
CNI/CST/ECR	3.4	2.5	5.9
FRC/ECR	3.7	2.1	5.8
None	2.2	3.0	5.2
CST	2.2	2.9	5.1
HPC/CST	2.2	2.3	4.5

Figure 5.12. Rating Table of Mitigation Methods in Region 6.

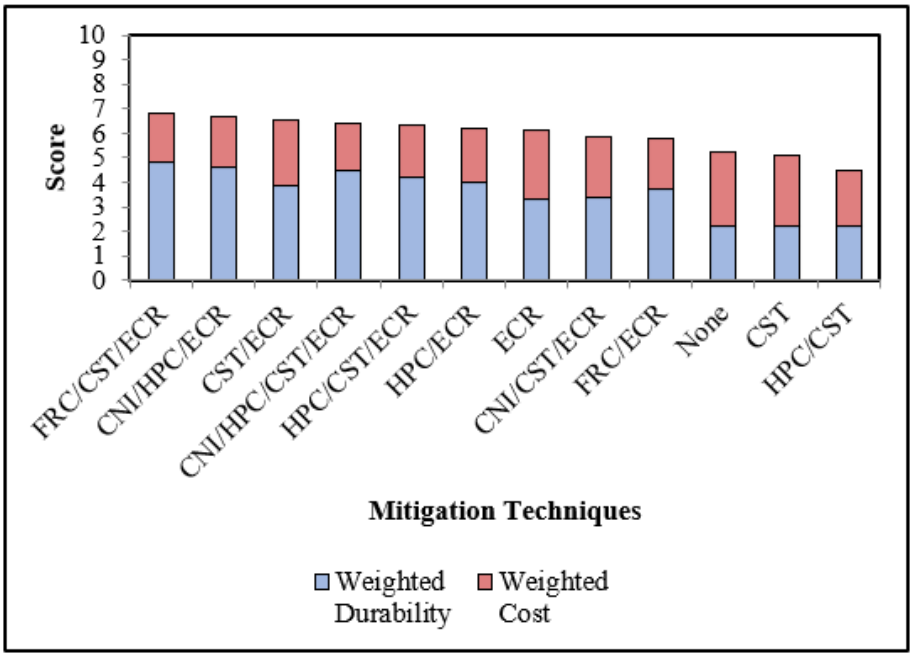

Figure 5.13. Rating Plot of Mitigation Methods in Region 6.

5.5 SUMMARY

This chapter described the development of a decision tool designed to evaluate corrosion mitigation methods that can be used on reinforced concrete bridge decks. The decision tool considers durability and cost as two primary categories and provides an evaluation of the effectiveness of corrosion prevention and mitigation methods in different risk environment. After studying the scores calculated for each mitigation method, it was concluded that a combination of black rebar and normal reinforced concrete exhibits decent performance in a low-risk corrosion environment. However, the effectiveness of this system to prevent corrosion damages decreases as the corrosivity of the environment increases. The application of CST(LO/SI) in this region also improved the performance of concrete decks against corrosion damages. In a medium to highly corrosive environment, the use of ECR in concrete is highly recommended. It was also concluded that ECR, or integrating ECR with CST(LO/SI), shows a promising approach to mitigate the risk of corrosion damage in concrete, specifically in more aggressive environments. In severe corrosive conditions, such as bridges located in Region 6, it is recommended to combine ECR with one or two additional mitigation techniques. The results of the current research show that the performance of ECR in reducing corrosion problems in concrete improves by combining CNI (in low-temperature environments) in the HPC admixture or employing HPCF in concrete deck slabs.

6 SUMMARY, CONCLUSION, AND RECOMMENDATIONS

Reinforced concrete can be an effective barrier against corrosive agents in the case no defects like cracks or concrete spalling occur in the structure. The durability of reinforced concrete is directly related to the extent of crack growth and water permeability since contaminants mixed with moisture can penetrate concrete, leading to corrosion on the steel surface. Ensuring the concrete bridge decks function properly, TxDOT recommends implementing corrosion prevention and mitigation methods, including the use of ECR and HPC, to enhance corrosion resistance of the system. Moreover, adding calcium nitrite in concrete mixed designs for hardening purposes is common in the northern part of the state, which experiences a significant annual number of freeze days. Calcium nitrite not only accelerates the early stage of concrete strength, it also acts as a corrosion inhibitor. Another solution to prevent corrosion in concrete is the use of surface treatment methods, which are widely applied on concrete decks across the state. Note that the treatments seldom exhibit long-term durability, and their protection characteristics decrease over the years.

A field inspection conducted in this research revealed minimal damage and spalling on concrete structures. Surface cracking was documented on some of the inspected concrete decks, and measurable cracking and spalling were recorded for some bridge abutments. Corrosion rate mapping developed for some bridges in Amarillo, El Paso, and Lubbock generally showed a moderate corrosion rate. Some cases with higher rates of corrosion were also documented in this report. Crack width and crack density were documented for inspected bridge decks, and these properties were found to be slightly greater in highly corrosive environments. Crack mapping created from the results of the field measurements showed surface crack distribution and the extent of surface cracks' growth on concrete decks.

Laboratory testing performed on core specimens obtained from inspected concrete decks revealed that the quality of concrete varies by age and environment. The electrical resistivity of the core specimens was found to decrease for aged samples and measured low for samples taken from structures in the Amarillo, Childress, and Lubbock Districts. The speed of sound waves in samples with low bulk resistivity was also found to be low, indicating high water content in those samples. In addition, the absorption rate of the concrete specimens correlated with the age of the structures, meaning the initial absorption rate increased and the secondary absorption rate

decreased for the aged samples. The average absorption rate was found to be higher for the specimens taken from corrosive environments.

The surface chloride concentration measured greater for samples obtained from shoulder lanes. In general, the volume of chloride content at the rebar level was higher for low-quality concrete samples. Aggravated corrosion activities such as corrosion rust and peeling of the epoxy coating were observed for the specimens, with chloride concentration at the rebar level exceeding 0.07 % wt. conc. It was concluded that calcium nitrite mitigates corrosion in high chloride concrete. It was also concluded that carbonation was not a significant problem in inspected concrete specimens. The depth of carbonation was found to be less than the concrete cover unless cracks occurred on the concrete surface and developed into the depth.

The results documented in the coating adhesion test showed a strong bond between reinforcing bars and epoxy coating, although there were a few exceptions of coating failures because of existing cracks on top of the steel. These cracks provided a pathway for corrosive agents to contact the reinforcing bars and degrade the epoxy coat. The coating deterioration was detected in concrete decks located in regions that had a high usage of deicing salt on roads. Additionally, impedance analyses performed on concrete specimens provided valuable insight into the quality of epoxy coating. All the reinforcing bars examined in EIS were found to have intact coatings with no sign of corrosion. The average logarithmic polarization resistance of these specimens was recorded as over 6 $\Omega\,cm^2$, indicating the protective ability of the epoxy coating. The average logarithmic polarization resistance of black rebar was found to be lower than ECR, and it was concluded that if it is lower than 5.4 $\Omega\,cm^2$ (equivalent to the polarization resistance of 240 $k\Omega\,cm^2$), then the low to moderate corrosion rate of steel is over 0.05 mpy. For these specimens, severe corrosion was observed on one side of rebar facing the concrete crack, while pitting corrosion was also found on other specimens in which the corrosion rate was measured to be approximately 0.05 mpy.

A metric was developed to evaluate the durability of corrosion prevention and mitigation methods employed in concrete decks. The metric served as a tool to help evaluate the effectiveness of the mitigation methods based on durability scores and cost of the protection systems in different risk environments. Based on the findings of this study, a combination of black rebar and normal reinforced concrete shows reasonable corrosion resistance in low-risk corrosion environments, and the use of a surface treatment can enhance the durability of concrete decks in these regions. It was

concluded that concrete structures reinforced with ECR exhibit greater corrosion resistance in medium to highly corrosive environments. Moreover, combining ECR with additional mitigation methods such as HPC proved an effective approach to decrease corrosion activities in aggressive environments such as Region 6.

6.1 CONCLUSIONS

This section summarizes the main findings of this study evaluating corrosion prevention and mitigation methods applied to TxDOT reinforced concrete decks. The outcomes of this research are divided into two categories. The conclusions drawn from field inspection conducted on concrete deck bridges are followed by the outcomes of laboratory testing performed on core specimens obtained from the inspected structures during the field visit.

6.1.1 Field Inspection

Conclusions obtained from field inspections are as follows:

- Corrosion mapping can show the location of corroded rebar.
- Surface crack mapping can provide valuable insight into current conditions of concrete decks. Although the severity of corrosion on steel rebar depends on the location of decks—whether in a high-risk environment or not—the deterioration of reinforcing bars due to corrosion generally is inevitable when cracks appear on the deck. Surface cracks can increase the rate of carbonation and the volume of chloride content and moisture in concrete.
- Thermal imaging can aid in identifying surface defects and provide a quick and efficient assessment of superficial defects not easily visible to the unaided eye. Thermal imaging results can also be utilized to create surface crack mapping.
- GPR helps locate embedded reinforcing bars in concrete. The results of the NDT can be used to develop corrosion rate mapping of reinforced concrete decks.
- UST results documented in this study did not show small defects or corroded steel members within concrete decks. Noise reflection was identified as a major problem during scanning of the concrete structures.

6.1.2 Laboratory Examinations

The laboratory examinations revealed details about the quality of concrete, the depth of pollutant penetration, and the condition of reinforcing rebars. The following conclusions were obtained from testing of core specimens:

- The volume of moisture and chloride content increases in concrete if the bulk resistivity of a concrete specimen measures below 10 kΩ cm. If the recorded sound wave in the sample is also lower than 10×10^3 ft/s, it indicates the potential of elevated water content in concrete.
- If initial water absorption rates measure lower than 6×10^{-3} mm/s$^{1/2}$ and the secondary absorption rate is lower than 1×10^{-3} mm/s$^{1/2}$, then the concrete must be assessed as dense with low pore distribution.
- The volume of chloride content at the rebar level was found to be less than the chloride threshold of 0.05 % wt. conc. for most of the core specimens. However, it generally exceeded this threshold for cores taken from concrete decks located in highly corrosive environments like Region 6.
- Carbonation was not significant in bridge decks if no surface crack appeared on the concrete surface. The depth of carbonation measured less than 1 in. for all core specimens. However, the depth was recorded more at the level crack extended for the fractured areas.
- A strong bond between the epoxy coat and steel rebar was found for most inspected specimens. However, delamination between the coating and steel substrate also occurred for a few specimens, indicating poor surface preparation during the manufacturing process. Additionally, corroded rebars were also obtained from core specimens with developed cracks and high initial sorptivity.
- The extent of corrosion is low if the average logarithmic polarization resistance of a specimen is 5.4 Ω cm^2 or greater. This threshold is equivalent to the polarization resistance of 240 kΩ cm^2 and a corrosion rate of 0.05 mpy. An epoxy coating provides electrical resistance; if logarithmic polarization resistance falls below 5.4 Ω cm^2, it indicates corrosion initiation.

6.2 RECOMMENDATIONS

The following recommendations are suggested based on the findings of this study:

- Routine maintenance and repair of concrete bridge decks are recommended regardless of the corrosivity of the environment. Corrosion is a localized problem that can readily progress if the environmental parameters required for the electrochemical reactions are present.
- The use of ECR combined with HPC is suggested for aggressive environments (Region 6). However, the application of normal reinforced concrete and surface treatments can be a potential solution for corrosion prevention and mitigation in low corrosive regions if routine inspections are conducted and the conditions of potential surface cracks are carefully monitored.
- In a medium corrosive environment (Region 3 and Region 4), the use of ECR is suggested to prevent and mitigate corrosion of reinforcing rebars embedded in concrete.
- Corrosion and surface crack mapping can help identify locations vulnerable to corrosion.
- To identify the quality of aged concrete specimens, bulk resistivity along with UPV is recommended to assess the volume of water content in concrete. In addition, water absorption tests can also help to identify the fraction of pour distribution and the presence of small defects in concrete specimens. Impedance measurements are also an effective approach to determine potential corrosion activities in concrete specimens.

REFERENCES

AASHTO. (2011). Guide manual for bridge element inspection. In. 444 North Capitol Street N.W., Suite 249 Washington, D.C. 20001: American Association of State Highway and Transportation Officials.

AASHTO T358. (2015). Surface resistivity indication of concrete's ability to resist chloride ion penetration, American Association of State Highway and Transportation Officials, 444 North Capitol Street N.W., Suite 249 Washington, D.C. 20001

Abushanab, A., & Alnahhal, W. (2021). Combined effects of treated domestic wastewater, fly ash, and calcium nitrite toward concrete sustainability. *Journal of Building Engineering, 44*, 103240.

ACI 228.2R-13. (2013). Nondestructive test methods for evaluation of concrete in structures, American Concrete Institute, Farmington Hills, MI

ACI 365.1R-17. (2017). Report on Service Life Prediction, American Concrete Institute, Farmington Hills, MI

ACI 440.5-08. (2008). Specification for construction with fiber-reinforced polymer reinforcing bars, American Concrete Institute, Farmington Hills, MI

ACI 440.6-08. (2008). Specification for carbon fiber-reinforced polymer bar material for concrete reinforcement, American Concrete Institute, Farmington Hills, MI

Ahmad, S. (2003). Reinforcement corrosion in concrete structures, its monitoring and service life prediction—a review. *Cement and Concrete Composites, 25*(4-5), 459-471.

Al-Amoudi, O. S. B., Maslehuddin, M., Lashari, A. N., & Almusallam, A. A. (2003). Effectiveness of corrosion inhibitors in contaminated concrete. *Cement and Concrete Composites, 25*(4), 439-449 '10.1016/S0958-9465(02)00084-7:' 10.1016/S0958-9465(02)00084-7.

Alampalli, S., & Ettouney, M. M. (2006). Long-term issues related to structural health of FRP bridge decks. *Bridge Structures, 2*(1), 1-11.

American Galvanizers Association. (2023). Retrieved from https://galvanizeit.org/

Angst, U., Elsener, B., Larsen, C. K., & Vennesland, Ø. (2009). Critical chloride content in reinforced concrete—A review. *Cement Concrete Research, 39*(12), 1122-1138.

Ann, K.-Y., Jung, H., Kim, H., Kim, S., & Moon, H. Y. (2006). Effect of calcium nitrite-based corrosion inhibitor in preventing corrosion of embedded steel in concrete. *Cement Concrete Research, 36*(3), 530-535.

Ann, K., Ahn, J., & Ryou, J. (2009). The importance of chloride content at the concrete surface in assessing the time to corrosion of steel in concrete structures. *Construction and Building Materials, 23*(1), 239-245.

Ann, K. Y., & Buenfeld, N. (2007). The effect of calcium nitrite on the chloride-induced corrosion of steel in concrete. *Magazine of concrete research, 59*(9), 689-697.

Aperador, W., Bautista-Ruiz, J., & Chunga, K. (2015). Determination of the efficiency of cathodic protection applied to alternative concrete subjected to carbonation and chloride attack. *International Journal of Electrochemical Science, 10*(9), 7073-7082.

Arya, C., & Ofori-Darko, F. (1996). Influence of crack frequency on reinforcement corrosion in concrete. *Cement Concrete Research, 26*(3), 345-353.

ASTM A240/A240M. (2023). Standard specification for chromium and chromium-nickel stainless steel plate, sheet, and strip for pressure vessels and for general applications, ASTM International, West Conshohocken, PA

ASTM A767/A767M. (2019). Standard specification for zinc-coated (galvanized) steel bars for concrete reinforcement, ASTM International, West Conshohocken, PA

ASTM A775/A775M. (2022). Standard specification for epoxy-coated steel reinforcing bars, ASTM International, West Conshohocken, PA

ASTM A934/A934M. (2022). Standard specification for epoxy-coated prefabricated steel reinforcing bars, ASTM International, West Conshohocken, PA

ASTM A995/A995M. (2020). Standard specification for castings, austenitic-ferritic (duplex) stainless steel, for pressure-containing parts, ASTM International, West Conshohocken, PA

ASTM A1035/A1035M. (2020). Standard specification for deformed and plain, low-carbon, chromium, steel bars for concrete reinforcement, ASTM International, West Conshohocken, PA

ASTM C597. (2016). Standard test method for pulse velocity through concrete, ASTM International, West Conshohocken, PA

ASTM C876. (2015). Standard test method for corrosion potentials of uncoated reinforcing steel in concrete, ASTM International, West Conshohocken, PA

ASTM C1152. (2004). Standard test method for acid-soluble chloride in mortar and concrete, ASTM International, West Conshohocken, PA

ASTM C1218. (2012). Standard test method for water-soluble chloride in mortar and concrete, ASTM International, West Conshohocken, PA

ASTM C1585. (2020). Standard test method for measurement of rate of absorption of water by hydraulic-cement concretes, ASTM International, West Conshohocken, PA

ASTM C1876. (2019). Standard test method for bulk electrical resistivity or bulk conductivity of concrete, ASTM International, West Conshohocken, PA

ASTM D3963/D3963M. (2021). Standard specification for fabrication and jobsite handling of epoxy-coated steel reinforcing bars, ASTM International, West Conshohocken, PA

ASTM D6677. (2018). Standard test method for evaluating adhesion by knife, ASTM International, West Conshohocken, PA

Atkinson, A., & Nickerson, A. (1984). The diffusion of ions through water-saturated cement. *Materials Science, 19*, 3068-3078.

Bastidas-Arteaga, E., Bressolette, P., Chateauneuf, A., & Sánchez-Silva, M. (2009). Probabilistic lifetime assessment of RC structures under coupled corrosion–fatigue deterioration processes. *Structural safety, 31*(1), 84-96.

Bavarian, B., & Reiner, L. (2002). *Corrosion protection of steel rebar in concrete using migrating corrosion inhibitors, MCI 2021 & 2022*.

Benedetto, A. (2013). A three dimensional approach for tracking cracks in bridges using GPR. *Journal of Applied Geophysics, 97*, 37-44.

Benmokrane, B., Wang, P., Ton-That, T. M., Rahman, H., & Robert, J.-F. (2002). Durability of glass fiber-reinforced polymer reinforcing bars in concrete environment. *Composites for Construction, 6*(3), 143-153.

Bentur, A., Berke, N., & Diamond, S. (1997). *Steel corrosion in concrete: fundamentals and civil engineering practice*: CRC press.

Bertolini, L., Elsener, B., Pedeferri, P., Redaelli, E., & Polder, R. B. (2013). *Corrosion of steel in concrete: prevention, diagnosis, repair*: John Wiley & Sons.

Bertolini, L., Elsener, B., Pedeferri, P., Redaelli, E., & Polder, R. B. (2014). *Corrosion of Steel in Concrete: Prevention, Diagnosis, Repair*: John Wiley & Sons.

Beushausen, H., & Luco, L. F. (2015). *Performance-based specifications and control of concrete durability: state-of-the-art report RILEM TC 230-PSC* (Vol. 18): Springer.

Blitz, J., & Simpson, G. (1995). *Ultrasonic methods of non-destructive testing* (Vol. 2): Springer Science & Business Media.

Böer, P., Holliday, L., Kang, T. H.-K. J. C., & Materials, B. (2013). Independent environmental effects on durability of fiber-reinforced polymer wraps in civil applications: A review. *Construction Building Materials, 48*, 360-370.

Broomfield, J. P. (2006). *Corrosion of steel in concrete: understanding, investigation and repair, second edition*: Taylor & Francis.

Broomfield, J. P. (2023). *Corrosion of steel in concrete: understanding, investigation and repair*: Crc Press.

Buth, E., Furr, H. L., & Jones, H. L. (1972). *Evaluation of a prestressed panel, cast-in-place concrete bridge*.

Castro, J., Bentz, D., Weiss, J. J. C., & Composites, C. (2011). Effect of sample conditioning on the water absorption of concrete. *Cement Concrete Composites, 33*(8), 805-813.

Cheesman, J. (1949). An ultrasonic method of deterioration and cracking in concrete structures. *ACI Journal Proceedings, 46*(9) '10.14359/12041:' 10.14359/12041.

Cheytani, M., & Chan, S. L. I. (2021). The applicability of the Wenner method for resistivity measurement of concrete in atmospheric conditions. *Case Studies in Construction Materials, 15*, e00663 '10.1016/j.cscm.2021.e00663:' 10.1016/j.cscm.2021.e00663.

Clear, K. C. (1989). Measuring rate of corrosion of steel in field concrete structures. *Transportation Research Record*(1211).

Connor, R. J., Dexter, R., & Mahmoud, H. (2005). *Inspection and management of bridges with fracture-critical details*: Transportation Research Board Washington, DC.

Cross, W. M., Duke, E. F., Kellar, J. J., Han, K. N., & Johnston, D. (2001). *Stainless steel clad rebar in bridge decks*.

Dallin, G., Gagné, M., Goodwin, F., & Pole, S. (2015). Continuously galvanized reinforcing steel. *ACI Fall Convention: Kansas City, MO, USA*.

Dang, Y., Xie, N., Kessel, A., McVey, E., Pace, A., & Shi, X. (2014). Accelerated laboratory evaluation of surface treatments for protecting concrete bridge decks from salt scaling. *Construction Building and Materials, 55*, 128-135.

Darwin, D., Browning, J., O'Reilly, M., & Xing, L. (2007). Critical chloride corrosion threshold for galvanized reinforcing bars. *ACI Materials*.

de Vries, J., & Polder, R. B. (1997). Hydrophobic treatment of concrete. *Construction and Building Materials, 11*(4), 259-265.

Deschner, F., Winnefeld, F., Lothenbach, B., Seufert, S., Schwesig, P., Dittrich, S., . . . Neubauer, J. (2012). Hydration of Portland cement with high replacement by siliceous fly ash. *Cement Concrete Research, 42*(10), 1389-1400.

Dhir, R., & Jones, M. (1999). Development of chloride-resisting concrete using fly ash. *Fuel, 78*(2), 137-142.

Elsener, B., Andrade, C., Gulikers, J., Polder, R., & Raupach, M. (2003). Half-cell potential measurements—Potential mapping on reinforced concrete structures. *Materials Structures, 36*(7), 461-471.

Euclid. (2023). Calcium Nitrite Inhibitor. Retrieved from https://www.euclidchemical.com/products/admixtures/specialty-admixtures/corrosion-inhibitors/eucon-cia/

Fahim, A., Ghods, P., Alizadeh, R., Salehi, M., & Decarufel, S. (2019). *CEPRA: A new test method for rebar corrosion rate measurement.* Paper presented at the Advances in electrochemical techniques for corrosion monitoring and laboratory corrosion measurements.

Fanous, F. S., & Wu, H.-C. (2000). *Service life of Iowa bridge decks reinforced with epoxy-coated bars.* Paper presented at the Mid-Continent Transportation Symposium Proceedings.

Farris, J. F. (2018). Bridge design manual updates, bridge design guide, and corrosion guidelines updates.

Fazio, R. (1999). The assessment and prediction of reinforcing steel corrosion on the Dickson Bridge.

Figueira, R. B., Sadovski, A., Melo, A. P., & Pereira, E. V. (2017). Chloride threshold value to initiate reinforcement corrosion in simulated concrete pore solutions: The influence of surface finishing and pH. *Construction and Building Materials, 141*, 183-200.

Fishburn, P. C. (1967). Additive utilities with incomplete product sets: Application to priorities and assignments. *Operations Research, 15*(3), 537-542.

Fontana, M. G., & Greene, N. D. (1986). *Corrosion engineering* (3rd ed.): McGraw-hill.

Franzoni, E., Pigino, B., & Pistolesi, C. (2013). Ethyl silicate for surface protection of concrete: Performance in comparison with other inorganic surface treatments. *Cement Concrete Composites, 44*, 69-76.

Freitag, S., & Bruce, S. (2010). *The influence of surface treatments on the service lives of concrete bridges*: New Zealand Transport Agency Wellington, NewZealand.

Frølund, T., Klinghoffer, O., & Sørensen, H. E. (2003). *Pro's and con's of half-cell potentials and corrosion rate measurements.* Paper presented at the International Conference on ''Structural faults.

Giannini, E. R., Lindly, J. K., & Dunn, J. R. (2015). *Comparative evaluation of concrete bridge deck sealers*.

Giatec. (2019). iCOR user manual. In. Smart Concrete Testing Technologies.

Gowripalan, N., Mohamed, H. J. C., & Research, C. (1998). Chloride–ion induced corrosion of galvanized and ordinary steel reinforcement in high-performance concrete. *Cement Concrete Research, 28*(8), 1119-1131.

Goyal, A., Pouya, H. S., Ganjian, E., & Claisse, P. (2018). A review of corrosion and protection of steel in concrete. *Arabian Journal for Science Engineering, 43*, 5035-5055.

Groover, M. P. (2020). *Fundamentals of modern manufacturing: materials, processes, and systems*: John Wiley & Sons.

Gucunski, N., Romero, F., Shokouhi, P., & Makresias, J. (2005). *Complementary impact echo and ground penetrating radar evaluation of bridge decks on I-84 interchange in Connecticut.* Paper presented at the Earthquake engineering and soil dynamics.

Hall, C. (1989). Water sorptivity of mortars and concretes: a review. *Magazine of concrete research, 41*(147), 51-61.

Hansson, C., Mammoliti, L., & Hope, B. (1998). Corrosion inhibitors in concrete–part I: the principles. *Cement Concrete Research, 28*(12), 1775-1781.

Hansson, C., Poursaee, A., & Jaffer, S. (2007). Corrosion of reinforcing bars in concrete. *R&D Serial, 3013*.

Hao, S. (2010). I-35W bridge collapse. *Journal of Bridge Engineering, 15*(5), 608-614.

Hartt, W. H., Powers, R. G., Leroux, V., & Lysogorski, D. K. (2004). Critical literature review of high-performance corrosion reinforcements in concrete bridge applications.

Hoegh, K., Khazanovich, L., Dai, S., & Yu, T. (2015). Evaluating asphalt concrete air void variation via GPR antenna array data. *Case Studies in Nondestructive Testing Evaluation, 3*, 27-33.

Hong, S., Lai, W. W.-L., Wilsch, G., Helmerich, R., Helmerich, R., Günther, T., & Wiggenhauser, H. (2014). Periodic mapping of reinforcement corrosion in intrusive chloride contaminated concrete with GPR. *Construction Building Materials, 66*, 671-684.

Howell, B., Hopwood II, T., Meade, B. W., & Palle, S. (2015). *Evaluation of deterioration of structural concrete due to chloride intrusion and other damaging mechanisms*.

Hurlebaus, S., Hueste, M., Karthik, M., & Terzioglu, T. (2016). *Condition assessment of bridge post-tensioning and stay cable systems using NDE methods*.

Ichi, E., & Dorafshan, S. (2022). Effectiveness of infrared thermography for delamination detection in reinforcedconcrete bridge decks. *Automation in Construction, 142*, 104523.

Im, S. B., & Hurlebaus, S. (2012). Non-destructive testing methods to identify voids in external post-tensioned tendons. *KSCE Journal of Civil Engineering, 16*, 388-397.

Iyer, S., Schokker, A. J., & Sinha, S. K. (2003). Ultrasonic C-scan imaging: Preliminary evaluation for corrosion and void detection in posttensioned tendons. *Transportation Research Record, 1827*(1), 44-52.

Jackson, A., Rainwater, K., Lawson, W. D., Senadheera, S., Liang, D., Surles, J., . . . Yan, W. (2017). Snow and ice control materials for Texas roads; VOLUME 1: literature and best practices review; VOLUME 2: field trials and laboratory study.

Kamde, D. K., & Pillai, R. G. (2021). Corrosion initiation mechanisms and service life estimation of concrete systems with fusion-bonded-epoxy (FBE) coated steel exposed to chlorides. *Construction Building Materials, 277*, 122314.

Keller, T. J. P. i. S. E., & Materials. (2001). Recent all-composite and hybrid fibre-reinforced polymer bridges and buildings. *Progress in Structural Engineering Materials, 3*(2), 132-140.

Kessler, R. J., Powers, R. G., Paredes, M. A., Sagüés, A. A., & Virmani, Y. P. (2007). *Corrosion inhibitors In concrete–results of a ten year study.* Paper presented at the CORROSION 2007.

Keßler, S., Angst, U., Zintel, M., & Gehlen, C. (2015). Defects in epoxy-coated reinforcement and their impact on the service life of a concrete structure: A study of critical chloride content and macro-cell corrosion. *Structural Concrete, 16*(3), 398-405.

Koch, G. H., Brongers, M. P., Thompson, N. G., Virmani, Y. P., & Payer, J. H. (2002). *Corrosion cost and preventive strategies in the United States*.

Kofman, L., Ronen, A., & Frydman, S. (2006). Detection of model voids by identifying reverberation phenomena in GPR records. *Journal of Applied Geophysics, 59*(4), 284-299.

Kogler, R., & Ocel, J. (2022). *Steel Bridge Design Handbook*.

Krause, M., Maierhofer, C., & Wiggenhauser, H. (1995). *Thickness measurement of concrete elements using radar and ultrasonic impulse echo techniques.* Paper presented at the Proc. 6th International Conf. on Structural Faults and Repair.

Lau, K., & Sabbir, M. A. (2015). *Corrosion evaluation of novel coatings for steel components of highway bridges*.

Lawler, J. S., Krauss, P. D., Kurth, J., & McDonald, D. J. T. r. r. (2011). Condition survey of older west Virginia bridge decks constructed with epoxy-coated reinforcing bars. *Transportation Research Record, 2220*(1), 57-65.

Layssi, H., Ghods, P., Alizadeh, A. R., & Salehi, M. (2015). Electrical resistivity of concrete. *Concrete International*(May), 41-46.

Leeco Steel, L. (2023). How Much Does Steel Plate Cost: 2023? Retrieved from https://www.leecosteel.com/news/post/cost-of-steel-plate/

Li, K., Han, J., Wang, S., Lian, H., Xiong, J., Wang, J., . . . Zhu, H. (2023). Long-term performance of structural concretes in China southeast coastal environments exposed to atmosphere and chlorides. *Cement and Concrete Research, 164*(107064), 107064 '10.1016/j.cemconres.2022.107064:' 10.1016/j.cemconres.2022.107064.

Lute, R. D., Folliard, K. J., Drimalas, T., & Murcia-Delso, J. (2021). *Alternate reinforcements for enhanced corrosion resistance in TxDOT Bridges*.

Manafpour, A., Hopper, T., Rajabipour, F., Radlińska, A., Warn, G. P., Shokouhi, P., . . . Jahangirnejad, S. (2016). Field investigation of in-service performance of concrete bridge decks in Pennsylvania. *Journal of Transportation Research Record, 2577*(1), 1-7.

Marchand, J., Pigeon, M., & Setzer, M. J. (1996). *Freeze-thaw durability of concrete*: CRC Press.

Martin, U., Ress, J., Bosch, J., & Bastidas, D. (2020). Stress corrosion cracking mechanism of AISI 316LN stainless steel rebars in chloride contaminated concrete pore solution using the slow strain rate technique. *Electrochimica Acta, 335*, 135565.

Martys, N. S., & Ferraris, C. F. (1997). Capillary transport in mortars and concrete. *Cement Concrete Research, 27*(5), 747-760.

Medeiros, M., & Helene, P. (2008). Efficacy of surface hydrophobic agents in reducing water and chloride ion penetration in concrete. *Materials Structures, 41*, 59-71.

Müller, A. (2015). 25 Milliarden Euro Schaden durch Staus. Retrieved from http://www.handelsblatt.com/unternehmen/handel-konsumgueter/ueberlastete-autobahnen-25-milliarden-euro-schaden-durch-staus/12053128.html.

National Academics of Sciences, E., & Medicine. (2020). *Guide specification for service life design of highway bridges* (I. Masters, J. Kulicki, R. U.-C. F. Moon, C. A.-M. Langlois, & L. L. C. Ncs GeoResources Naresh Samtani Eds.). Washington, DC: The National Academies Press.

Neville, A. M. (1995). *Properties of concrete* (Vol. 4): Longman London.

Noumowe, A. N., Siddique, R., & Debicki, G. (2009). Permeability of high-performance concrete subjected to elevated temperature (600 C). *Construction Building and Materials, 23*(5), 1855-1861.

Nycon. (2023). Polypropylene fibers. Retrieved from https://nycon.com/collections/polypropylene-fibers

Omar, T., & Nehdi, M. L. (2017). Remote sensing of concrete bridge decks using unmanned aerial vehicle infrared thermography. *Automation in Construction, 83*, 360-371.

Otieno, M., Alexander, M., & Beushausen, H.-D. (2010). Corrosion in cracked and uncracked concrete–influence of crack width, concrete quality and crack reopening. *Magazine of concrete research, 62*(6), 393-404.

Pan, X., Shi, Z., Shi, C., Ling, T.-C., & Li, N. (2017a). A review on surface treatment for concrete–Part 2: Performance. *Construction and Building Materials, 133*, 81-90.

Pan, X., Shi, Z., Shi, C., Ling, T.-C., & Li, N. (2017b). A review on surface treatment for concrete – Part 2: Performance. *Construction and Building Materials, 133*, 81-90 '10.1016/j.conbuildmat.2016.11.128:' 10.1016/j.conbuildmat.2016.11.128.

Pianca, F., Schell, H., Cautillo, G. J. I. J. o. M., & Technology, P. (2005). The performance of epoxy coated reinforcement: experience of the Ontario ministry of transportation. *International Journal of Materials Product Technology, 23*(3-4), 286-308.

Pincheira, J. A., Aramayo, A., Fratta, D., & Kim, K.-S. (2015). Corrosion performance of epoxy-coated bars in four bridge decks subjected to deicing salts: 30-year perspective. *Performance of Constructed Facilities, 29*(4), 04014097.

Popov, B. N. (2015). *Corrosion engineering: principles and solved problems*: Elsevier.

Pradhan, B., & Bhattacharjee, B. (2009). Half-cell potential as an indicator of chloride-induced rebar corrosion initiation in RC. *Journal of Materials in Civil Engineering, 21*(10), 543-552.

Presuel-Moreno, F., Scully, J., & Sharp, S. (2010). Literature review of commercially available alloys that have potential as low-cost, corrosion-resistant concrete reinforcement. *Corrosion, 66*(8), 086001-086001-086013.

Pritzl, M. D., Tabatabai, H., Ghorbanpoor, A. J. C., & Materials, B. (2015). Long-term chloride profiles in bridge decks treated with penetrating sealer or corrosion inhibitors. *Construction and Building Materials, 101*, 1037-1046.

Pyc, W. A., Weyers, R. E., Sprinkel, M. M., & Weyers, R. M. (2000). Field performance of epoxy coated reinforcing steel in concrete bridge decks in Virginia. *Concrete International, 22*(2), 57-62.

Ramniceanu, A., Weyers, R. E., Riffle, J. S., & Sprinkel, M. M. J. A. M. J. (2008). Parameters governing corrosion protection efficacy of fusion-bonded epoxy coatings on reinforcing bar. *ACI Materials, 105*(5), 459.

Rasheeduzzafar, D. F., Bader, M., & Khan, M. M. J. A. M. J. (1992). Performance of corrosion resisting steels in chloride-bearing concrete. *ACI Materials, 89*(5), 439-448.

Ribeiro, D., & Abrantes, J. (2016). Application of electrochemical impedance spectroscopy (EIS) to monitor the corrosion of reinforced concrete: A new approach. *Construction Building Materials, 111*, 98-104.

RILEM CPC-18. (1988). Measurement of hardened concrete carbonation depth, RILEM Recommendations CPC-18, Materials and Structures,

Rockey, A. (2022). *Metallic coatings as peripheral barriers to diminish the adverse effects of cathodic protection on prestressing members.* (Ph.D. Ph.D. Thesis), Texas A&M University.,

Rodrigues, R., Gaboreau, S., Gance, J., Ignatiadis, I., & Betelu, S. (2021). Reinforced concrete structures: A review of corrosion mechanisms and advances in electrical methods for corrosion monitoring. *Construction Building Materials, 269*, 121240.

Rupnow, T. D. (2012). *Evaluation of ternary cementitious combinations*.

Ryan, T. W., Mann, J. E., Chill, Z. M., & Ott, B. T. J. P. N. F. N. (2012). *Bridge inspector's reference manual (BIRM)*.

Safiuddin, M., Kaish, A. A., Woon, C.-O., & Raman, S. N. (2018). Early-age cracking in concrete: Causes, consequences, remedial measures, and recommendations. *Applied Sciences, 8*(10), 1730.

Schickert, M. (1995). *Towards SAFT-imaging in ultrasonic inspection of concrete.* Paper presented at the International Symposium Non Destructive Testing in Civil Engineering (NDT-CE).

Scully, J. R., Hurley, M. F., & Sharp, S. R. (2007). *Investigation of the corrosion propagation characteristics of new metallic reinforcing bars*.

Smith, J., & Virmani, Y. P. (2000). *Materials and methods for corrosion control of reinforced and prestressed concrete structures in new construction*.

Söylev, T. A., & Richardson, M. (2008). Corrosion inhibitors for steel in concrete: State-of-the-art report. *Construction and Building Materials, 22*(4), 609-622.

Spragg, R. P., Bu, Y., Snyder, K., Bentz, D., & Weiss, J. (2013). Electrical testing of cement-based materials: role of testing techniques, sample conditioning, and accelerated curing. '10.5703/1288284315230:' 10.5703/1288284315230.

Sun, H., Pashoutani, S., & Zhu, J. (2018). Nondestructive evaluation of concrete bridge decks with automated acoustic scanning system and ground penetrating radar. *Sensors, 18*(6), 1955.

TCEQ. (2023). Texas commision on environmental quality.

Tittarelli, F., & Moriconi, G. (2010). The effect of silane-based hydrophobic admixture on corrosion of galvanized reinforcing steel in concrete. *Construction Science, 52*(9), 2958-2963.

Triantaphyllou, E., & Mann, S. H. (1989). An examination of the effectiveness of multi-dimensional decision-making methods: A decision-making paradox. *Decision support systems, 5*(3), 303-312.

Tuutti, K. (1982). *Corrosion of steel in concrete*: Cement-och betonginst.

TxDOT. (2015). *University Handbook 2016*: Texas Department of Transportation, The Research and Technology Implementation Office.

TxDOT. (2021). Concrete repair manual. Austin, Tx.: Texas Department of Transportation

TxDOT. (2022a). Average unit cost. Austin, Tx.: Texas Department of Transportation

TxDOT. (2022b). Structure design - corrosion protection guide. Austin, Tx.: Texas Department of Transportation

TxDOT. (2023). TxDOT Bridges. *TxDOT Open Data Portal.* Retrieved from https://gis-txdot.opendata.arcgis.com/datasets/83af0d2957ca4c2eb340e4bd04a1046f/explore

US Bureau of Labour Statistics. (2023). US Bureau of Labour Statistics (St. Louis Federal Reserve). Retrieved from https://www.bls.gov/.htm

Vaca-Cortés, E., Lorenzo, M. A., Jirsa, J. O., Wheat, H. G., & Carrasquillo, R. L. (1998). *Adhesion testing of epoxy coating* (1265-6).

Van Dyke, C., Meade, B., Wells, D., Palle, S., & Hopwood, I. (2017). Long-term corrosion protection of bridge elements reinforcing materials in concrete.

Vu, K. A. T., & Stewart, M. G. (2000). Structural reliability of concrete bridges including improved chloride-induced corrosion models. *Structural safety, 22*(4), 313-333.

Yang, Z. (2004). *Assessing cumulative damage in concrete and quantifying its influence on life cycle performance modeling.* Purdue University,

Yehia, S., Abudayyeh, O., Nabulsi, S., & Abdelqader, I. (2007). Detection of common defects in concrete bridge decks using nondestructive evaluation techniques. *Journal of Bridge Engineering, 12*(2), 215-225.

Yeomans, S. (2004). *Galvanized steel reinforcement in concrete*: Elsevier.

Yodsudjai, W., & Pattarakittam, T. (2017). Factors influencing half-cell potential measurement and its relationship with corrosion level. *Measurement, 104*, 159-168.

Zhang, J. (2001). *Noninvasive surface measurement of the corrosion impedance of rebar in concrete*: University of California, Berkeley.

Zou, Z., Wu, J., Wang, Z., & Wang, Z. (2016). Relationship between half-cell potential and corrosion level of rebar in concrete. *Corrosion Engineering, 51*(8), 588-595.

APPENDIX A VALUE OF RESEARCH

A.1 MOTIVATION AND SIGNIFICANCE

The deterioration of steel girder and reinforced concrete deck bridges due to corrosion impose a major safety risk and financial allocations in Texas. Hao (2010) reported a significant annual cost of corrosion damages to infrastructure in Texas, including the cost associated with proactive monitoring and regular maintenance of bridge structures. The long-term performance and structural safety of steel and concrete bridges are essential to ensure efficient transportation and economic growth of the state. According to the Texas bridge inventory database (TxDOT, 2023), most bridges in Texas are built between 1940 and 2000. These structures have been in service for a sufficient period, making them susceptible to significant deterioration caused by corrosion.

As electrochemical reactions proceed, metal loss takes place in oxidized location while corrosion products accumulate and expand on reduction sites, causing metal loss in steel girders as well as surface cracking and concrete spalling in concrete decks. Identifying corrosion problems in both steel and concrete bridge structures is a cumbersome task and requires destructive testing in many events, making repair and maintenance expensive. The rate of corrosion for different types of bridges is different and is dependent on the surrounding “micro” and “macro” environmental conditions.

Texas has a wide range of environments from high rainfall areas, dry areas with less rainfall, coastal areas with high air borne chloride concentration, and areas with heavy usage of deicing salt. These environmental variations impose varying corrosion risks on different regions. This research project proposes a corrosion risk map for Texas to diminish corrosion activities on steel and concrete bridge structures. Based on the results of field inspections and laboratory testing, it demonstrates an analysis of corrosion prevention and mitigation techniques implemented on steel girders and concrete decks, and if these strategies have been suitable to reduce the adverse effects of corrosion in the state bridge structures. It also provides a guideline for the laboratory examinations, which can aid in determining corrosion related issues in steel girders and concrete specimens.

The findings of this research benefits state agency and affiliated departments to select the best suitable corrosion prevention methods for new and existing steel and reinforced concrete bridges across Texas. This study provides a modified Patina Rating Index based on field and

laboratory analysis to aid bridge inspectors performing accurate analysis on the protective state of patina layer developed on weathering steel surface. It addresses quantitative guidelines to enable consistent corrosion assessments of coating systems by implementing field and laboratory testing strategies of paint system performance. In addition, this research proposes an analytical approach based on corrosion fatigue models to estimate the average service life of weathering steel girders in different corrosive environments. Furthermore, it evaluates different corrosion mitigation systems employed in concrete decks, including high-performance concrete (HPC), fiber reinforced concrete (FRC), epoxy coated rebar (ECR), calcium nitrate corrosion inhibitor (CNI), and concrete surface treatment. It provides guidelines to conducting corrosion assessments of concrete decks by studying the results of field testing and proper laboratory testing for aged concrete specimens.

A.2 ECONOMIC VALUE

This research project aimed to deliver economic benefits to the Texas Department of Transportation by suggesting efficient and durable corrosion prevention and mitigation strategies that can be implemented in a particular corrosive risk region. This will result in less frequent repairs and replacements, eventually increasing the lifespan of the structures. The potential economic value of this research is to reduce construction, operations, and maintenance cost of steel and concrete bridge structures based on a developed decision tool.

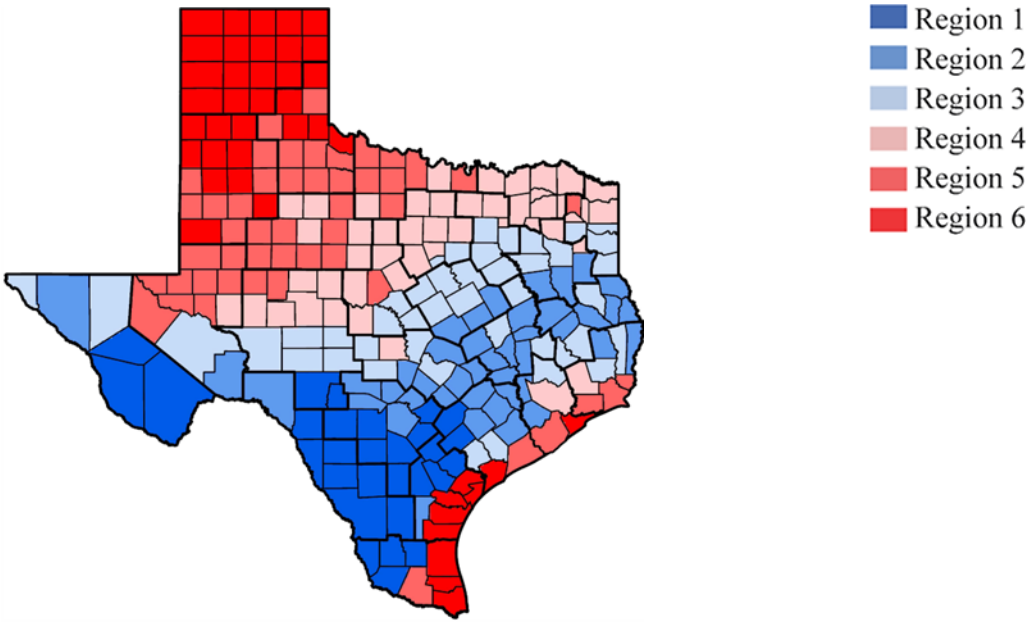

Figure A.1. Corrosion Risk Assessment Map

The Corrosion Risk Assessment Map in Figure A.1 illustrates the varying corrosivity risks across Texas counties. The map divides the state into six regions based on the average predicted corrosion risk for each county. Region 1 and Region 2 in southwest Texas show low corrosion risk environments. In addition, Region 3 and Region 4 across central Texas exhibit medium corrosion risk, and Region 5 and Region 6 in north Texas and along the coastline demonstrate high corrosion risk. The northern counties face more corrosion problems due to the increased application of deicing salt. However, the coastline counties are also in corrosion risk because of higher TOW, more airborne chloride deposition, and substantial industrial activity.

The Table A-1 provides a detailed breakdown of bridge constructed across multiple regions, categorized by weathering steel, and painted steel girders, as well as reinforced concrete bridges. Considering steel and concrete bridges across the state, there are 492 weathering Steel, 6,287 painted steel, and 28,914 reinforced concrete bridges that is a total of 35,693 structures in Texas (TxDOT, 2023).

Table A-1. Total Number of Weathering Steel, Painted Steel, and Reinforced Concrete Bridges Distributed Across All Six Regions

Region	Weathering Steel Bridge	Painted Steel Bridge	Concrete Bridge	Total
Region 1	7	268	1,620	1,895
Region 2	63	1,809	5,891	7,763
Region 3	195	2,045	9,377	11,617
Region 4	185	1,540	7,491	9,216
Region 5	22	388	2,456	2,866
Region 6	20	237	2,079	2,336
All Regions	492	6,287	28,914	35,693

A.2.1 Steel Bridge

A.2.1.1 Alleviating Traffic Congestion

Employing weathering steel in construction of steel girders in Region 1 to Region 4 result in a smaller number of repair and maintenance over the bridge service life, while regular maintenance and repainting are expected for the painted steel girders to maintain the integrity of painted steel girders. As a result, application of weathering steel reduces the number of lane closures required for the corrosion maintenance, hence it reduce indirect cost of lane closures and associated traffic congestion. Although the cost has not been considered in the cost analysis in this report, the results of the current project have a direct positive effect on public transportation by reducing the time spent on the roads. Indirect costs include wasted time for drivers stuck in congestion, excess fuel consumption, and environmental impact of traffic jams. According to NCHRP Synthesis 354, lane closures incur an economic loss of $11,000 per hour per lane (Connor et al., 2005). This estimate aligns with European analysis finding that a 4 km traffic jam on a two-lane autobahn causes an economic loss of $9,200 per hour (Müller, 2015).

A.2.1.2 Upfront Cost and Maintenance Cost

Upfront cost is the initial cost for installation of corrosion mitigation method, such as using weathering steel or coating the steel girders by paint. In Texas, three coating systems are common for painted steel girders, System I, System II, and System III. Maintenance cost includes water washing and replacing corroded parts for weathering and painted steel members. It can also include touch-up, maintenance repaint, and full repaint after blast cleaning of the steel surface. Table A-2 provides the detailing of the cost associated with corrosion prevention and mitigation methods in low corrosive environments. Additionally, Table A-3 gives the cost data for medium corrosive

environments, and Table A-4 shows the pricing information for high corrosive regions. The data represented in these tables are divided into four categories; original paint cost, touch-up, maintenance repaint, and full repaint. Note that the cost of touch-up and maintenance repainting does not depend on the regions for a particular paint system and can be estimated to be $\$2.28/ft^2$ and $\$3.99/ft^2$. The cost of a full repaint is also assumed to be constant across different regions at $\$7.70/ft^2$. However, the time of repainting of steel girders varies by regions and the corrosivity of the environment, (American Galvanizers Association, 2023).

Table A-2. Upfront Cost and Maintenance Cost for System I in Region 1 and Region 2 (American Galvanizers Association, 2023)

Paint Application	Cost ($/ft^2)	In-Service (year)
Original Paint	5.70	–
Touch up	2.28	23
Maintenance Repaint	3.99	34
Full Repaint	7.70	46
Touch up	2.28	69
Maintenance Repaint	3.99	80
Full Repaint	7.70	92

Table A-3. Upfront Cost and Maintenance Cost for System I for Region 3 And Region 4 (American Galvanizers Association, 2023)

Paint Application	Cost ($/ft^2)	In-Service (year)
Original Paint	5.70	–
Touch up	2.28	17
Maintenance Repaint	3.99	25
Full Repaint	7.70	34
Touch up	2.28	51
Maintenance Repaint	3.99	59
Full Repaint	7.70	69
Touch up	2.28	85
Maintenance Repaint	3.99	93

Table A-4. Upfront Cost and Maintenance Cost for System I Region 5 and Region 6 (American Galvanizers Association, 2023)

Paint Application	Cost ($/ft^2)	In-Service (year)
Original Paint	5.70	–
Touch up	2.28	13
Maintenance Repaint	3.99	19
Full Repaint	7.70	26
Touch up	2.28	39
Maintenance Repaint	3.99	45
Full Repaint	7.70	52
Touch up	2.28	65
Maintenance Repaint	3.99	71
Full Repaint	7.70	78
Touch up	2.28	91
Maintenance Repaint	3.99	97

The cost data for System II type paint across different regions over time are listed in the Table A-5, Table A-6, and Table A-7. The different costs presented in the table are original cost, touch up cost, maintenance repaint cost, and full repaint cost, which is \$4.49/ft^2, \$1.79/ft^2, \$3.14/ft^2, and \$6.06/ft^2 respectively. A similar observation can be made based on these tables that the frequency of maintenance requirement increases with the increase in corrosivity of the region. The table provides the cost listed for touch-up painting which is performed at different intervals in different regions (e.g., Year 24, 17, 11), maintenance repainting at different intervals (e.g., Year 36, 25, 16), and full repainting at different intervals (e.g., Year 48, 34, 22. Regions 3 and Regions 4 have the same touch-up, maintenance, and full repainting costs as Region 1 and Region 2, but the maintenance must be done in different years (Table A-6). Similarly, Regions 5 and 6 have the same costs as the other regions, but the maintenance is scheduled in different years (Table A-7) (American Galvanizers Association, 2023).

Table A-5. Upfront Cost and Maintenance Cost for System II in Region 1 and Region 2 (American Galvanizers Association, 2023)

Paint Application	Cost ($/ft^2)	In-Service (year)
Original Paint	4.49	–
Touch up	1.79	24
Maintenance Repaint	3.14	36
Full Repaint	6.06	48
Touch up	1.79	72
Maintenance Repaint	3.14	84
Full Repaint	6.06	96

Table A-6. Upfront Cost and Maintenance Cost for System II Region 3 and Region 4 (American Galvanizers Association, 2023)

Paint Application	Cost ($/ft^2)	In-Service (year)
Original Paint	4.49	–
Touch up	1.79	17
Maintenance Repaint	3.14	25
Full Repaint	6.06	34
Touch up	1.79	51
Maintenance Repaint	3.14	59
Full Repaint	6.06	68
Touch up	1.79	85
Maintenance Repaint	3.14	93

Table A-7. Upfront Cost and Maintenance Cost for System II Region 5 and Region 6 (American Galvanizers Association, 2023)

Paint Application	Cost ($/ft^2)	In-Service (year)
Original Paint	4.49	–
Touch up	1.79	11
Maintenance Repaint	3.14	16
Full Repaint	6.06	22
Touch up	1.79	33
Maintenance Repaint	3.14	38
Full Repaint	6.06	44
Touch up	1.79	55
Maintenance Repaint	3.14	60
Full Repaint	6.06	66
Touch up	1.79	77
Maintenance Repaint	3.14	82
Full Repaint	6.06	88
Touch up	1.79	99

In a low corrosive environment (Region 1 and Region 2), the original paint is \$5.77/ft^2, while touch-up cost is \$2.31/ft^2, the maintenance repainting cost is \$4.04/ft^2, and full repainting cost is \$7.79/ft^2 (Table A-8). Similarly for paint System II, the timing of these applications varies across regions and more frequent maintenance applications are needed in aggressive corrosive condition such as Region 5 and Region 6. In medium and high corrosive environments, the cost is still similar to the low corrosive regions, but touch-ups, maintenance repaints, and full repaints are expected in different intervals (Table A-9 and Table A-10) (American Galvanizers Association, 2023).

Table A-8. Upfront Cost and Maintenance Cost for System III in Region 1 and Region 2 (American Galvanizers Association, 2023)

Paint Application	Cost ($/ft^2)	In-Service (year)
Original Paint	5.77	–
Touch up	2.31	29
Maintenance Repaint	4.04	43
Full Repaint	7.79	58
Touch up	2.31	87

Table A-9. Upfront Cost and Maintenance Cost for System III Region 3 and Region 4 (American Galvanizers Association, 2023)

Paint Application	Cost ($/ft^2)	In-Service (year)
Original Paint	5.77	–
Touch up	2.31	20
Maintenance Repaint	4.04	30
Full Repaint	7.79	40
Touch up	2.31	60
Maintenance Repaint	4.04	70
Full Repaint	7.79	80

Table A-10. Upfront Cost and Maintenance Cost for System III Region 5 and Region 6 (American Galvanizers Association, 2023)

Paint Application	Cost ($/ft^2)	In-Service (year)
Original Paint	5.77	–
Touch up	2.31	14
Maintenance Repaint	4.04	21
Full Repaint	7.79	28
Touch up	2.31	42
Maintenance Repaint	4.04	49
Full Repaint	7.79	56
Touch up	2.31	70
Maintenance Repaint	4.04	77
Full Repaint	7.79	84
Touch up	2.31	98

Kogler and Ocel (2022) estimated the price of weathering steel to be $1/lbs. in 2013. Factoring an inflation rate of 2.4% (US Bureau of Labour Statistics, 2023) in the cost analysis, it was estimated that the cost of weathering steel is $1.27/lbs. in 2023. Assuming hot-rolled carbon steel is $0.41/lbs. (Leeco Steel, 2023), the cost associated four standard beams sizes commonly used in Texas calculated and reported in Table A-11. Density of steel was assumed 490 lbs./ft^3. As shown in Table A-11, the cost of corrosion prevention and mitigation strategies is varied and

increased from Region 1 to Region 6, with System-I from \$26.7/ft^2 to \$51.6/ft^2, System-II from \$21.4/ft^2 to \$48.8/ft^2, and System-III from \$22.0/ft^2 to \$48.8/ft^2.

Table A-11. Calculated Cost for Corrosion Protection Systems in Different Regions

Corrosion Protection System	Region 1-2 (\$/ft^2)	Region 3 (\$/ft^2)	Region 4 (\$/ft^2)	Region 5 (\$/ft^2)	Region 6 (\$/ft^2)
System I	28.6	39.0	39.0	51.6	51.6
System II	21.4	30.8	30.8	48.8	48.8
System III	22.0	34.0	34.0	48.8	48.8

At the time this report was being prepared, 57520 bridges had been constructed in Texas according to TxDOT (2023). Most of these structures (about 35693 bridges) are concrete and steel bridges, which is about 62% of all bridges in the state. Among these, 492 are weathering steel, and 6,287 are painted steel bridges. This is about 0.9% weathering steel and 11% painted steel of the total overpasses. In addition, according to Texas bridge database (TxDOT, 2023) on an average 6000 new bridges will be built in every 10 years, including 708 steel bridges (12 % of total), and 3000 concrete overpasses (50% of total).

Table A-12 provides detailed distribution of steel and concrete bridges across Texas. The data were divided into six corrosive regions according to Texas corrosion risk assessment map developed in this study (Figure A.1). It was concluded that 32% of steel bridges fall in low corrosive environments (Region 1 and Region 2), over 58% falls in medium corrosive regions (Region 3 and Region 4), and about 10% are located in high corrosive environments (Region 5 and Region 6). Therefore, if TxDOT does not change the current pattern, it could be a fair assumption that the new steel bridges will be built in the state in next 10 years consists of 225 structures in Region 1 and Region 2, 415 bridges in Region 3 and Region 4, and 68 overpasses in Region 5 and Region 6.

It was concluded from the experimental examinations conducted in this study, weathering steel should be employed in Region 1 to Region 4 and paint system III should be used in Region 5 and 6. However, TxDOT recommends using System II everywhere except in coastal areas in South East in addition to locations that deicing salt is frequently used in North. TxDOT recommends the application of System III for these areas (Table A-13). A comparison between findings of this research and TxDOT recommendations, a cost saving estimation is reported in Table A-13.

Table A-12. Region Wise Distribution of Steel Bridges (Based on Texas Corrosion Map)

Region	Number of Steel Bridges	Percentage of Steel Bridges (%)	Percentage of Steel Bridges (%)
Region 1	275	4.06	31.7
Region 2	1,872	27.6	
Region 3	2,240	33.0	58.5
Region 4	1,725	25.5	
Region 5	410	6.05	9.84
Region 6	257	3.79	

Table A-13. Recommended Mitigation for Steel Bridges and TxDOT Recommendation

Regions	TxDOT Recommendation	Project 0-7040 Recommendation	Savings or Loss
Region 1	System II	WS	May result in cost saving but needs validation
Region 2	System II	WS	
Region 3	System II	WS	
Region 4	System II	WS	
Region 5	System III	System III	No cost saving
Region 6	System III	System III	

For the cost analysis, a 30 feet wide bridge with various lengths, different cross-section is considered based on TxDOT recommendation. The details about 30 feet wide plate girder bridge are listed in the Table A-14. Detailing of length and cross-sectional properties provided in this table encloses the short and long span steel bridges built by TxDOT.

Table A-15 provides the cost per pound of weathering steel (WS) and carbon steel (CS) beams. It also gives the cost of paint per square ft, assuming a fixed paint cost rate. The number of girders, weight per linear foot, and total paint cost per square ft are provided for each wide flange represented in the Table A-15. Note that the values given in this table were calculated for low corrosive environments.

Table A-14. Bridge Girder Details Considered for Calculation

Span Width (ft)	Min Length (ft)	Beam	t_{tf} (in.)	b_{tf} (in.)	t_{bf} (in.)	b_{bf} (in.)	t_{web}	d_{web}
30	30	W18×130	1.00	12	1.25	12	0.5	17.0
30	90	W40×199	0.87	16	1.25	16	0.5	36.5
30	95	W40×215	1.00	16	1.37	16	0.5	36.5
30	60	W40×149	0.75	12	1.00	12	0.5	36.5

Table A-15. Cost Information for Weathering Steel (WS), Carbon Steel (CS), Paint Cost for System II in Region 1 and Region 2

Beam	Painted Area	WS ($/lbs.)	CS ($/lbs.)	No. of Girders	Paint Cost ($/ft^2)	Weight (lbs./ft)
W18×130	203	$1.27	$0.41	5	$21.4	130
W40×199	1,020	$1.27	$0.41	5	$21.4	199
W40×215	1,077	$1.27	$0.41	5	$21.4	215
W40×149	600	$1.27	$0.41	5	$21.4	149

Table A-16 provides a cost comparison between weathering steel bridge and painted steel bridges, considering a span with 5 wide flange girders. The painted steel is considered to be a carbon steel with a coat of paint system II. The painting cost is represented as PS Cost and PS total is sum of carbon steel and the cost of using System II. The average saving was determined by taking average saving of all four cases that estimated at $22,539.

Table A-16. Cost Calculation for Region 1 and Region 2

Beam	WS ($)	CS ($)	PS Cost ($)	PS total ($)	Saving Using WS ($)	Average Saving ($)
W18×130	24,765	$7,995	$21,668	$29,663	$4,897	$22,539
W40×199	113,729	$36,716	$109,140	$145,86	$32,127	
W40×215	129,699	$41,871	$115,203	$157,075	$27,376	
W40×149	56,769	$18,327	$64,200	$82,527	$25,758	

Based on the Texas bridge inventory, each steel bridge has an average around 3 main spans, thus the cost saving per bridge was calculated for a 3-span steel bridges. Table A-16 shows an average saving of around $22,539 per span. Therefore, the total saving per bridge of 3 span in Region 1 and Region 2 is $67,617. As mentioned earlier, since 215 bridges will be probably built every 10 years in Texas, employing weathering steel in super structures will result in a cost saving of $14,537,655 which is about $1,453,766 every year.

Table A-17 provides cost and weight of different wide flanges for weathering steel and painted steel located in Region 3 and Region 4. It is evident that the cost associated with painting in Region 3 and Region 4 is more compared to Region 1 and Region 2. As corrosivity of environment increases, it results in more repair and maintenance, touch up and full repaint during the bridge service life.

Table A-17. Cost Information for Weathering Steel (WS), Carbon Steel (CS), Paint Cost for System II in Region 3 and Region 4

Beam	Painted Area	WS ($/lbs.)	CS ($/lbs.)	No of girder	Paint cost ($/ft^2)	Weight (lbs./ft)
W18×130	203	$1.27	$0.41	5	$30.8	130
W40×199	1,020	$1.27	$0.41	5	$30.8	199
W40×215	1,077	$1.27	$0.41	5	$30.8	215
W40×149	600	$1.27	$0.41	5	$30.8	149

Table A-18 shows the cost calculation for a single span bridge consisting of 5 wide flange steel girders. Utilizing weathering steel in bridge structures located in Region 3 and Region 4 results in an average saving of $56,605 per span. Hence, the cost saving for a 3 span bridge can be estimated at $169,815. Therefore, the total cost saving for a potential of 415 new bridges constructed in Region 3 and Region 4 is $70,473,225 every 10 years. This can be reduced to $7,047,323 per year. Therefore, the total cost saving using weathering steel in Region 1 to Region 4 is $8,501,088 per year.

Table A-18 Cost Calculation for Region 3 and Region 4

Beam	WS	CS	PS Cost	PS total	Saving Using WS	Average Saving
W18×130	24,765	$7,995	$31,185	$39,180	$14,415	$56,605
W40×199	113,729	$36,716	$157,080	$193,796	$80,067	
W40×215	129,699	$41,871	$165,807	$207,678	$77,979	
W40×149	56,769	$18,327	$92,400	$110,727	$53,958	

A.2.2 Concrete Bridge

A.2.2.1 Construction and Maintenance Cost

The cost associated to construction is a significant factor for the selection of corrosion prevention and mitigation methods employed in reinforced concrete bridges. Assuming the process of deck construction (including labor, machinery, and engineering and design) remains the same regardless of the chosen mitigation method, the cost of the materials was only factored in the cost analysis in this study. Table A-19 provides the cost of each mitigation of concrete deck according to Average Low Bid Unit Price (TxDOT, 2022a). The cost of a High-Performance Concrete (HPC) slab was estimated to be $22.0/ft^2, while a regular concrete slab was estimated at $18.2/ft^2. Therefore, the price difference between HPC and regular concrete can be estimated $3.88/ft^2. This was further considered as the price of HPC for determining the scores. The cost associated with

mitigation methods include the concrete surface treatment (CST) that was estimated \$0.91/ft^2 (\$85/yd^2). High performance concrete with micro-fibers (HPCF) (polypropylene fibers) was estimated to be \$4.45/ft^2 (0.033 lbs. of polypropylene fibrillated fiber per cubic feet in 4.5 in. thick cast-in-place concrete (CIP)) (Nycon, 2023). The cost of calcium nitrite inhibitor was found to be \$9 per gallon (Euclid, 2023). To this end, 3 gallons of CNI per cubic yard was assumed to add to concrete mix design for CIP with 4.5 in. thick. Hence, the cost of CNI was calculated to be \$1.13/ft^2. Note that additional cementitious materials that should be added to concrete mix in addition to CNI may contribute to an increase in the overall cost.

As reported by Lute et al. (2021), the cost of Epoxy-Coated Reinforcement (ECR) was estimated to be \$0.63/lbs., while black rebar (ASTM A615 Grade 60) cost \$0.42/lbs. On average, 6.5 lbs. of ECR per square feet were assumed in the concrete deck. Therefore, the cost of ECR can be estimated at \$4.1/ft^2. Similar to HPC, the price difference between ECR and black steel rebar was factored in the price of ECR for the purpose of cost evaluation.

Table A-19. Cost of Mitigation Methods

Mitigation Methods	Cost (\$/ft^2)
Latex Modified Concrete Overlay (LMCO)	9.44
Fiber Reinforced Concrete (FRC)	4.45
High Performance Concrete (HPC)	3.88
Epoxy Coated Rebar (ECR)	1.40
Calcium Nitrate Inhibitor (CNI)	1.13
Concrete Surface Treatment (CST)	0.91
None	0.00

In general, a combination of corrosion prevention and mitigation methods were employed in reinforced concrete decks in Texas. While the cost of each method was determined individually, the overall cost was estimated by adding up the individual costs of each mitigation method. Table A-20 shows the total cost of combined mitigation methods employed in the inspected concrete decks. It was assumed that the highest cost is when all mitigation methods are implemented in the concrete structure, and the lowest cost is when no mitigation method is applied, resulting in a cost of \$0.

Table A-20. Cost of Mitigation Methods

Mitigation Methods Used in Bridges	Cost ($/ft^2)
None	3.44
CNI/CST(LO/SI)/ECR	2.31
CST(LO/SI)/ECR	1.40
ECR	3.88
HPC	5.92
HPC/CNI/CST(LO/SI)	7.32
HPC/CNI/CST(LO/SI)/ECR	6.41
HPC/CNI/ECR	4.79
HPC/CST(LO/SI)	6.19
HPC/CST(LO/SI)/ECR	5.28
HPC/ECR	6.76
HPCF/CST(LO/SI)/ECR	5.85
HPCF/ECR	3.44

In Chapter 5 of the report Volume 2, durability-driven rankings of corrosion prevention and mitigation techniques were developed using the weighted sum model with 70% weight of durability and 30% weight of cost. It was concluded that a combination of HPCF/CST(LO/SI)/ECR is suitable for structures located in Region 6. In addition, the use of HPC is recommended in Region 5, and ECR in Regions 3 and Region 4. Concrete surface treatment (CST) is also recommended for low corrosive environment such as Region 1 and Region 2 (Figure A**.2** to Figure A**.6**).

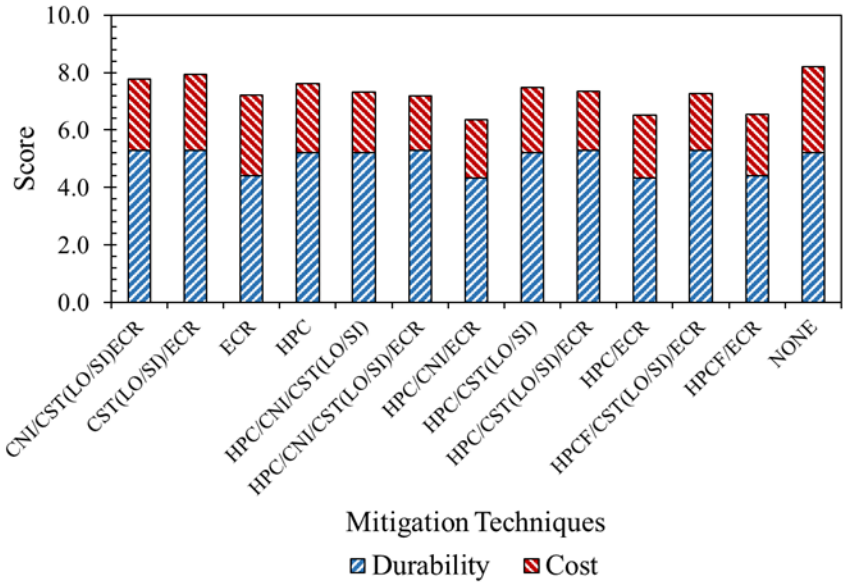

Figure A.2. Total Score of Mitigation Methods in Region 1 and Region 2

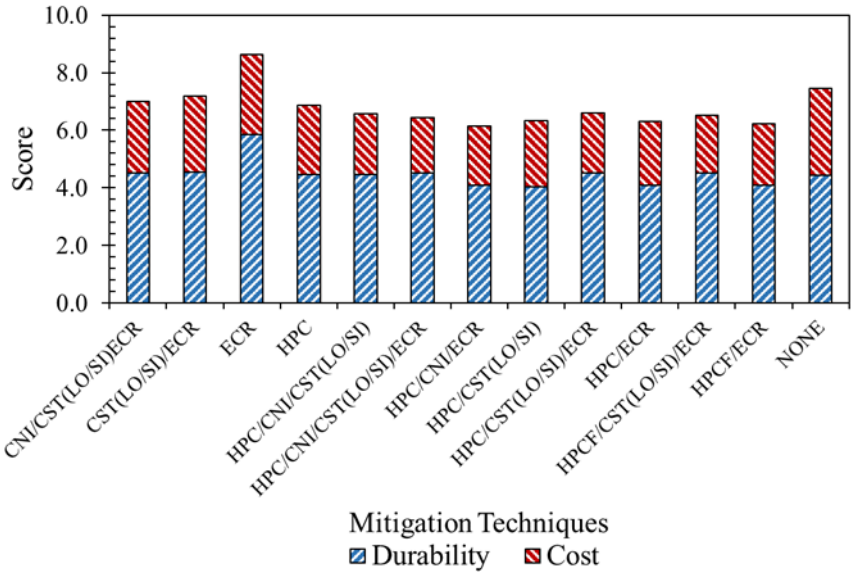

Figure A.3. Total Score of Mitigation Methods in Region 3

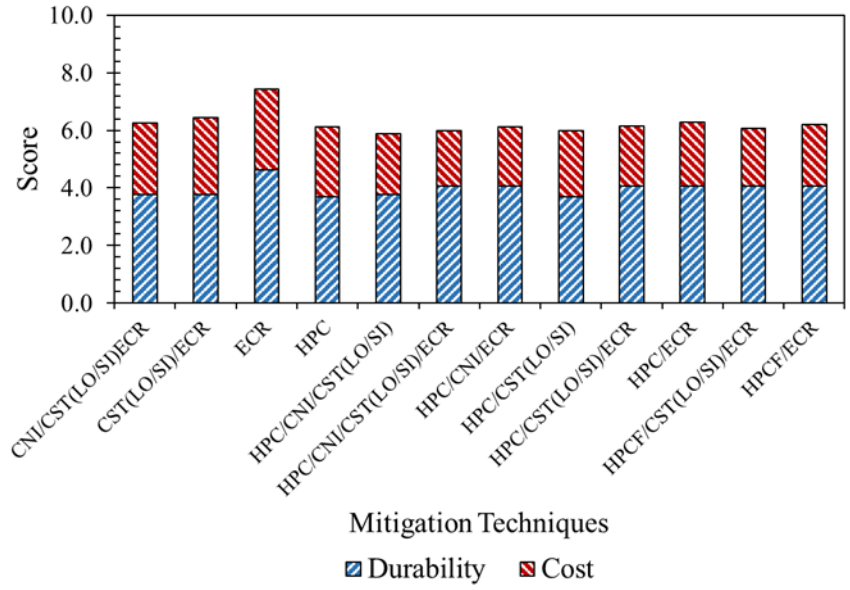

Figure A.4. Total Score of Mitigation Methods in Region 4

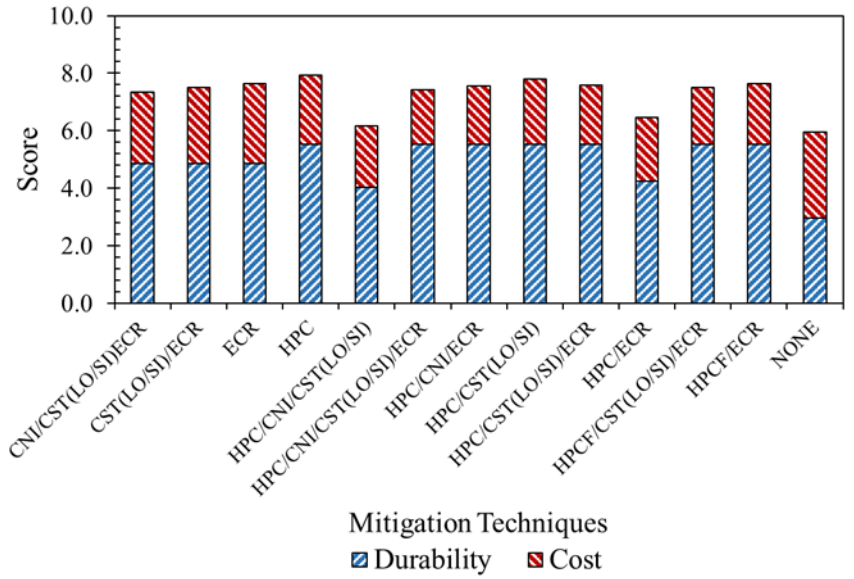

Figure A.5. Total Score of Mitigation Methods in Region 5

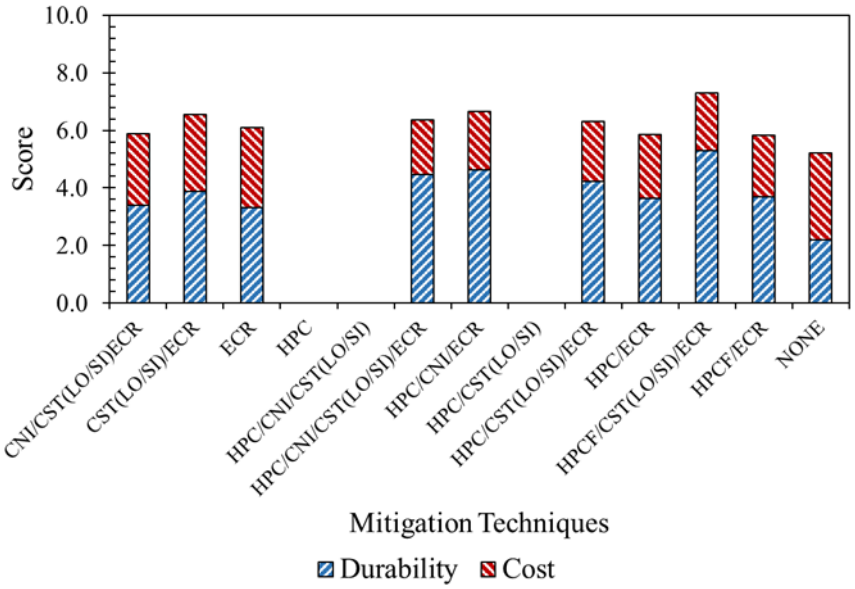

Figure A.6. Total Score of Mitigation Methods in Region 6

Table A-21 and Table A-22 show TxDOT recommendation for concrete super structures in Texas. For example, in Amarillo district, TxDOT recommends HPC and poly fibers on bridge deck in addition to ECR, continuously galvanized reinforcing (CGR), glass fiber reinforced polymer reinforcing (GFRP), and hot dipped galvanized reinforcing (HDG) as recommended corrosion resistant reinforcement.

Table A-21. Concrete Durability Recommendations for Structures (Farris, 2018)

Districts	Bridge Rail	Bridge Deck		P/S Beams	Bridge Substructure		
	HPC	HPC	Poly Fibers	Corrosion Inhibiting Admixture	HPC	Corrosion Inhibiting Admixture	Surface Protective Coatings Sub-structure
ABL	Y	Y	Y	Y	Y	Y	Y
AMA	Y	Y	Y	Y	Y	Y	Y
ATL	Y	Y	N	Y	Y	Y	Y
AUS	N	N	N	N	N	N	N
BMT	N	N	N	N	N	N	N
BRY	N	N	N	N	N	N	N
BWD	Y	Y	Y	Y	Y	Y	Y
CHS	Y	Y	Y	Y	Y	Y	Y
CRP	N	N	N	N	N	N	N
DAL	Y	Y	N	Y	Y	Y	Y
ELP	Y	Y	Y	Y	Y	Y	Y
FTW	Y	Y	N	Y	Y	Y	Y
HOU	N	N	N	N	N	N	N
LBB	Y	Y	Y	Y	Y	Y	Y
LFK	N	N	N	N	N	N	N
LRD	N	N	N	N	N	N	N
ODA	Y	Y	Y	Y	N	Y	Y
PAR	Y	Y	N	Y	Y	Y	Y
PHR	N	N	N	N	N	N	N
SAT	N	N	N	N	N	N	N
SJT	N	N	Y	N	N	Y	Y
TYL	N	N	N	N	Y	Y	Y
WAC	N	N	N	N	Y	N	Y
WFS	Y	Y	Y	Y	Y	Y	Y
YKM	N	N	N	N	N	N	N

Note:
Y indicates Districtwide application of the specific recommendation
P/S: Prestressed Concrete

Table A-22. Recommended Options for Corrosion Resistant Reinforcement for Structures (Farris, 2018)

Districts	Bridge Rail	Bridge Deck	Substructure Reinforcing	
	CGR, ECR, HDG	ECR, CGR, GFRP, HDG	ECR	HDG, LCCR
ABL	Y	Y	Y	Y
AMA	Y	Y	Y	Y
ATL	Y	Y	N	N
AUS	N	N	N	N
BMT	N	N	N	N
BRY	N	N	N	N
BWD	Y	Y	Y	Y
CHS	Y	Y	Y	Y
CRP	N	N	N	N
DAL	Y	Y	Y	Y
ELP	Y	Y	Y	Y
FTW	Y	Y	Y	Y
HOU	N	N	N	N
LBB	Y	Y	Y	Y
LFK	N	N	N	N
LRD	N	N	N	N
ODA	Y	Y	Y	Y
PAR	Y	Y	N	N
PHR	N	N	N	N
SAT	N	N	N	N
SJT	Y	Y	Y	Y
TYL	N	N	N	N
WAC	Y	Y	Y	Y
WFS	Y	Y	Y	Y
YKM	N	N	N	N

Abbreviations:
CGR: Continuously galvanized reinforcing
ECR: Epoxy-coated reinforcing
GFRP: Glass fiber reinforced polymer reinforcing
HDG: Hot dipped galvanized reinforcing
LCCR: Low Carbon-Chromium Reinforcing Steel

The cost of corrosion prevention of mitigation methods recommended by TxDOT and those from the findings of this study were compared to calculate the cost saving for each county. Since the decision tool suggests mitigation methods based on counties and TxDOT recommendations are based on districts, all counties within each district were first identified, and then the recommended mitigation methods for each county were compared. Table A-23 shows the difference of the two recommendations.

Table A-23. Corrosion Mitigation Recommendation based on District and Region

County	TxDOT Recommendation			Decision Tool Recommendation		
	District	Mitigation Methods	Cost ($/ft^2)	Region	Mitigation Methods	Cost ($/ft^2)
Borden	Abilene	HPC/CNI/ECR	7.0	4	ECR	1.4
Haskell	Abilene	HPC/CNI/ECR	7.0	4	ECR	1.4
Bowie	Atlanta	HPC/CNI/ECR	7.0	4	ECR	1.4
Moore	Atlanta	HPC/CNI/ECR	7.0	4	ECR	1.4
Live Oak	Austin	None	0.0	4	ECR	1.4
Leon	Beaumont	None	0.0	4	ECR	1.4
Lubbock	Lubbock	HPC/CNI/ECR	7.0	5	HPC	3.1
Terrell	Lubbock	HPC/CNI/ECR	7.0	5	HPC	3.1
Parker	Lubbock	HPCF/CNI/ECR	7.0	6	HPCF/CST(LO/SI)/ ECR	6.8
Sutton	Lubbock	HPCF/CNI/ECR	7.0	6	HPCF/CST(LO/SI)/ ECR	6.8
Crane	Odessa	HPC/CNI/ECR	7.0	5	HPC	3.1
Ector	Odessa	HPC/CNI/ECR	7.0	5	HPC	3.1
Kendall	Pharr	HPC/CNI/ECR	6.4	6	HPCF/CST(LO/SI)/ ECR	6.8
Willacy	Pharr	HPC/CNI/ECR	6.4	6	HPCF/CST(LO/SI)/ ECR	6.8

Table A-24 shows the average cost saving in each region. Because Region 6 is a highly corrosive environment, there wasn't any cost saving. In fact, recommendations from study seems to be more costly because bridges with multiple corrosion prevention and mitigation methods performed higher durability in this region. On the other hand, the findings of this research for the application of corrosion mitigation methods in all other regions create cost saving, particularly in Region 4 where the cost saving was $\$3.93/ft^2$.

Table A-24. Calculated Cost Saving for each Region and All Regions

Region	Cost Saving ($/ft^2)
Region 1	1.70
Region 2	0.32
Region 3	1.17
Region 4	3.93
Region 5	2.20
Region 6	-1.04

Two bridge decks were considered for the cost analysis of reinforced concrete to estimate the amount of cost saving per bridge. The dimensions of the concrete decks are given in Table A-25. As the dimension of the bridge deck increases, it generally results in greater cost savings from mitigation methods. According to the Texas Bridge Inventory (TxDOT, 2023), the average deck area for all bridges in Texas is approximately 8,750 ft^2, with a structure length of 214 ft. and a width of 41 ft. Structure 1 in Table A-25 closely matches the average deck size of Texas bridges. Structure 1 was used to calculate the cost savings per bridge by multiplying the saving cost ($/ft^2) by deck area of Structure 1. Table A-26 shows the calculated cost saving per bridge for each corrosive region. As the cost saving per bridge is calculated, it was multiplied by the number of bridges in each region to determine the total saving per region in Texas.

Table A-25. Concrete Deck Dimensions

Structure ID	Structure Length (ft.)	Deck Width (ft.)	Deck Area (ft.^{2})
1	300	30	9,000
2	60	26	1,560

Table A-26. Cost Saving Based on Structure Sizes

Region	Cost Saving from Structure 1 ($)
Region 1	15,300
Region 2	2,880
Region 3	10,530
Region 4	35,370
Region 5	19,800
Region 6	-9,360

As mentioned before, approximately 6,000 bridges are probably built every 10 years. Since all bridges have concrete decks and mitigation methods are applied on decks, cost saving from all bridges can be calculated by multiplying the cost saving of each region to the number of bridges in each region. The number of bridges located in different regions were also calculated using the

proportionality of bridges located in different regions (Table A-1). Among 57520 bridges in Texas, 62% are concrete and steel bridges with concrete deck that were factored in the calculation of cost saving. The total saving amounts to $55, 757,619 in 10 years which is $5,575,762 every year.

Table A-27. Number of Bridges and Cost Saving in 10 Years

Region	Number of Bridges	Cost Saving in 10 Years ($)
Region 1	198	3,024,357
Region 2	810	2,332,139
Region 3	1,212	12,760,119
Region 4	961	34,002,426
Region 5	299	5,919,346
Region 6	244	-2,280,768
All Regions	3,723	55,757,619

A.2.2.2 Economic Value of Research

The evaluation of the total savings can be generated by subtracting the project budget and the one-time engineering cost from the sum of the expected values per year. The expected total yearly saving was calculated as sum of savings as a result of findings of this research on steel ($8,501,088) and concrete bridges ($5,575,762) that is estimated to be $14,076,850 every year. The payback period of this research project was calculated 0.06 years.

The net present value (NPV) determines the current value of future cash flow by accounting for the time value of money. It provides a dynamic approach for evaluating project costs and benefits over time. The NPV formula used by TxDOT (2015) is:

$$NPV = \sum_{t=1}^{T} \frac{C_t}{(1+r)^t} - C_0 \quad (1)$$

where C_t represents net cash inflow during the period, C_0 is the initial investment, r is the discount rate, and *t* stands for the number of time periods. The discount rate is typically 5% (TxDOT, 2015), and the cost analysis is estimated for a 10-year period. Figure A**.7** shows the progression of NPV over the next 10 years, illustrating a positive value at the beginning of the first year and ultimately reaching $107,840,620 after a decade. Finally, the benefit-cost ratio (BCR) can be determined by:

$$BCR = \frac{NPV}{Project\ Budget} \quad (2)$$

The benefit-cost ratio was calculated 126, which indicates that Texas Department of Transportation can expect a benefit of $126 with each dollar invested in this research project.

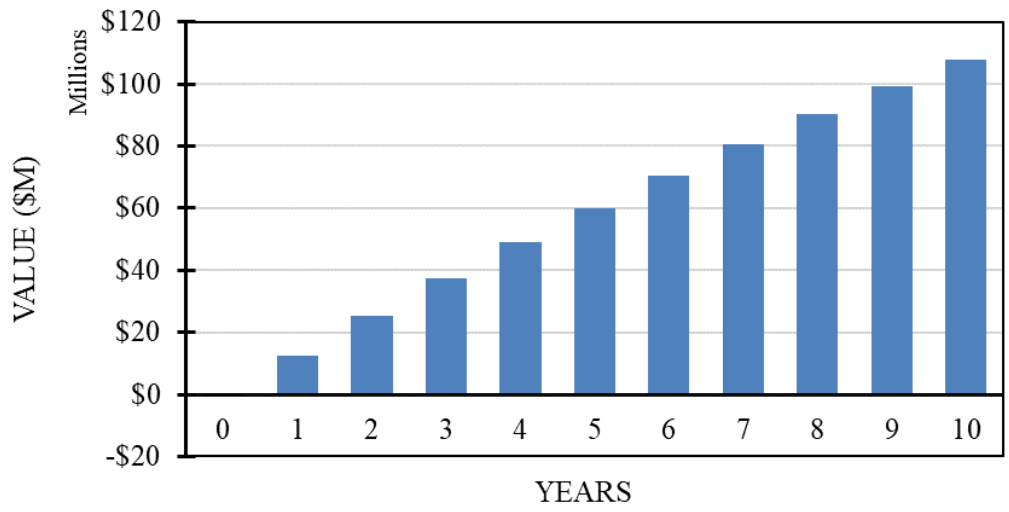

Figure A.7. Progression of NPV over 10 Years

Figure A**.8** shows a snipped image of value of research calculation. The image also shows the cost saving in terms of net present value for next 10 years in the form of bar chart along with data presented in tabular form as well.

	Project #	0-7040		
	Project Name:	Evaluation of Corrosion Prevention and Mitigation Approaches Used on Texas Bridges		
	Agency:	TTI	Project Budget	$ 857,084
	Project Duration (Yrs)	4	Exp. Value (per Yr)	$ 14,076,850
	Expected Value Duration (Yrs)	10	Discount Rate	5%
Total Savings:	$ 139,911,416		Net Present Value (NPV):	$ 107,840,620
Payback Period (Yrs):	0.06		Cost Benefit Ratio (NPV / Project Budget):	$ 126

Year	Expected Value per year	Savings	Net Present Value in $M
0	$ -857,084.00	$ -857,084	$ -857,084
1	$ 14,076,850.00	$ 13,219,766	$ 12,549,440
2	$ 14,076,850.00	$ 27,296,616	$ 25,317,558
3	$ 14,076,850.00	$ 41,373,466	$ 37,477,670
4	$ 14,076,850.00	$ 55,450,316	$ 49,058,729
5	$ 14,076,850.00	$ 69,527,166	$ 60,088,310
6	$ 14,076,850.00	$ 83,604,016	$ 70,532,672
7	$ 14,076,850.00	$ 97,680,866	$ 80,596,826
8	$ 14,076,850.00	$ 111,757,716	$ 90,124,593
9	$ 14,076,850.00	$ 125,834,566	$ 99,198,656
10	$ 14,076,850.00	$ 139,911,416	$ 107,840,620

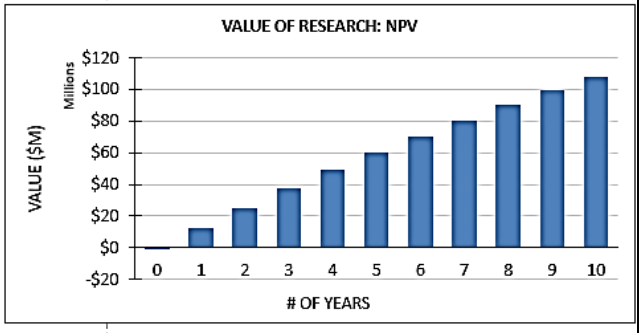

Data for the chart

Year	Expected Value per year	Expected Value	Expected Value/1,000,000	NPV/1,000,000
0	-$857,084.00	-$857,084.00	-$0.86	-$0.86
1	$14,076,850.00	$13,219,766.00	$13.22	$12.55
2	$14,076,850.00	$27,296,616.00	$27.30	$25.32
3	$14,076,850.00	$41,373,466.00	$41.37	$37.48
4	$14,076,850.00	$55,450,316.00	$55.45	$49.06
5	$14,076,850.00	$69,527,166.00	$69.53	$60.09
6	$14,076,850.00	$83,604,016.00	$83.60	$70.53
7	$14,076,850.00	$97,680,866.00	$97.68	$80.60
8	$14,076,850.00	$111,757,716.00	$111.76	$90.12
9	$14,076,850.00	$125,834,566.00	$125.83	$99.20
10	$14,076,850.00	$139,911,416.00	$139.91	$107.84

Figure A.8. Snapshot of Value of Research Spreadsheet

A.3 SUMMARY

A comprehensive evaluation including field inspection, laboratory examinations, and theoretical modeling were carried out in this study to improve understanding of corrosion mechanisms impacting weathering and painted steel girders as well as reinforced concrete decks under Texas environmental conditions. This research provides valuable insight into the protection strategies used in bridge structures by analyzing the performance of corrosion prevention and mitigation methods implemented in over than one hundred steel girders and concrete decks across the state. The findings of this study can be used for decision making, prioritizing maintenance efforts and efficiently allocating resources to develop suitable corrosion prevention strategies for bridge structures in different corrosive environments in Texas. In addition, cost analysis provided in this research study provides a comprehensive understanding of the cost-effectiveness of different corrosion prevention methods in particular corrosive regions that can helps the Texas Department of Transportation and affiliated departments to decide suitable protection systems and maintenance strategies to protect steel and concrete bridges from corrosion attack. Furthermore, the broader implications of this study provide guidance not only to professionals in Texas but also to those working on similar projects facing environmental corrosion challenges.

This research project is estimated to save Texas Department of Transportation and the state of Texas around $108 million within 10 years of completion. The positive net present value indicates that this research study was profitable for Texas Department of Transportation, with a 126:1 cost-benefit ratio, meaning there is $126 in benefit for each dollar invested. Payback period was estimated to be 0.06-year, and total estimated 10-year saving was calculated to be $139,911,416.

APPENDIX B

B.1 AMA-RC-01, SH 136 OVER ANTELOPE CREEK

- Bridge ID: 41180037901027 (Hutchinson County)
- Built in 1995
- Mitigation methods: Linseed oil, ECR
- Observed CIP depth: 3.5 in.
- Observed clear cover: 1.1 in.
- 3 spans, 3-concrete PS girder @ 8’ spacing with 3’ overhangs
- Inspected on June 16, 2021

Figure B.9. Concrete Deck of the Bridge (source: google maps)

B.1.1 Observed Condition

Top surface of the deck has hairline diagonal, transverse, and longitudinal cracks.

B.1.2 NDE Results

Grid 1 was located on the WB lane, and grid 2 was located on the WB shoulder of the span 2 as shown in Figure B.10.

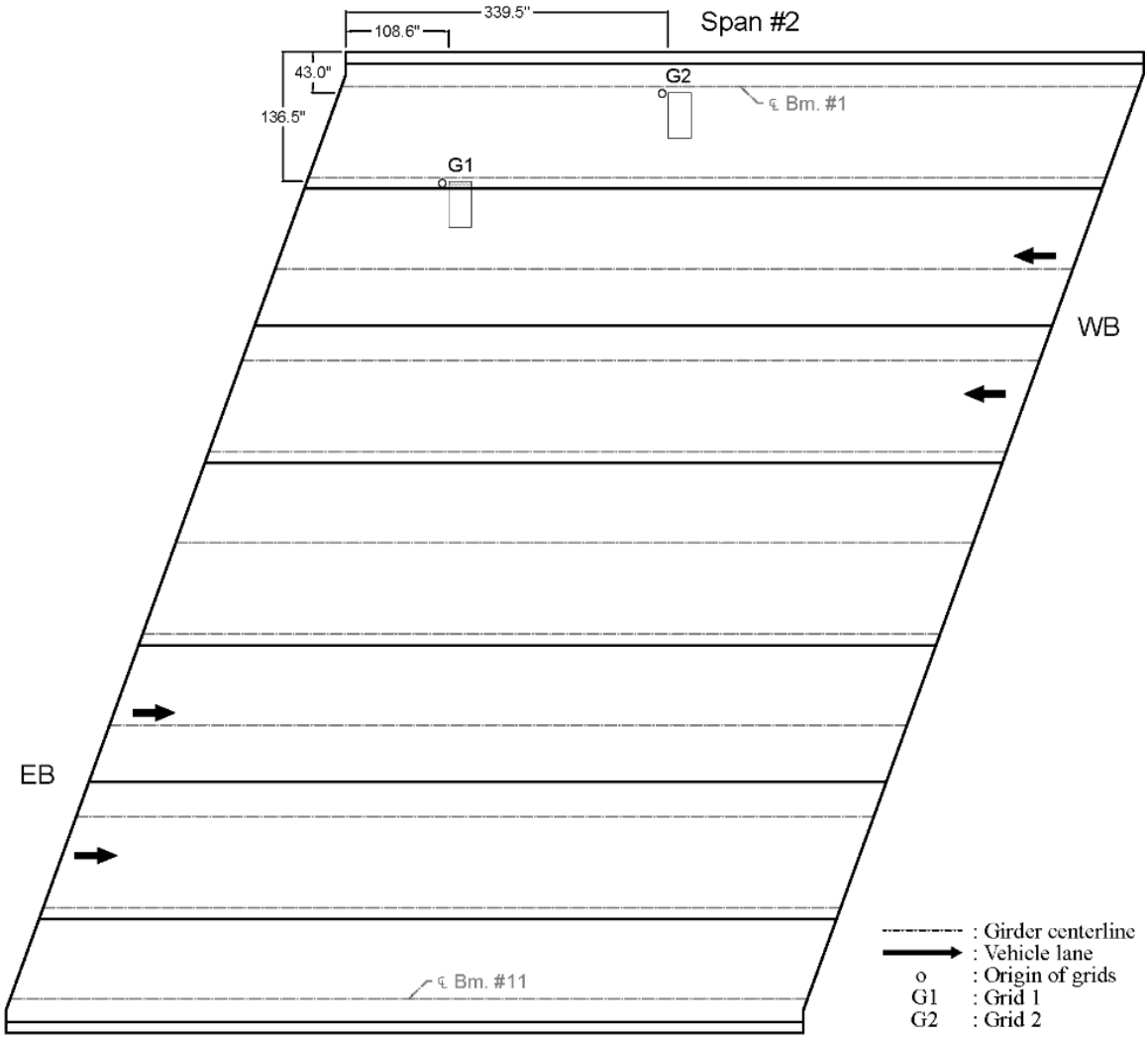

Figure B.10. Plan View of the Bridge and Location of Grids

As shown in Figure B.11 (a), grid 1 had various range of cracks from a hairline crack to 0.025 in. crack. As shown in Figure A.1.5 (a), grid 2 had hairline cracks mostly, with one 0.008 in. transverse crack possibly caused by joint of two PCPs.

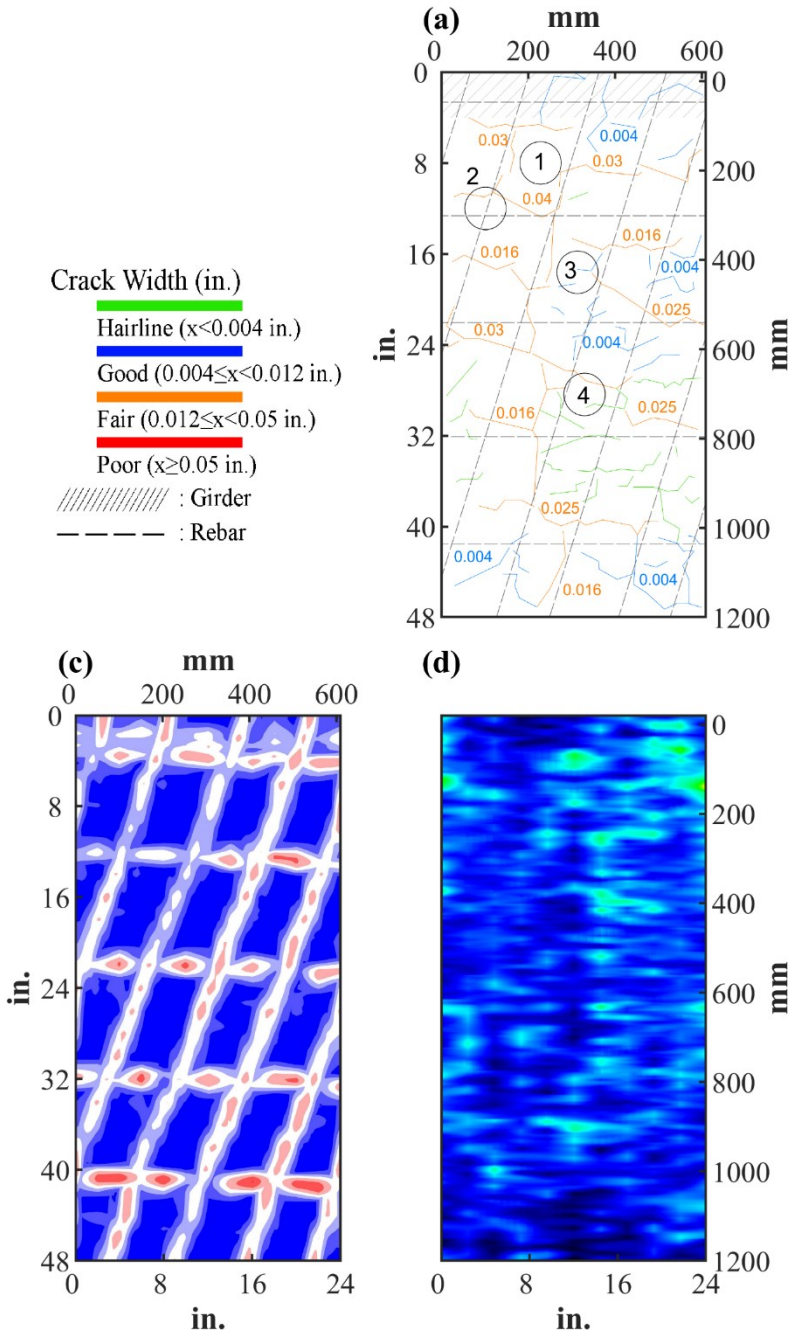

Figure B.11. Crack Map and NDE Results of Grid 1: (a) Crack Map and Location of Cores; (c) GPR C-scan at 1.2 in. to 2.25 in. Depth; (d) UST C-scan at 2.56 in. Depth

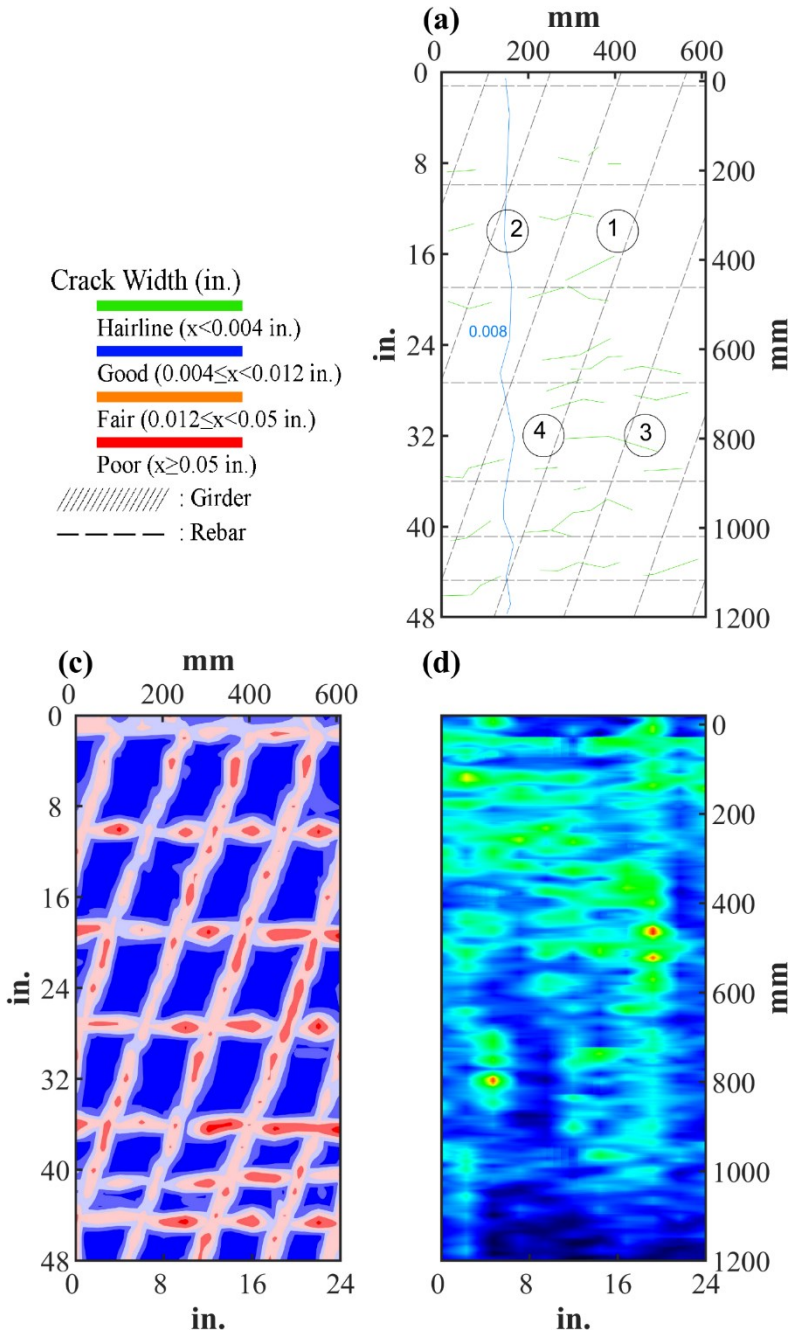

Figure B.12. Crack Map and NDE Results of Grid 2: (a) Crack Map and Location of Cores; (c) GPR C-scan at 0.95 in. to 2.05 in. Depth; (d) UST C-scan at 3.35 in. Depth

B.1.3 Concrete Cores

Table B-28. Detail Information of Concrete Cores

Core	dia. x height (in.)	Rebar depth (in.)	Rebar size (#)	Epoxy (Y/N)	Crack type	Crack width (in)	Notes
1-1	3.75 x 5.3	-	-	-	-	-	Panel joint
1-2	3.75 x 4.3	1.4; 2.0	5; 4	Y; Y	transverse; longitudinal	0.04	-
1-3	3.75 x 5.1	-	-	-	transverse; longitudinal	0.025	A crack propagates along intersection of aggregates
1-4	-	-	-	-	-	-	-
2-1	3.75 x 5.5	1.2	5	Y	-	-	-
2-2	3.75 x 5.5	1.1	5	Y	transverse; longitudinal	0.008	Panel joint
2-3	3.75 x 5.1	1.1	5	Y	-	-	-
2-4	3.75 x 4.1	1.1	5	Y	-	-	-

Table B-29. Core Pictures

Core	Side	Top	Bottom
1-1	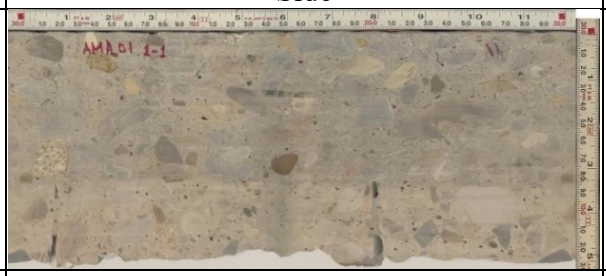	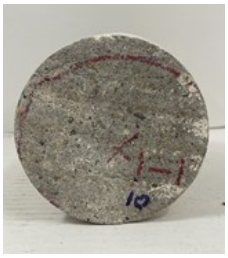	
1-2	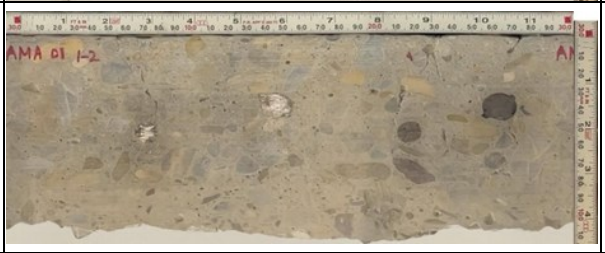		
1-3			

1-4	(Broken Core)	-	-
2-1			
2-2			
2-3			
2-4			

B.1.4 Laboratory Experiment Results

B.1.4.1 Resistivity

Core Number	Surface Resistivity (kΩ·m)	Bulk Resistivity (kΩ·m)
-	-	-

B.1.4.2 Ultrasonic Pulse Velocity

Core Number	Ultrasonic Pulse Velocity (m/s)
1-1	4060

B.1.4.3 Carbonation Depth

Core Number	Carbonation Depth (in.)
1-3	0.12
2-1	0.08

B.1.4.4 Acid-Soluble Chloride Content

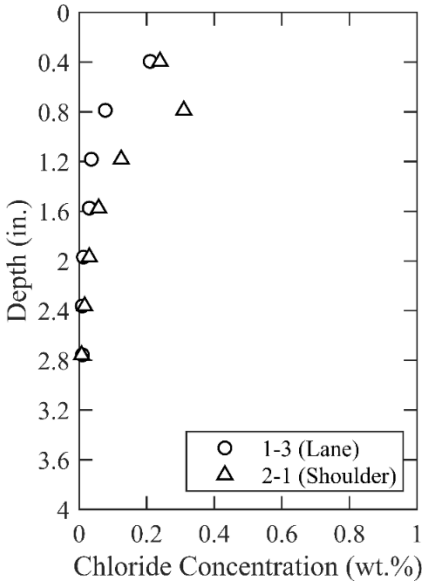

Figure B.13. Chloride Content at Different Depth

B.1.4.5 Knife Test

Core Number	Score	Picture
2-1	10	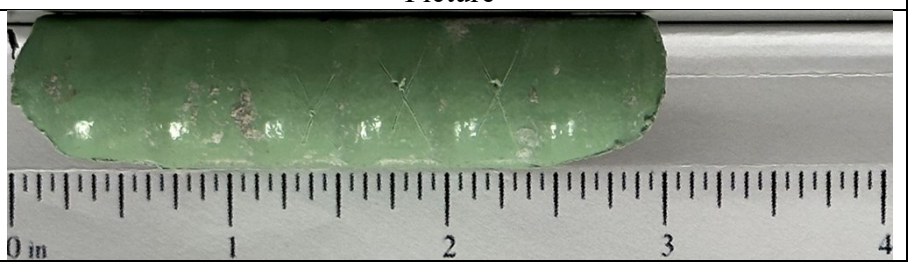

B.2 AMA-RC-02, IH 40 WB OVER IVY RD.

- Bridge ID: 41800009002048 (Oldham County)
- Built in 2006
- Mitigation methods: HPC, MLPO, ECR
- Observed CIP depth: 4.33 in.
- Observed clear cover: 2.6 – 2.8 in.
- 2 spans, 5-concrete PS girder @ 8.5’ spacing with 3’ overhangs
- Inspected on June 15, 2021

Figure B.14. Concrete Deck of the Bridge (source: google maps)

B.2.1 Observed Condition

Spalling occurred on the abutment backwall possible due to the settlement of the bridge approach, and the exposed and corroded rebar is found inside as shown in Figure B.15 (a) and (b). There is hairline diagonal cracking on the web of prestressed beam at the end of support as shown in Figure B**.15** (c).

(a) (b) (c)

Figure B.15. Deteriorations on the Bridge: (a) Severe Cracks and Corroded Rebar On the abutment; (b) Spalling at abutment and Exposed, Corroded Rebar; (c) Hairline Diagonal Cracking on the Web of Girder

B.2.2 NDE Results

Both Grid 1 and Grid 2 were located on the WB lane of the span 1 as shown in Figure B**.16**.

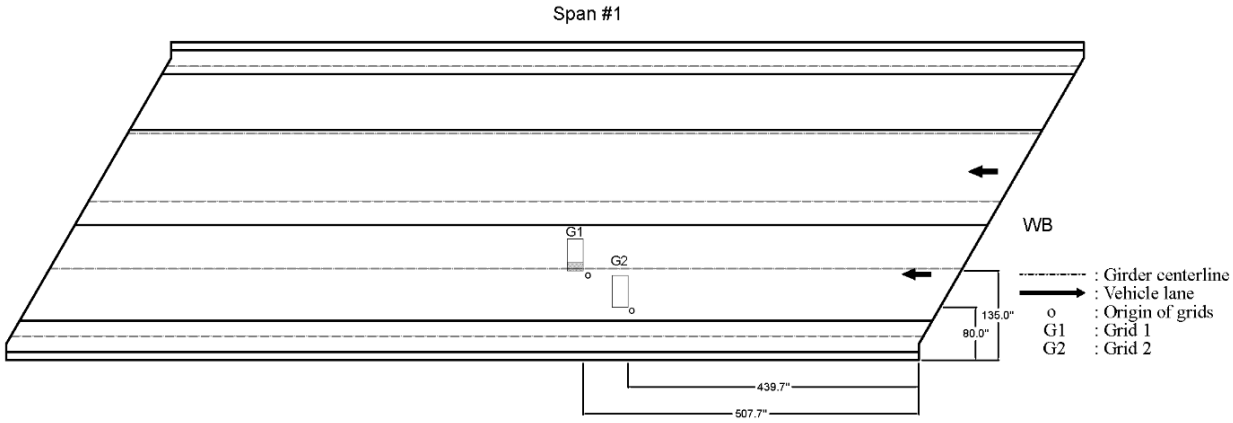

Figure B.16. Plan View of the Bridge and Location of Grids

As there was MLPO on the bridge, both grids did not have any cracks.

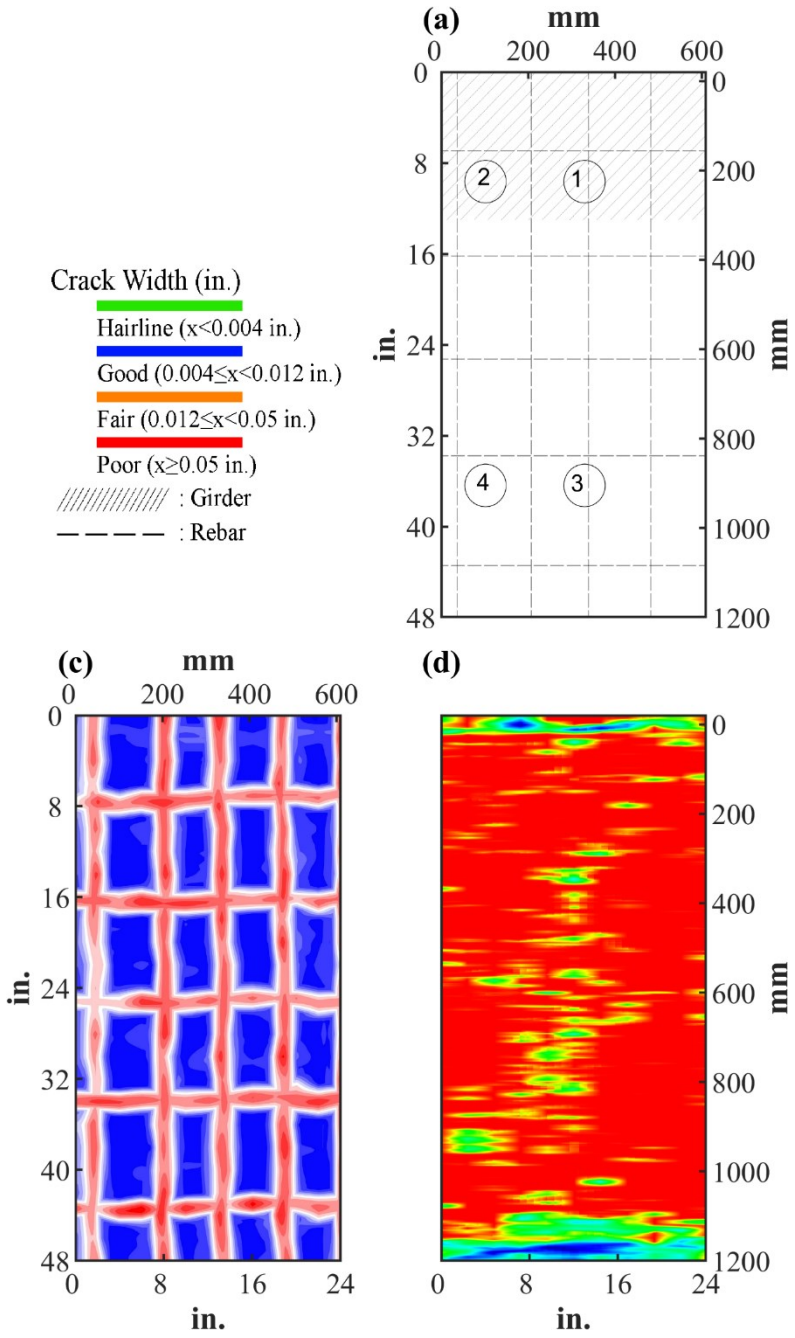

Figure B.17. Crack Map and NDE Results of Grid 1: (a) Crack Map and Location of Cores; (c) GPR C-scan at 1.85 in. to 2.85 in. Depth; (d) UST C-scan at 2.7 in. Depth

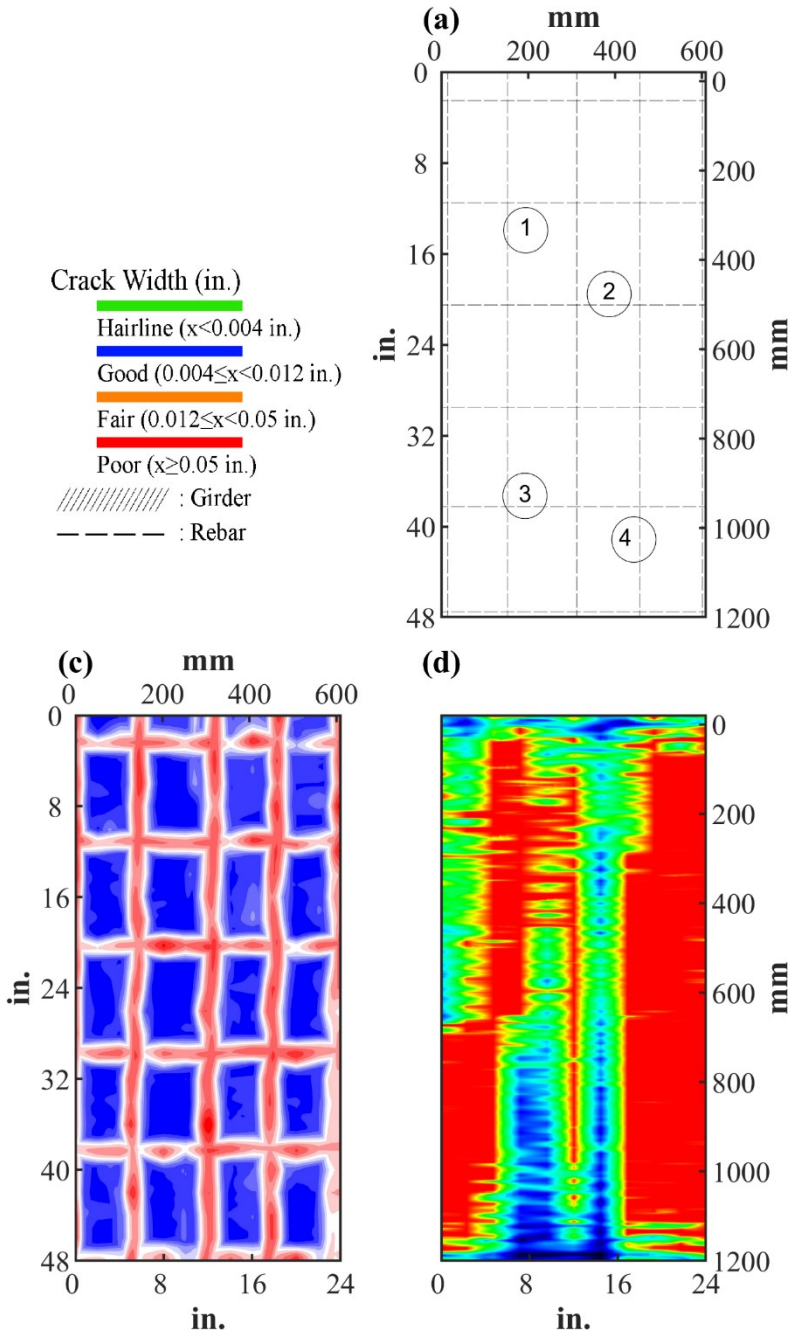

Figure B.18. Crack Map and NDE Results of Grid 2: (a) Crack Map and Location of Cores; (c) GPR C-scan at 2.25 in. to 3.25 in. Depth; (d) UST C-scan at 2.0 in. Depth

B.2.3 Concrete Cores

Table B-30. Detail Information of Concrete Cores

Core	dia. × height (in.)	Rebar depth (in.)	Rebar size (#)	Epoxy (Y/N)	Crack type	Crack width (in)	Notes
1-1	3.75 × 5.1	2.6	5	Y	-	-	-
1-2	3.75 × 5.1	-	-	-	-	-	-
1-3	3.75 × 5.5	2.6	5	Y	-	-	-
1-4	3.75 × 5.5	-	-		-	-	-
2-1	3.75 × 5.5	2.8	5	Y	-	-	-
2-2	3.75 × 5.5	4.1	-	Y	-	-	-
2-3	3.75 × 5.5	2.6; 3.3	5; 4	Y; Y	-	-	-
2-4	3.75 × 5.3	3.3	5	Y	-	-	-

Table B-31. Core Pictures

Core	Side	Top	Bottom
1-1			
1-2			

1-3			
1-4	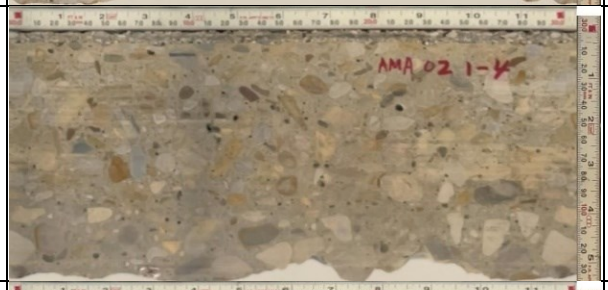		
2-1			
2-2			
2-3			
2-4			

B.2.4 Laboratory Experiment Results

B.2.4.1 Resistivity

Core Number	Surface Resistivity (kΩ·m)	Bulk Resistivity (kΩ·m)
1-2	145	-

B.2.4.2 Ultrasonic Pulse Velocity

Core Number	Ultrasonic Pulse Velocity (m/s)
1-2	4146
1-4	4162

B.2.4.3 Carbonation Depth

Core Number	Carbonation Depth (in.)
1-3	0.00
2-4	0.00

B.2.4.4 Acid-Soluble Chloride Content

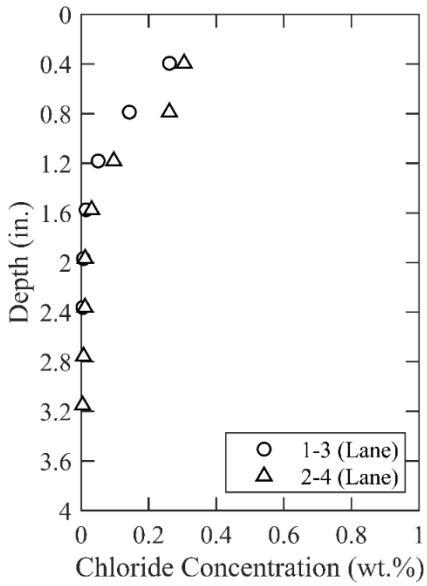

Figure B.19. Chloride Content at Different Depth

B.2.4.5 Sorptivity

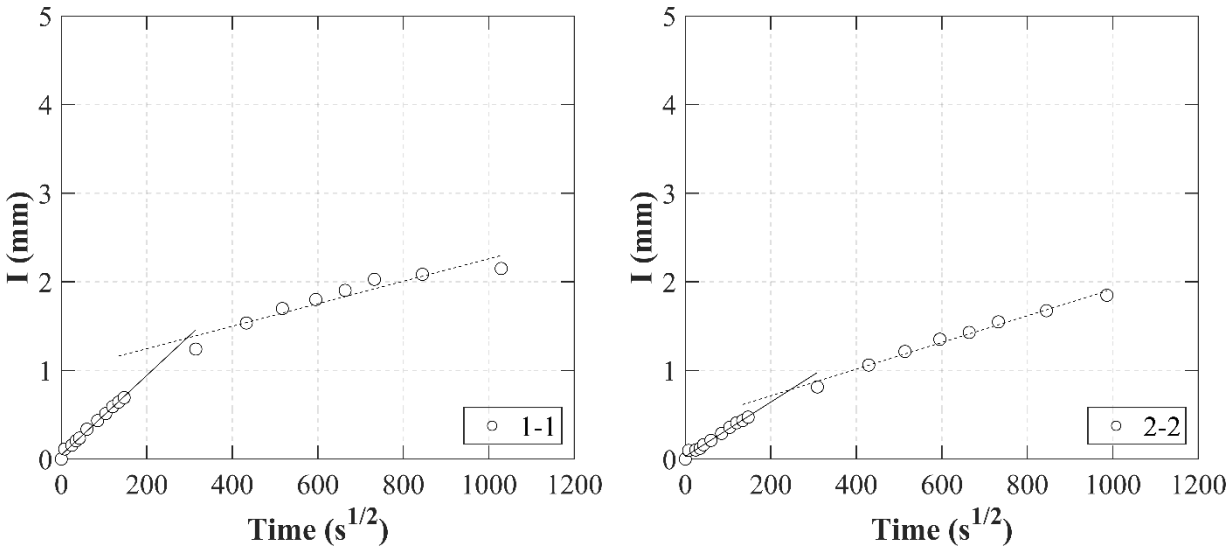

(a) Core 1–1 (b) Core 2–2

Figure B.20. Absorption and Sorptivity of: (a) Core 1–1; (b) Core 2–2

Table B-32. Initial and Secondary Sorptivity Results

Core Number	Sorptivity	Results (mm/s$^{1/2}$)
Core 1–1	Initial Sorptivity	0.00449
	Secondary Sorptivity	0.00127
Core 2–2	Initial Sorptivity	0.00306
	Secondary Sorptivity	0.00150

B.2.4.6 Knife Test

Core Number	Score	Picture
1-3	10	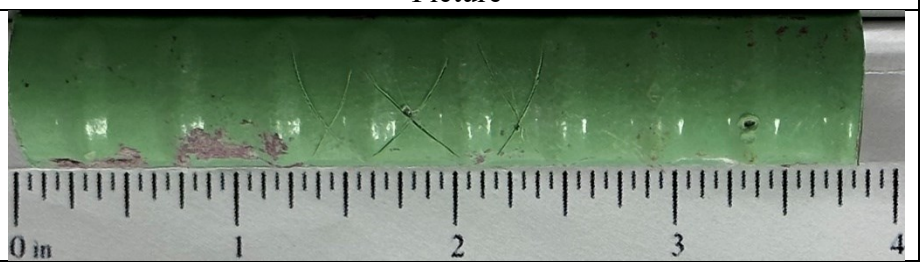

B.3 AMA-RC-03, US 385 OVER CANADIAN RIVER

- Bridge ID: 41800022602024 (Oldham County)
- Built in 2005
- Mitigation methods: HPC, CNI (2 gal./CY.), Linseed oil, ECR
- Observed CIP depth: 3.15 in.
- Observed clear cover: 1.4 in.
- 14 spans, 9-concrete PS girder @ 6.75’ spacing with 3’ overhangs
- Inspected on June 15, 2021

Figure B.21. Concrete Deck of the Bridge (source: google maps)

B.3.1 Observed Condition

There are widespread of minor transverse and longitudinal cracking on the concrete deck surface.

B.3.2 NDE Results

Grid 1 was located on the NB lane of the 14th span and grid 2 was located on the NB shoulder lane of the span 13 as shown in Figure B.22.

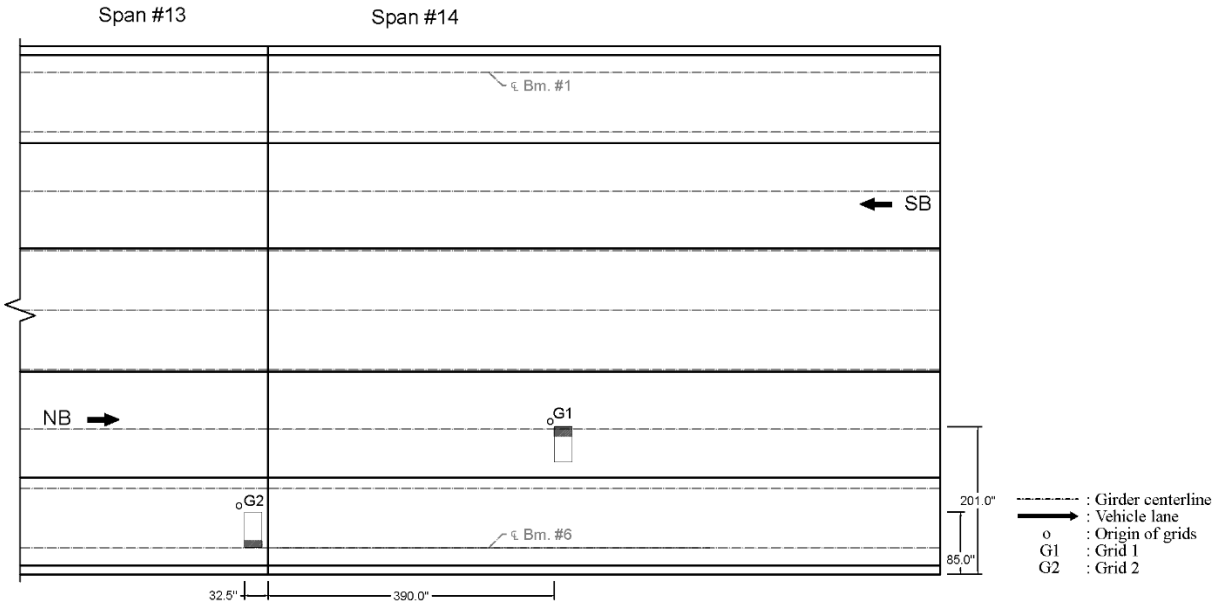

Figure B.22. Plan View of the Bridge and Location of Grids

Figure B.23 and Figure B.24 show detailed information of the grids. As shown in Figure A.3.3 (a), grid 1 had little to no hairline cracks with one 0.008 in. transverse crack possibly caused by a joint of precast concrete panels. As shown in Figure A.3.4 (a), grid 2 had few hairline cracks with one 0.008 in. longitudinal crack.

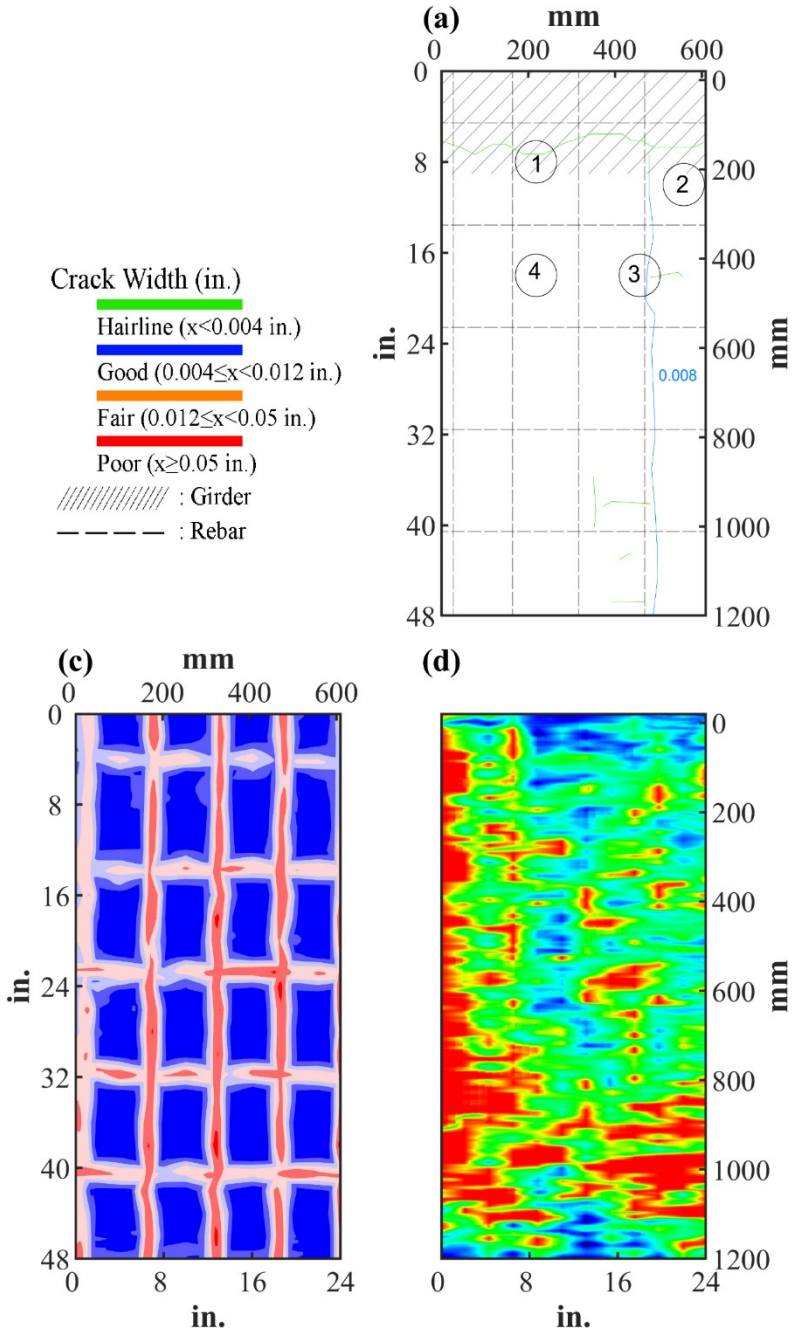

Figure B.23. Crack Map and NDE Results of Grid 1: (a) Crack Map and Location of Cores; (c) GPR C-scan at 1.45 in. to 2.45 in. Depth; (d) UST C-scan at 2.37 in. Depth

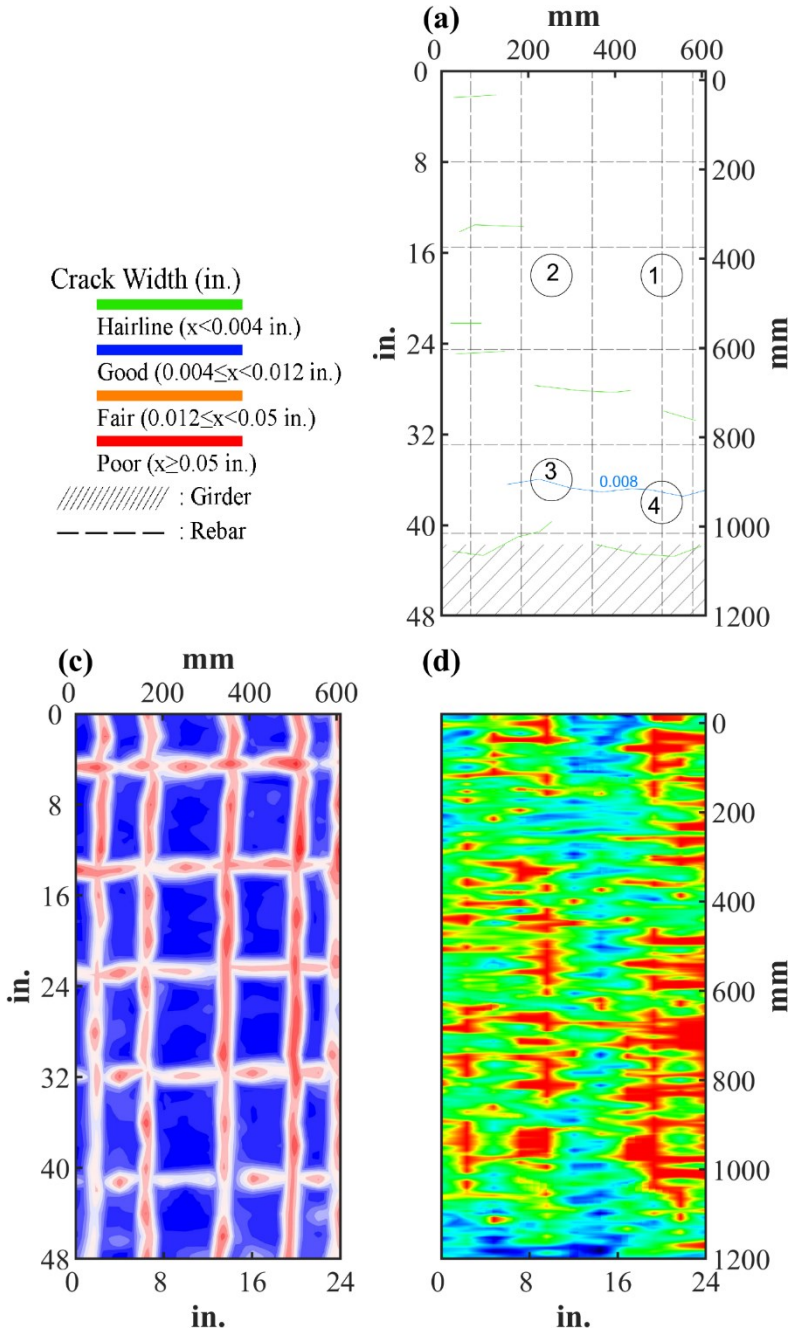

Figure B.24. Crack Map and NDE Results of Grid 2: (a) Crack Map and Location of Cores; (c) GPR C-scan at 2.25 in. to 3.25 in. Depth; (d) UST C-scan at 2.78 in. Depth

B.3.3 Concrete Cores

Table B-33. Detail Information of Concrete Cores

Core	dia. × height (in.)	Rebar depth (in.)	Rebar size (#)	Epoxy (Y/N)	Crack type	Crack width (in)	Notes
1-1	3.75 × 5.3	-	-	-	longitudinal	HL	Crack propagating from panel joint
1-2	3.75 × 1.3	-	-	-	-	-	-
1-3	3.75 × 3.1	1.4	5	Y	transverse	0.008	Crack propagating from panel joint
1-4	3.75 × 5.5	-	-	-	-	-	-
2-1	3.75 × 5.9	2.6	5	Y	longitudinal	HL	-
2-2	3.75 × 4.4	-	-	-	-	-	-
2-3	3.75 × 5.6	-	-	-	longitudinal	0.008	A crack propagates along intersection of aggregates
2-4	3.75 × 5.8	2.6	5	Y	longitudinal	0.008	-

Table B-34. Core Pictures

Core	Side	Top	Bottom
1-1			
1-2			

1-3			
1-4			
2-1			
2-2			
2-3			
2-4			

B.3.4 Laboratory Experiment Results

B.3.4.1 Resistivity

Core Number	Surface Resistivity (kΩ·m)	Bulk Resistivity (kkΩ·m)
2-3	202	26

B.3.4.2 Ultrasonic Pulse Velocity

Core Number	Ultrasonic Pulse Velocity (m/s)
2-2	4193
2-3	4261

B.3.4.3 Carbonation Depth

Core Number	Carbonation Depth (in.)
1-4	0.00
2-4	0.20

B.3.4.4 Acid-Soluble Chloride Content

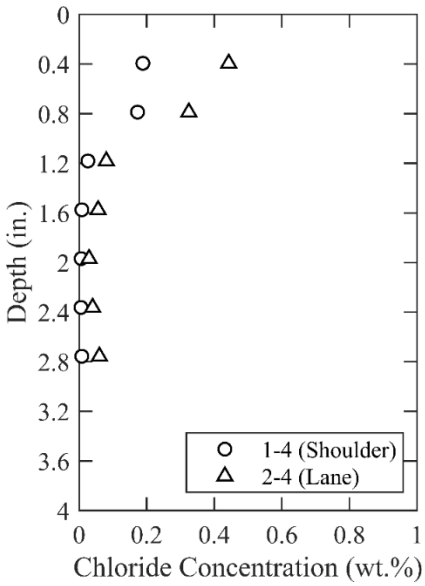

Figure B.25. Chloride Content at Different Depth

B.3.4.5 Sorptivity

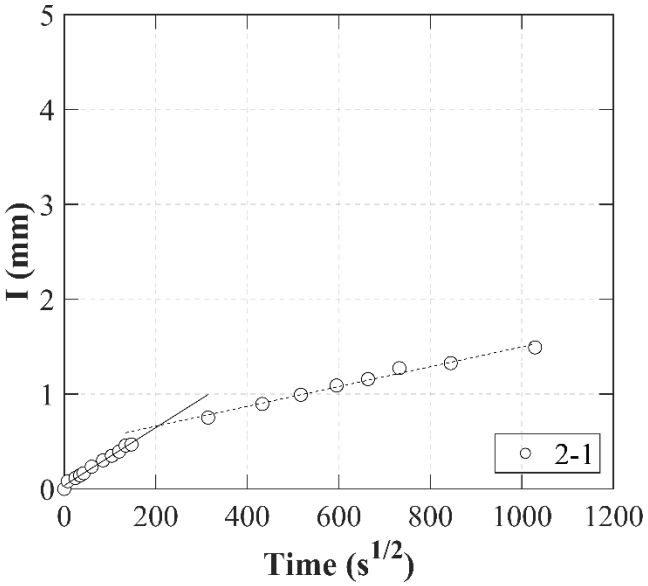

Figure B.26. Absorption and Sorptivity of Core 2–1

Table B-35. Initial and Secondary Sorptivity Results

Core Number	Sorptivity	Results (mm/s$^{1/2}$)
Core 2–1	Initial Sorptivity	0.00305
	Secondary Sorptivity	0.00105

B.3.4.6 Knife Test

Core Number	Score	Picture
2-4	10	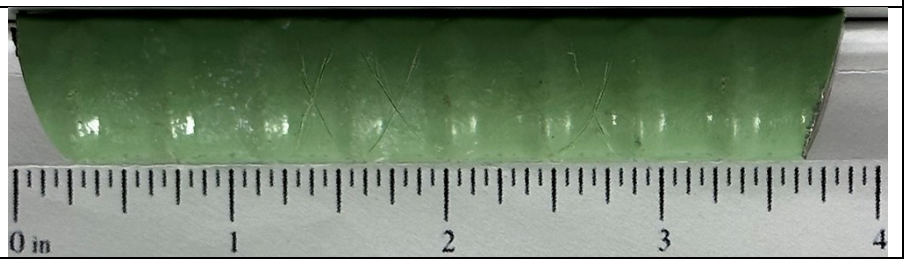

B.4 AMA-RC-04, US 60 SB (PIERCE ST.) OVER RNSF RAILYARD

- Bridge ID: 41880004107068 (Potter County)
- Built in 1996
- Mitigation methods: CNI (4 gal./CY.), Linseed oil, ECR
- Observed CIP depth: 4.33 in.
- Inspected Clear cover: 2.5 – 2.8 in.
- 11 spans, 7-concrete PS girder @ 5.143’ spacing with 3’ overhangs at spans 2 and 3; 6 concrete PS girder @ 6’ spacing with 3’ overhangs at spans 1, 4, 5, and 6
- Inspected on June 18, 2021

Figure B.27. Concrete Deck of the Bridge (source: google maps)

B.4.1 Observed Condition

Hairline map cracking is found on the top surface of the deck. There is minor delamination and spalling along the railing bottom as shown in Figure B.28 (a). There is spalling at the end of girders and shows sign of corrosion as shown in Figure B.28 (b). And severe rust on the permanent metal deck from under expansion joint is present as shown in Figure B.28 (c).

On Abutment 1, a small horizontal crack and exposed strand at the end of a girder was observed. Additionally, horizontal and vertical cracks (0.012 in.) were observed below the girders on the vertical wall. Otherwise, it was in better condition. The PCP panels were offset with PMDF at the link slab and abutment. The girders in the center of the bridge appeared to be in better condition than the ones on east and west. A west girder showed exposed steel on its end.

The overhang displayed cracking with efflorescence, occurring at intervals slightly less than the panel length and not corresponding to panel locations. Bent 2 consisted of two columns

with midspan flexural cracks spaced approximately 3 feet apart. It also exhibited diagonal cracks at the columns and longitudinal cracks along the top reinforcement, along with flexural cracks at the bottom near the center. Bent 11 exhibited positive and negative flexure cracks, although these were positioned a bit high and were not clearly visible in photographs. The south face had a discernible diagonal crack in the west overhang.

(a)

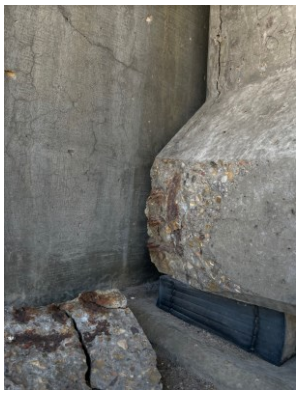

(b)

(c)

Figure B.28. Deterioration on the Bridge: (a) Spalling at Railing Bottom; (b) Spalling and Exposed Rebar and Strands on Bottom of a Beam; (c) Corrosion on the Metal Deck Form

B.4.2 NDE Results

Both Grid 1 and Grid 2 were located on the SB lane of the 5th span of the bridge. Figure B.29 shows the location of the grids on the deck.

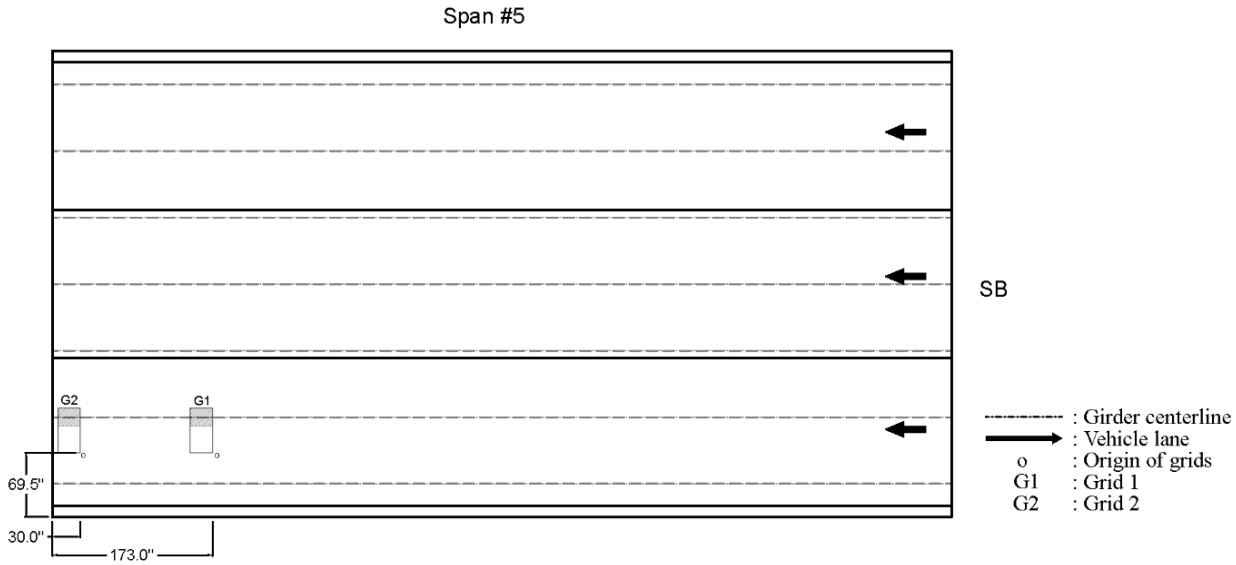

Figure B.29. Plan View of the Bridge and Location of Grids

As shown in Figure B.30 (a) cracks with different width exist. On grid 1, the widest crack with 0.3 in. width was located on top. Figure B.30 (e) shows possibility of corrosion near lower left of the grid. Based on Figure A.4.5 (b), the widest crack on grid 2 was also 0.3 in. wide, but in overall, cracks were wider in grid 2. Based on Figure B.31 (e) grid 2 has very low possibility of corrosion.

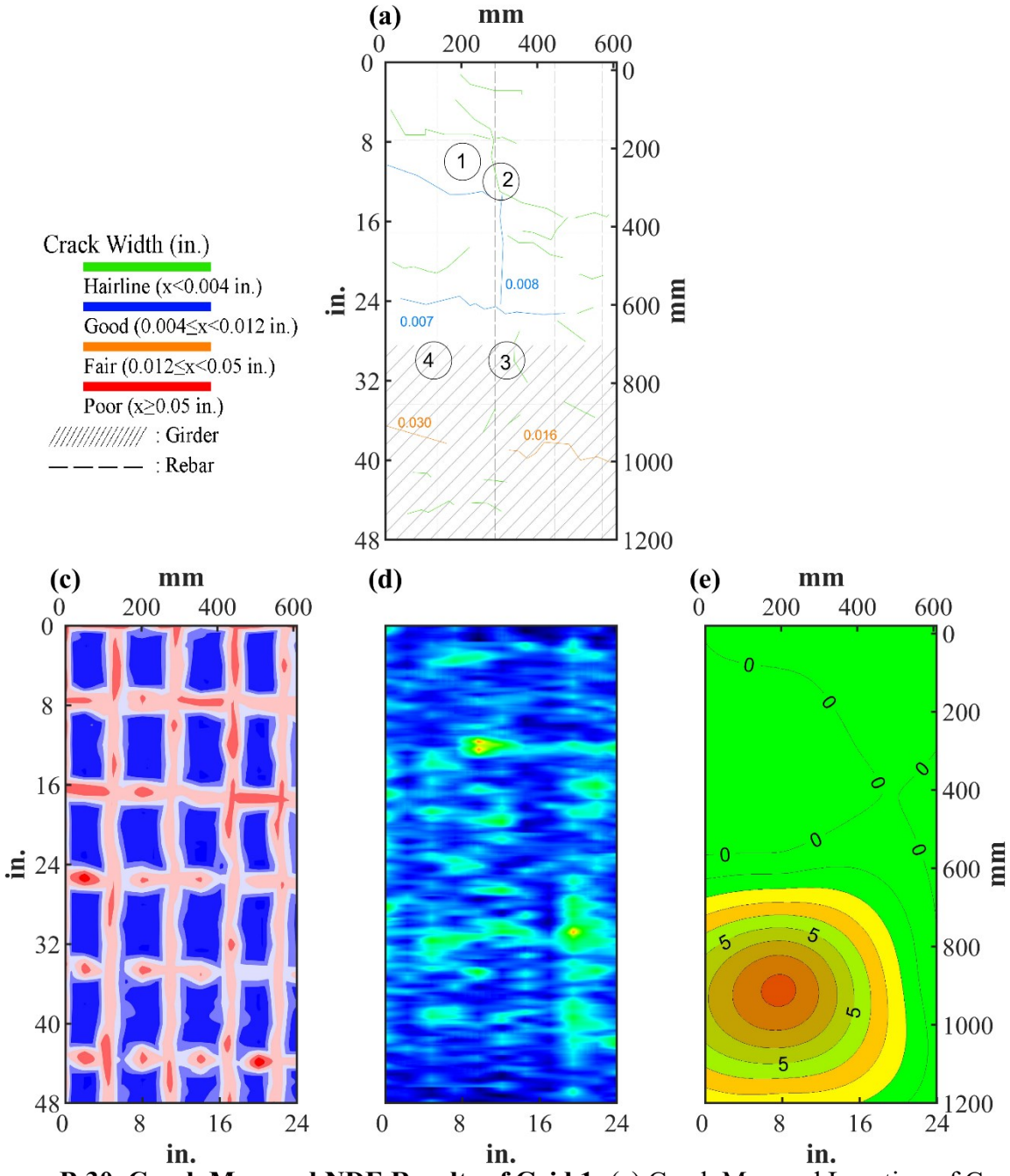

Figure B.30. Crack Map and NDE Results of Grid 1: (a) Crack Map and Location of Cores; (c) GPR C-scan at 1.9 in. to 3.1 in. Depth; (d) UST C-scan at 4.32 in. Depth; (e) Corrosion Rate Map

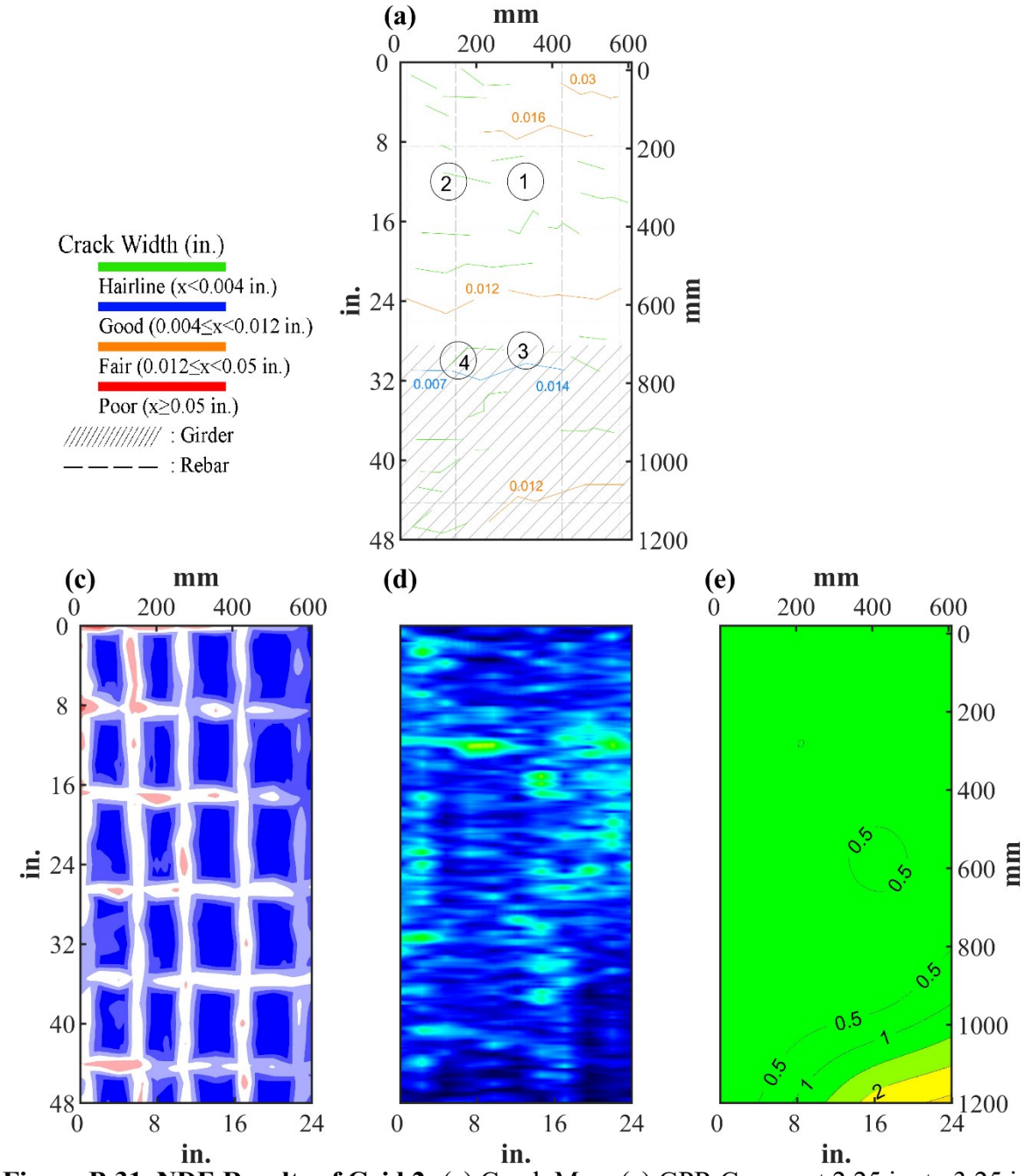

Figure B.31. NDE Results of Grid 2: (a) Crack Map; (c) GPR C-scan at 2.25 in. to 3.25 in. Depth; (d) UST C-scan at 2.01 in. Depth; (e) Corrosion Rate Map

B.4.3 Concrete Cores

Table B-36. Detail Information of Concrete Cores

Core	dia. × height (in.)	Rebar depth (in.)	Rebar size (#)	Epoxy (Y/N)	Crack type	Crack width (in)	Notes
1-1	3.75 × 4.3	-	-	-	-	-	Void at 1.5 in. depth; Delamination between CIP and PCP
1-2	3.75 × 4.3	2.5	5	Y	-	-	Delamination between CIP and PCP
1-3	3.75 × 6.2	2.5	5	Y	longitudinal	HL	-
1-4	3.75 × 5.7	-	-	-	-	-	Void near CIP and PCP intersection
2-1	3.75 × 6.0	-	-	-	-	-	-
2-2	3.75 × 4.1	2.8	5	Y	longitudinal	HL	Delamination between CIP and PCP
2-3	3.75 × 6.2	-	-	-	-	-	Void at 1 in. depth
2-4	3.75 × 4.0	2.8	5	Y	diagonal	HL	Delamination between CIP and PCP

Table B-37. Core Pictures

Core	Side	Top	Bottom
1-1			
1-2			

1-3			
1-4			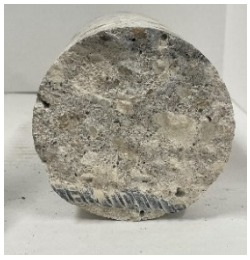
2-1			
2-2			
2-3			

2-4			

B.4.4 Laboratory Experiment Results

B.4.4.1 Resistivity

Core Number	Surface Resistivity (kΩ·m)	Bulk Resistivity (kΩ·m)
1-1	-	6

B.4.4.2 Ultrasonic Pulse Velocity

Core Number	Ultrasonic Pulse Velocity (m/s)
1-1	3449

B.4.4.3 Carbonation Depth

Core Number	Carbonation Depth (in.)
1-2	0.07
2-4	0.00

B.4.4.4 Acid-Soluble Chloride Content

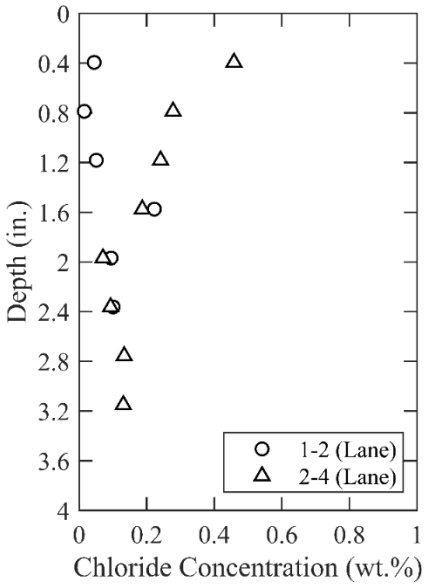

Figure B.32. Chloride Content at Different Depth

B.4.4.5 Sorptivity

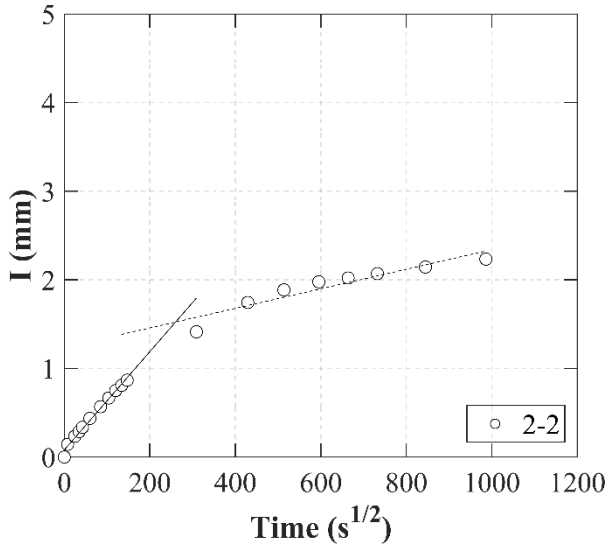

Figure 0.33. Absorption and Sorptivity of Core 2–2

Table B-38. Initial and Secondary Sorptivity Results

Core Number	Sorptivity	Results (mm/s$^{1/2}$)
Core 2–2	Initial Sorptivity	0.00554
	Secondary Sorptivity	0.00110
Core 2–4	Initial Sorptivity	0.00746
	Secondary Sorptivity	0.00087

B.4.4.6 Knife Test

Core Number	Score	Picture
1-2	10	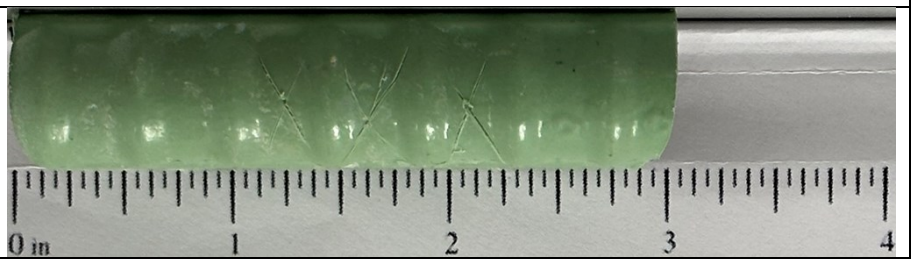

B.4.4.7 Electrochemical Impedance Spectroscopy

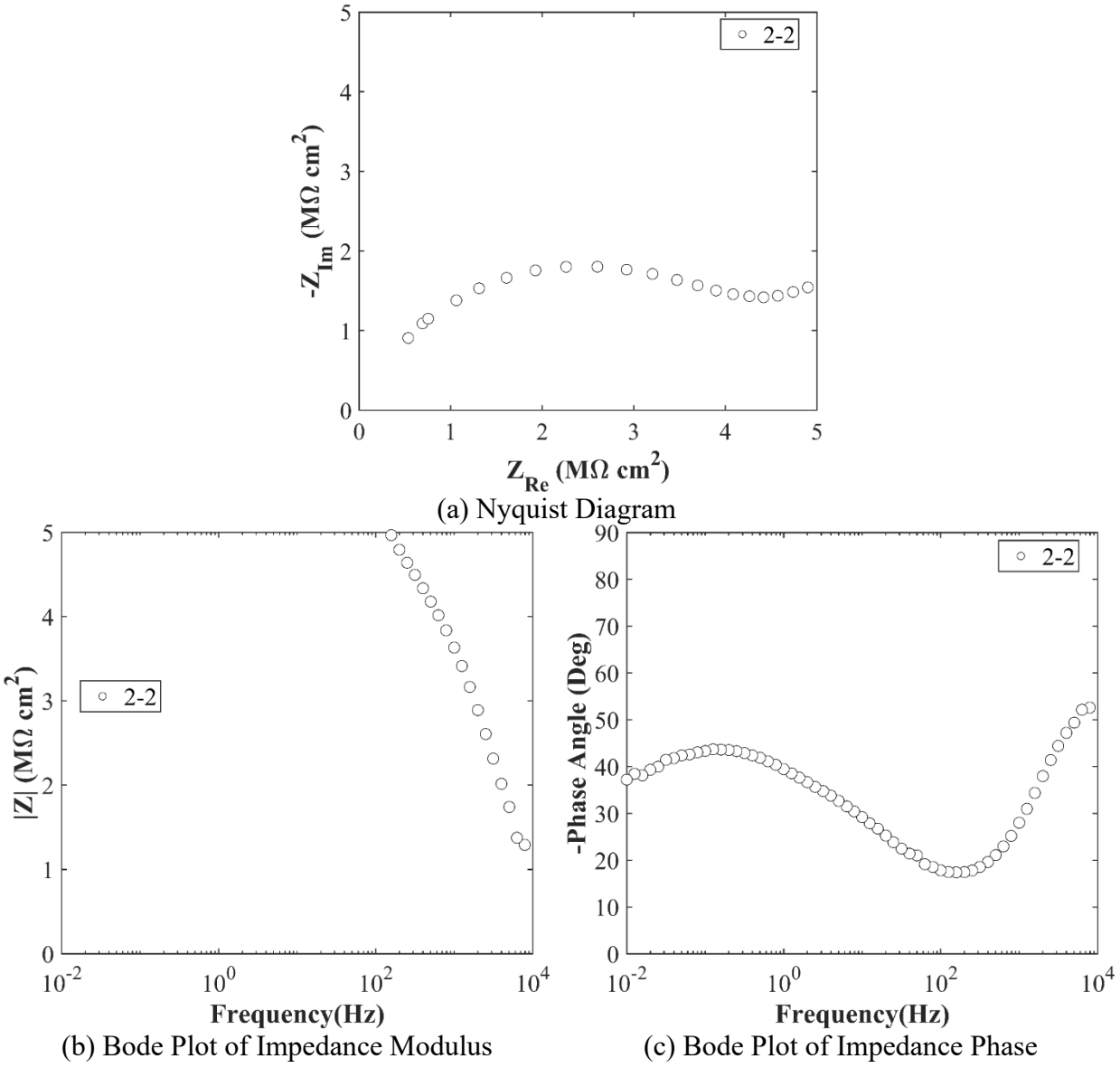

(a) Nyquist Diagram

(b) Bode Plot of Impedance Modulus

(c) Bode Plot of Impedance Phase

Figure 0.34. EIS Results: (a) Nyquist Diagram; (b) Bode Plot of Impedance Modulus; (c) Bode Plot of Impedance Phase

B.5 AMA-RC-05, US 60 OVER BNSF RR

- Bride ID: 41880016902028 (Potter County)
- Built in 1997
- Mitigation methods: CNI (2 gal./CY.), Silane, ECR
- Observed CIP depth: 5 in.
- Inspected Clear cover: 1.6 – 2.2 in.
- 3 spans, 8-concrete PS girder @ 6.857’ spacing with 3’ overhangs
- Inspected on June 18, 2021

Figure 0.35. Concrete Deck of the Bridge (source: google maps)

B.5.1 Observed Condition

Hairline map cracking is present on the deck. The web and bottom flange of south beam at span 1 has horizontal and vertical moderate cracks. The deck exhibited extensive cracking, including transverse cracks at panel ends and longitudinal cracks at girders, with diagonal cracks at PBJ. Girders were painted on the outside, and the bottom of the overhang exhibited some signs of cracking and efflorescence. The deck consisted of PCP offset at the PBJ, and while most panels were in good condition, the link slabs displayed cracks with efflorescence. Flexural cracks were observed at the bottom of the bent cap of Bent 3, spaced approximately 2 feet apart, with diagonal cracks at the outer columns. The condition of Abutment 1 mirrored that of the east abutment.

B.5.2 NDE Results

Grid 1 located on the WB lane of the span 1, and Grid 2 was located on the joint of the 1st and 2nd span of the WB lane of the bridge.

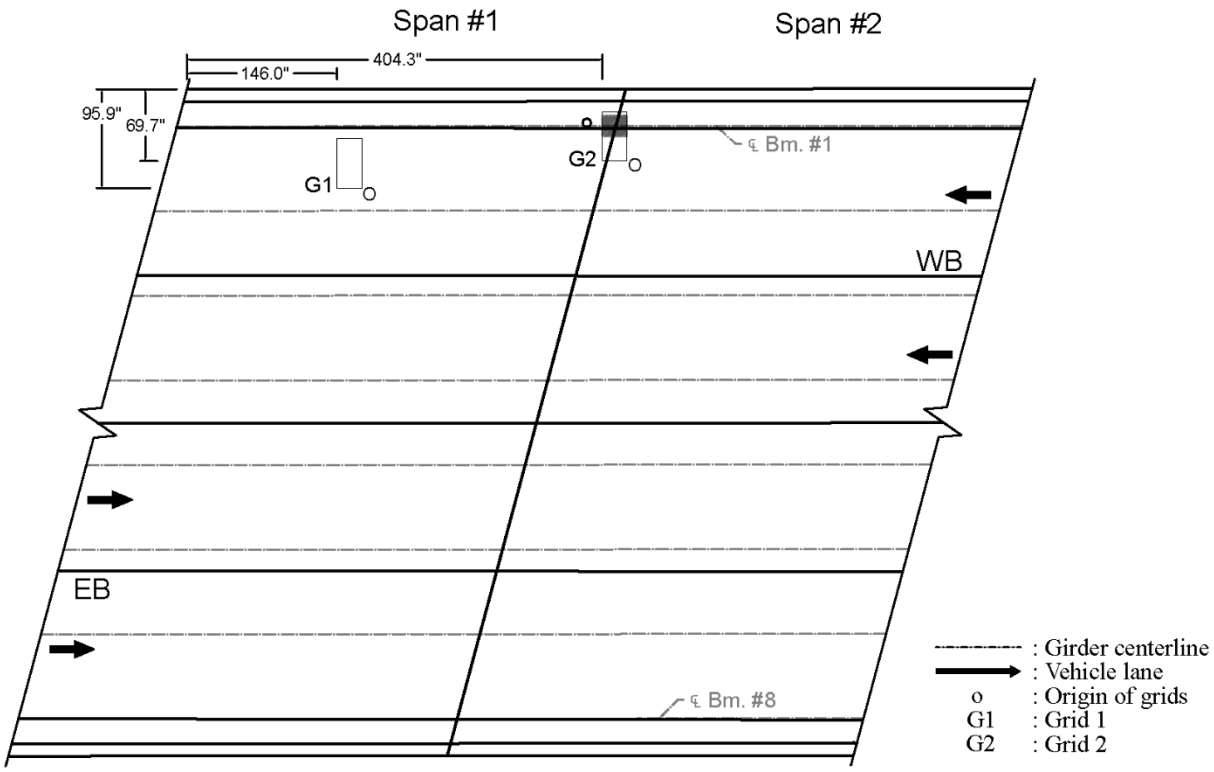

Figure 0.36. Plan View of the Bridge and Location of Grids

As shown in Figure 0.37 (a), grid 1 was drawn on top of the joint and 0.007 in. wide crack and 0.014 crack were spreading from the joint. Other than the two cracks, it only showed hairline cracks. As shown in Figure 0.38 (a), the widest crack on grid 2 was 0.02 in. wide, but hairline cracks were dominant.

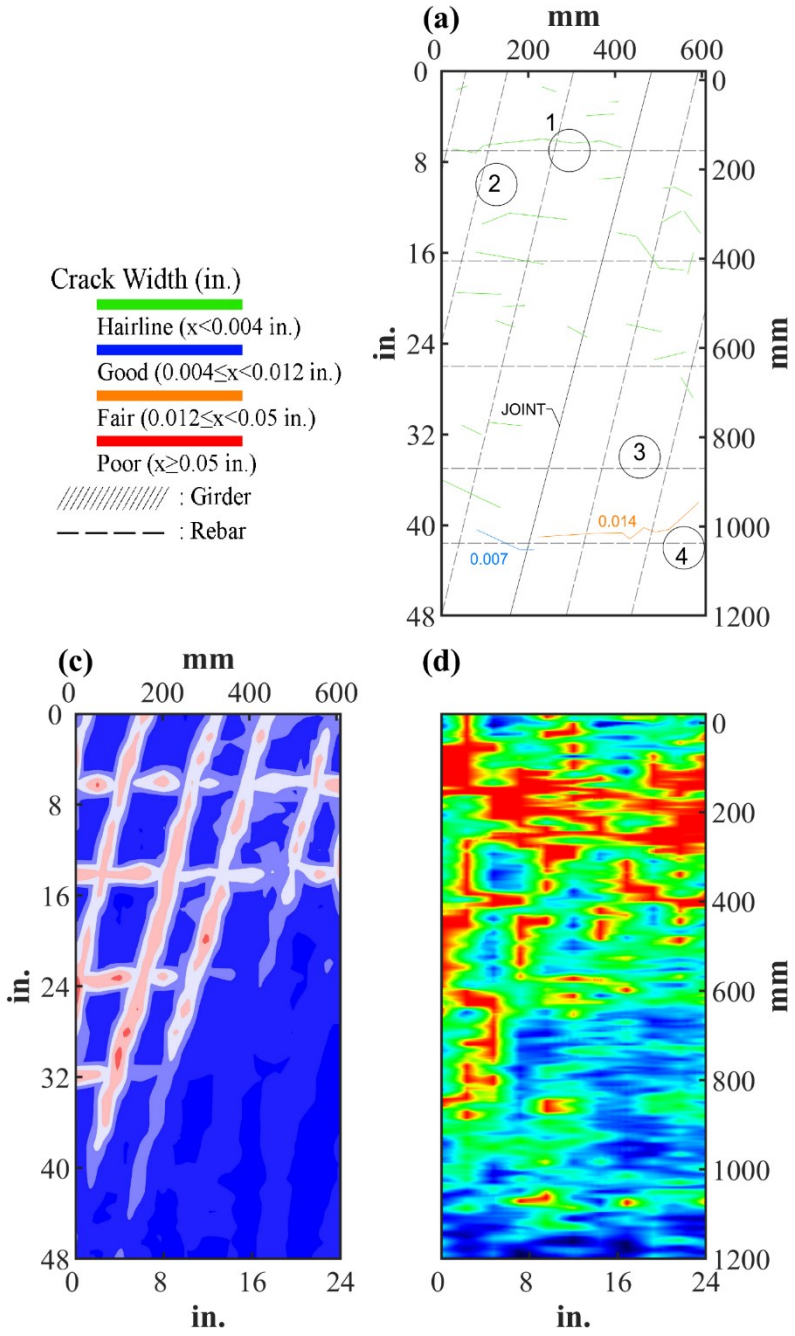

Figure 0.37. Crack Map and NDE Results of Grid 1: (a) Crack Map and Location of Cores; (c) GPR C-scan at 1.85 in. to 2.85 in. Depth; (d) UST C-scan at 2.97 in. Depth

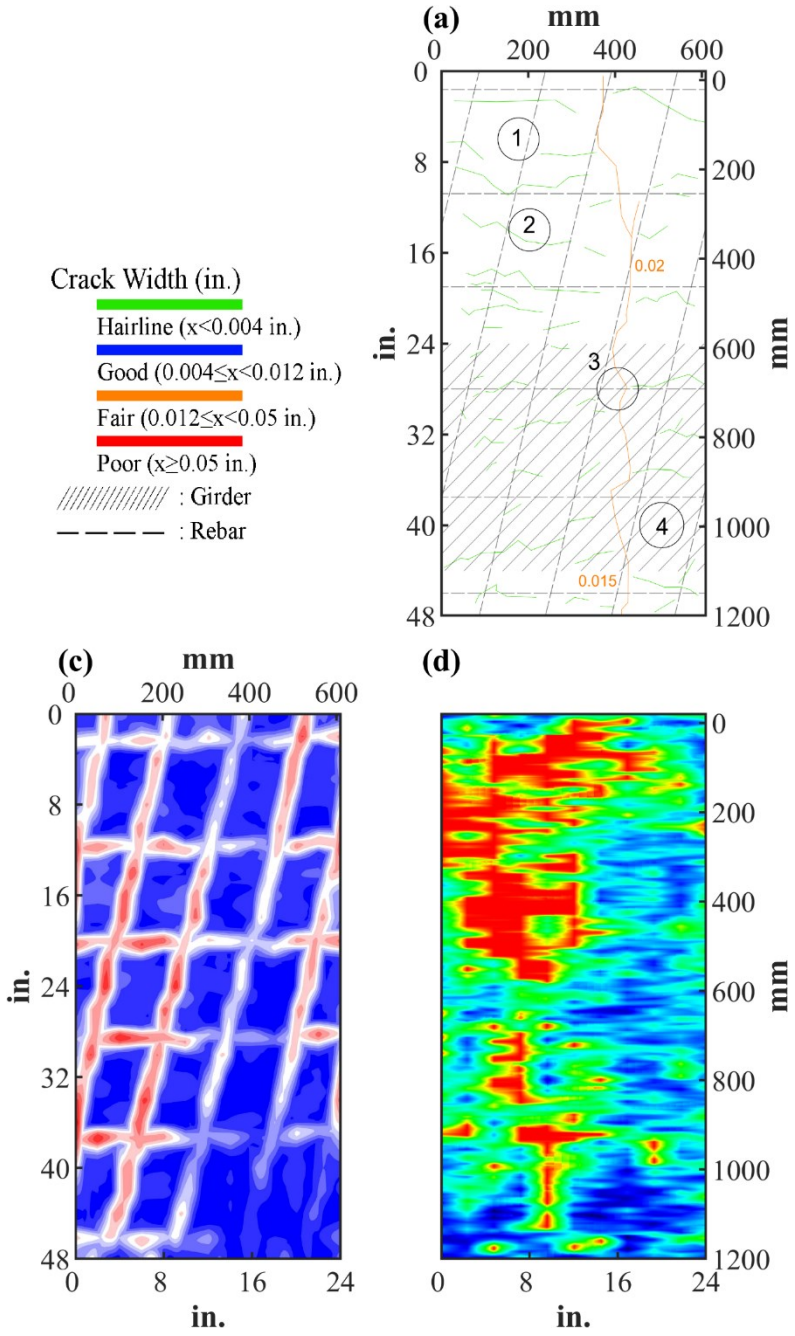

Figure 0.38. Crack Map and NDE Results of Grid 2: (a) Crack Map and Location of Cores; (c) GPR C-scan at 2.00 in. to 3.00 in. Depth; (d) UST C-scan 2.97 in. Depth

B.5.3 Concrete Cores

Table B-39. Detail Information of Concrete Cores

Core	dia. × height (in.)	Rebar depth (in.)	Rebar size (#)	Epoxy (Y/N)	Crack type	Crack width (in)	Notes
1-1	3.75 × 5.8	1.8; 2.6	5; 4	Y; Y	longitudinal	0.1	-
1-2	3.75 × 5.2	1.6	5	Y	-	-	-
1-3	3.75 × 5.5	-	-	-	-	-	-
1-4	-	-	5, 4	Y; Y	-	-	Corroded bottom rebar
2-1	3.75 × 6.1	2.2	5	Y	longitudinal	HL	-
2-2	3.75 × 4.6	-	-	-	-	-	-
2-3	3.75 × 2.0	2.6	4	Y	longitudinal; transverse	0.25, 0.45	Core split due to crack; Corroded rebar
2-4	3.75 × 1.5	-	-	-	-	-	Delamination between CIP and PCP

Table B-40. Core Pictures

Core	Side	Top	Bottom
1-1			
1-2			

1-3			
1-4	-		
2-1			
2-2			
2-3			
2-4			

ECR extracted from the core 2-3 was corroded and the epoxy coating fell off from the rebar surface.

B.5.4 Laboratory Experiment Results

B.5.4.1 Resistivity

Core Number	Surface Resistivity (kΩ·m)	Bulk Resistivity (kΩ·m)
1-3	8	2

B.5.4.2 Ultrasonic Pulse Velocity

Core Number	Ultrasonic Pulse Velocity (m/s)
1-3	3345
2-2	3021

B.5.4.3 Carbonation Depth

Core Number	Carbonation Depth (in.)
1-1	0.00
2-3	0.00

B.5.4.4 Acid-Soluble Chloride Content

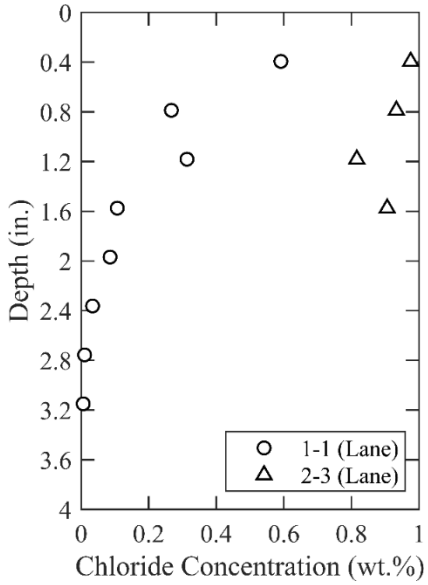

Figure 0.39. Chloride Content at Different Depth

B.5.4.5 Sorptivity

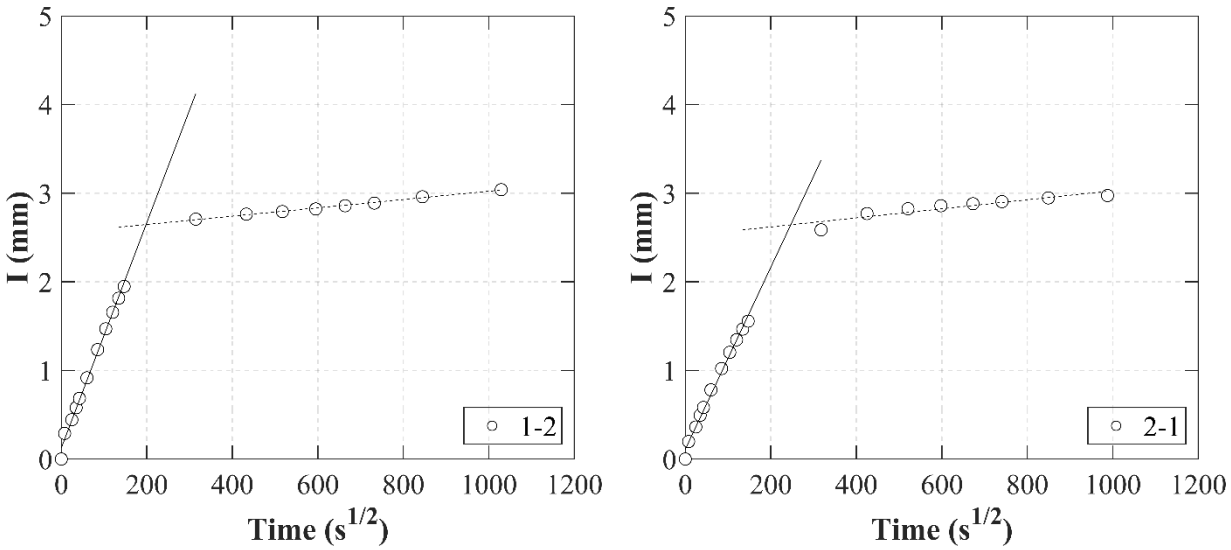

(a) Core 1–2 (b) Core 2–1

Figure 0.40. Absorption and Sorptivity of: (a) Core 1–2; (b) Core 2–1

Table B-41. Initial and Secondary Sorptivity Results

Core Number	Sorptivity	Results (mm/s$^{1/2}$)
Core 1–2	Initial Sorptivity	0.0127
	Secondary Sorptivity	0.00047
Core 2–1	Initial Sorptivity	0.0103
	Secondary Sorptivity	0.00051

B.5.4.6 Knife Test

Core Number	Score	Picture
1-1	10	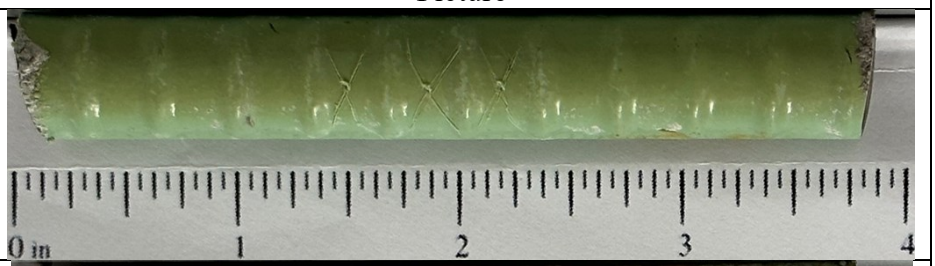
2-3	0	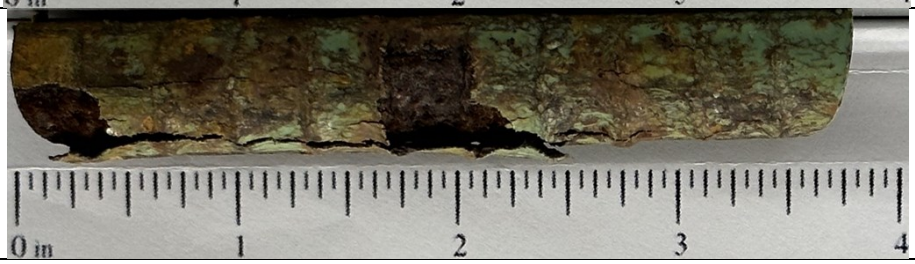

B.5.4.7 Electrochemical Impedance Spectroscopy

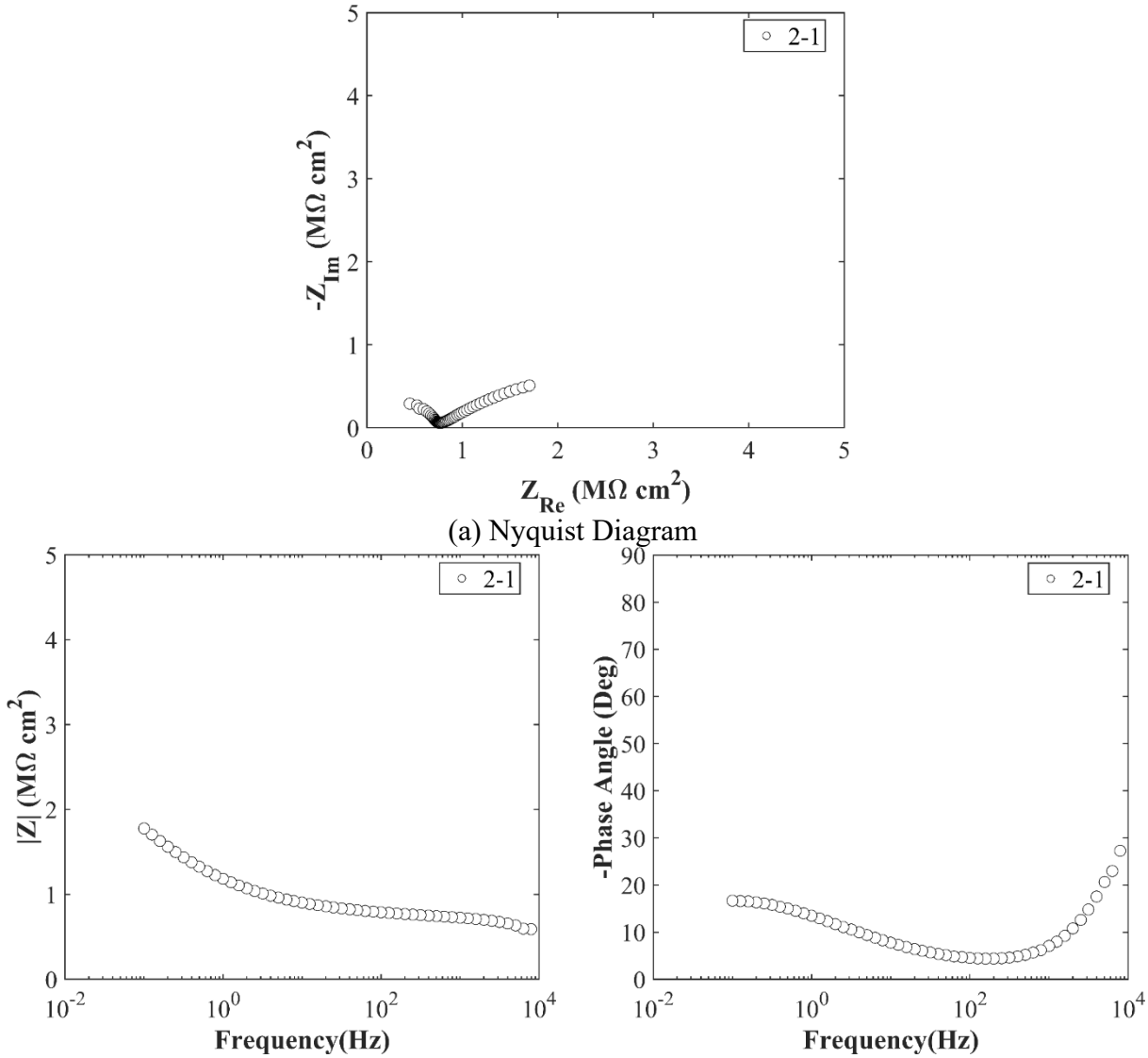

(a) Nyquist Diagram

(b) Bode Plot of Impedance Modulus

(c) Bode Plot of Impedance Phase

Figure 0.41. EIS Results: (a) Nyquist Diagram; (b) Bode Plot of Impedance Modulus; (c) Bode Plot of Impedance Phase

B.6 AMA-RC-06, GRAND ST. E. T/A OVER IH 40

- Bridge ID: 41880027501104 (Potter County)
- Built in 2000
- Mitigation methods: HPC, CNI (2 gal./CY.), ECR
- Observed CIP depth: 4.33 in.
- Observed clear cover: 2.2 – 2.8 in.
- 4 spans, 7-concrete PS girder @ 4.75’ spacing with varying overhangs at span 1; 6-concrete ps girder @ 6.4’ spacing with varying overhangs at span 2, 3, and 4
- Inspected on June 16, 2021

Figure 0.42. Concrete Deck of the Bridge (source: google maps)

B.6.1 Observed Condition

The east bridge rail is damaged due to an impact, and exposed rebar is corroded as shown in Figure 0.43 (a) and (b).

(a) (b)

Figure 0.43. Deterioration on the Bridge: (a) Impact Damage on the East Rail of the Bridge; (b) Exposed and Corroded Rebar

B.6.2 NDE Results

Both Grid 1 and Grid 2 were located on the 3rd span of the east turnaround bridge as shown in Figure 0.44.

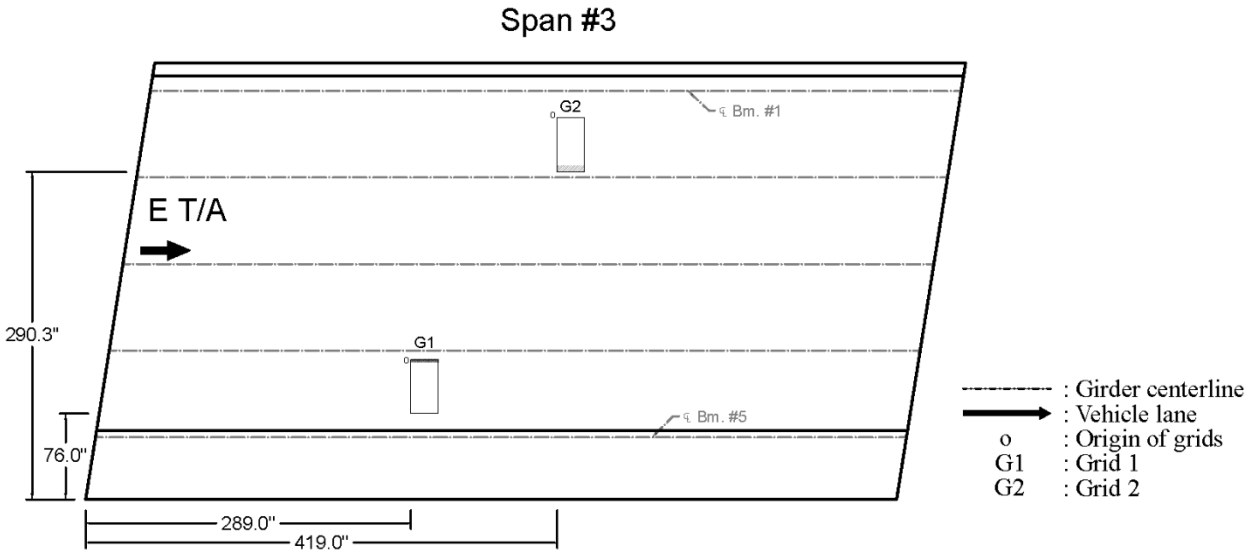

Figure 0.44. Plan View of the Bridge and Location of Grids

As shown in Figure 0.45 (a), there was hairline cracks throughout the grid. On the other hand, as shown in Figure 0.46 (a), grid 2 did not have any cracks on its surface.

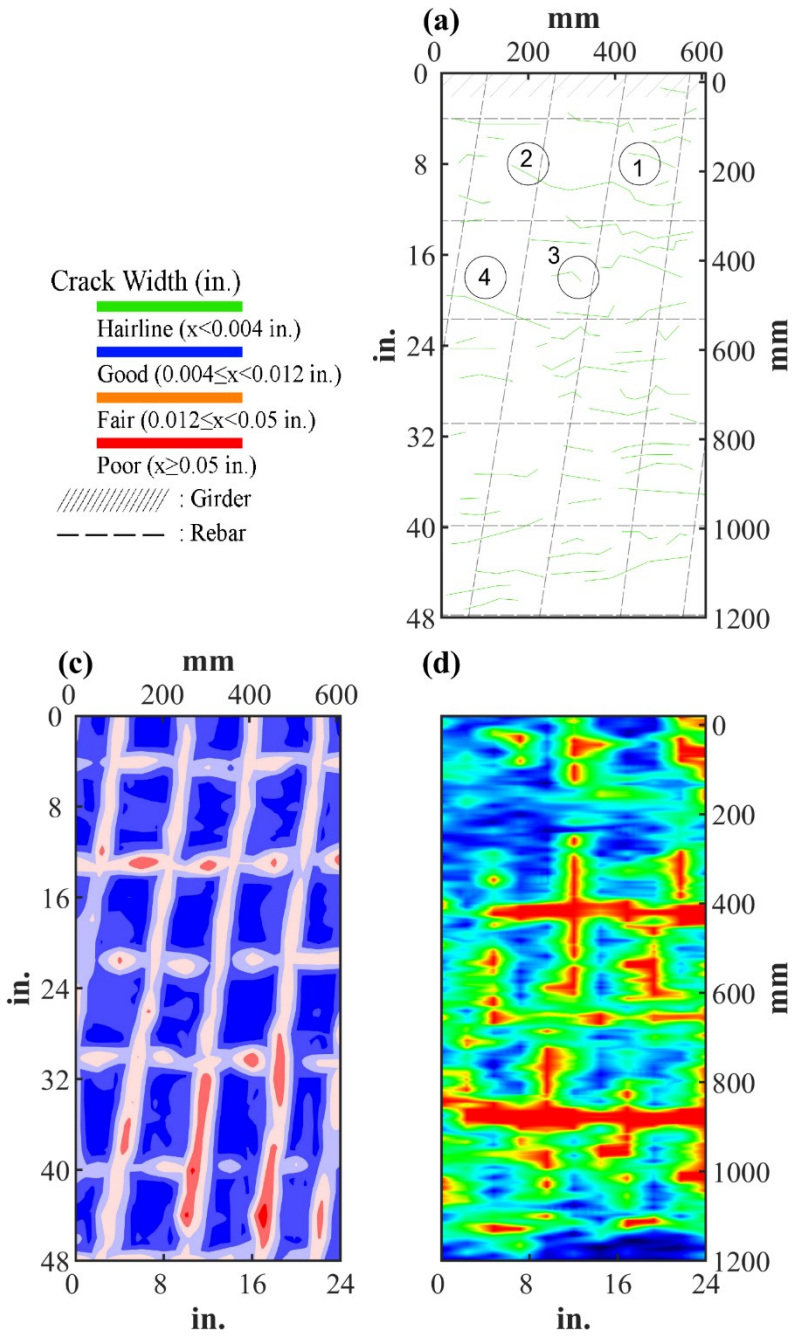

Figure 0.45. Crack Map and NDE Results of Grid 1: (a) Crack Map and Location of Cores; (c) GPR C-scan at 2.1 in. to 3.4 in. Depth; (d) UST C-scan at 3.93 in. Depth

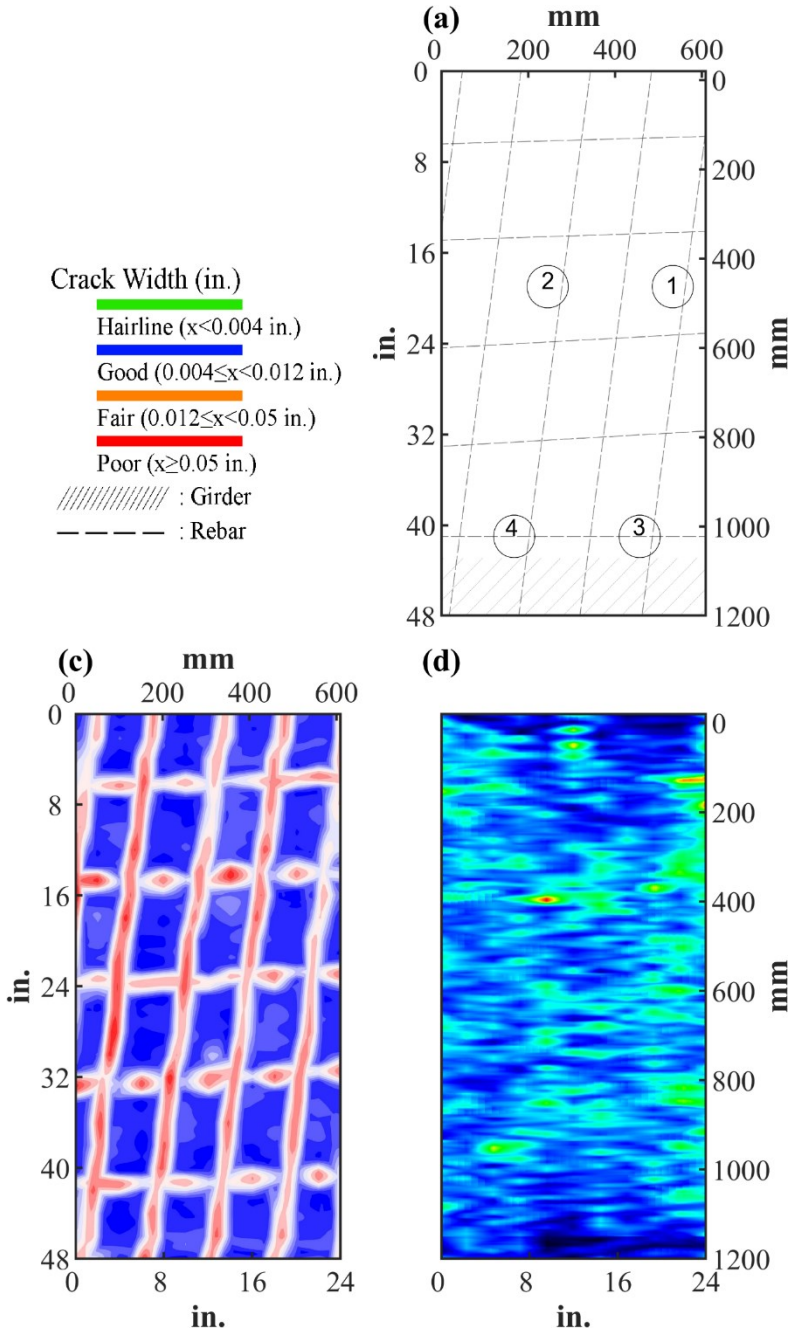

Figure 0.46. Crack Map and NDE Results of Grid 2: (a) Crack Map and Location of Cores; (c) GPR C-scan at 1.85 in. to 2.85 in. Depth; (d) UST C-scan at 1.97 in. Depth

B.6.3 Concrete Cores

Table B-42. Detail Information of Concrete Cores

Core	dia. × height (in.)	Rebar depth (in.)	Rebar size (#)	Epoxy (Y/N)	Crack type	Crack width (in)	Notes
1-1	3.75 × 6.0	-	-	-	-	-	-
1-2	3.75 × 5.9	2.8	5	Y	-	-	-
1-3	3.75 × 5.9	2.7	5	Y	-	-	-
1-4	3.75 × 5.7	-	-	-	-	-	-
2-1	3.75 × 6.2	2.2	5	Y	-	-	-
2-2	3.75 × 4.1	2.2	5	Y	-	-	-
2-3	3.75 × 4.1	2.2; 2.8	5; 4	Y; Y	-	-	-
2-4	3.75 × 4.2	2.2; 6.7	5; 4	Y; Y	-	-	-

Table B-43. Core Pictures

Core	Side	Top	Bottom
1-1			
1-2	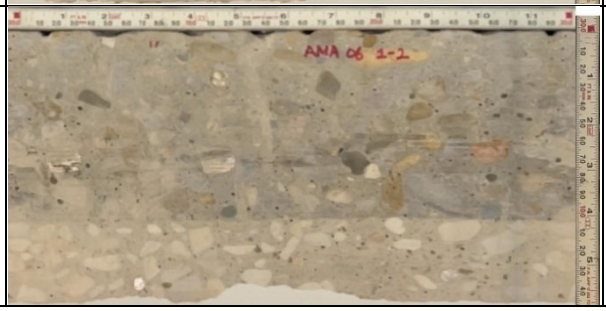		

1-3			
1-4			
2-1			
2-2			
2-3			
2-4			

All rebar was epoxy coated and showed no sign of corrosion.

B.6.4 Laboratory Experiment Results

B.6.4.1 Resistivity

Core Number	Surface Resistivity (kΩ·m)	Bulk Resistivity (kΩ·m)
1-4	63	7

B.6.4.2 Ultrasonic Pulse Velocity

Core Number	Ultrasonic Pulse Velocity (m/s)
1-1	4180
1-4	3352

B.6.4.3 Carbonation Depth

Core Number	Carbonation Depth (in.)
1-2	0.00
2-4	0.20

B.6.4.4 Acid-Soluble Chloride Content

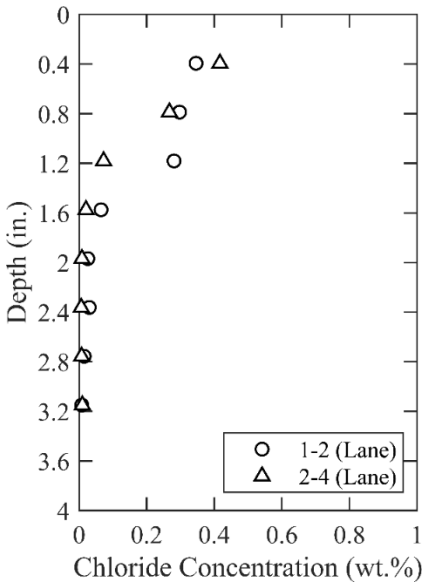

Figure 0.47. Chloride Content at Different Depth

B.6.4.5 Sorptivity

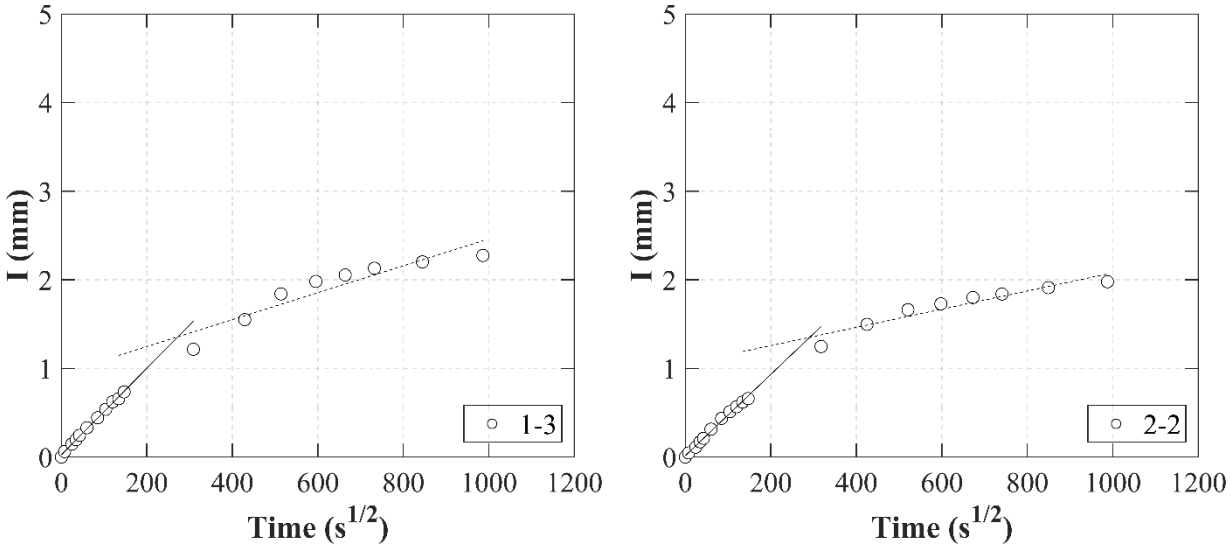

(a) Core 1–3 (b) Core 2–2

Figure 0.48. Absorption and Sorptivity of: (a) Core 1–3; (b) Core 2–2

Table B-44. Initial and Secondary Sorptivity Results

Core Number	Sorptivity	Results (mm/s$^{1/2}$)
Core 1–3	Initial Sorptivity	0.00489
	Secondary Sorptivity	0.00152
Core 2–2	Initial Sorptivity	0.00459
	Secondary Sorptivity	0.00103

B.6.4.6 Knife Test

Core Number	Score	Picture
2-4	10	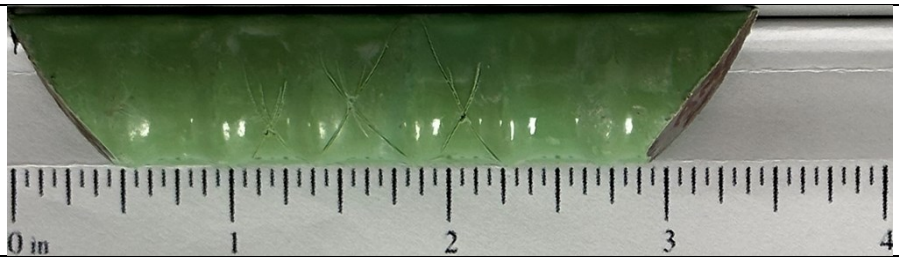

B.6.4.7 Electrochemical Impedance Spectroscopy

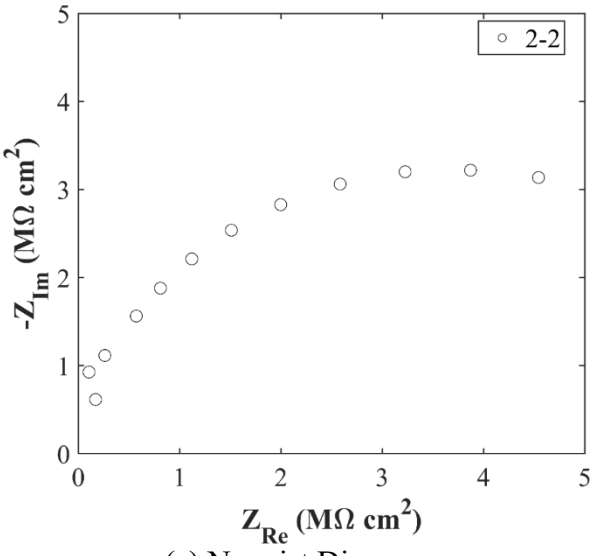

(a) Nyquist Diagram

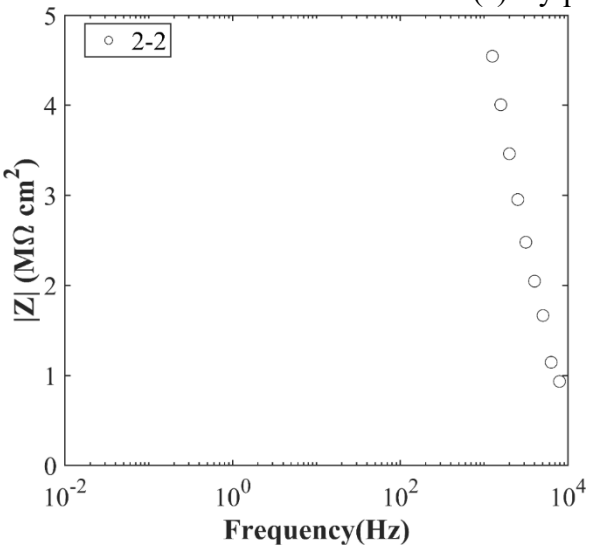

(b) Bode Plot of Impedance Modulus

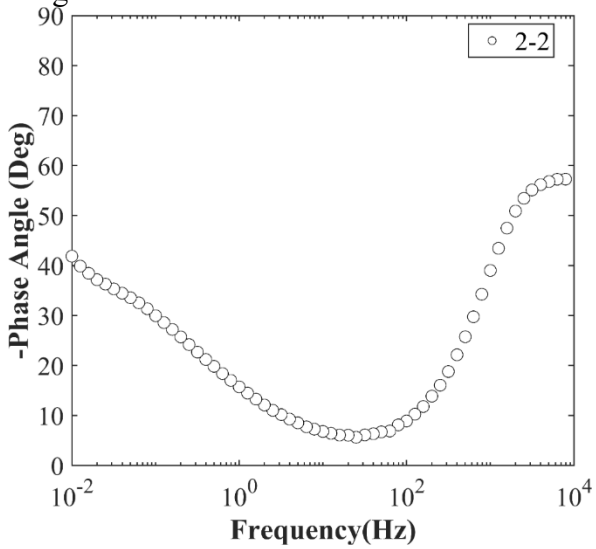

(c) Bode Plot of Impedance Phase

Figure 0.49. EIS Results: (a) Nyquist Diagram; (b) Bode Plot of Impedance Modulus; (c) Bode Plot of Impedance Phase

B.7 AMA-RC-07, BELL ST. W. T/A OVER IH 40

- Bridge ID: 41880027501160 (Potter County)
- Built in 2001
- Mitigation methods: HPC, CNI (2 gal./CY.), ECR
- Observed CIP depth: 4.33 in.
- Observed clear cover: 1.8 – 2.4 in.
- 4 spans, 5-concrete PS girder @ 4.75’ spacing with varying overhangs at span 1; 4-concrete PS girder @ 6.40’ spacing with varying overhangs at span 2, 3, and 4
- Inspected on June 17, 2021

Figure 0.50. Concrete Deck of the Bridge (source: google maps)

B.7.1 Observed Condition

Epoxy overlay is placed on deck. The west bridge rail in the south span has an impact damage. The deck, covered with an overlay, appears crack-free. The girders and abutment have been painted, including the bearing pad. The painted substructure shows no visible cracks, but there is paint loss at the bottom of one column. Abutment 5 is generally in good condition, except for one exposed rebar on the west end and a crack at the top of the east end.

B.7.2 NDE Results

Both Grid 1 and Grid 2 were located on the 4th span of the west turnaround bridge as shown in Figure 0.51.

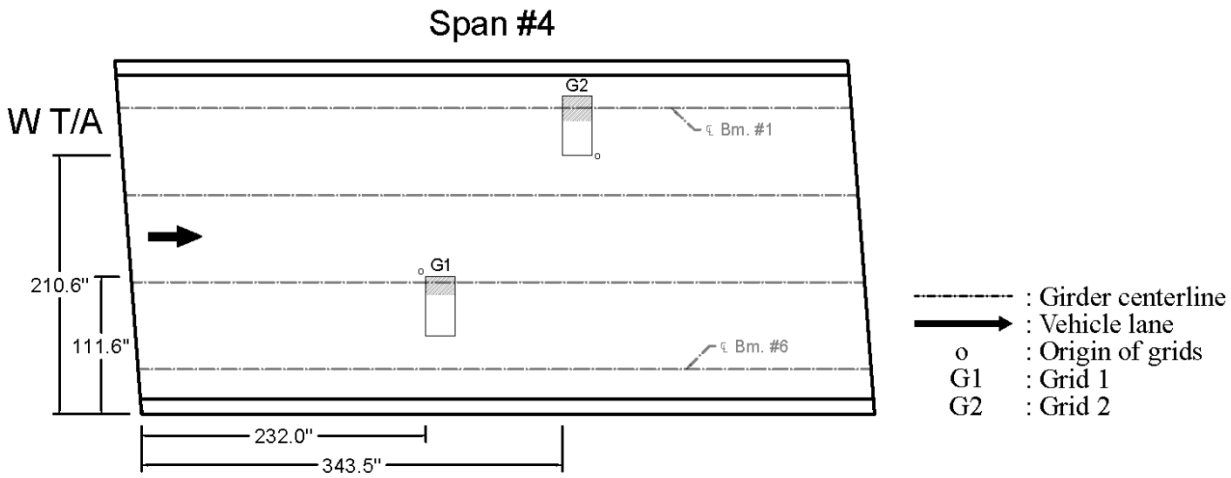

Figure 0.51. Plan View of the Bridge and Location of Grids

Epoxy overlay was applied to the bridge deck surface. As a result, no cracks were visible as shown in Figure 0.52 (a) and Figure 0.53 (a)

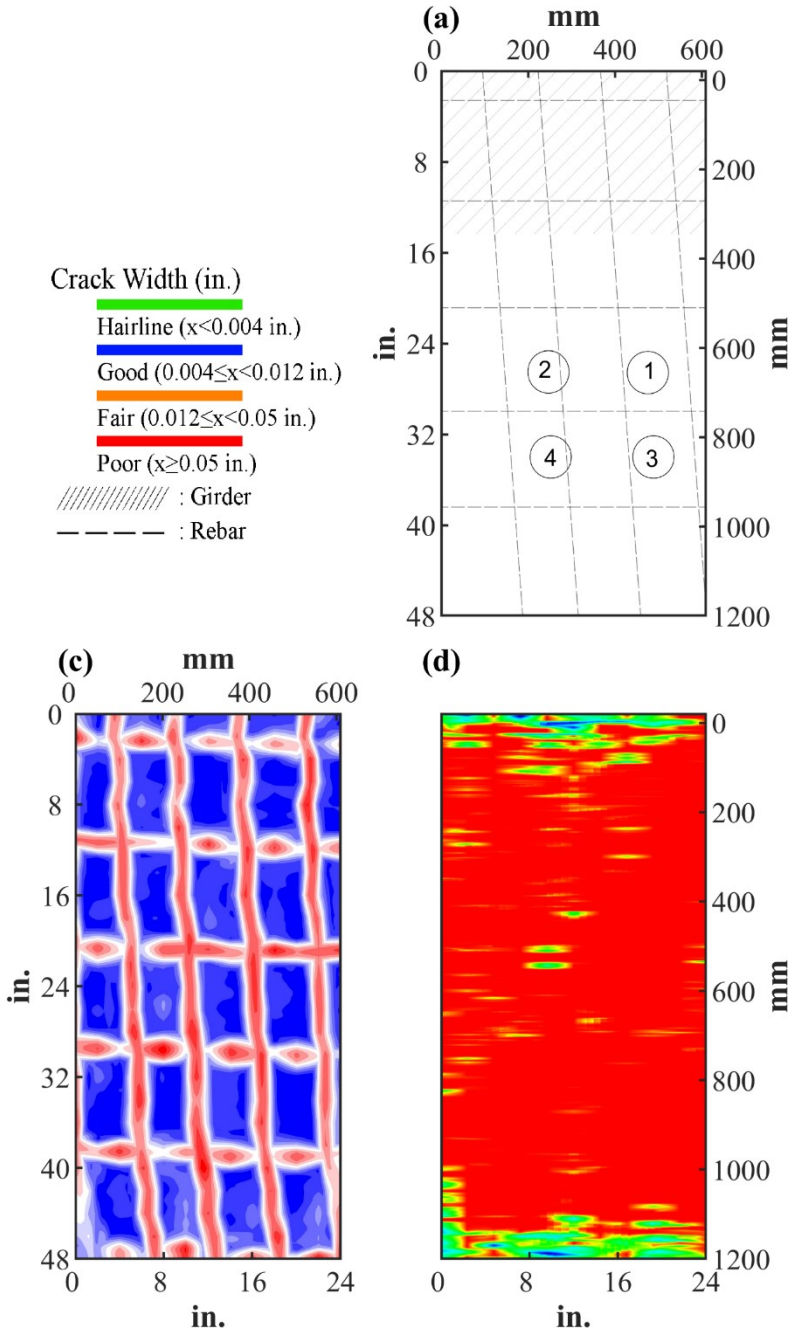

Figure 0.52. Crack Map and NDE Results of Grid 1: (a) Crack Map and Location of Cores; (c) GPR C-scan at 1.85 in. to 2.85 in. Depth; (d) UST C-scan at 1.97 in. Depth

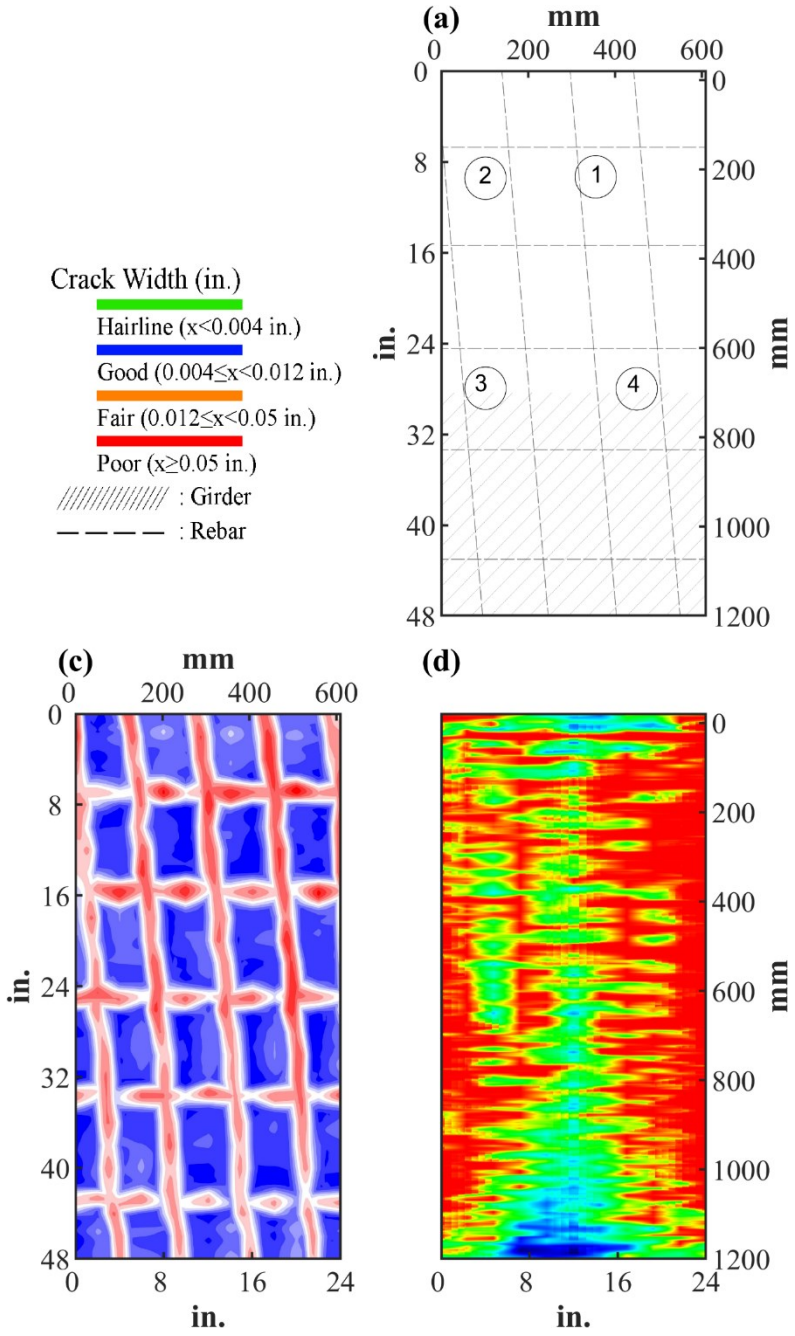

Figure 0.53. Crack Map and NDE Results of Grid 2: (a) Crack Map and Location of Cores; (c) GPR C-scan at 1.85 in. to 2.85 in. Depth; (d) UST C-scan at 1.97 in. Depth

B.7.3 Concrete Cores

Table B-45. Detail Information of Concrete Cores

Core	dia. × height (in.)	Rebar depth (in.)	Rebar size (#)	Epoxy (Y/N)	Crack type	Crack width (in)	Notes
1-1	3.75 × 5.9	-	-	-	-	-	-
1-2	3.75 × 5.9	1.9	5	Y	-	-	-
1-3	3.75 × 6.3	1.8	-	-	-	-	-
1-4	3.75 × 6.3	1.9	5	Y	-	-	-
2-1	3.75 × 5.5	2.4	5	Y	-	-	-
2-2	3.75 × 5.3	-	-	-	-	-	-
2-3	3.75 × 5.0	-	-	-	-	-	-
2-4	3.75 × 5.1	-	-	-	-	-	-

Table B-46. Core Pictures

Core	Side	Top	Bottom
1-1			
1-2			

1-3			
1-4			
2-1			
2-2			
2-3			
2-4	-	-	-

B.7.4 Laboratory Experiment Results

B.7.4.1 Resistivity

Core Number	Surface Resistivity (kΩ·m)	Bulk Resistivity (kΩ·m)
2-2	-	17
2-3	62	-

B.7.4.2 Ultrasonic Pulse Velocity

Core Number	Ultrasonic Pulse Velocity (m/s)
1-1	4101
1-3	4059
2-2	4002
2-3	4221
2-4	4207

B.7.4.3 Carbonation Depth

Core Number	Carbonation Depth (in.)
1-2	0.00
2-3	0.00

B.7.4.4 Acid-Soluble Chloride Content

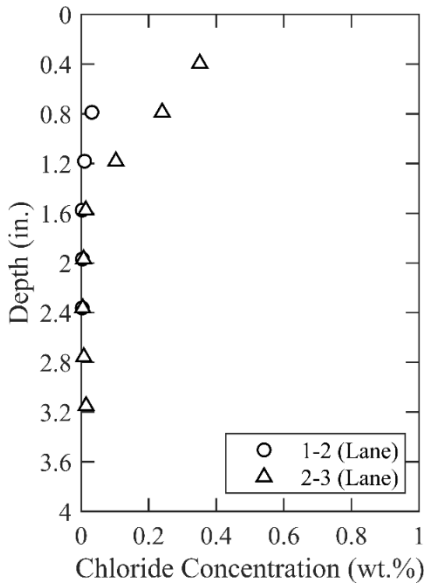

Figure 0.54. Chloride Content at Different Depth

B.7.4.5 Sorptivity

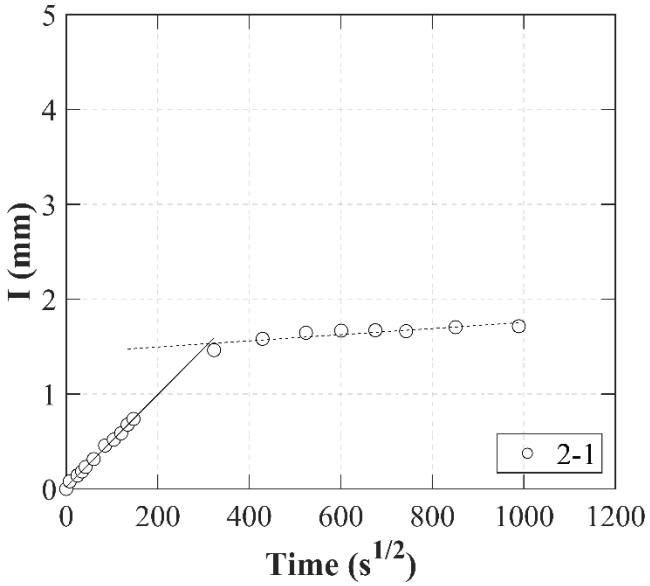

Figure 0.55. Absorption and Sorptivity of Core 2–1

Table B-47 Initial and Secondary Sorptivity Results

Core Number	Sorptivity	Results (mm/s$^{1/2}$)
Core 2–1	Initial Sorptivity	0.00486
	Secondary Sorptivity	0.00032

B.7.4.6 Knife Test

Core Number	Score	Picture
1-3	10	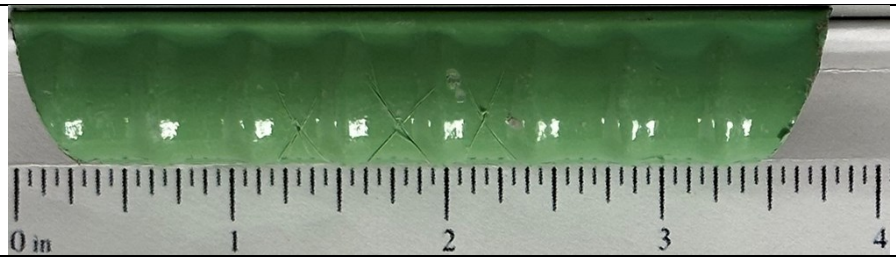

B.8 AMA-RC-08, RM 1061 OVER SIERRITA DE LA CRUZ CREEK

- Bridge ID: 41880124502017 (Potter County)
- Built in 2001
- Mitigation methods: HPC, CNI (2 gal./CY.), Linseed oil, ECR, GFRP (only in span 6 and 7)
- Observed CIP depth: 6.3 in.
- Observed clear cover: 1.9 – 2.4 in.
- 7 spans, 6-concrete PS girder @ 7.87’ spacing with 3’ overhangs
- Inspected on June 17, 2021

Figure 0.56. Concrete Deck of the Bridge (source: google maps)

B.8.1 Observed Condition

There are hairline longitudinal and transverse cracks on the top surface of deck. The bottom surface of deck around joint has diagonal cracks as shown in Figure 0.57 (a). The undersurface of one span is with seepage in progress and obvious stains as shown in Figure 0.57 (b). There is moderate map crack at the epoxy surface of south approach pavement.

Abutment 1 displayed horizontal cracks at both its top and bottom. The overhangs on the north and south sides exhibit cracking, with efflorescence occurring every few feet on the north side and at panel spacing on the south side. The north bent cap has sustained vertical and horizontal cracks, while girders ends exhibit hairline diagonal cracks. Notably, rust is present at the expansion joints.

(a) (b)

Figure 0.57. Deterioration on the Bridge: (a) Diagonal Crack at the deck bottom surface; (b) Leakage and stains on bottom surface of deck

B.8.2 NDE Results

Grid 1 was located on the WB lane of the span 1 (Figure 0.58), Grid 2 was located on the 2nd span of the WB shoulder lane (Figure 0.58), and the grid 3 was located on the WB shoulder lane of 7th span as shown in Figure 0.58.

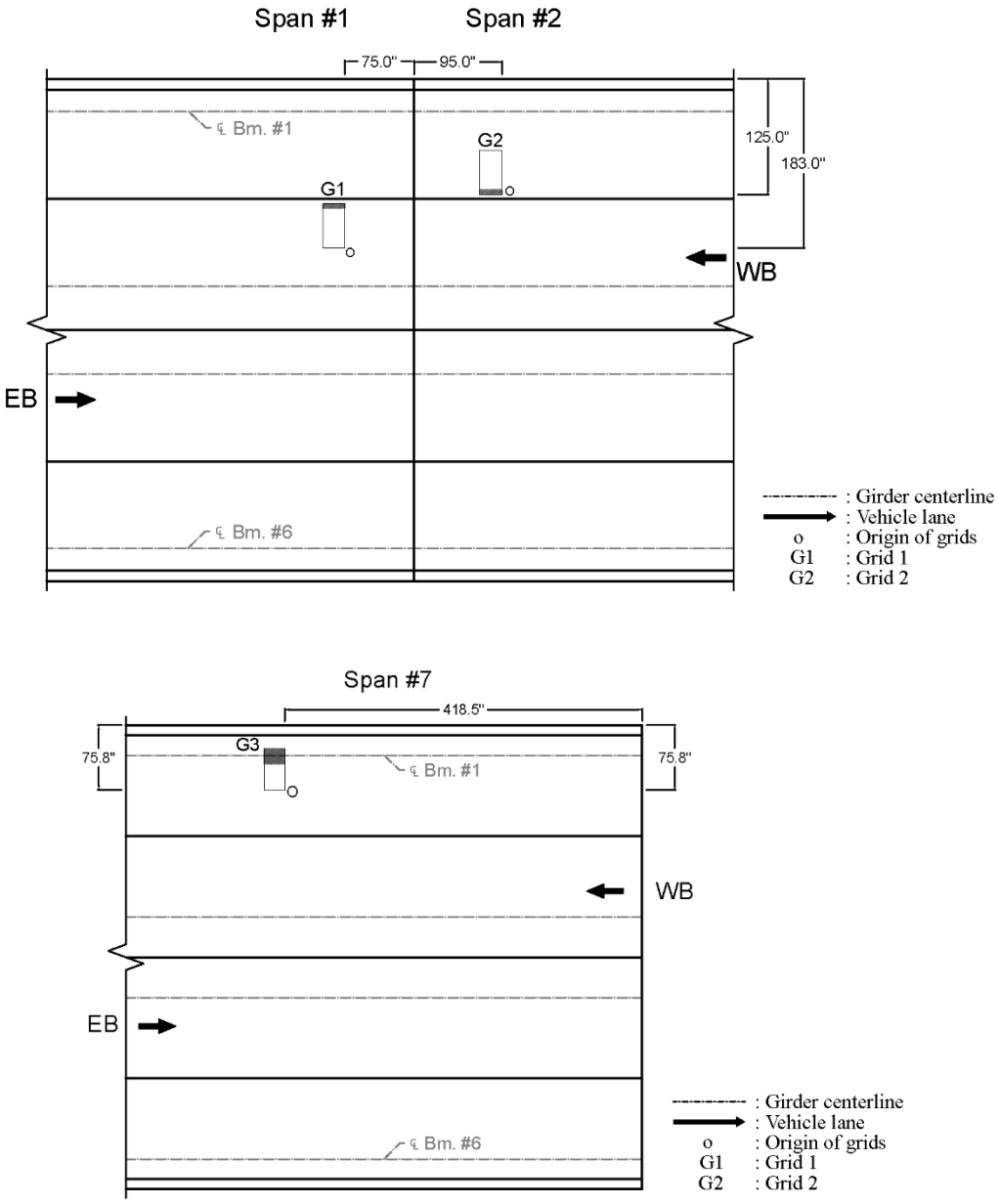

Figure 0.58. Plan View of the Bridge and Location of Three Grids

As shown in Figure 0.58 (a), 0.05 in. crack was present in Grid 1, and 0.02 in. transverse crack possibly caused by PCP. As shown in Figure 0.59 (a), 0.007 in. transverse crack was visible in Grid 2 which was possibly caused by PCP as well.

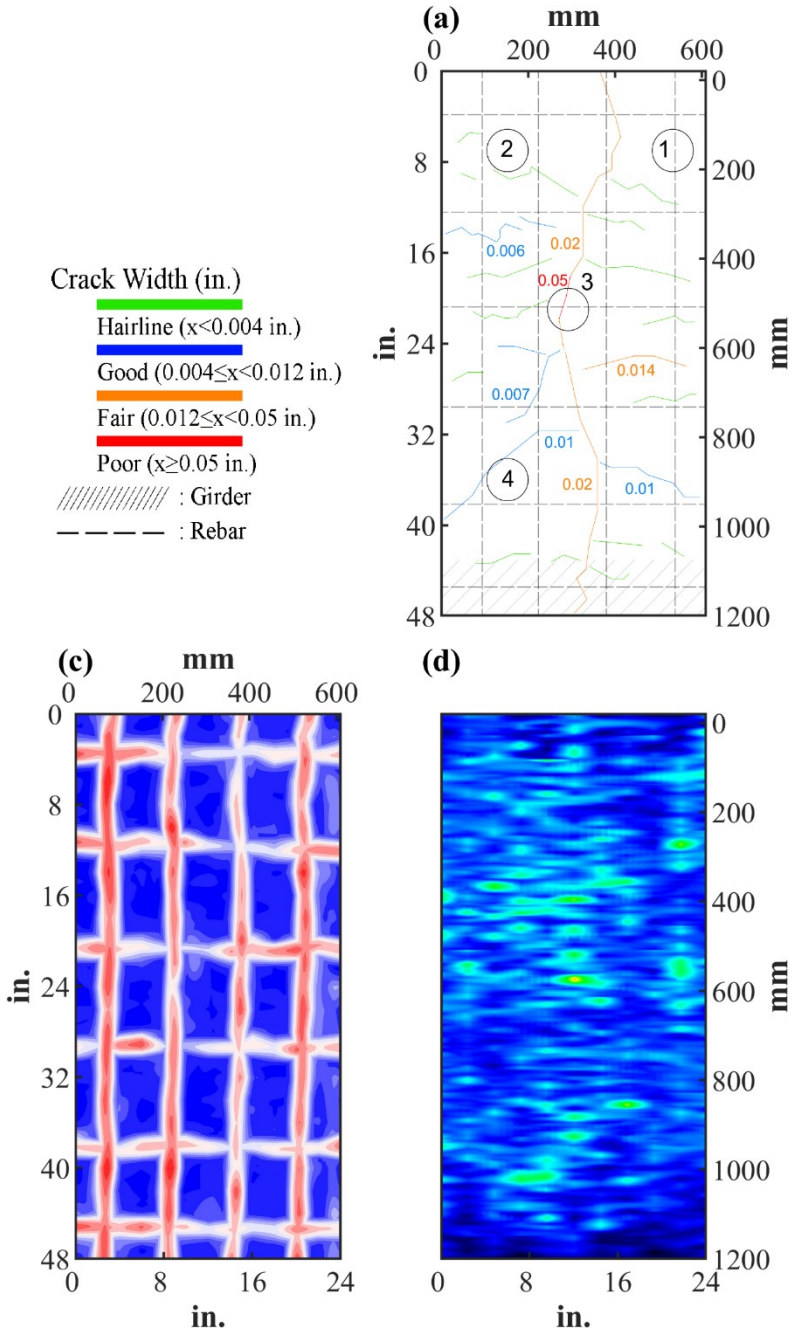

Figure 0.59. Crack Map and NDE Results of Grid 1: (a) Crack Map and Location of Cores; (c) GPR C-scan at 2.8 in. to 3.9 in. Depth; (d) UST C-scan at 2.0 in. Depth

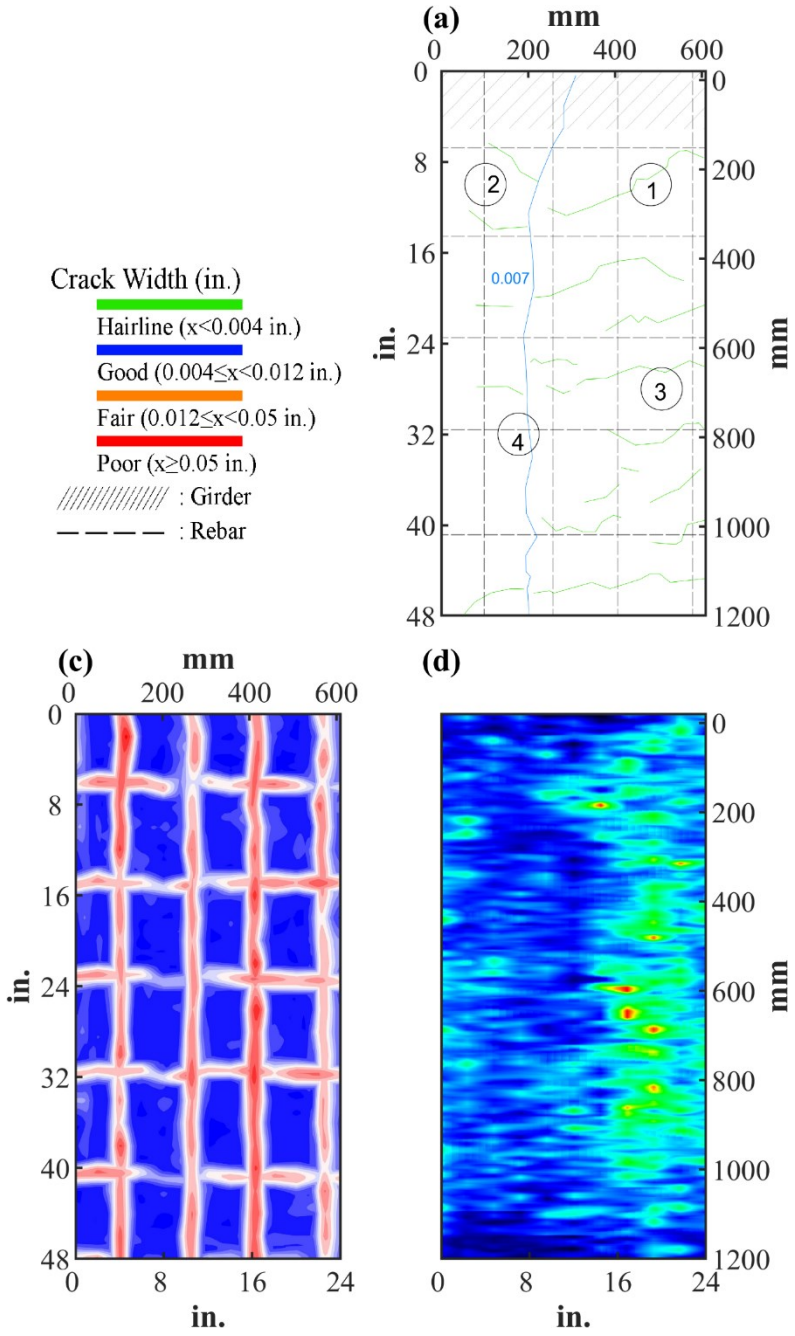

Figure 0.60. Crack Map and NDE Results of Grid 2: (a) Crack Map and Location of Cores; (c) GPR C-scan at 2.45 in. to 3.55 in. Depth; (d) UST C-scan at 2.0 in. Depth

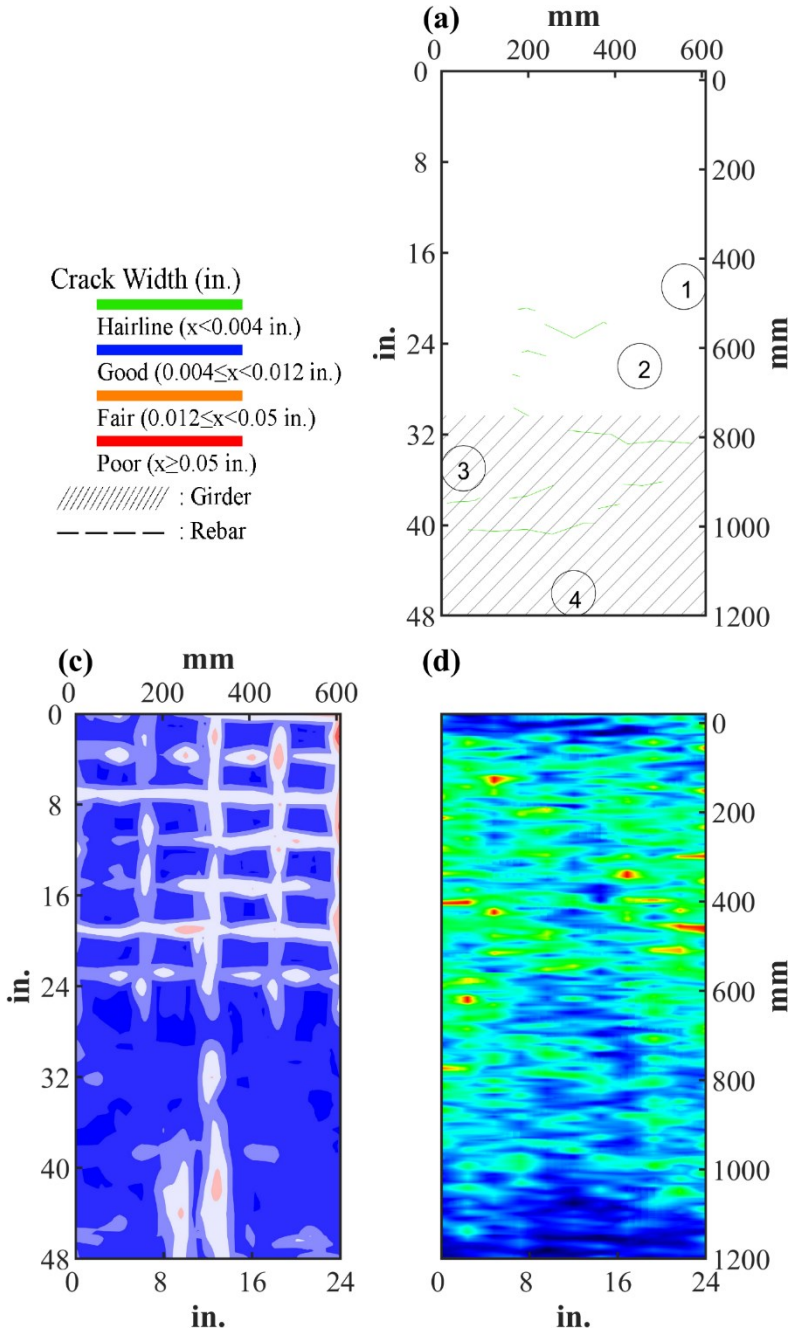

Figure 0.61. Crack Map and NDE Results of Grid 3: (a) Crack Map and Location of Cores; (b) Infrared Picture; (c) GPR C-scan at 2.45 in. to 3.55 in. Depth; (d) UST C-scan at 2.0 in. Depth; (e) Corrosion Rate Map

B.8.3 Concrete Cores

Table B-48. Detail Information of Concrete Cores

Core	dia. × height (in.)	Rebar depth (in.)	Rebar size (#)	Epoxy (Y/N)	Crack type	Crack width (in)	Notes
1-1	3.75 × 6.0	3.2	5	Y	-	-	-
1-2	3.75 × 6.3	-	-	-	-	-	-
1-3	3.75 × 4.0	3.9	4	Y	transverse	0.5	Core broken due to crack
1-4	3.75 × 6.3	-	-	-	-	-	-
2-1	3.75 × 5.1	-	-	-	-	-	-
2-2	3.75 × 6.3	2.6	5	Y	longitudinal	HL	-
2-3	3.75 × 6.3	-	-	-	-	-	-
2-4	3.75 × 6.3	3.2	4	Y	transverse	0.25	A crack propagates along intersection of aggregates
3-1	3.75 × 5.7	1.9; 2.7	6	N; N	-	-	GFRP
3-2	3.75 × 5.9	2.0	6	N	-	-	GFRP
3-3	3.75 × 5.9	2.0; 2.0	6; 6	N; N	-	-	GFRP
3-4	3.75 × 6.3	2.4; 3.2	6; 5	N; N	longitudinal	HL	GFRP

Table B-49. Core Pictures

Core	Side	Top	Bottom
1-1			

1-2			
1-3			
1-4			
2-1			
2-2			

2-3			
2-4			
3-1			
3-2			
3-3	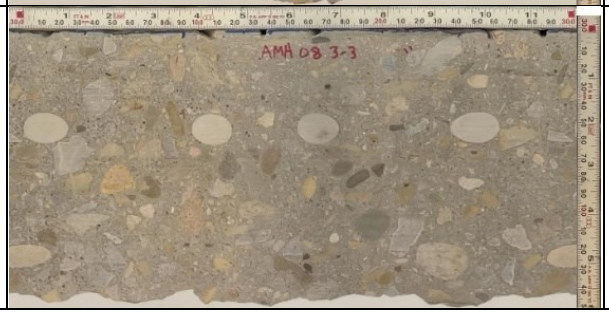		

3-4			

B.8.4 Laboratory Experiment Results

B.8.4.1 Resistivity

Core Number	Surface Resistivity (kΩ·m)	Bulk Resistivity (kΩ·m)
1-2	34	-
1-4	40	10
2-1	27	6
2-3	27	-

B.8.4.2 Ultrasonic Pulse Velocity

Core Number	Ultrasonic Pulse Velocity (m/s)
1-2	4084
1-4	4176
2-1	3927
2-3	3909

B.8.4.3 Carbonation Depth

Core Number	Carbonation Depth (in.)
1-3	0.04
2-2	0.00

B.8.4.4 Acid-Soluble Chloride Content

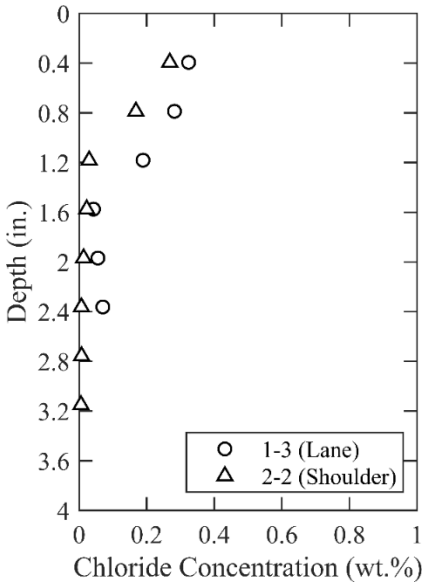

Figure 0.62. Chloride Content at Different Depth

B.8.4.5 Sorptivity

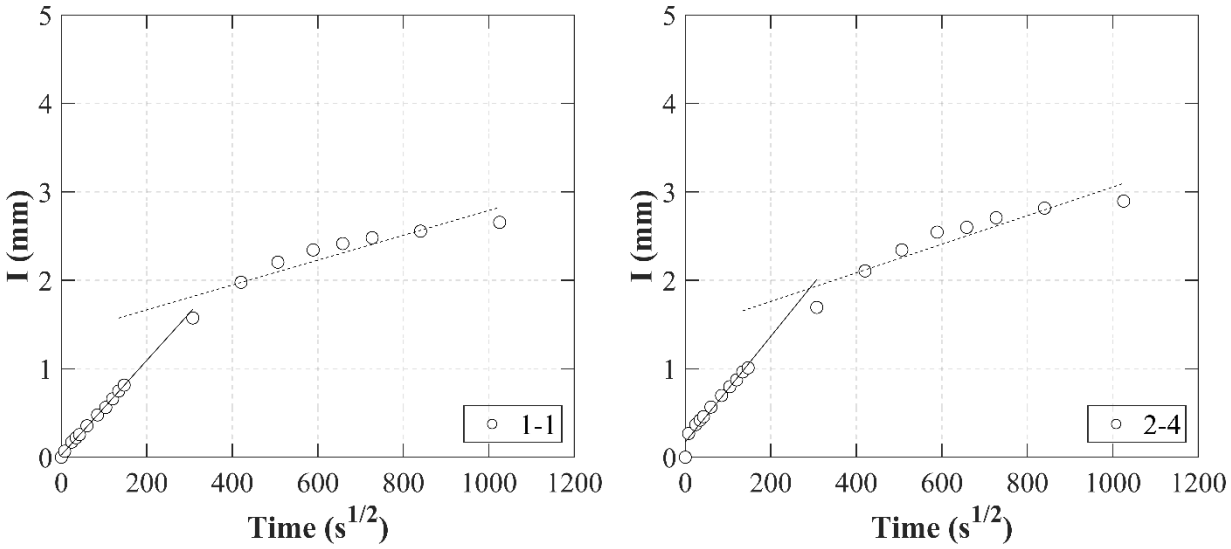

(a) Core 1–1 (b) Core 2–4

Figure 0.63. Absorption and Sorptivity of: (a) Core 1–1; (b) Core 2–4

Table B-50. Initial and Secondary Sorptivity Results

Core Number	Sorptivity	Results (mm/s$^{1/2}$)
Core 1–1	Initial Sorptivity	0.00535
	Secondary Sorptivity	0.00140
Core 2–4	Initial Sorptivity	0.00597
	Secondary Sorptivity	0.00162

B.8.4.6 Knife Test

Core Number	Score	Picture
2-2	10	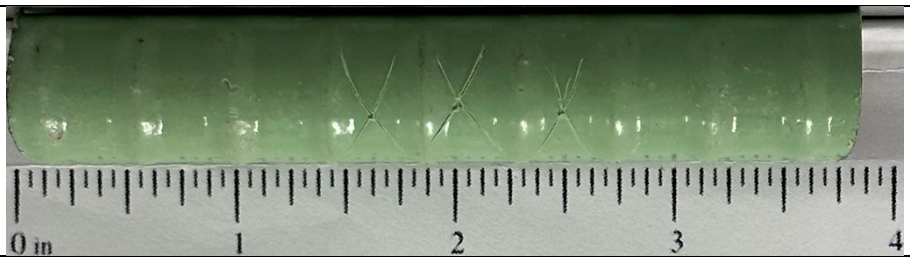

B.8.4.7 Electrochemical Impedance Spectroscopy

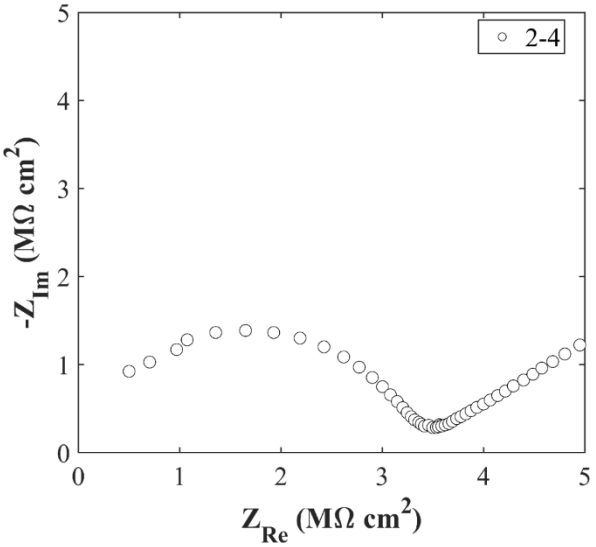

(a) Nyquist Diagram

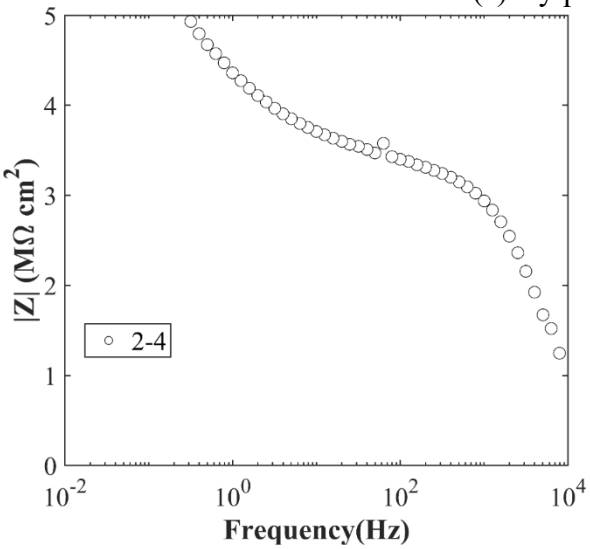

(b) Bode Plot of Impedance Modulus

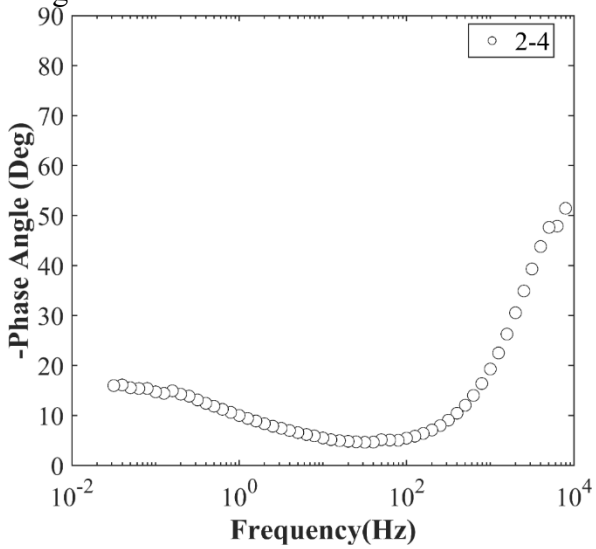

(c) Bode Plot of Impedance Phase

Figure 0.64. EIS Results: (a) Nyquist Diagram; (b) Bode Plot of Impedance Modulus; (c) Bode Plot of Impedance Phase

B.9 AMA-RC-09, LP 335 OVER AMARILLO CREEK

- Bridge ID: 41880263504028 (Potter County)
- Built in 1997
- Mitigation methods: CNI (2 gal./CY.), Silane, ECR
- Observed CIP depth: 5.11 in.
- Observed clear cover: 2.1 – 2.2 in.
- 3 spans, 6-concrete PS girder @ 8’ spacing with varying overhangs
- Inspected on June 19, 2021

Figure 0.65. Concrete Deck of the Bridge (source: google maps)

B.9.1 Observed Condition

The top surface of deck has some hairline longitudinal and transverse cracks. The bridge deck exhibits transverse cracks at regular intervals in the main lane. Numerous longitudinal cracks were also present, which were more frequent but shorter than typical longitudinal cracks associated with beams. At PBJ, a longitudinal crack, presumably originating from the girder, was 0.018 in. wide. A horizontal crack was inspected near the top of the backwall of Abutment 4. No visible cracks are seen on the girder ends, and the girder line does not appear to be straight. The overhang cracks are spaced at regular intervals and exhibit efflorescence.

B.9.2 NDE Results

Grid 1 was located on the NB lane of the span 2, and Grid 2 was located on the 2nd span of the NB shoulder lane as shown in Figure 0.66.

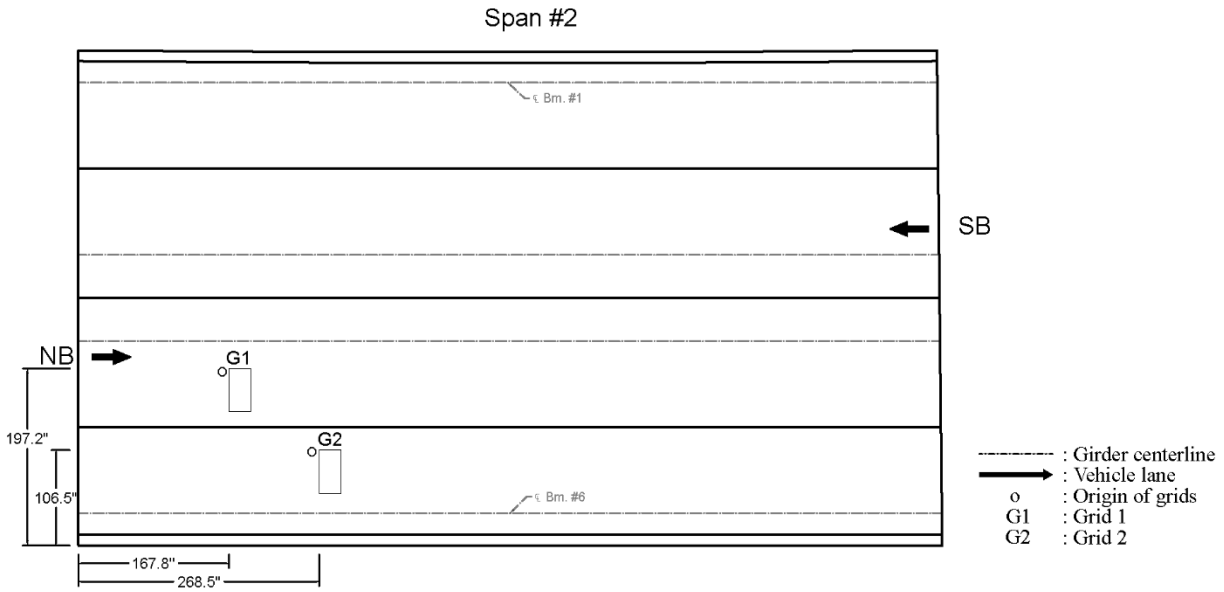

Figure 0.66. Plan View of the Bridge and Location of Grids

Figure 0.67 (a) shows that there was widespread of 0.004 in. wide cracks with one 0.012 wide transverse crack. The Grid 2 had one crack that was 0.004 in. wide as shown in Figure 0.68 (a).

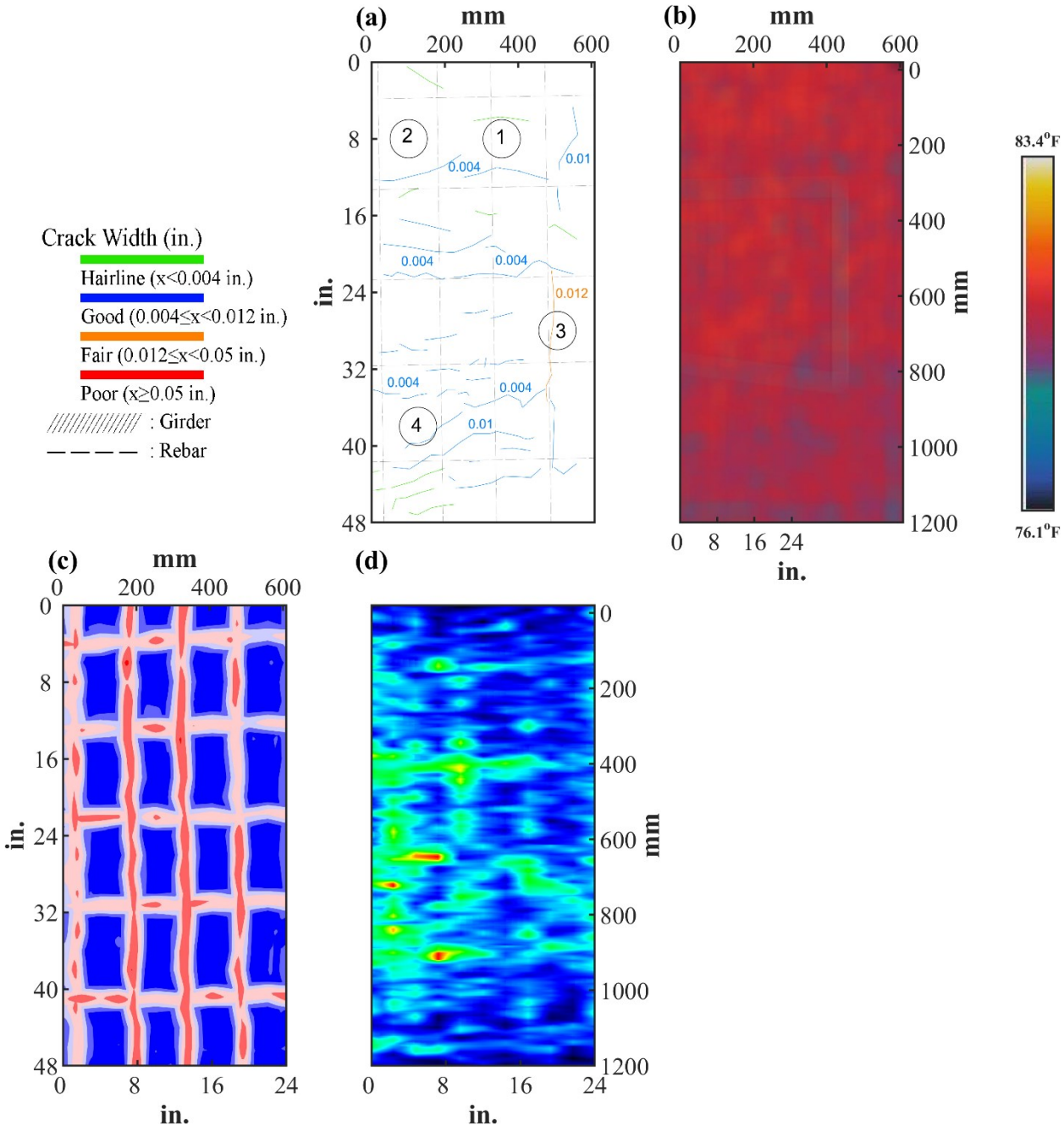

Figure 0.67. Crack Map and NDE Results of Grid 1: (a) Crack Map and Location of Cores; (b) Infrared Picture; (c) GPR C-scan at 1.8 in. to 2.9 in. Depth; (d) UST C-scan at 4.11 in. Depth

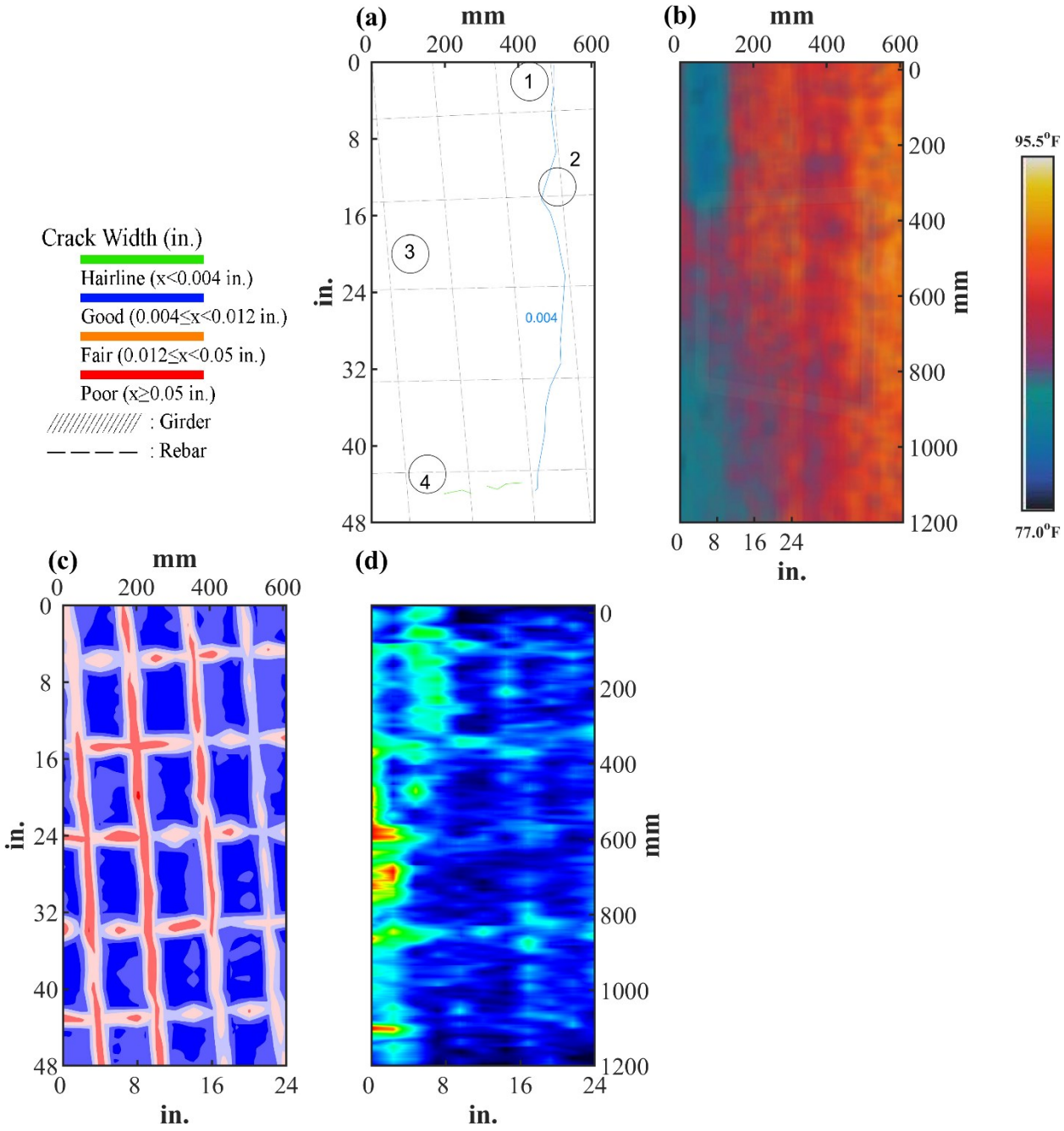

Figure 0.68. Crack Map and NDE Results of Grid 2: (a) Crack Map and Location of Cores; (b) Infrared Picture; (c) GPR C-scan at 1.8 in. to 2.9 in. Depth; (d) UST C-scan at 3.93 in. Depth

B.9.3 Concrete Cores

Table B-51. Detail Information of Concrete Cores

Core	dia. × height (in.)	Rebar depth (in.)	Rebar size (#)	Epoxy (Y/N)	Crack type	Crack width (in)	Notes
1-1	3.75 × 5.7	2.2	5	Y	-	-	Delamination between CIP and PCP
1-2	3.75 × 5.3	-	-	-	-	-	Delamination between CIP and PCP
1-3	3.75 × 5.1	2.1	5	Y	transverse	0.45	A crack propagates along intersection of aggregates; delamination between CIP and PCP
1-4	3.75 × 5.1	-	-	-	longitudinal	HL	Delamination between CIP and PCP
2-1	3.75 × 5.2	-	-	-	longitudinal	HL	Delamination between CIP and PCP; 2 cm void
2-2	3.75 × 5.3	2.2; 2.8	5; 4	Y; Y	diagonal	0.2	Delamination between CIP and PCP
2-3	3.75 × 4.7	-	-	-	-		-
2-4	3.75 × 4.7	2.8	5	Y	longitudinal	HL	-

Table B-52. Core Pictures

Core	Side	Top	Bottom
1-1			
1-2			

1-3			
1-4			
2-1	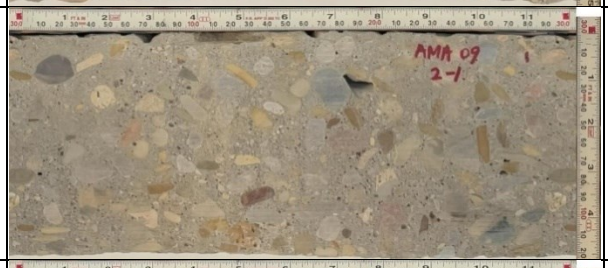		
2-2			
2-3			
2-4			

B.9.4 Laboratory Experiment Results

B.9.4.1 Resistivity

Core Number	Surface Resistivity (kΩ·m)	Bulk Resistivity (kΩ·m)
1-2	39	6
2-1	-	4

B.9.4.2 Ultrasonic Pulse Velocity

Core Number	Ultrasonic Pulse Velocity (m/s)
1-2	3261
1-4	3347
2-1	3767

B.9.4.3 Carbonation Depth

Core Number	Carbonation Depth (in.)
1-1	0.02
2-2	0.00

B.9.4.4 Acid-Soluble Chloride Content

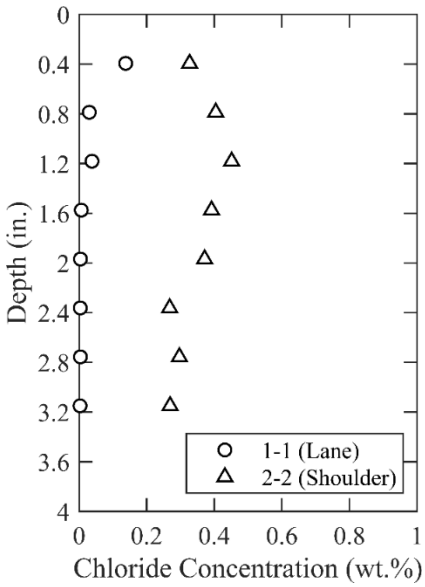

Figure 0.69. Chloride Content at Different Depth

B.9.4.5 Sorptivity

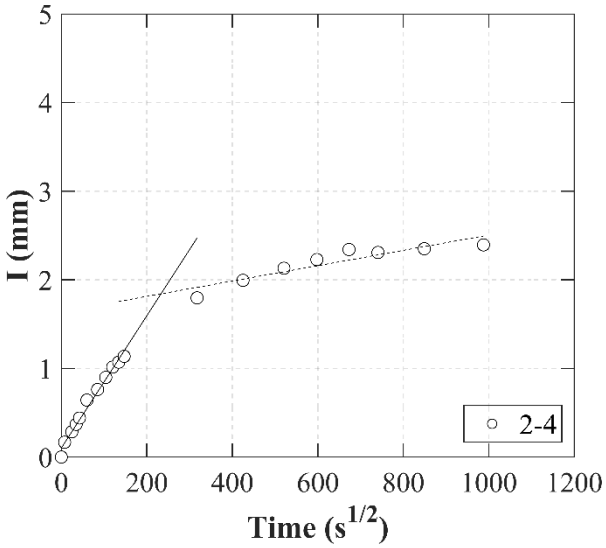

Figure 0.70. Absorption and Sorptivity of Core 2–4

B.9.4.6 Knife Test

Core Number	Score	Picture
2-2	10	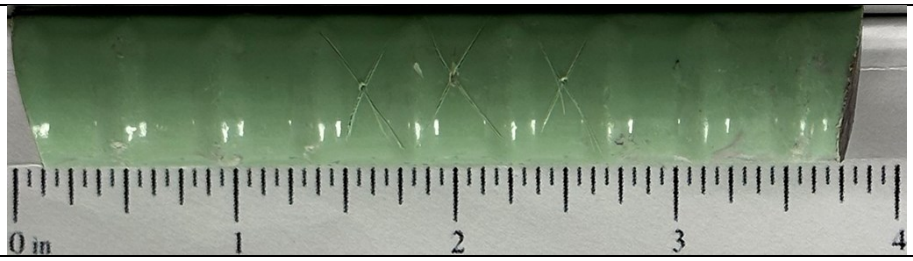

B.9.4.7 Electrochemical Impedance Spectroscopy

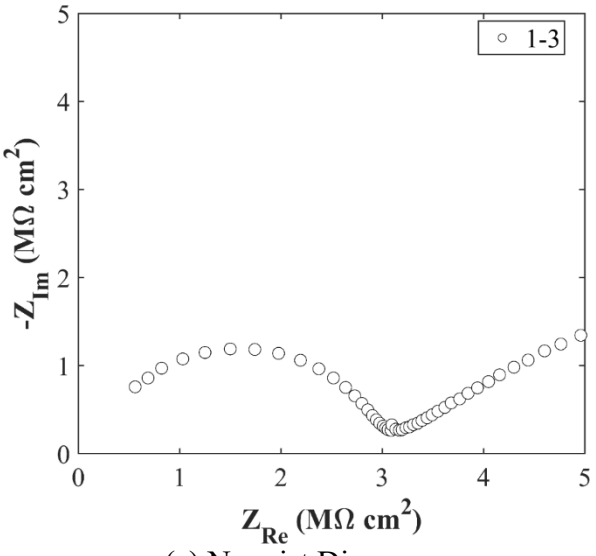

(a) Nyquist Diagram

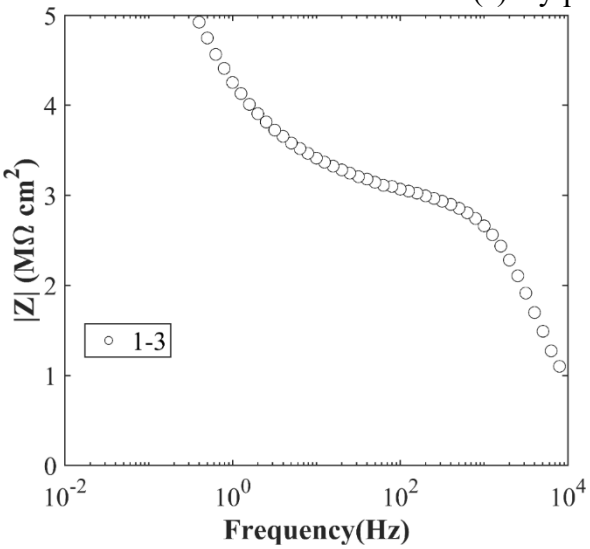

(b) Bode Plot of Impedance Modulus

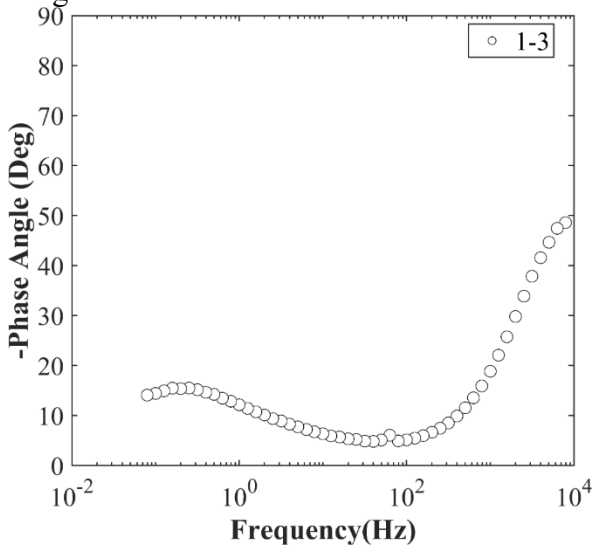

(c) Bode Plot of Impedance Phase

Figure 0.71. EIS Results: (a) Nyquist Diagram; (b) Bode Plot of Impedance Modulus; (c) Bode Plot of Impedance Phase

B.10 AMA-RC-10, LP 335 EB OVER FM 1719

- Bridge ID: 41880263504079 (Potter County)
- Built in 2005
- Mitigation methods: HPC, CNI (2 gal./CY.) Linseed oil, ECR
- Observed CIP depth: 4.33 in.
- Observed clear cover: 2.0 – 2.2 in.
- 3 spans, 5-concrete PS girder @ 8.5’ spacing with 3’ overhangs
- Inspected on June 19, 2021

Figure 0.72. Concrete Deck of the Bridge (source: google maps)

B.10.1 Observed Condition

There are widespread longitudinal and transverse moderate cracks on the top surface of deck. Minor vertical and diagonal cracks were evident in the paint on the abutment backwall, along with staining between the girders. The overhang displayed some transverse cracks, although they did not span the full width of the overhang, and there was efflorescence near the girder flanges. All girder ends featured hairline diagonal cracks. The deck was constructed using PCP with thickened CIP link slabs. A few hairline longitudinal cracks were observed, and efflorescence was noted in some panel joints.

B.10.2 NDE Results

Grid 1 was located on the EB lane of the span 2, and Grid 2 was located on the 2nd span of the EB shoulder lane.

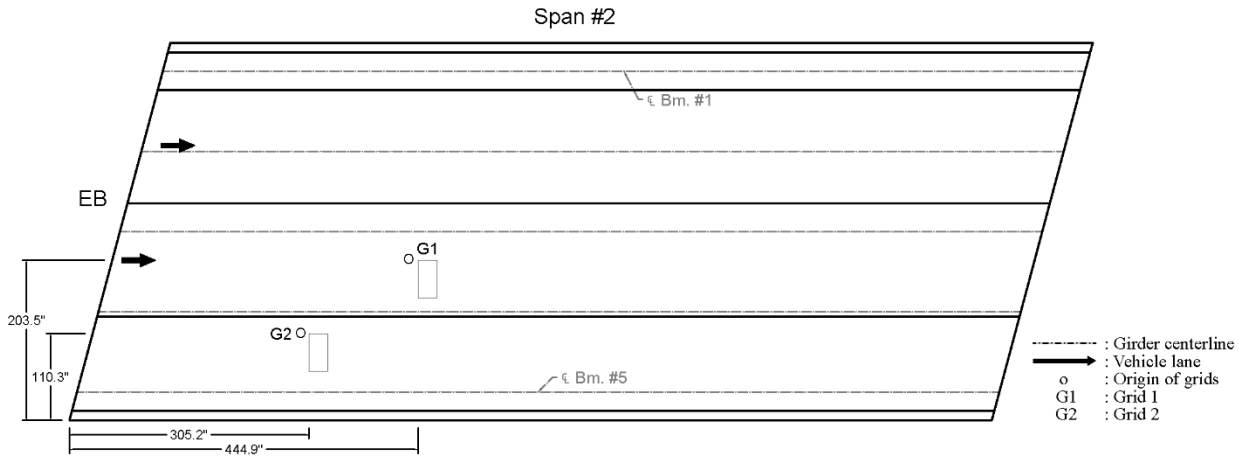

Figure 0.73. Plan View of the Bridge and Location of Grids

As shown in Figure 0.74 (a), there were cracks with width ranging from 0.006 in. to 0.01in. 0.01 in. transverse crack could have been caused by panel joints. Based on the Figure A. 10.3 (e), there is a possibility of corrosion on upper left corner of the Grid 1. Grid 2 has cracks ranging from 0.004 in. to 0.006 in. as shown in Figure 0.75 (a). The cracks could have been caused by panel joints.

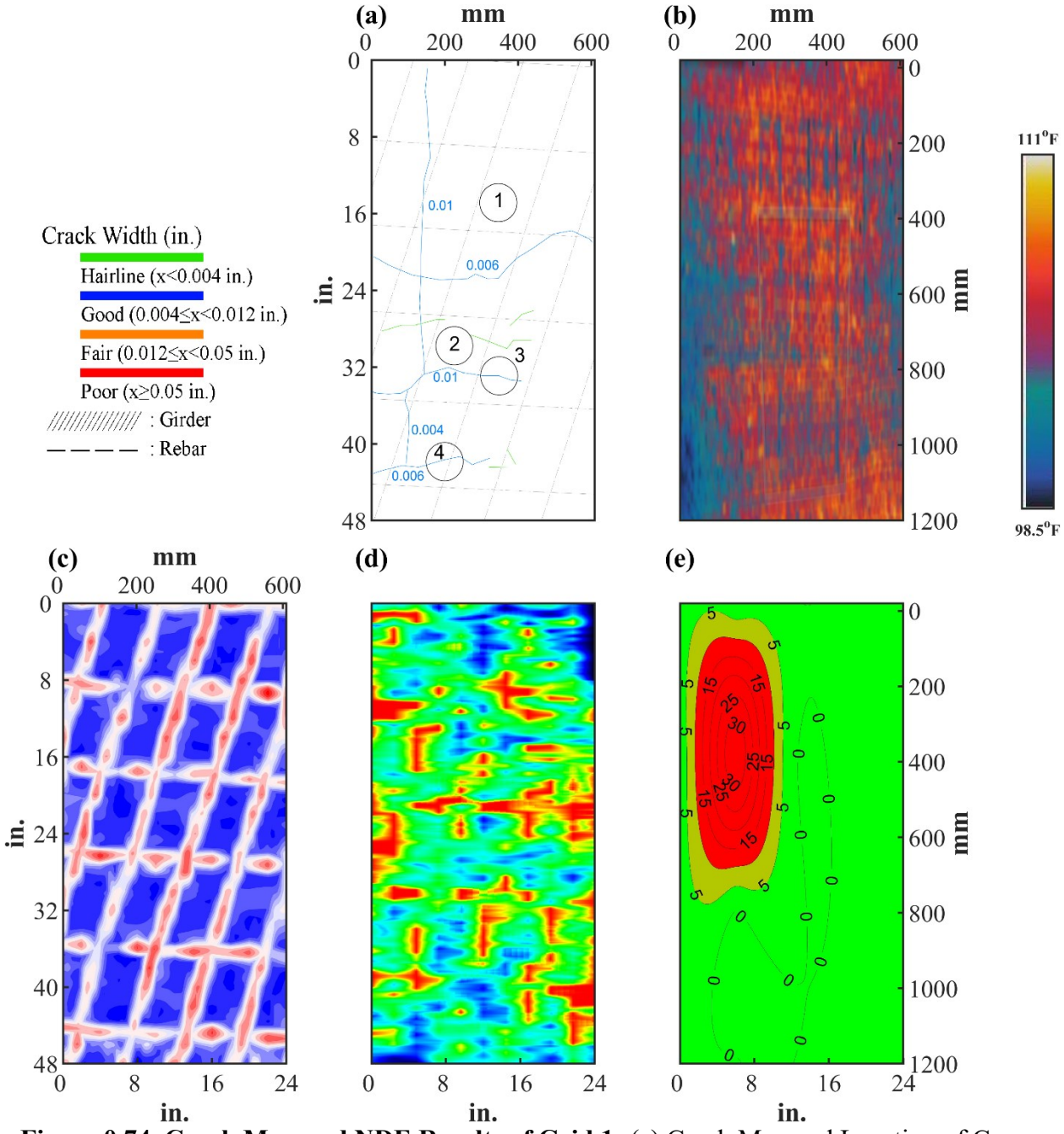

Figure 0.74. Crack Map and NDE Results of Grid 1: (a) Crack Map and Location of Cores; (b) Infrared Picture; (c) GPR C-scan at 1.8 in. to 2.9 in. Depth; (d) UST C-scan at 3.97 in. Depth; (e) Corrosion Rate Map

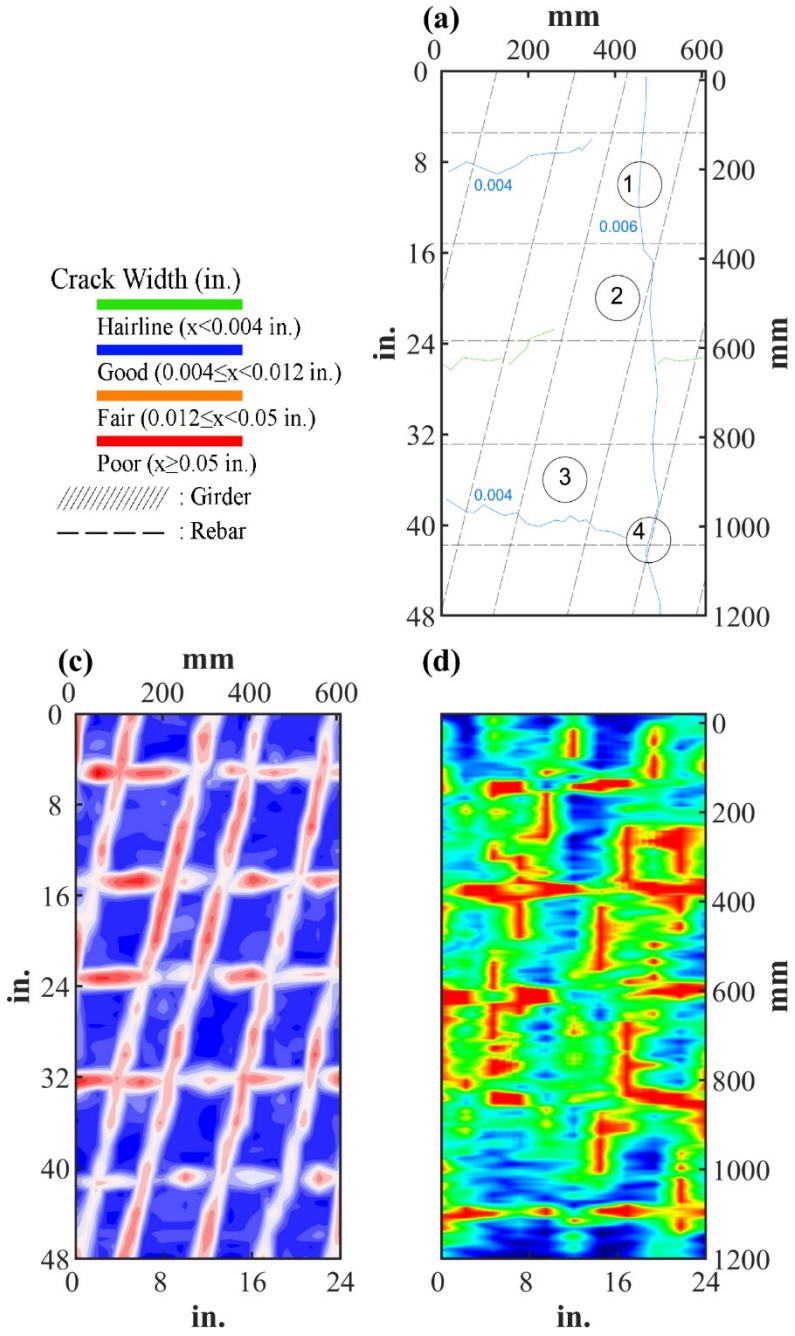

Figure 0.75. Crack Map and NDE Results of Grid 2: (a) Crack Map and Location of Cores; (c) GPR C-scan at 1.95 in. to 3.05 in. Depth; (d) UST C-scan at 3.56 in. Depth

B.10.3 Concrete Cores

Table B-53. Detail Information of Concrete Cores

Core	dia. × height (in.)	Rebar depth (in.)	Rebar size (#)	Epoxy (Y/N)	Crack type	Crack width (in)	Notes
1-1	3.75 × 5.9	-	-	-	-	-	-
1-2	3.75 × 5.9	-	-	-	-	-	-
1-3	3.75 × 5.9	-	-	-	diagonal	0.25	A crack propagates along intersection of aggregates
1-4	3.75 × 5.5	2.0	5	Y	diagonal	0.25	-
2-1	3.75 × 4.3	-	-	-	transverse	0.2	A crack propagates along intersection of aggregates; delamination between CIP and PCP
2-2	3.75 × 4.3	-	-	-	-	-	Delamination between CIP and PCP
2-3	-	-	-	-	-	-	Crushed core
2-4	3.75 × 4.5	2.2, 2.7	5, 4	Y, Y	diagonal	0.3	Delamination between CIP and PCP; Crack propagating from rebar

Table B-54. Core Pictures

Core	Side	Top	Bottom
1-1			
1-2			

1-3			
1-4			
2-1			
2-2			
2-3	-	-	-
2-4			

B.10.4 Laboratory Experiment Results

B.10.4.1 Resistivity

Core Number	Surface Resistivity (kΩ·m)	Bulk Resistivity (kΩ·m)
1-1	193	15
1-2	217	-
2-2	-	21

B.10.4.2 Ultrasonic Pulse Velocity

Core Number	Ultrasonic Pulse Velocity (m/s)
1-1	4253
1-2	4381
2-1	4286
2-2	4458

B.10.4.3 Carbonation Depth

Core Number	Carbonation Depth (in.)
1-3	0.00
2-4	0.00

B.10.4.4 Acid-Soluble Chloride Content

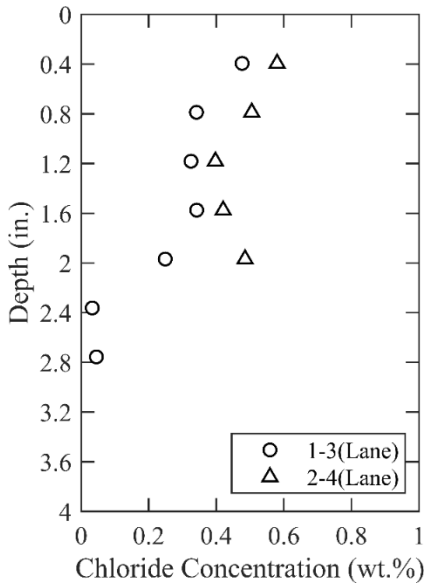

Figure 0.76. Chloride Content at Different Depth

B.10.4.5 Knife Test

Core Number	Score	Picture
2-4	2	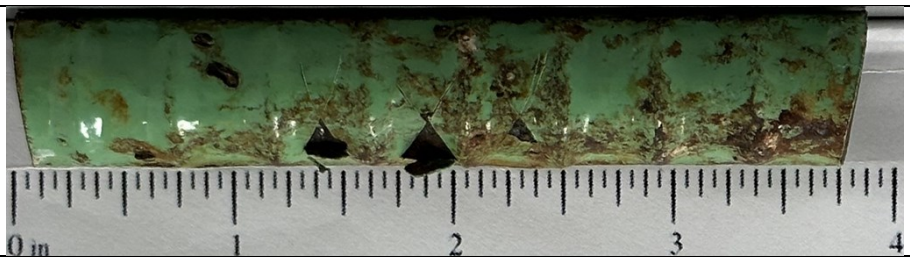

B.10.4.6 Electrochemical Impedance Spectroscopy

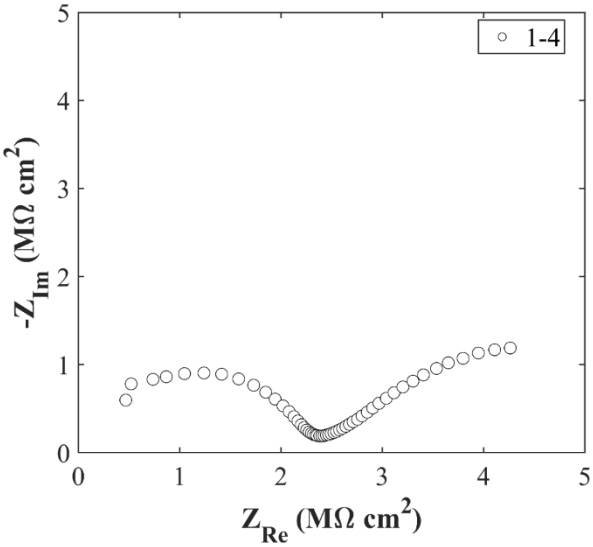

(a) Nyquist Diagram

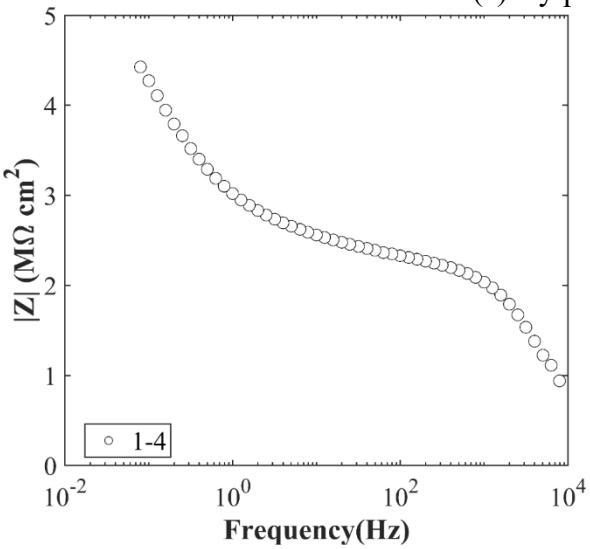

(b) Bode Plot of Impedance Modulus

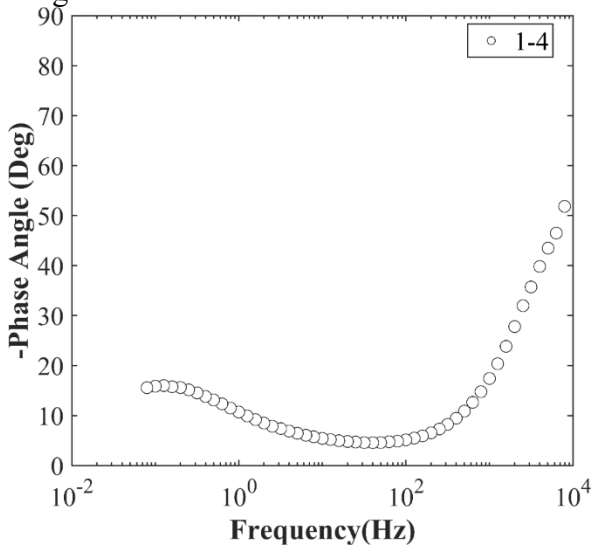

(c) Bode Plot of Impedance Phase

Figure 0.77. EIS Results: (a) Nyquist Diagram; (b) Bode Plot of Impedance Modulus; (c) Bode Plot of Impedance Phase

B.11 AMA-RC-11, US 287 SB OVER SOUTH PALO DURO CREEK

- Bridge ID: 41710006604030 (Moore County)
- Built in 2004
- Mitigation methods: MLPO, ECR
- Observed CIP depth: 4 in.
- Observed clear cover: 1.8 in.
- 3 spans, 5-concrete PS girder @ 8.5’ spacing with 3’ overhangs
- Inspected on June 14, 2021

Figure 0.78. Concrete Deck of the Bridge (source: google maps)

B.11.1 Observed Condition

The top surface of deck has asphalt overlay, and no crack was visible.

B.11.2 NDE Results

Grid 1 was located on the SB lane of the span 2, and Grid 2 was located on the 2nd span of the SB shoulder lane as shown in Figure 0.79.

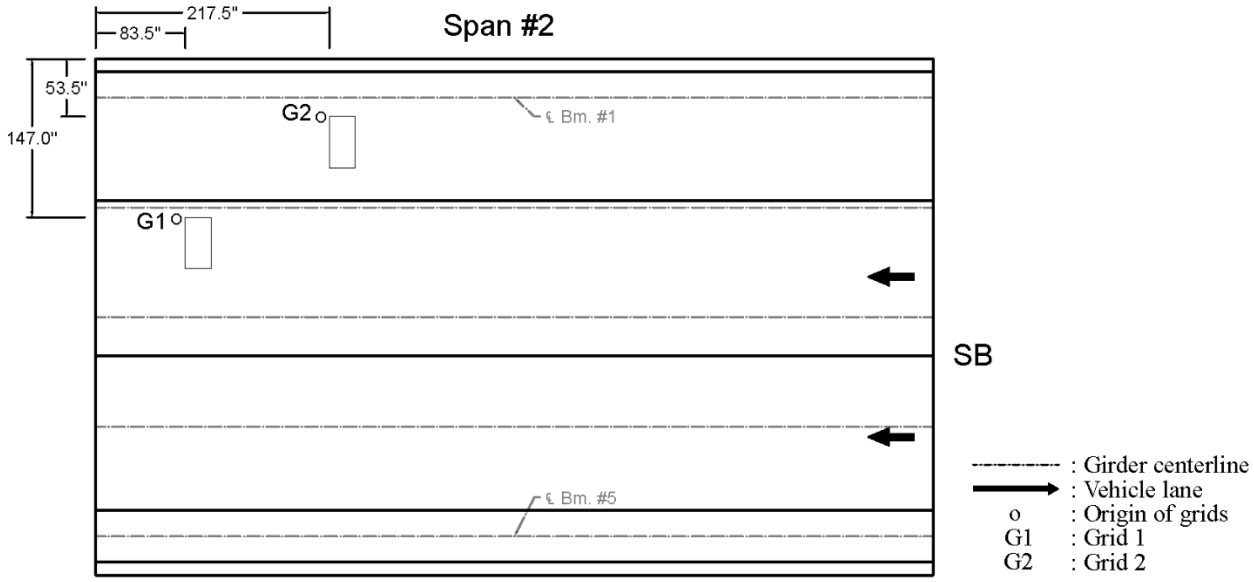

Figure 0.79. Plan View of the Bridge and Location of Grids

Asphalt overlay was applied on the bridge, and as a result, no cracks were visible on the deck as shown in Figure 0.80 (a) and Figure 0.81Figure 0.81 (a).

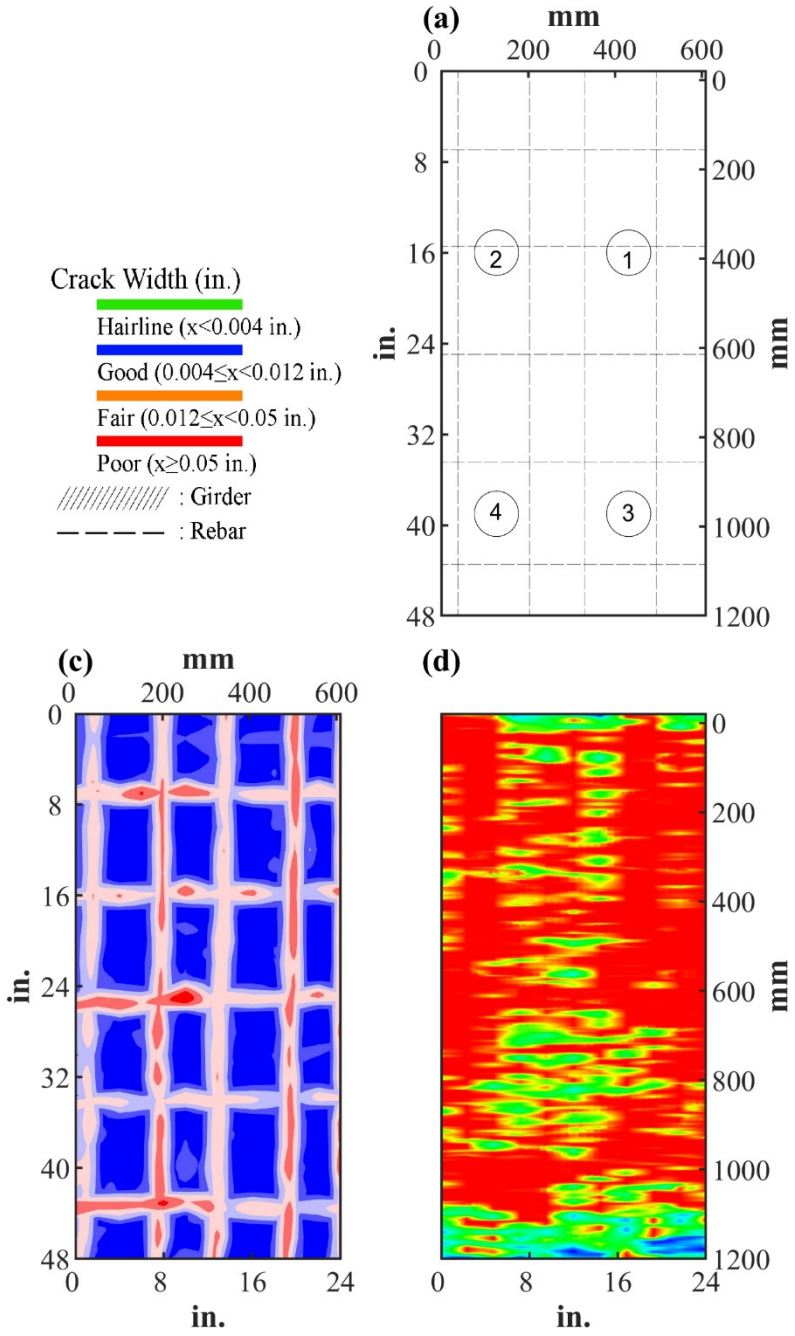

Figure 0.80. Crack Map and NDE Results of Grid 1: (a) Crack Map and Location of Cores; (c) GPR C-scan at 1.8 in. to 2.9 in. Depth; (d) UST C-scan at 1.96 in. Depth

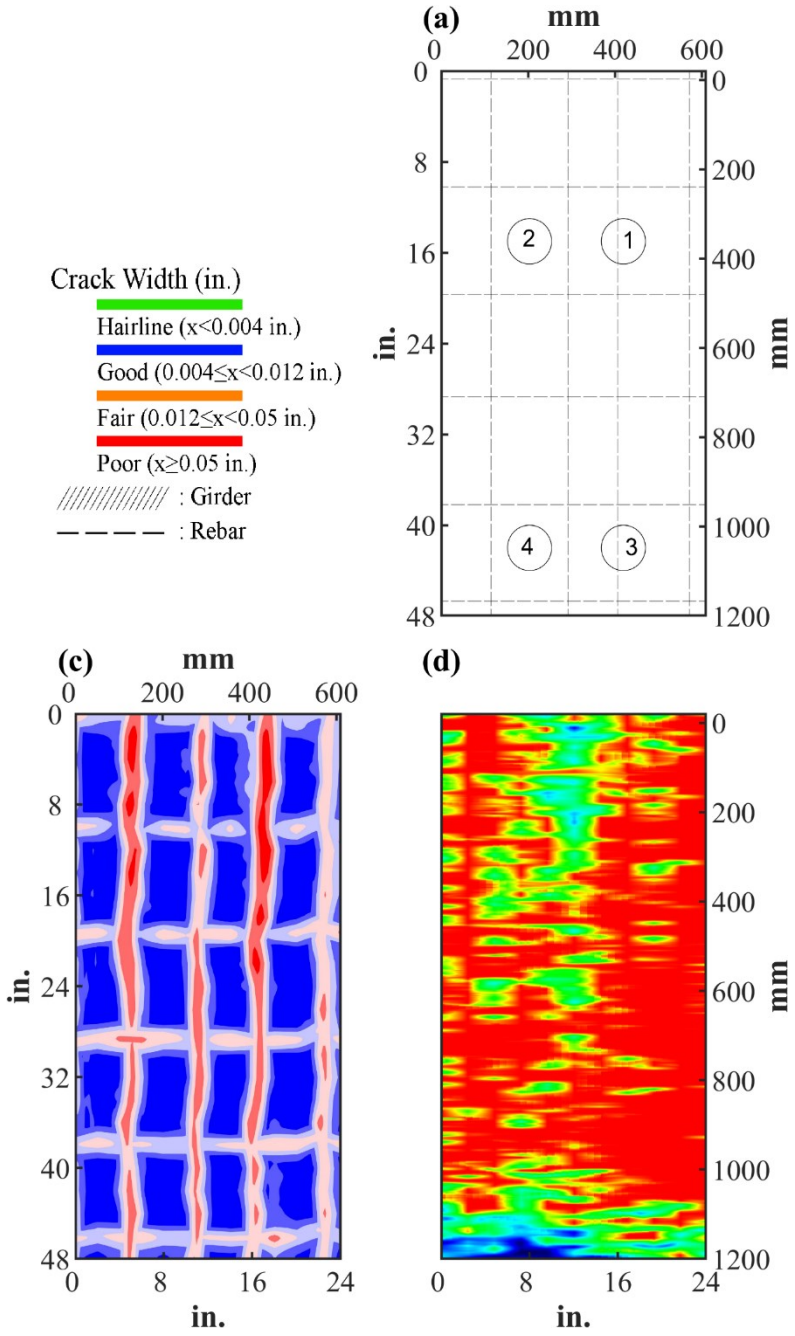

Figure 0.81. Crack map and NDE Results of Grid 2: (a) Crack Map and Location of Cores; (c) GPR C-scan at 1.45 in. to 2.55' Depth; (d) UST C-scan at 1.96 in. Depth

B.11.3 Concrete Cores

Table B-55. Detail Information of Concrete Cores

Core	dia. × height (in.)	Rebar depth (in.)	Rebar size (#)	Epoxy (Y/N)	Crack type	Crack width (in)	Notes
1-1	3.75 × 4.7	1.8	5	Y	-	-	-
1-2	3.75 × 4.7	-	-	-	-	-	-
1-3	3.75 × 4.7	1.8	5	Y	-	-	-
1-4	3.75 × 4.7	-	-	-	-	-	-
2-1	3.75 × 4.1	2.9	4	Y	-	-	-
2-2	3.75 × 5.5	2.9	4	Y	-	-	-
2-3	3.75 × 5.9	-	-	-	-	-	-
2-4	3.75 × 6.3	-	-	-	-	-	-

Table B-56. Core Pictures

Core	Side	Top	Bottom
1-1			
1-2			
1-3			

1-4			
2-1			
2-2			
2-3			
2-4		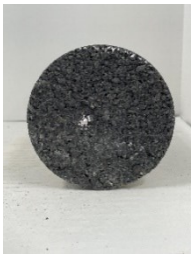	

B.11.4 Laboratory Experiment Results

B.11.4.1 Resistivity

Core Number	Surface Resistivity (kΩ·m)	Bulk Resistivity (kΩ·m)
1-4	187	21
2-2	151	-
2-4	-	22

B.11.4.2 Ultrasonic Pulse Velocity

Core Number	Ultrasonic Pulse Velocity (m/s)
1-3	4255
1-4	4242
2-2	4135
2-4	4239

B.11.4.3 Carbonation Depth

Core Number	Carbonation Depth (in.)
1-2	0.00
2-1	0.00

B.11.4.4 Acid-Soluble Chloride Content

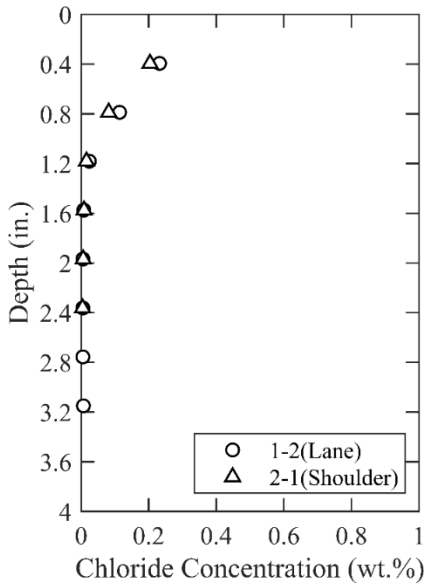

Figure 0.82. Chloride Content at Different Depth

B.11.4.5 Sorptivity

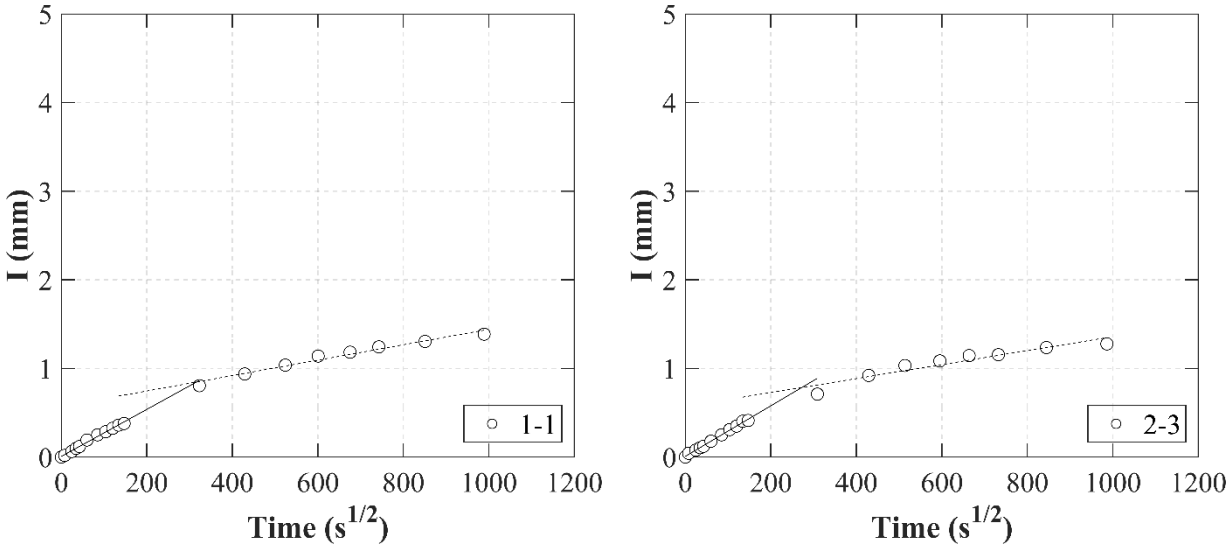

(a) Core 1–1 (b) Core 2–3

Figure 0.83. Absorption and Sorptivity of: (a) Core 1–1; (b) Core 2–3

Table B-57. Initial and Secondary Sorptivity Results

Core Number	Sorptivity	Results (mm/s$^{1/2}$)
Core 1–1	Initial Sorptivity	0.00266
	Secondary Sorptivity	0.00087
Core 2–3	Initial Sorptivity	0.00285
	Secondary Sorptivity	0.00079

B.11.4.6 Knife Test

Core Number	Score	Picture
2-1	10	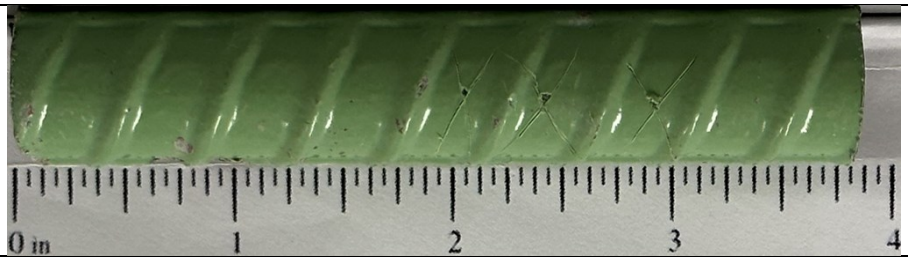

B.11.4.7 Electrochemical Impedance Spectroscopy

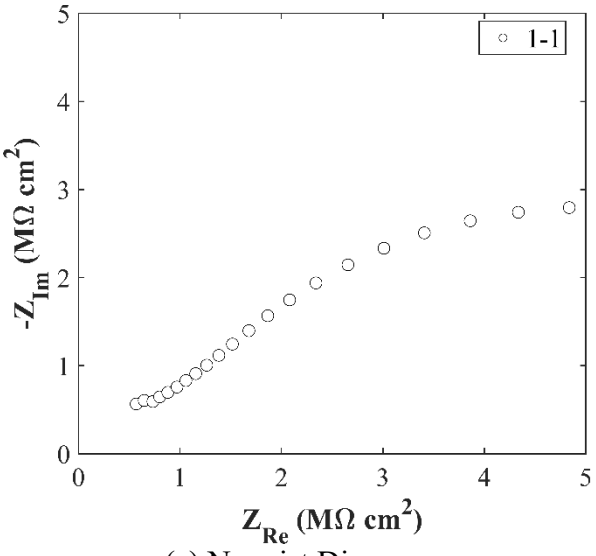

(a) Nyquist Diagram

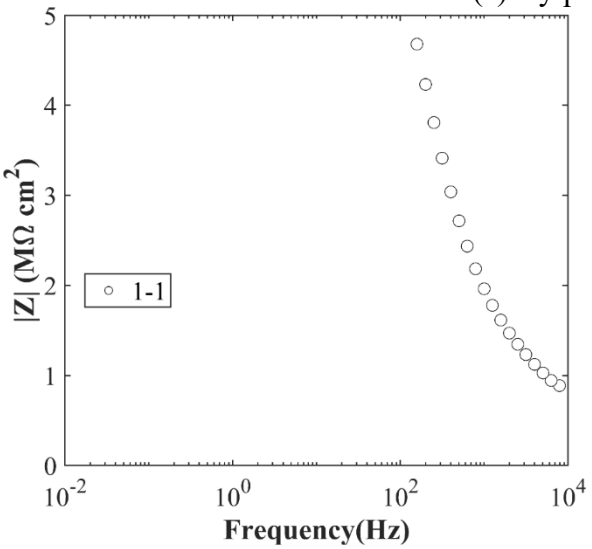

(b) Bode Plot of Impedance Modulus

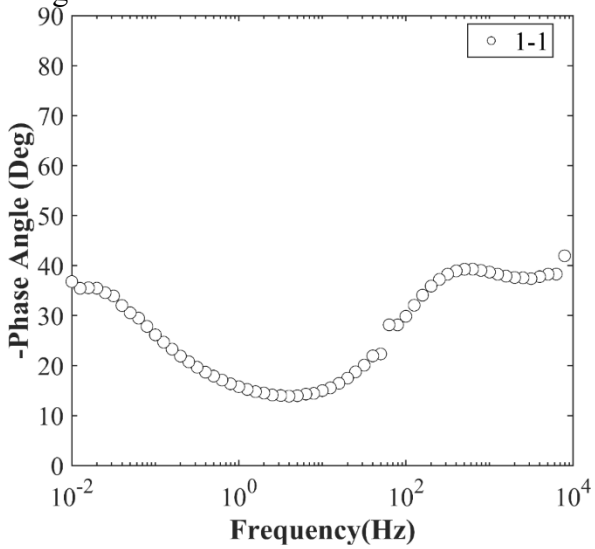

(c) Bode Plot of Impedance Phase

Figure 0.84. EIS Results: (a) Nyquist Diagram; (b) Bode Plot of Impedance Modulus; (c) Bode Plot of Impedance Phase

B.12 AMA-RC-12, US 287 SB OVER COLDWATER CREEK

- Bridge ID: 42110006603003 (Sherman County)
- Built in 2003
- Mitigation methods: MLPO, ECR
- Observed CIP depth: 4.33 in.
- Observed clear cover: 2.5 in.
- 3 spans, 5-concrete PS girder @ 8.5’ spacing with 3’ overhangs
- Inspected on June 14, 2021

Figure 0.85. Concrete Deck of the Bridge (source: google maps)

B.12.1 Observed Condition

The top surface of deck has asphalt overlay, and no crack was visible.

B.12.2 NDE Results

Grid 1 was located on the SB lane of the span 2, and Grid 2 was located on the 2nd span of the SB shoulder lane.

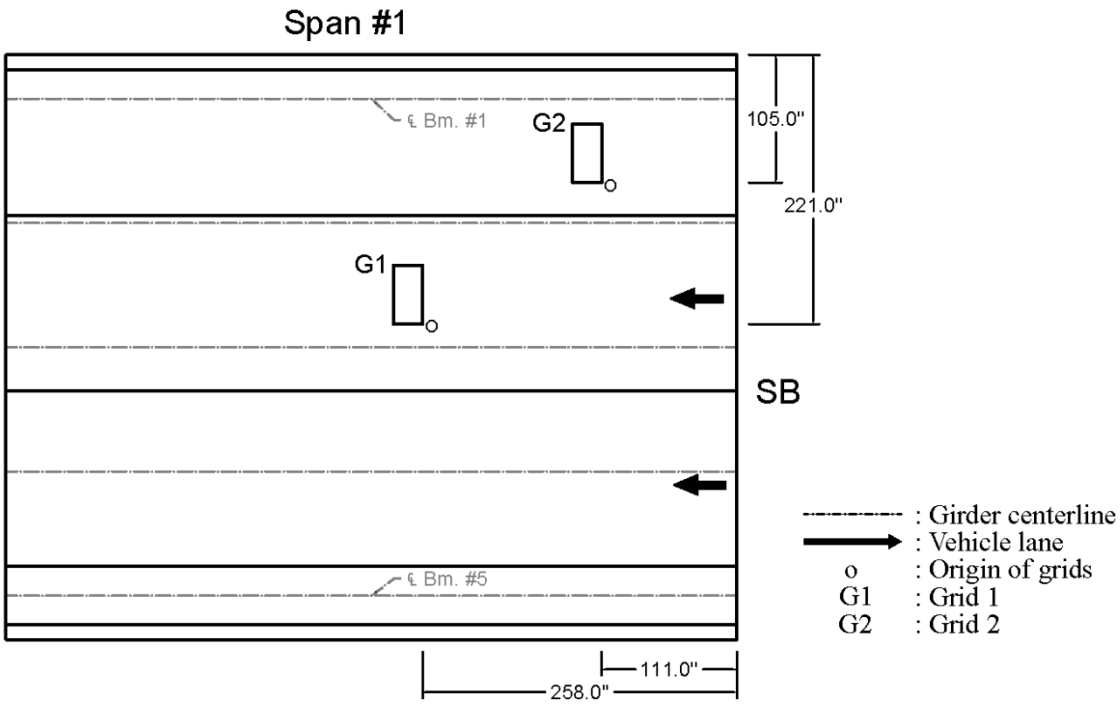

Figure 0.86. Plan View of the Bridge and Location of Grids

Asphalt overlay was applied on the bridge, and as a result, no cracks were visible on the deck as shown in Figure 0.87 (a) and Figure 0.88Figure 0.81 (a).

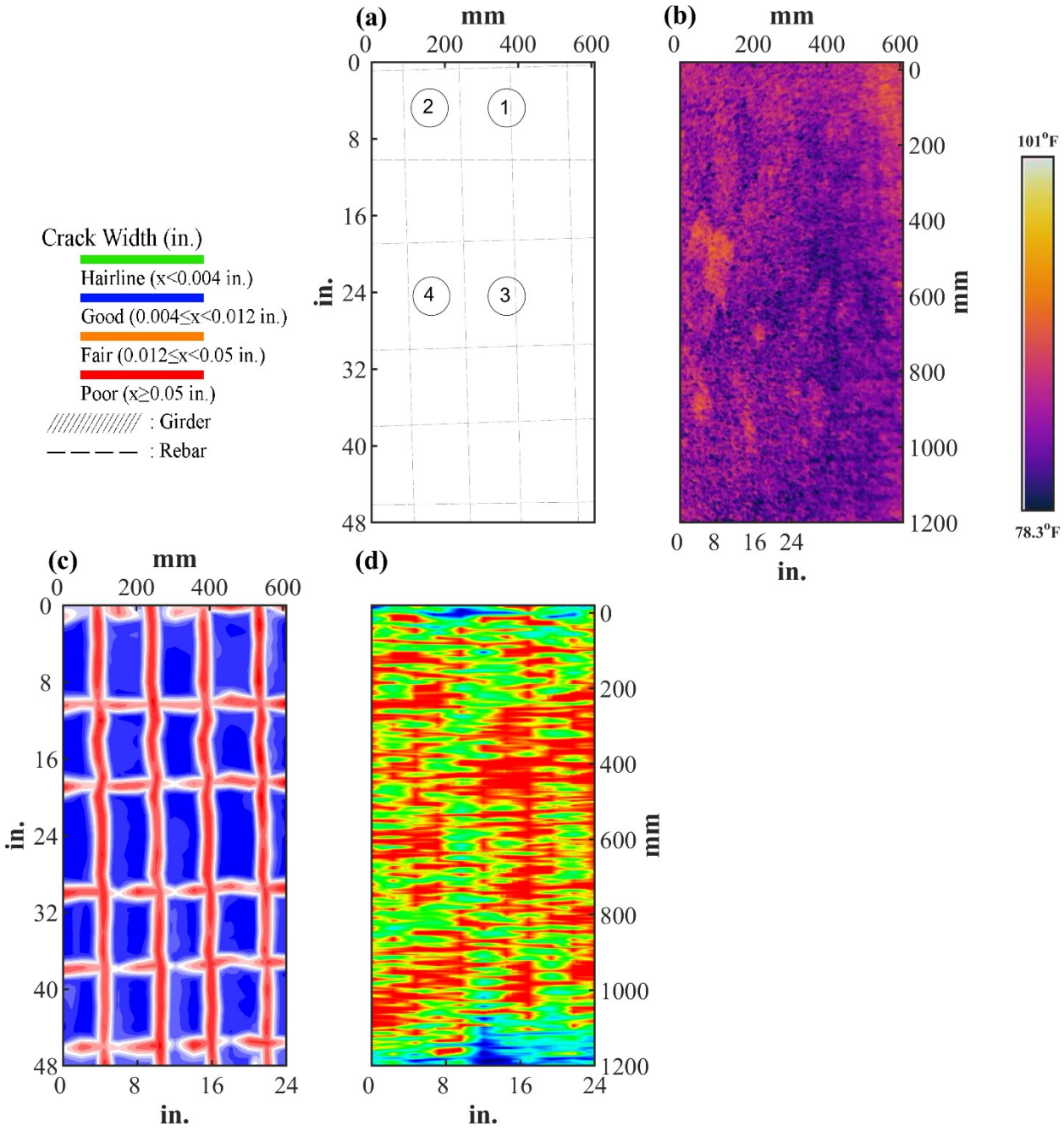

Figure 0.87. Crack Map and NDE Results of Grid 1: (a) Crack Map and Location of Cores; (b) Infrared Picture; (c) GPR C-scan at 1.95 in. to 3.05 in. Depth; (d) UST C-scan at 1.96 in. Depth

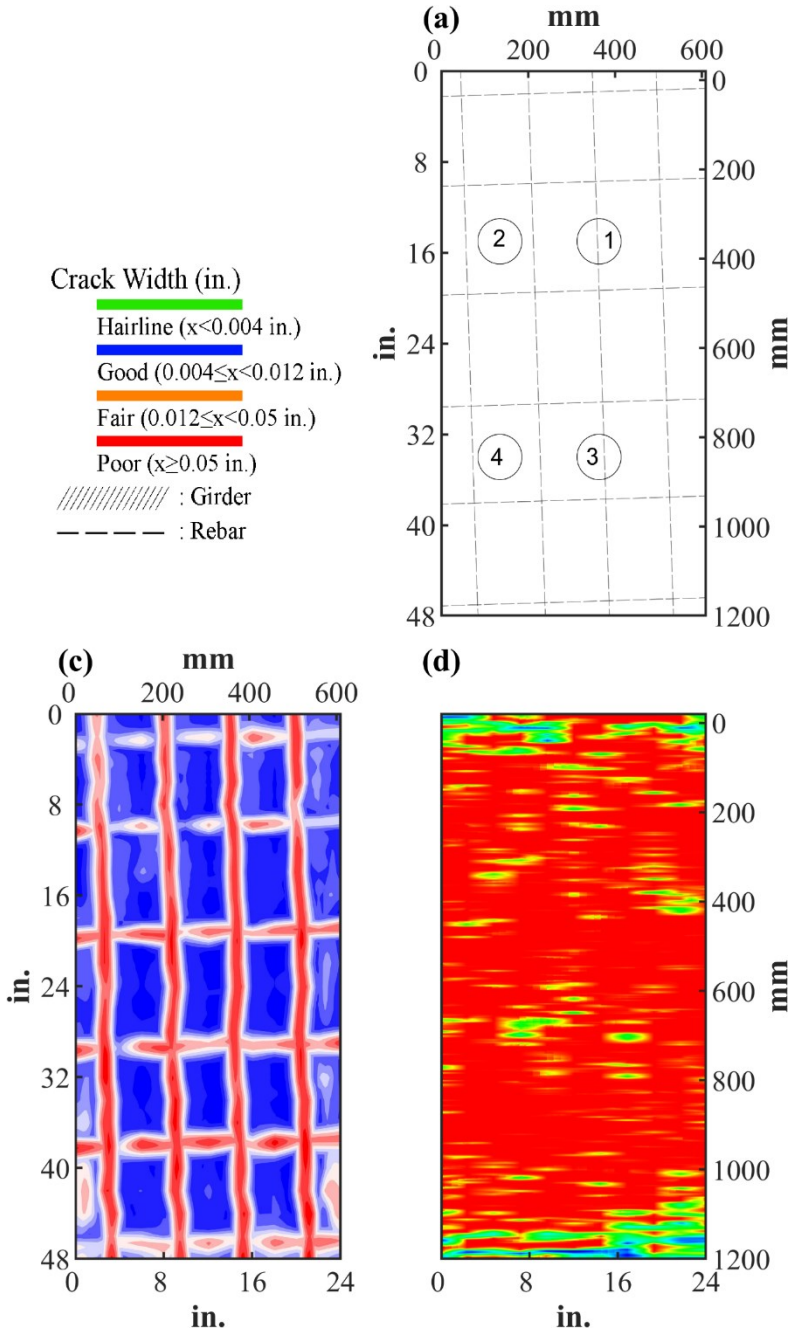

Figure 0.88. Crack Map and NDE Results of Grid 2: (a) Crack Map and Location of Cores; c) GPR C-scan at 2.2 in. to 3.3 in. Depth; (d) UST C-scan at 1.96 in. Depth

B.12.3 Concrete Cores

Table B-58. Detail Information of Concrete Cores

Core	dia. × height (in.)	Rebar depth (in.)	Rebar size (#)	Epoxy (Y/N)	Crack type	Crack width (in)	Notes
1-1	3.75 × 5.9	2.5	5	Y	-	-	-
1-2	3.75 × 5.9	-	-	-	-	-	-
1-3	3.75 × 5.9	2.5	5	Y	-	-	-
1-4	3.75 × 6.1	-	-	-	-	-	-
2-1	3.75 × 6.5	2.6	5	Y	-	-	-
2-2	3.75 × 4.1	-	-	-	-	-	-
2-3	3.75 × 6.1	2.4	5	Y	-	-	-
2-4	3.75 × 6.0	-	-	-	-	-	-

Table B-59. Core Pictures

Core	Side	Top	Bottom
1-1			
1-2	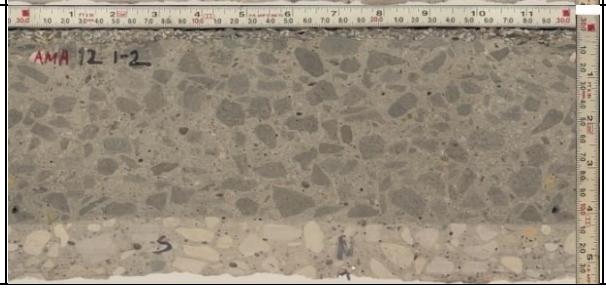		

1-3			
1-4			
2-1			
2-2			
2-3			

2-4			

B.12.4 Laboratory Experiment Results

B.12.4.1 Resistivity

Core Number	Surface Resistivity (kΩ·m)	Bulk Resistivity (kΩ·m)
1-2	44	6
1-4	44	-
2-2	35	-
2-4	32	5

B.12.4.2 Ultrasonic Pulse Velocity

Core Number	Ultrasonic Pulse Velocity (m/s)
1-2	3968
1-4	4036
2-2	4261
2-4	3892

B.12.4.3 Carbonation Depth

Core Number	Carbonation Depth (in.)
1-1	0.00
2-3	0.16

B.12.4.4 Acid-Soluble Chloride Content

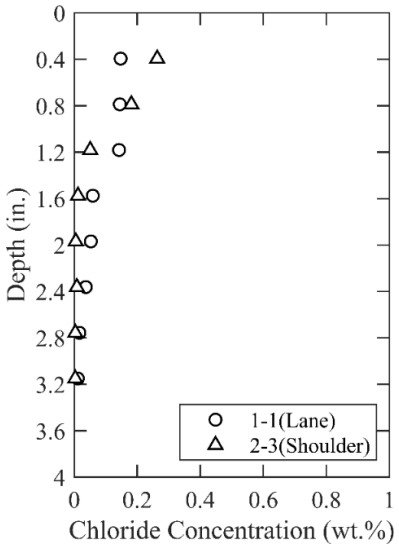

Figure 0.89. Chloride Content at Different Depth

B.12.4.5 Sorptivity

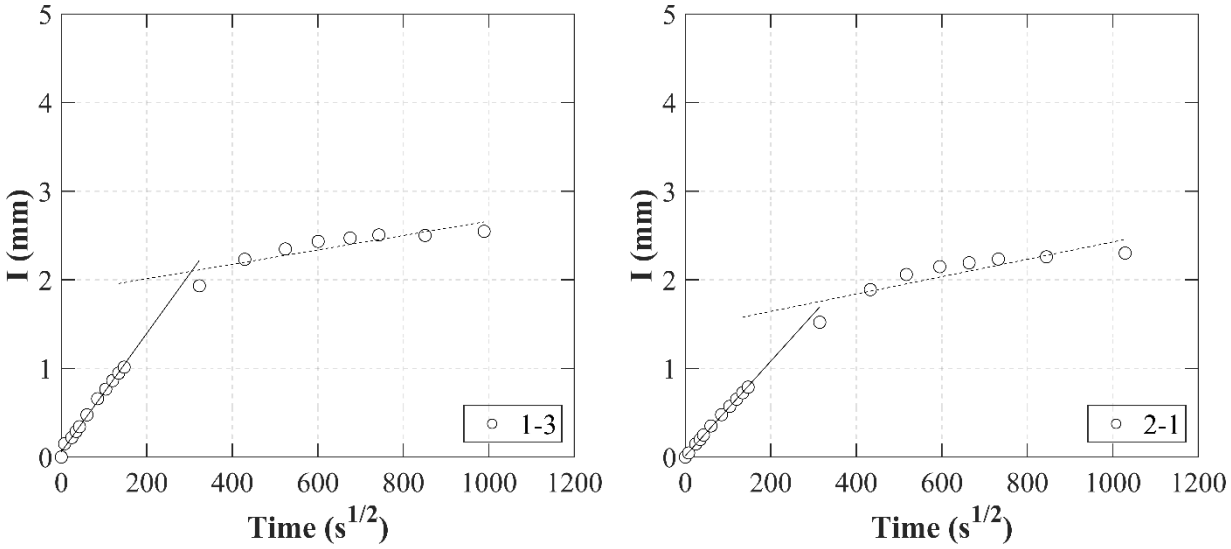

(a) Core 1–3 (b) Core 2–1

Figure 0.90. Absorption and Sorptivity of: (a) Core 1–3; (b) Core 2–1

Table B-60. Initial and Secondary Sorptivity Results

Core Number	Sorptivity	Results (mm/s$^{1/2}$)
Core 1–3	Initial Sorptivity	0.00669
	Secondary Sorptivity	0.00081
Core 2–1	Initial Sorptivity	0.00534
	Secondary Sorptivity	0.00098

B.12.4.6 Knife Test

Core Number	Score	Picture
1-1	10	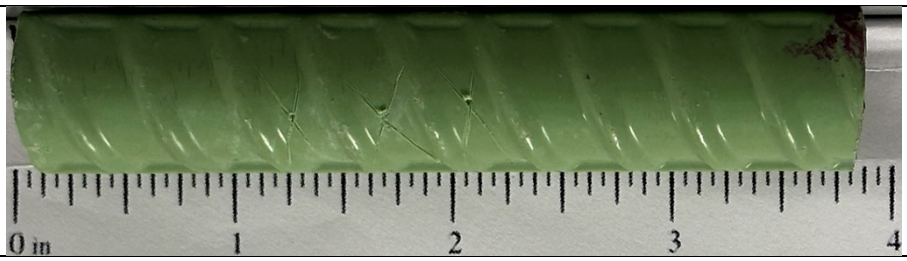

B.12.4.7 Electrochemical Impedance Spectroscopy

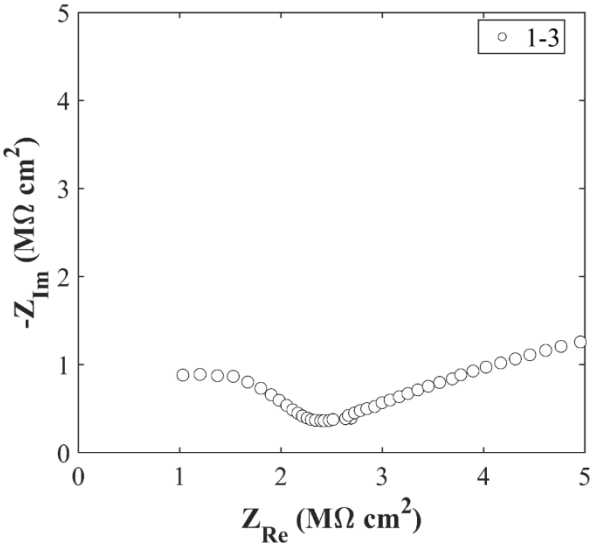

(a) Nyquist Diagram

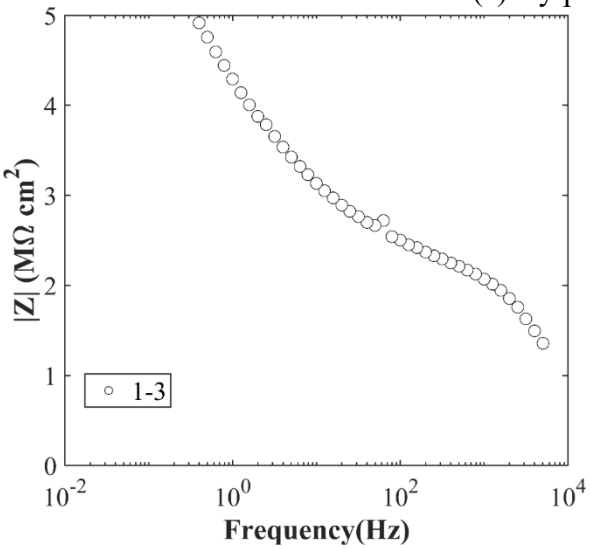

(b) Bode Plot of Impedance Modulus

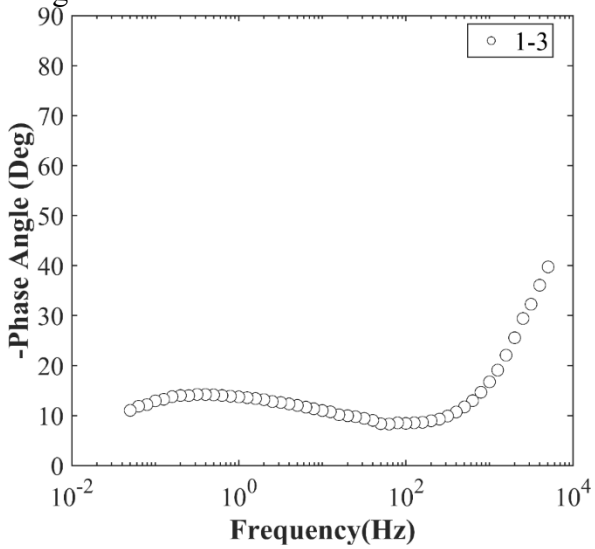

(c) Bode Plot of Impedance Phase

Figure 0.91. EIS Results: (a) Nyquist Diagram; (b) Bode Plot of Impedance Modulus; (c) Bode Plot of Impedance Phase

B.13 ATL-RC-01, IH 369 SB OVER UPRR & FINDLEY ST

- Bridge ID: 190190021802051 (Bowie County)
- Built in 1981
- Mitigation methods: None
- Observed CIP depth: 5 in.
- Observed clear cover: 3.0 in.
- 5 spans, 5-concrete PS girder @ 8.5’ spacing with 3’ overhangs
- Inspected on July 12, 2021

Figure 0.92. Concrete Deck of the Bridge (source: google maps)

B.13.1 Observed Condition

The top surface of deck has hairline and some transverse, longitudinal cracks. The west rails have minor spalling and exposed rebar along its bottom is corroded as shown in Figure 0.93. Spalling at the both west and east end of the backwall of Abutment 1. Water staining was visible at the bottom of the overhang, but no cracks were apparent. The girders bottom flanges exhibited honeycombing. Water leakage through the west overhangs at the bents was apparent.

Figure 0.93. Exposed and Corroded Rebar at the Bottom of Railing

B.13.2 NDE Results

Grid 1 was located on the SB lane, and Grid 2 was located on the SB shoulder lane of the span 1 of the bridge as shown in Figure 0.94.

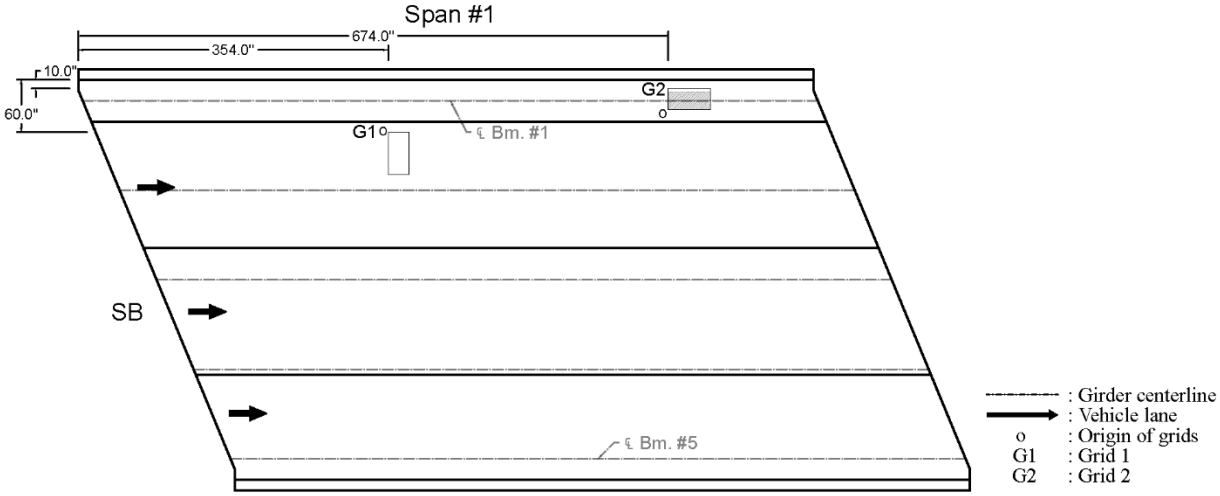

Figure 0.94. Plan View of Bridge and Location of Grids

As shown in Figure 0.95 (a), one 0.006 in. wide crack in transverse direction was visible, possibly caused by panel joints. The Grid 2 had transverse cracks that are 0.007 in. and 0.008 in. wide as shown in Figure 0.96. It is possible that the cracks were caused by panel joints.

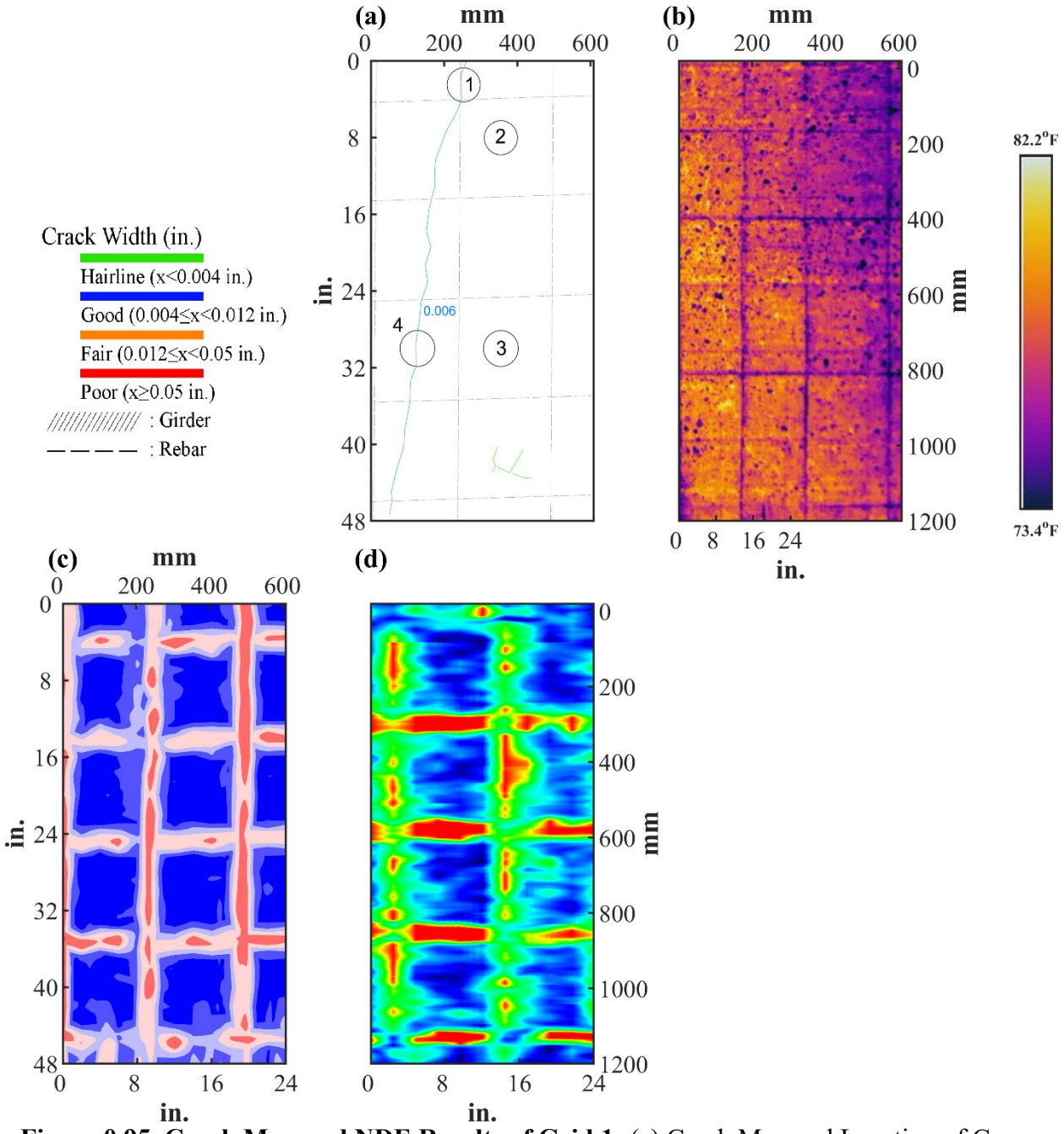

Figure 0.95. Crack Map and NDE Results of Grid 1: (a) Crack Map and Location of Cores; (b) Infrared Picture; (c) GPR C-scan at 2.2 in. to 3.3 in. Depth; (d) UST C-scan at 4.3 in. Depth

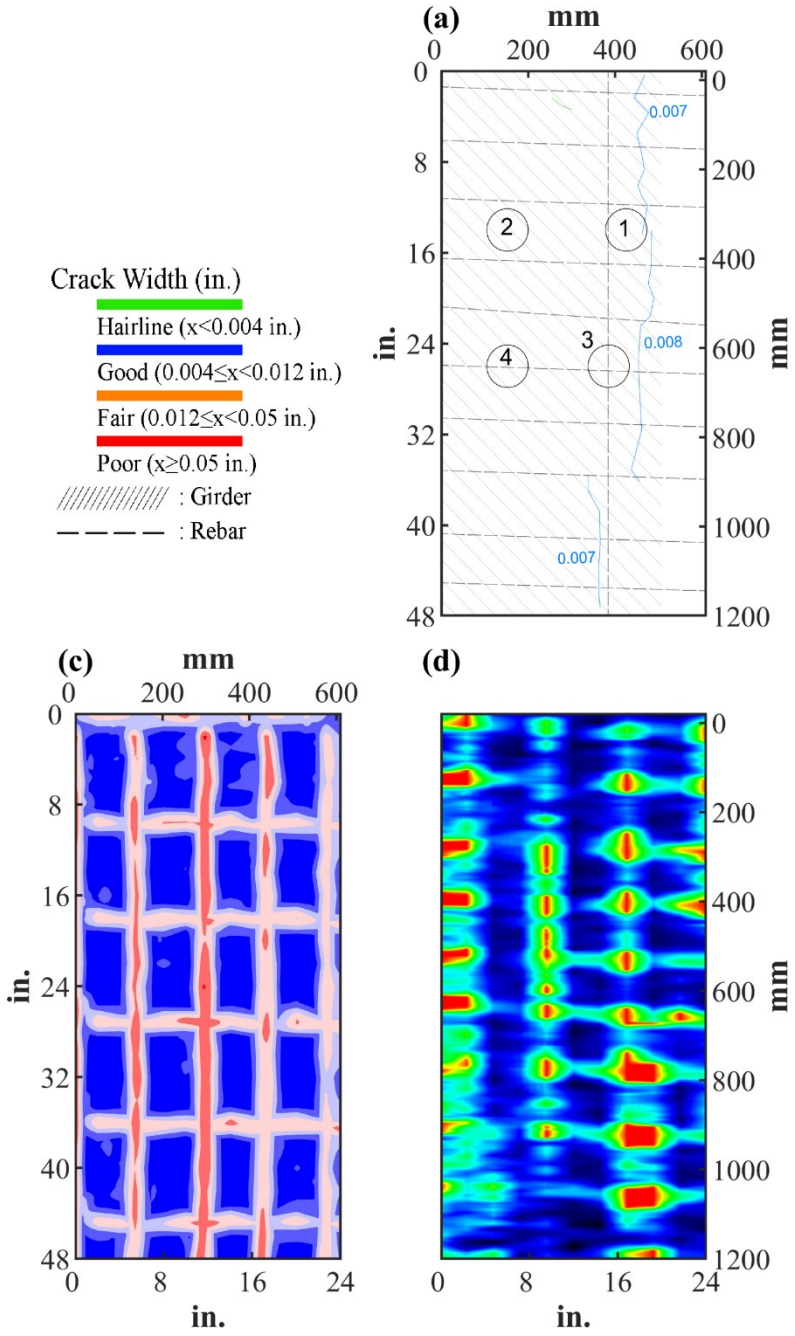

Figure 0.96. Crack Map and NDE Results of Grid 2: (a) Crack Map and Location of Cores; (c) GPR C-scan at 1.95 in. to 3.05 in. Depth; (d) UST C-scan at 4.3 in. Depth

B.13.3 Concrete Cores

Table B-61. Detail Information of Concrete Cores

Core	dia. x height (in.)	Rebar depth (in.)	Rebar size (#)	Epoxy (Y/N)	Crack type	Crack width (in)	Notes
1-1	3.75 x 5.9	2.91; 3.62	5	-	transverse	0.006	A crack propagates along intersection of aggregates
1-2	3.75 x 5.1	-	-	-	-	-	-
1-3	3.75 x 5.9	-	-	-	-	-	-
1-4	3.75 x 5.5	-	-	-	transverse	0.007	-
2-1	3.75 x 5.5	3.54	5	-	longitudinal	HL	A crack propagates along intersection of aggregates
2-2	3.75 x 5.9	-	-	-	-	-	-
2-3	3.75 x 6.2	3.54; 4.21	5	-	-	-	-
2-4	3.75 x 5.9	3.43	5	-	-	-	-

Table B-62. Core Pictures

Core	Pictures of the Cores
1-1	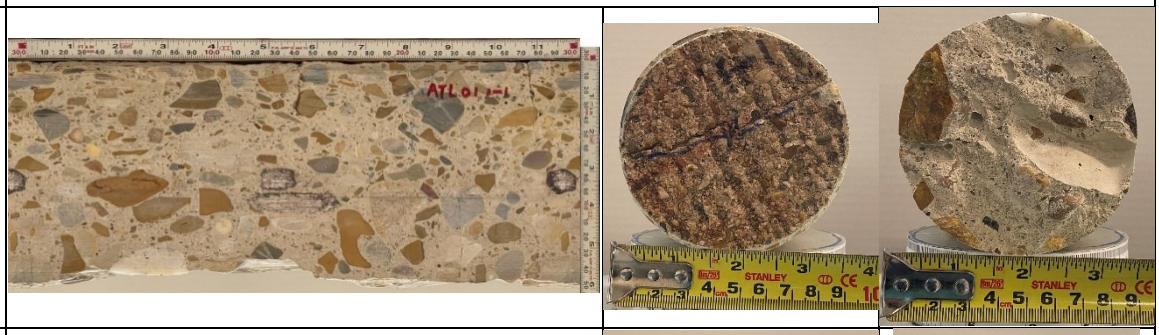
1-2	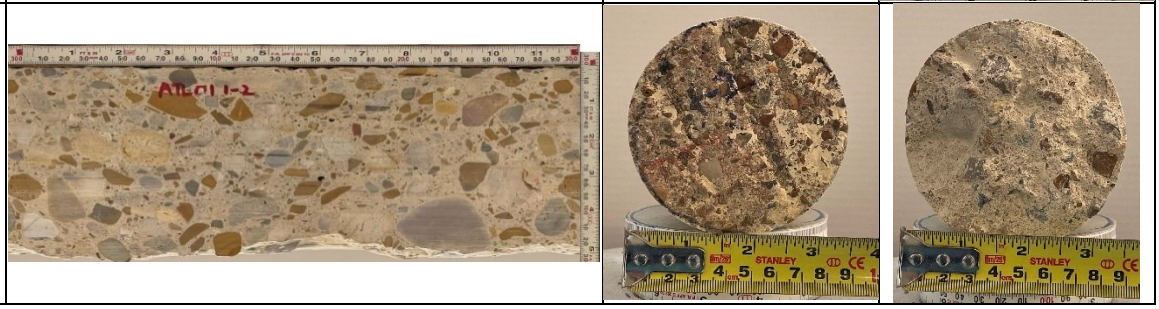

1-3		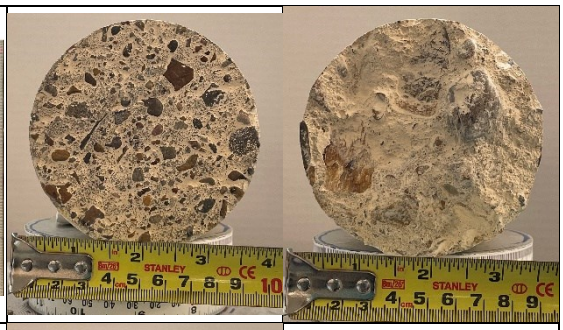
1-4		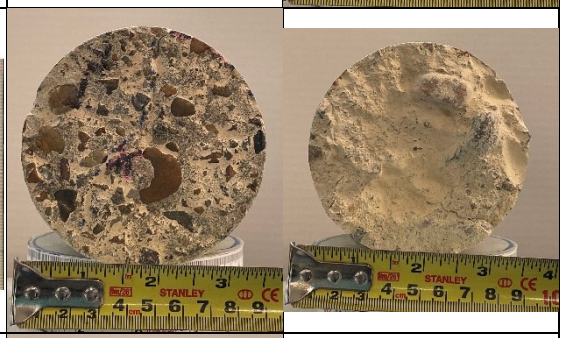
2-1		
2-2		
2-3		

2-4		

B.13.4 Laboratory Experiment Results

B.13.4.1 Resistivity

Core Number	Surface Resistivity (kΩ·m)	Bulk Resistivity (kΩ·m)
1-2	50.4	7.3
1-3	36.9	-
1-4	39.0	-
2-2	44.8	7.7

B.13.4.2 Ultrasonic Pulse Velocity

Core Number	Ultrasonic Pulse Velocity (m/s)
1-2	4274
1-3	4261
1-4	4212
2-2	4220

B.13.4.3 Carbonation Depth

Core Number	Carbonation Depth (in.)
1-4	0.00
2-3	0.00

B.13.4.4 Acid-Soluble Chloride Content

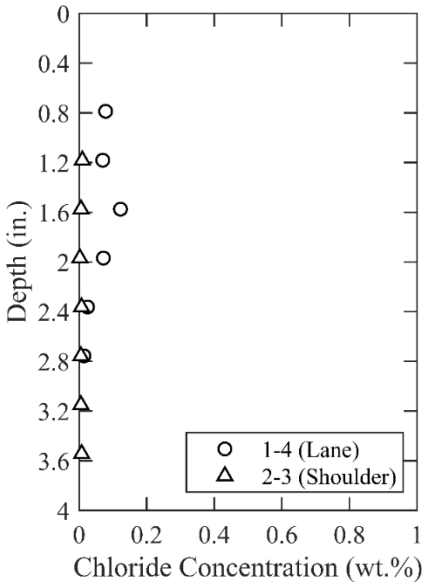

Figure 0.97. Chloride Content at Different Depth

B.13.4.5 Sorptivity

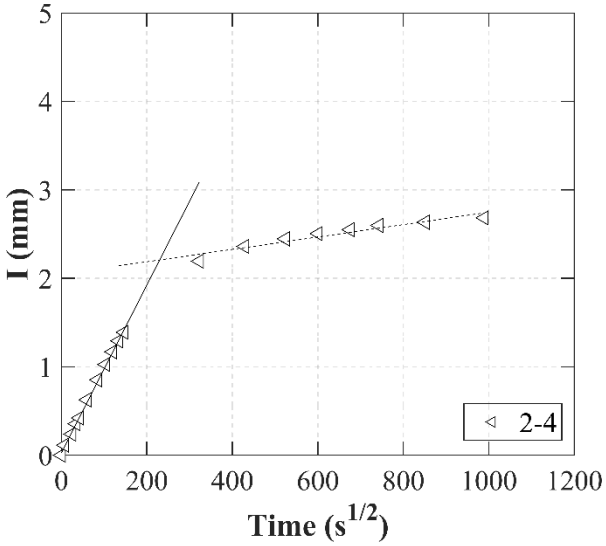

Figure 0.98. Absorption and Sorptivity of Core 2–4

Table B-63. Initial and Secondary Sorptivity Results

Core Number	Sorptivity	Results (mm/s$^{1/2}$)
Core 2–4	Initial Sorptivity	0.00948
	Secondary Sorptivity	0.00070

B.14 ATL-RC-02, IH 30 OVER COWHORN CREEK RD

- Bridge ID: 190190061007190 (Bowie County)
- Built in 1999
- Mitigation methods: None
- Observed CIP depth: 3 in.
- Observed clear cover: 0.3 in.
- 6 spans, 7-concrete PS girder @ 8.64’ spacing with 3’ overhangs at spans 1, 2, 3, 4, and 5; 8-concrete PS girder @ 7.4’ spacing with 3’ overhangs at span 6
- SB lane and shoulder inspected on July 13, 2021

Figure 0.99. Concrete Deck of the Bridge (source: google maps)

B.14.1 Observed Condition

Transverse cracks were present at the panel joints, and a longitudinal crack was visible, likely over a girder. Drains at the barrier were found to be plugged. Underneath the bridge, on the southwest side, a horizontal crack measuring 0.005 in. was observed at the top of the abutment backwall. The exterior of Beam 7 end exhibited a longitudinal crack on top of the bottom flange, measuring 0.004 in. wide. The overhang showed no visible cracks.

B.14.2 NDE Results

Grid 1 was located on the SB lane, and Grid 2 was located on the SB shoulder lane of the span 4 of the bridge as shown in Figure 0.100.

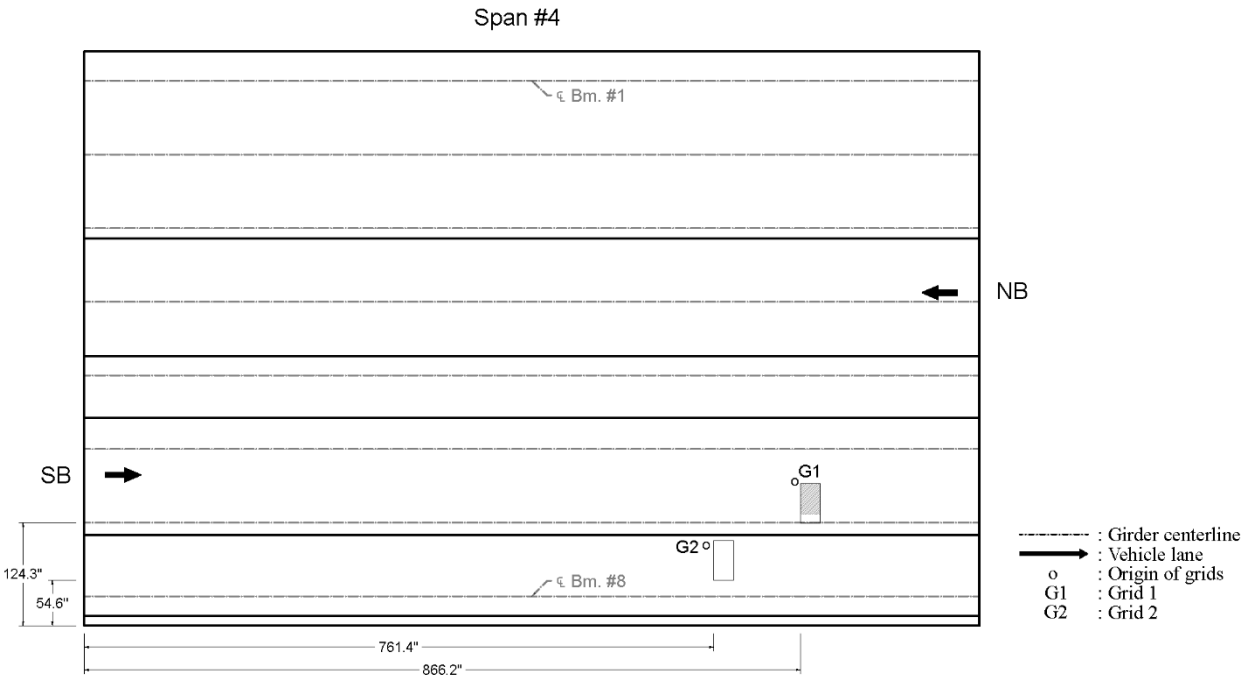

Figure 0.100. Plan View of the Bridge and Location of Grids

As shown in Figure 0.101 (a), G1 had widespread of hairline cracks with one 0.004 in. wide transverse crack and one 0.004 in. wide longitudinal cracks. It is possible that the longitudinal crack was caused by a girder and transverse crack was caused by panel joints. As shown in Figure 0.102 (a), hairline cracks were wide spread, and there were two 0.004 in. wide transverse cracks.

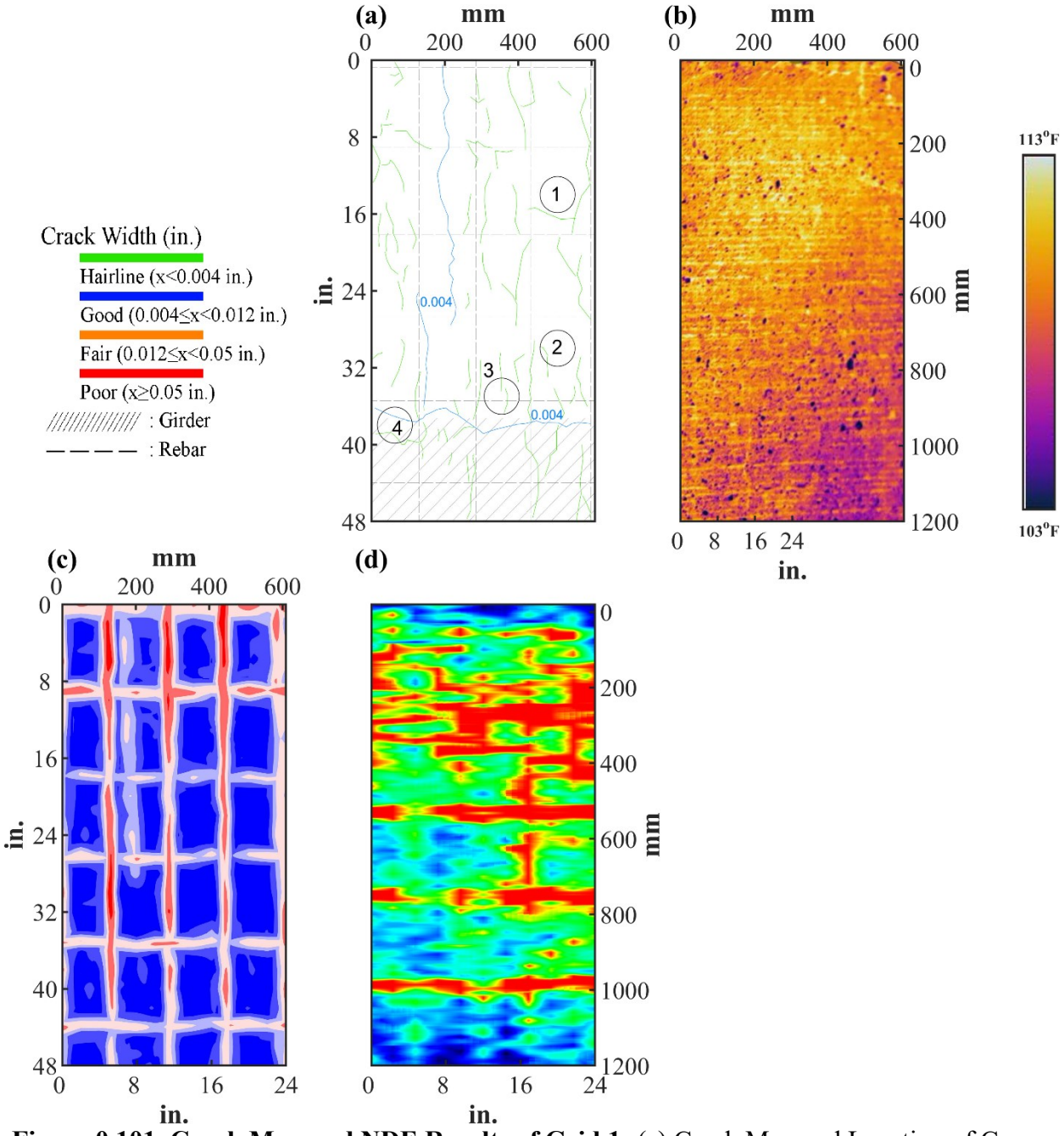

Figure 0.101. Crack Map and NDE Results of Grid 1: (a) Crack Map and Location of Cores; (b) Infrared Picture; (c) GPR C-scan at 1.2 in. to 2.3 in. Depth; (d) UST C-scan at 3.1 in. Depth

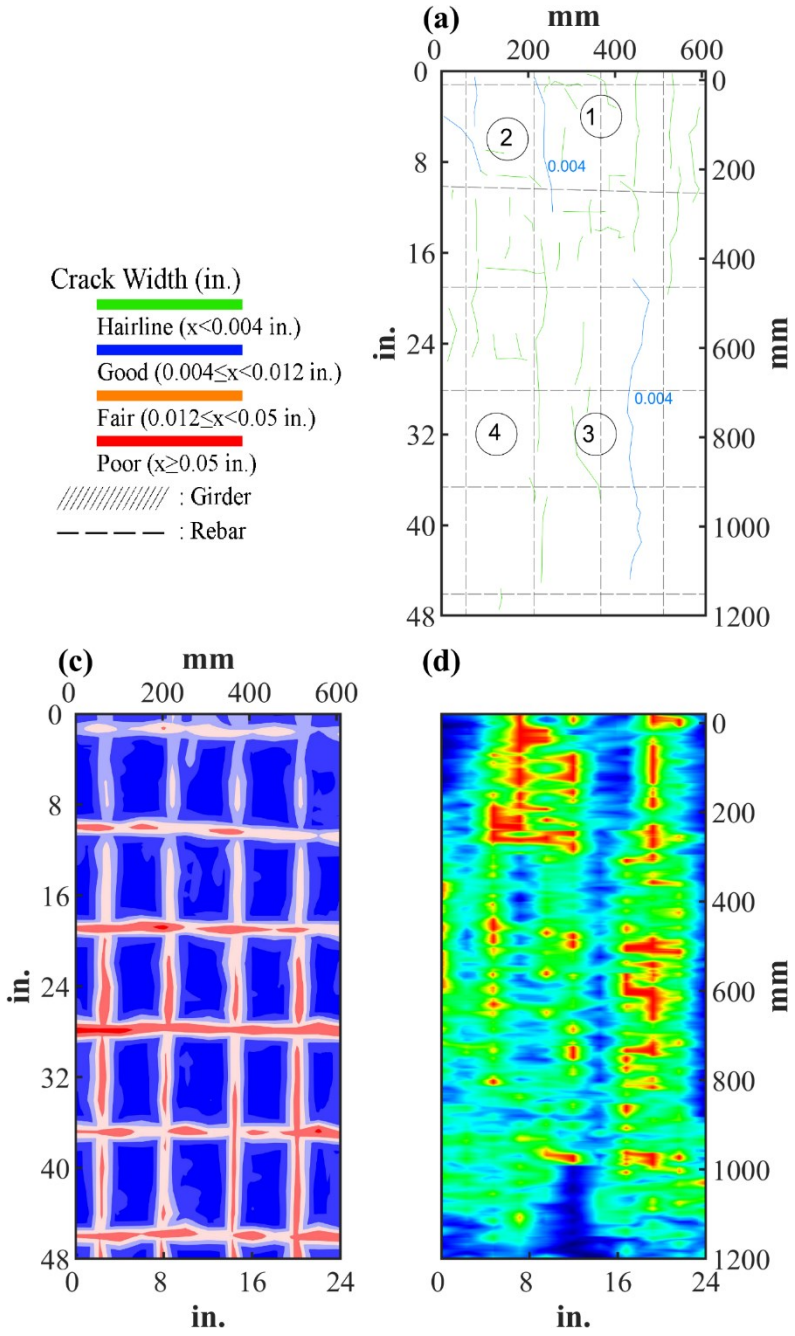

Figure 0.102. Crack Map and NDE Results of Grid 2: (a) Crack Map and Location of Cores; (c) GPR C-scan at 0.7 in. to 1.8 in. Depth; (d) UST C-scan at 1.5 in. Depth

B.14.3 Concrete Cores

Table B-64. Detail Information of Concrete Cores

Core	dia. x height (in.)	Rebar depth (in.)	Rebar size (#)	Epoxy (Y/N)	Crack type	Crack width (in)	Notes
1-1	3.75 x 6.3	-	-	-	-	-	-
1-2	3.75 x 6.4	-	-	-	longitudinal	0.004	-
1-3	3.75 x 3.1	-	-	-	-	-	-
1-4	3.75 x 6.3	-	-	-	-	-	Delamination of top surface of deck
2-1	3.75 x 6.3	0.3	5	N	-	-	-
2-2	3.75 x 4.9	-	-	-	-	-	-
2-3	3.75 x 6.7	0.4	5	N	-	-	-
2-4	3.75 x 6.5	-	-	-	-	-	-

Table B-65. Core Pictures

Core	Pictures of the Cores		
1-1		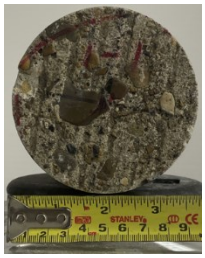	
1-2			

1-3			
1-4			
2-1			
2-2			
2-3			

2-4			

B.14.4 Laboratory Experiment Results

B.14.4.1 Resistivity

Core Number	Surface Resistivity (kΩ·m)	Bulk Resistivity (kΩ·m)
-	-	-

B.14.4.2 Ultrasonic Pulse Velocity

Core Number	Ultrasonic Pulse Velocity (m/s)
1-2	3936
2-2	4140

B.14.4.3 Acid-Soluble Chloride Content

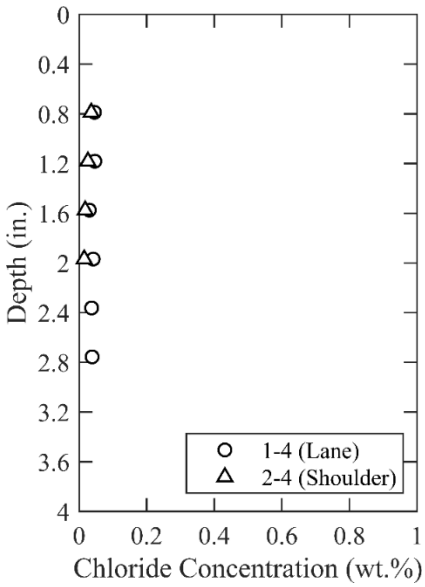

Figure 0.103. Chloride Content at Different Depth

B.14.4.4 Sorptivity

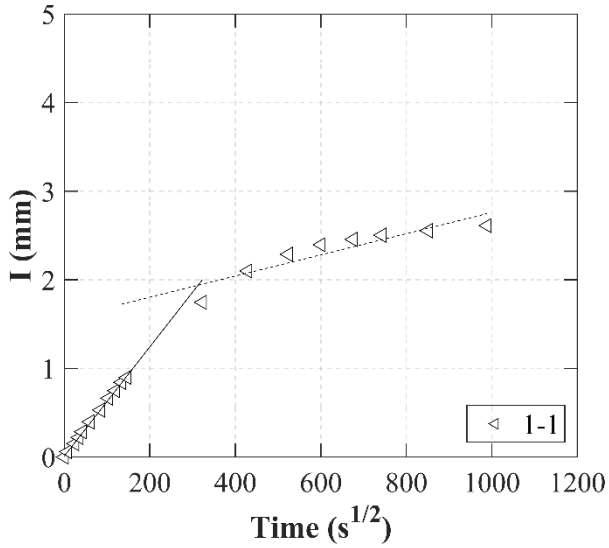

Figure 0.104. Absorption and Sorptivity of Core 1–1

Table B-66. Initial and Secondary Sorptivity Results

Core Number	Sorptivity	Results (mm/s$^{1/2}$)
Core 1–1	Initial Sorptivity	0.00616
	Secondary Sorptivity	0.00120

B.15 ATL-RC-03, IH 30 FR E U-TURN

- Bridge ID: 190190061007207 (Bowie County)
- Built in 2009
- Mitigation methods: ECR
- Observed CIP depth: 4.5 in.
- Observed clear cover: 2.0 in.
- 4 spans, 4-concrete PS girder @ 8’ spacing with 3’ overhangs at spans 1, 2, 3, and 4
- Inspected on July 13, 2021

Figure 0.105. Concrete Deck of the Bridge (source: google maps)

B.15.1 Observed Condition

The top surface of deck has widespread transverse and longitudinal cracks. Some of them have been sealed. The cracks were saw-cut and treated, displaying a different visual color. Diagonal cracks were prominent with some transverse cracks on Span 4. The exterior overhangs exhibited cracks, while the interior had no cracks.

B.15.2 NDE Results

Grid 1, Grid 2, and Grid 3 were located on the 1st span, 2nd, and 4th span of the east turnaround bridge, respectively, as shown in Figure 0.106 and Figure 0.107.

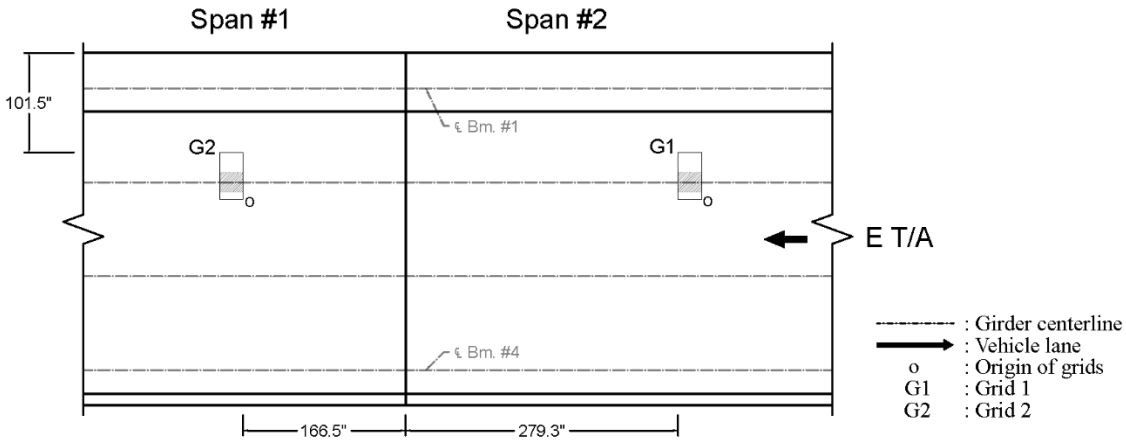

Figure 0.106. Plan View of the Bridge and Location of Two Grids

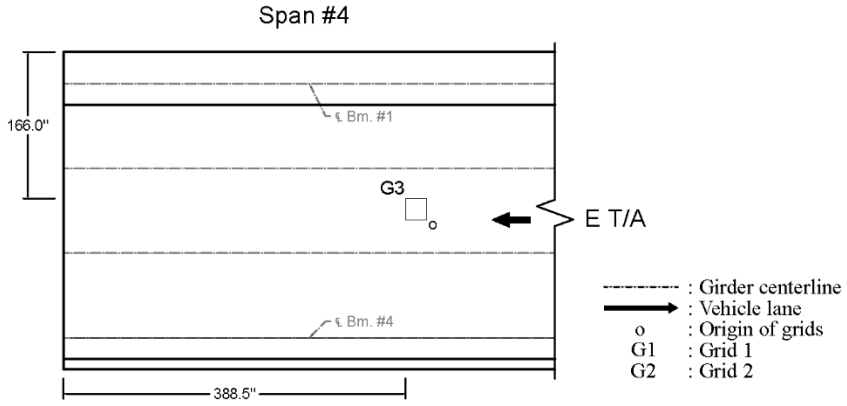

Figure 0.107. Plan View of the Bridge and Location of Grid 3

As shown in Figure 0.108 (a), the width of a transverse crack ranged from 0.01 in. to 0.03 in. It is possible that panel joints caused the crack. The Grid 2 had 0.004 in wide diagonal cracks and some hairline cracks as shown in Figure 0.109 (a). The Grid 3 had sealant applied on the crack as shown in Figure 0.110 (a).

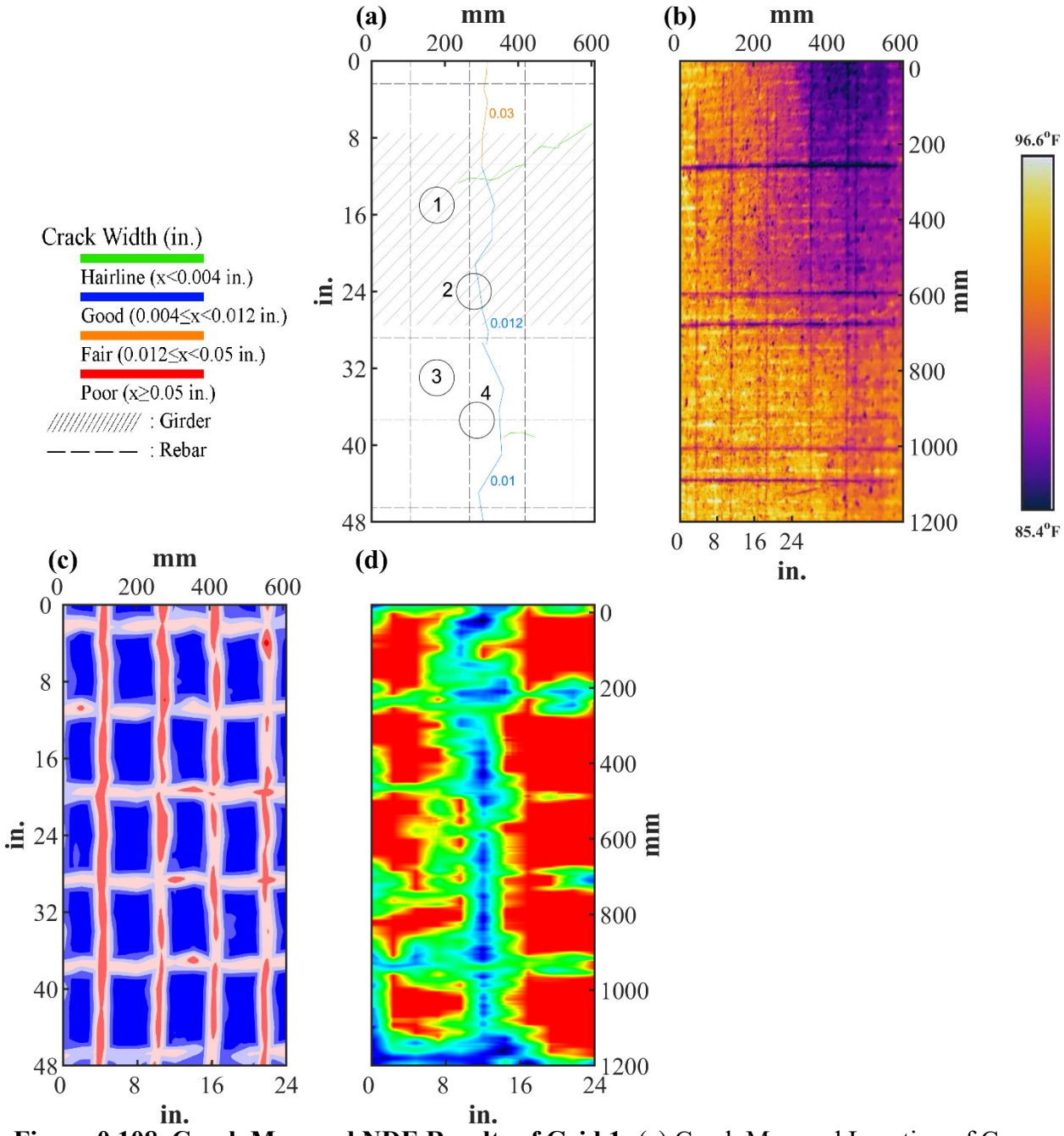

Figure 0.108. Crack Map and NDE Results of Grid 1: (a) Crack Map and Location of Cores; (b) Infrared Picture; (c) GPR C-scan at 1.7 in. to 2.8 in. Depth; (d) UST C-scan at 4.6 in. Depth

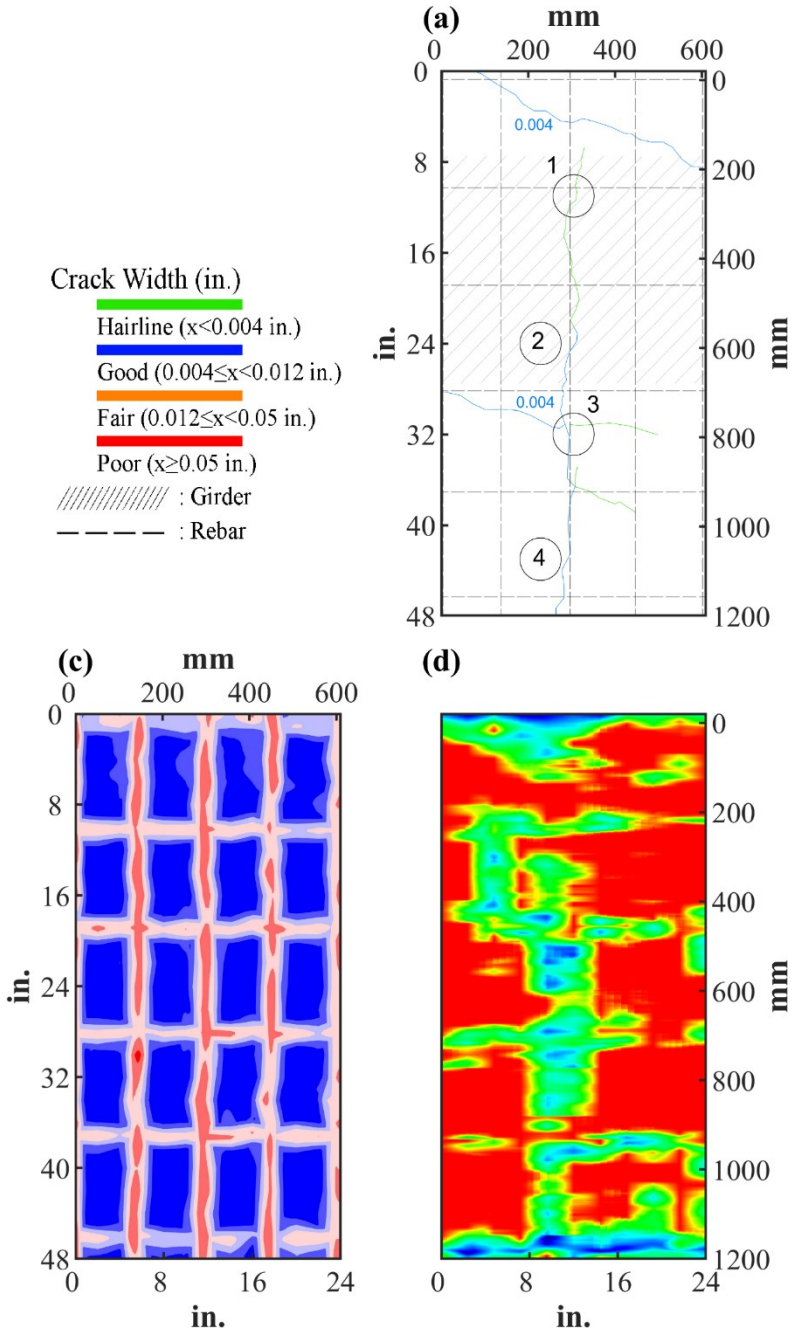

Figure 0.109. Crack Map and NDE Results of Grid 2: (a) Crack Map and Location of Cores; (c) GPR C-scan at 1.7 in. to 2.8 in. Depth; (d) UST C-scan at 4.4 in. Depth

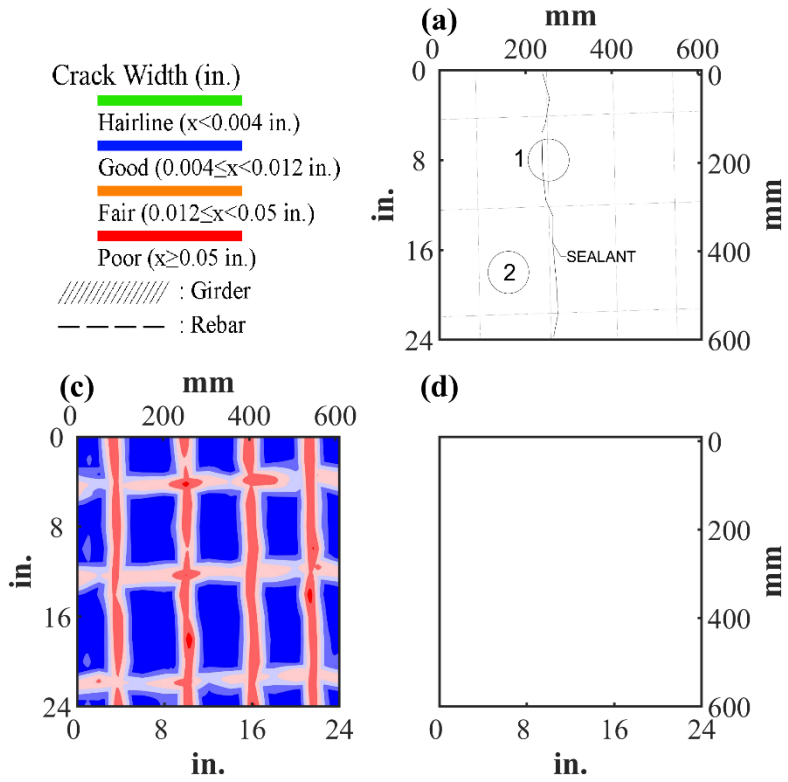

Figure 0.110. Crack Map and NDE Results of Grid 3: (a) Crack Map and Location of Cores; (c) GPR C-scan at 1.7 in. to 2.8 in. Depth; (d) UST C-scan

B.15.3 Concrete Cores

Table B-67. Detail Information of Concrete Cores

Core	dia. x height (in.)	Rebar depth (in.)	Rebar size (#)	Epoxy (Y/N)	Crack type	Crack width (in)	Notes
1-1	3.75 x 4.3	-	-	-	-	-	Delamination between CIP and PCP
1-2	3.75 x 4.3	2.2	5	Y	transverse	0.012	Delamination between CIP and PCP; A crack propagates from a rebar
1-3	3.75 x 4.5	-	-	Y, Y	-	-	Delamination between CIP and PCP
1-4	3.75 x 4.6	2.2, 2.3	5, 4	Y, Y	-	-	Delamination between CIP and PCP
2-1	3.75 x 4.8	2.2, 2.3	5, 4	Y, Y	diagonal	HL	Delamination between CIP and PCP; A crack propagates along intersection of aggregates
2-2	3.75 x 4.8	-	-	-	-	-	Delamination between CIP and PCP
2-3	3.75 x 4.8	2.2	5	Y	transverse	0.004	Delamination between CIP and PCP
2-4	3.75 x 4.8	-	-	-	longitudinal	0.004	Delamination between CIP and PCP; A crack propagates along intersection of aggregates
3-1	3.75 x 4.3	2.0	5	Y	-	-	Delamination between CIP and PCP
3-2	3.75 x 4.3	-	-	-	-	-	Delamination between CIP and PCP

Table B-68. Core Pictures

Core	Pictures of the Cores		
1-1			

1-2		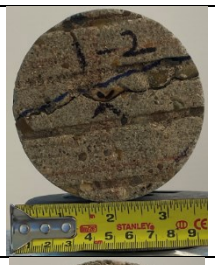	
1-3			
1-4		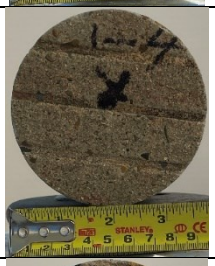	
2-1			
2-2			
2-3			

2-4			
3-1			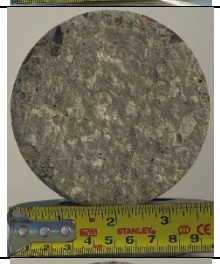
3-2			

B.15.4 Laboratory Experiment Results

B.15.4.1 Resistivity

Core Number	Surface Resistivity (kΩ·m)	Bulk Resistivity (kΩ·m)
1-3	-	20.6
2-2	161.2	21.9
2-4	237.7	-

B.15.4.2 Ultrasonic Pulse Velocity

Core Number	Ultrasonic Pulse Velocity (m/s)
1-3	4309
2-2	4342
2-4	3909
3-2	4385

B.15.4.3 Carbonation Depth

Core Number	Carbonation Depth (in.)
1-1	0.00
2-1	0.00

B.15.4.4 Acid-Soluble Chloride Content

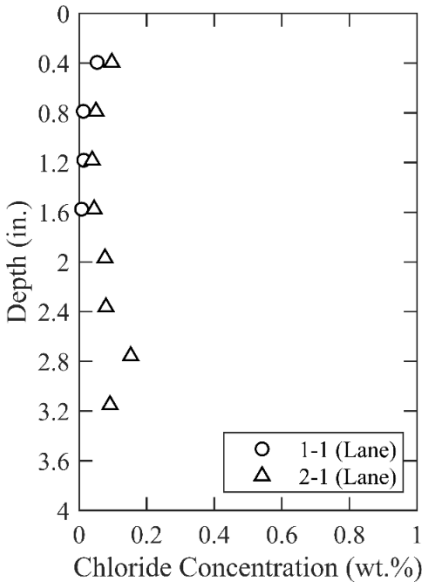

Figure 0.111. Chloride Content at Different Depth

B.15.4.5 Sorptivity

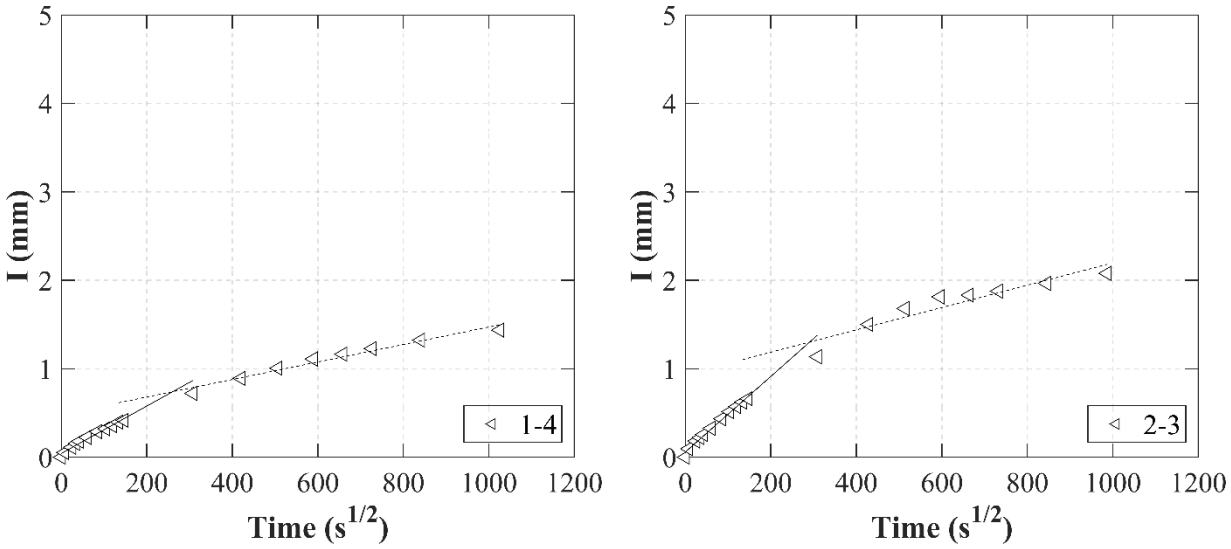

(a) Core 1–4 (b) Core 2–3

Figure 0.112. Absorption and Sorptivity of: (a) Core 1–4; (b) Core 2–3

Table B-69. Initial and Secondary Sorptivity Results

Core Number	Sorptivity	Results ($mm/s^{1/2}$)
Core 1–4	Initial Sorptivity	0.00268
	Secondary Sorptivity	0.00099
Core 2–3	Initial Sorptivity	0.00427
	Secondary Sorptivity	0.00126

B.15.4.6 Knife Test

Core Number	Score	Picture
1-2	10	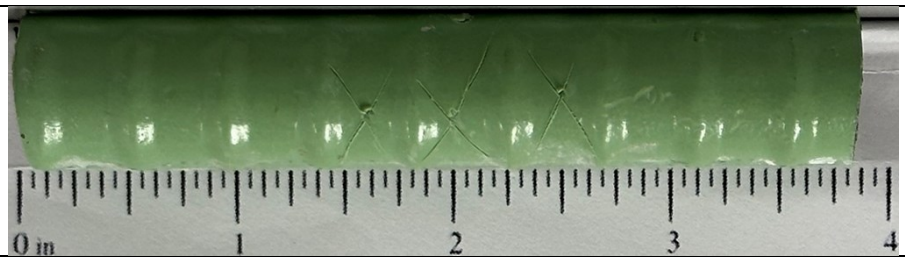

B.15.4.7 Electrochemical Impedance Spectroscopy

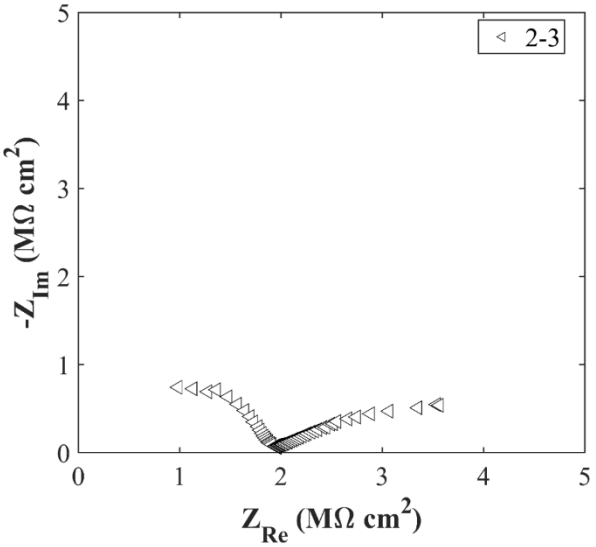

(a) Nyquist Diagram

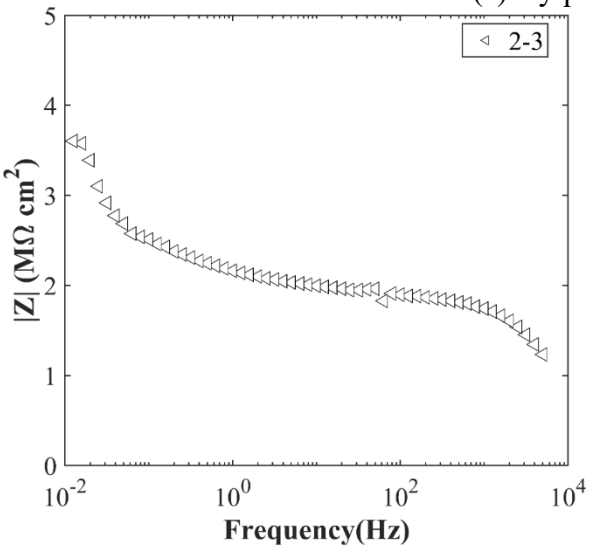

(b) Bode Plot of Impedance Modulus

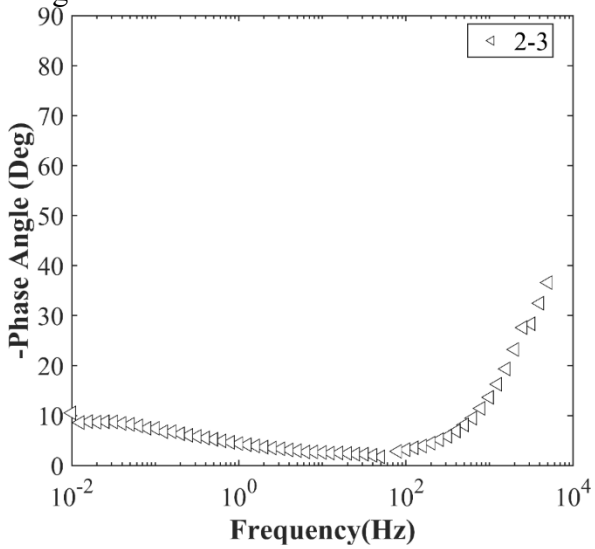

(c) Bode Plot of Impedance Phase

Figure 0.113. EIS Results: (a) Nyquist Diagram; (b) Bode Plot of Impedance Modulus; (c) Bode Plot of Impedance Phase

B.16 ATL-RC-04, FM 3129 OVER UPRR & CR 3676

- Bridge ID: 190340319501003 (Cass County)
- Built in 2011
- Mitigation methods: HPC, ECR
- Observed CIP depth: unknown
- Observed clear cover: 2.0 in.
- 6 spans, 6-concrete PS girder @ 8’ spacing with 3’ overhangs at spans 1, 2, 3, 4, and 6; 8-concrete PS girder @ 5.714’ spacing with 3’ overhangs at span 5
- Inspected on July 12, 2021

Figure 0.114. Concrete Deck of the Bridge (source: google maps)

B.16.1 Observed Condition

The top surface of deck has hairline cracks. On the south overhang, several flexure cracks with efflorescence were observed, although they did not follow a regular pattern. The north overhang had fewer cracks than the south side, but a substantial crack was found at Bent 3, along with staining and efflorescence. Minor efflorescence was present near PMDFs.

B.16.2 NDE Results

Both Grid 1 and grid 2 were located on the joint of the span 1 and span 2 of the WB lane. Grid 1 was located on the car lane, and Grid 2 was located on the shoulder lane of the bridge as shown in Figure 0.115.

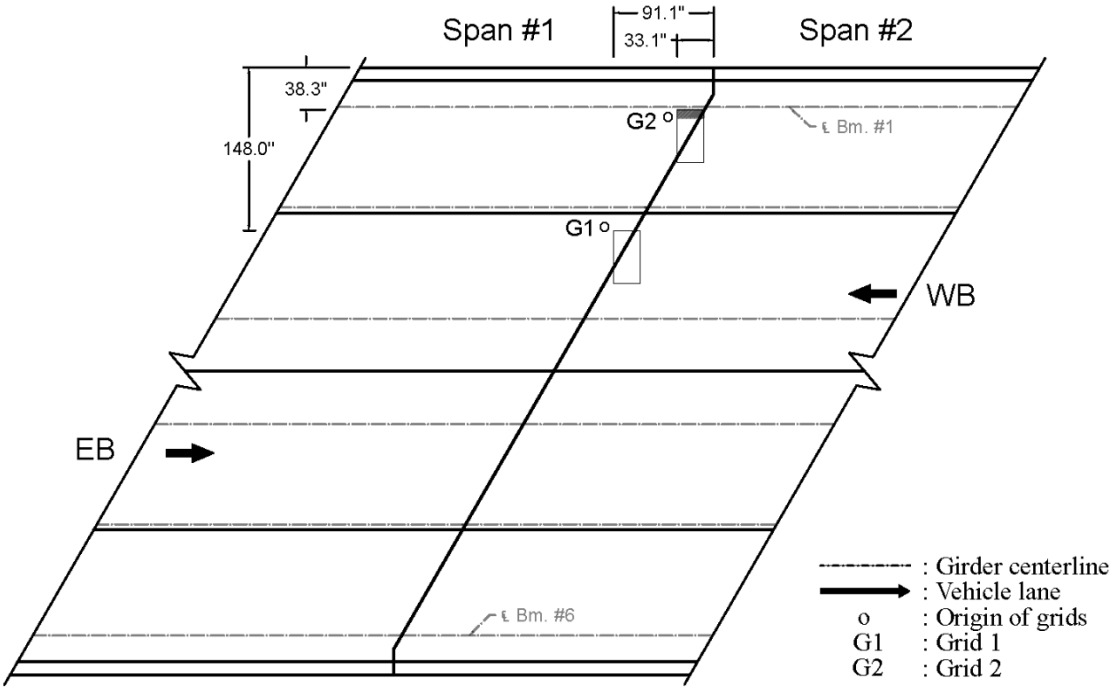

Figure 0.115. Plan view of the Bridge and Location of Grids

As shown in Figure 0.116 (a), the Grid 1 had cracks with their widths ranging from 0.004 in. to 0.02 in. wide. The grid 1 was located on the joint and cracks propagate from the joint. The grid 2 was also located on the joint, and a crack ranging from 0.02 in. wide to 0.03 in. wide was propagating from the joint as shown in Figure 0.117 (a).

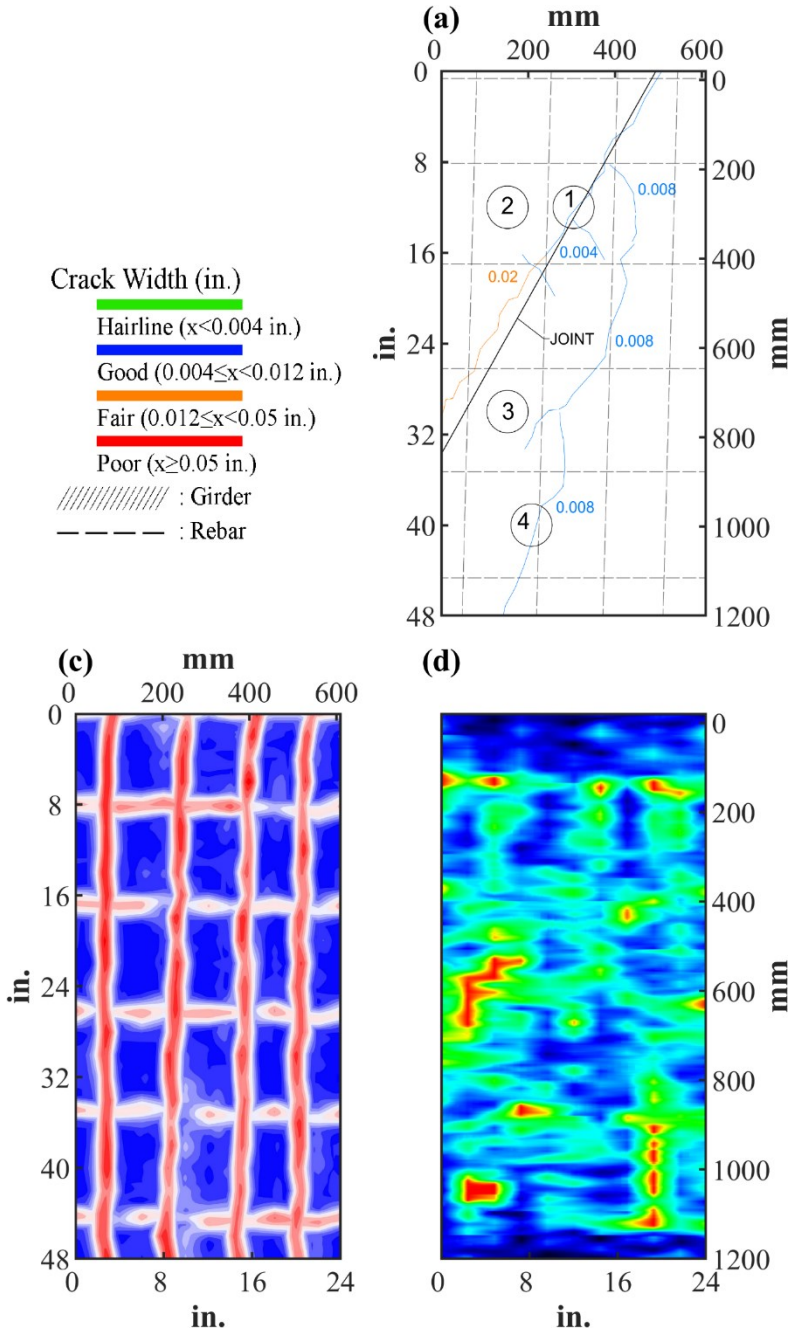

Figure 0.116. Crack Map and NDE Results of Grid 1: (a) Crack Map and Location of Cores; (c) GPR C-scan at 1.7 in. to 2.8 in. Depth; (d) UST C-scan at 6.2 in. Depth

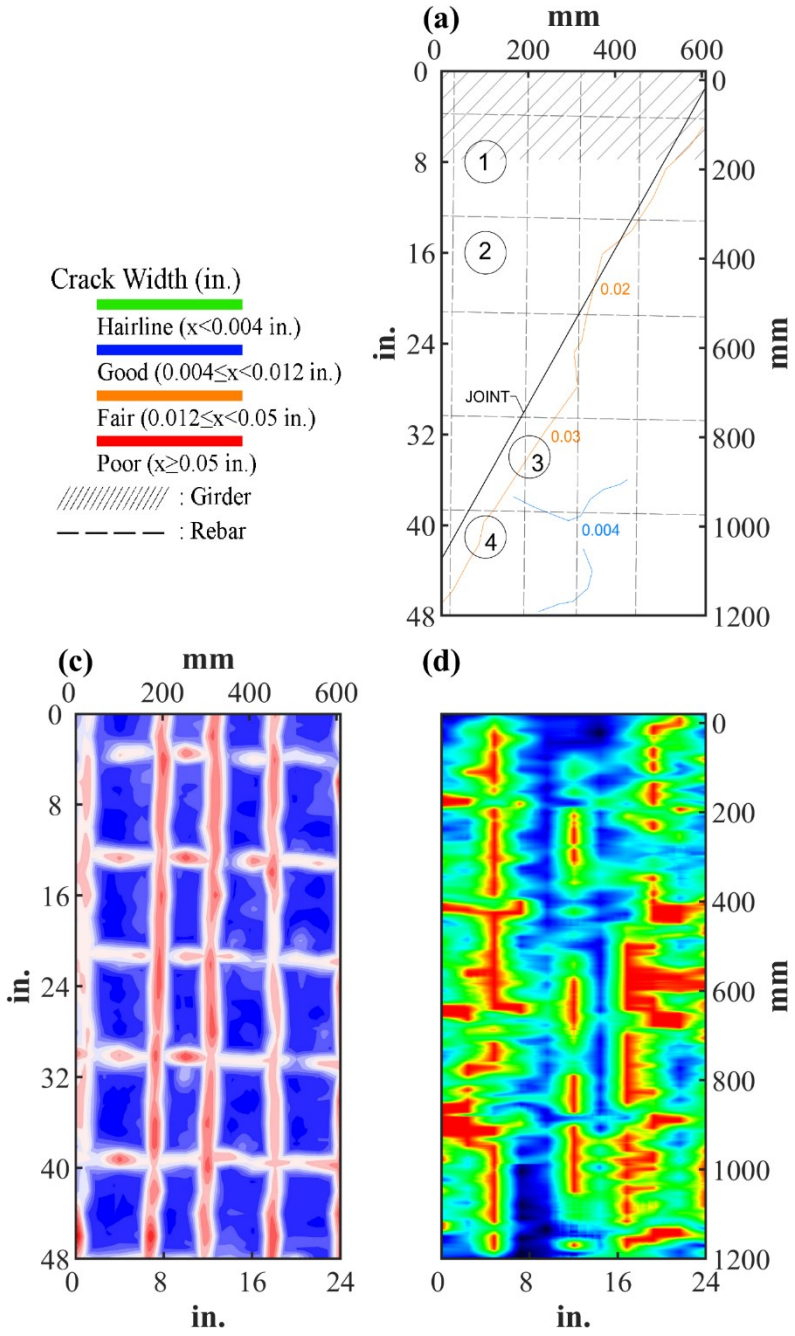

Figure 0.117. Crack Map and NDE Results of Grid 2: (a) Crack Map and Location of Cores; (c) GPR C-scan at 1.95 in. to 3.05 in. Depth; (d) UST C-scan at 3.7 in. Depth

B.16.3 Concrete Cores

Table B-70. Detail Information of Concrete Cores

Core	dia. x height (in.)	Rebar depth (in.)	Rebar size (#)	Epoxy (Y/N)	Crack type	Crack width (in)	Notes
1-1	3.75 x 4.7	-	-	-	diagonal	0.004	A crack propagates along intersection of aggregates
1-2	3.75 x 5.5	5.3	5	Y	-	-	Void at 1 in. depth
1-3	3.75 x 6.1	5.1	5	Y	-	-	-
1-4	3.75 x 5.3	2.0	5	Y	transverse	0.008	A crack propagates along intersection of aggregates
2-1	3.75 x 5.5	-	-	-	-	-	-
2-2	3.75 x 6.5	-	-	-	-	-	=-
2-3	3.75 x 6.3	2.3	5	Y	diagonal	0.03	Spilt due to a crack
2-4	3.75 x 2.9	-	-	-	diagonal	0.03	Spilt due to a crack

Table B-71. Core Pictures

Core	Pictures of the Cores		
1-1			
1-2			

1-3			
1-4			
2-1			
2-2			
2-3			

2-4			

B.16.4 Laboratory Experiment Results

B.16.4.1 Resistivity

Core Number	Surface Resistivity (kΩ·m)	Bulk Resistivity (kΩ·m)
2-1	185.1	20.1
2-2	184.0	-

B.16.4.2 Ultrasonic Pulse Velocity

Core Number	Ultrasonic Pulse Velocity (m/s)
1-4	4474
2-1	4291
2-2	4389

B.16.4.3 Carbonation Depth

Core Number	Carbonation Depth (in.)
1-3	0.00
2-3	0.08

B.16.4.4 Acid-Soluble Chloride Content

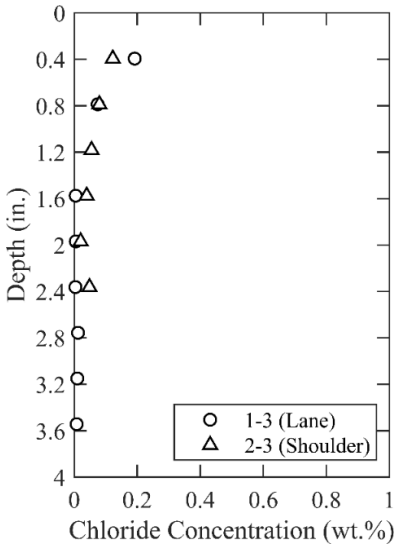

Figure 0.118. Chloride Content at Different Depth

B.16.4.5 Knife Test

Core Number	Score	Picture
2-3	6	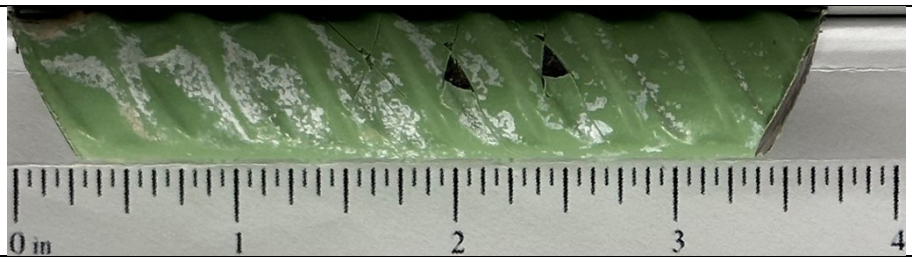

B.16.4.6 Electrochemical Impedance Spectroscopy

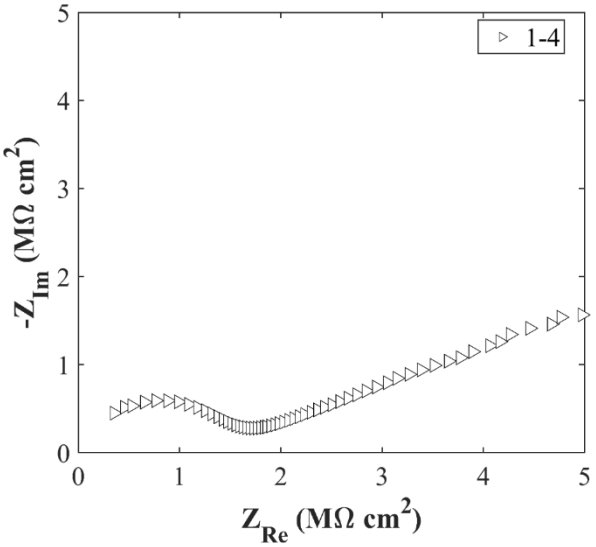

(a) Nyquist Diagram

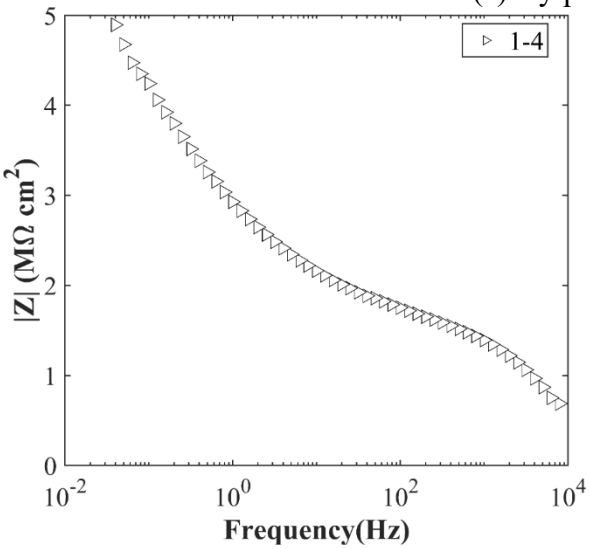

(b) Bode Plot of Impedance Modulus

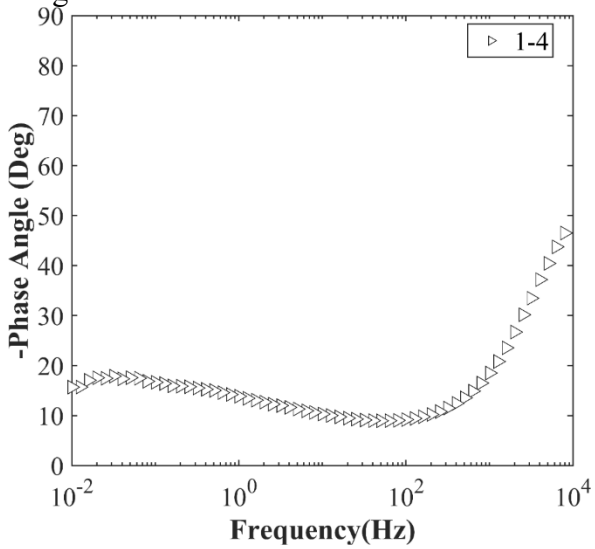

(c) Bode Plot of Impedance Phase

Figure 0.119. EIS Results: (a) Nyquist Diagram; (b) Bode Plot of Impedance Modulus; (c) Bode Plot of Impedance Phase

B.17 ATL-RC-05, FM 10 OVER MURVAUL CREEK

- Bridge ID: 191830122201007 (Panola County)
- Built in 2013
- Mitigation methods: ECR
- Observed CIP depth: 5.0 in.
- Observed clear cover: 2.8 in.
- 7 spans, 6-concrete PS girder @ 8’ spacing with 3’ overhangs
- Inspected on July 15, 2021

Figure 0.120. Concrete Deck of the Bridge (source: google maps)

B.17.1 Observed Condition

The top surface of deck has transverse and longitudinal cracks.

B.17.2 NDE Results

Grid 1 was located on the SB lane, and Grid 2 was located on the SB shoulder lane of the span 2 of the bridge as shown in Figure 0.121.

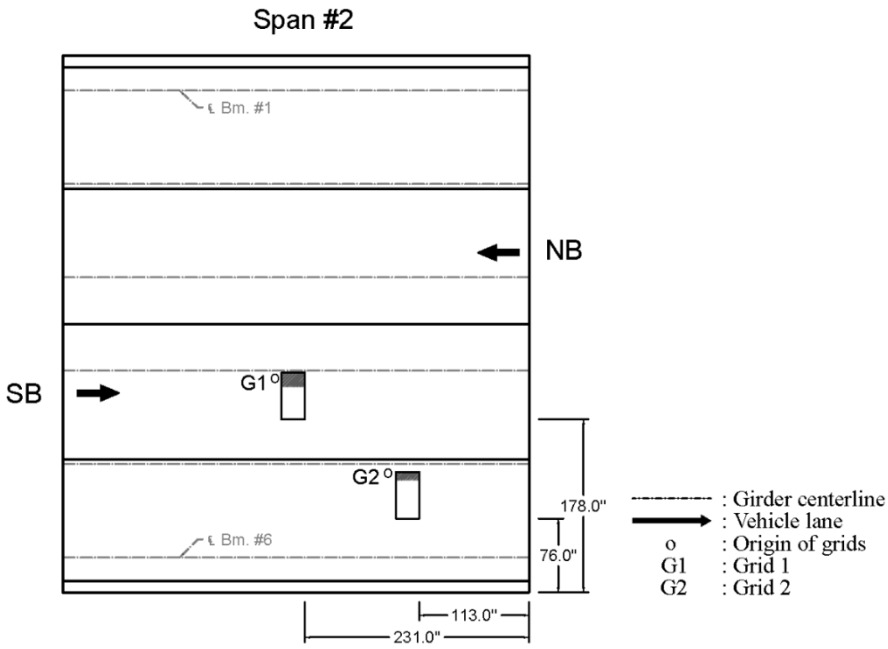

Figure 0.121. Plan View of the Bridge and Location of Grids

As shown in Figure 0.122 (a), it is possible that longitudinal and transverse cracks are cause by panel joints and they were 0.008 and 0.012 wide, respectively. The Grid 2 had 0.006 in. wide transverse crack, possibly cause by panel joints as shown in Figure 0.123 (a).

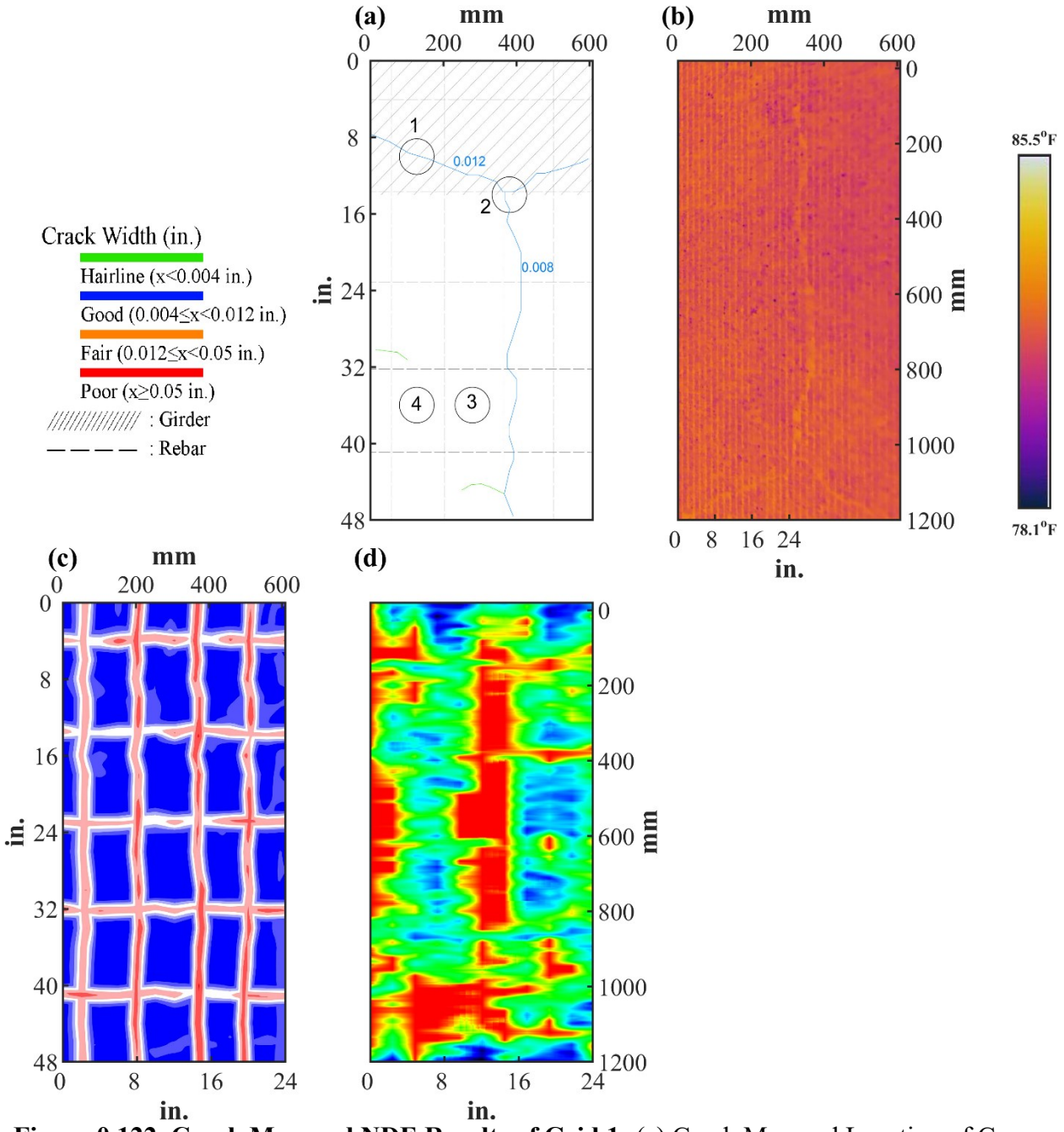

Figure 0.122. Crack Map and NDE Results of Grid 1: (a) Crack Map and Location of Cores; (b) Infrared Picture; (c) GPR C-scan at 2.7 in. to 3.8 in. Depth; (d) UST C-scan at 4.6 in. Depth

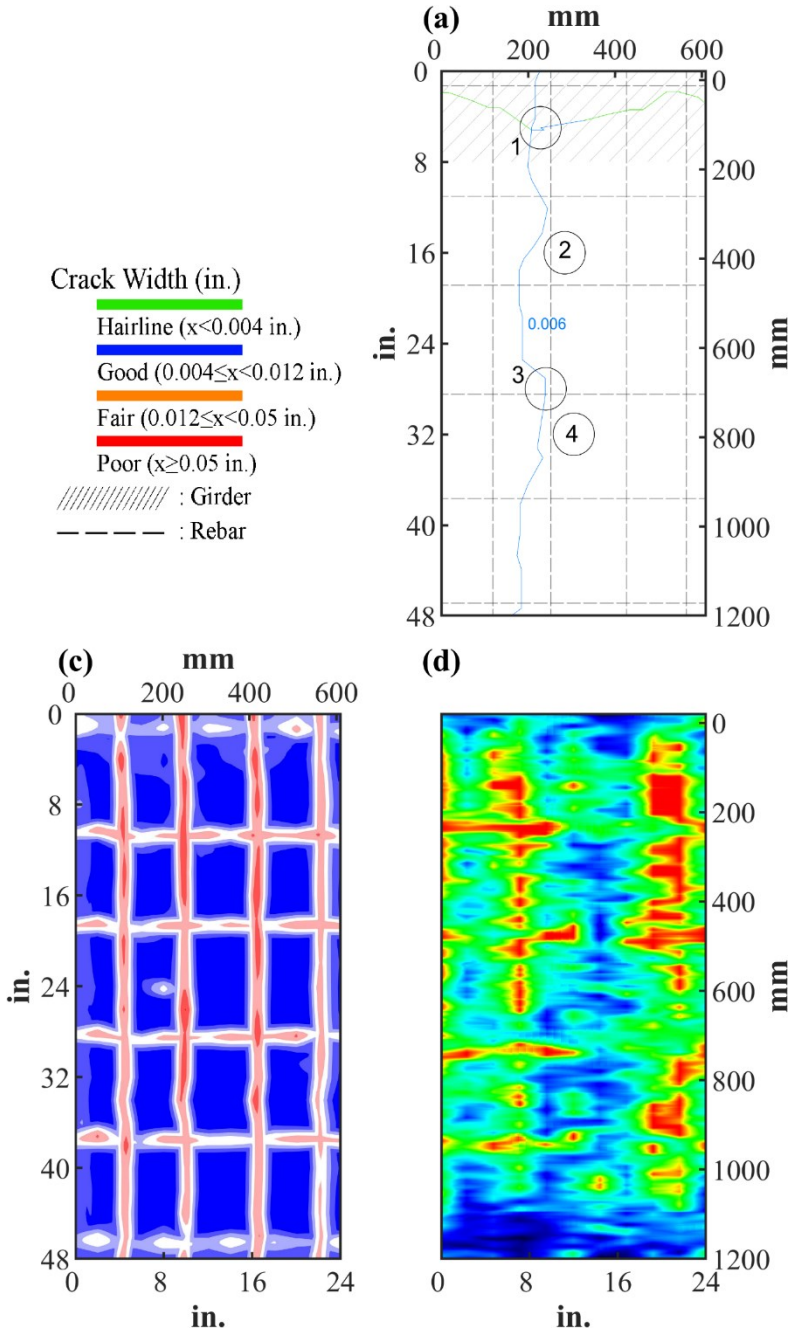

Figure 0.123. Crack Map and NDE Results of Grid 2: (a) Crack Map and Location of Cores; (c) GPR C-scan at 2.7 in. to 3.8 in. Depth; (d) UST C-scan at 4.2 in. Depth

B.17.3 Concrete Cores

Table B-72. Detail Information of Concrete Cores

Core	dia. x height (in.)	Rebar depth (in.)	Rebar size (#)	Epoxy (Y/N)	Crack type	Crack width (in)	Notes
1-1	3.75 x 4.9	-	-	-	diagonal	0.012	Delamination between CIP and PCP; A crack propagates along intersection of aggregates
1-2	3.75 x 4.7	2.8, 3.4	5, 4	Y, Y	transverse; diagonal	0.008; 0.012	Delamination between CIP and PCP; A crack propagates along intersection of aggregates
1-3	3.75 x 4.6	-	-	-	-	-	Delamination between CIP and PCP
1-4	3.75 x 6.1	-	-	-	-	-	-
2-1	3.75 x 2.9	2.8	5	Y	transverse	0.004	A crack propagates along intersection of aggregates
2-2	3.75 x 5.9	2.8	5	Y	-	-	-
2-3	3.75 x 5.1	2.8, 3.4	5, 4	Y, Y	transverse	0.006	A crack propagates along intersection of aggregates
2-4	3.75 x 5.1	-	-	-			Delamination between CIP and PCP

Table B-73. Core Pictures

Core	Pictures of the Cores		
1-1			
1-2			

1-3			
1-4			
2-1			
2-2			
2-3			
2-4			

B.17.4 Laboratory Experiment Results

B.17.4.1 Resistivity

Core Number	Surface Resistivity (kΩ·m)	Bulk Resistivity (kΩ·m)
1-4	93.2	11.0
2-4	74.3	8.4

B.17.4.2 Ultrasonic Pulse Velocity

Core Number	Ultrasonic Pulse Velocity (m/s)
1-3	4303
1-4	4396
2-4	4123

B.17.4.3 Carbonation Depth

Core Number	Carbonation Depth (in.)
1-1	0.10
2-1	0

B.17.4.4 Acid-Soluble Chloride Content

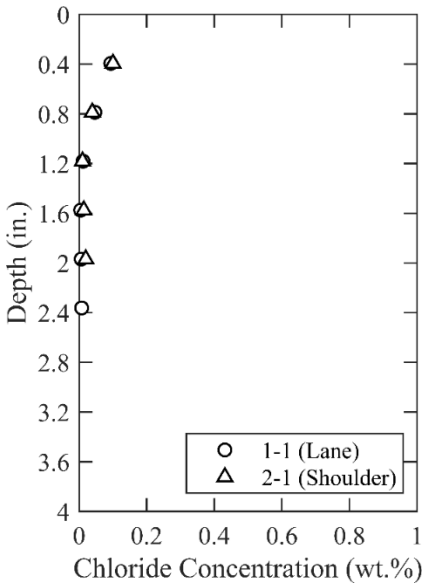

Figure 0.124. Chloride Content at Different Depth

B.17.4.5 Sorptivity

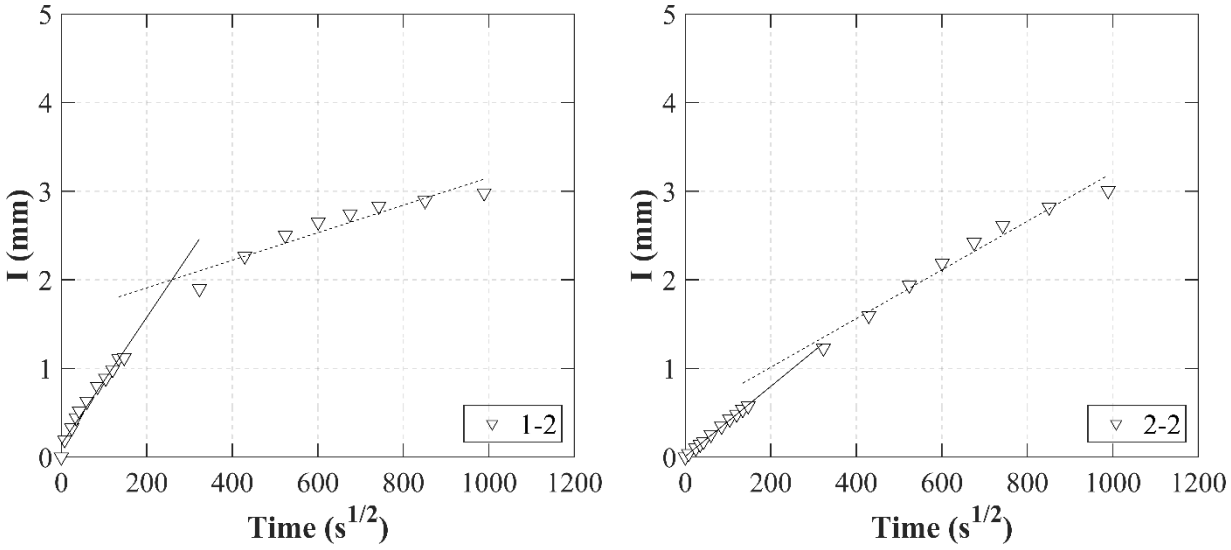

(a) Core 1–2 (b) Core 2–2

Figure 0.125. Absorption and Sorptivity of: (a) Core 1–2; (b) Core 2–2

Table B-74. Initial and Secondary Sorptivity Results

Core Number	Sorptivity	Results (mm/s$^{1/2}$)
Core 1–2	Initial Sorptivity	0.00717
	Secondary Sorptivity	0.00155
Core 2–2	Initial Sorptivity	0.00395
	Secondary Sorptivity	0.00275

B.17.4.6 Electrochemical Impedance Spectroscopy

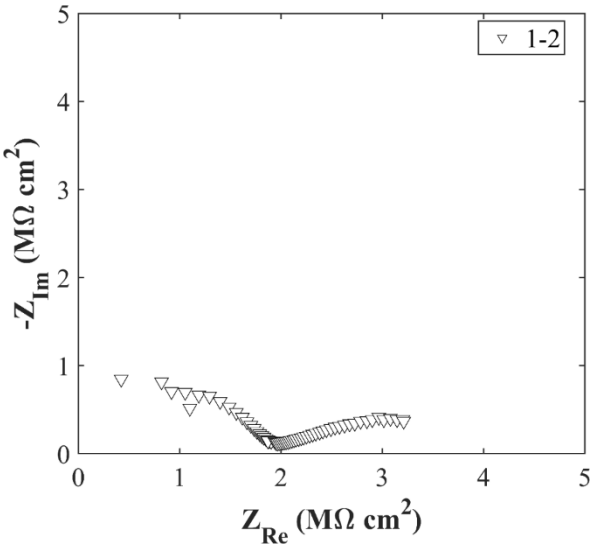

(a) Nyquist Diagram

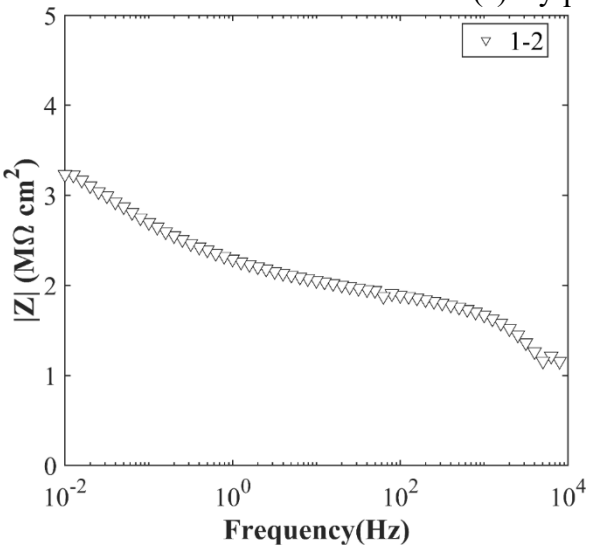

(b) Bode Plot of Impedance Modulus

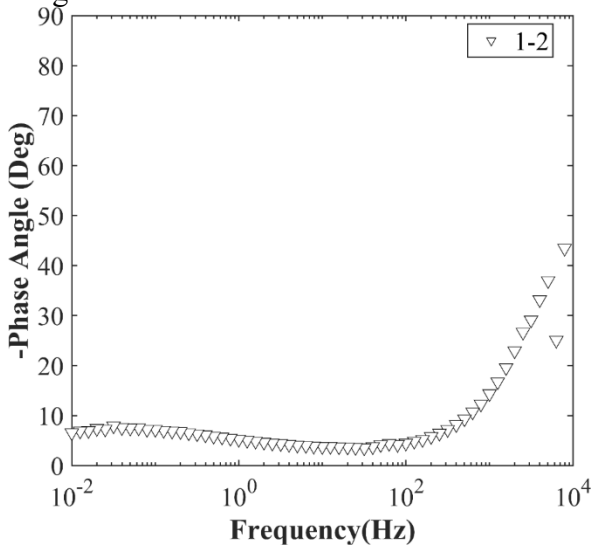

(c) Bode Plot of Impedance Phase

Figure 0.126. EIS Results: (a) Nyquist Diagram; (b) Bode Plot of Impedance Modulus; (c) Bode Plot of Impedance Phase

B.18 ATL-RC-06, FM 2348 OVER UPRR & EVANS CREEK

- Bridge ID: 192250224001002 (Titue County)
- Built in 2013
- Mitigation methods: HPC, ECR
- Observed CIP depth: 4.33 in.
- Observed clear cover: 2.0 in.
- 4 spans, 6-concrete PS girder @ varying spacing with 2.989’ max and 2.113’ min overhangs at span 1; 6-concrete PS girder @ 8.2’ spacing with 2.984’ max and 2.022’ min overhangs at span 2; 7-concrete PS girder @ 6.833’ spacing with 3.133’ max and 1.876’ min overhangs at span 3; 6-concrete PS girder @ 8.2’ spacing with 2.818’ max and 2.187’ min overhangs at span 3
- Inspected on July 14, 2021

Figure 0.127. Concrete Deck of the Bridge (source: google maps)

B.18.1 Observed Condition

Numerous transverse cracks were observed on the deck. Notably, a wide crack with up to 0.035 in. width and spalling was observed south of the SEJ. The west side of Abutment 1 back wall exhibited a 0.008 in. wide vertical crack, with the top of the abutment displaying longitudinal and transverse cracks up to 0.014 in. wide. The backwall showed various cracks, primarily horizontal and up to 0.016 in. wide, along with diagonal and vertical cracks. Significant cracking was present between the west exterior and interior of Beam 6. Additional issues included erosion under the bent cap, spalling, exposed rebar and strand on the west girder, and deformation of the bearing pad.

B.18.2 NDE Results

Grid 1 was located on the SB lane, and Grid 2 was located on the SB shoulder lane of the span 3 of the bridge as shown in Figure 0.128.

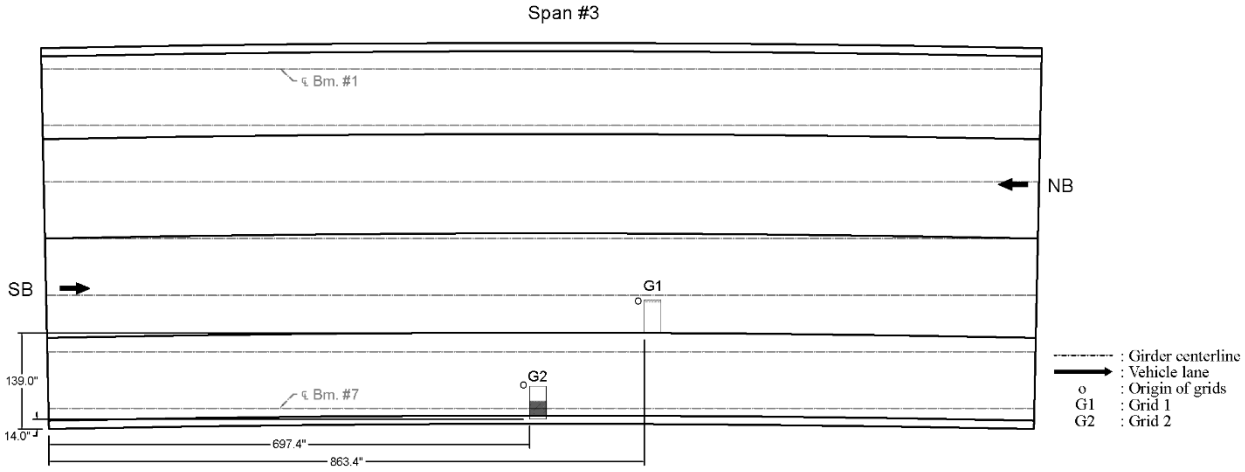

Figure 0.128. Plan View of the Bridge and Location of Grids

As shown in Figure 0.129 (a), the Grid 1 had cracks that are 0.004 in. wide in both transverse and longitudinal directions. The Grid 2 had short cracks that were 0.006 in wide and 0.012 in. wide as shown in Figure 0.130 (a).

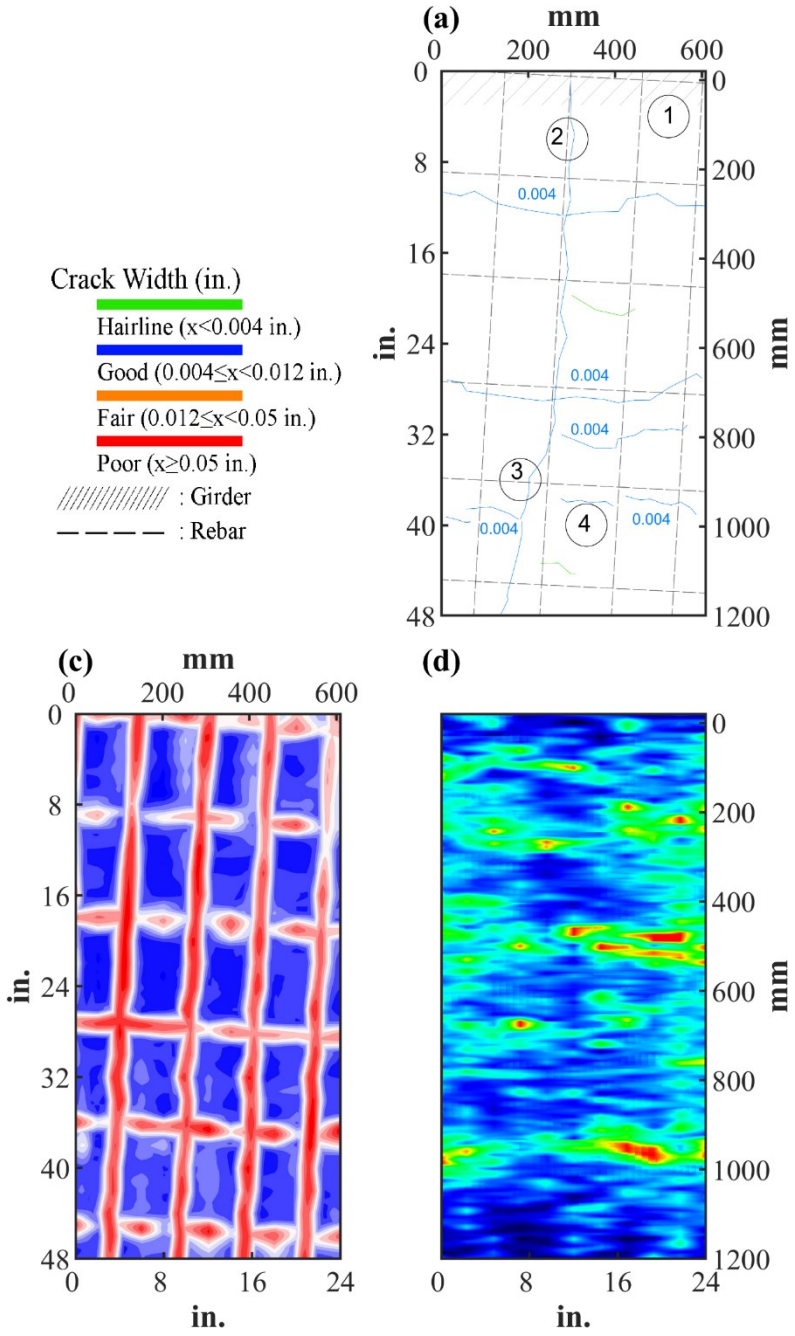

Figure 0.129. Crack Map and NDE Results of Grid 1: (a) Crack Map and Location of Cores; (c) GPR C-scan at 1.7 in. to 2.8 in. Depth; (d) UST C-scan at 1.6 in. Depth

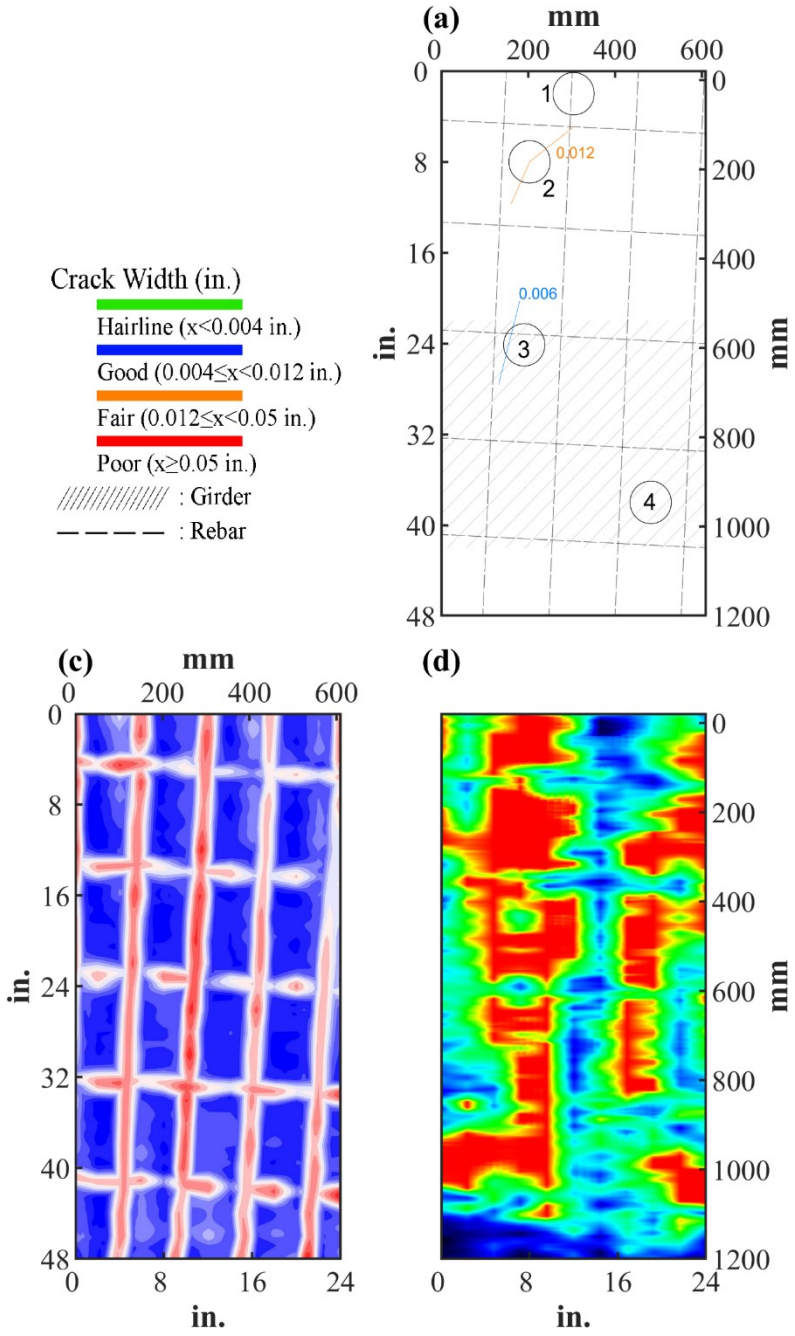

Figure 0.130. Crack Map and NDE Results of Grid 2: (a) Crack Map and Location of Cores; (c) GPR C-scan at 1.95 in. to 3.05 in. Depth; (d) UST C-scan at 4.3 in. Depth

B.18.3 Concrete Cores

Table B-75. Detail Information of Concrete Cores

Core	dia. x height (in.)	Rebar depth (in.)	Rebar size (#)	Epoxy (Y/N)	Crack type	Crack width (in)	Notes
1-1	3.75 x 5.5	-	-	-	-	-	-
1-2	3.75 x 5.9	2.0	5	Y	transverse	0.004	-
1-3	3.75 x 4.1	2.6	4	Y	transverse	0.004	A crack propagates along intersection of aggregates
1-4	3.75 x 4.0	-	-	-	map	HL	-
2-1	3.75 x 5.6	2.4	5	Y	diagonal	HL	A crack propagates along intersection of aggregates
2-2	3.75 x 4.3	-	-	-	-	-	-
2-3	3.75 x 4.4	3.0	4	Y	longitudinal	0.006	A crack propagates along intersection of aggregates
2-4	3.75 x 4.6	-	-	-	-	-	-

Table B-76. Core Pictures

Core	Pictures of the Cores		
1-1			
1-2			

1-3			
1-4			
2-1			
2-2			
2-3			
2-4			

B.18.4 Laboratory Experiment Results

B.18.4.1 Resistivity

Core Number	Surface Resistivity (kΩ·m)	Bulk Resistivity (kΩ·m)
1-1	91.4	11.2
2-2	-	6.8

B.18.4.2 Ultrasonic Pulse Velocity

Core Number	Ultrasonic Pulse Velocity (m/s)
1-1	4006
2-2	3870
2-3	3903

B.18.4.3 Carbonation Depth

Core Number	Carbonation Depth (in.)
1-4	0.14
2-4	0.00

B.18.4.4 Acid-Soluble Chloride Content

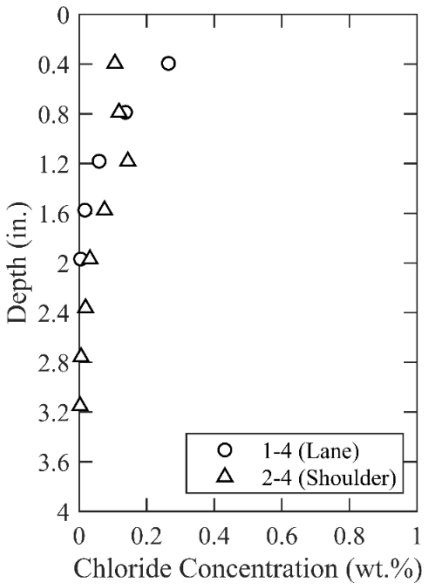

Figure 0.131. Chloride Content at Different Depth

B.18.4.5 Sorptivity

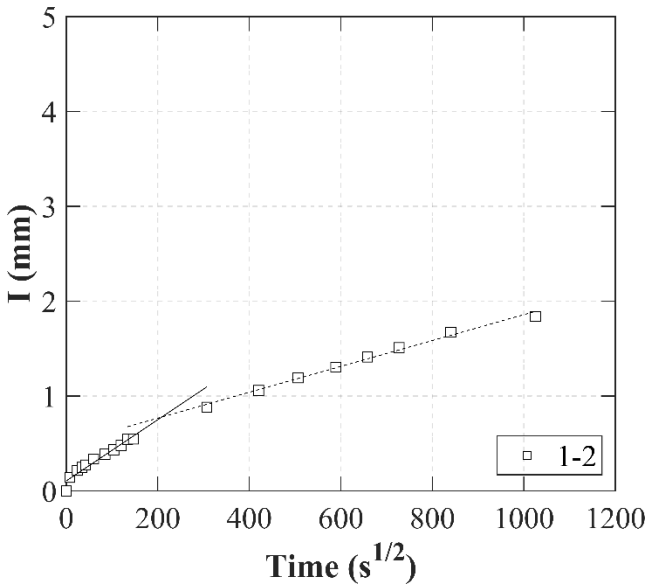

Figure 0.132. Absorption and Sorptivity of Core 1–2

Table B-77. Initial and Secondary Sorptivity Results

Core Number	Sorptivity	Results (mm/s$^{1/2}$)
Core 1–2	Initial Sorptivity	0.00323
	Secondary Sorptivity	0.00136

B.18.4.6 Knife Test

Core Number	Score	Picture
1-1	10	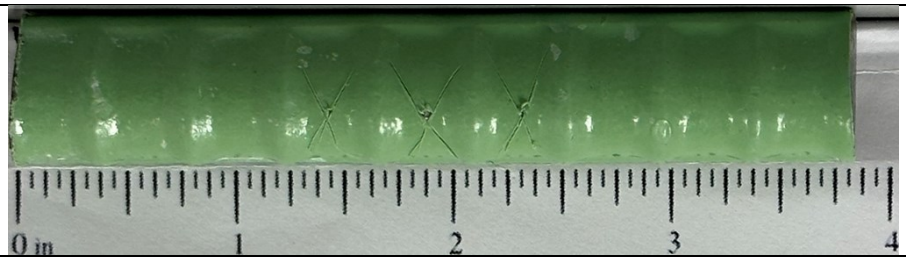

B.18.4.7 Electrochemical Impedance Spectroscopy

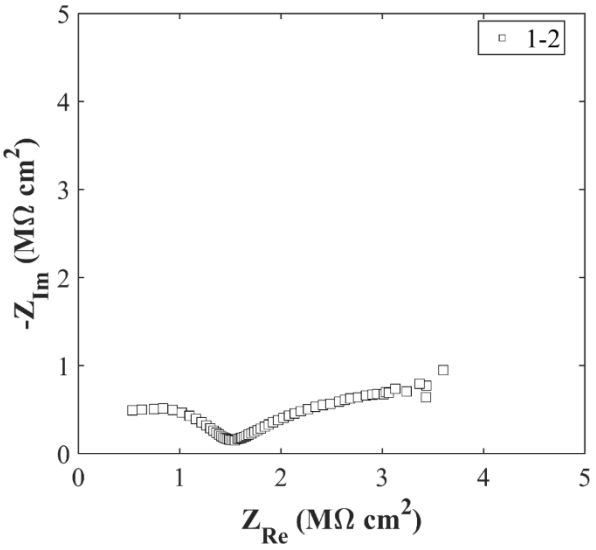

(a) Nyquist Diagram

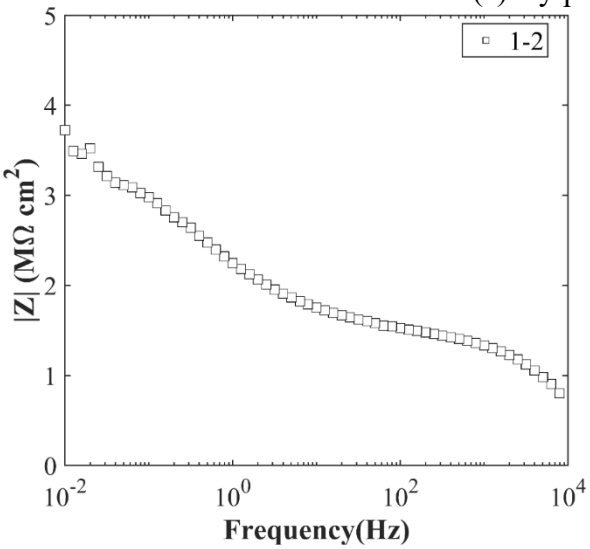

(b) Bode Plot of Impedance Modulus

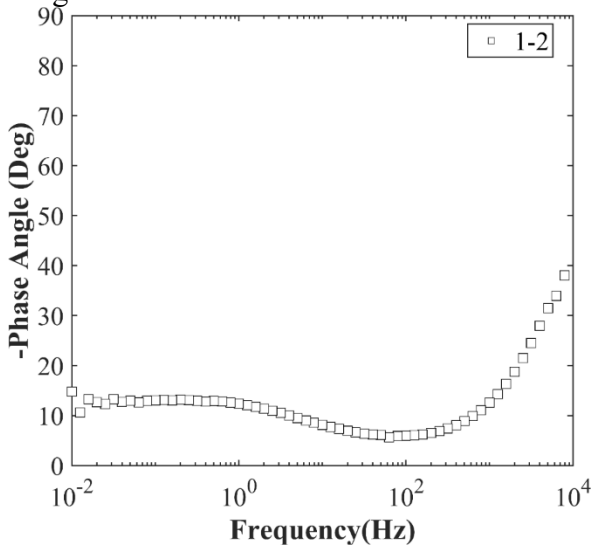

(c) Bode Plot of Impedance Phase

Figure 0.133. EIS Results: (a) Nyquist Diagram; (b) Bode Plot of Impedance Modulus; (c) Bode Plot of Impedance Phase

B.19 ATL-RC-07, SH 155 OVER UNION PACIFIC RR

- Bridge ID: 192300052002178 (Upshur County)
- Built in 2011
- Mitigation methods: ECR
- Observed CIP depth: 3.9 in.
- Observed clear cover: 2.0 in.
- 3 spans, 17-concrete ps girder @ 4’ spacing with 3’ overhangs at span 2; 9-concrete ps girder @ 8’ spacing with 3’ overhangs at span 1 and 3
- Inspected on July 14, 2021

Figure 0.134. Concrete Deck of the Bridge (source: google maps)

B.19.1 Observed Condition

The top surface of deck has transverse cracks. These cracks are perpendicular to the skew joints. The overall condition of the bridge was deemed to be in good shape.

B.19.2 NDE Results

Grid 1 was located on the WB lane, and Grid 2 was located on the WB shoulder lane of the span 3 of the bridge as shown in Figure 0.135.

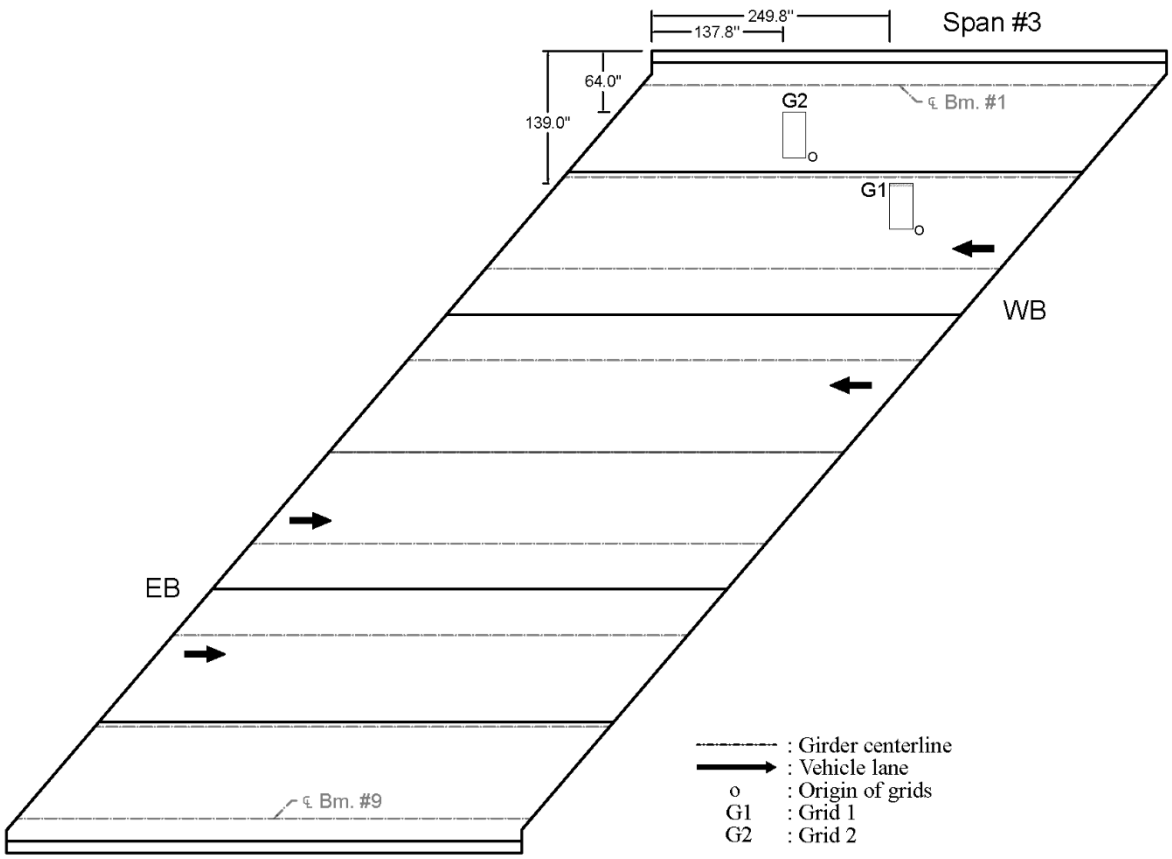

Figure 0.135. Plan View of the Bridge and Location of Grids

As shown in Figure 0.136 (a), there were widespread of hairline cracks and 0.01 in. wide transverse crack which was possibly caused by panel joints. On Grid 2, 0.004 in. wide transverse crack was observed which was possibly cause by panel joints as well as shown in Figure 0.137 (a).

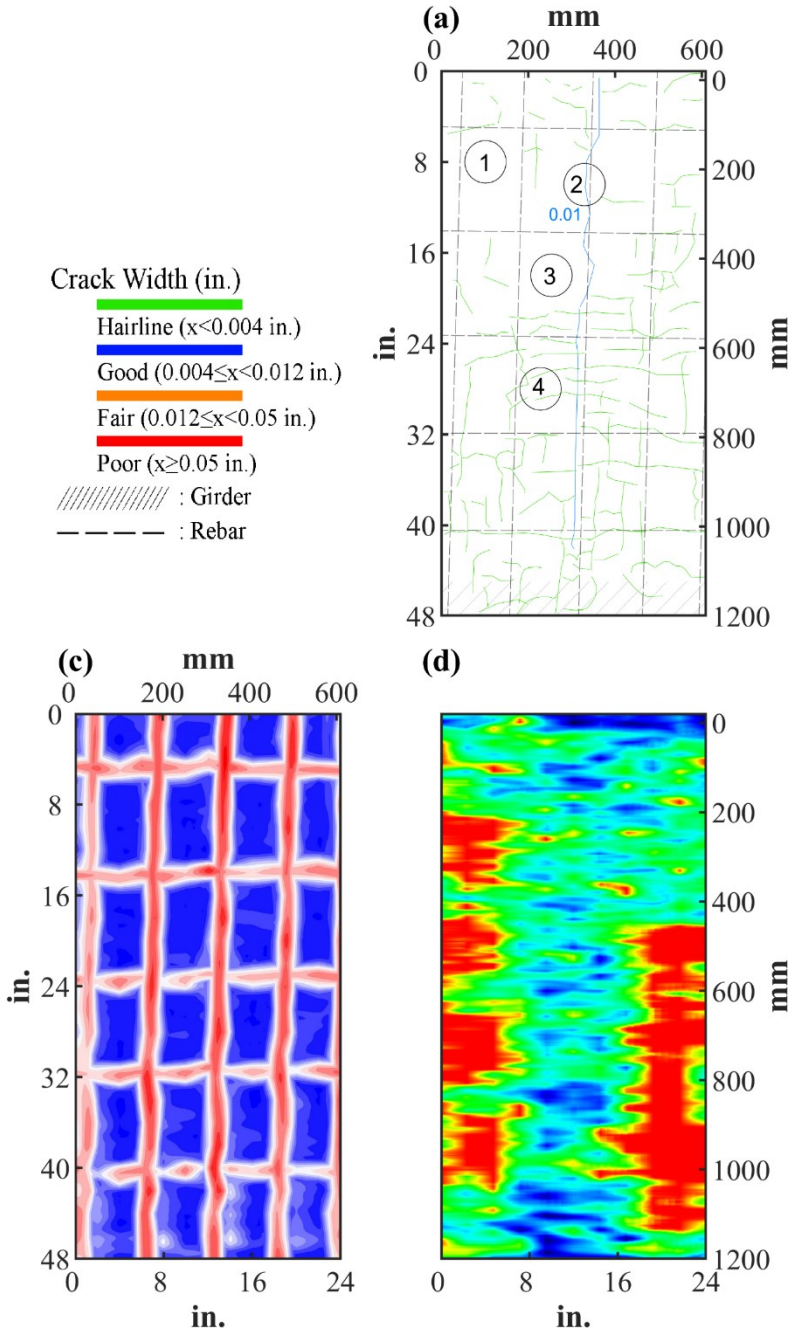

Figure 0.136. Crack Map and NDE Results of Grid 1: (a) Crack Map and Location of Cores; (c) GPR C-scan at 1.7 in. to 2.8 in. Depth; (d) UST C-scan at 6.7 in. Depth

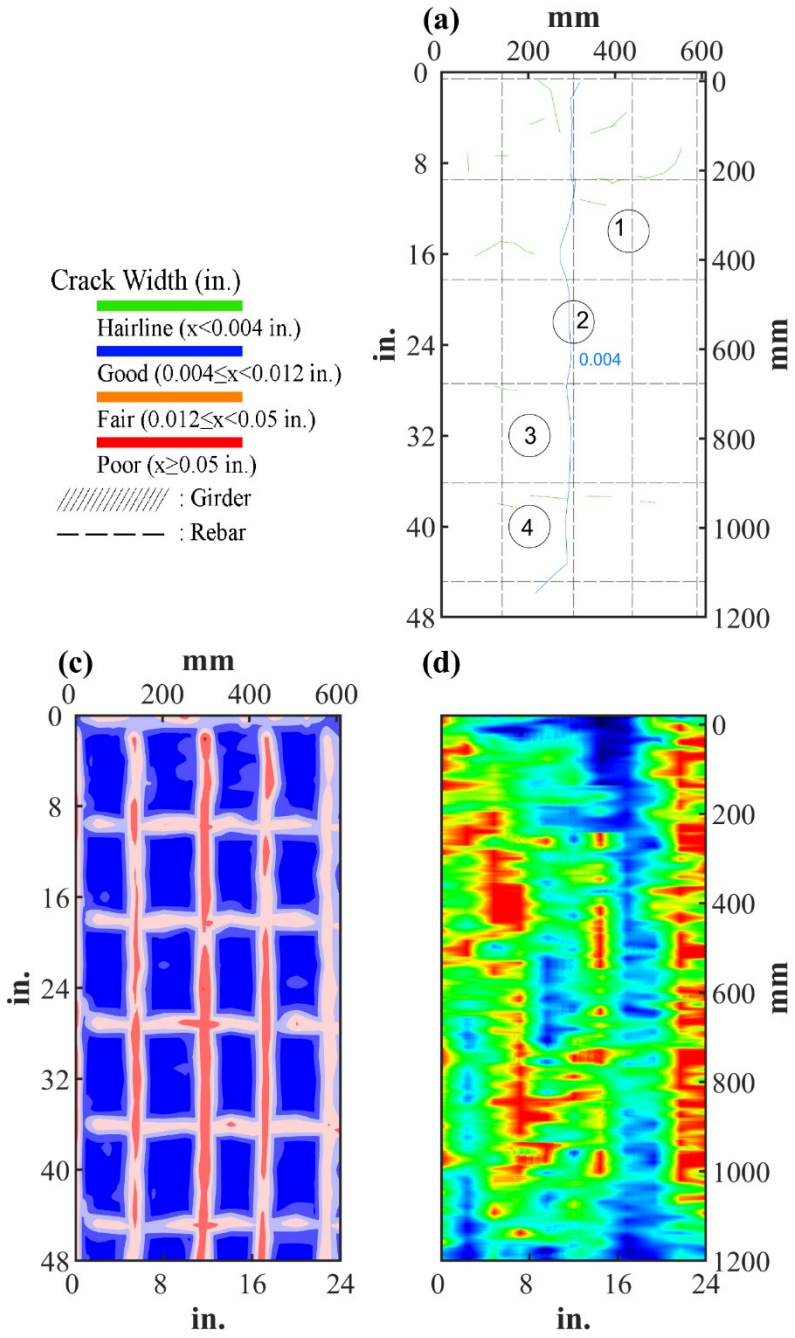

Figure 0.137. Crack Map and NDE Results of Grid 2: (a) Crack Map and Location of Cores; (c) GPR C-scan at 1.6 in. to 3.0 in. Depth; (d) UST C-scan at 3.2 in. Depth

B.19.3 Concrete Cores

Table B-78. Detail Information of Concrete Cores

Core	dia. x height (in.)	Rebar depth (in.)	Rebar size (#)	Epoxy (Y/N)	Crack type	Crack width (in)	Notes
1-1	3.75 x 5.5	-	-	-	-	-	-
1-2	3.75 x 6.4	2.1	5	Y	transverse	0.01	A crack propagates from panel joint
1-3	3.75 x 3.9	-	-	-	-	-	Delamination between CIP and PCP
1-4	3.75 x 5.0	-	-	-	map	HL	-
2-1	3.75 x 5.5	2.0	5	Y	-	-	-
2-2	3.75 x 3.6	2.1	5	Y	transverse	0.004	A crack propagates along intersection of aggregates
2-3	3.75 x 5.5	-	-	-	-	-	-
2-4	3.75 x 5.2	-	-	-	-	-	-

Table B-79. Core Pictures

Core	Pictures of the Cores		
1-1			
1-2			

1-3			
1-4			
2-1			
2-2			
2-3			
2-4			

B.19.4 Laboratory Experiment Results

B.19.4.1 Resistivity

Core Number	Surface Resistivity (kΩ·m)	Bulk Resistivity (kΩ·m)
-	-	-

B.19.4.2 Ultrasonic Pulse Velocity

Core Number	Ultrasonic Pulse Velocity (m/s)
1-3	4061
1-4	4516
2-3	4480

B.19.4.3 Carbonation Depth

Core Number	Carbonation Depth (in.)
1-2	0.00
2-4	0.13

B.19.4.4 Acid-Soluble Chloride Content

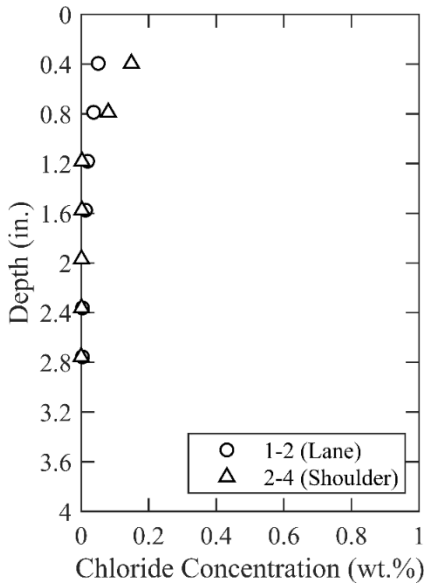

Figure 0.138. Chloride Content at Different Depth

B.19.4.5 Sorptivity

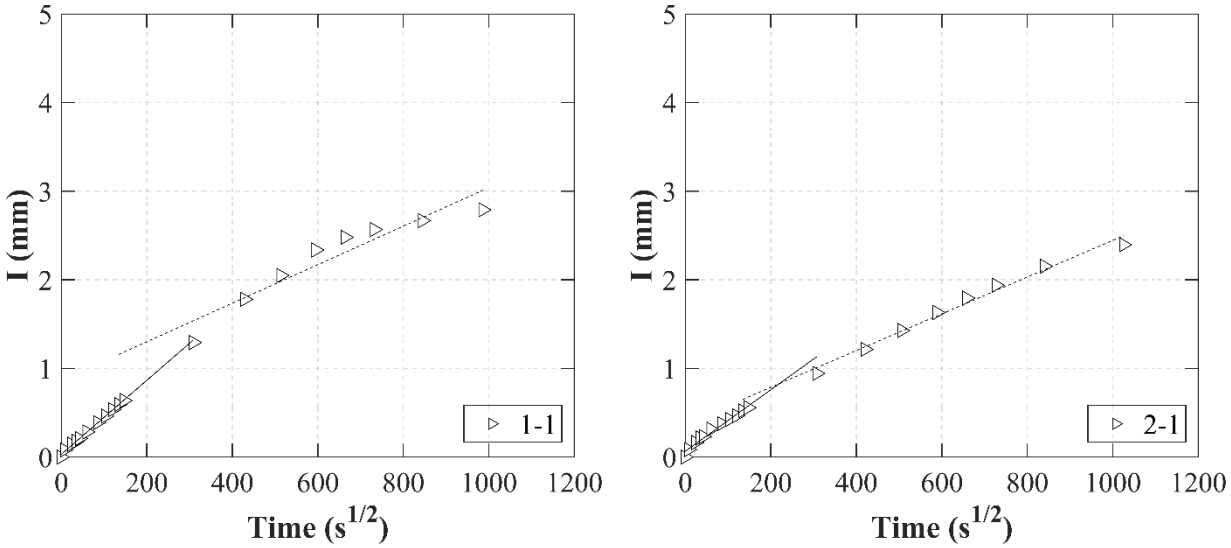

(a) Core 1–1 (b) Core 2–1

Figure 0.139. Absorption and Sorptivity of: (a) Core 1–1; (b) Core 2–1

Table B-80. Initial and Secondary Sorptivity Results

Core Number	Sorptivity	Results (mm/s$^{1/2}$)
Core 1–1	Initial Sorptivity	0.00418
	Secondary Sorptivity	0.00217
Core 2–1	Initial Sorptivity	0.00347
	Secondary Sorptivity	0.00207

B.19.4.6 Knife Test

Core Number	Score	Picture
1-2	10	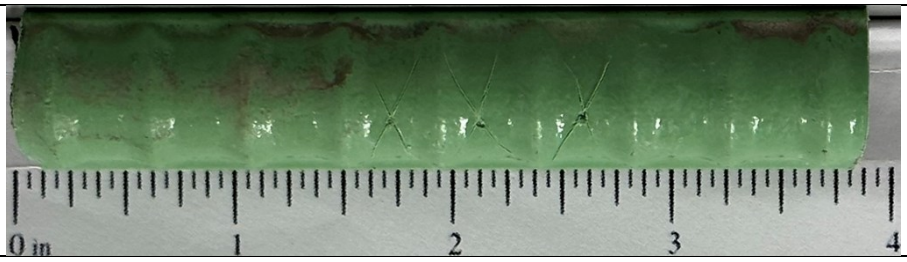

B.19.4.7 Electrochemical Impedance Spectroscopy

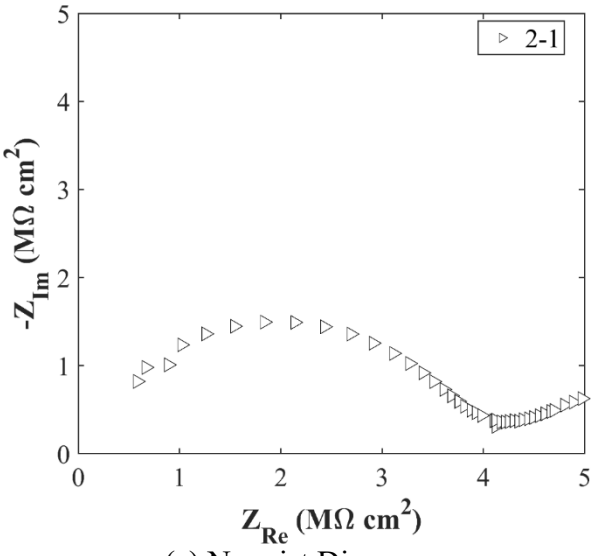

(a) Nyquist Diagram

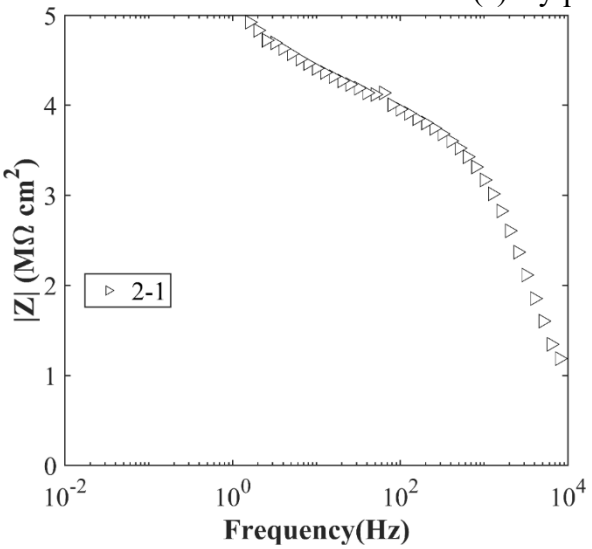

(b) Bode Plot of Impedance Modulus

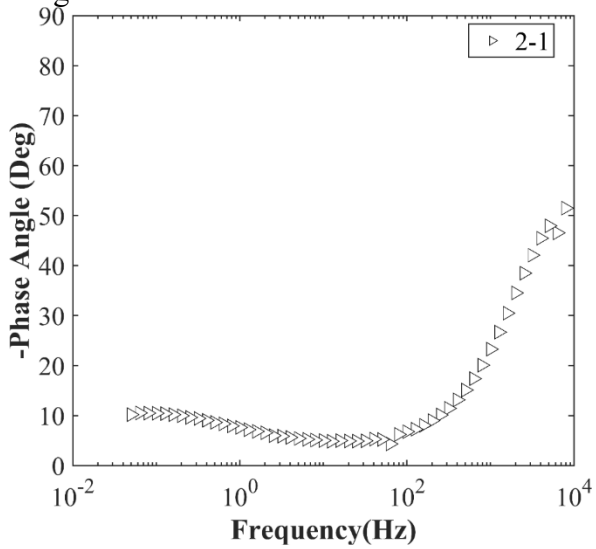

(c) Bode Plot of Impedance Phase

Figure 0.140. EIS Results: (a) Nyquist Diagram; (b) Bode Plot of Impedance Modulus; (c) Bode Plot of Impedance Phase

B.20 BMT-RC-01, SH 87 SB OVER CRANE BAYOU

- Bridge ID: 201240030603240, (Jefferson County)
- Built in 2015
- Mitigation methods: HPC
- Observed CIP depth: 4.8 in.
- Observed clear cover: 2.7 in.
- 3 spans, 6-PS concrete girder @ max 6.8’ spacing with 3’overhangs
- Inspected on June 08, 2021

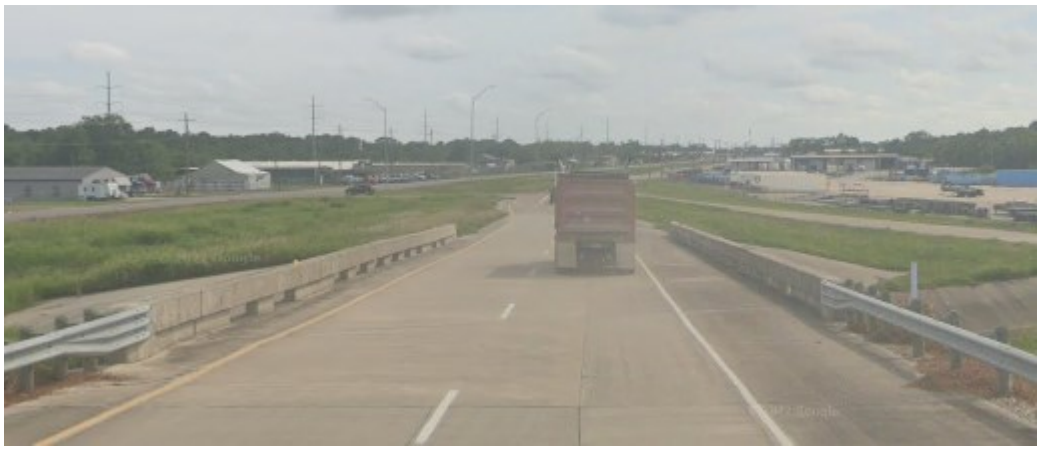

Figure 0.141. Concrete Deck of the Bridge (source: google maps)

B.20.1 Observed Condition

The top surface of deck is in good condition with only minor cracks.

B.20.2 NDE Results

Grid 1 was located on the span 2, and Grid 2 was located on the span 1 of the bridge as shown in Figure 0.142.

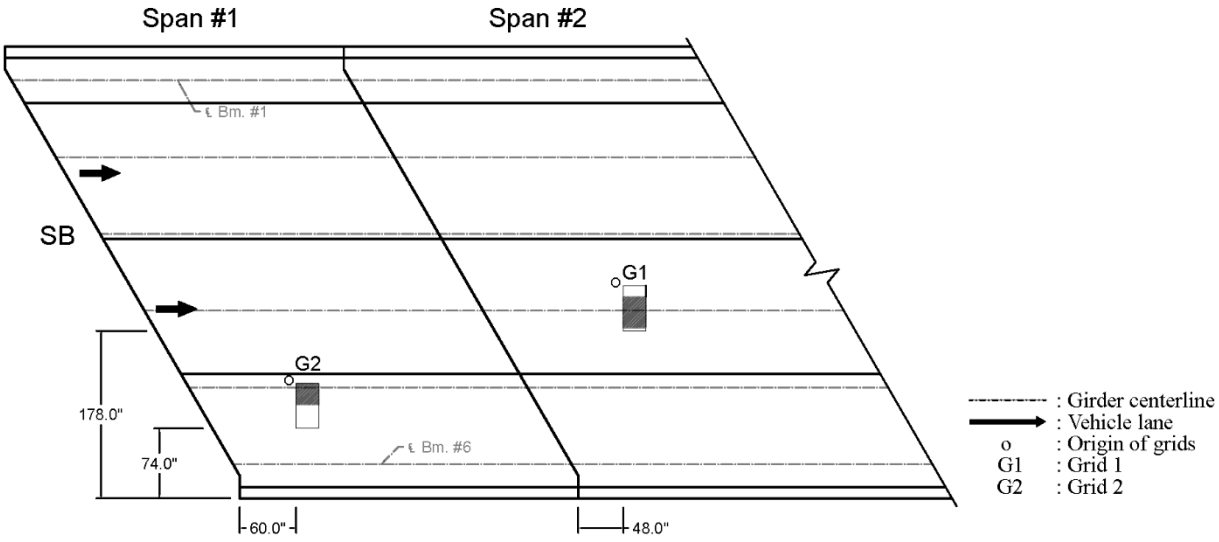

Figure 0.142. Plan View of the Bridge and Location of Grids

As shown in Figure 0.143 (a), Grid 1 was located on the longitudinal construction joint. On Grid 2, there was a 0.004 in. wide diagonal crack as shown in Figure 0.144 (a). The deck was in very good condition with almost no cracks.

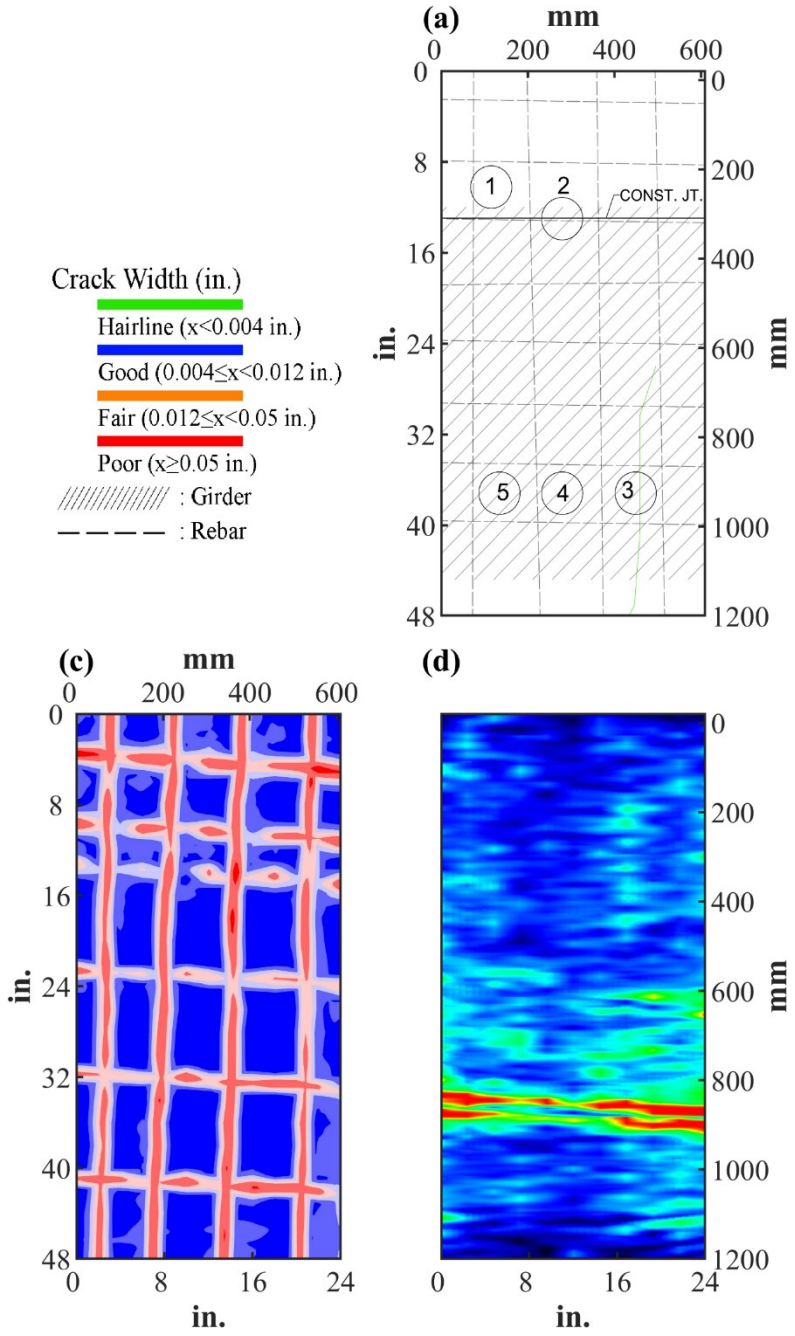

Figure 0.143. Crack Map and NDE Results of Grid 1: (a) Crack Map and Location of Cores; (c) GPR C-scan at 1.7 in. to 2.8 in. Depth; (d) UST C-scan at 6.7 in. Depth

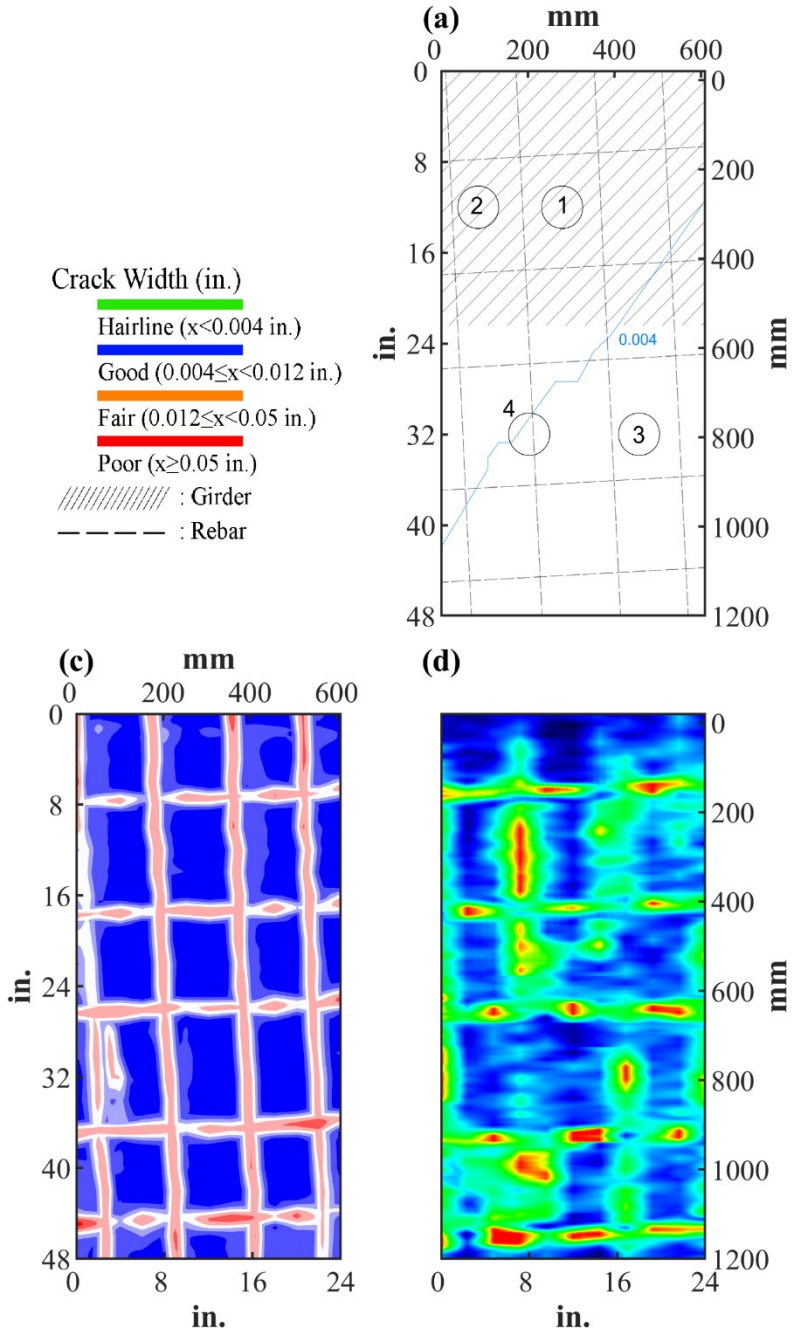

Figure 0.144. Crack Map and NDE Results of Grid 1: (a) Crack Map and Location of Cores; (c) GPR C-scan at 1.7 in. to 2.8 in. Depth; (d) UST C-scan at 6.7 in. Depth

B.20.3 Concrete Cores

Table B-81. Detail Information of Concrete Cores

Core	dia. x height (in.)	Rebar depth (in.)	Rebar size (#)	Epoxy (Y/N)	Crack type	Crack width (in)	Notes
1-1	3.75 x 6.3	2.7	5	N	-	-	-
1-2	3.75 x 6.4	3.1	5	N	-	-	Core split due to construction joint
1-3	3.75 x 4.7	-	-	-	transverse	HL	-
1-4	3.75 x 4.8	-	-	-	-	-	-
1-5	3.75 x 4.8	-	-	-	-	-	-
2-1	3.75 x 4.9	-	-	-	-	-	-
2-2	3.75 x 6.7	-	-	-	-	-	-
2-3	3.75 x 6.6	-	-	-	-	-	-
2-4	3.75 x 5.2	2.4	5	N	diagonal	HL	-

Table B-82. Core Pictures

Core	Pictures of the Cores		
1-1		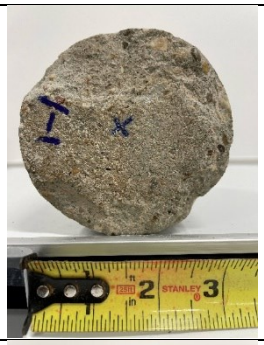	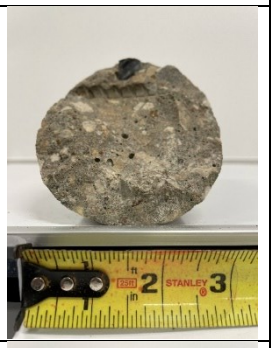
1-2	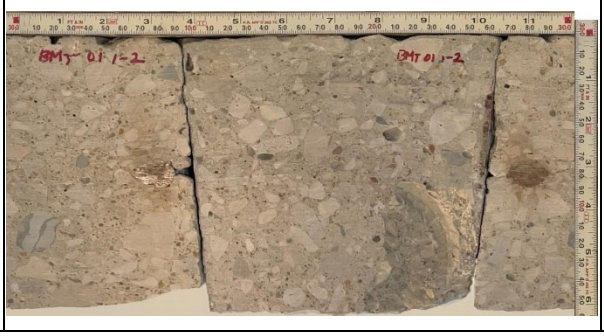		

1-3			
1-4			
1-5		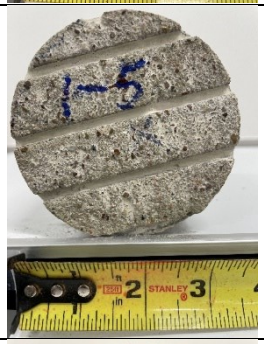	
2-1		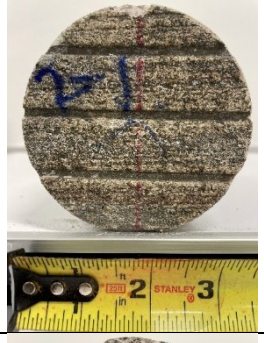	
2-2		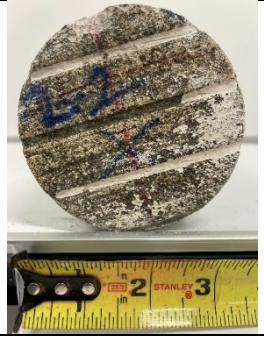	

2-3	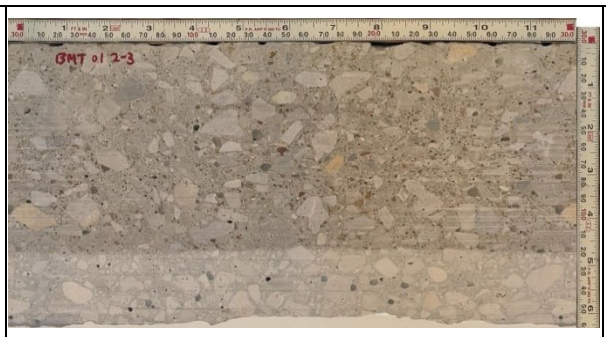	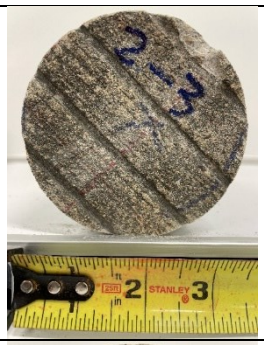	
2-4		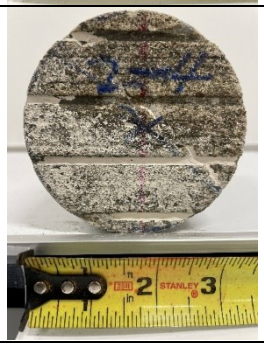	

B.20.4 Laboratory Experiment Results

B.20.4.1 Resistivity

Core Number	Surface Resistivity (kΩ·m)	Bulk Resistivity (kΩ·m)
1-4	517	-
1-5	399	61.8
2-1	-	39.6
2-2	245	-

B.20.4.2 Ultrasonic Pulse Velocity

Core Number	Ultrasonic Pulse Velocity (m/s)
1-4	4847
1-5	4969
2-1	4606
2-2	4819
2-3	5000

B.20.4.3 Carbonation Depth

Core Number	Carbonation Depth (in.)
1-2	0.00

B.20.4.4 Acid-Soluble Chloride Content

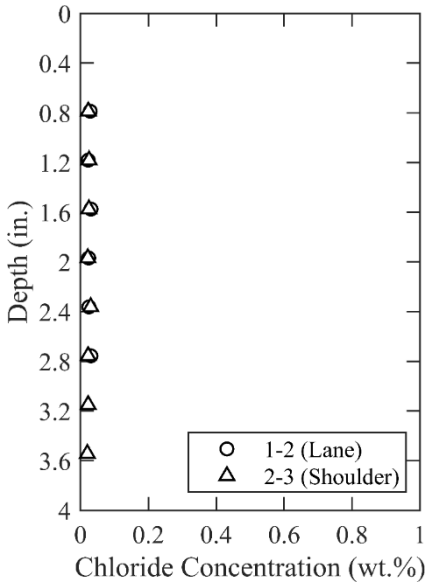

Figure 0.145. Chloride Content at Different Depth

B.20.4.5 Sorptivity

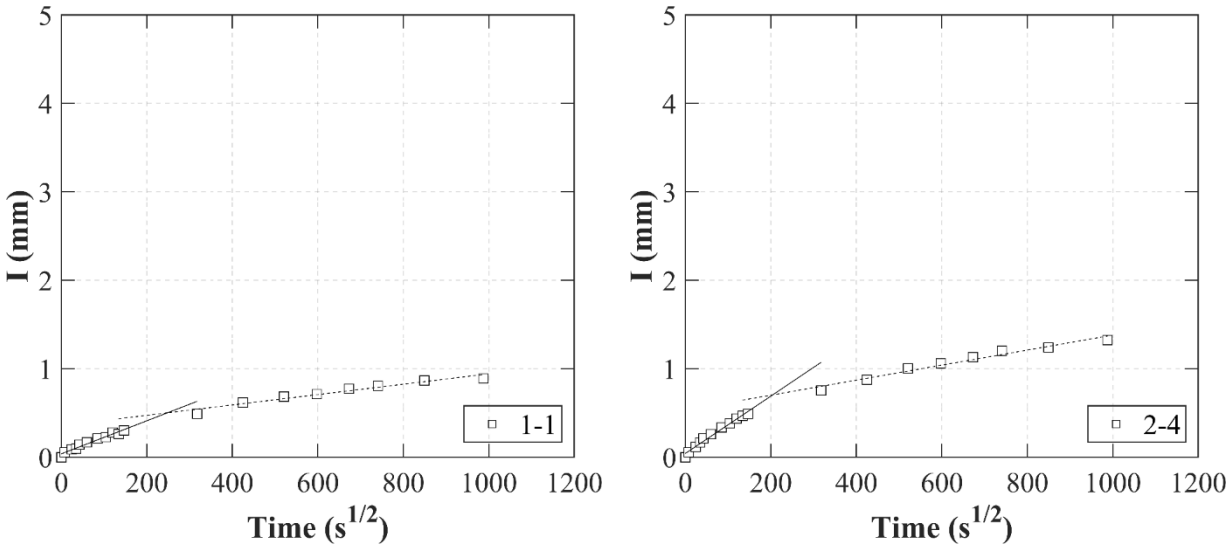

(a) Core 1–1 (b) Core 2–4

Figure 0.146. Absorption and Sorptivity of: (a) Core 1–1; (b) Core 2–4

Table B-83. Initial and Secondary Sorptivity Results

Core Number	Sorptivity	Results (mm/s$^{1/2}$)
Core 1–1	Initial Sorptivity	0.00187
	Secondary Sorptivity	0.00059
Core 2–4	Initial Sorptivity	0.00324
	Secondary Sorptivity	0.00085

B.21 CHS-RC-01, US 62 OVER RED RIVER

- Bridge ID: 250380003105019, (Childress County)
- Built in 1994
- Mitigation methods: ECR
- Deck: 7.25 in.
- Observed clear cover: 2.0 in.
- 12 spans, 7-PS concrete girder @ max 8-8 in. spacing with 3'-1.5 in. overhangs
- Inspected on Feb 18, 2022

Figure 0.147. Concrete Deck of the Bridge (source: google maps)

B.21.1 Observed Condition

The concrete railing had been demolished, and some corroded rebar was found on the edge of railing as shown in Figure 0.148 (a). It was noted that the epoxy-coated rebar was used for top rebar whereas the bottom rebars were black rebars without any coating. As can be seen from Figure A.1.2 (a), bottom black rebar displayed severe corrosion. Expansion joint is partially failed and full of dirt and debris as shown in Figure A.1.2 (b). In the superstructure, extensive delamination was found along the deck overhang as shown in Figure A.1.2 (c). Spalling and exposed rebar were found on the end of beam at bent 25 as shown in Figure 0.148 (d). Severe vertical cracking was found the bent 29 as shown in Figure 0.148 (e).

(a)

(b)

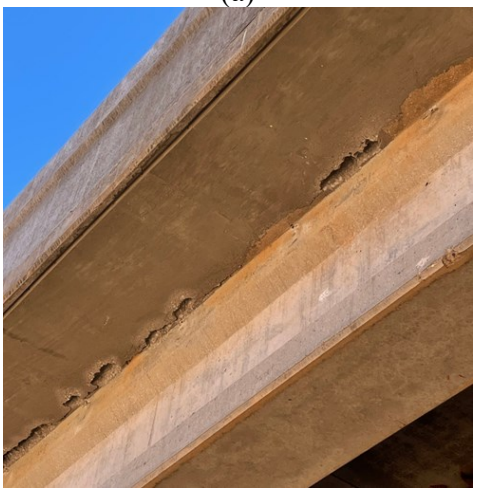

(c)

(d)

(e)

Figure 0.148. Deteriorations on the Bridge Deck: (a) Corroded black rebar at the railing edge; (b) Spalling of overlay at Joint; (c) Delamination along the west overhang of Span 26; (d) Spalling and exposed rebar of girders at bent 25; (e) Sealed cracks at bent 29

B.21.2 NDE Results

Grid 1 was located on SB shoulder lane. Because bridge was under construction and had asphalt overlay, an arbitrary location on the shoulder of span 29 where the asphalt overlay could be taken out was decided. As shown in Figure 0.149 (a), grid 1 did not have any cracks partly because the deck was originally covered by asphalt overlay.

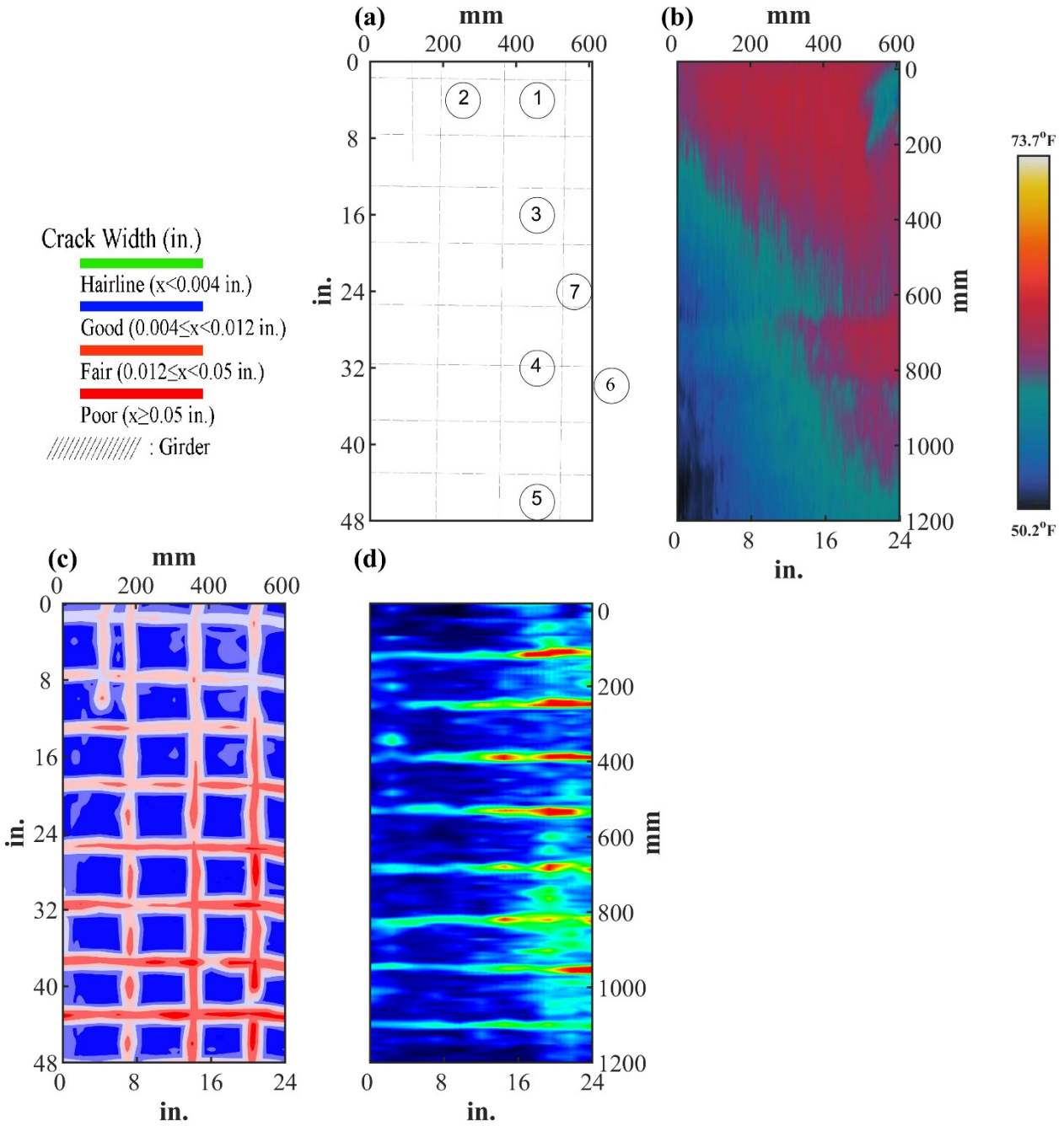

Figure 0.149. Crack Map and NDE Results of Grid 1: (a) Crack Map and Location of Cores; (b) Infrared Picture; (c) GPR C-scan at 1.5 in. to 3.4 in. Depth; (d) UST C-scan at 2.0 in. Depth

B.21.3 Concrete Cores

Table B-84. Detail Information of concrete cores

Core	dia. x height (in.)	Rebar depth (in.)	Rebar size (#)	Epoxy (Y/N)	Crack type	Crack width (in)	Notes
1-1	3.75 x6.7	-	-	-	-	-	-
1-2	3.75 x 7.9	-	-	-	-	-	-
1-3	3.75 x 7.9	-	-	-	-	-	-
1-4	3.75 x 7.9	2	5	Y	-	-	-
1-5	3.75 x 7.9	-	-	-	-	-	-
1-6	3.75 x 7.9	2.6; 5.0	5; 5	Y; Y	-	-	-
1-7	3.75 x 7.9	2.2; 5.1	5; 5	Y; Y	-	-	-

Table B-85. Core Pictures

Core	Pictures of the Cores
1-1	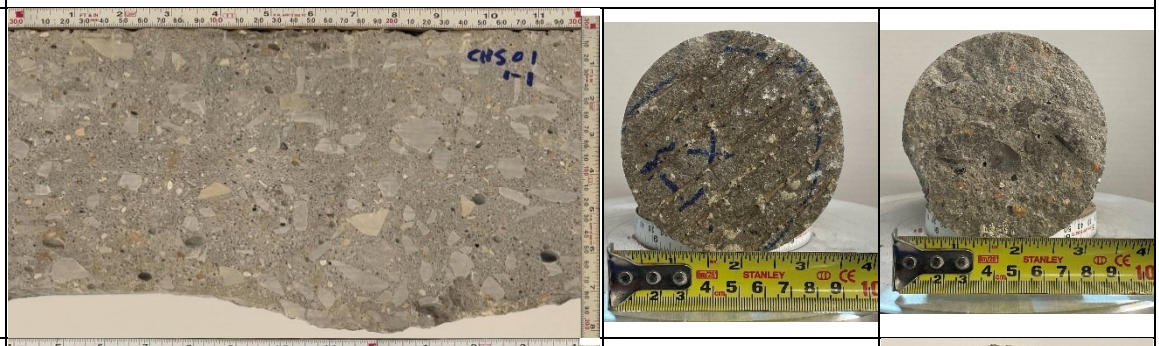
1-2	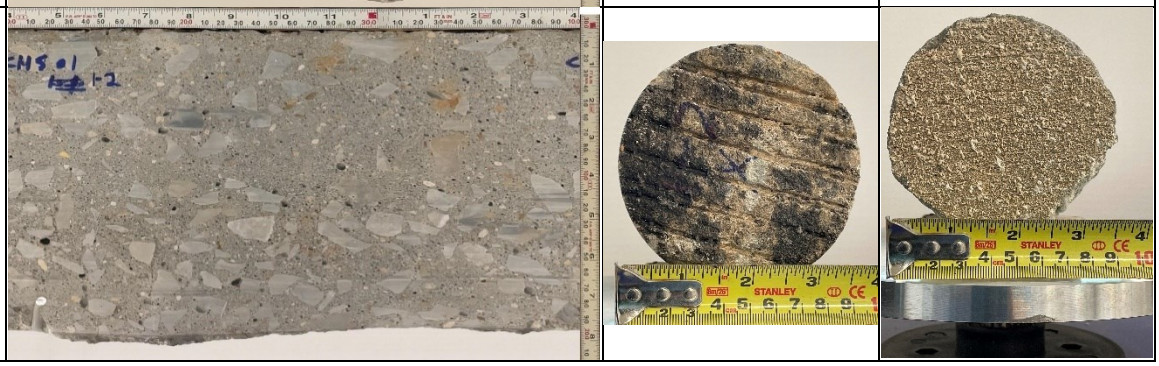

1-3			
1-4			
1-5			
1-6			
1-7			

B.21.4 Laboratory Experiment Results

B.21.4.1 Resistivity

Core Number	Surface Resistivity (kΩ·m)	Bulk Resistivity (kΩ·m)
1-1	20	6.6
1-2	20	-
1-3	27	-
1-5	23	10.6

B.21.4.2 Ultrasonic Pulse Velocity

Core Number	Ultrasonic Pulse Velocity
1-1	3417
1-2	3513
1-3	3651
1-5	4221

B.21.4.3 Carbonation Depth

Core Number	Carbonation Depth
1-3	0.00
1-7	0.10

B.21.4.4 Acid-Soluble Chloride Content

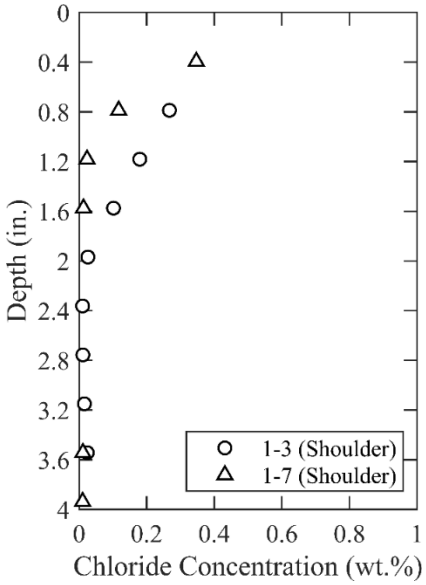

Figure 0.150. Chloride Content at Different Depth

B.21.4.5 Sorptivity

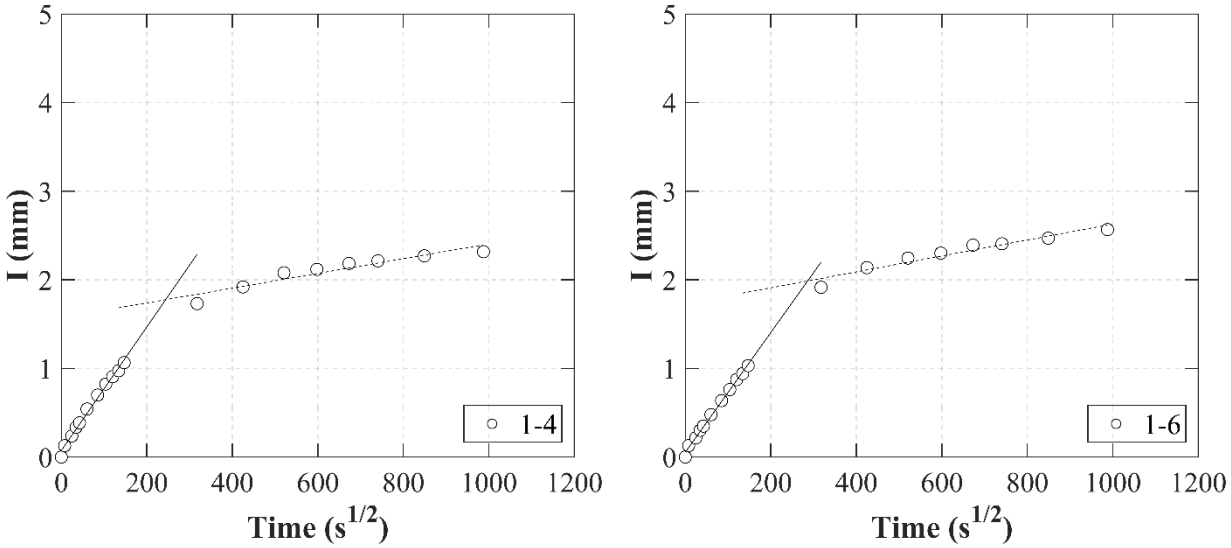

(a) Core 1–4 (b) Core 1–6

Figure 0.151. Absorption and Sorptivity of: (a) Core 1–4; (b) Core 1–6

Table B-86. Initial and Secondary Sorptivity Results

Core Number	Sorptivity	Results (mm/s$^{1/2}$)
Core 1–4	Initial Sorptivity	0.00697
	Secondary Sorptivity	0.00083
Core 1–6	Initial Sorptivity	0.00676
	Secondary Sorptivity	0.00090

B.21.4.6 Knife Test

Core Number	Score	Picture
1-7	10	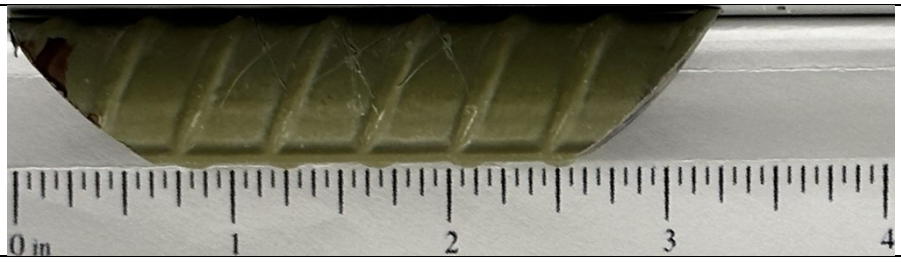

B.21.4.7 Electrochemical Impedance Spectroscopy

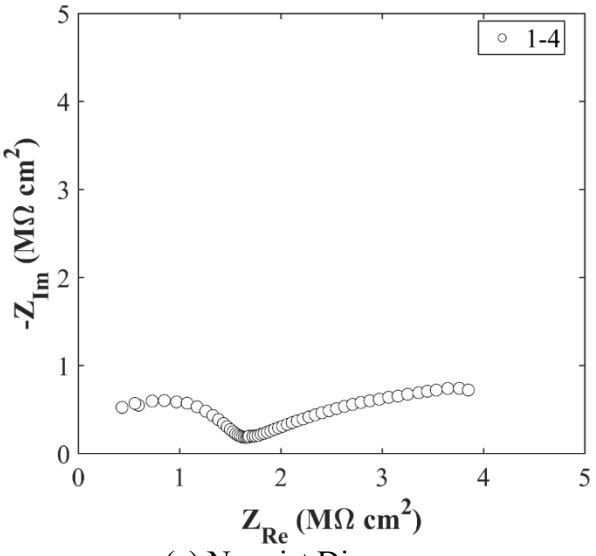

(a) Nyquist Diagram

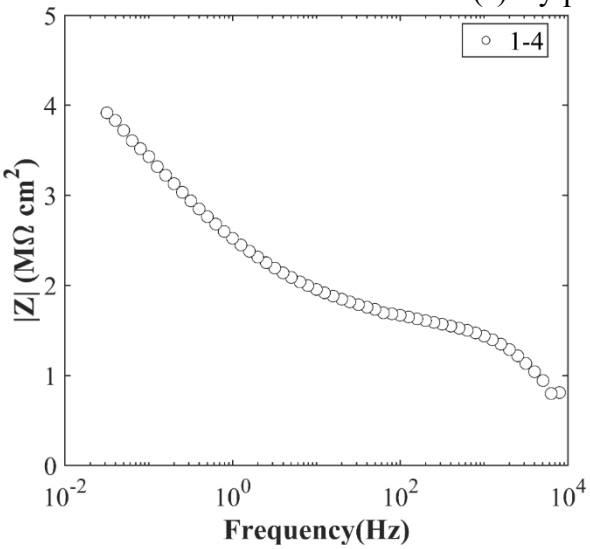

(b) Bode Plot of Impedance Modulus

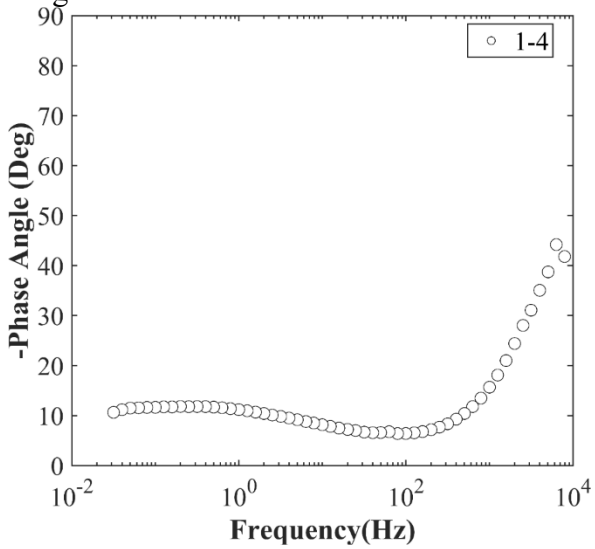

(c) Bode Plot of Impedance Phase

Figure 0.152. EIS Results: (a) Nyquist Diagram; (b) Bode Plot of Impedance Modulus; (c) Bode Plot of Impedance Phase

B.22 CHS-RC-02, US 83 OVER BUCK CREEK

- Bridge ID: 250380003105020 (Childress County)
- Built in 1997
- Mitigation methods: CNI (4 gal./CY.), Silane, ECR
- Observed CIP depth: unknown
- Observed clear cover: 2.2 in.
- 7 spans, 6-PS concrete girder @ 7.6’ spacing with max 3’ overhangs
- Inspected on Feb 18, 2022

Figure 0.153. Concrete Deck of the Bridge (source: google maps)

B.22.1 Observed Condition

Deck surface has transverse and longitudinal cracks as shown in Figure 0.154 (a), and there were hairline cracks on the abutment.

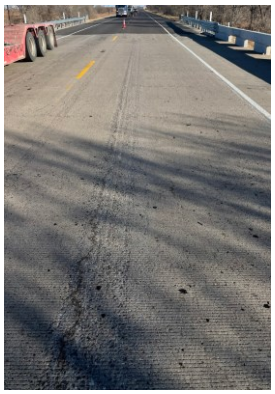

(a)

(b)

Figure 0.154. Deteriorations on the Bridge Deck: (a) Transverse and Longitudinal Cracks on the Deck Surface; (b) Hairline cracks at Abutment

B.22.2 NDE Results

Grid 1 was located on the SB lane and grid 2 was located on the SB shoulder lane of the span 4 of the bridge.

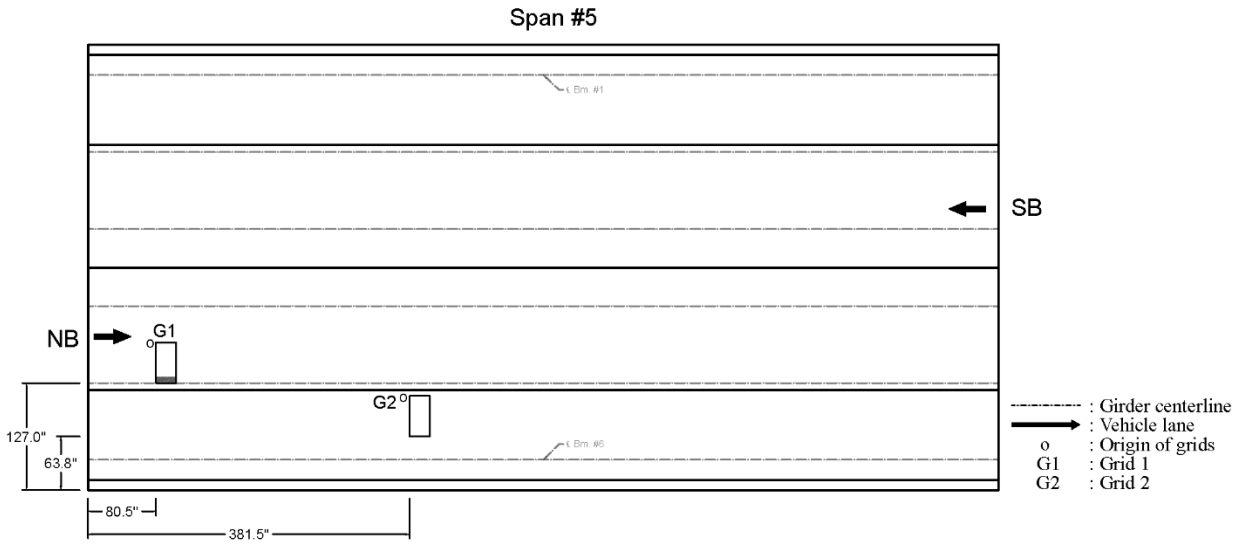

Figure 0.155. Plan View of the Bridge and Location of Grids

As shown in Figure 0.156 (a), there are widespread of cracks that range from 0.006 in. and 0.008 in. wide. The widest crack width was 0.02 in. transverse crack. It is possible that transverse crack was caused by panel joints. The Grid 2 had one 0.004 in. wide transverse crack as shown in Figure 0.157 (a).

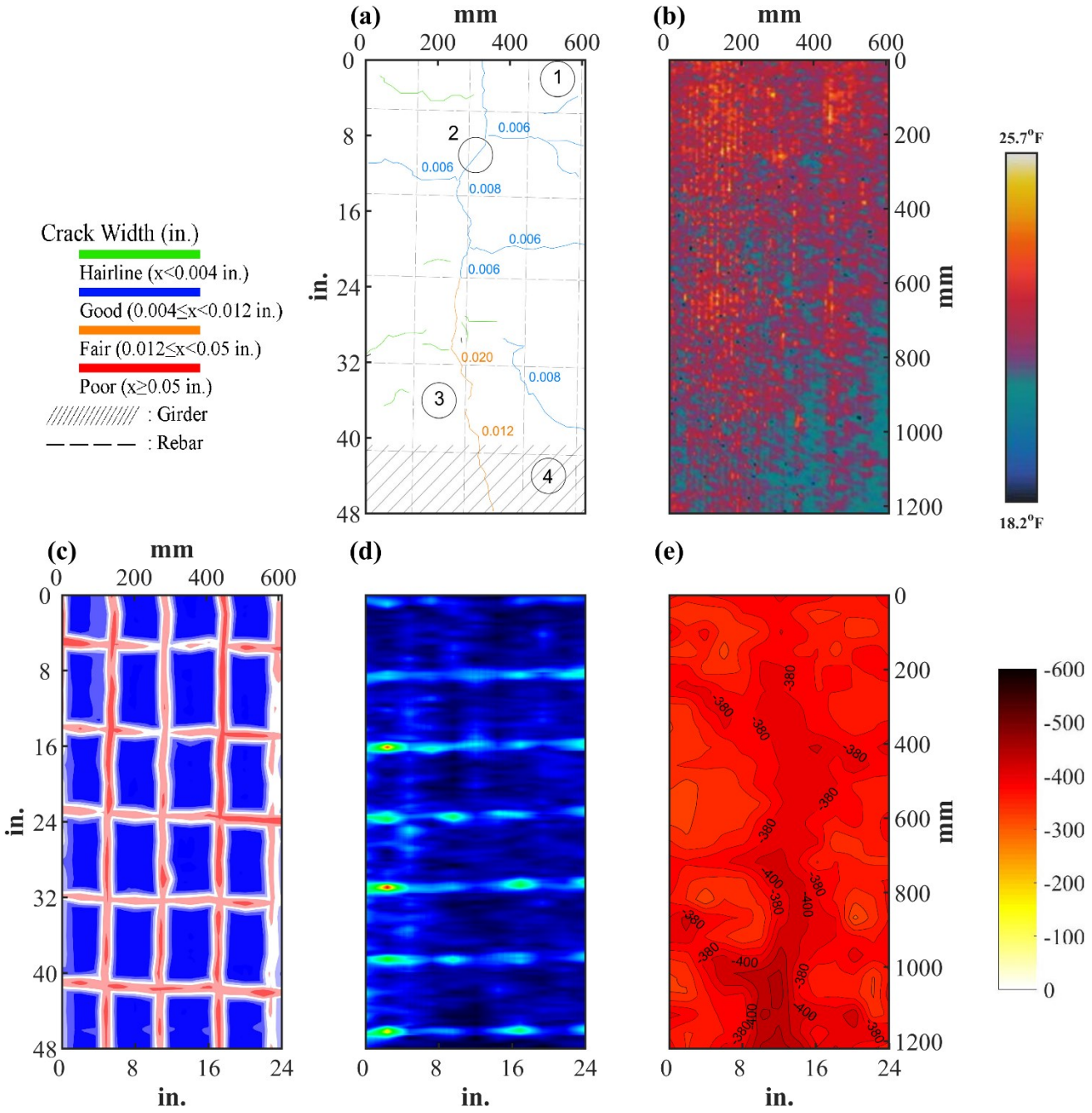

Figure 0.156. NDE Results of Grid 1: (a) Crack Map and Location of Cores; (b) Infrared Picture; (c) GPR C-scan at 1.75 in. to 3.15 in. Depth; (d) UST C-scan at 2.9 in. Depth; (e) Corrosion Rate Map

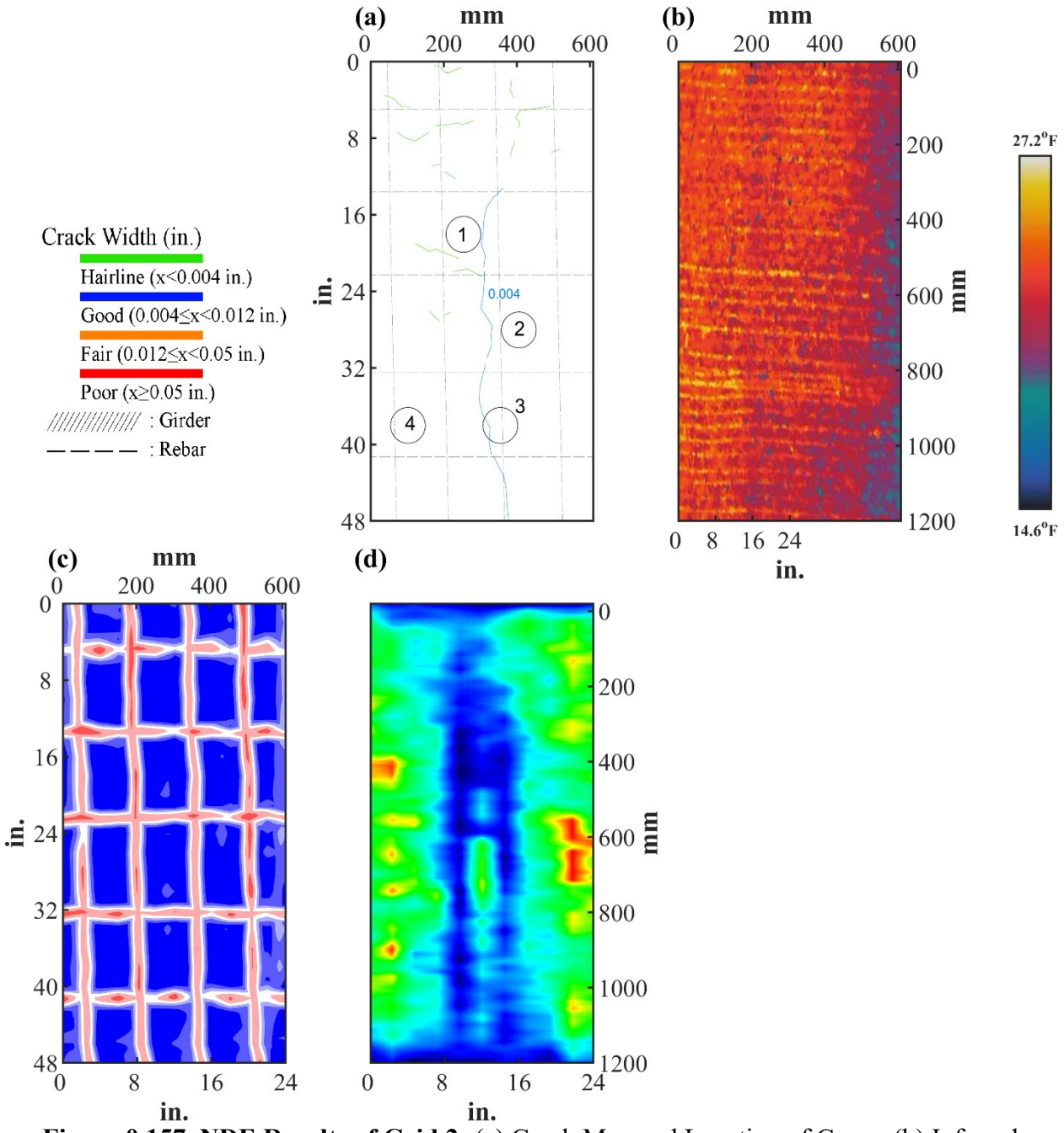

Figure 0.157. NDE Results of Grid 2: (a) Crack Map and Location of Cores; (b) Infrared Picture; (c) GPR C-scan at 2 in. to 3.4 in. Depth; (d) UST C-scan at 9.3 in. Depth

B.22.3 Concrete Cores

Table B-87. Detail Information of concrete cores

Core	dia. x height (in.)	Rebar depth (in.)	Rebar size (#)	Epoxy (Y/N)	Crack type	Crack width (in)	Notes
1-1	3.75 x 5.5	-	-	-	-	-	-
1-2	3.75 x 2.4	2.4	5	Y	diagonal	0.008	Corroded rebar; A crack propagates from rebar
1-3	3.75 x 5.1	-	-	-	-	-	-
1-4	3.75 x 5.5	-	-	-	-	-	-
2-1	3.75 x 5.3	-	-	-	transverse	0.004	-
2-2	3.75 x 6.3	2.2	5	Y	-	-	-
2-3	3.75 x 6.5	2.3	5	Y	-	-	-
2-4	3.75 x 5.0	2.4	5	Y	-	-	-

Table B-88. Core Pictures

Core	Pictures of the Cores
1-1	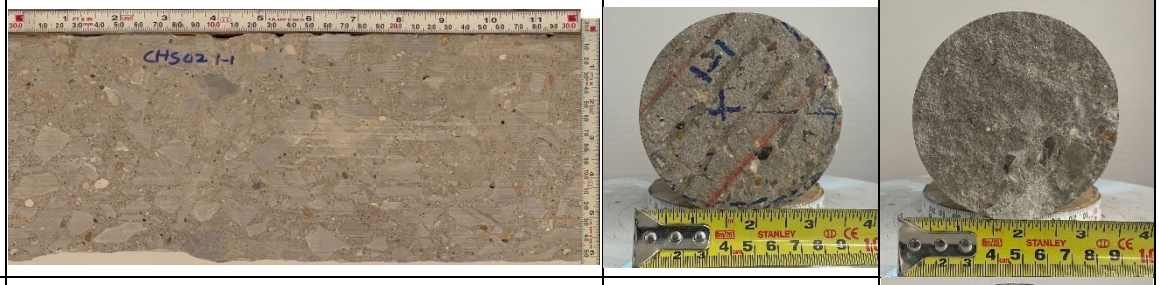
1-2	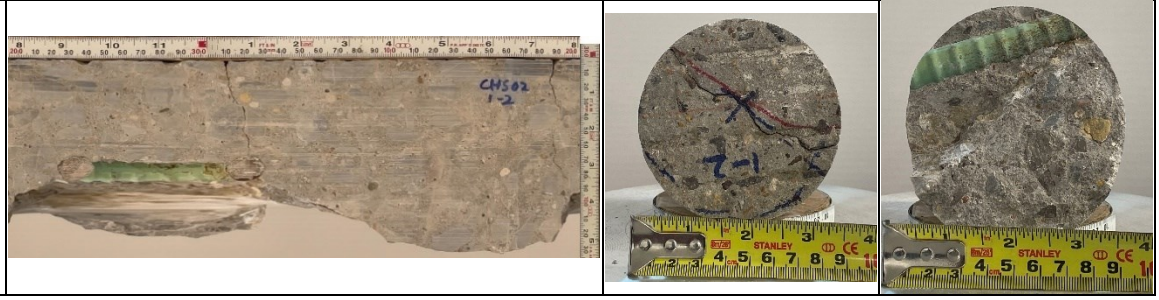

1-3			
1-4			
2-1			
2-2			
2-3			

2-4	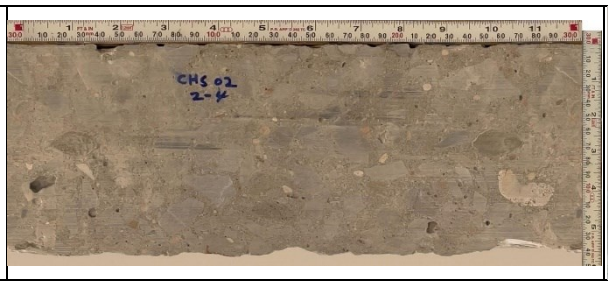		

B.22.4 Laboratory Experiment Results

B.22.4.1 Resistivity

Core Number	Surface Resistivity (kΩ·m)	Bulk Resistivity (kΩ·m)
1-1	23	-
1-3	21	4.4
1-4	21	-
2-1	26	-
2-2	26	6.1

B.22.4.2 Ultrasonic Pulse Velocity

Core Number	Ultrasonic Pulse Velocity (m/s)
1-1	4337
1-3	4080
1-4	4196
2-1	4452
2-2	4693

B.22.4.3 Carbonation Depth

Core Number	Carbonation Depth (in.)
1-2	0.00
2-4	0.21

B.22.4.4 Acid-Soluble Chloride Content

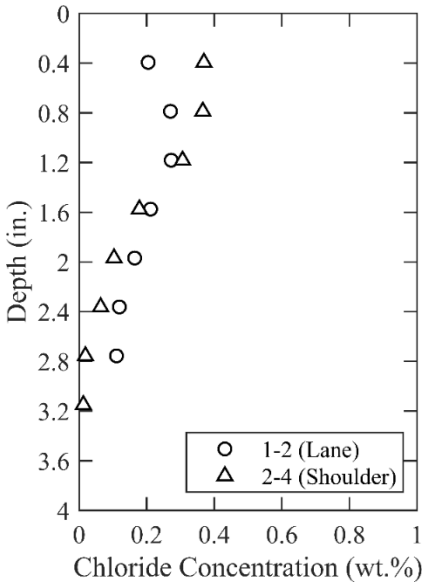

Figure 0.158. Chloride Content at Different Depth

B.22.4.5 Sorptivity

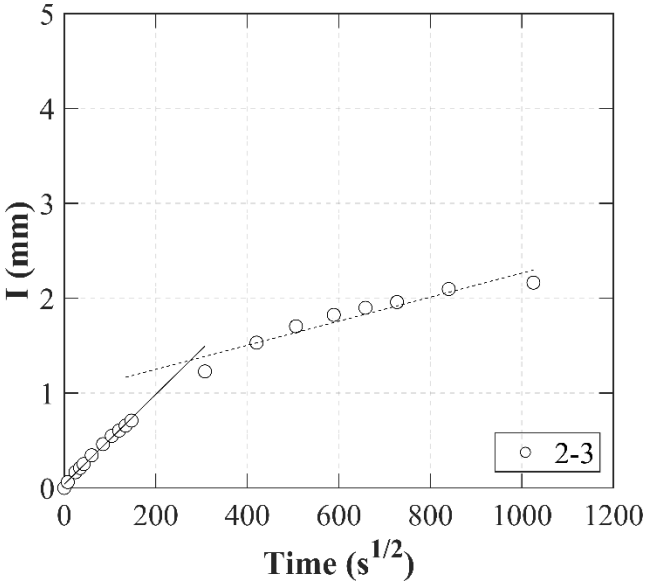

Figure 0.159. Absorption and Sorptivity of Core 2–3

Table B-89. Initial and Secondary Sorptivity Results

Core Number	Sorptivity	Results ($mm/s^{1/2}$)
Core 2–3	Initial Sorptivity	0.00474
	Secondary Sorptivity	0.00127

B.22.4.6 Knife Test

Core Number	Score	Picture
1-2	4	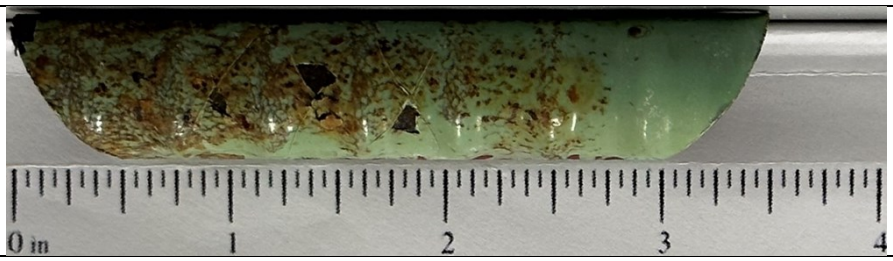

B.22.4.7 Electrochemical Impedance Spectroscopy

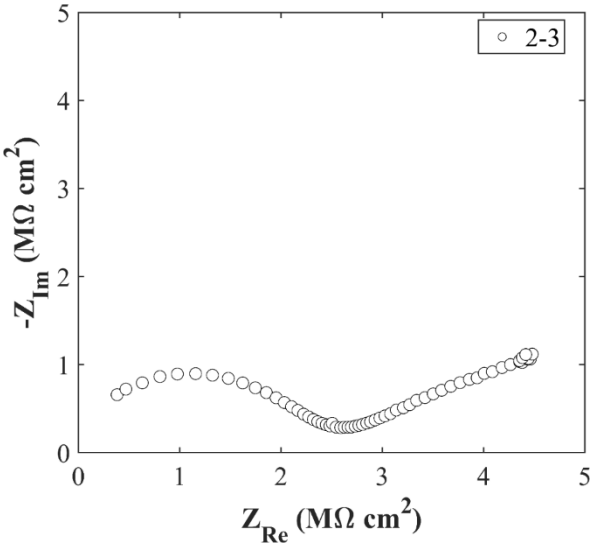

(a) Nyquist Diagram

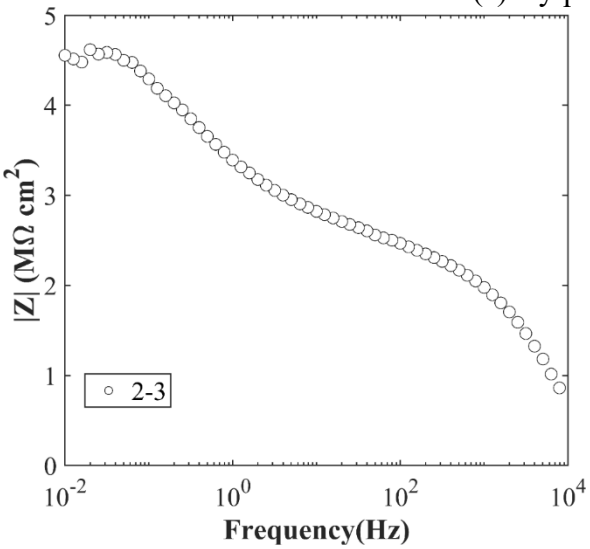

(b) Bode Plot of Impedance Modulus

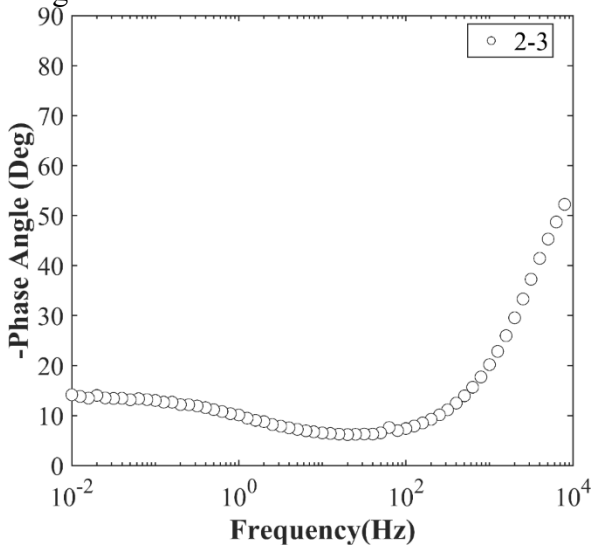

(c) Bode Plot of Impedance Phase

Figure 0.160. EIS Results: (a) Nyquist Diagram; (b) Bode Plot of Impedance Modulus; (c) Bode Plot of Impedance Phase

B.23 CHS-RC-03, US 83 OVER N SCATTERBRANCH CRK

- Bridge ID: 250380003201023 (Childless County)
- Built in 2002
- Mitigation methods: HPC, ECR
- Observed CIP depth: 4.1 in.
- Observed clear cover: 2 in.
- 2 spans, 6-concrete PS girder @ 8’ spacing with 3’ overhangs
- Inspected on Feb 17 2022

Figure 0.161. Concrete Deck of the Bridge (source: google maps)

B.23.1 Observed Condition

Deck surface has hairline to minor diagonal, transverse, and longitudinal cracks.

B.23.2 NDE Results

Grid 1 was located on the SB lane and grid 2 was located on the SB shoulder lane of the span 4 of the bridge.

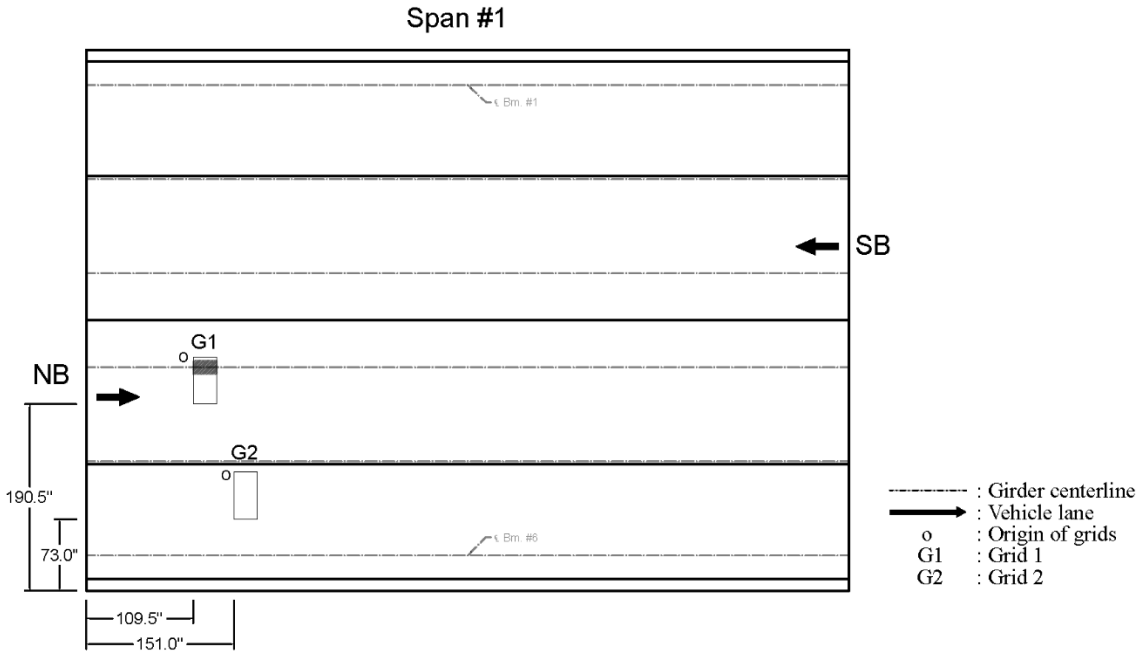

Figure 0.162. Plan View of the Bridge and Location of Grids

As shown in Figure 0.163 (a), there was a 0.004 in. wide longitudinal crack on top of girder and 0.006 in. wide transverse crack on grid 1. On grid 2, there was two short cracks that are 0.004 in. wide as shown in Figure 0.164 (a).

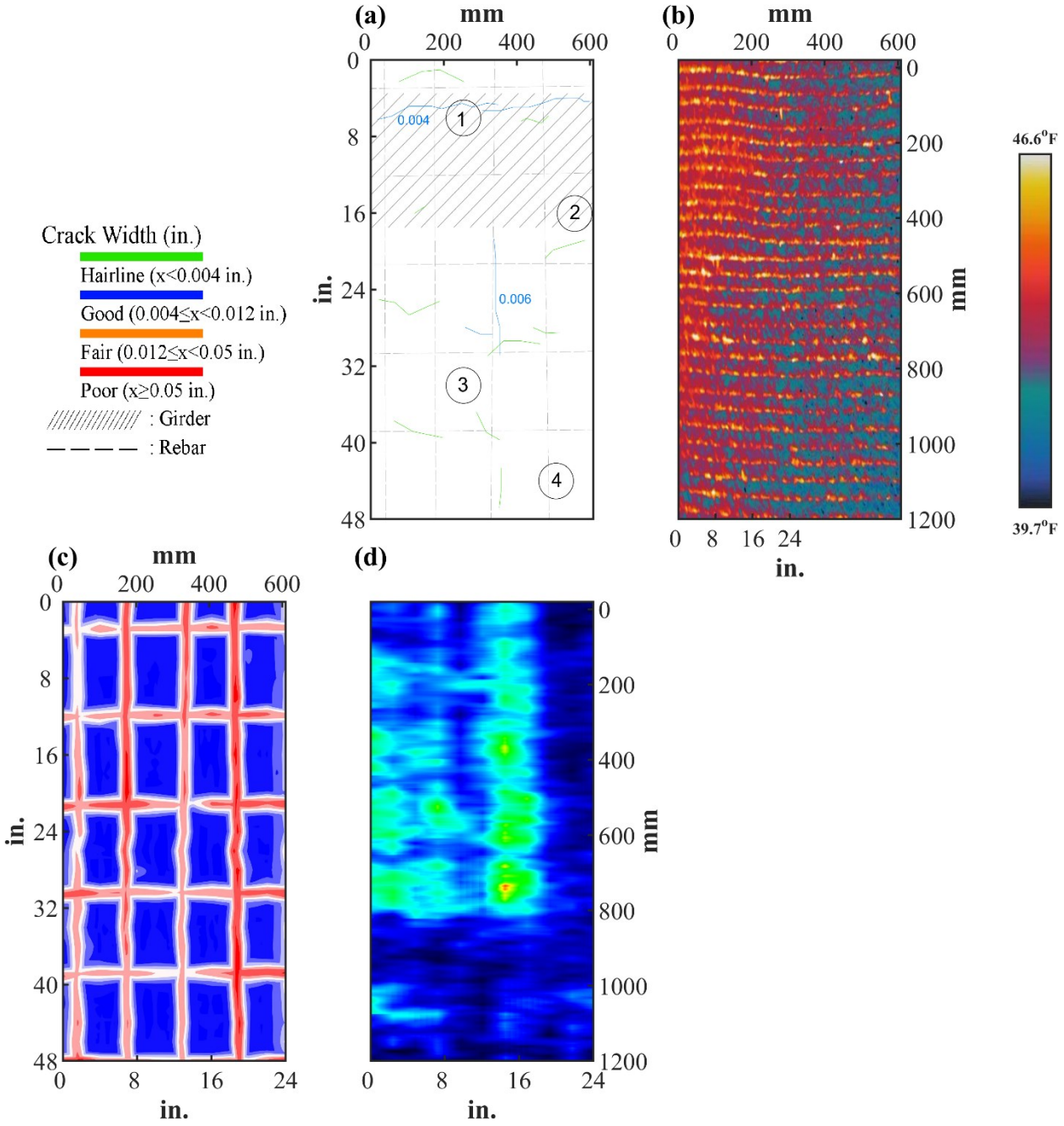

Figure 0.163. NDE Results of Grid 1: (a) Crack Map and Location of Cores; (b) Infrared Picture; (c) GPR C-scan at 1.25 in. to 2.65 in. Depth; (d) UST C-scan at 4.5 in. Depth

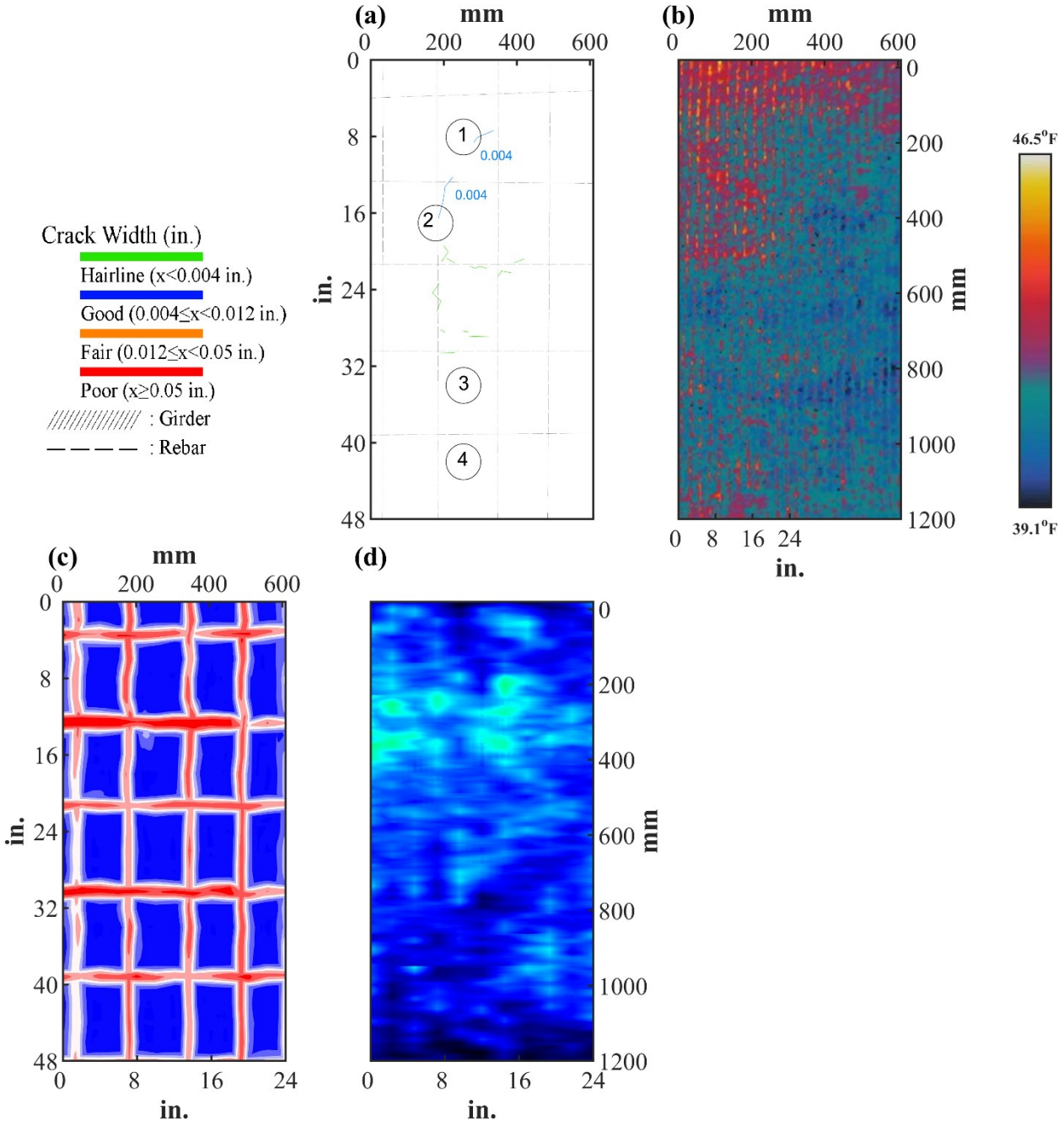

Figure 0.164. NDE Results of Grid 2: (a) Crack Map and Location of Cores; (b) Infrared Picture; (c) GPR C-scan at 1.25 in. to 2.65 in. Depth; (d) UST C-scan at 8.5 in. Depth

B.23.3 Concrete Cores

Table B-90. Detail Information of concrete cores

Core	dia. x height (in.)	Rebar depth (in.)	Rebar size (#)	Epoxy (Y/N)	Crack type	Crack width (in)	Notes
1-1	3.75 x 4.2	-	-	-	longitudinal	0.004	-
1-2	3.75 x 4.1	-	-	-	-	-	Delamination between CIP and PCP; A crack propagates from CIP and PCP intersection
1-3	3.75 x 4.1	-	-	-	-	-	Delamination between CIP and PCP
1-4	3.75 x 3.9	2.9	5	Y	-	-	A void near rebar; Delamination between CIP and PCP
2-1	3.75 x 3.7	-	-	-	longitudinal	0.004	A crack propagates along intersection of aggregates
2-2	3.75 x 3.7	2	5	Y	transverse	0.004	A crack propagates from rebar
2-3	3.75 x 3.7	-	-	-	-	-	-
2-4	3.75 x 3.7	-	-	-	-	-	-

Table B-91. Core Pictures

Core	Pictures of the Cores		
1-1			
1-2			

1-3			
1-4			
2-1			
2-2			
2-3			
2-4			

B.23.4 Laboratory Experiment Results

B.23.4.1 Resistivity

Core Number	Surface Resistivity (kΩ·m)	Bulk Resistivity (kΩ·m)
1-2	-	4.1

B.23.4.2 Ultrasonic Pulse Velocity

Core Number	Ultrasonic Pulse Velocity (m/s)
1-2	3904
1-3	4036
2-1	4246
2-3	3913

B.23.4.3 Carbonation Depth

Core Number	Carbonation Depth (in.)
1-1	0.00
2-2	0.09

B.23.4.4 Acid-Soluble Chloride Content

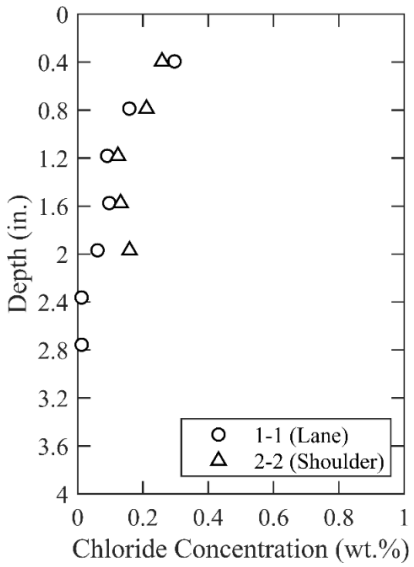

Figure 0.165. Chloride Content at Different Depth

B.23.4.5 Sorptivity

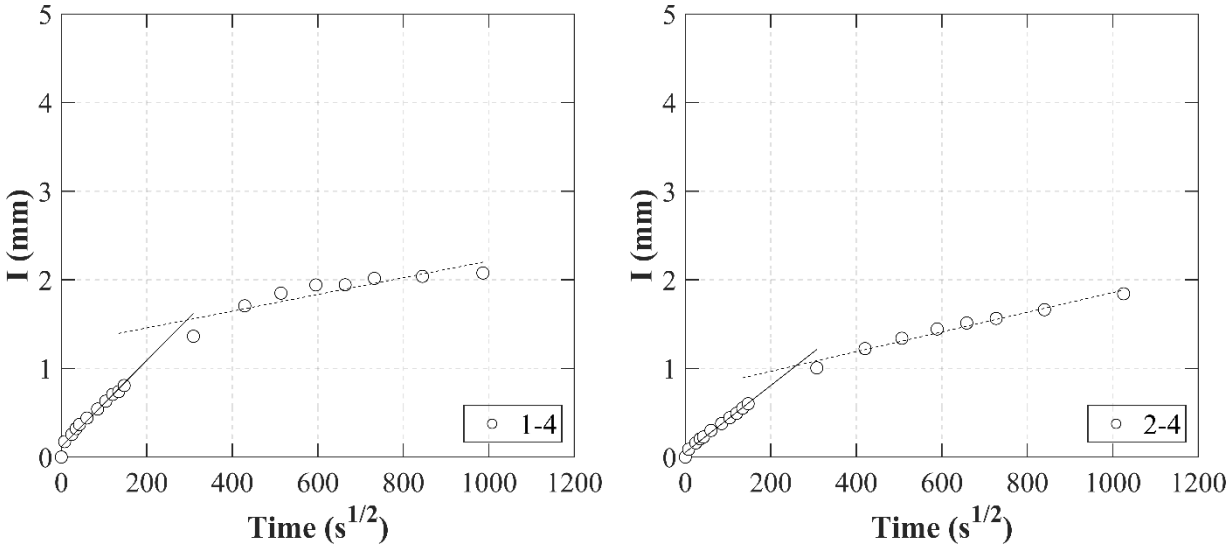

(a) Core 1–4 (b) Core 2–4

Figure 0.166. Absorption and Sorptivity of: (a) Core 1–4; (b) Core 2–4

Table B-92. Initial and Secondary Sorptivity Results

Core Number	Sorptivity	Results (mm/s$^{1/2}$)
Core 1–4	Initial Sorptivity	0.00487
	Secondary Sorptivity	0.00094
Core 2–4	Initial Sorptivity	0.00377
	Secondary Sorptivity	0.00111

B.23.4.6 Knife Test

Core Number	Score	Picture
2-2	10	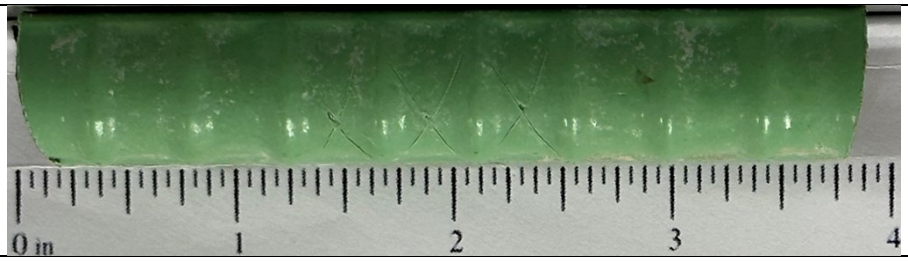

B.23.4.7 Electrochemical Impedance Spectroscopy

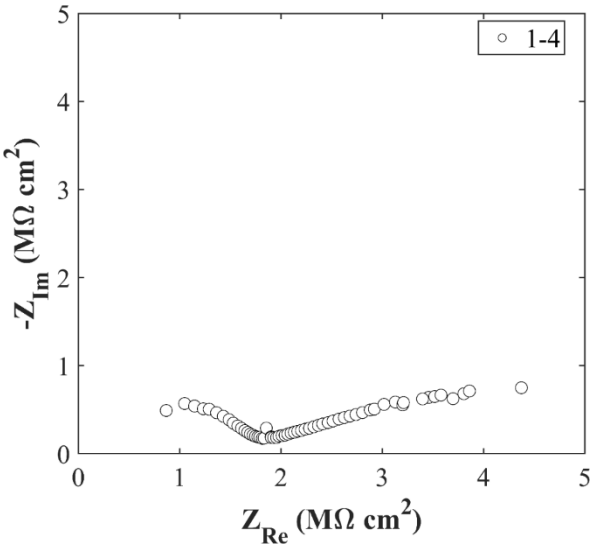

(a) Nyquist Diagram

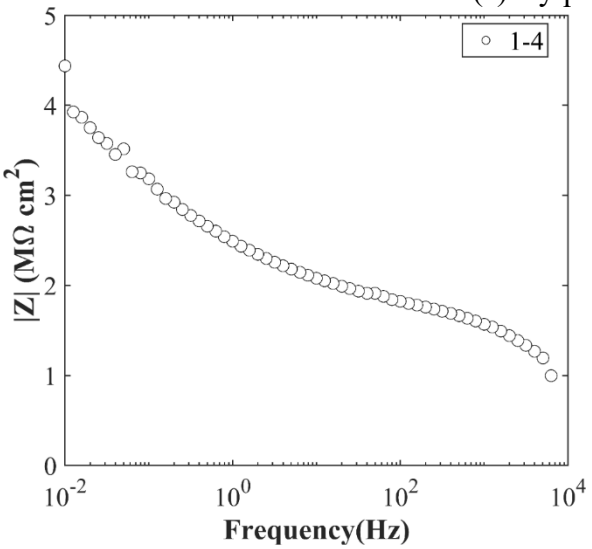

(b) Bode Plot of Impedance Modulus

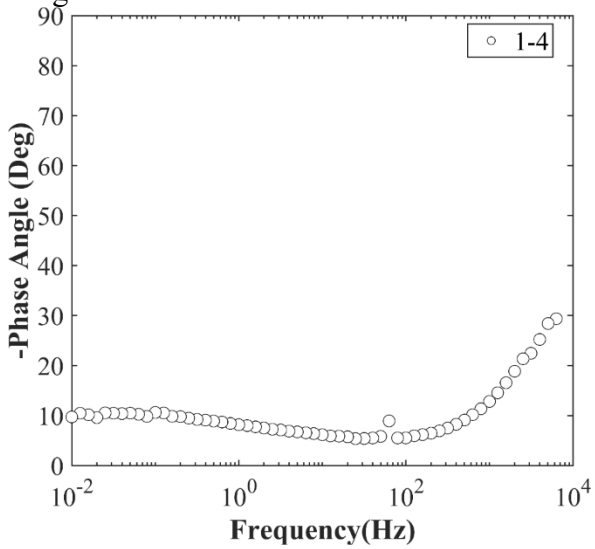

(c) Bode Plot of Impedance Phase

Figure 0.167. EIS Results: (a) Nyquist Diagram; (b) Bode Plot of Impedance Modulus; (c) Bode Plot of Impedance Phase

B.24 CHS-RC-04, US 62 OVER MIDDLE SCATTERBRANCH CRK

- Bridge ID: 250380003201024 (Childress County)
- Built in 2002
- Mitigation methods: HPC, ECR
- Observed CIP depth: 3.9 in.
- Observed clear cover: 2 in.
- 2 spans, 6-concrete PS-concrete girder @ 8’ spacing with 3’ overhangs
- Inspected Feb 17, 2022

Figure 0.168. Concrete Deck of the Bridge (source: google maps)

B.24.1 Observed Condition

There were hairline cracks on abutment backwall as shown in Figure 0.169.

Figure 0.169. Deteriorations on the Bridge: Hairline Cracks on Abutment

B.24.2 NDE Results

Grid 1 was located on the SB lane and grid 2 was located on the SB shoulder lane of the span 4 of the bridge.

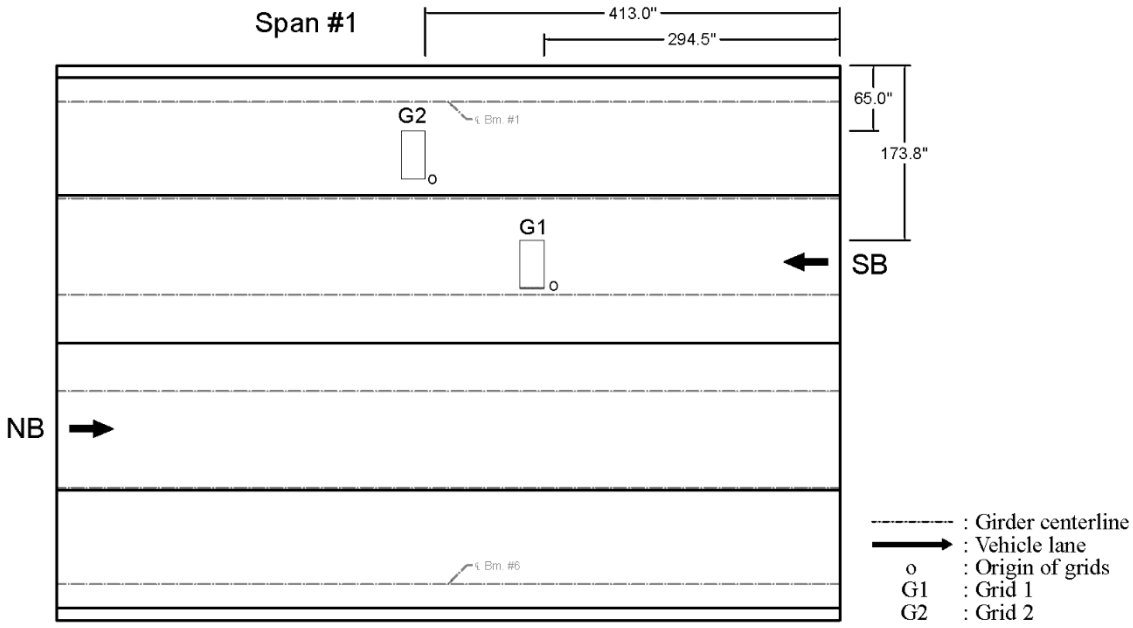

Figure 0.170. Plan View of the Bridge and Location of Grids

As shown in Figure 0.171 (a), grid 1 had a 0.008 in. wide longitudinal crack, maybe caused by panel joints, and some cracks that are 0.004 in. and 0.007 in. wide. On grid 2, there wasn't any cracks as shown in Figure 0.172 (a).

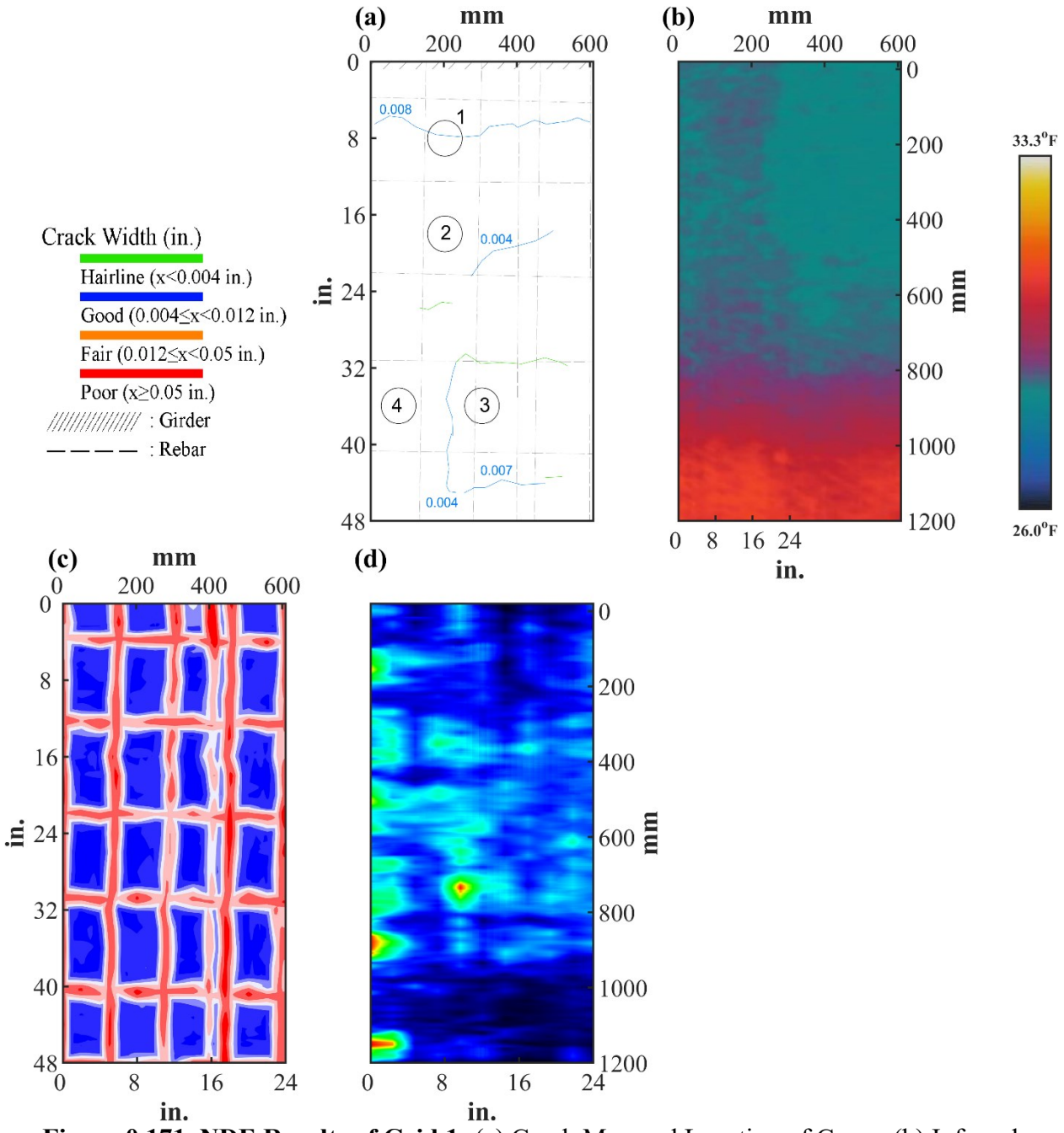

Figure 0.171. NDE Results of Grid 1: (a) Crack Map and Location of Cores; (b) Infrared Picture; (c) GPR C-scan at 1.25 in. to 3.15 in. Depth; (d) UST C-scan at 4.0 in. Depth

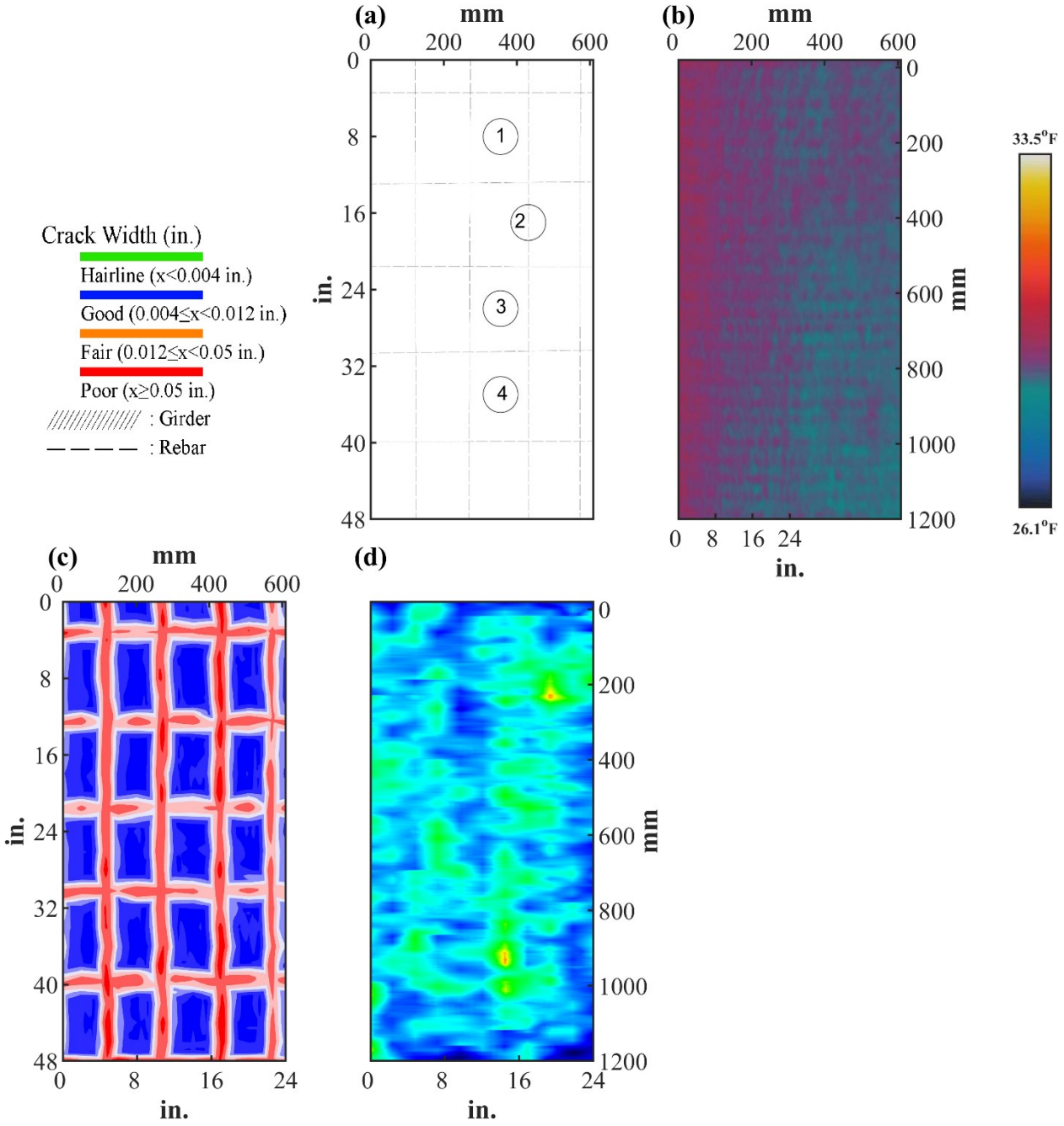

Figure 0.172. NDE Results of Grid 2: (a) Crack Map and Location of Cores; (b) Infrared Picture; (c) GPR C-scan at 1.6 in. to 3.0 in. Depth; (d) UST C-scan at 11.1 in. Depth

B.24.3 Concrete Cores

Table B-93. Detail Information of concrete cores

Core	dia. x height (in.)	Rebar depth (in.)	Rebar size (#)	Epoxy (Y/N)	Crack type	Crack width (in)	Notes
1-1	3.75 x 3.9	-	-	-	longitudinal	0.008	Delamination between CIP and PCP
1-2	3.75 x 3.9	-	-	-	-	-	Delamination between CIP and PCP
1-3	3.75 x 3.9	2	5	Y	-	-	Delamination between CIP and PCP
1-4	3.75 x 4.3	-	-	-	-	-	Delamination between CIP and PCP
2-1	3.75 x 4.3	-	-	-	-	-	Delamination between CIP and PCP
2-2	3.75 x 4.3	2	5	Y	-	-	Delamination between CIP and PCP
2-3	3.75 x 4.3	-	-	-	-	-	Delamination between CIP and PCP
2-4	3.75 x 4.1	-	-	-	-	-	Delamination between CIP and PCP

Table B-94. Core Pictures

Core	Pictures of the Cores		
1-1			
1-2			

1-3			
1-4			
2-1			
2-2			
2-3			
2-4			

B.24.4 Laboratory Experiment Results

B.24.4.1 Resistivity

Core Number	Surface Resistivity (kΩ·m)	Bulk Resistivity (kΩ·m)
1-4	-	5.0
2-1	-	3.1

B.24.4.2 Ultrasonic Pulse Velocity

Core Number	Ultrasonic Pulse Velocity (m/s)
1-2	3564
1-4	3760
2-1	3684
2-4	3750

B.24.4.3 Carbonation Depth

Core Number	Carbonation Depth (in.)
1-1	0.00
2-3	0.00

B.24.4.4 Acid-Soluble Chloride Content

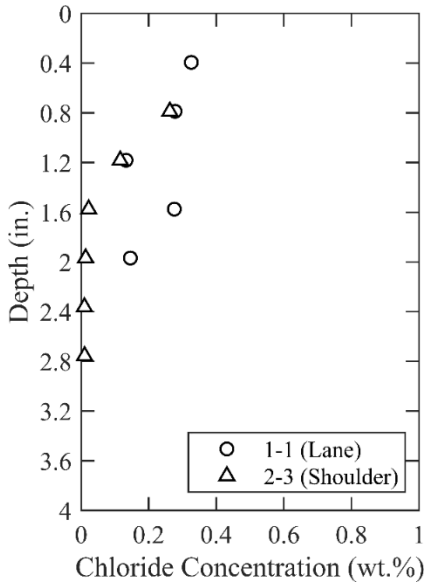

Figure 0.173. Chloride Content at Different Depth

B.24.4.5 Sorptivity

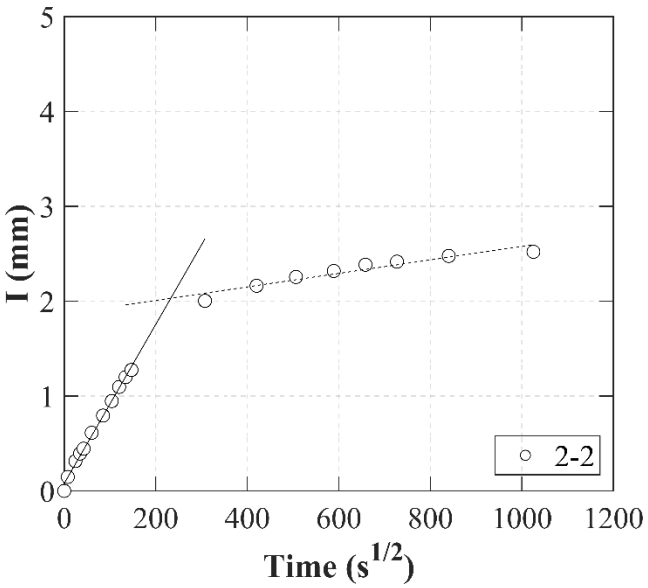

Figure 0.174. Absorption and Sorptivity of Core 2–2

Table B-95. Initial and Secondary Sorptivity Results

Core Number	Sorptivity	Results (mm/s$^{1/2}$)
Core 2–2	Initial Sorptivity	0.00838
	Secondary Sorptivity	0.00071

B.24.4.6 Knife Test

Core Number	Score	Picture
1-3	10	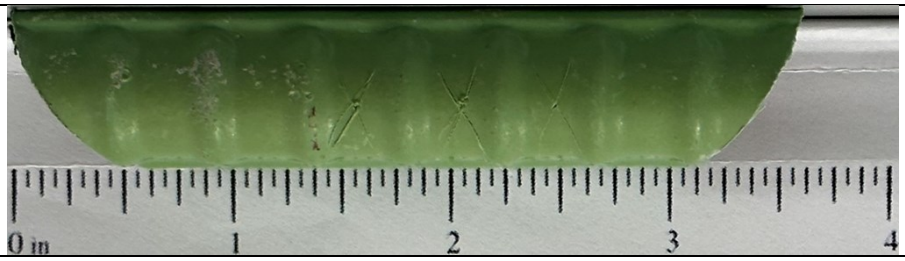

B.24.4.7 Electrochemical Impedance Spectroscopy

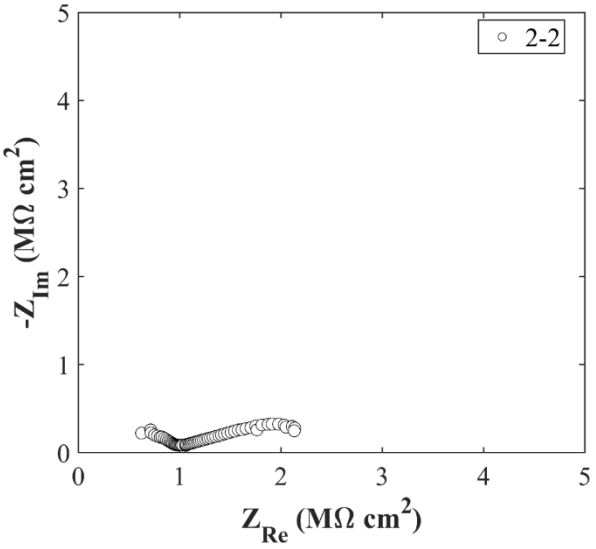

(a) Nyquist Diagram

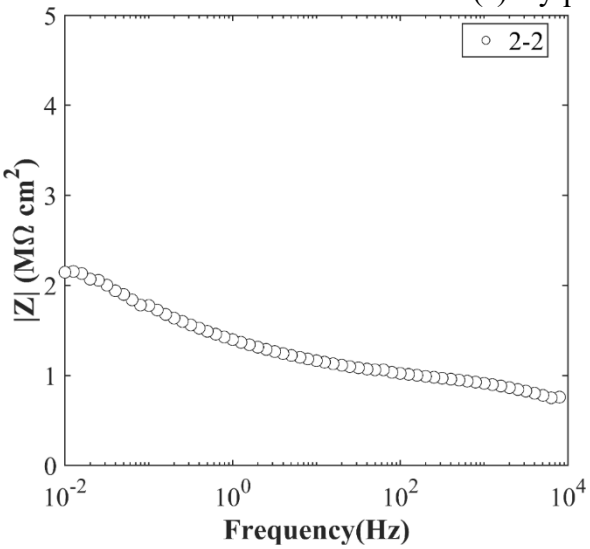

(b) Bode Plot of Impedance Modulus

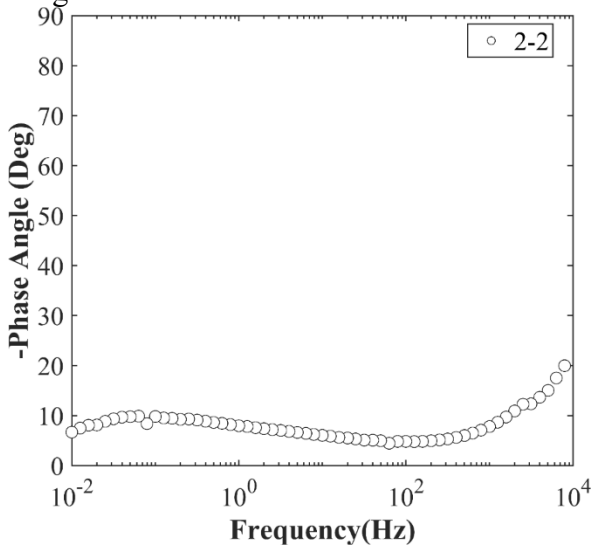

(c) Bode Plot of Impedance Phase

Figure 0.175. EIS Results: (a) Nyquist Diagram; (b) Bode Plot of Impedance Modulus; (c) Bode Plot of Impedance Phase

B.25 CHS-RC-05, US 62 OVER SOUTH PEASE RIVER

- Bridge ID: 250510003202039 (Cottle County)
- Built in 1998
- Mitigation methods: ECR
- Observed CIP depth: 4.0 in.
- Observed clear cover: 2.6 in.
- 12 spans, 6-concrete PS girder @ 8’ spacing with 3’ overhangs
- Inspected on Feb 16, 2022

Figure 0.176. Concrete Deck of the Bridge (source: google maps)

B.25.1 Observed Condition

Moderate shrinkage cracks are found on the bottom of deck as shown in the Figure 0.177 (a). There were some cracks and delamination of asphalt overlay on the deck as shown in Figure 0.177 (b).

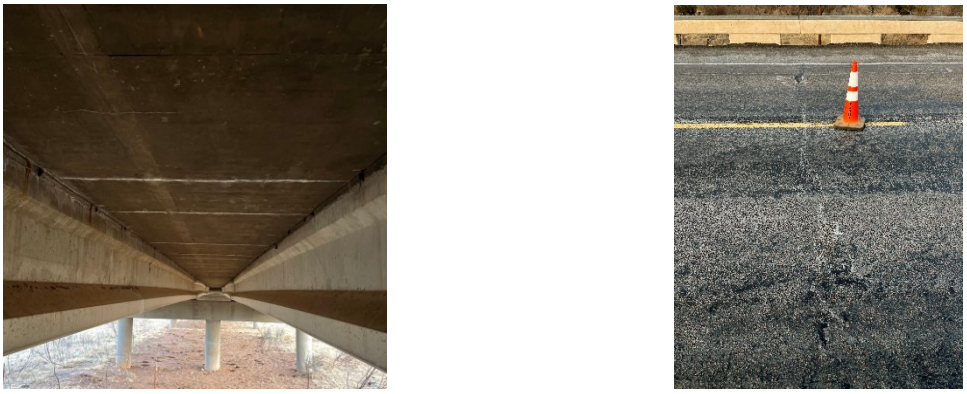

(a) (b)

Figure 0.177. Deteriorations on the Bridge: (a) Moderate Cracks on Bottom Surface of Deck; (b) Cracks and Delamination of Asphalt Overlay

B.25.2 NDE Results

Grid 1 was located on the SB lane and grid 2 was located on the SB shoulder lane of the span 4 of the bridge.

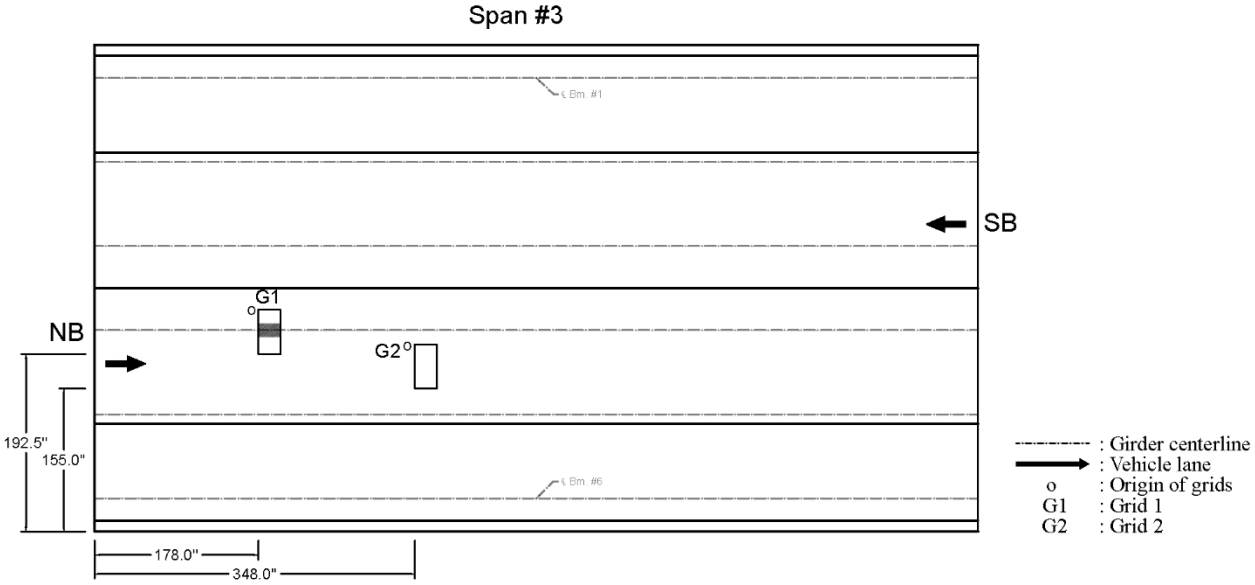

Figure 0.178. Plan View of the Bridge and Location of Grids

As shown in Figure 0.179 (a) and Figure 0.180 (a), both grid 1 and 2 had only one hairline crack.

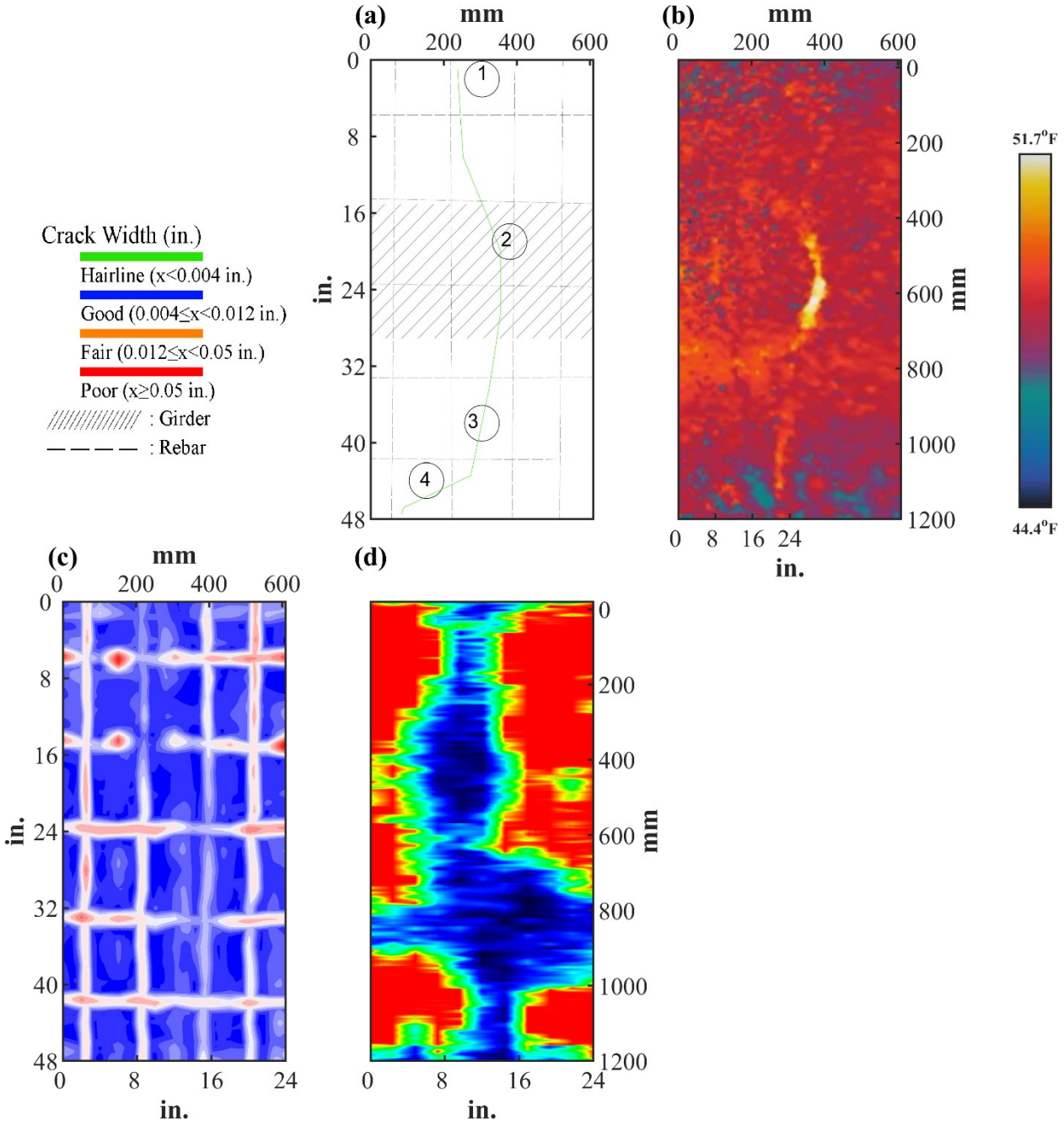

Figure 0.179. NDE Results of Grid 1: (a) Crack Map and Location of Cores; (b) Infrared Picture; (c) GPR C-scan at 4.4 in. to 6.4 in. Depth; (d) UST C-scan at 2.4 in. Depth

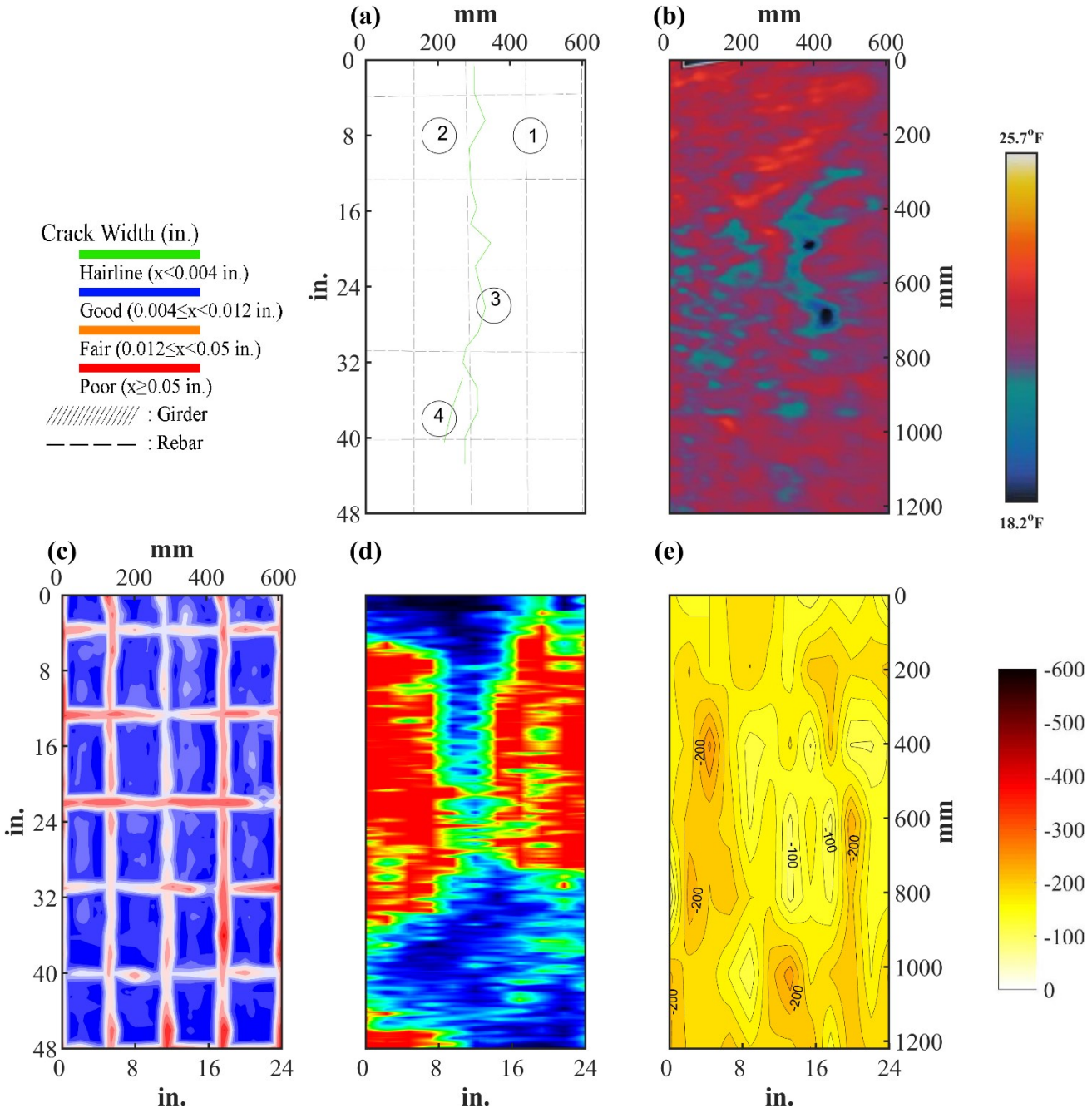

Figure 0.180. NDE Results of Grid 2: (a) Crack Map and Location of Cores; (b) Infrared Picture; (c) GPR C-scan at 4.1 in. to 6.3 in. Depth; (d) UST C-scan at 2.4 in. Depth; (e) Corrosion Rate Map

B.25.3 Concrete Cores

Table B-96. Detail Information of concrete cores

Core	dia. x height (in.)	Rebar depth (in.)	Rebar size (#)	Epoxy (Y/N)	Crack type	Crack width (in)	Notes
1-1	3.75 x 5.5	5.1	5	Y	-	-	-
1-2	3.75 x 5.1	2.6; 3.3	4,5	Y; Y	-	-	-
1-3	3.75 x 5.9	-	-	-	-	-	-
1-4	3.75 x 5.7	-	-	-	-	-	-
2-1	3.75 x 4.3	2.6	5	Y	-	-	Delamination between CIP and PCP
2-2	3.75 x 4.0	-	-	-	-	-	Delamination between CIP and PCP
2-3	3.75 x 5.1	-	-	-	-	-	-
2-4	3.75 x 5.5	3.1	4	Y	-	-	-

Table B-97. Core Pictures

Core	Pictures of the Cores
1-1	
1-2	

1-3			
1-4			
2-1			
2-2			
2-3	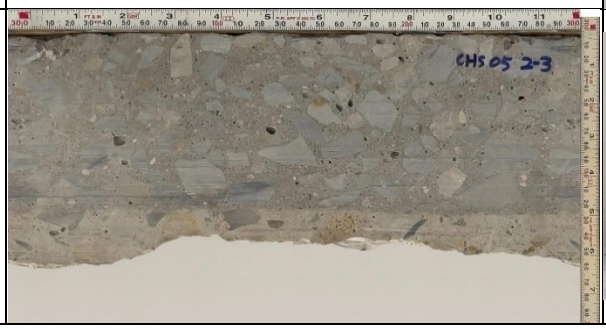		

2-4			

B.25.4 Laboratory Experiment Results

B.25.4.1 Resistivity

Core Number	Surface Resistivity (kΩ·m)	Bulk Resistivity (kΩ·m)
1-3	51	11.1
2-3	64	11.2

B.25.4.2 Ultrasonic Pulse Velocity

Core Number	Ultrasonic Pulse Velocity (m/s)
1-3	4735
1-4	4512
2-2	4465
2-3	4656

B.25.4.3 Carbonation Depth

Core Number	Carbonation Depth (in.)
1-2	0.00
2-1	0.25
2-4	0.00

B.25.4.4 Acid-Soluble Chloride Content

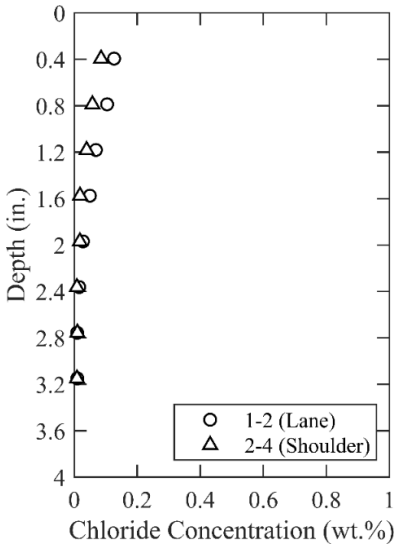

Figure 0.181. Chloride Content at Different Depth

B.25.4.5 Sorptivity

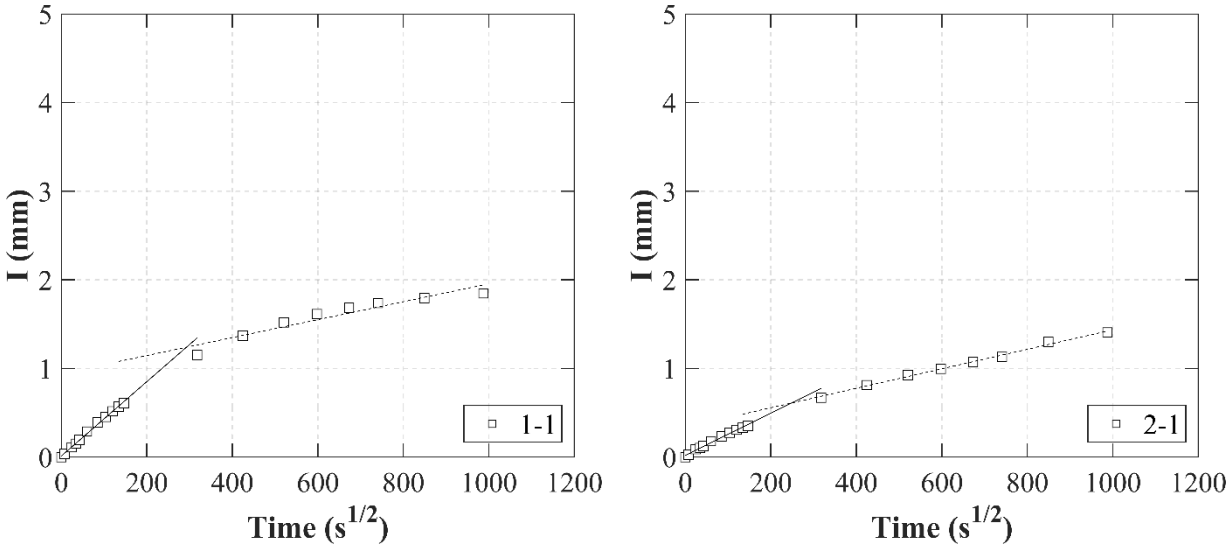

(a) Core 1–1 (b) Core 2–1

Figure 0.182. Absorption and Sorptivity of: (a) Core 1–1; (b) Core 2–1

Table B-98. Initial and Secondary Sorptivity Results

Core Number	Sorptivity	Results (mm/s$^{1/2}$)
Core 1–1	Initial Sorptivity	0.00419
	Secondary Sorptivity	0.00101
Core 2–1	Initial Sorptivity	0.00238
	Secondary Sorptivity	0.00110

B.25.4.6 Knife Test

Core Number	Score	Picture
1-1	10	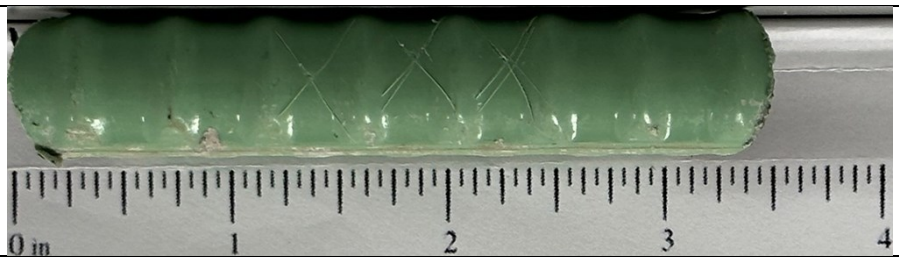

B.25.4.7 Electrochemical Impedance Spectroscopy

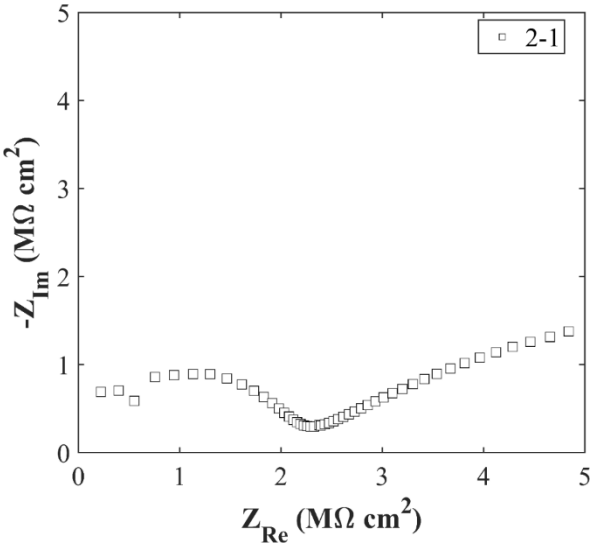

(a) Nyquist Diagram

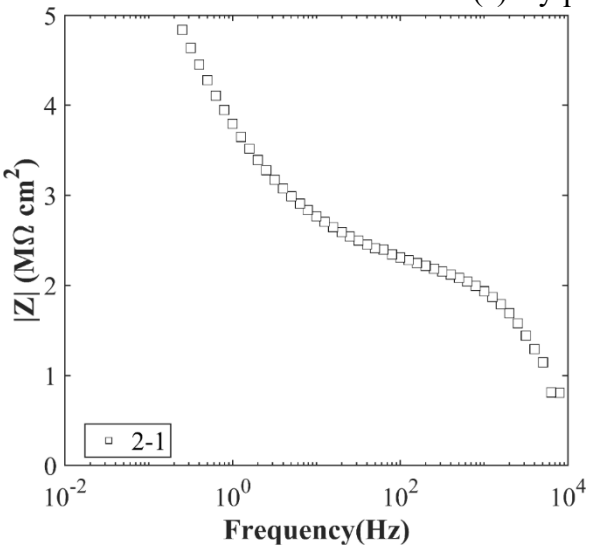

(b) Bode Plot of Impedance Modulus

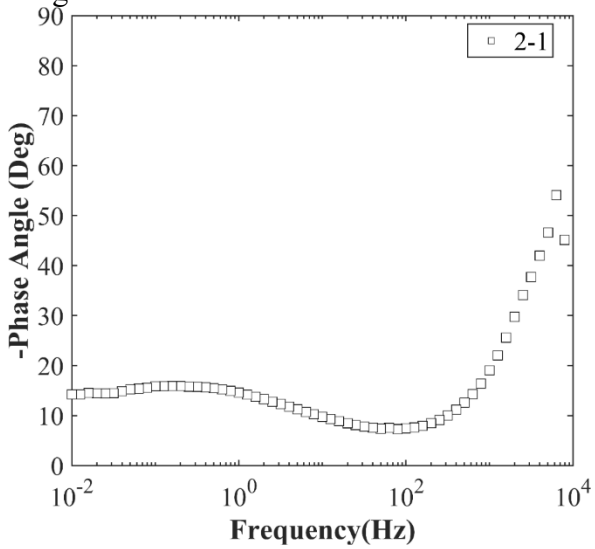

(c) Bode Plot of Impedance Phase

Figure 0.183. EIS Results: (a) Nyquist Diagram; (b) Bode Plot of Impedance Modulus; (c) Bode Plot of Impedance Phase

B.26 CHS-RC-06, US 62 OVER NORTH PEASE RIVER

- Bridge ID: 250510003202041 (Cottle County)
- Built in 1997
- Mitigation methods: ECR
- Observed CIP depth: 4.1 in.
- Observed clear cover: 1.5 in.
- 12 spans, 4-concrete PS girder @ 7.61’ spacing with 3’ overhangs
- Inspected on Feb 16, 2022

Figure 0.184. Concrete Deck of the Bridge (source: google maps)

B.26.1 Observed Condition

Deck surface has moderate transverse and longitudinal cracks. There are moderate cracks on the abutment backwalls as shown in

Figure 0.185. Deteriorations on the Bridge: (a) Cracks at Abutment Backwall

B.26.2 NDE Results

Grid 1 was located on the SB lane and grid 2 was located on the SB shoulder lane of the span 4 of the bridge.

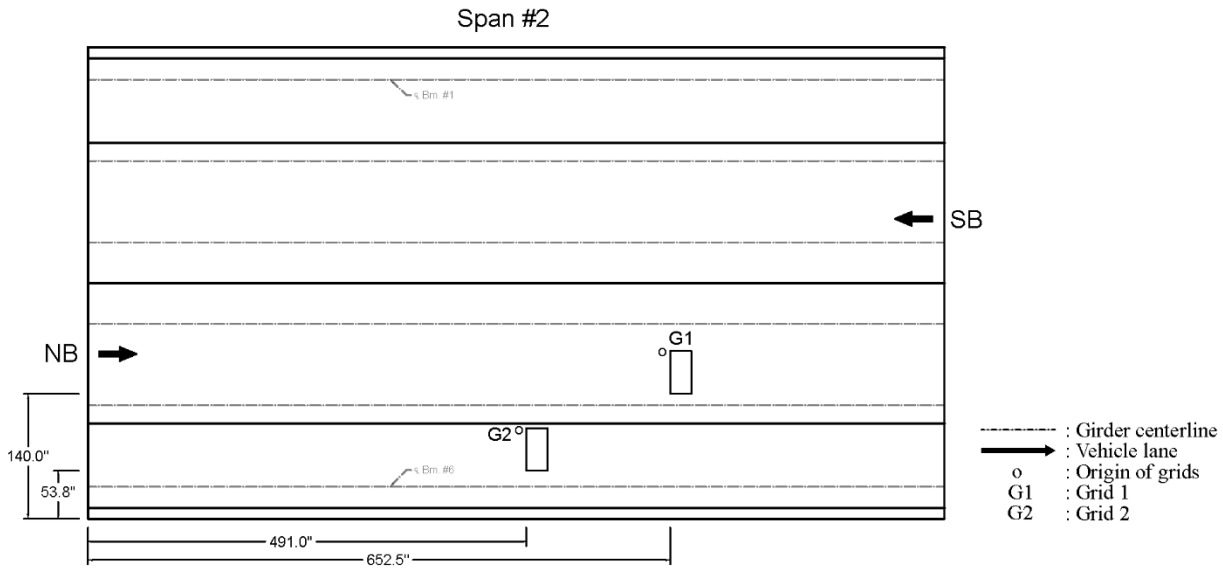

Figure 0.186. Plan View of the Bridge and Location of Grids

As shown in Figure 0.187 (a), there are widespread of transverse and longitudinal cracks with them width ranging from 0.006 in. to 0.03 in. wide on grid 1. On grid 2, there are longitudinal and diagonal cracks, and they are 0.01 in. and 0.012 in., and 0.01 in. wide, respectively, as shown in Figure 0.188 (a).

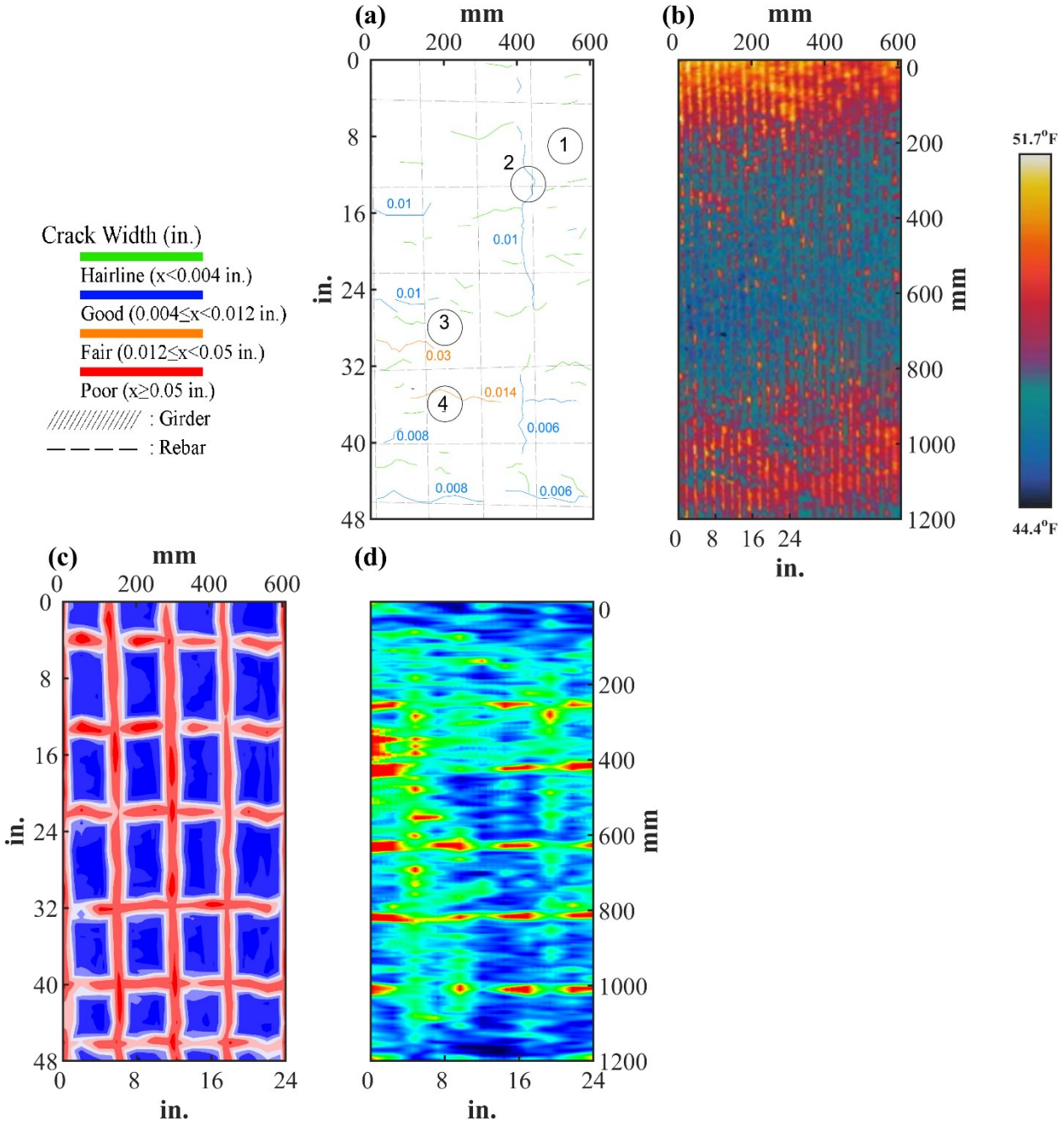

Figure 0.187. NDE Results of Grid 1: (a) Crack Map and Location of Cores; (b) Infrared Picture; (c) GPR C-scan at 1.25 in. to 3.15 in. Depth; (d) UST C-scan at 6.3 in. Depth

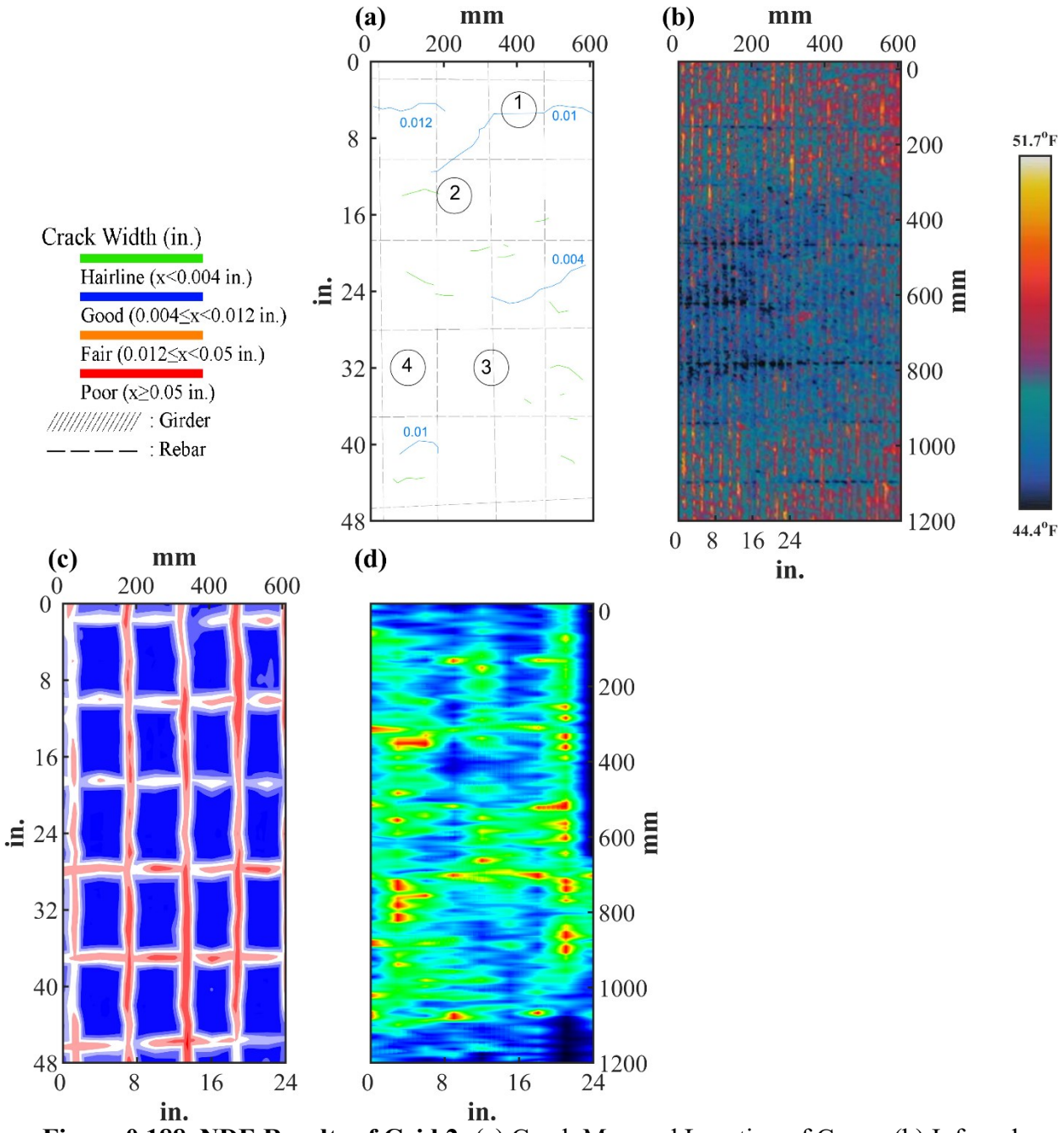

Figure 0.188. NDE Results of Grid 2: (a) Crack Map and Location of Cores; (b) Infrared Picture; (c) GPR C-scan at 1.25 in. to 3.15 in. Depth; (d) UST C-scan at 2.4 in. Depth

B.26.3 Concrete Cores

Table B-99. Detail Information of concrete cores

Core	dia. x height (in.)	Rebar depth (in.)	Rebar size (#)	Epoxy (Y/N)	Crack type	Crack width (in)	Notes
1-1	3.75 x 4.1	-	-	-	-	-	A crack propagates; delamination between CIP and PCP
1-2	3.75 x 4.1	2; 2.7	5,5	Y; Y	transverse	0.01	A crack propagates along aggregates
1-3	3.75 x 4.2	2	5	Y	-	-	Delamination between CIP and PCP
1-4	3.75 x 4.3	-	-	-	longitudinal	0.014	A void at 0.8 in. from the surface; Delamination between CIP and PCP
2-1	3.75 x 4.7	-	-	-	longitudinal	0.01	A crack propagates along aggregates
2-2	3.75 x 5.1	-	-	-	-	-	-
2-3	3.75 x 3.6	1.5	5	Y	-	-	Delamination between CIP and PCP
2-4	3.75 x 5.5	-	-	-	-	-	-

Table B-100. Core Pictures

Core	Pictures of the Cores
1-1	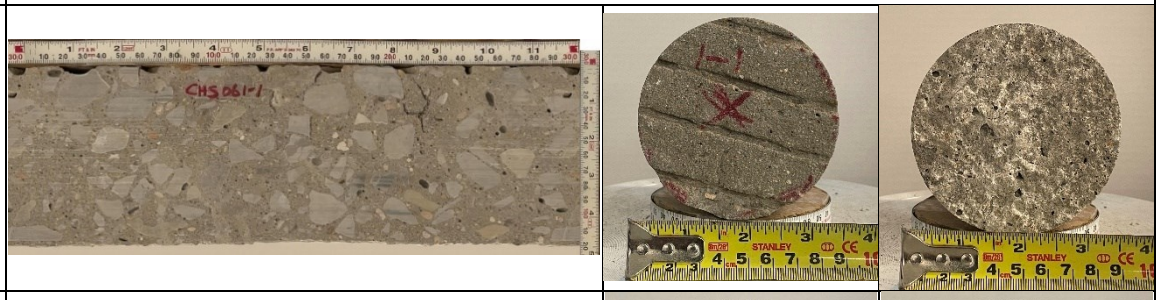
1-2	

1-3			
1-4			
2-1			
2-2			
2-3			
2-4			

B.26.4 Laboratory Experiment Results

B.26.4.1 Resistivity

Core Number	Surface Resistivity (kΩ·m)	Bulk Resistivity (kΩ·m)
2-1	43	-

B.26.4.2 Ultrasonic Pulse Velocity

Core Number	Ultrasonic Pulse Velocity (m/s)
1-1	4079
1-4	4075
2-1	4317
2-4	4028

B.26.4.3 Carbonation Depth

Core Number	Carbonation Depth (in.)
1-3	0.00
2-2	0.00

B.26.4.4 Acid-Soluble Chloride Content

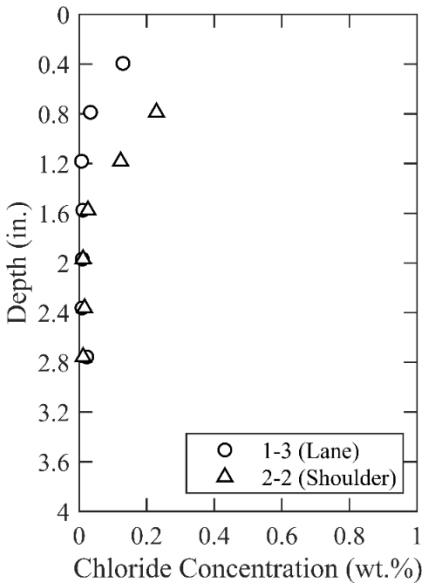

Figure 0.189. Chloride Content at Different Depth

B.26.4.5 Sorptivity

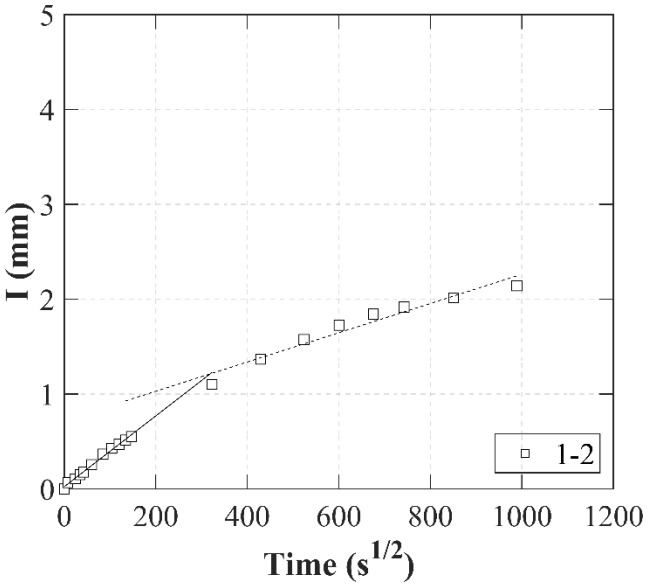

Figure 0.190. Absorption and Sorptivity of Core 1–2

Table B-101. Initial and Secondary Sorptivity Results

Core Number	Sorptivity	Results ($mm/s^{1/2}$)
Core 1–2	Initial Sorptivity	0.00373
	Secondary Sorptivity	0.00154

B.26.4.6 Knife Test

Core Number	Score	Picture
1-2	10	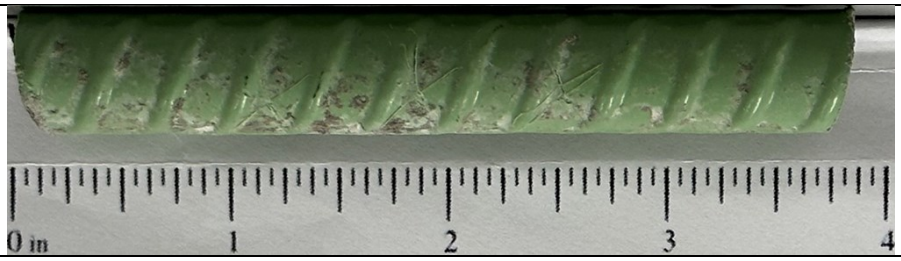

B.26.4.7 Electrochemical Impedance Spectroscopy

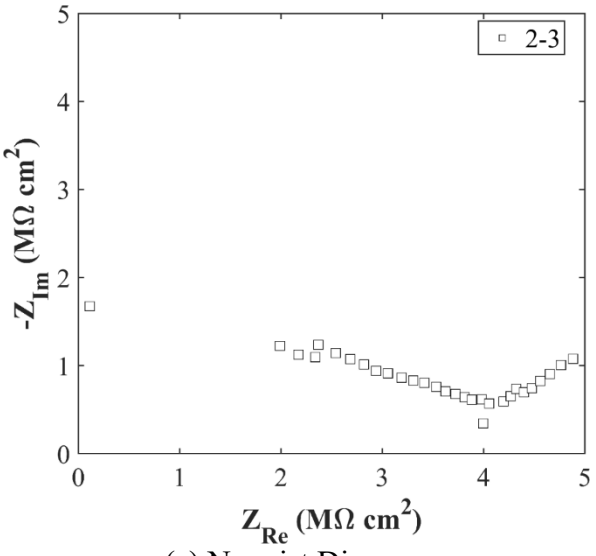

(a) Nyquist Diagram

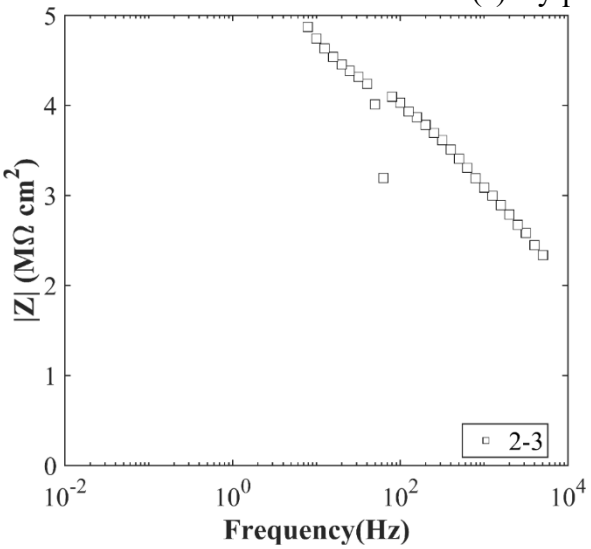

(b) Bode Plot of Impedance Modulus

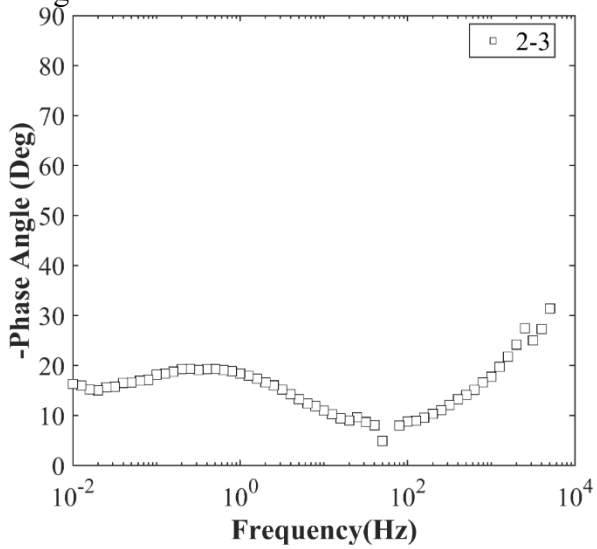

(c) Bode Plot of Impedance Phase

Figure 0.191. EIS Results: (a) Nyquist Diagram; (b) Bode Plot of Impedance Modulus; (c) Bode Plot of Impedance Phase

B.27 ELP-RC-01, IH 10 WB OVER CARRIZO CREEK

- Bridge ID: 240550000211273 (Culberson County)
- Built in 2010
- Mitigation methods: HPC, linseed oil
- Observed CIP depth: Unknown
- Observed clear cover: 2.8 in.
- 3 spans, 8-concrete PS Box Beam
- Inspected on June 28, 2021

Figure 0.192. Concrete Deck of the Bridge (source: google maps)

B.27.1 Observed Condition

There are isolated transverse and longitudinal hairline cracks that are propagating from a joint as shown in Figure 0.193 (a). The leakage and cracks are found on the abutment as shown in Figure 0.193 (b).

(a) (b)

Figure 0.193. Deterioration on the Bridge: (a) Map Cracks Propagating from a Joint; (b) Cracks and Leakage at Abutment

B.27.2 NDE Results

Grid 1 was located on the WB lane, and grid 2 was located on the WB shoulder lane of the span 1 of the bridge.

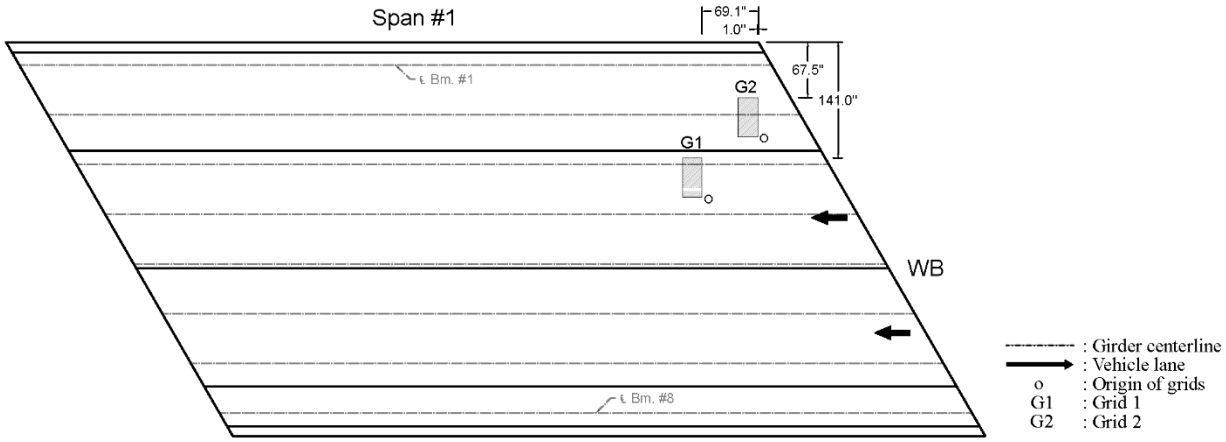

Figure 0.194. Plan View of the Bridge and Location of Grids

As shown in Figure 0.195 (a), there are widespread of hairline cracks and cracks that are 0.004 in. to 0.025 in. wide on grid 1. Map, transverse, and longitudinal cracks exist on grid 1. On grid 2, there are widespread of hairline cracks, and transverse cracks that are 0.004 in. to 0.012 in. wide as shown in Figure 0.196.

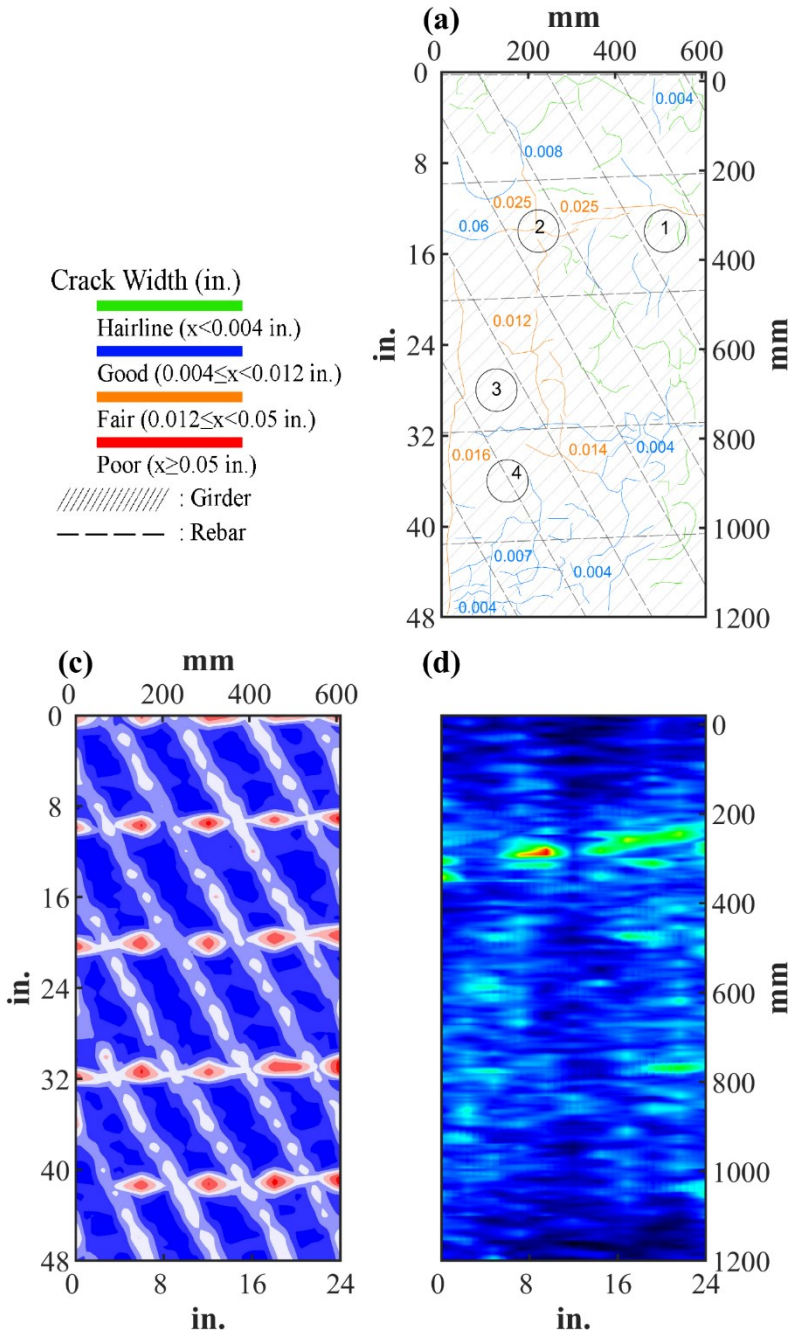

Figure 0.195. Crack Map and NDE Results of Grid 1: (a) Crack map and Location of Cores; (c) GPR C-scan at 1.5 in. to 3.2 in. Depth; (d) UST C-scan at 2.0 in. Depth

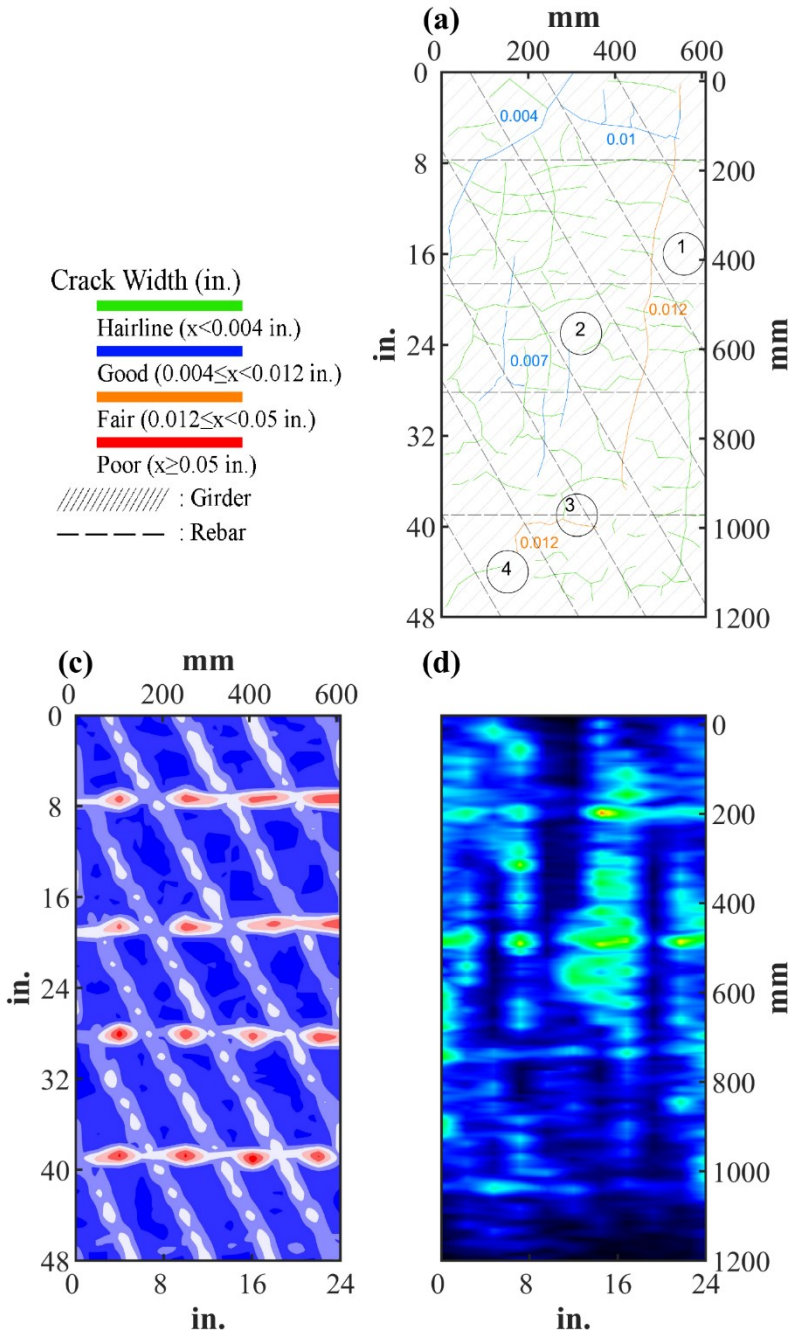

Figure 0.196. Crack Map and NDE Results of Grid 2: (a) Crack map and Location of Cores; (c) GPR C-scan at 2.55 in. to 4.0 in. Depth; (d) UST C-scan at 3.3 in. Depth

B.27.3 Concrete Cores

Table B-102. Detail Information of concrete cores

Core	dia. x height (in.)	Rebar depth (in.)	Rebar size (#)	Epoxy (Y/N)	Crack type	Crack width (in)	Notes
1-1	3.75 x 5.3	-	-	-	-	-	A void at 3.5 in. depth
1-2	3.75 x 4.9	-	-	-	transverse; longitudinal	0.025; 0.025	A crack propagates along aggregates
1-3	3.75 x 5.3	-	-	-	-	-	-
1-4	3.75 x 5.1	2.8	5	N	-	-	-
2-1	3.75 x 4.7	-	-	-	-	-	-
2-2	3.75 x 5.1	-	-	-	-	-	A void at 0.8 in. depth
2-3	3.75 x 5.1	3.2, 3.7	4,4	N	map	0.012	-
2-4	3.75 x 5.1	-	-	-	-	-	-

Table B-103. Core Pictures

Core	Pictures of the Cores		
1-1			
1-2			
1-3			

1-4			
2-1		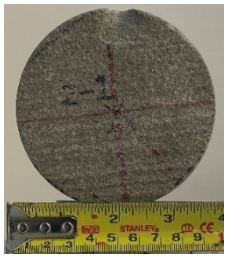	
2-2	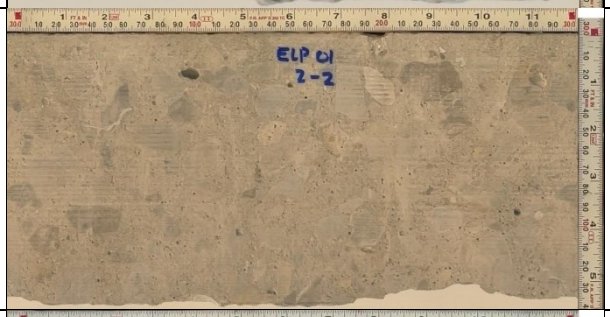		
2-3			
2-4	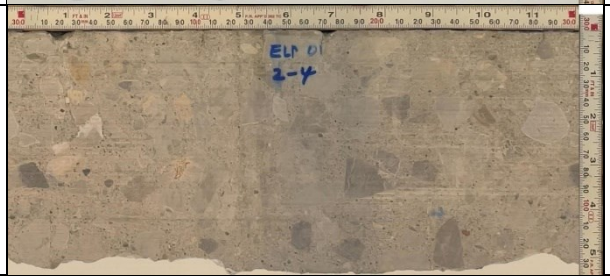	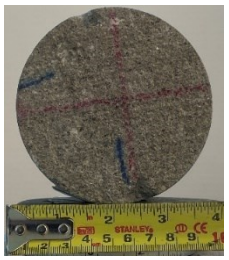	

B.27.4 Laboratory Experiment Results

B.27.4.1 Resistivity

Core Number	Surface Resistivity (kΩ·m)	Bulk Resistivity (kΩ·m)
1-1	80	11.2
1-2	113	-
1-3	55	-
2-1	75	12.1
2-2	71	-
2-4	93	-

B.27.4.2 Ultrasonic Pulse Velocity

Core Number	Ultrasonic Pulse Velocity (m/s)
1-1	4425
1-2	3863
1-3	4488
2-1	4376
2-2	4313
2-4	4337

B.27.4.3 Carbonation Depth

Core Number	Carbonation Depth (in.)
1-3	0.00
2-4	0.00

B.27.4.4 Acid-Soluble Chloride Content

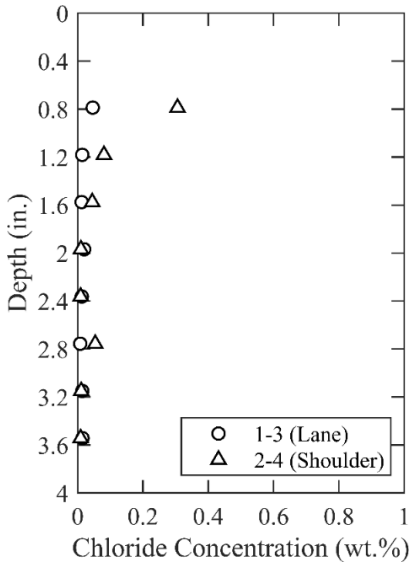

Figure 0.197. Chloride Content at Different Depth

B.27.4.5 Sorptivity

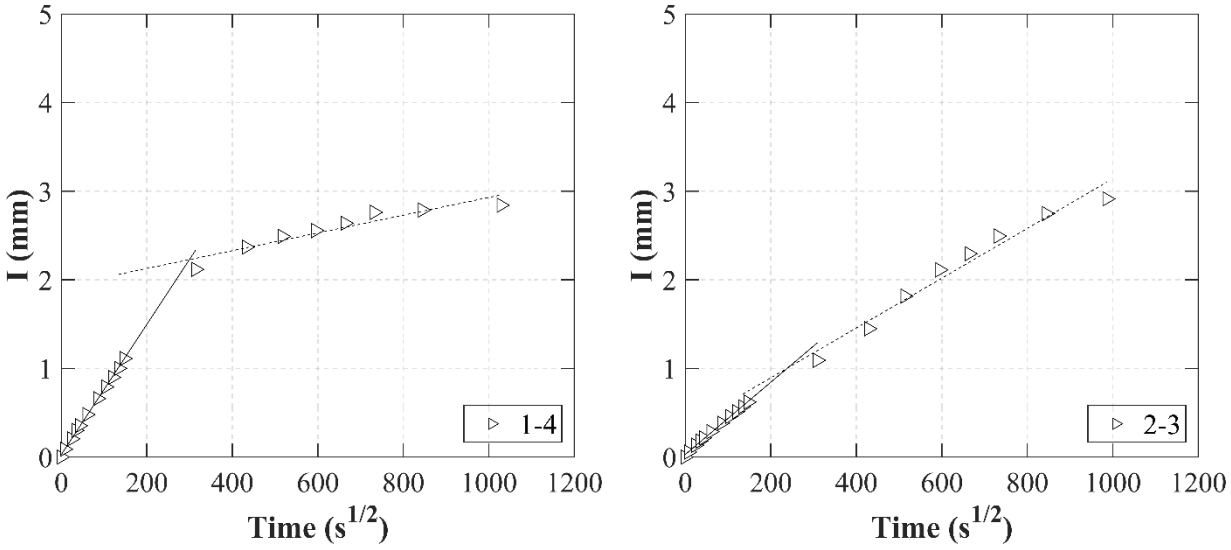

(a) Core 1–4 (b) Core 2–3

Figure 0.198. Absorption and Sorptivity of: (a) Core 1–4; (b) Core 2–3

Table B-104. Initial and Secondary Sorptivity Results

Core Number	Sorptivity	Results (mm/s$^{1/2}$)
Core 1–4	Initial Sorptivity	0.00734
	Secondary Sorptivity	0.00100
Core 2–3	Initial Sorptivity	0.00408
	Secondary Sorptivity	0.00281

B.27.4.6 Electrochemical Impedance Spectroscopy

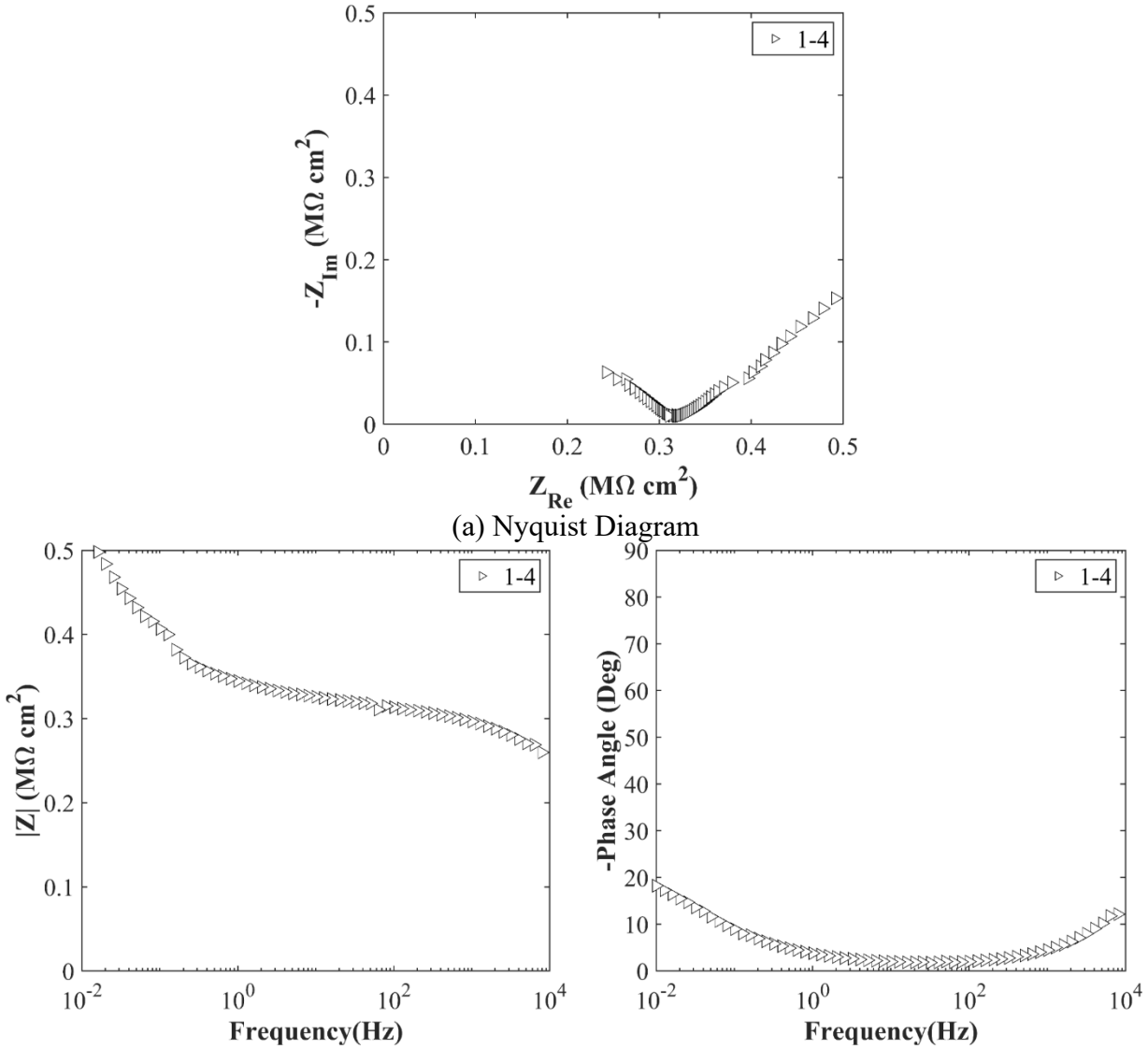

(a) Nyquist Diagram

(b) Bode Plot of Impedance Modulus

(c) Bode Plot of Impedance Phase

Figure 0.199. EIS Results: (a) Nyquist Diagram; (b) Bode Plot of Impedance Modulus; (c) Bode Plot of Impedance Phase

B.28 ELP-RC-02, FM 3380 OVER SH 20 (ALAMEDA ST.) / UPRR

- Bridge ID: 240720000203278 (El Paso County)
- Built in 2016
- Mitigation methods: HPC, linseed oil
- Observed CIP depth: 6.0 in.
- Observed clear cover: 3.6 in.
- 17 spans, 7-concrete PS girder @ varying spacing with 3’ overhangs at span 1 and 2, 6-concrete PS girder @ varying spacing with 3’ overhangs at span 3 and 4, 6-concrete PS girder @ 8’ with 3’ overhangs at other spans
- Inspected on June 28, 2021

Figure 0.200. Concrete Deck of the Bridge (source: google maps)

B.28.1 Observed Condition

There are transverse and longitudinal hairline cracks on the top surface of deck.

B.28.2 NDE Results

Grid 1 was located on the EB lane, and grid 2 was located on the EB shoulder lane of the span 6 of the bridge.

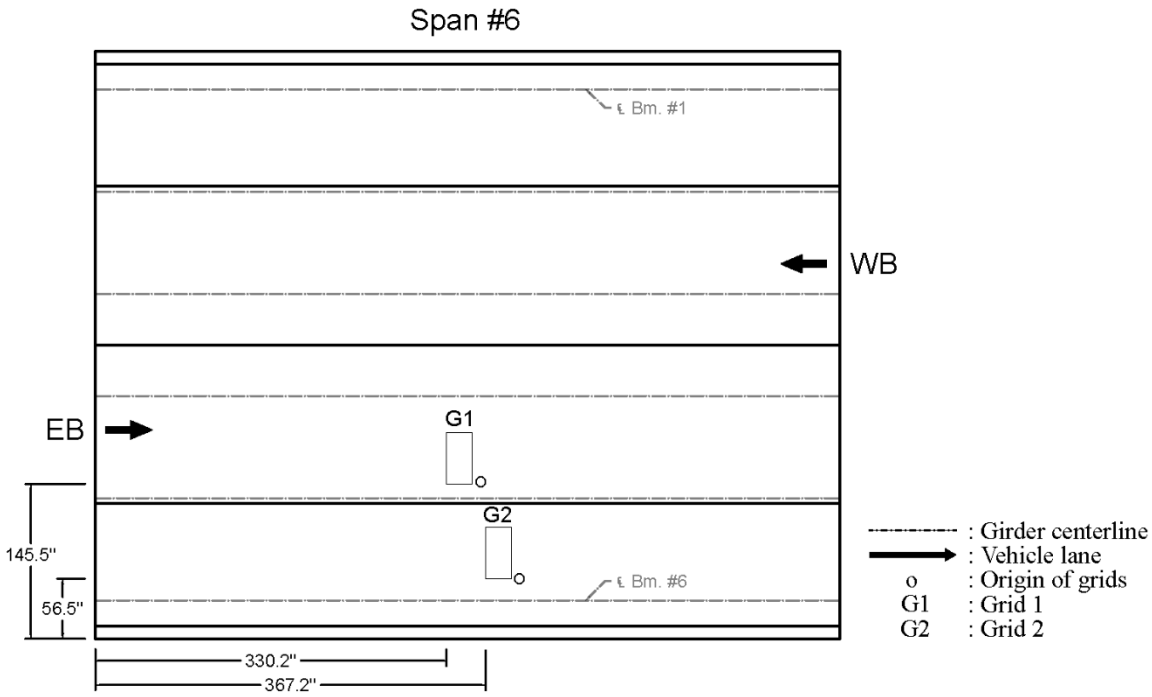

Figure 0.201. Plan View of the Bridge and Location of Grids

As shown in Figure 0.202 (a), there are transverse and diagonal cracks that are 0.007 in. to 0.01 in. wide on grid 1. On grid 2, there were only hairline cracks and 0.004 in. wide cracks as shown in Figure 0.203 (a).

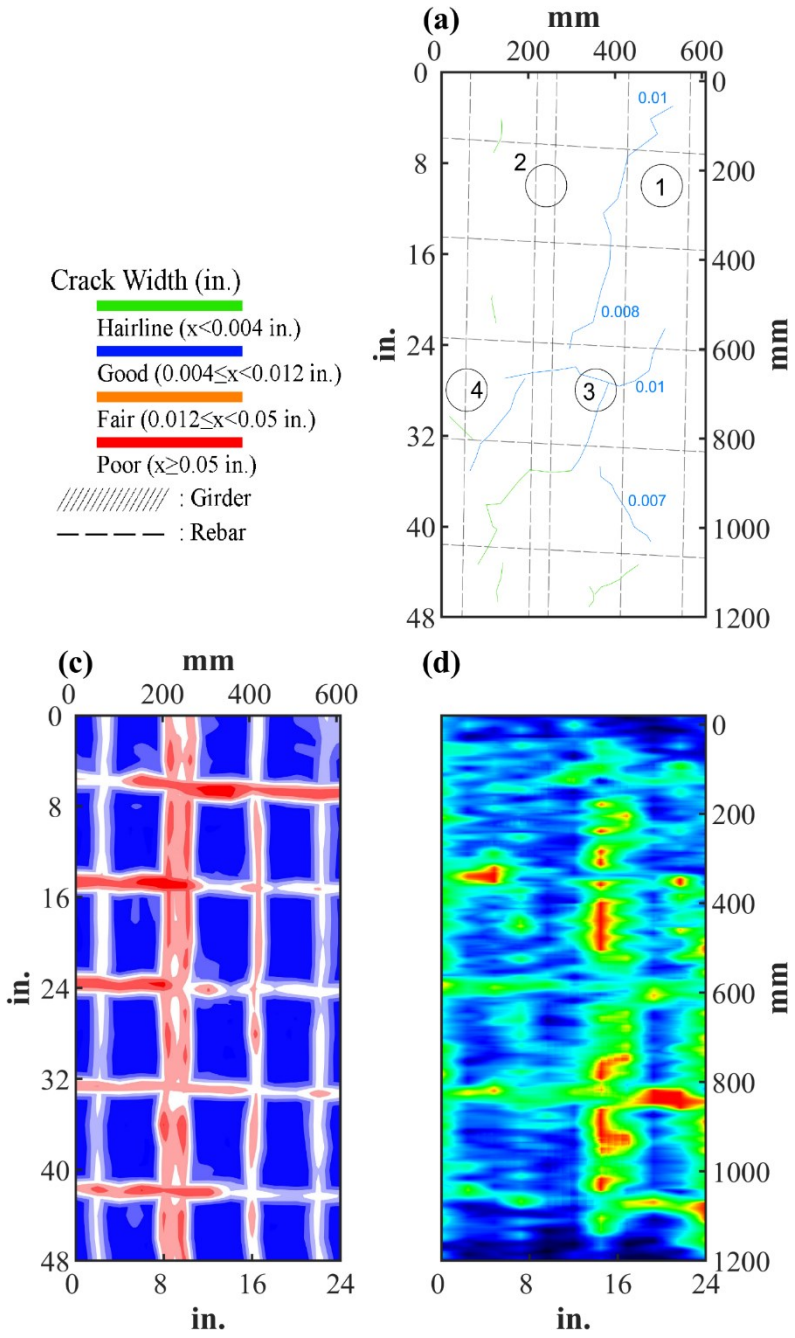

Figure 0.202. Crack Map and NDE Results of Grid 1: (a) Crack map and Location of Cores; (b) Infrared Picture; (c) GPR C-scan at 3.8 in. to 5.2 in. Depth; (d) UST C-scan at 4.3 in. Depth

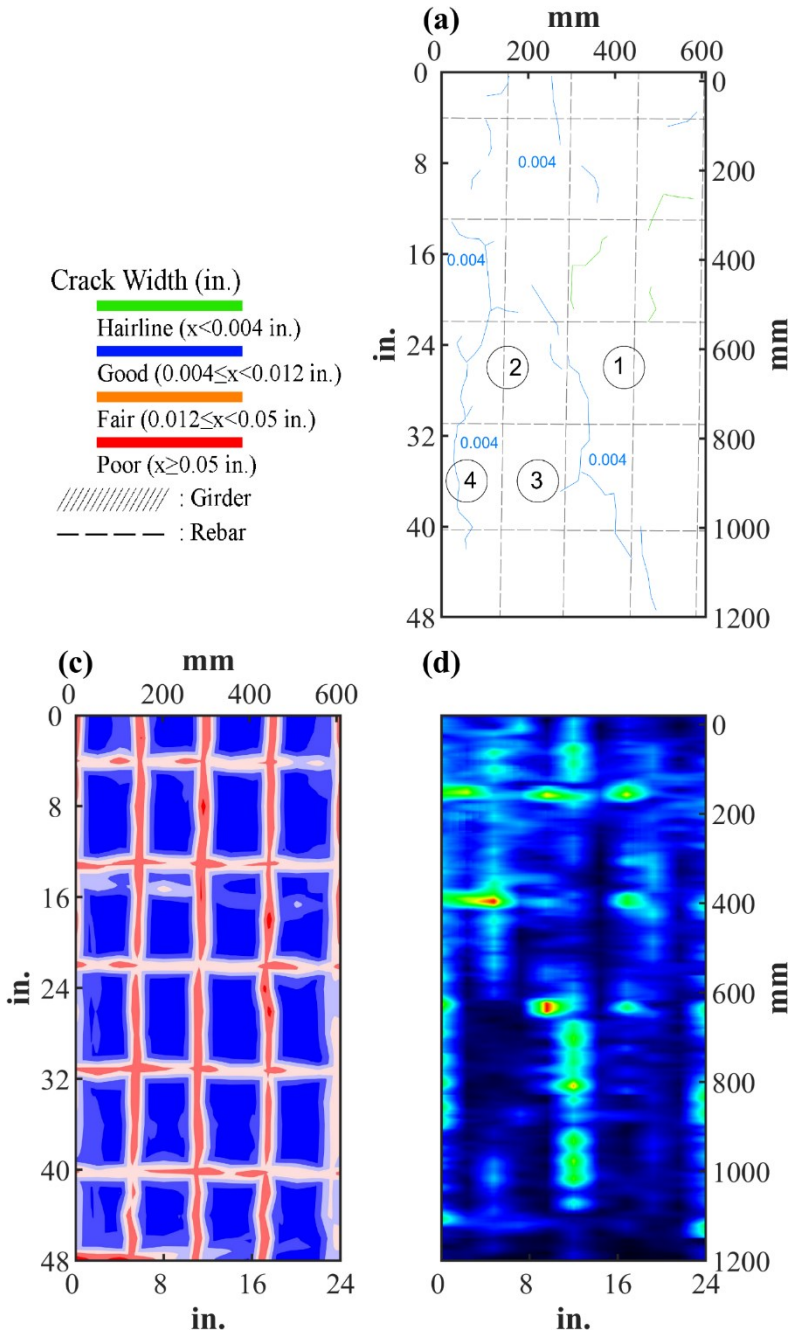

Figure 0.203. Crack Map and NDE Results of Grid 2: (a) Crack map and Location of Cores; (b) Infrared Picture; (c) GPR C-scan at 3.25 in. to 4.6 in. Depth; (d) UST C-scan at 4.3 in. Depth

B.28.3 Concrete Cores

Table B-105. Detail Information of concrete cores

Core	dia. x height (in.)	Rebar depth (in.)	Rebar size (#)	Epoxy (Y/N)	Crack type	Crack width (in)	Notes
1-1	3.75 x 5.9	-	-	-	-	-	Delamination between CIP and PCP
1-2	3.75 x 7.2	4.1,4.1	5,5	N	-	-	-
1-3	3.75 x 6.1	-	-	-	diagonal	0.01	A void at 1.7 in. depth; delamination between CIP and PCP
1-4	3.75 x 6.2	3.6	5	N	-	-	Delamination between CIP and PCP
2-1	3.75 x 6.0	3.6	5	N	-	-	Delamination between CIP and PCP
2-2	3.75 x 6.0	3.6	5	N	-	-	Delamination between CIP and PCP
2-3	3.75 x 6.0	-	-	-	-	-	Delamination between CIP and PCP
2-4	3.75 x 5.9	-	-	-	transverse	0.004	Delamination between CIP and PCP

Table B-106. Core Pictures

Core	Pictures of the Cores		
1-1			
1-2			

1-3			
1-4		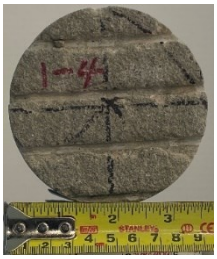	
2-1	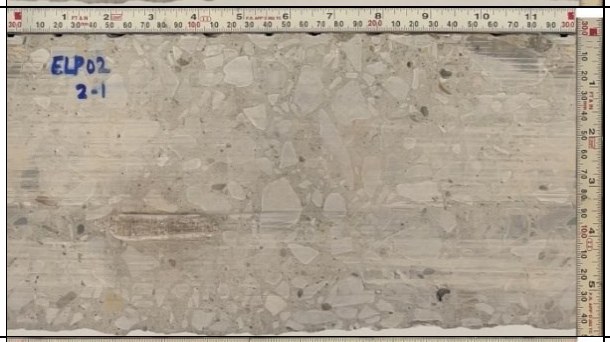		
2-2		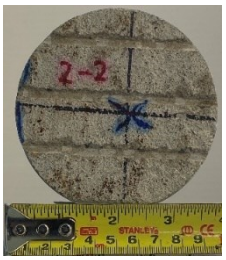	
2-3	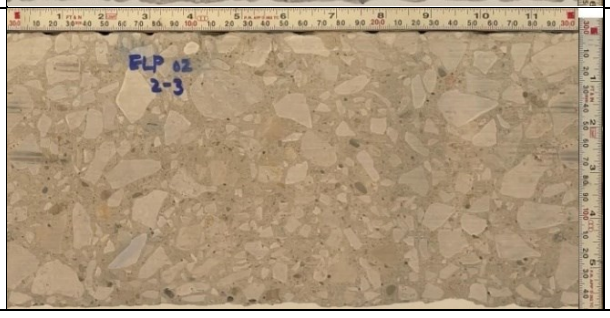		

2-4		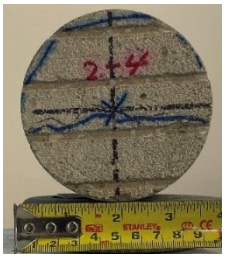	

B.28.4 Laboratory Experiment Results

B.28.4.1 Resistivity

Core Number	Surface Resistivity (kΩ·m)	Bulk Resistivity (kΩ·m)
1-3	60.8	12.8
2-3	67.4	-
2-4	50.3	11.2

B.28.4.2 Ultrasonic Pulse Velocity

Core Number	Ultrasonic Pulse Velocity (m/s)
1-1	4431
1-3	4540
2-3	4665
2-4	4456

B.28.4.3 Carbonation Depth

Core Number	Carbonation Depth (in.)
1-4	0.24
2-1	0.19

B.28.4.4 Acid-Soluble Chloride Content

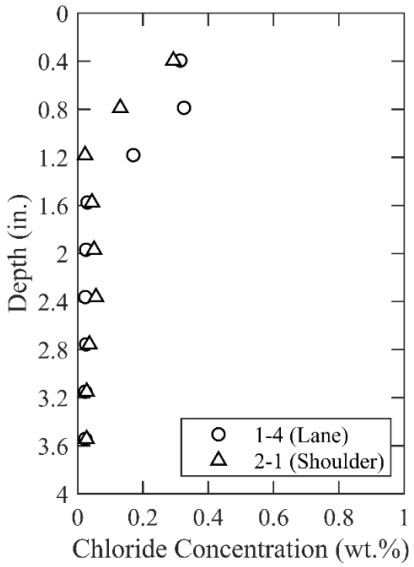

Figure 0.204. Chloride Content at Different Depth

B.28.4.5 Sorptivity

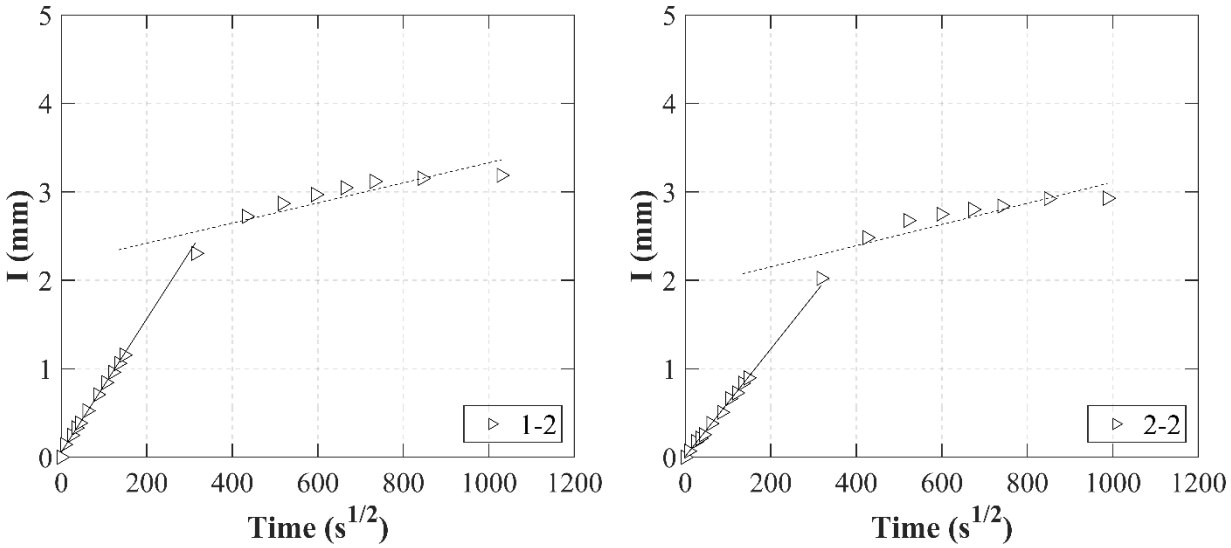

(a) Core 1–2 (b) Core 2–2

Figure 0.205. Absorption and Sorptivity of: (a) Core 1–2; (b) Core 2–2

Table B-107. Initial and Secondary Sorptivity Results

Core Number	Sorptivity	Results (mm/s$^{1/2}$)
Core 1–2	Initial Sorptivity	0.00754
	Secondary Sorptivity	0.00114
Core 2–2	Initial Sorptivity	0.00607
	Secondary Sorptivity	0.00120

B.28.4.6 Electrochemical Impedance Spectroscopy

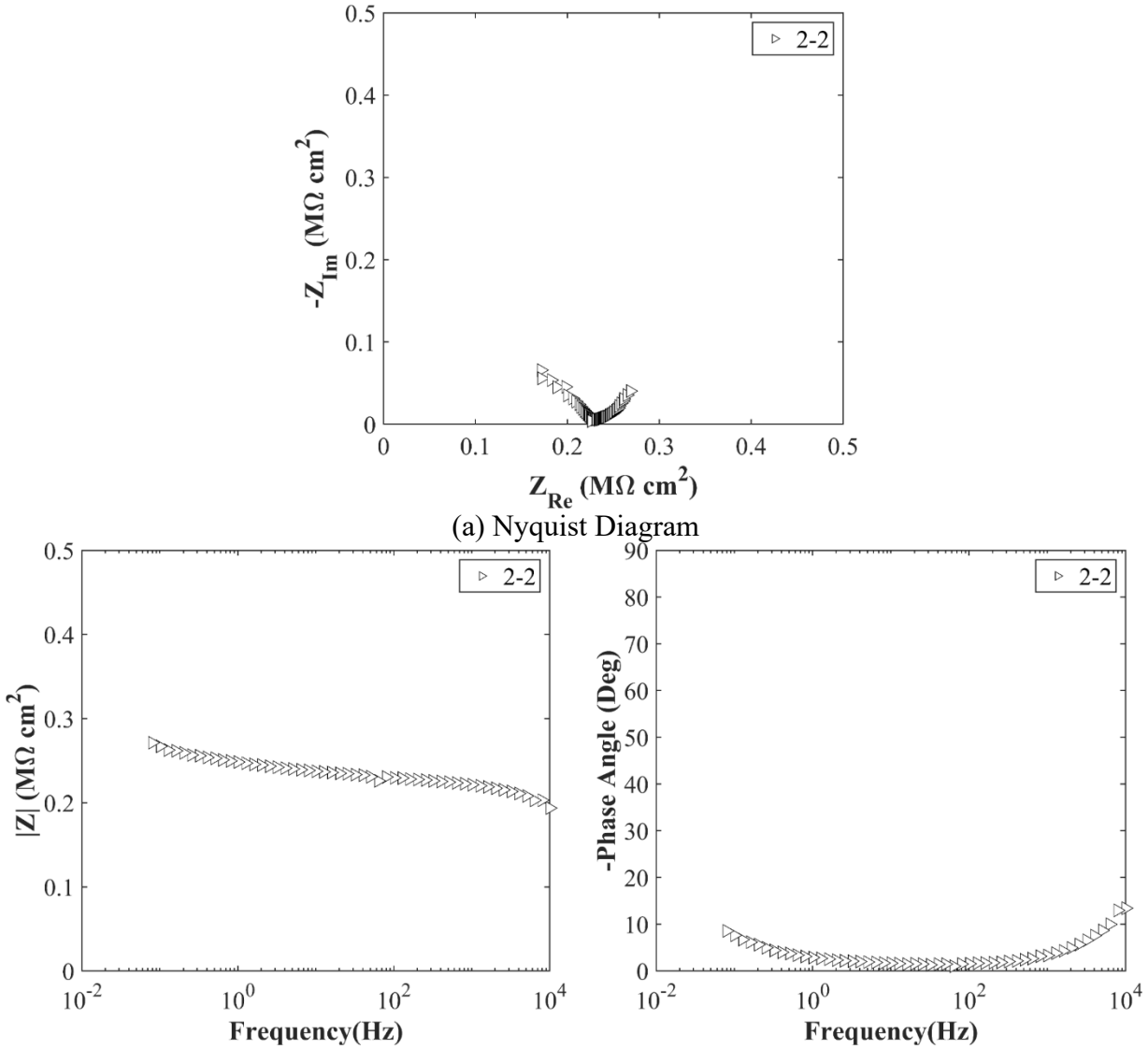

(a) Nyquist Diagram

(b) Bode Plot of Impedance Modulus

(c) Bode Plot of Impedance Phase

Figure 0.206. EIS Results: (a) Nyquist Diagram; (b) Bode Plot of Impedance Modulus; (c) Bode Plot of Impedance Phase

B.29 ELP-RC-03, BU 54 WB OVER FLOOD CHANNEL

- Bridge ID: 240720016702107 (El Paso County)
- Built in 1989
- Mitigation methods: HPC, ECR
- Observed CIP depth: N/A
- Observed clear cover: 1.8 in.
- 4 spans, 7-concrete PS girder @ varying spacing with 3’ overhangs at span 1 and 2, 6-concrete PS girder @ varying spacing with 3’ overhangs at span 3 and 4, 6-concrete PS girder @ 8’ with 3’ overhangs at other spans
- Inspected on June 29, 2021

Figure 0.207. Concrete Deck of the Bridge (source: google maps)

B.29.1 Observed Condition

There are transverse and longitudinal cracks on the top surface of deck.

B.29.2 NDE Results

The grid 1 was located on the SB lane, and the grid 2 was located on the pedestrian of the span 1 of the bridge.

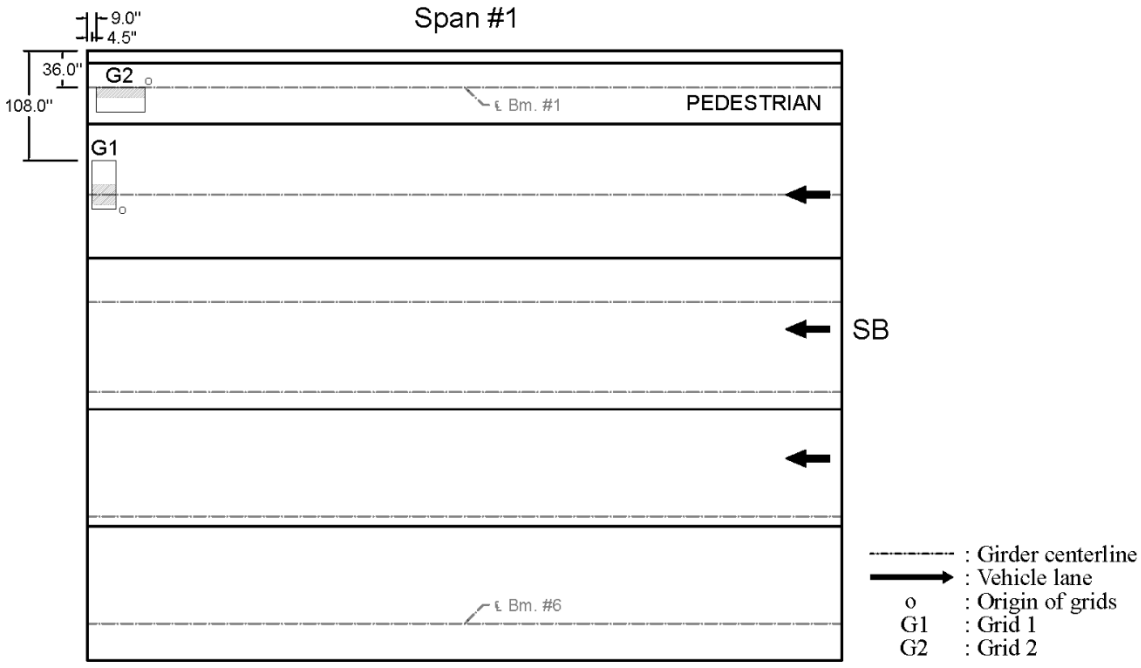

Figure 0.208. Plan View of the Bridge and Location of Grids

As shown in Figure 0.209 (a), only hairline cracks were visible on grid 1. On grid 2, 0.004 in. wide transverse cracks were visible as shown in Figure 0.210 (a).

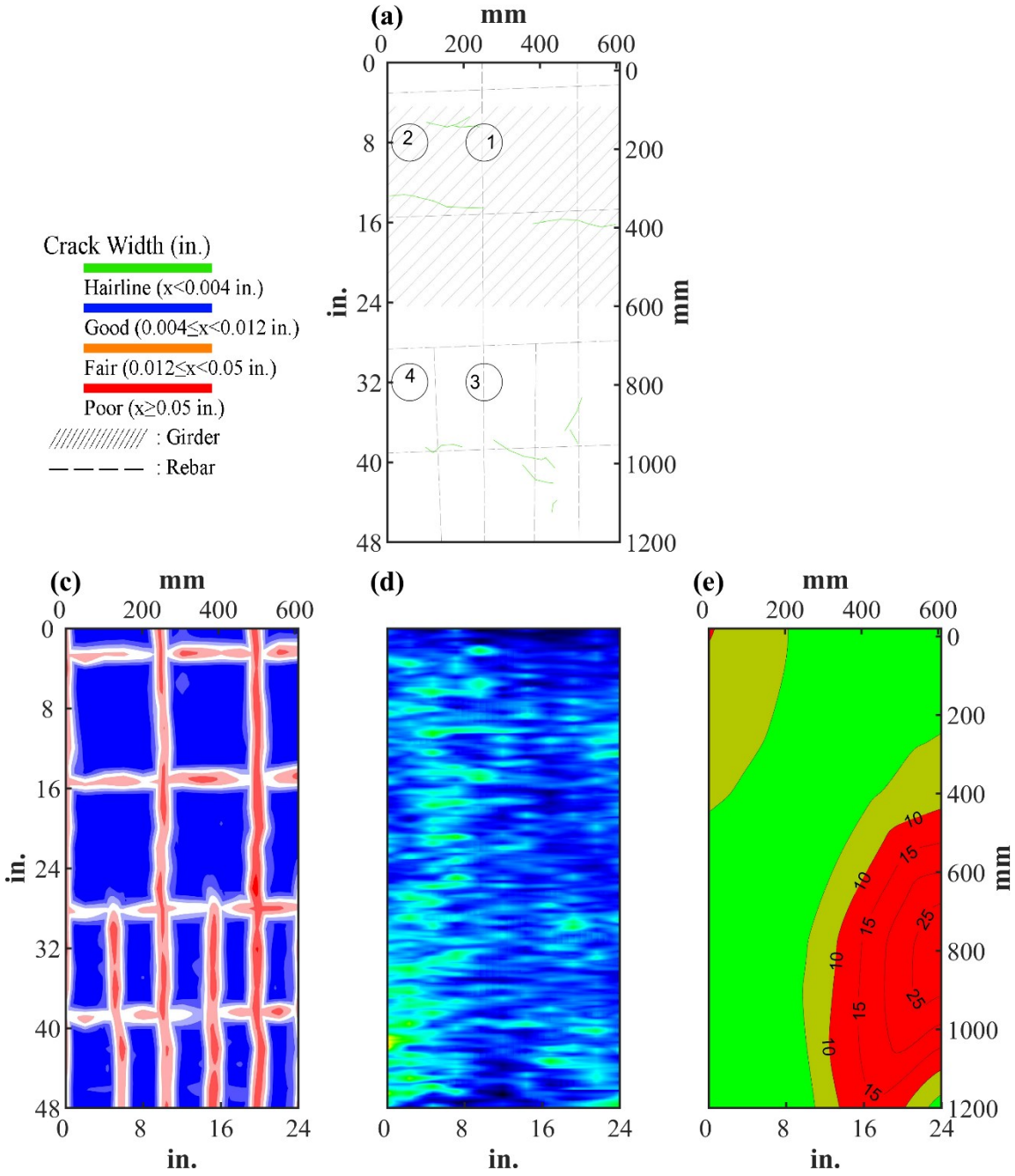

Figure 0.209. Crack Map and NDE Results of Grid 1: (a) Crack map and Location of Cores; (b) Infrared Picture; (c) GPR C-scan at 1.0 in. to 2.4 in. Depth; (d) UST C-scan at 2.0 in. Depth; (e) Corrosion Rate Map

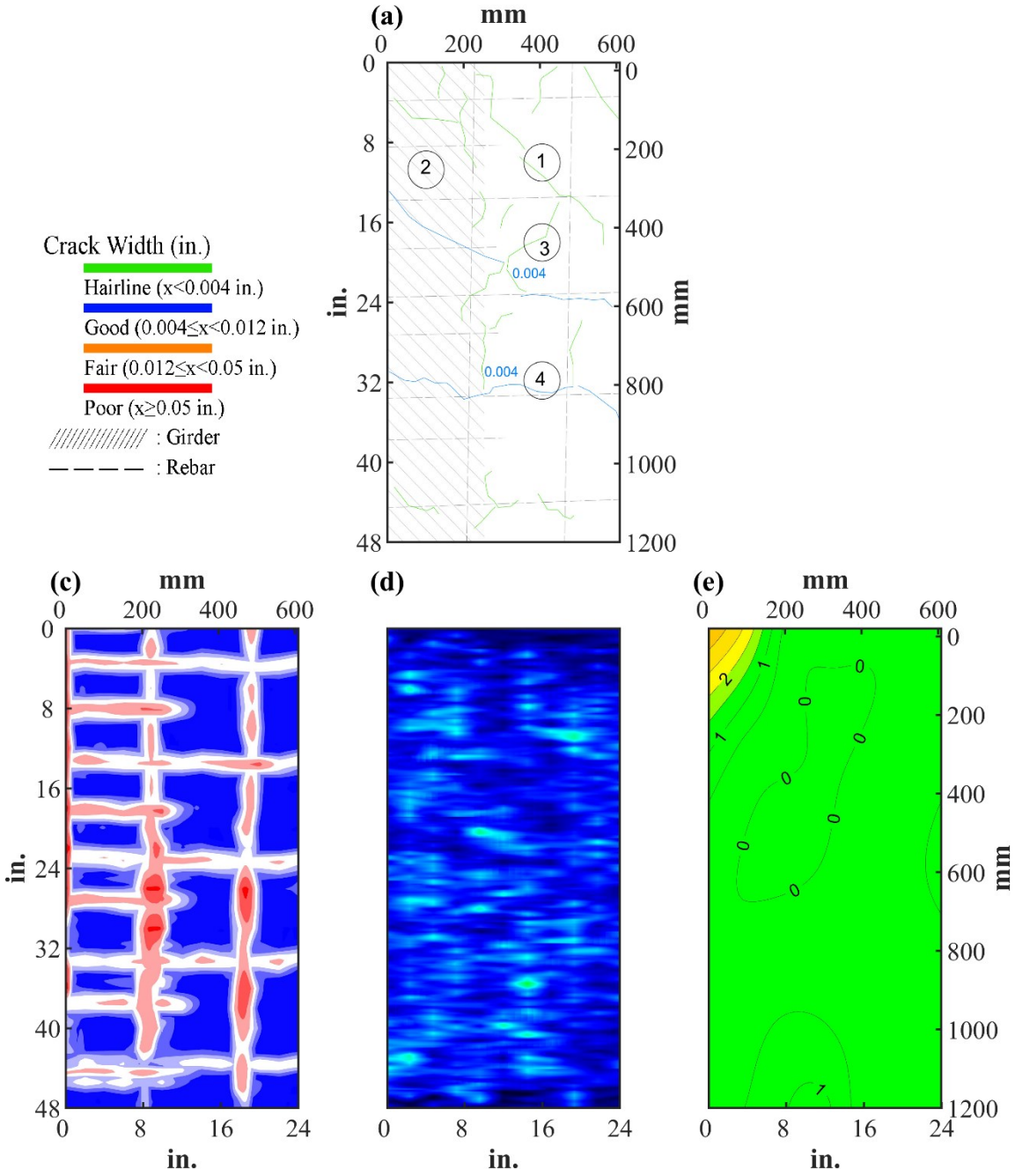

Figure 0.210. Crack Map and NDE Results of Grid 2: (a) Crack map and Location of Cores; (b) Infrared Picture; (c) GPR C-scan at 1.9 in. to 3.3 in. Depth; (d) UST C-scan at 2.2 in. Depth; (e) Corrosion Rate Map

B.29.3 Concrete Cores

Table B-108. Detail Information of concrete cores

Core	dia. x height (in.)	Rebar depth (in.)	Rebar size (#)	Epoxy (Y/N)	Crack type	Crack width (in)	Notes
1-1	3.75 x 5.5	1.8, 5.6	5,4	Y, Y	-	-	-
1-2	3.75 x 5.8	-	-	-	-	-	-
1-3	3.75 x 5.4	1.8	5	Y	transverse	0.1	-
1-4	3.75 x	-	-	-	-	-	Crushed core
2-1	3.75 x 9.7	-	-	-	-	-	
2-2	3.75 x 5.3	-	-	-	-	-	A void at 0.4 in. depth
2-3	3.75 x 9.0	-	-	-	-	-	-
2-4	3.75 x 8.8	3.1	4	Y	longitudinal	HL	-

Table B-109. Core Pictures

Core	Pictures of the Cores		
1-1		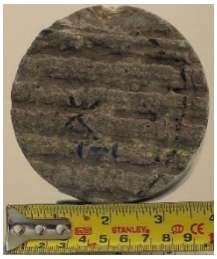	
1-2		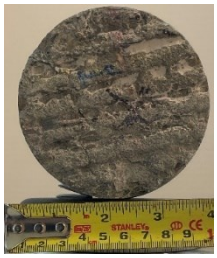	

1-3		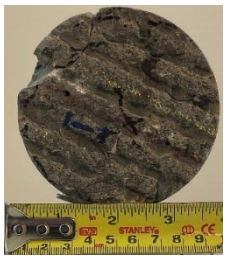	
1-4	-	-	-
2-1			
2-2			
2-3		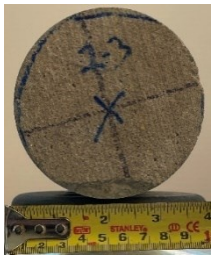	

2-4			

B.29.4 Laboratory Experiment Results

B.29.4.1 Resistivity

Core Number	Surface Resistivity (kΩ·m)	Bulk Resistivity (kΩ·m)
1-2	17.3	4.0
2-1	21.3	-
2-2	26.6	8.5
2-3	15.9	-

B.29.4.2 Ultrasonic Pulse Velocity

Core Number	Ultrasonic Pulse Velocity (m/s)
1-2	2673
2-1	3146
2-2	2901
2-3	3107

B.29.4.3 Carbonation Depth

Core Number	Carbonation Depth (in.)
1-1	0.00
2-1	0.00

B.29.4.4 Acid-Soluble Chloride Content

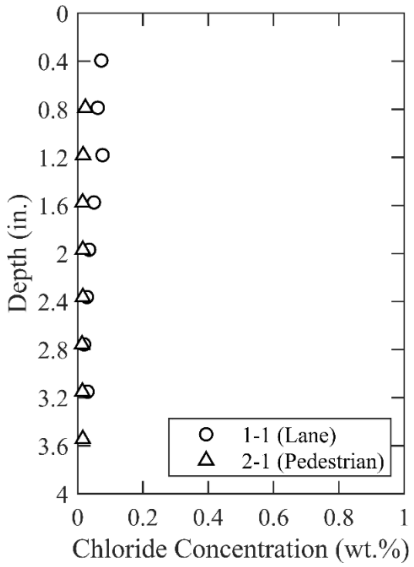

Figure 0.211. Chloride Content at Different Depth

B.29.4.5 Sorptivity

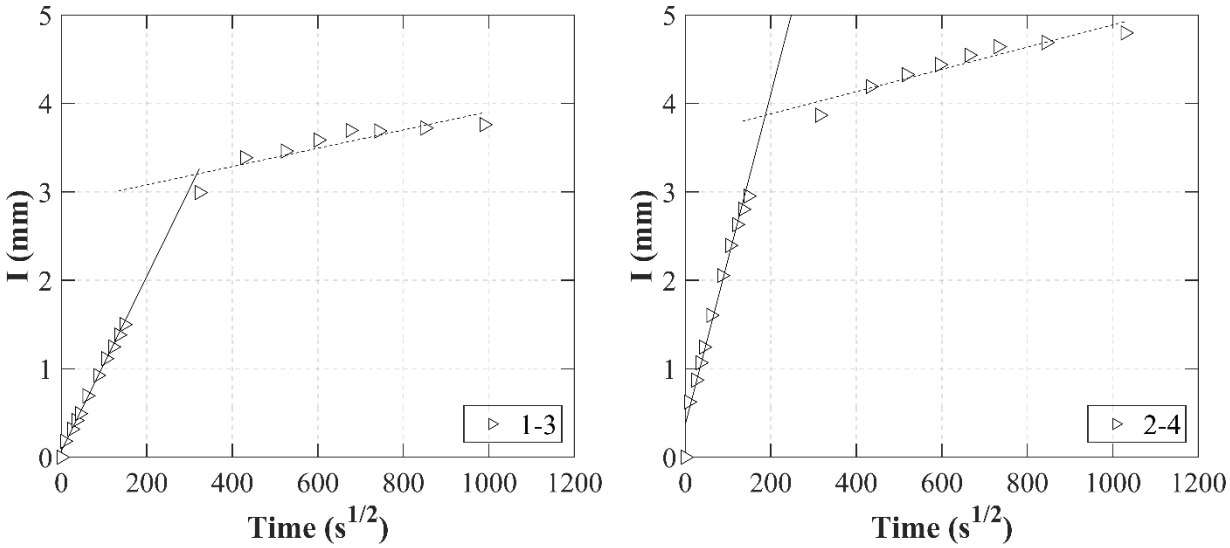

(a) Core 1–3 (b) Core 2–4

Figure 0.212. Absorption and Sorptivity of: (a) Core 1–3; (b) Core 2–4

Table B-110. Initial and Secondary Sorptivity Results

Core Number	Sorptivity	Results (mm/s$^{1/2}$)
Core 1–3	Initial Sorptivity	0.00988
	Secondary Sorptivity	0.00103
Core 2–4	Initial Sorptivity	0.0187
	Secondary Sorptivity	0.00126

B.29.4.6 Knife Test

Core Number	Score	Picture
1-1	8	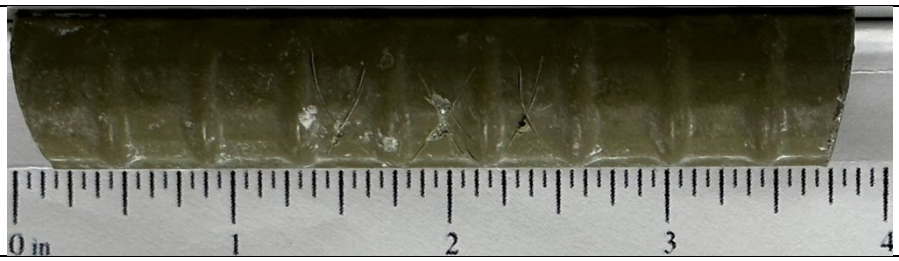

B.29.4.7 Electrochemical Impedance Spectroscopy

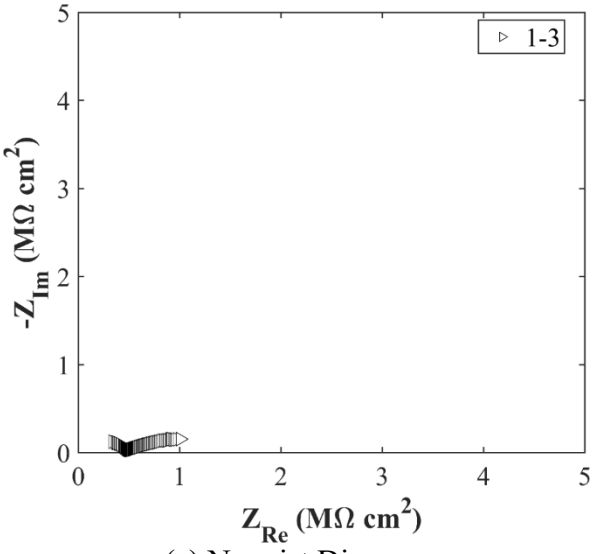

(a) Nyquist Diagram

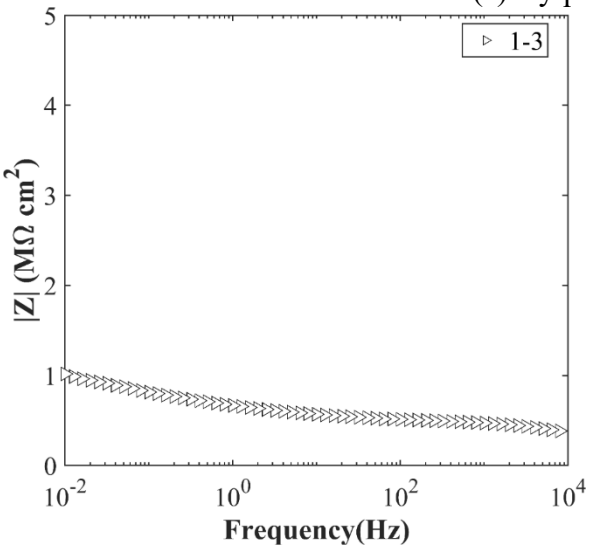

(b) Bode Plot of Impedance Modulus

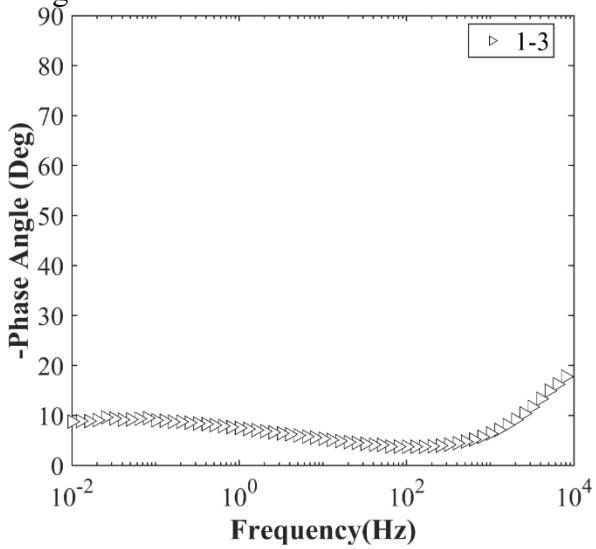

(c) Bode Plot of Impedance Phase

Figure 0.213. EIS Results: (a) Nyquist Diagram; (b) Bode Plot of Impedance Modulus; (c) Bode Plot of Impedance Phase

B.30 ELP-RC-04, US 62/180 OVER FM 659

- Bridge ID: 240720037402112 (El Paso County)
- Built in 2010
- Mitigation methods: HPC, silane
- Observed CIP depth: 5.0 in.
- Observed clear cover: 2.5 in.
- 1 span, 12-concrete PS girder @ 6.333’ with 3’ overhangs
- Inspected on July 1, 2021

Figure 0.214. Concrete Deck of the Bridge (source: google maps)

B.30.1 Observed Condition

The deck is in good condition. Concrete railing has vertical hairline and minor cracks and impact scrapes.

B.30.2 NDE Results

Grid 1 was located on the EB lane, and grid 2 was located on the EB shoulder lane of the span 1 of the bridge.

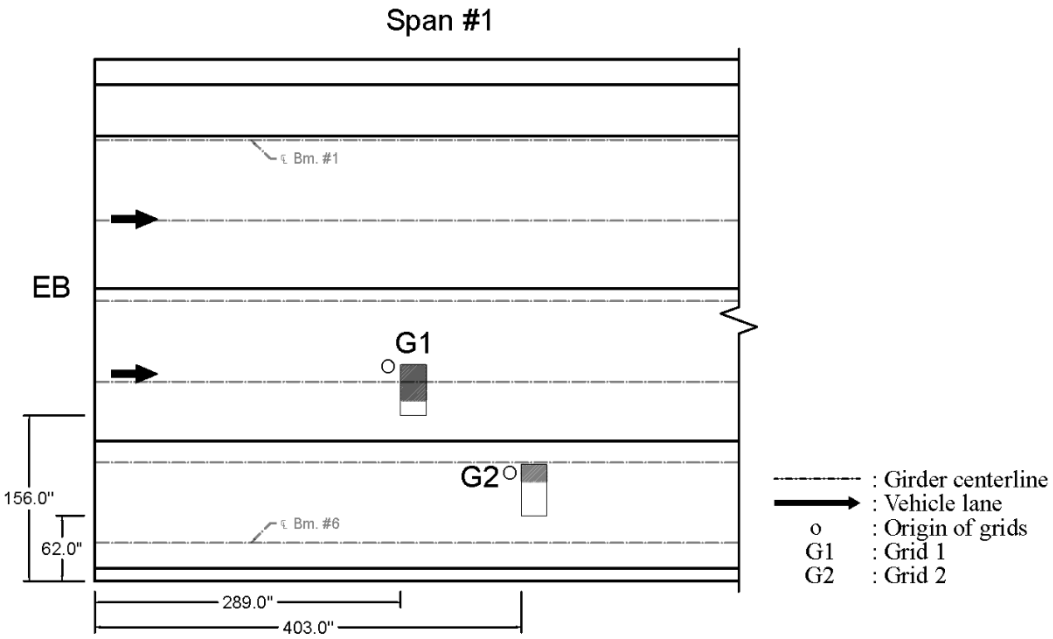

Figure 0.215. Plan View of the Bridge and Location of Grids

As shown in Figure 0.216 (a), one 0.004 in. wide transverse crack was visible on grid 1. On grid 2, there were two short transverse crack that are 0.004 in. wide as shown in Figure 0.217 (a).

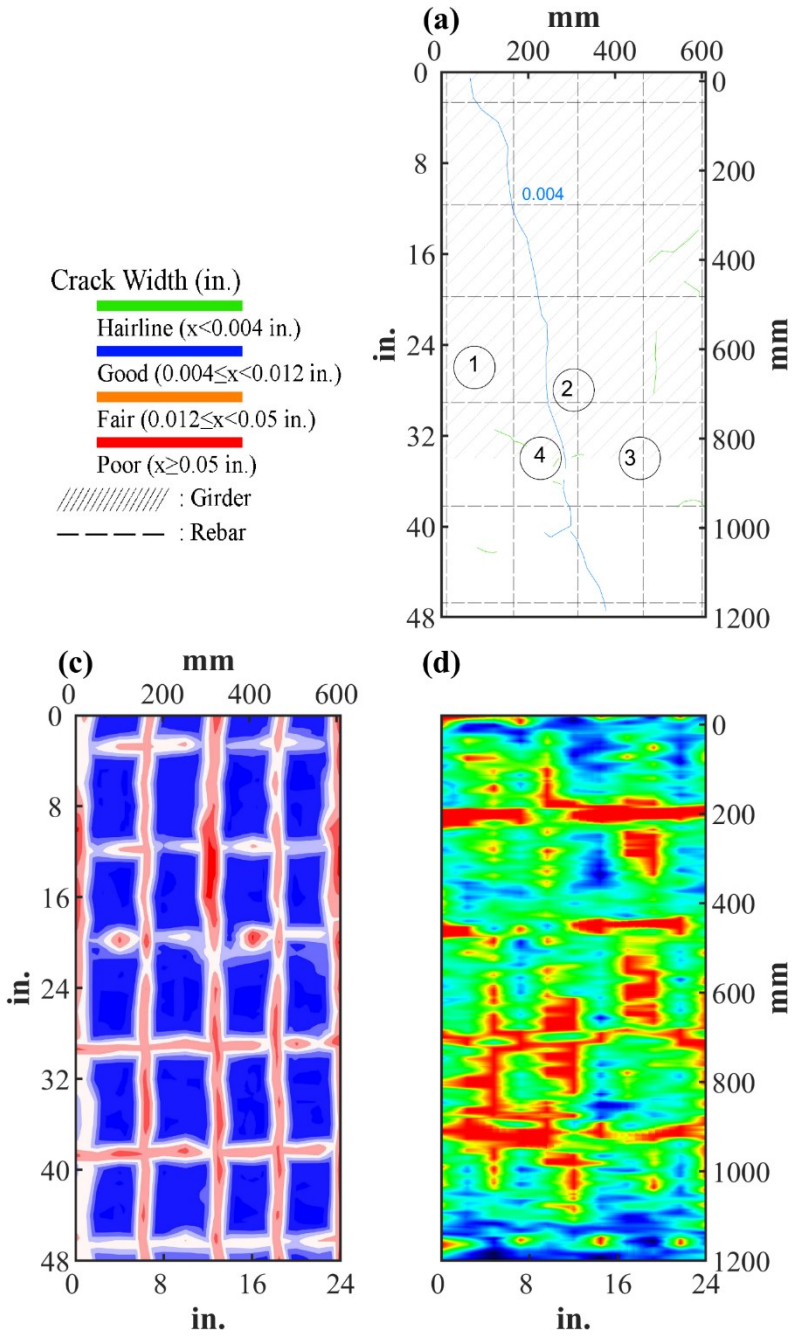

Figure 0.216. Crack Map and NDE Results of Grid 1: (a) Crack map and Location of Cores; (c) GPR C-scan at 2.6 in. to 4.0 in. Depth; (d) UST C-scan at 3.4 in. Depth

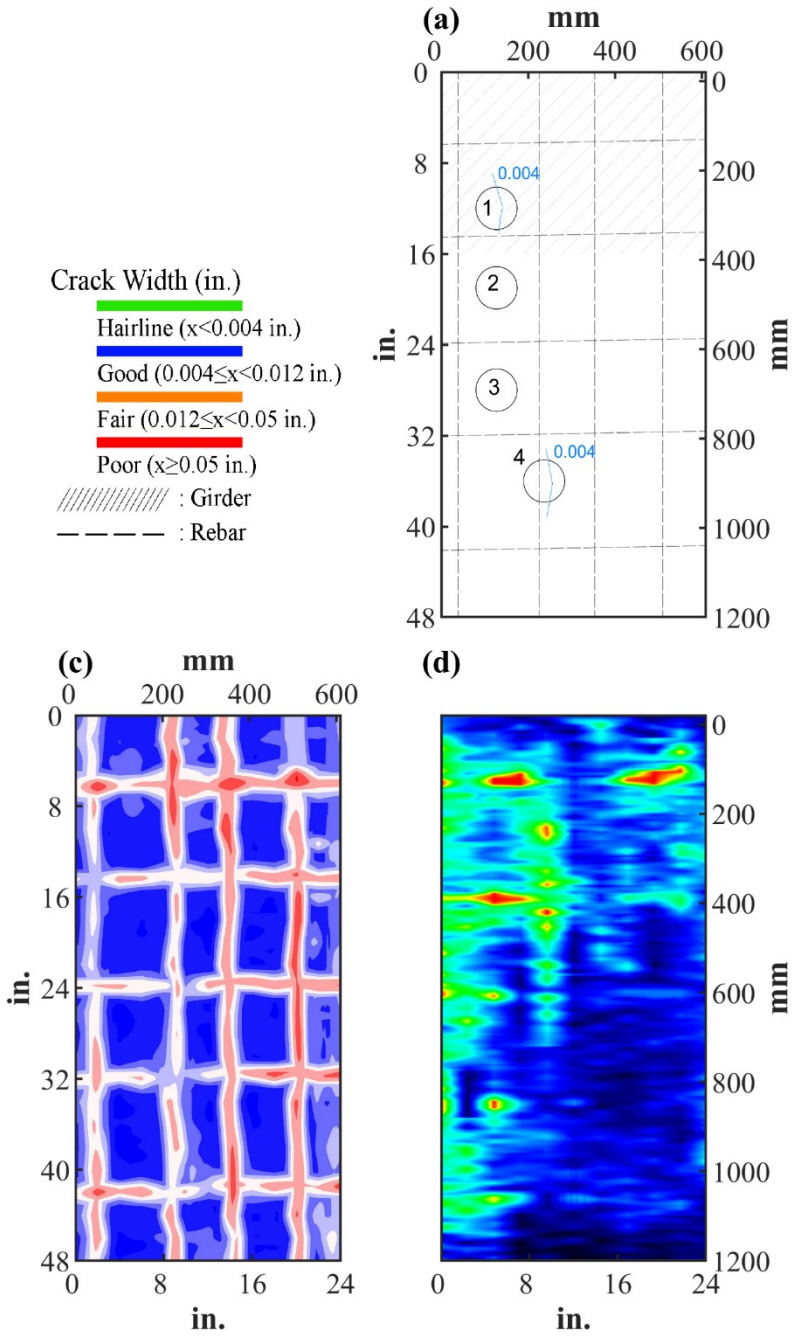

Figure 0.217. Crack Map and NDE Results of Grid 2: (a) Crack map and Location of Cores; (c) GPR C-scan at 2.9 in. to 4.1 in. Depth; (d) UST C-scan at 3.9 in. Depth

B.30.3 Concrete Cores

Table B-111. Detail Information of concrete cores

Core	dia. x height (in.)	Rebar depth (in.)	Rebar size (#)	Epoxy (Y/N)	Crack type	Crack width (in)	Notes
1-1	3.75 x 6.3	2.5, 3.5	5,4	N, N	-	-	-
1-2	3.75 x 5.9	-	-	-	-	-	-
1-3	3.75 x 6.1	3.1	5	N	-	-	-
1-4	3.75 x 5.7	-	-	-	-	-	-
2-1	3.75 x 6.4	-	-	-	transverse	0.004	-
2-2	3.75 x 5.7	-	-	-	-	-	-
2-3	3.75 x 5.7	-	-	-	-	-	-
2-4	3.75 x 6.1	3.1	5	N	transverse	0.004	-

Table B-112 Core Pictures

Core	Pictures of the Cores		
1-1			
1-2	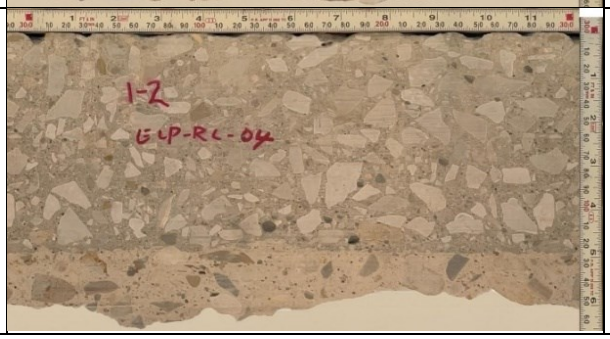		

1-3			
1-4	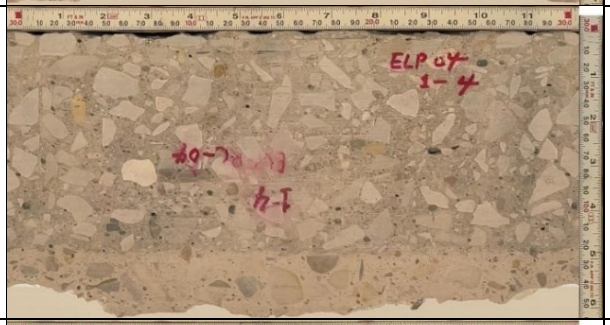		
2-1		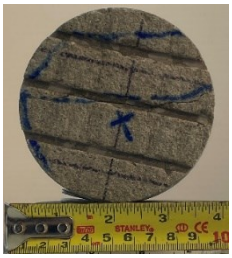	
2-2			
2-3		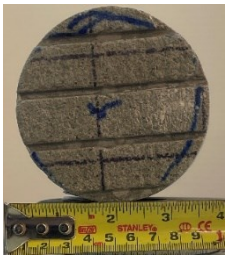	

2-4			

B.30.4 Laboratory Experiment Results

B.30.4.1 Resistivity

Core Number	Surface Resistivity (kΩ·m)	Bulk Resistivity (kΩ·m)
1-2	77.3	13.6
1-4	53.5	-
2-2	68.1	-
2-3	47.4	16.5

B.30.4.2 Ultrasonic Pulse Velocity

Core Number	Ultrasonic Pulse Velocity (m/s)
1-2	4480
1-4	4366
2-2	4302
2-3	4371

B.30.4.3 Carbonation Depth

Core Number	Carbonation Depth (in.)
1-1	0.31
2-1	0.00

B.30.4.4 Acid-Soluble Chloride Content

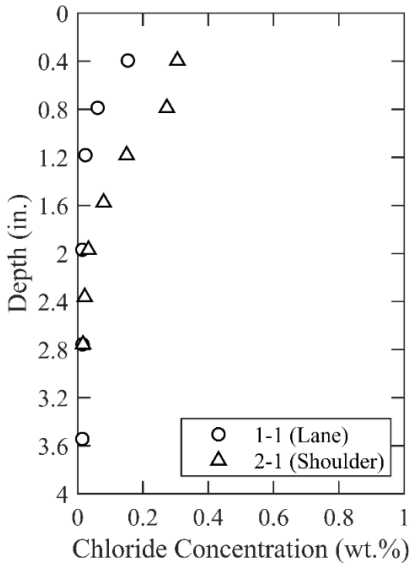

Figure 0.218. Chloride Content at Different Depth

B.30.4.5 Sorptivity

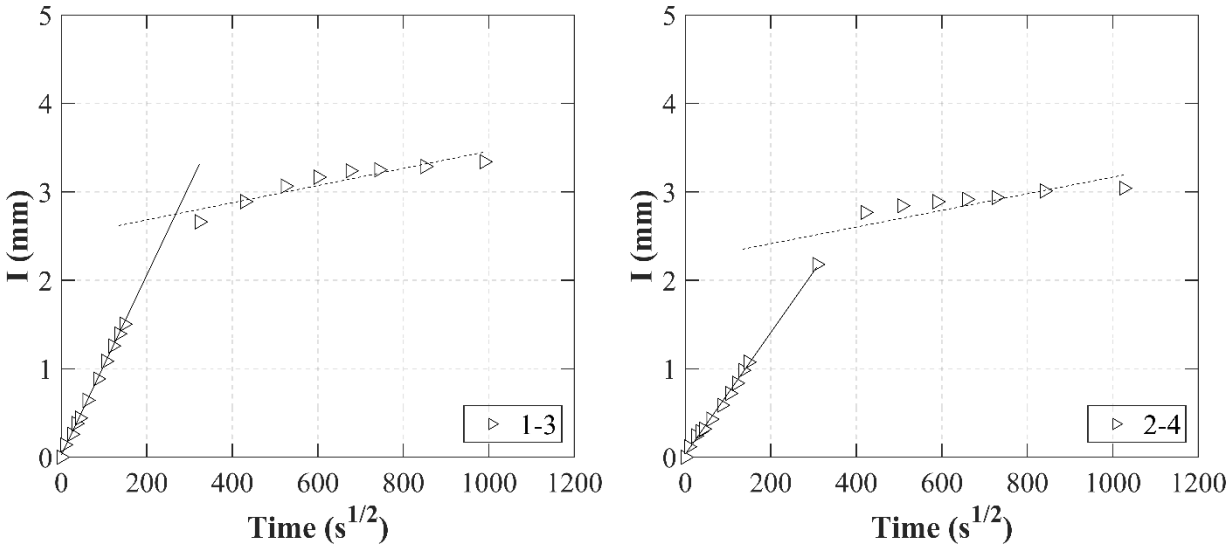

(a) Core 1–3 (b) Core 2–4

Figure 0.219. Absorption and Sorptivity of: (a) Core 1–3; (b) Core 2–4

Table B-113. Initial and Secondary Sorptivity Results

Core Number	Sorptivity	Results (mm/s$^{1/2}$)
Core 1–3	Initial Sorptivity	0.0102
	Secondary Sorptivity	0.00097
Core 2–4	Initial Sorptivity	0.00688
	Secondary Sorptivity	0.00094

B.30.4.6 Electrochemical Impedance Spectroscopy

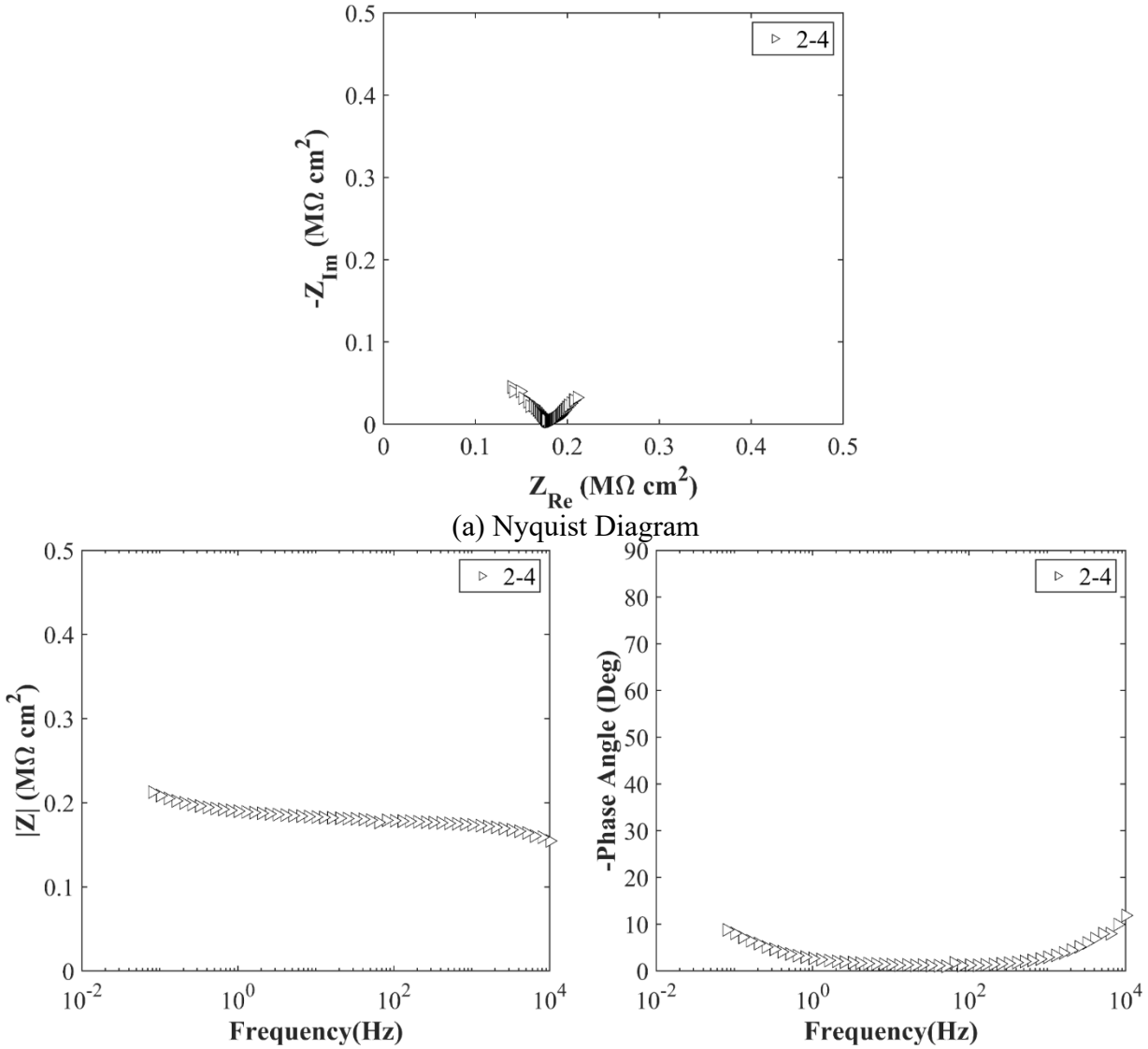

(a) Nyquist Diagram

(b) Bode Plot of Impedance Modulus

(c) Bode Plot of Impedance Phase

Figure 0.220. EIS Results: (a) Nyquist Diagram; (b) Bode Plot of Impedance Modulus; (c) Bode Plot of Impedance Phase

B.31 ELP-RC-05, LP 375 OVER ALCAN ST.

- Bridge ID: 240720255201295 (El Paso County)
- Built in 2014
- Mitigation methods: HPC, silane
- Observed CIP depth: 4.2 in.
- Observed clear cover: 2.8 in.
- 3 spans, 9-concrete PS girder @ 9.5’ with 3’ overhangs
- Inspected on June 29, 2021

Figure 0.221. Concrete Deck of the Bridge (source: google maps)

B.31.1 Observed Condition

There are transverse and longitudinal hairline to minor cracks on the top surface of deck.

B.31.2 NDE Results

The grid 1 was located on the SB lane, and the grid 2 was located on the SB shoulder lane of the span 1 of the bridge.

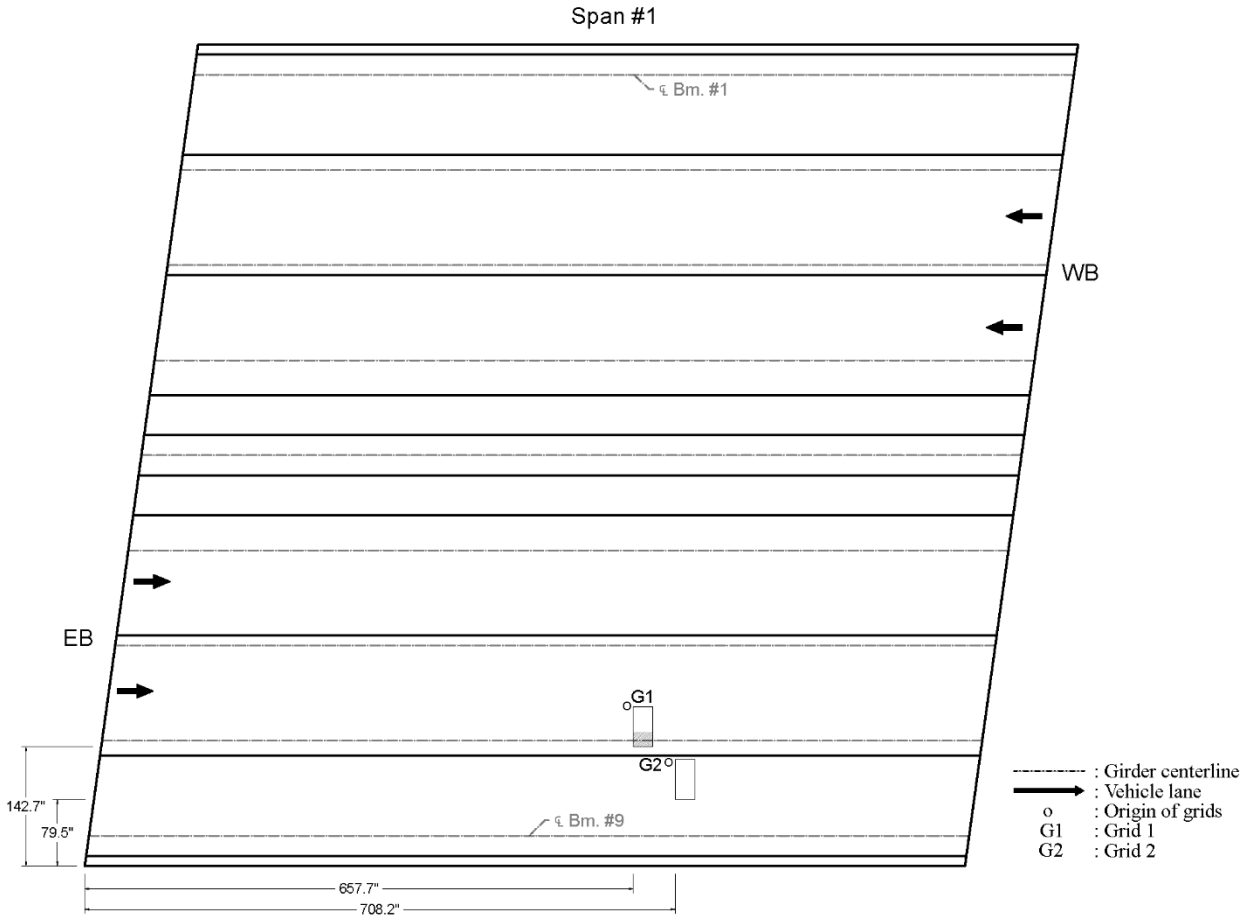

Figure 0.222. Plan View of the Bridge and Location of Grids

As shown in Figure 0.223 (a), there are widespread of hairline cracks and cracks ranging from 0.004 in. to 0.01 in. wide. 0.01 in wide crack was in transverse direction and 0.004 in. cracks were mostly in longitudinal direction on grid 1. On grid 2, most of the cracks were in longitudinal direction and their width ranged from 0.004 in. to 0.025 in. wide as shown in Figure 0.224 (a).

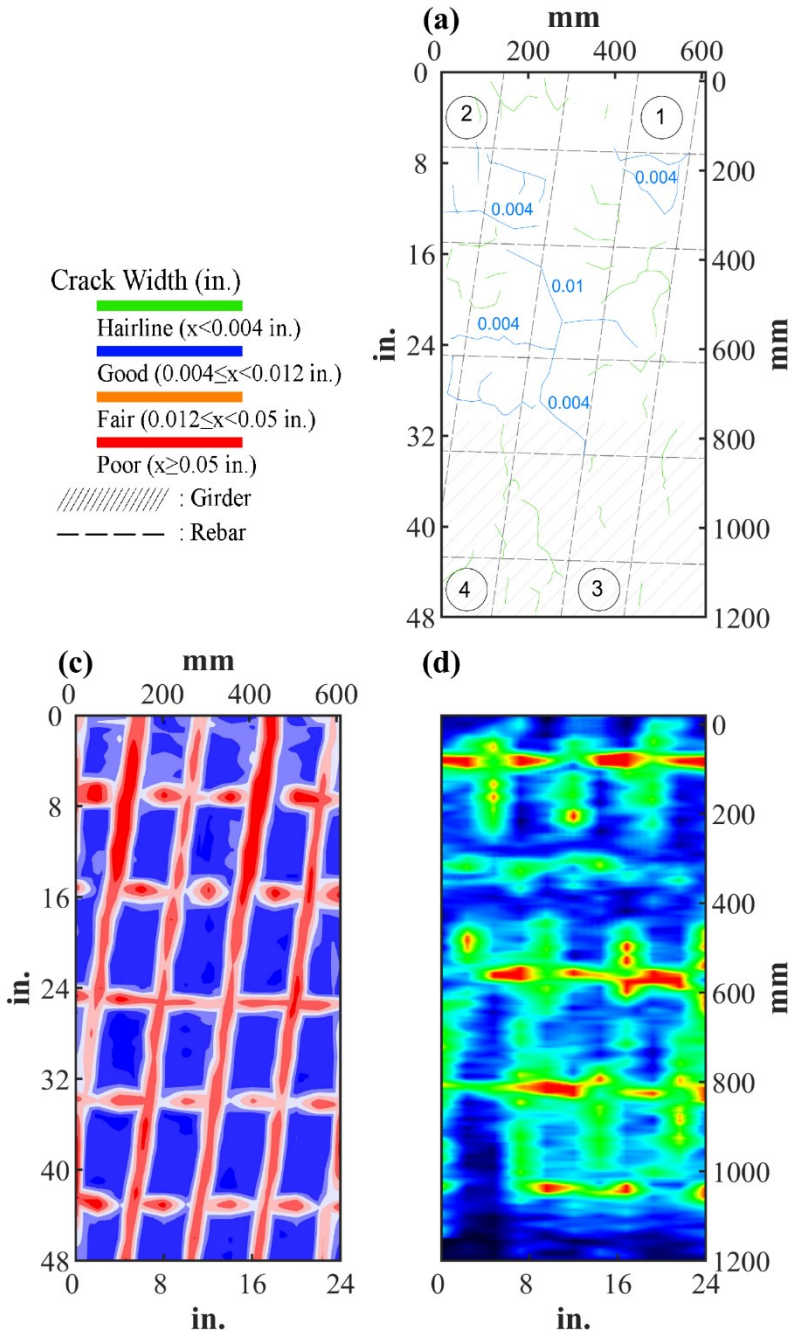

Figure 0.223. Crack Map and NDE Results of Grid 1: (a) Crack map and Location of Cores; (c) GPR C-scan at 2.3 in. to 3.5 in. Depth; (d) UST C-scan at 3.7 in. Depth

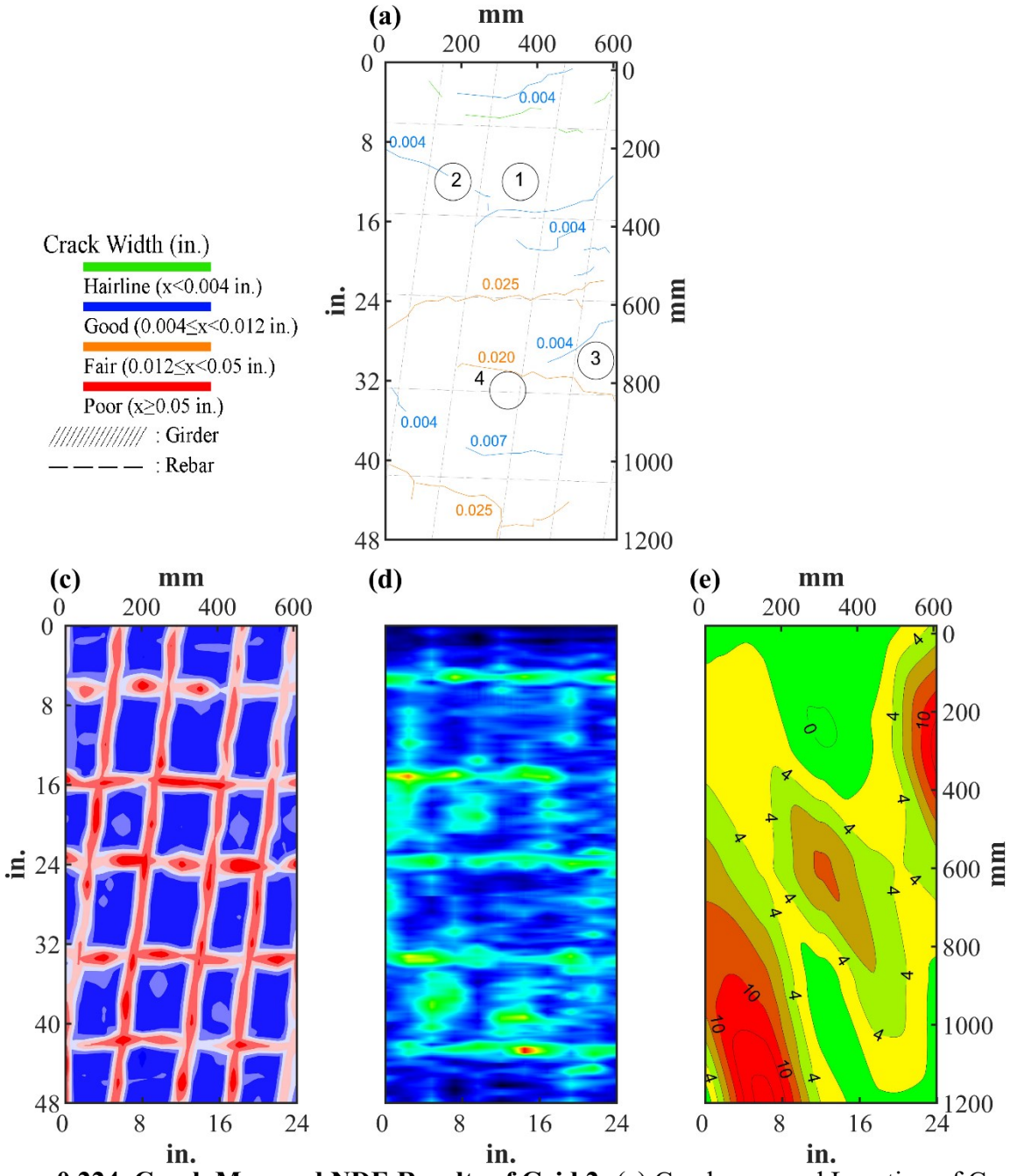

Figure 0.224. Crack Map and NDE Results of Grid 2: (a) Crack map and Location of Cores; (b) Infrared Picture; (c) GPR C-scan at 2.55 in. to 4.0 in. Depth; (d) UST C-scan at 3.7 in. Depth; (e) Corrosion Rate Map

B.31.3 Concrete Cores

Table B-114. Detail Information of concrete cores

Core	dia. x height (in.)	Rebar depth (in.)	Rebar size (#)	Epoxy (Y/N)	Crack type	Crack width (in)	Notes
1-1	3.75 x 6.3	-	-	-	-	-	-
1-2	3.75 x 6.3	-	-	-	transverse	HL	-
1-3	3.75 x 5.1	-	-	-	-	-	-
1-4	3.75 x 5.1	-	-	-	-	-	-
2-1	3.75 x 6.7	-	-	-	-	-	-
2-2	3.75 x 6.5	-	-	-	-	-	-
2-3	3.75 x 6.1	-	-	-	-	-	-
2-4	3.75 x 6.5	2.8, 3.3	5,4	N, N	-	-	-

Table B-115. Core Pictures

Core	Pictures of the Cores		
1-1			
1-2			

1-3			
1-4			
2-1			
2-2			

2-3			
2-4			

B.31.4 Laboratory Experiment Results

B.31.4.1 Resistivity

Core Number	Surface Resistivity (kΩ·m)	Bulk Resistivity (kΩ·m)
1-2	148.9	-
1-3	94.3	19.2
1-4	83.4	-
2-3	95.0	15.0

B.31.4.2 Ultrasonic Pulse Velocity

Core Number	Ultrasonic Pulse Velocity (m/s)
1-2	4554
1-3	4580
1-4	4492
2-3	4702

B.31.4.3 Carbonation Depth

Core Number	Carbonation Depth (in.)
1-1	0.00
2-1	0.17

B.31.4.4 Acid-Soluble Chloride Content

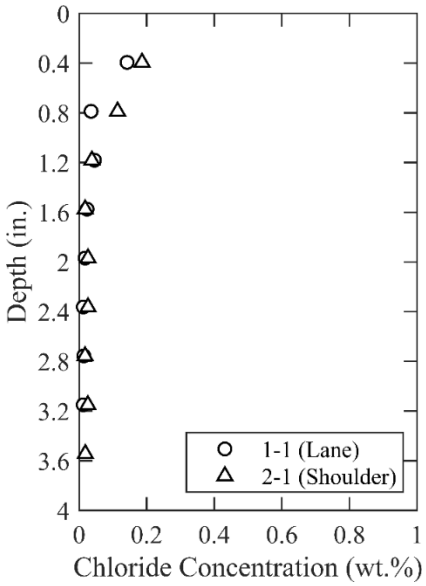

Figure 0.225. Chloride Content at Different Depth

B.31.4.5 Sorptivity

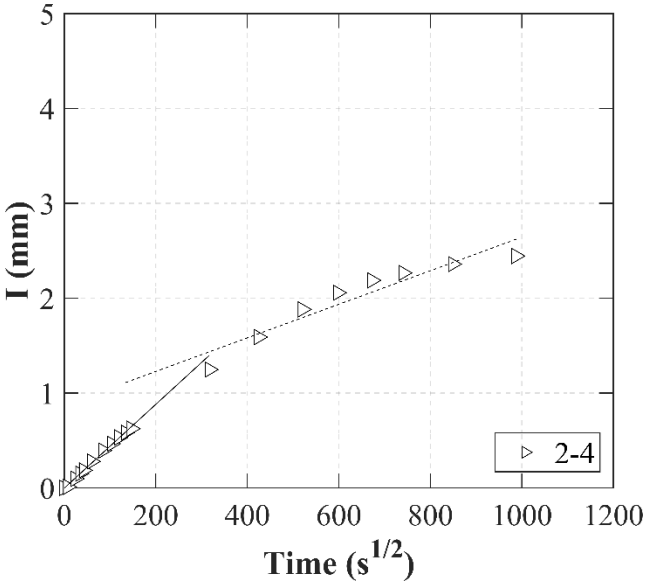

Figure 0.226. Absorption and Sorptivity of Core 2–4

Table B-116. Initial and Secondary Sorptivity Results

Core Number	Sorptivity	Results ($mm/s^{1/2}$)
Core 2–4	Initial Sorptivity	0.00442
	Secondary Sorptivity	0.00177

B.31.4.6 Electrochemical Impedance Spectroscopy

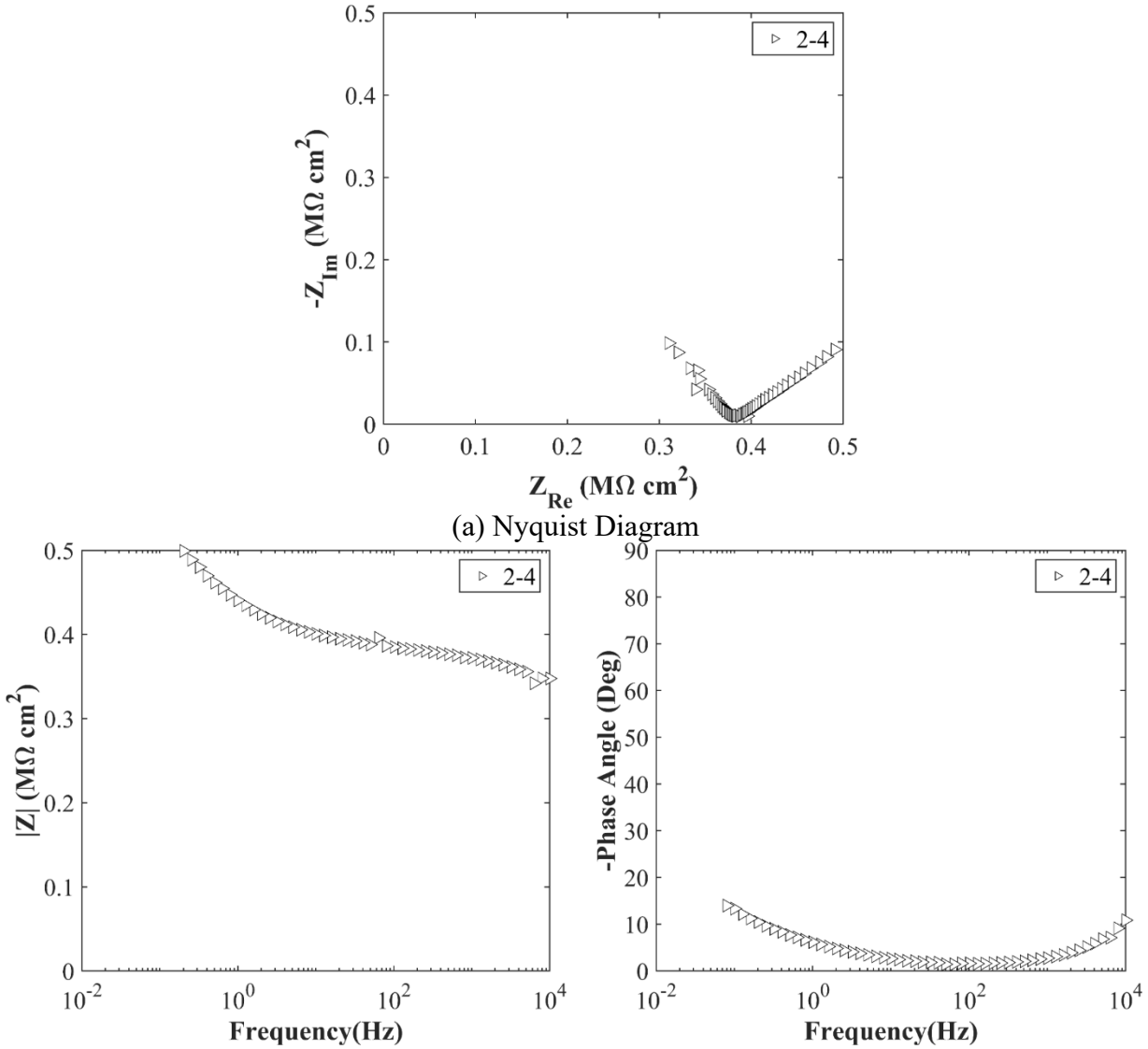

(a) Nyquist Diagram

(b) Bode Plot of Impedance Modulus

(c) Bode Plot of Impedance Phase

Figure 0.227. EIS Results: (a) Nyquist Diagram; (b) Bode Plot of Impedance Modulus; (c) Bode Plot of Impedance Phase

B.32 ELP-RC-06, LP 375 OVER MILITARY TANK XING & UPRR

- Bridge ID: 240720255202037 (El Paso County)
- Built in 1994
- Mitigation methods: None
- Observed CIP depth: N/A.
- Observed clear cover: 2.4 in.
- 7 spans
- Inspected on June 30, 2021

Figure 0.228. Concrete Deck of the Bridge (source: google maps)

B.32.1 Observed Condition

There are transverse and longitudinal hairline to minor cracks on the top surface of deck. The joint is partially failed and full of debris. The concrete railing has minor vertical cracks. Obvious soot stains are found on the beams over the railroad tracks. The metal deck form at the end of abutment has serious corrosion. The abutment has deep spalling and exposed rebar as shown in Figure 0.229

Figure 0.229. Corrosion at metal deck form and abutment

B.32.2 NDE Results

The grid 1 was located on the WB lane, and the grid 2 was located on the WB shoulder lane of the span 1 of the bridge.

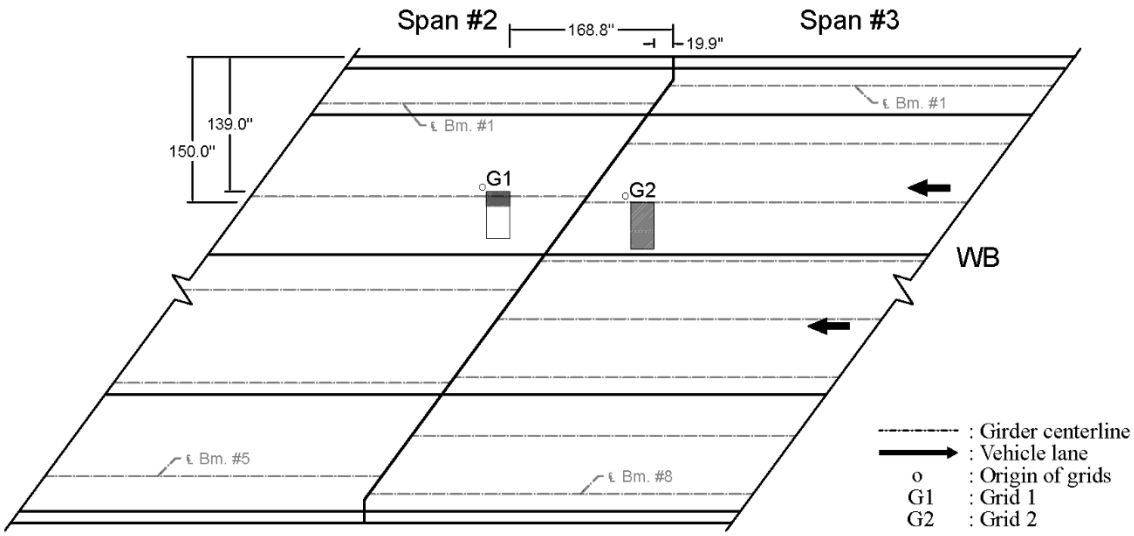

Figure 0.230. Plan View of the Bridge and Location of Grids

As shown in Figure 0.231 (a), there were widespread of cracks range from 0.004 in. to 0.01 in. wide on grid 1. There was one 0.01 in. wide crack that was caused by girder. On grid 2, there were cracks ranging from 0.004 in. to 0.008 in. wide. The direction of cracks was transverse, longitudinal, and diagonal as shown in Figure 0.232 (a).

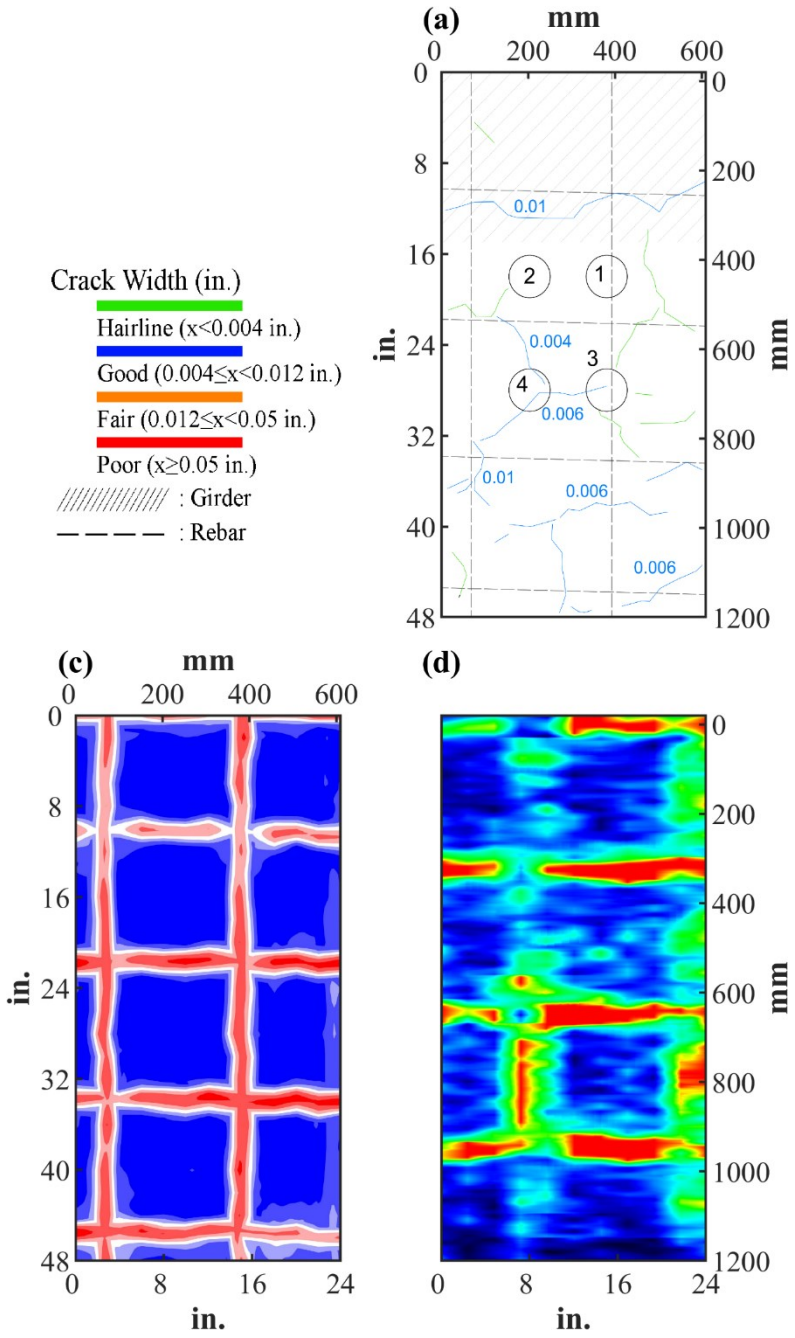

Figure 0.231. Crack Map and NDE Results of Grid 1: (a) Crack map and Location of Cores; (c) GPR C-scan at 2.2 in. to 3.6 in. Depth; (d) UST C-scan at 4.2 in. Depth

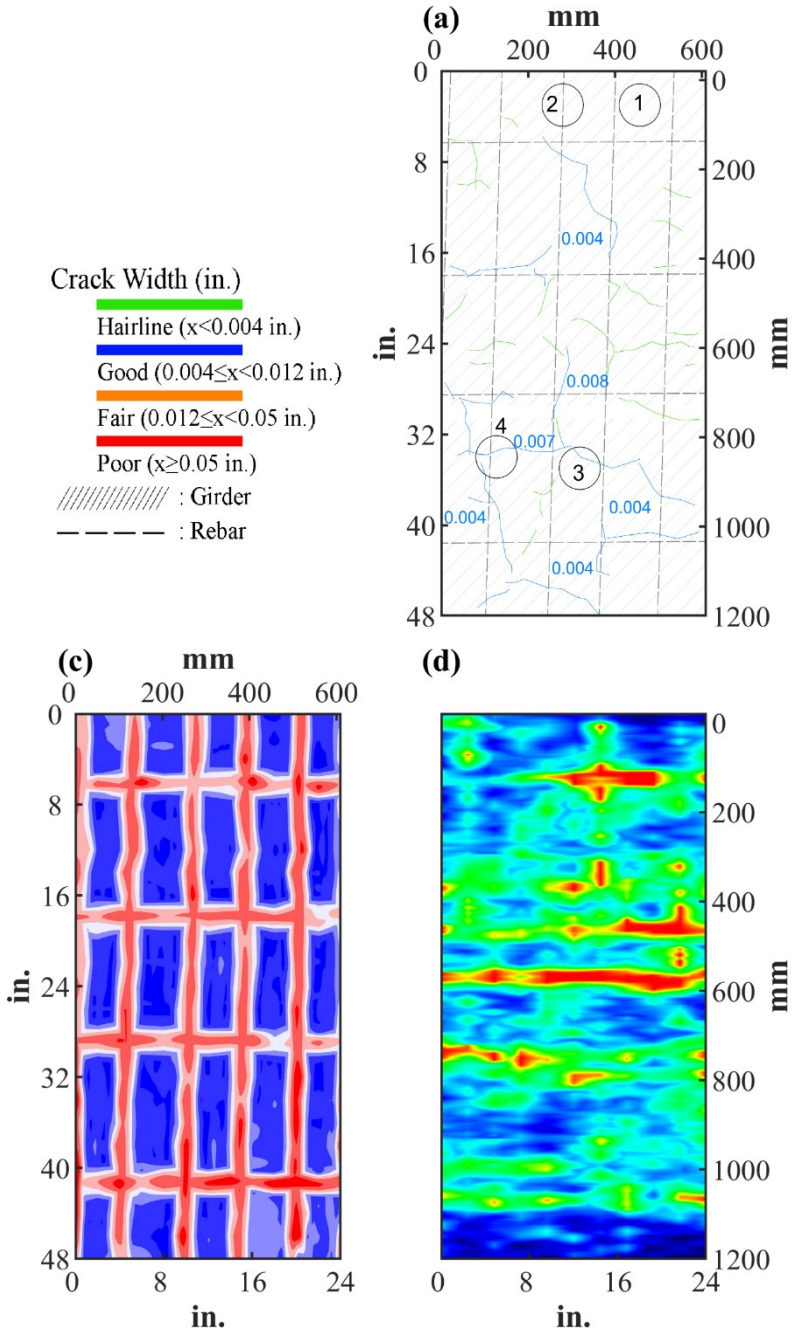

Figure 0.232. Crack Map and NDE Results of Grid 2: (a) Crack map and Location of Cores; (c) GPR C-scan at 1.9 in. to 3.3 in. Depth; (d) UST C-scan at 3.4 in. Depth

B.32.3 Concrete Cores

Table B-117. Detail Information of concrete cores

Core	dia. x height (in.)	Rebar depth (in.)	Rebar size (#)	Epoxy (Y/N)	Crack type	Crack width (in)	Notes
1-1	3.75 x 5.1	2.8	5	Y	-	-	-
1-2	3.75 x 5.5	-	-	-	-	-	-
1-3	3.75 x 4.7	2.8	5	Y	diagonal	0.006	-
1-4	3.75 x 5.9	-	-	-	diagonal	0.006	A crack propagating along aggregates
2-1	3.75 x 8.1	-	-	-	-	-	Core split while coring
2-2	3.75 x 7.7	2.4, 5.3, 5.9	5,5,5	Y, Y,Y		-	-
2-3	3.75 x 4.9	5.3	5	N	diagonal	0.008	-
2-4	3.75 x 5.7	-	5,5	Y,Y	longitudinal	0.007	-

Table B-118. Core Pictures

Core	Pictures of the Cores		
1-1		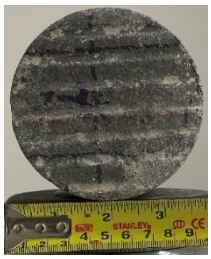	
1-2			

1-3	 ELP 06 1-3		
1-4	 ELP 06 1-4		
2-1	 ELP 06 2-1-1 ELP 06 2-1-2		
2-2	 ELP 06 2-2		
2-3	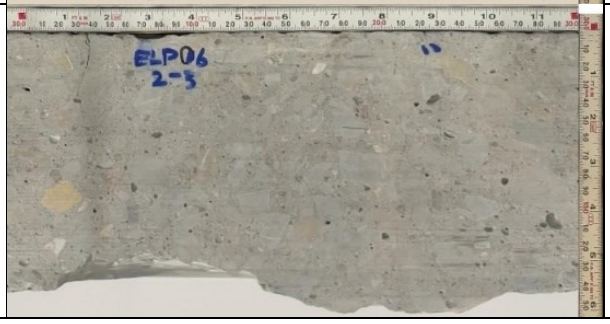 ELP 06 2-3	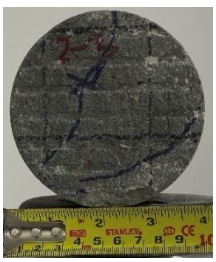	

2-4	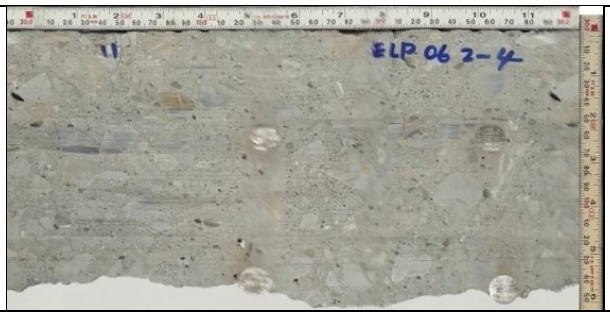		

B.32.4 Laboratory Experiment Results

B.32.4.1 Resistivity

Core Number	Surface Resistivity (kΩ·m)	Bulk Resistivity (kΩ·m)
1-2	33.7	4.7
1-4	31.8	-
2-1	24.7	4.4

B.32.4.2 Ultrasonic Pulse Velocity

Core Number	Ultrasonic Pulse Velocity (m/s)
1-2	4379
1-4	4216
2-1	3416

B.32.4.3 Carbonation Depth

Core Number	Carbonation Depth (in.)
1-3	0.10
2-2	0.00

B.32.4.4 Acid-Soluble Chloride Content

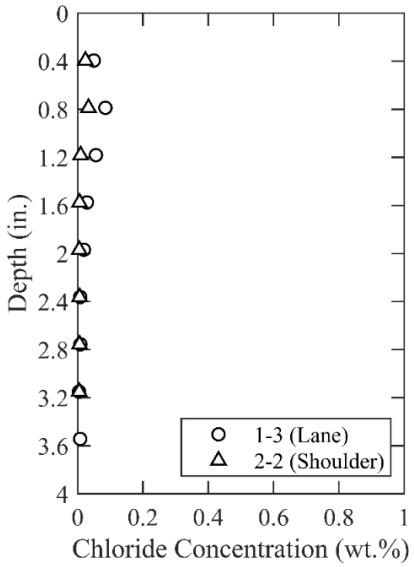

Figure 0.233. Chloride Content at Different Depth

B.32.4.5 Sorptivity

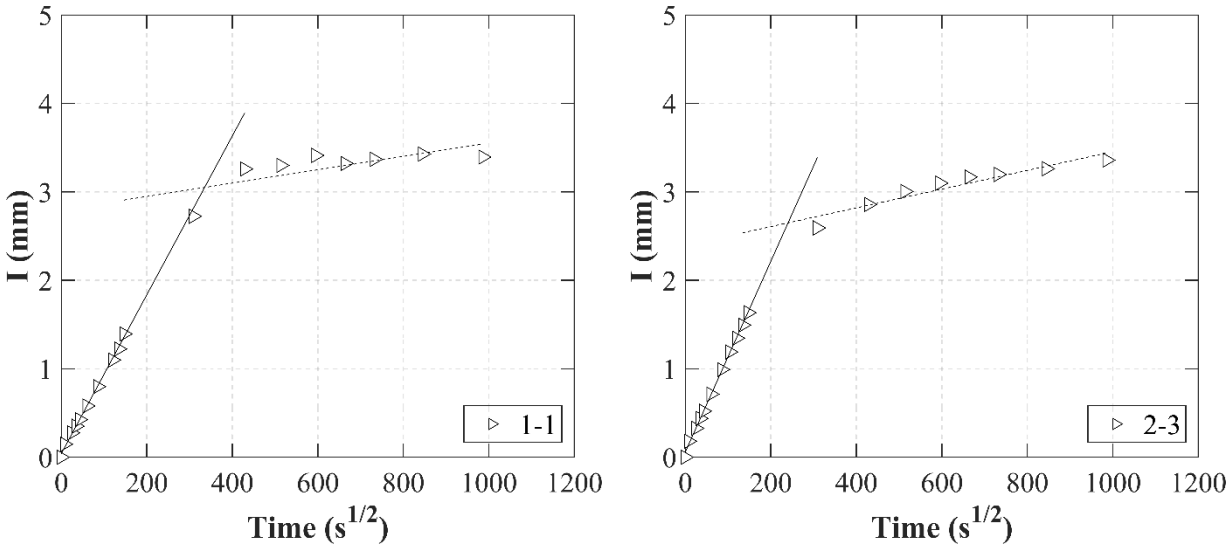

(a) Core 1–1 (b) Core 2–3

Figure 0.234. Absorption and Sorptivity of: (a) Core 1–1; (b) Core 2–3

Table B-119. Initial and Secondary Sorptivity Results

Core Number	Sorptivity	Results (mm/s$^{1/2}$)
Core 1–1	Initial Sorptivity	0.00898
	Secondary Sorptivity	0.00075
Core 2–3	Initial Sorptivity	0.0108
	Secondary Sorptivity	0.00106

B.32.4.6 Knife Test

Core Number	Score	Picture
1-3	10	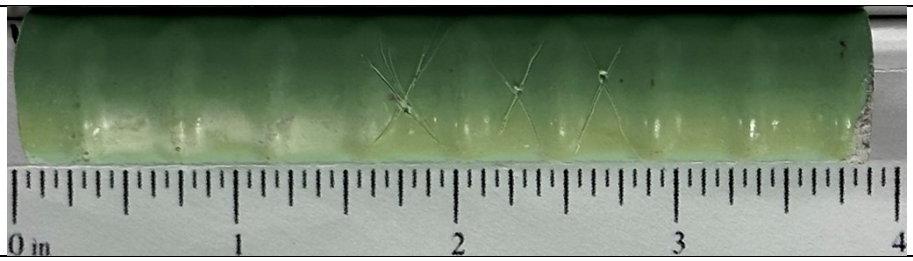

B.32.4.7 Electrochemical Impedance Spectroscopy

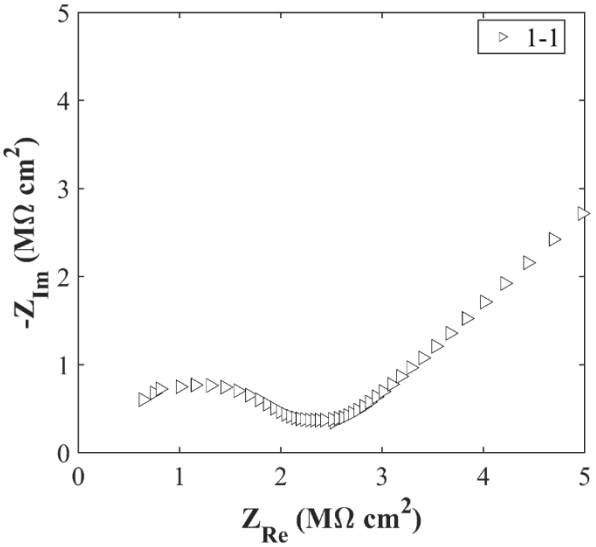

(a) Nyquist Diagram

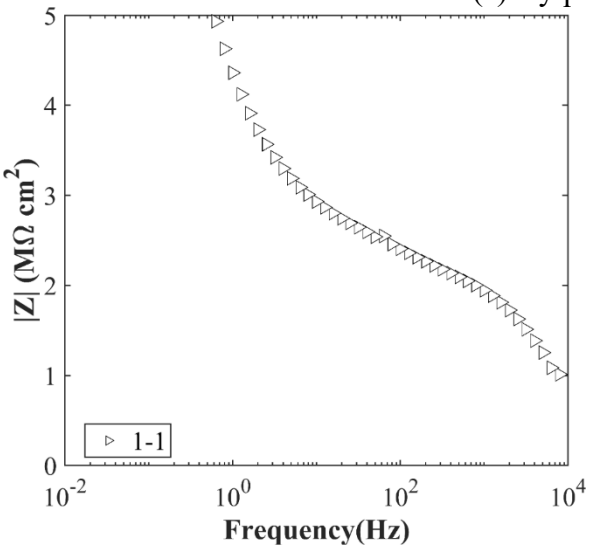

(b) Bode Plot of Impedance Modulus

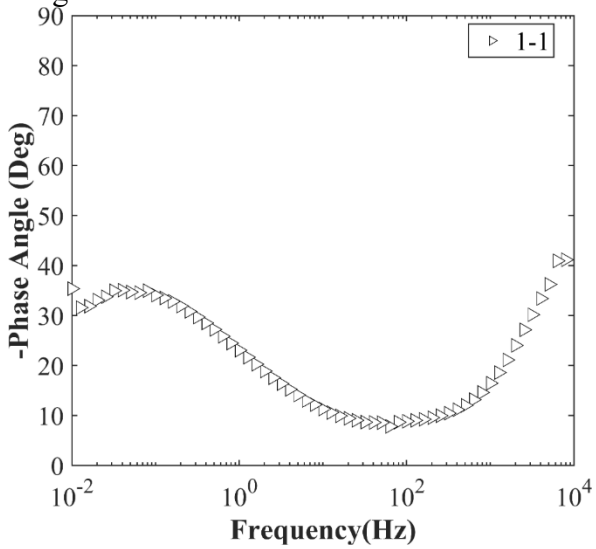

(c) Bode Plot of Impedance Phase

Figure 0.235. EIS Results: (a) Nyquist Diagram; (b) Bode Plot of Impedance Modulus; (c) Bode Plot of Impedance Phase

B.33 ELP-RC-07, LP 375 OVER MONTWOOD DR.

- Bridge ID: 240720255203273 (El Paso County)
- Built in 2006
- Mitigation methods: Linseed oil, ECR
- Observed CIP depth: Unknown
- Observed clear cover: 2.2 in.
- 3 spans, 18-concrete PS girder @ 6’ 8.25 in. with 3’ overhangs
- Inspected on June 30, 2021

Figure 0.236. Concrete Deck of the Bridge (source: google maps)

B.33.1 Observed Condition

There are isolated transverse and longitudinal hairline cracks on the top surface of deck. The joint is partially filled with debris and small gravel. There is one isolated up to 48-inch failure on the south relief joint. The bridge and median railings have vertical hairline to minor cracks and minor collision scrapes. The interior beam near abutment 4 has minor spalling at its corner. The beam 2 at abutment 1 has diagonal hairline cracks at its end.

B.33.2 NDE Results

Grid 1 was located on the SB lane, and grid 2 was located on the SB shoulder lane of the span 1 of the bridge.

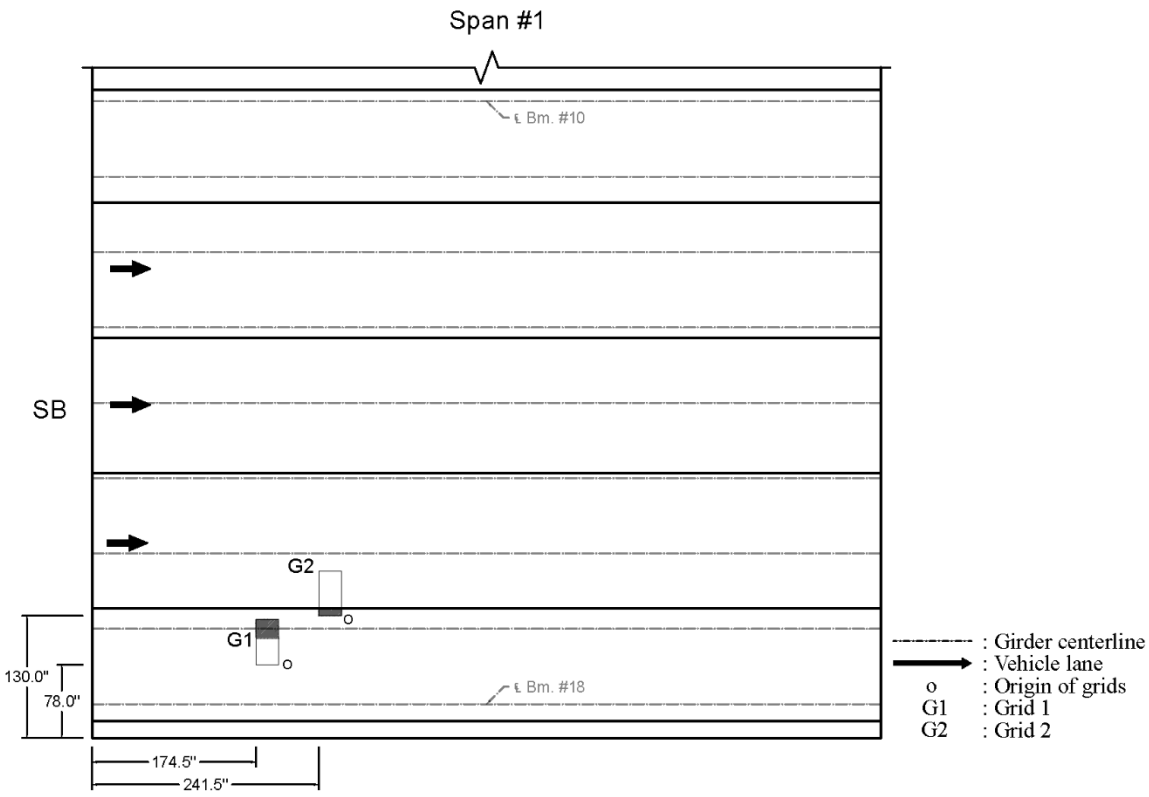

Figure 0.237. Plan View of the Bridge and Location of Grids

As shown in Figure 0.238 (a), there was one 0.012 in. to 0.014 in wide longitudinal crack on top of a girder and transverse cracks that were 0.008 in and 0.01 in. wide on grid 1. On grid 2, there were no cracks as shown in Figure 0.239 (a).

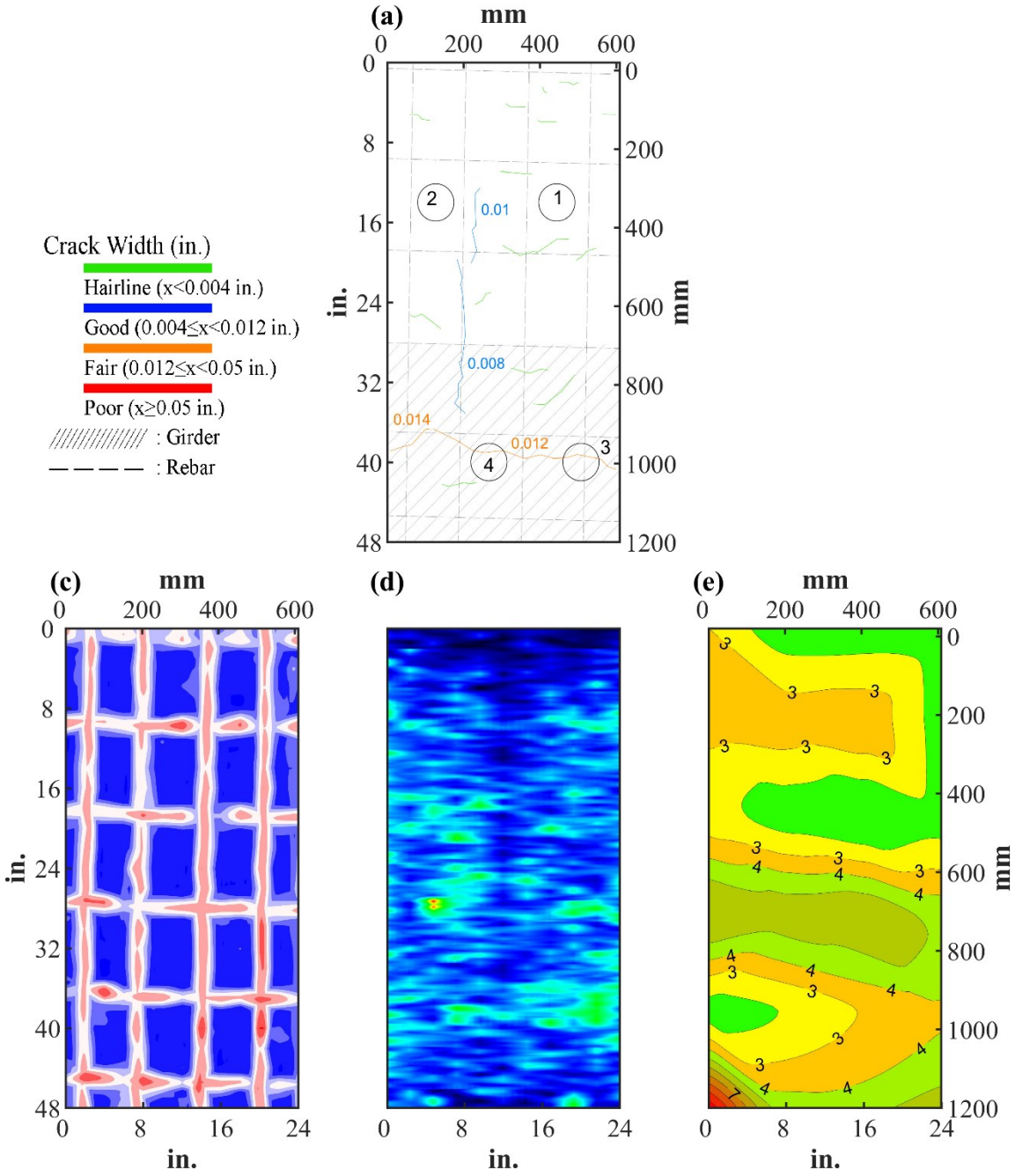

Figure 0.238. Crack Map and NDE Results of Grid 1: (a) Crack map and Location of Cores; (b) Infrared Picture; (c) GPR C-scan at 1.9 in. to 3.3 in. Depth; (d) UST C-scan at 3.9 in. Depth; (e) Corrosion Rate Map

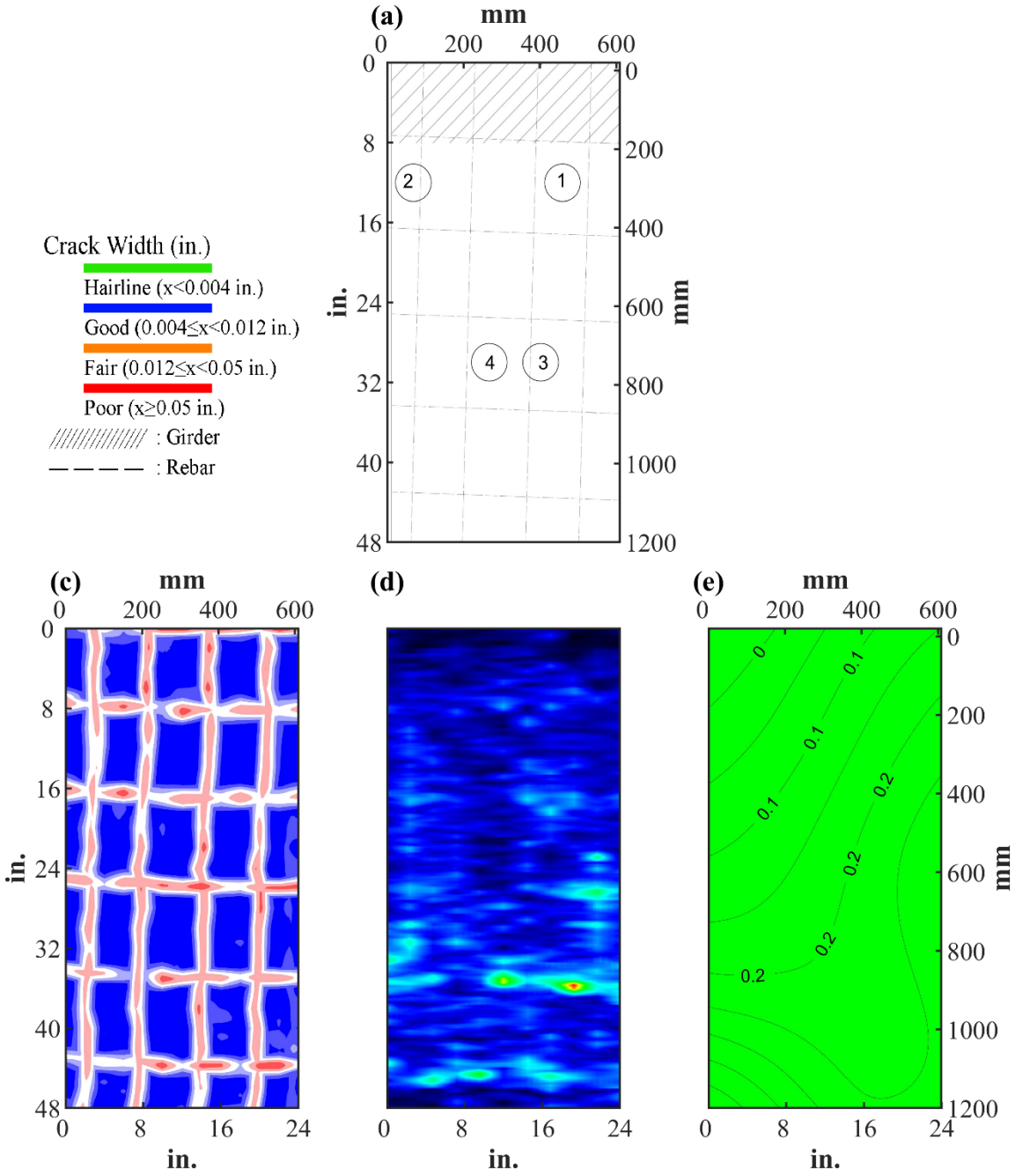

Figure 0.239. Crack Map and NDE Results of Grid 2: (a) Crack map and Location of Cores; (b) Infrared Picture; (c) GPR C-scan at 1.9 in. to 3.3 in. Depth; (d) UST C-scan at 4.1 in. Depth; (e) Corrosion Rate Map

B.33.3 Concrete Cores

Table B-120. Detail Information of concrete cores

Core	dia. x height (in.)	Rebar depth (in.)	Rebar size (#)	Epoxy (Y/N)	Crack type	Crack width (in)	Notes
1-1	3.75 x 6.8	0.0			-	-	-
1-2	3.75 x 7.2	6.5	4	Y	-	-	-
1-3	3.75 x 6.4	2.2	5	Y	longitudinal	0.012	-
1-4	3.75 x 7.1	6.4	5	Y	longitudinal	0.012	-
2-1	3.75 x 6.1	6.1	5	Y	-	-	-
2-2	3.75 x 6.1	2.6, 6.1	5,5	Y,Y	-	-	-
2-3	3.75 x 6.8	2.6, 6.7	5,5	Y,Y	-	-	-
2-4	3.75 x 3.7	1.4,3.5,4,2	5	Y	-	-	-

Table B-121. Core Pictures

Core	Pictures of the Cores		
1-1			
1-2			

1-3			
1-4			
2-1			
2-2			

2-3			

B.33.4 Laboratory Experiment Results

B.33.4.1 Resistivity

Core Number	Surface Resistivity (kΩ·m)	Bulk Resistivity (kΩ·m)
1-1	58.0	15.7

B.33.4.2 Ultrasonic Pulse Velocity

Core Number	Ultrasonic Pulse Velocity (m/s)
1-1	4282

B.33.4.3 Carbonation Depth

Core Number	Carbonation Depth (in.)
2-1	0.50

B.33.4.4 Acid-Soluble Chloride Content

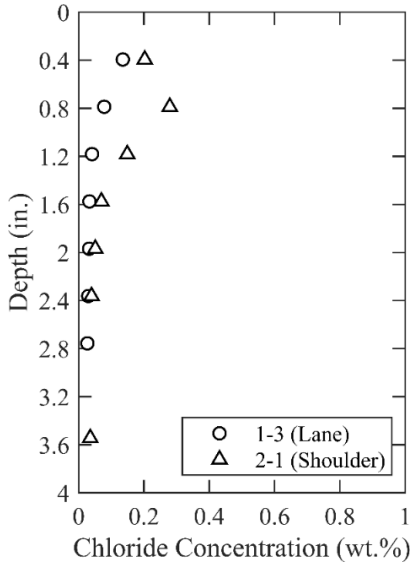

Figure 0.240. Chloride Content at Different Depth

B.33.4.5 Sorptivity

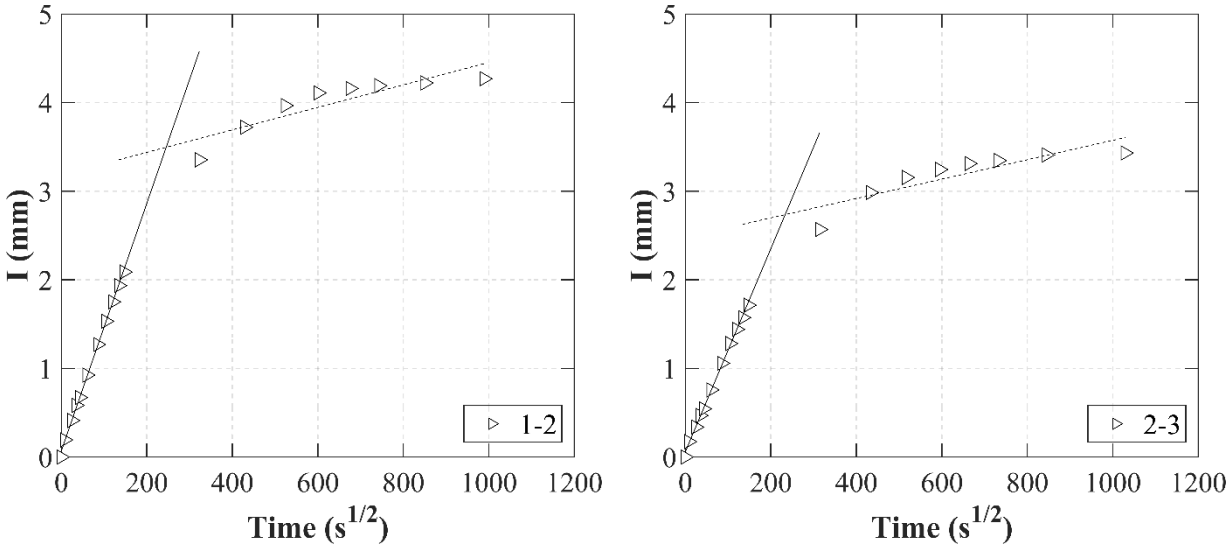

(a) Core 1–2 (b) Core 2–3

Figure 0.241. Absorption and Sorptivity of: (a) Core 1–2; (b) Core 2–3

Table B-122. Initial and Secondary Sorptivity Results

Core Number	Sorptivity	Results (mm/s$^{1/2}$)
Core 1–2	Initial Sorptivity	0.0140
	Secondary Sorptivity	0.00127
Core 2–3	Initial Sorptivity	0.0115
	Secondary Sorptivity	0.00109

B.33.4.6 Knife Test

Core Number	Score	Picture
1-3	2	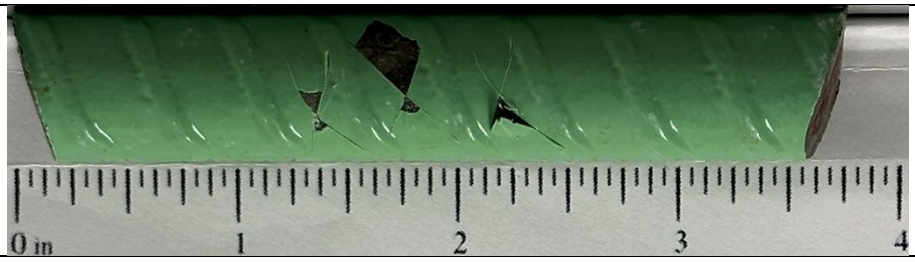

B.33.4.7 Electrochemical Impedance Spectroscopy

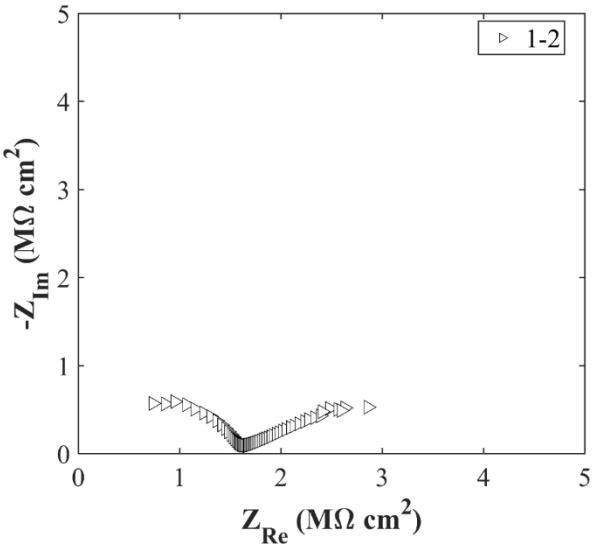

(a) Nyquist Diagram

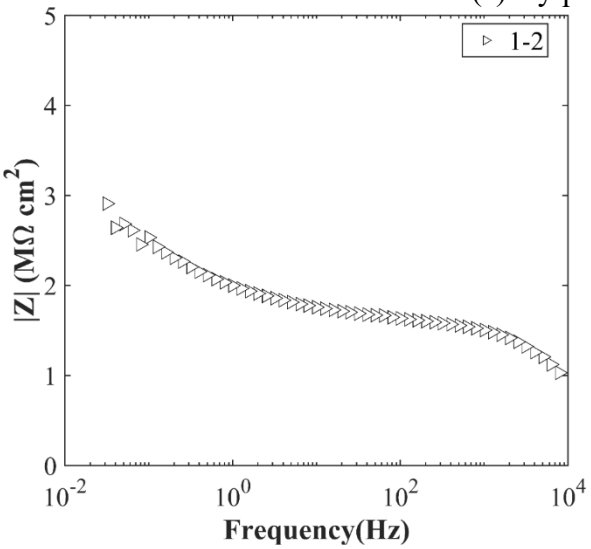

(b) Bode Plot of Impedance Modulus

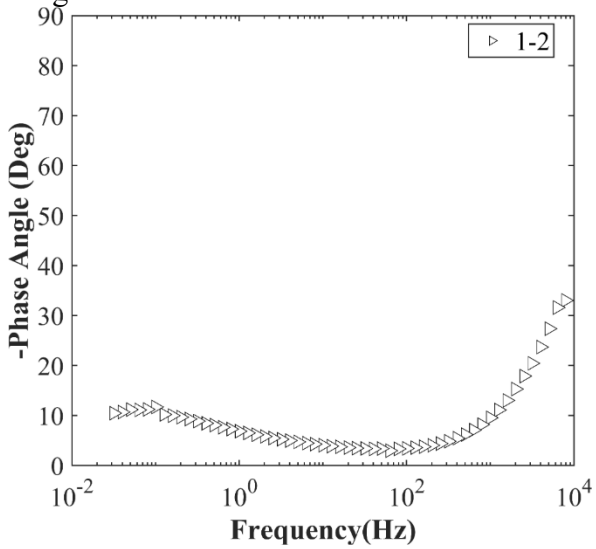

(c) Bode Plot of Impedance Phase

Figure 0.242. EIS Results: (a) Nyquist Diagram; (b) Bode Plot of Impedance Modulus; (c) Bode Plot of Impedance Phase

B.34 ELP-RC-08, HAAN RD. OVER AIRPORT RD.

- Bridge ID: 240720B00560004 (El Paso County)
- Built 2008
- Mitigation methods: Linseed oil, ECR
- Observed CIP depth: N/A
- Observed clear cover: 2.6 in.
- 2 spans, 7-concrete PS girder @ 6.792’ with 2.792’ overhangs
- Inspected on July 1, 2021

Figure 0.243. Concrete Deck of the Bridge

B.34.1 Observed Condition

There are transverse and longitudinal hairline cracks on the top surface of deck. Abutment joints are intact and in good condition. There are minor vertical cracks in the rail. The concrete railing at the west relief joint has moderate spalling. The north beam at west abutment has spalling due to the settlement of backwall.

B.34.2 NDE Results

Grid 1 was located on the NB lane of span 1, and grid 2 was located on the joint of NB lane span 1 and span 2 of the bridge.

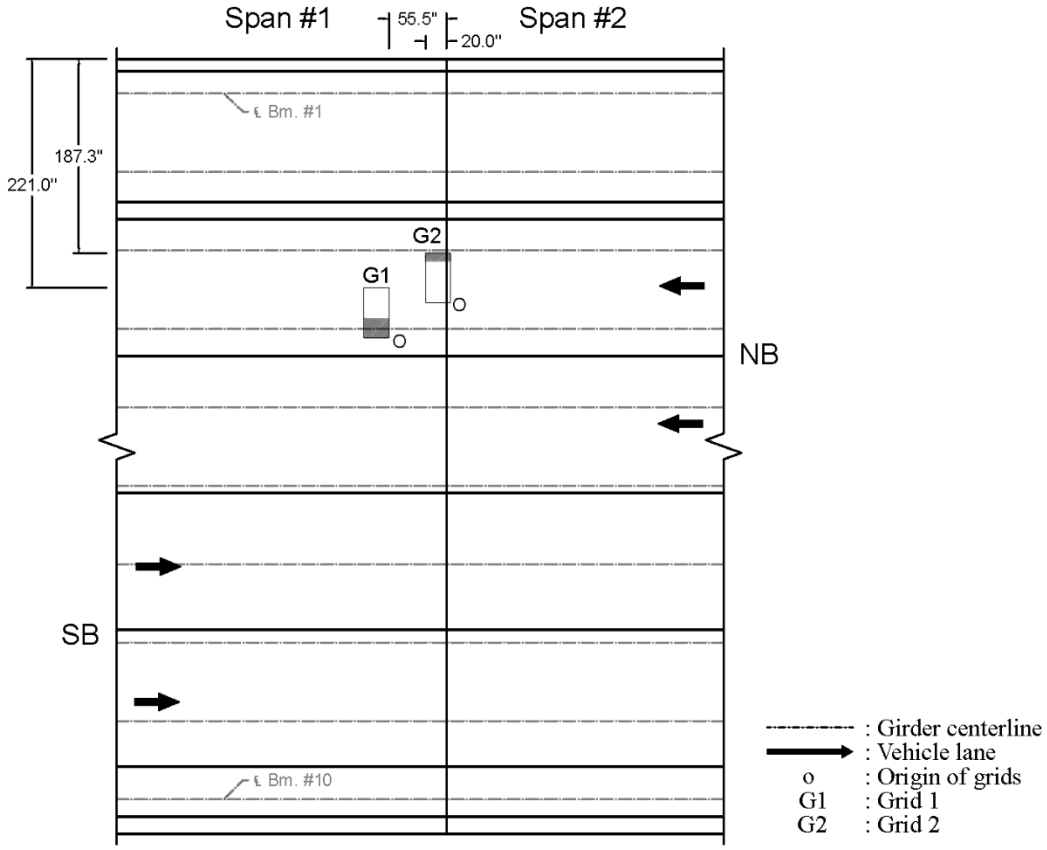

Figure 0.244. Plan View of the Bridge and Location of Grids

As shown in Figure 0.245 (a), 0.004 in. wide cracks were visible on grid 1. Grid 2 was located on the joint, and 0.004 in. and 0.006 in wide cracks were propagating from the joint. In addition, there was a short diagonal crack that was 0.012 wide as shown in Figure 0.246 (a).

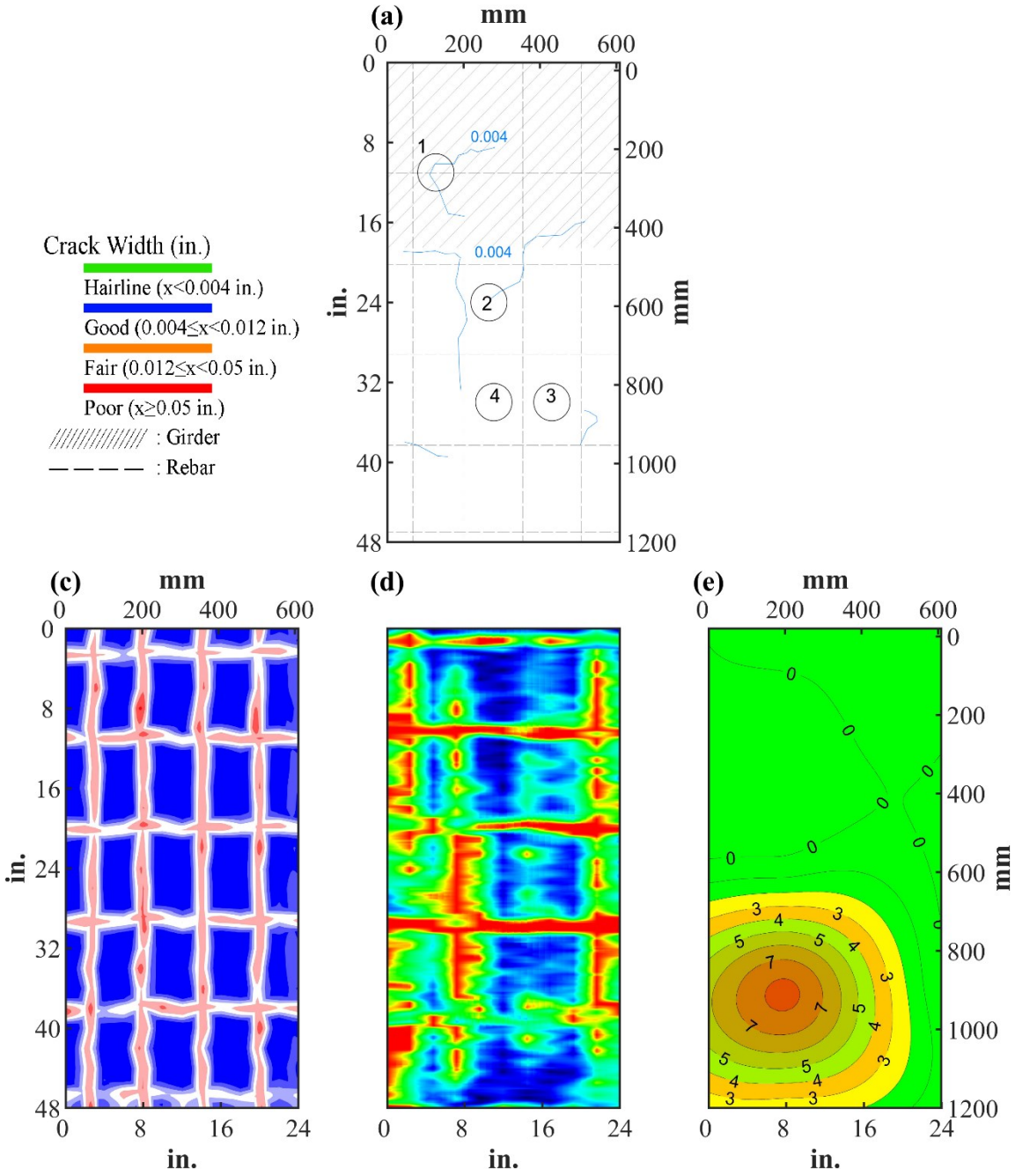

Figure 0.245. Crack Map and NDE Results of Grid 1: (a) Crack map and Location of Cores; (b) Infrared Picture; (c) GPR C-scan at 1.9 in. to 3.3 in. Depth; (d) UST C-scan at 3.5 in. Depth; (e) Corrosion Rate Map

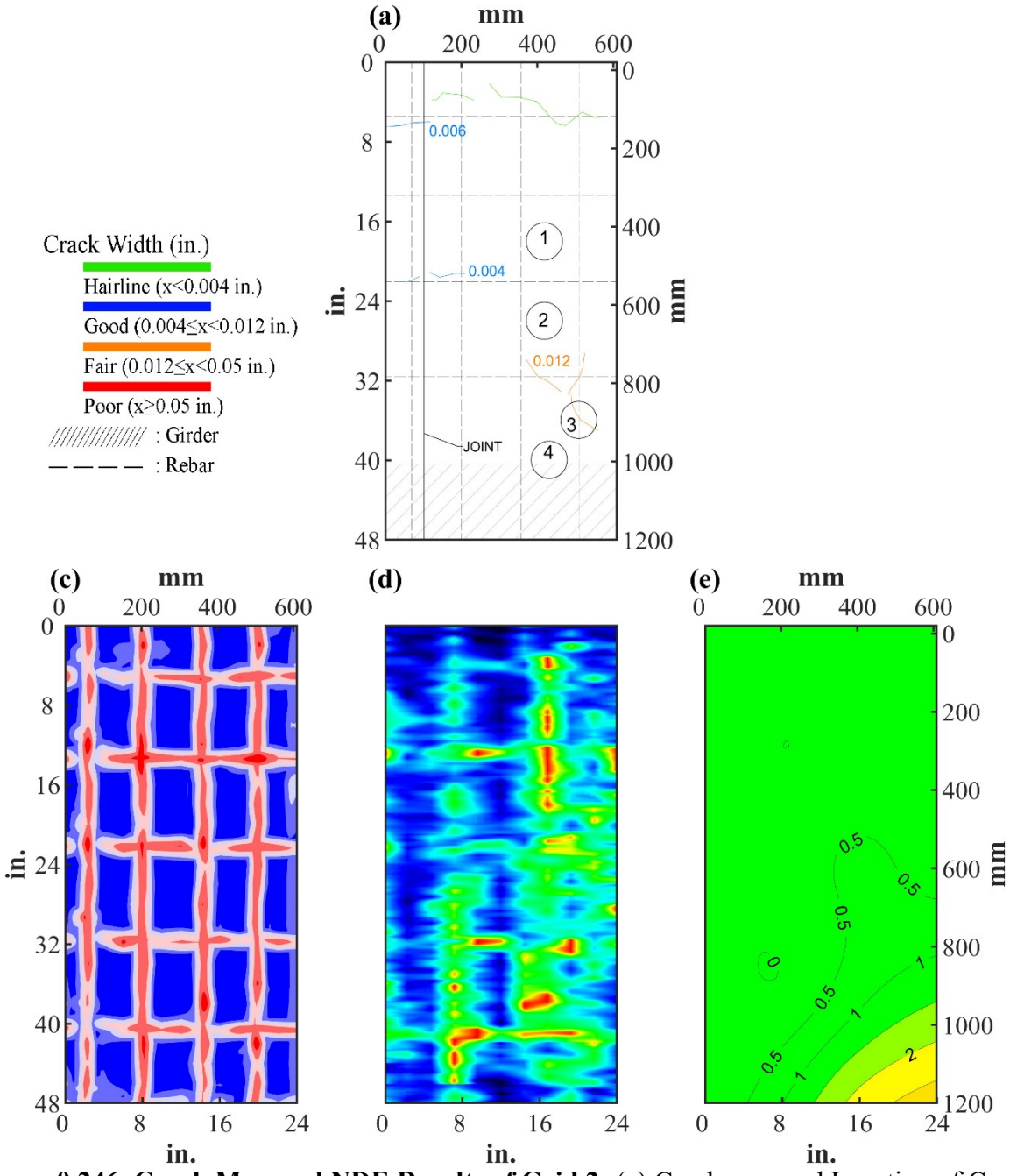

Figure 0.246. Crack Map and NDE Results of Grid 2: (a) Crack map and Location of Cores; (b) Infrared Picture; (c) GPR C-scan at 1.9 in. to 3.3 in. Depth; (d) UST C-scan at 4.0 in. Depth; (e) Corrosion Rate Map

B.34.3 Concrete Cores

Table B-123. Detail Information of concrete cores

Core	dia. x height (in.)	Rebar depth (in.)	Rebar size (#)	Epoxy (Y/N)	Crack type	Crack width (in)	Notes
1-1	3.75 x 6.9	3.1	4	Y	transverse	0.004	-
1-2	3.75 x 6.3	-	-	-	map	0.004	0.08 in. diagonal void at 8.5 in. depth
1-3	3.75 x 7.1	-	-	-	-	-	-
1-4	3.75 x 7.6	-	-	-	-	-	-
2-1	3.75 x 3.9	-	-	-	-	-	0.4 in. void at 4.7 in. depth
2-2	3.75 x 3.9	-	-	-			-
2-3	3.75 x 7.0	2.6	5	Y	diagonal	0.012	-
2-4	3.75 x 3.9	3.3	4	Y	-	-	-

Table B-124. Core Pictures

Core	Pictures of the Cores		
1-1			
1-2	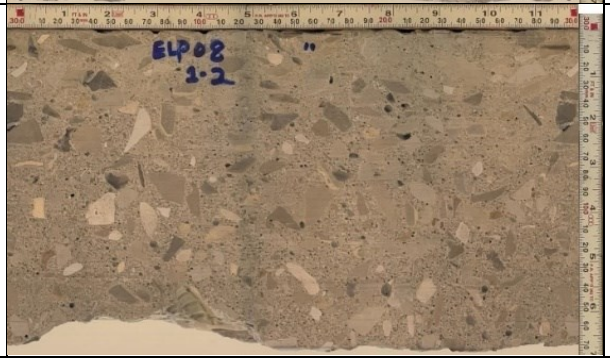		

1-3			
1-4	-	-	-
2-1			
2-2			
2-3			
2-4			

B.34.4 Laboratory Experiment Results

B.34.4.1 Resistivity

Core Number	Surface Resistivity (kΩ·m)	Bulk Resistivity (kΩ·m)
1-2	133.4	-
1-3	93.1	-
1-4	118.0	28.8

B.34.4.2 Ultrasonic Pulse Velocity

Core Number	Ultrasonic Pulse Velocity (m/s)
1-2	4324
1-3	4301
1-4	4558
2-2	3845

B.34.4.3 Carbonation Depth

Core Number	Carbonation Depth (in.)
1-2	0.00
2-1	0.35

B.34.4.4 Acid-Soluble Chloride Content

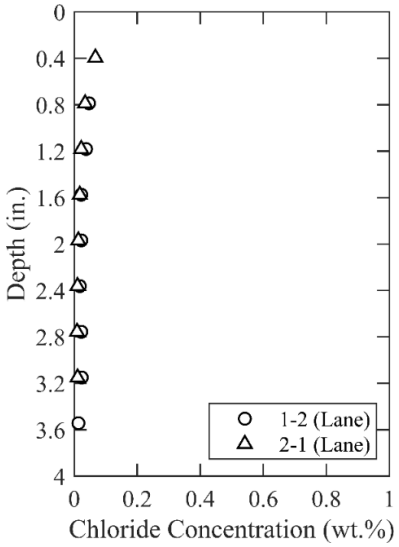

Figure 0.247. Chloride Content at Different Depth

B.34.4.5 Sorptivity

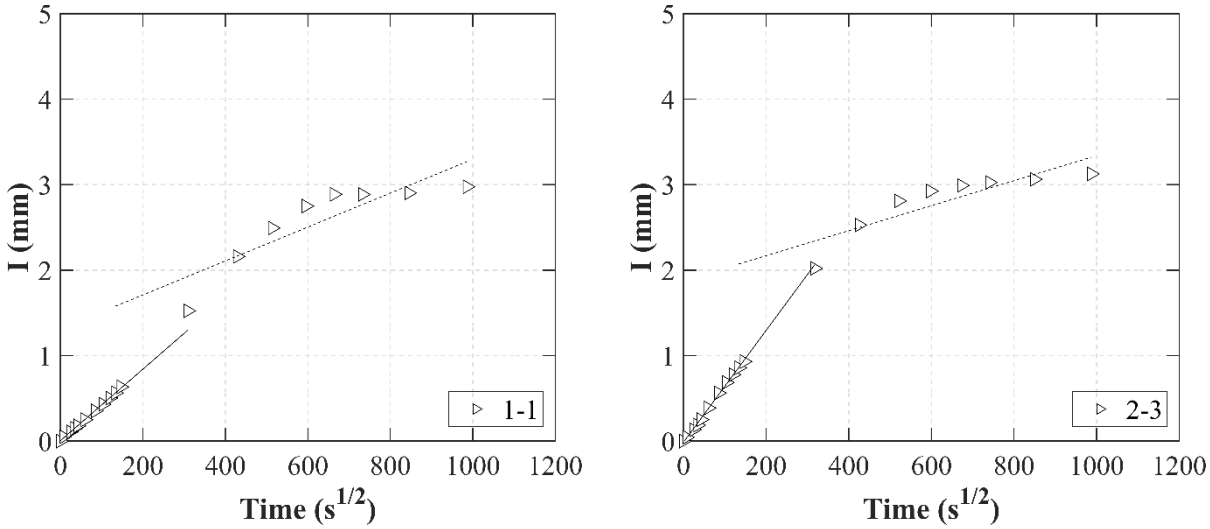

(a) Core 1–1 (b) Core 2–3

Figure 0.248. Absorption and Sorptivity of: (a) Core 1–1; (b) Core 2–3

Table B-125. Initial and Secondary Sorptivity Results

Core Number	Sorptivity	Results (mm/s$^{1/2}$)
Core 1–1	Initial Sorptivity	0.00419
	Secondary Sorptivity	0.00198
Core 2–3	Initial Sorptivity	0.00654
	Secondary Sorptivity	0.00146

B.34.4.6 Electrochemical Impedance Spectroscopy

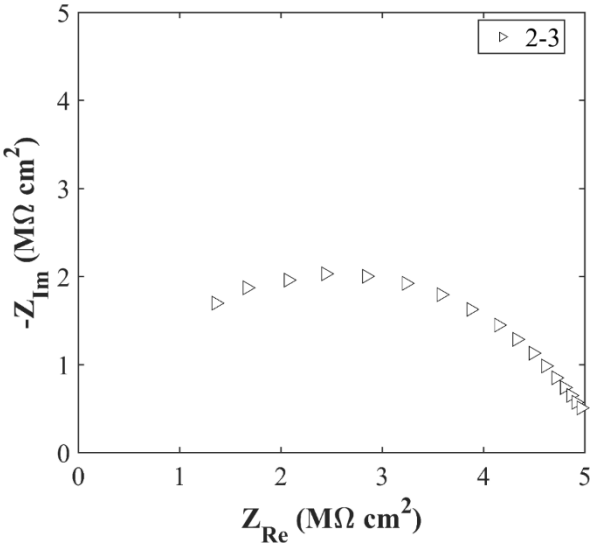

(a) Nyquist Diagram

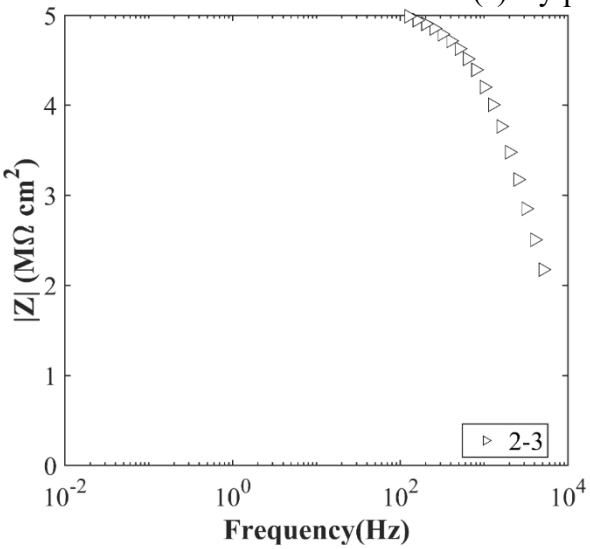

(b) Bode Plot of Impedance Modulus

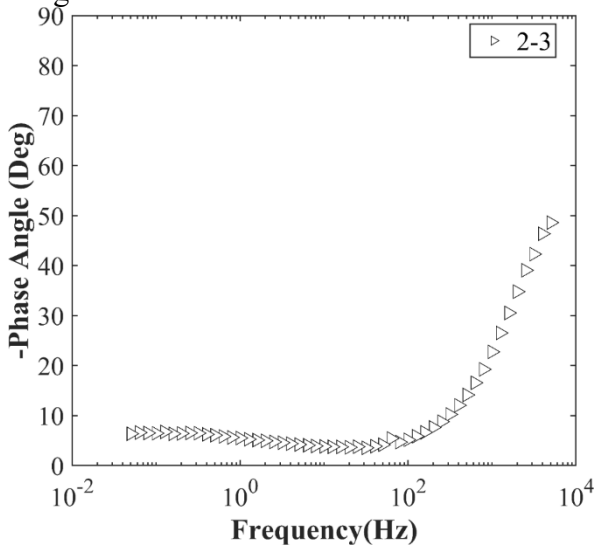

(c) Bode Plot of Impedance Phase

Figure 0.249. EIS Results: (a) Nyquist Diagram; (b) Bode Plot of Impedance Modulus; (c) Bode Plot of Impedance Phase

B.35 FTW-RC-01, BUS 377 OVER LAKE GRANBURY

- Bridge ID: 21120008010025 (Hood County)
- Built in 1992
- Mitigation methods: Linseed oil, ECR
- Observed CIP depth: 4.3 in.
- Observed clear cover: 2.6 in.
- 13 spans, 7-concrete PS girder @ 7.833’ with 3’ to 4’ overhangs
- Inspected on June 28, 2021

Figure 0.250. Concrete Deck of the Bridge (source: google maps)

B.35.1 Observed Condition

There are map pattern transverse hairline cracks on the top surface of deck. There are minor vertical cracks in the rail.

B.35.2 NDE Results

Both grid 1 and grid 2 were located on the EB lane of the bridge.

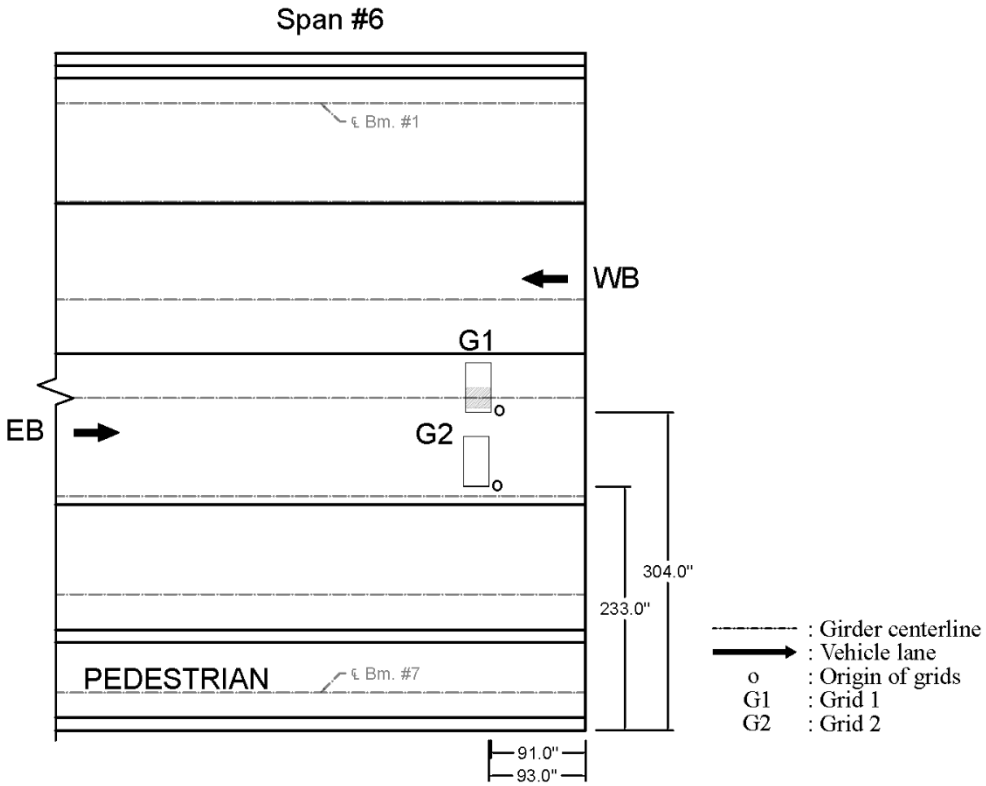

Figure 0.251. Plan View of the Bridge and Location of Grids

As shown in Figure 0.252 (a), there were two diagonal cracks that were 0.008 in. wide and one transverse crack that ranged from 0.012 in. to 0.08 in. wide on grid 1. On grid 2, one 0.004 in. wide longitudinal crack and 0.012 in. wide transverse crack were visible as shown in Figure 0.253 (a).

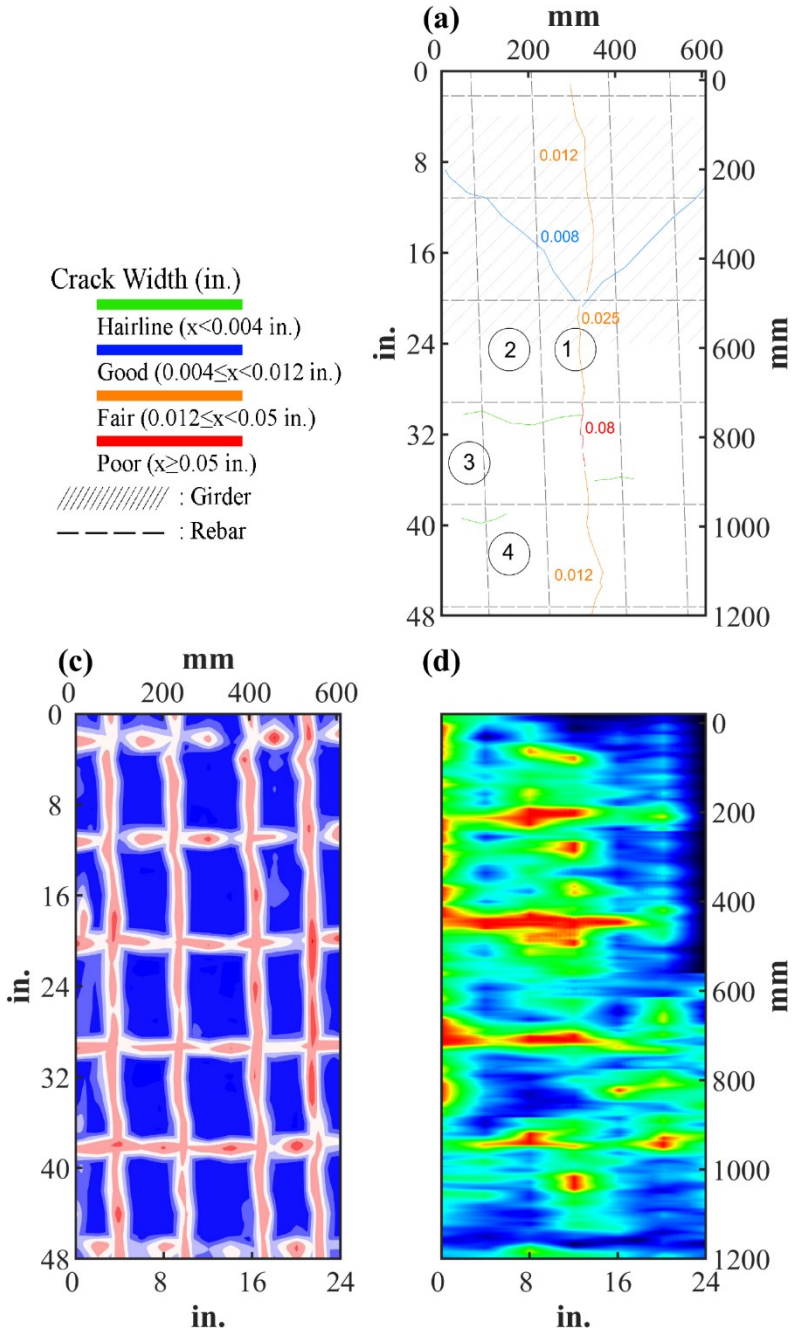

Figure 0.252. Crack Map and NDE Results of Grid 1: (a) Crack Map and Location of Cores; (c) GPR C-scan at 2.0 in. to 3.2 in. Depth; (d) UST C-scan at 4.1 in. Depth

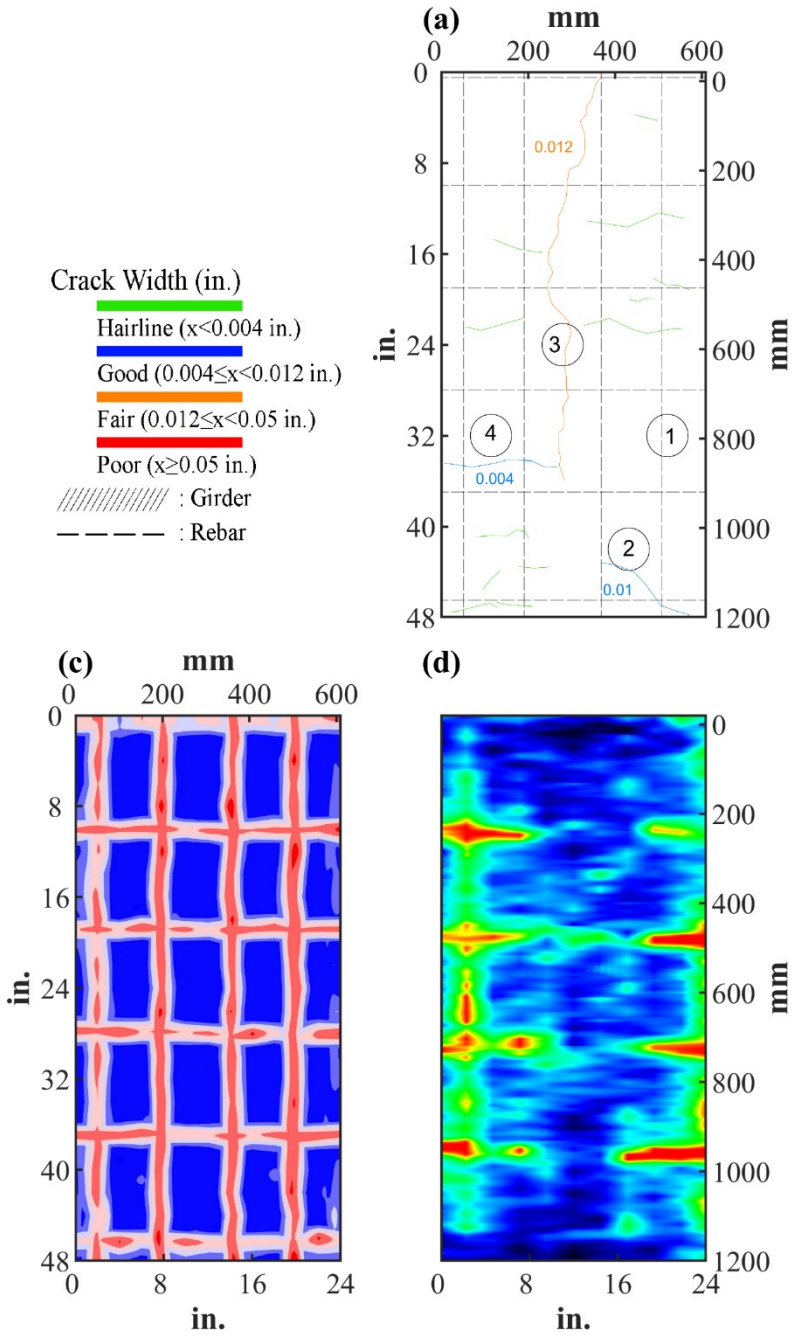

Figure 0.253. Crack Map and NDE Results of Grid 2: (a) Crack Map and Location of Cores; (c) GPR C-scan at 2.0 in. to 3.2 in. Depth; (d) UST C-scan at 4.4 in. Depth

B.35.3 Concrete Cores

Table B-126. Detail Information of concrete cores

Core	dia. x height (in.)	Rebar depth (in.)	Rebar size (#)	Epoxy (Y/N)	Crack type	Crack width (in)	Notes
1-1	3.75 x 4.5	-	-	-	transverse	0.025	Split core due to crack at intersection between column and PCP
1-2	3.75 x 5.5	-	-	-	-	-	-
1-3	3.75 x 4.7	2.6	1.7	Y	-	-	Delamination between CIP and PCP
1-4	3.75 x 5.9	-	-	-	-	-	-
2-1	3.75 x 5.3	2.6	1.7	Y	-	-	-
2-2	3.75 x 5.7	-	-	-	longitudinal	0.01	-
2-3	3.75 x 5.5	-	-	-	transverse	0.012	A crack propagates from panel joint
2-4	3.75 x 5.6	-	-	-	-	-	-

Table B-127. Core Pictures

Core	Pictures of the Cores		
1-1			
1-2			

1-3			
1-4			
2-1			
2-2			
2-3		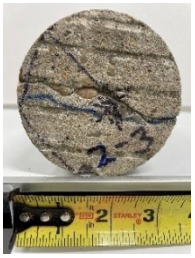	
2-4		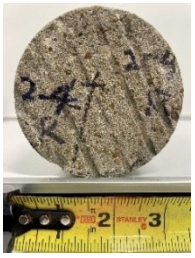	

B.35.4 Laboratory Experiment Results

B.35.4.1 Resistivity

Core Number	Surface Resistivity (kΩ·m)	Bulk Resistivity (kΩ·m)
1-2	33.7	6.1
1-4	29.7	-
2-2	32.8	-
2-3	47.0	-
2-4	28.1	6.1

B.35.4.2 Ultrasonic Pulse Velocity

Core Number	Ultrasonic Pulse Velocity (m/s)
1-2	4102
1-4	4078
2-2	4368
2-3	4142
2-4	4239

B.35.4.3 Carbonation Depth

Core Number	Carbonation Depth (in.)
1-1	0.00
2-3	0.00

B.35.4.4 Acid-Soluble Chloride Content

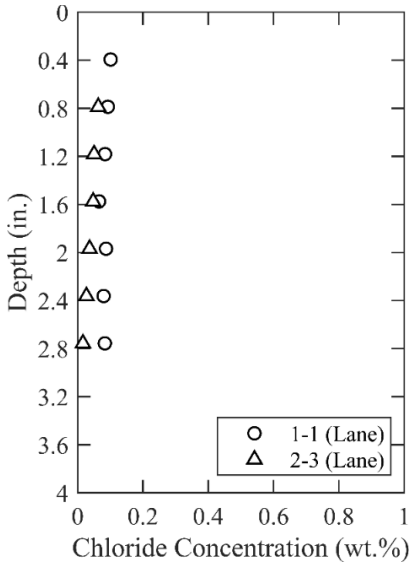

Figure 0.254. Chloride Content at Different Depth

B.35.4.5 Sorptivity

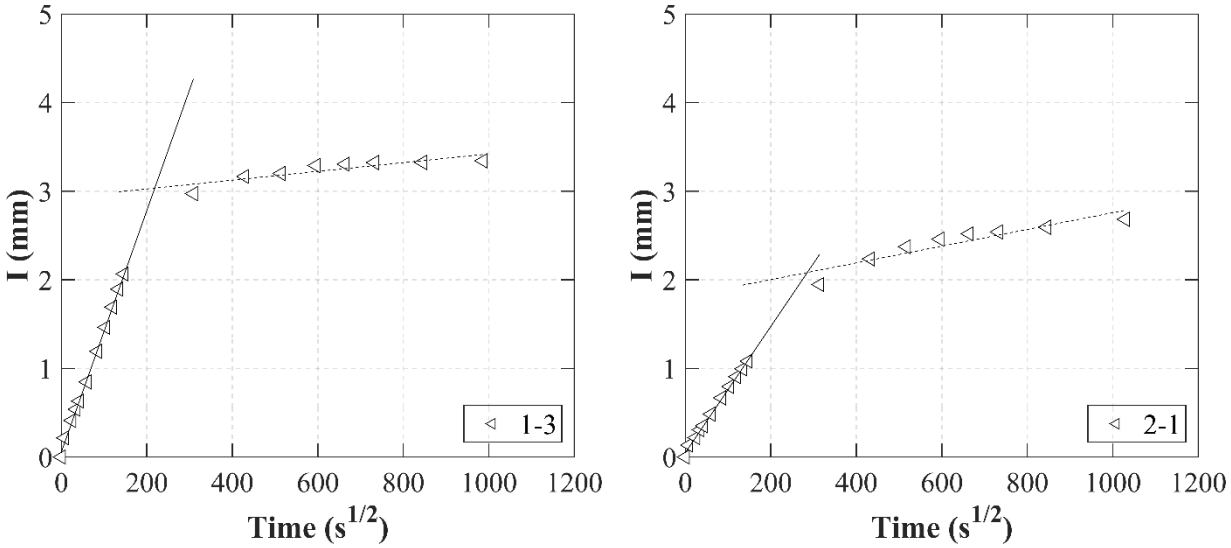

(a) Core 1–3 (b) Core 2–1

Figure 0.255. Absorption and Sorptivity of: (a) Core 1–3; (b) Core 2–1

Table B-128. Initial and Secondary Sorptivity Results

Core Number	Sorptivity	Results (mm/s$^{1/2}$)
Core 1–3	Initial Sorptivity	0.0136
	Secondary Sorptivity	0.00049
Core 2–1	Initial Sorptivity	0.00713
	Secondary Sorptivity	0.00094

B.35.4.6 Knife Test

Core Number	Score	Picture
2-1	10	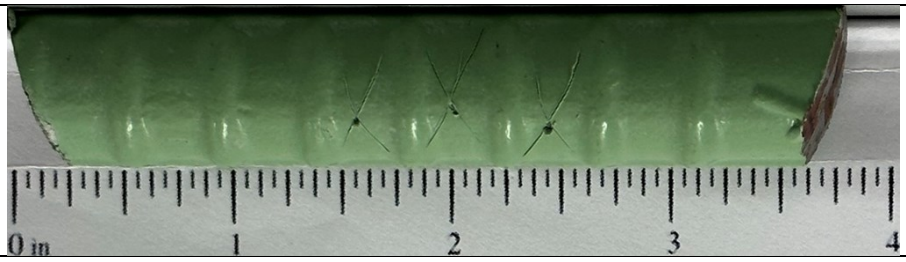

B.35.4.7 Electrochemical Impedance Spectroscopy

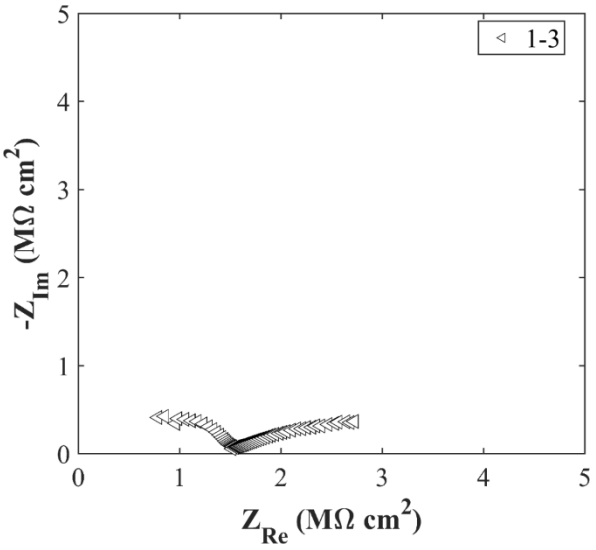

(a) Nyquist Diagram

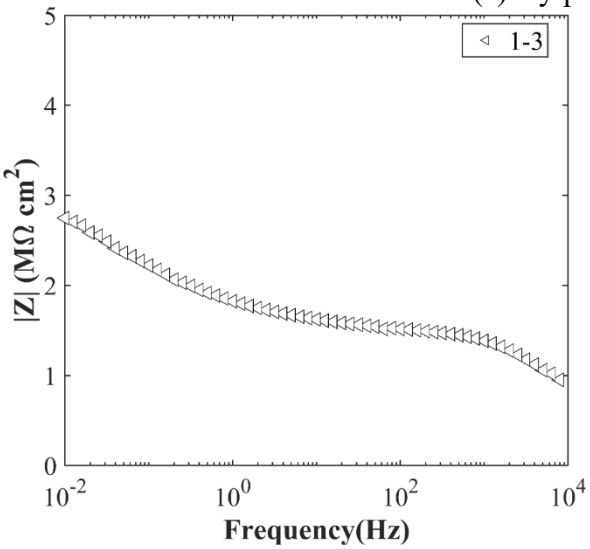

(b) Bode Plot of Impedance Modulus

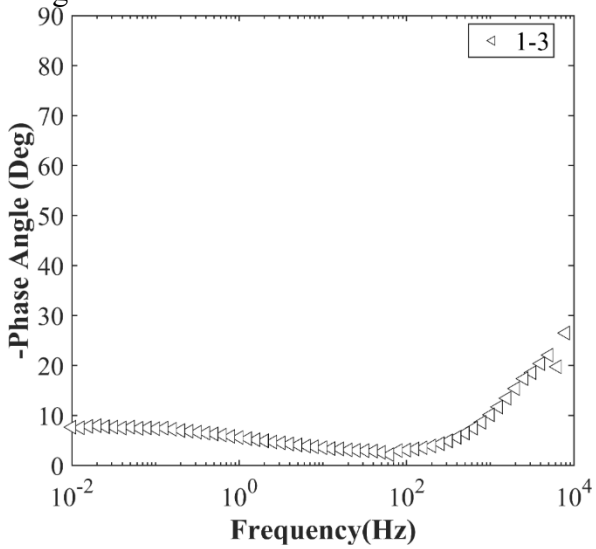

(c) Bode Plot of Impedance Phase

Figure 0.256. EIS Results: (a) Nyquist Diagram; (b) Bode Plot of Impedance Modulus; (c) Bode Plot of Impedance Phase

B.36 FTW-RC-02 US, 67 OVER PALUXY RIVER

- Bridge ID: 22130025902021 (Somervell County)
- Built in 2005
- Mitigation methods: Silane, ECR
- Observed CIP depth: 5.0 in.
- Observed clear cover: 2.6 in.
- Inspected on June 16, 2021

Figure 0.257. Concrete Deck of the Bridge (source: google maps)

B.36.1 Observed Condition

There are cracks on the top surface of deck. The deck overhang has minor cracks with efflorescence. Damage to the edge of joints results in leakage as shown in Figure 0.258 (a). The concrete railing is in good condition. There is 0.08 in. crack at the back wall of abutment as shown in Figure 0.258 (b).

(a)

(b)

Figure 0.258. Deteriorations on the Bridge: (a) Leakage at Joint; (b) Moderate Crack at Abutment

B.36.2 NDE Results

Both grid 1 and grid 2 were located on the NB lane of the bridge.

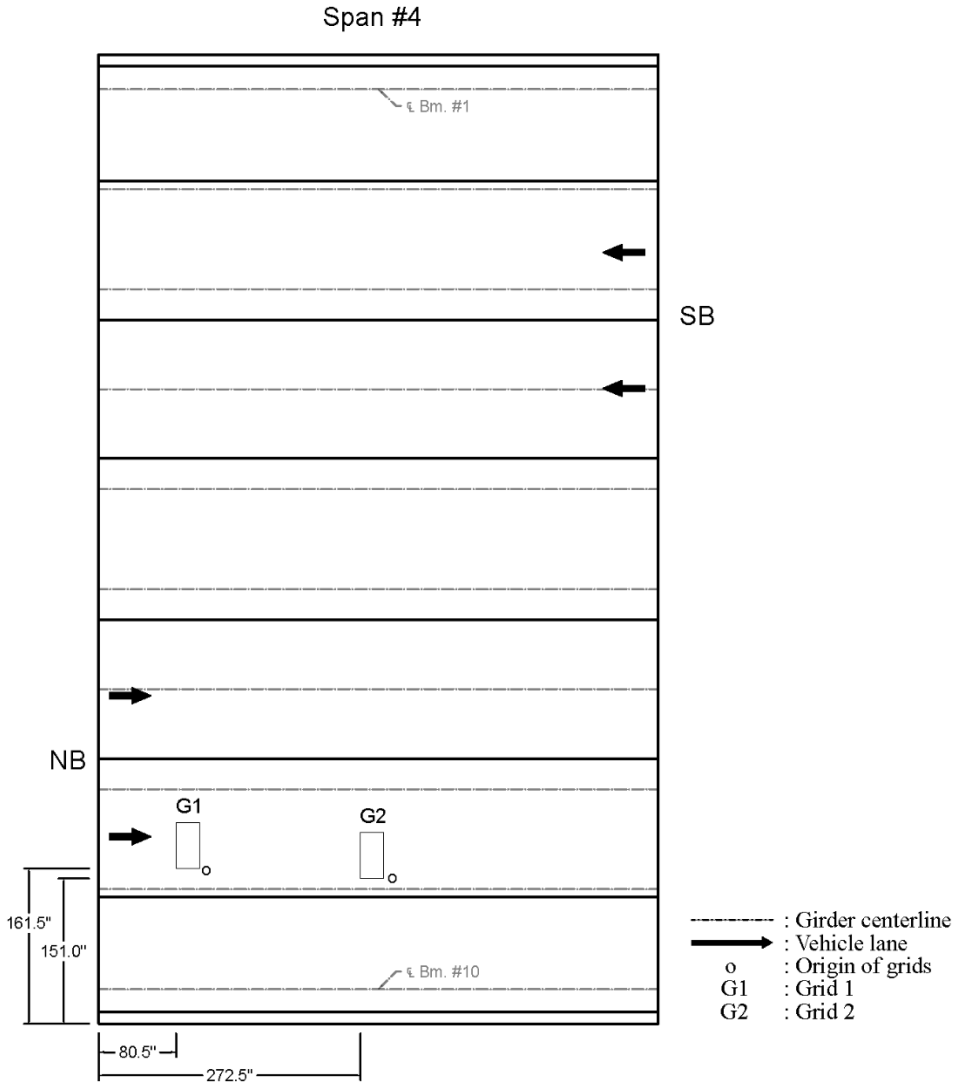

Figure 0.259. Plan View of the Bridge and Location of Grids

As shown in Figure 0.260 (a), there were cracks ranging from 0.008 in to 0.025 in. wide on grid 1. On grid 2, there were transverse cracks that were 0.004 in. and .008 in. wide as shown in Figure 0.261 (a).

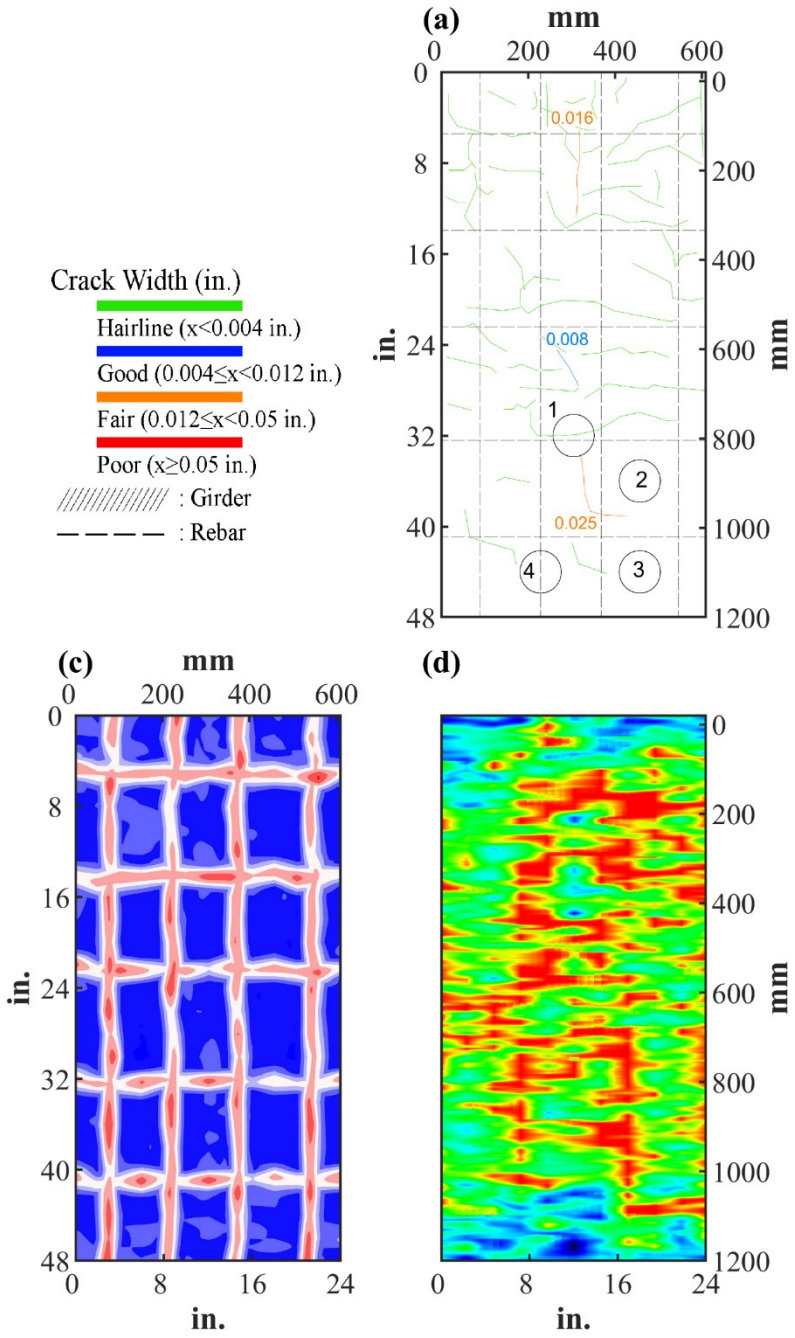

Figure 0.260. Crack Map and NDE Results of Grid 1: (a) Crack Map and Location of Cores; (c) GPR C-scan at 3.1 in. to 4.7 in. Depth; (d) UST C-scan at 3.1 in. Depth

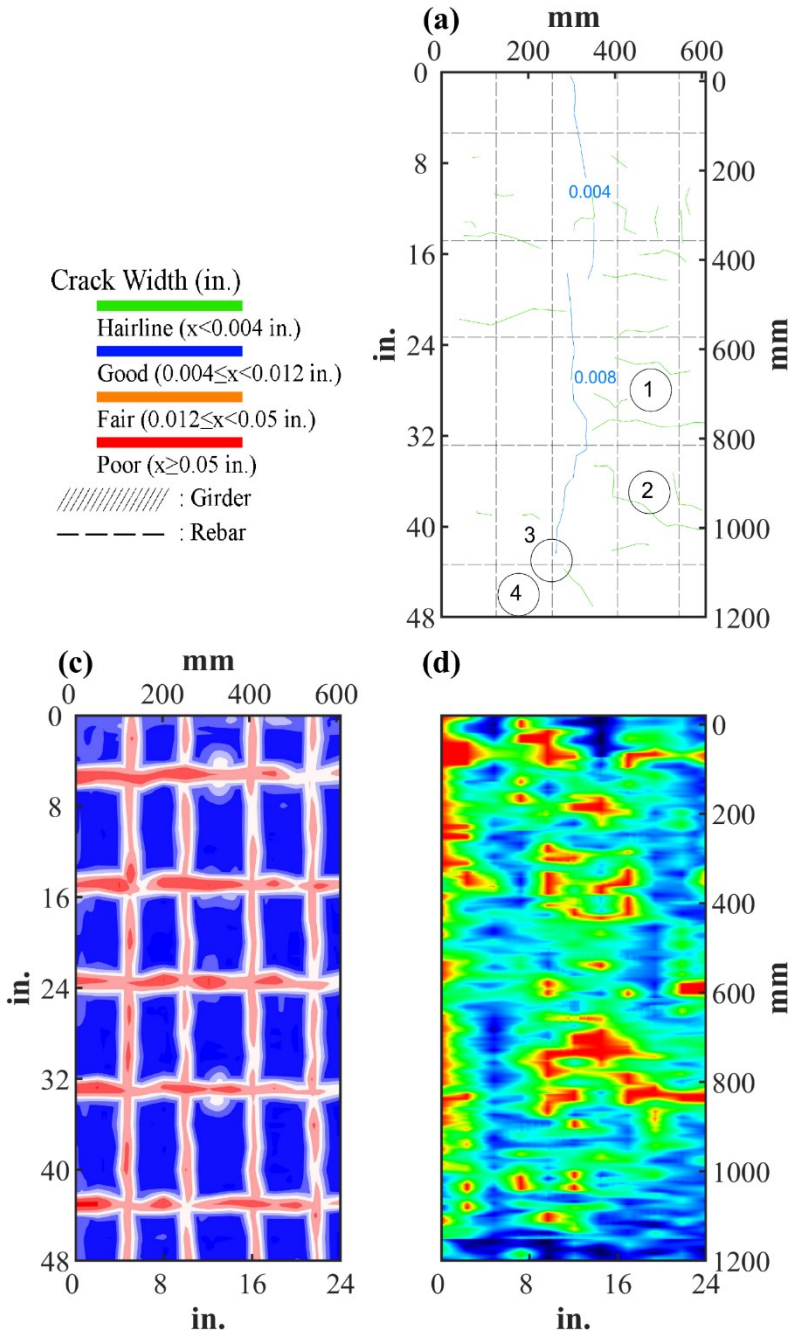

Figure 0.261. Crack Map and NDE Results of Grid 2: (a) Crack Map and Location of Cores; (c) GPR C-scan at 1.8 in. to 3.4 in. Depth; (d) UST C-scan at 4.0 in. Depth

B.36.3 Concrete Cores

Table B-129. Detail Information of concrete cores

Core	dia. x height (in.)	Rebar depth (in.)	Rebar size (#)	Epoxy (Y/N)	Crack type	Crack width (in)	Notes
1-1	3.75 x 5.5	4.1	4	Y	transverse	0.025	Delamination between CIP and PCP
1-2	3.75 x 5.5	-	-	-	-	-	Delamination between CIP and PCP
1-3	3.75 x 5.5	-	-	-	-	-	Delamination between CIP and PCP
1-4	3.75 x 5.2	3.6	5	Y	-	-	Delamination between CIP and PCP
2-1	3.75 x 4.7	-	-	-	-	-	Delamination between CIP and PCP
2-2	3.75 x 4.5	-	-	-	longitudinal	HL	Delamination between CIP and PCP
2-3	3.75 x 5.0	2.6; 3.3	5; 4	Y; Y	transverse	0.008	Delamination between CIP and PCP
2-4	3.75 x 5.0	-	-	-	-	-	Delamination between CIP and PCP

Table B-130. Core Pictures

Core	Pictures of the Cores		
1-1			
1-2		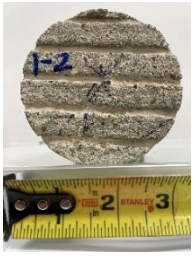	

1-3			
1-4			
2-1			
2-2			
2-3			
2-4		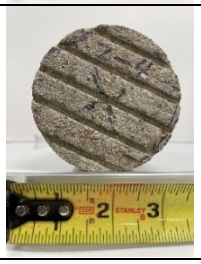	

B.36.4 Laboratory Experiment Results

B.36.4.1 Resistivity

Core Number	Surface Resistivity (kΩ·m)	Bulk Resistivity (kΩ·m)
1-2	86.7	18.0
1-3	81.2	-
2-1	-	11.8
2-2	65.5	-
2-4	71.0	-

B.36.4.2 Ultrasonic Pulse Velocity

Core Number	Ultrasonic Pulse Velocity (m/s)
1-2	4446
1-3	4316
2-1	4350
2-2	3386
2-4	4429

B.36.4.3 Carbonation Depth

Core Number	Carbonation Depth (in.)
1-1	0.00
2-3	0.00

B.36.4.4 Acid-Soluble Chloride Content

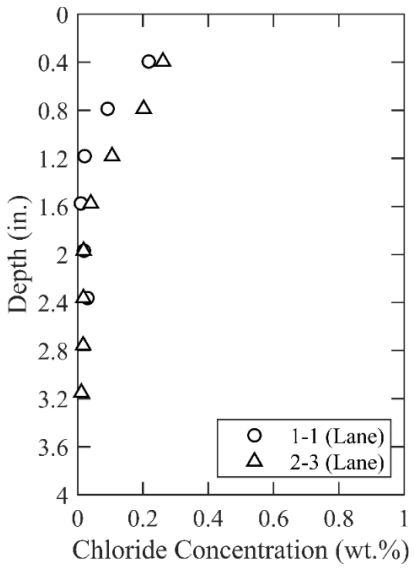

Figure 0.262. Chloride Content at Different Depth

B.36.4.5 Sorptivity

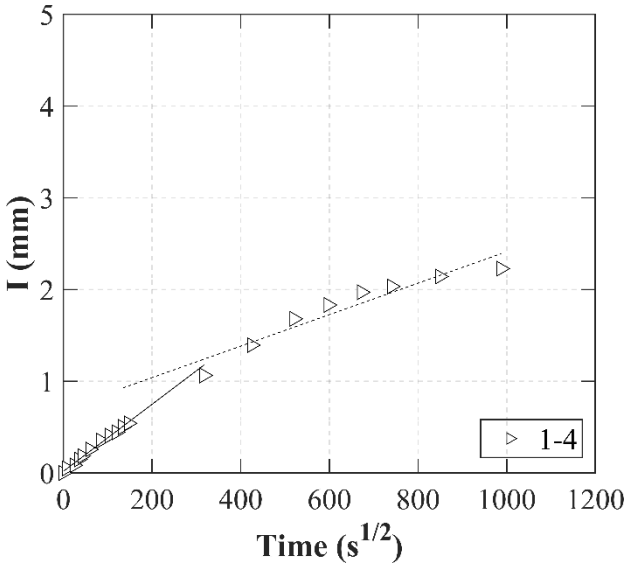

Figure 0.263. Absorption and Sorptivity of Core 1–4

Table B-131. Initial and Secondary Sorptivity Results

Core Number	Sorptivity	Results ($mm/s^{1/2}$)
Core 2–1	Initial Sorptivity	0.00365
	Secondary Sorptivity	0.00172

B.36.4.6 Knife Test

Core Number	Score	Picture
2-3	10	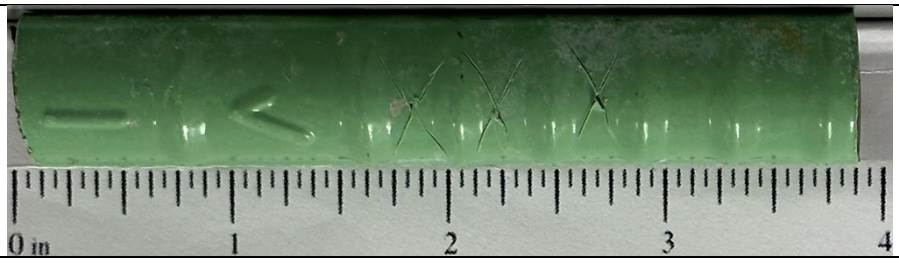

B.36.4.7 Electrochemical Impedance Spectroscopy

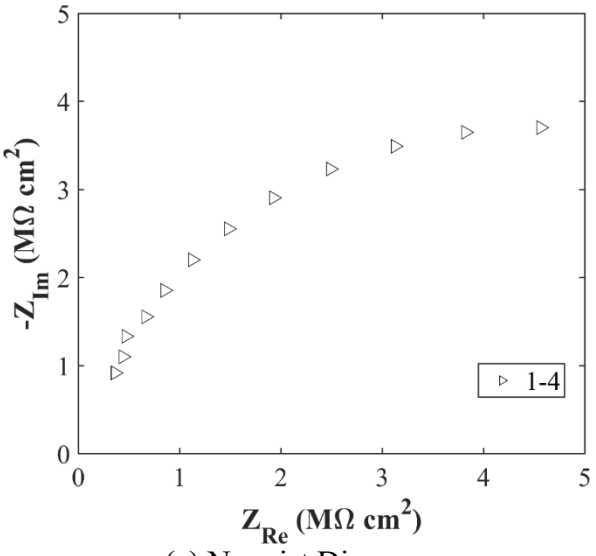

(a) Nyquist Diagram

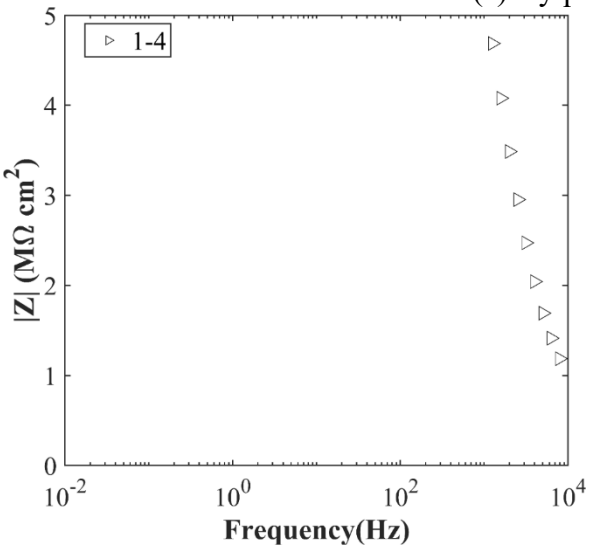

(b) Bode Plot of Impedance Modulus

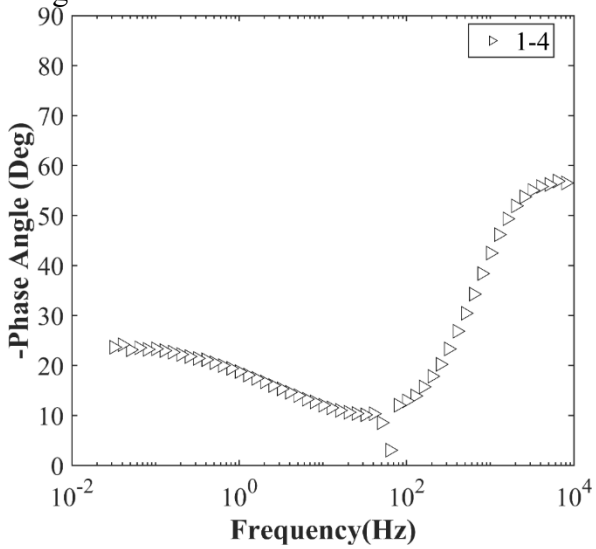

(c) Bode Plot of Impedance Phase

Figure 0.264. EIS Results: (a) Nyquist Diagram; (b) Bode Plot of Impedance Modulus; (c) Bode Plot of Impedance Phase

B.37 FTW-RC-03, IH 20 OVER HARTMAN RD.

- Bridge ID: 22200000813343 (Tarrant County)
- Built 1988
- Mitigation methods: Linseed oil, ECR
- Observed CIP depth: N/A
- Observed clear cover: 1.8 in.
- 3 spans, 32-concrete PS girder @ 5.167’ with 3’ overhangs
- Inspected on June 28, 2021

Figure 0.265. Concrete Deck of the Bridge (source: google maps)

B.37.1 Observed Condition

There are spalling on the top surface of deck. The concrete railing near southwest corner has severe cracking and minor spalling. Abutment back wall has serious corrosion and 0.15 in. crack as shown in Figure 0.266.

Figure 0.266. Corrosion near Bearing Pad

B.37.2 NDE Results

Grid 1 was located on the EB lane and grid 2 was located on the EB shoulder lane of the span 3 of the bridge.

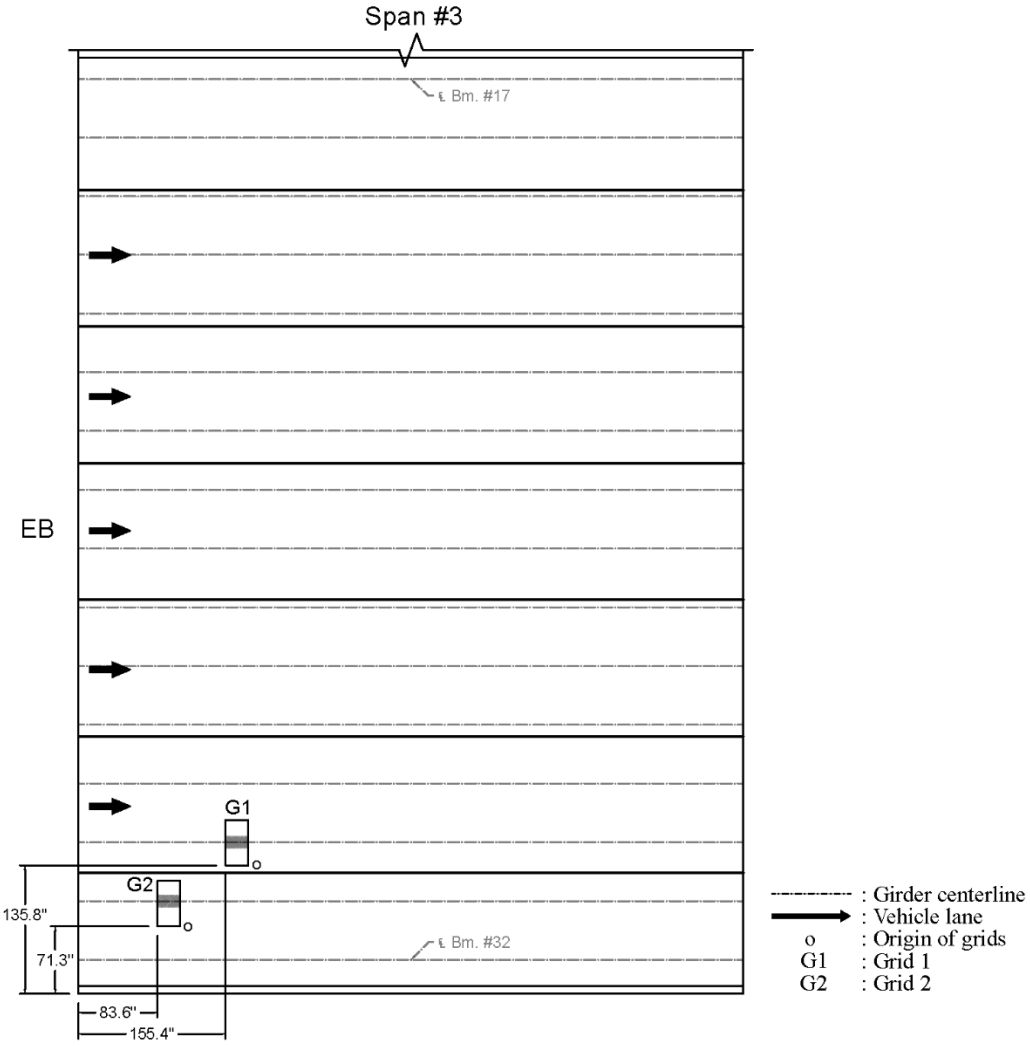

Figure 0.267. Plan View of the Bridge and Location of Grids

As shown in Figure 0.268 (a), longitudinal racks ranging from 0.004 in. to 0.008 in. were located on top of a girder and 0.012 in. wide longitudinal crack was about 8 in. away from a girder on grid 1. On grid 2, there were no cracks as shown in Figure 0.269 (a).

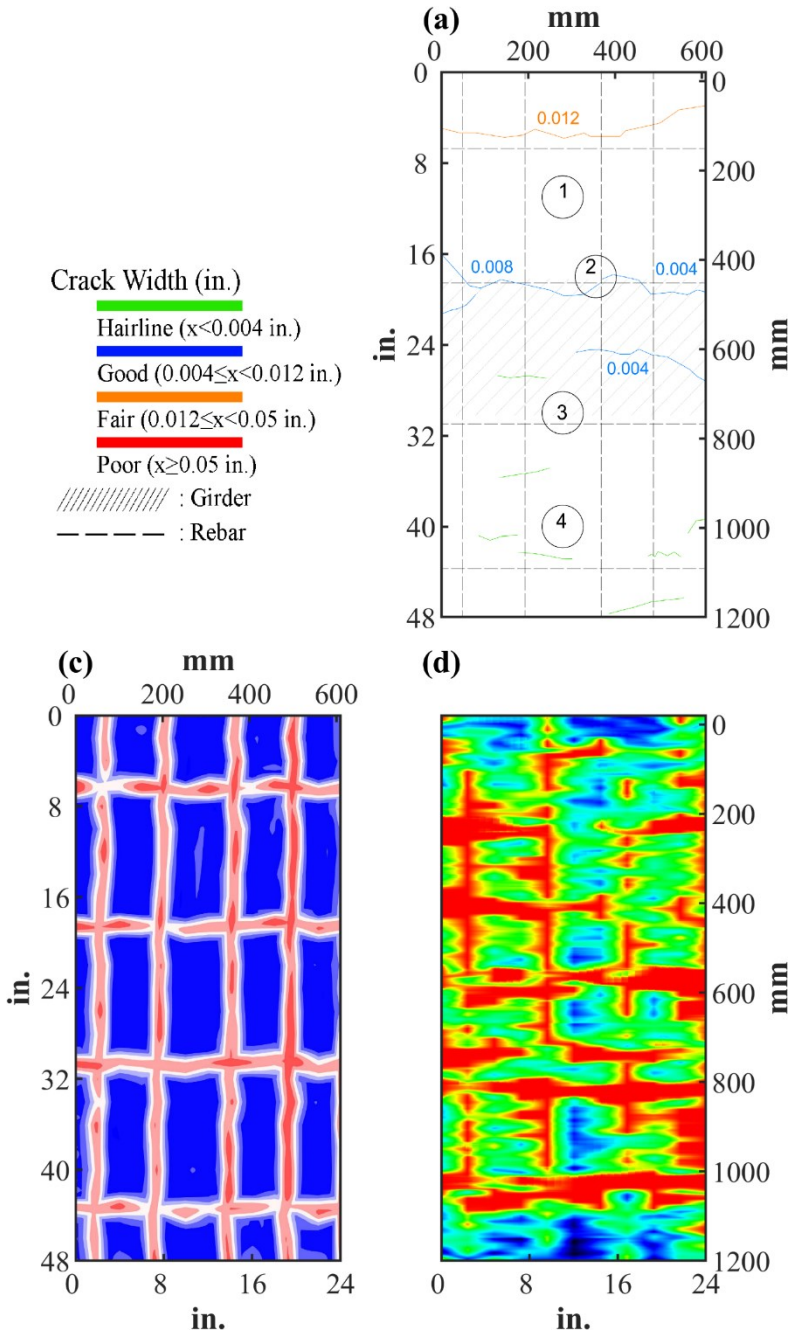

Figure 0.268. Crack Map and NDE Results of Grid 1: (a) Crack Map and Location of Cores; (c) GPR C-scan at 1.9 in. to 3.3 in. Depth; (d) UST C-scan at 4.0 in. Depth

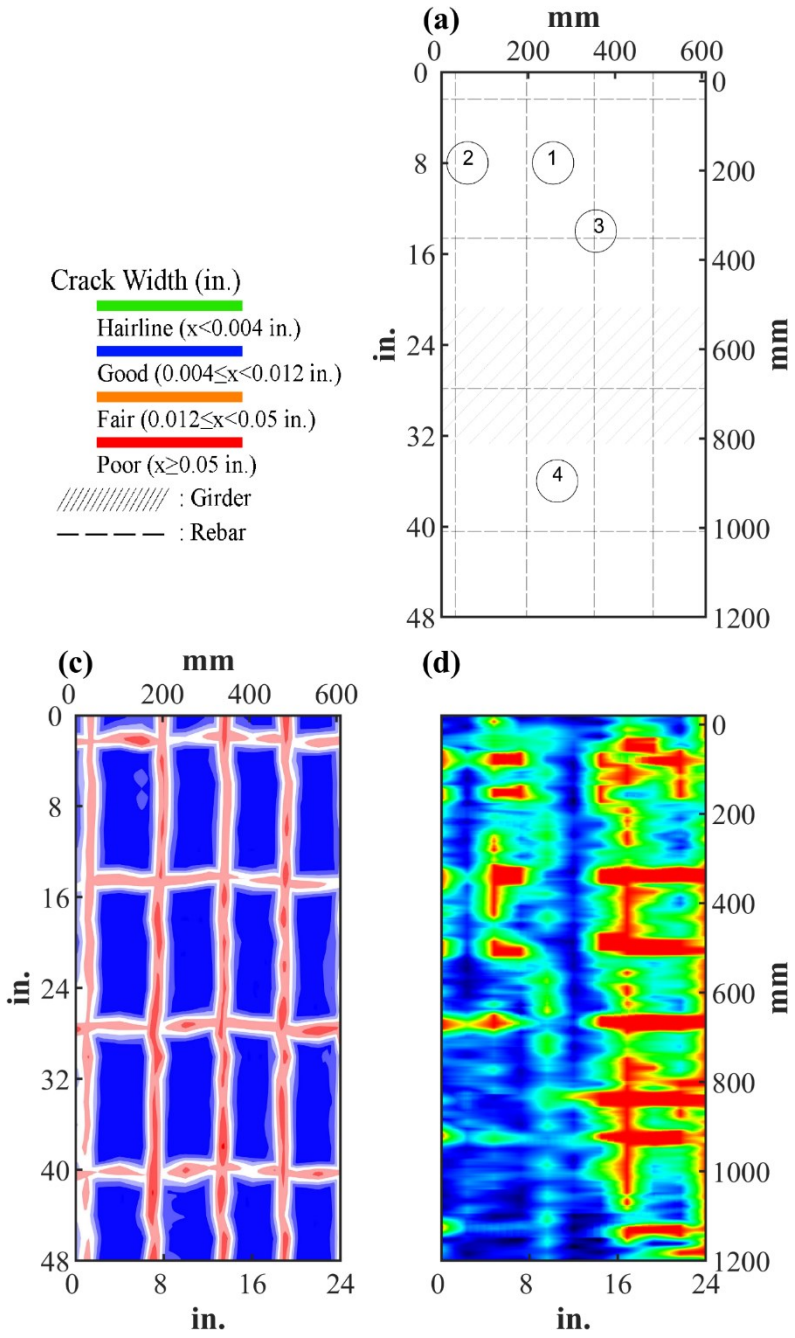

Figure 0.269. Crack Map and NDE Results of Grid 2: (a) Crack Map and Location of Cores; (c) GPR C-scan at 1.25 in. to 3.3 in. Depth; (d) UST C-scan at 3.5 in. Depth

B.37.3 Concrete Cores

Table B-132. Detail Information of concrete cores

Core	dia. x height (in.)	clear cover (in.)	Rebar size (#)	Epoxy (Y/N)	Crack type	Crack width (in)	Notes
1-1	3.75 x 5.2	-	-	-	-	-	-
1-2	3.75 x 6.3	2.0; 2.6; 5.1	5; 5; 5	Y; Y; Y			A void near rebar
1-3	3.75 x 4.5	2.6	5	Y	map	0.004	A void near rebar
1-4	3.75 x 5.3	-	-	-	-	-	-
2-1	3.75 x 5.9	5.1	5	Y			A void at 3.7 in. depth
2-2	3.75 x 5.5	-	-	-	-	-	-
2-3	3.75 x 6.1	1.8; 2.6; 5.1	5; 5; 5	Y; Y; Y	-	-	-
2-4	3.75 x 6.1	0.0	-	-	-	-	-

Table B-133. Core Pictures

Core	Pictures of the Cores		
1-1			
1-2			

1-3			
1-4		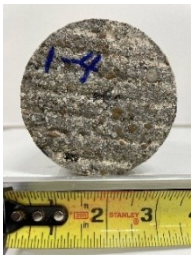	
2-1			
2-2		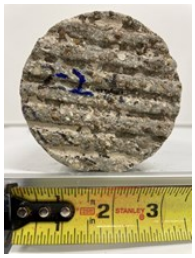	
2-3			
2-4			

B.37.4 Laboratory Experiment Results

B.37.4.1 Resistivity

Core Number	Surface Resistivity (kΩ·m)	Bulk Resistivity (kΩ·m)
1-1	40.0	-
1-4	24.3	6.5
2-2	39.7	-
2-4	40.5	10.6

B.37.4.2 Ultrasonic Pulse Velocity

Core Number	Ultrasonic Pulse Velocity (m/s)
1-1	4291
1-4	4008
2-2	4137
2-4	4249

B.37.4.3 Carbonation Depth

Core Number	Carbonation Depth (in.)
1-2	0.00
2-3	0.00

B.37.4.4 Acid-Soluble Chloride Content

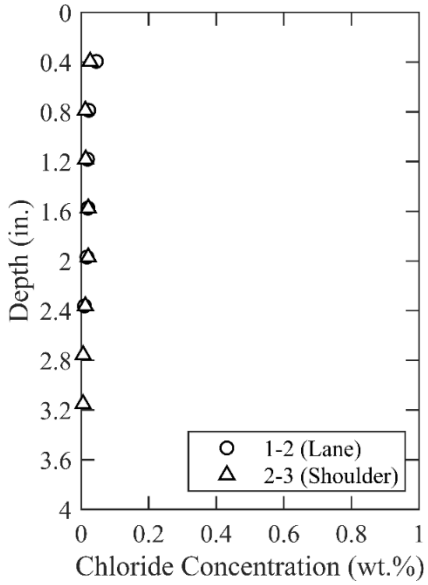

Figure 0.270. Chloride Content at Different Depth

B.37.4.5 Sorptivity

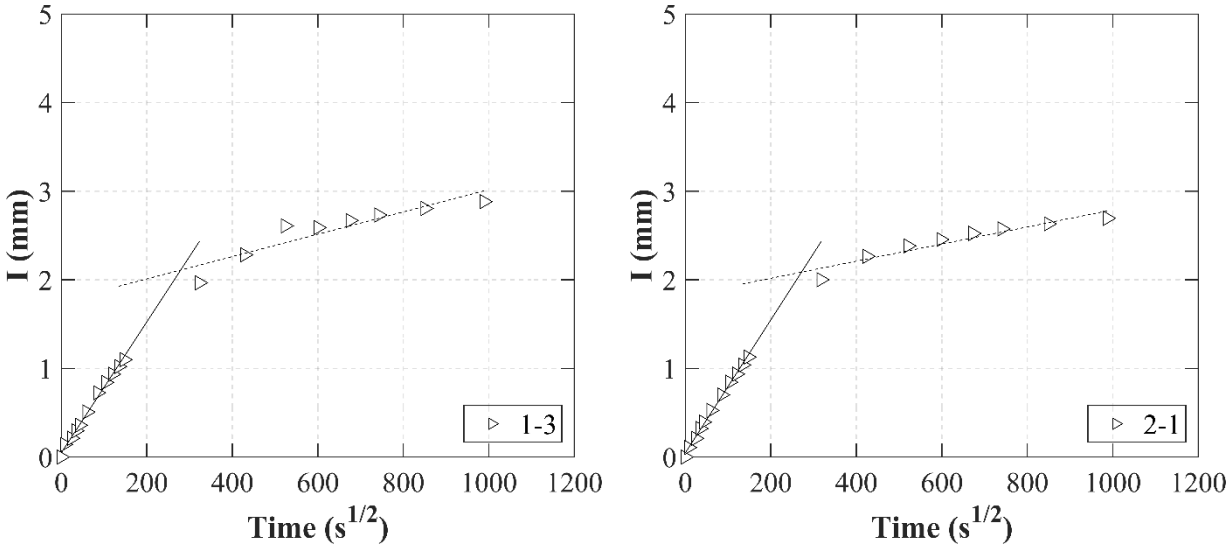

(a) Core 1–3 (b) Core 2–1

Figure 0.271. Absorption and Sorptivity of: (a) Core 1–3; (b) Core 2–1

Table B-134. Initial and Secondary Sorptivity Results

Core Number	Sorptivity	Results (mm/s$^{1/2}$)
Core 1–3	Initial Sorptivity	0.00738
	Secondary Sorptivity	0.00126
Core 2–1	Initial Sorptivity	0.00751
	Secondary Sorptivity	0.00097

B.37.4.6 Knife Test

Core Number	Score	Picture
2-3	8	

B.38 FTW-RC-04, IH 820 SB OVER BRENTWOOD STAIR RD.

- Bridge ID: 22200000813438 (Tarrant County)
- Built in 1991
- Mitigation methods: Linseed oil, ECR
- Observed CIP depth: N/A
- Observed clear cover: 2.2 in.
- 3 spans, 20-concrete PS girder @ varying spacing with 3’ overhangs
- Inspected on June 28, 2021

Figure 0.272. Concrete Deck of the Bridge (source: google maps)

B.38.1 Observed Condition

The main superstructure members are in good condition; however, there is corrosion at the metal deck form as shown in Figure 0.273 (a). A horizontal crack is found at the abutment as shown in Figure 0.273 (b).

(a)

(b)

Figure 0.273. Deteriorations on the Bridge: (a) Corrosion at Metal Deck Form; (b) Serious Crack at Abutment

B.38.2 NDE Results

Both grid 1 were located on the SB lane of the span 2 of the bridge.

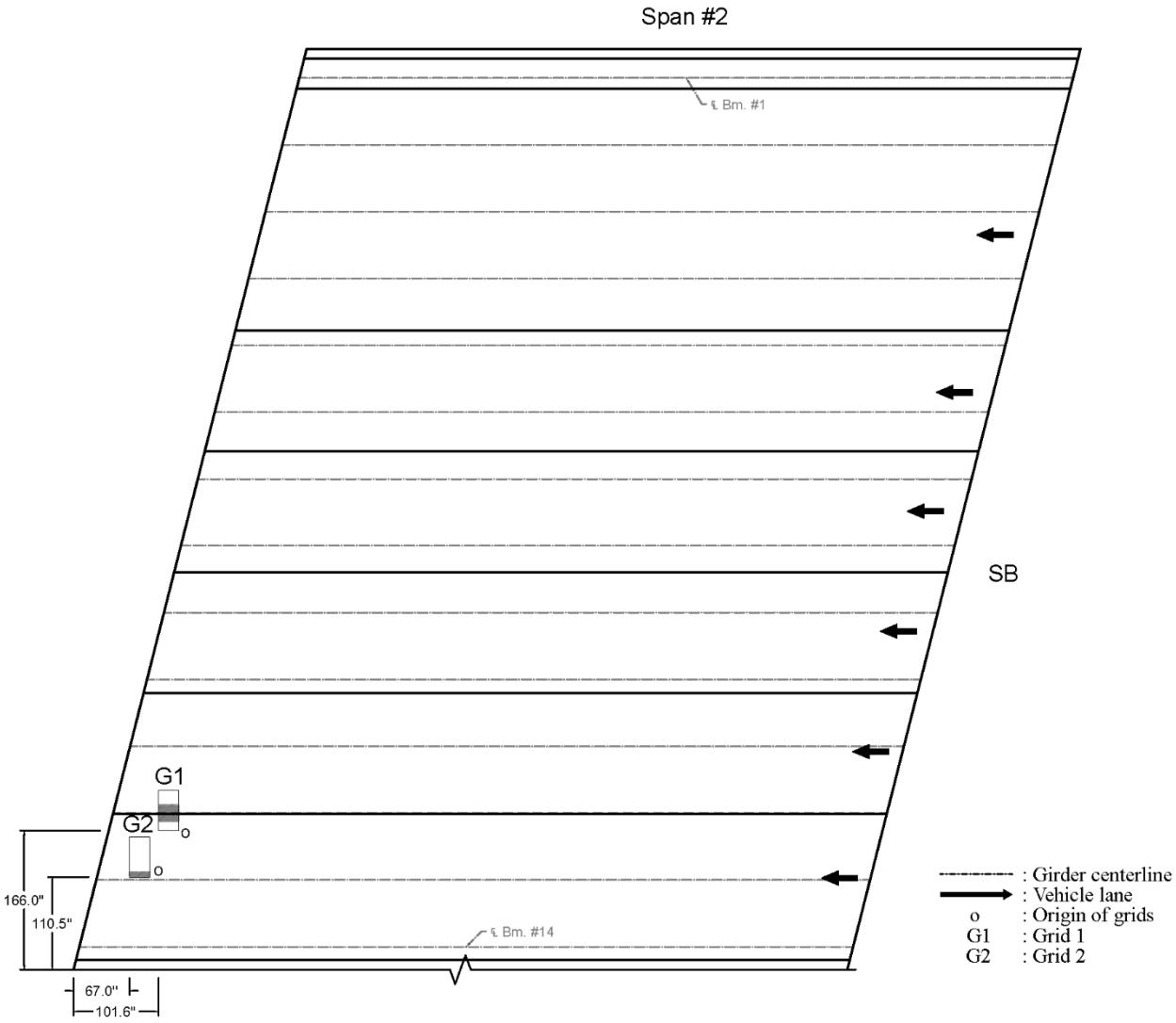

Figure 0.274. Plan View of the Bridge and Location of Grids

As shown in Figure 0.275 (a), there were widespread of hairline cracks and some cracks ranging from 0.004 in. to 0.008 in. wide were located on top of a girder on grid 1. On grid 2, some hairline cracks and 0.004 in. wide longitudinal cracks were visible as shown in Figure 0.276 (a).

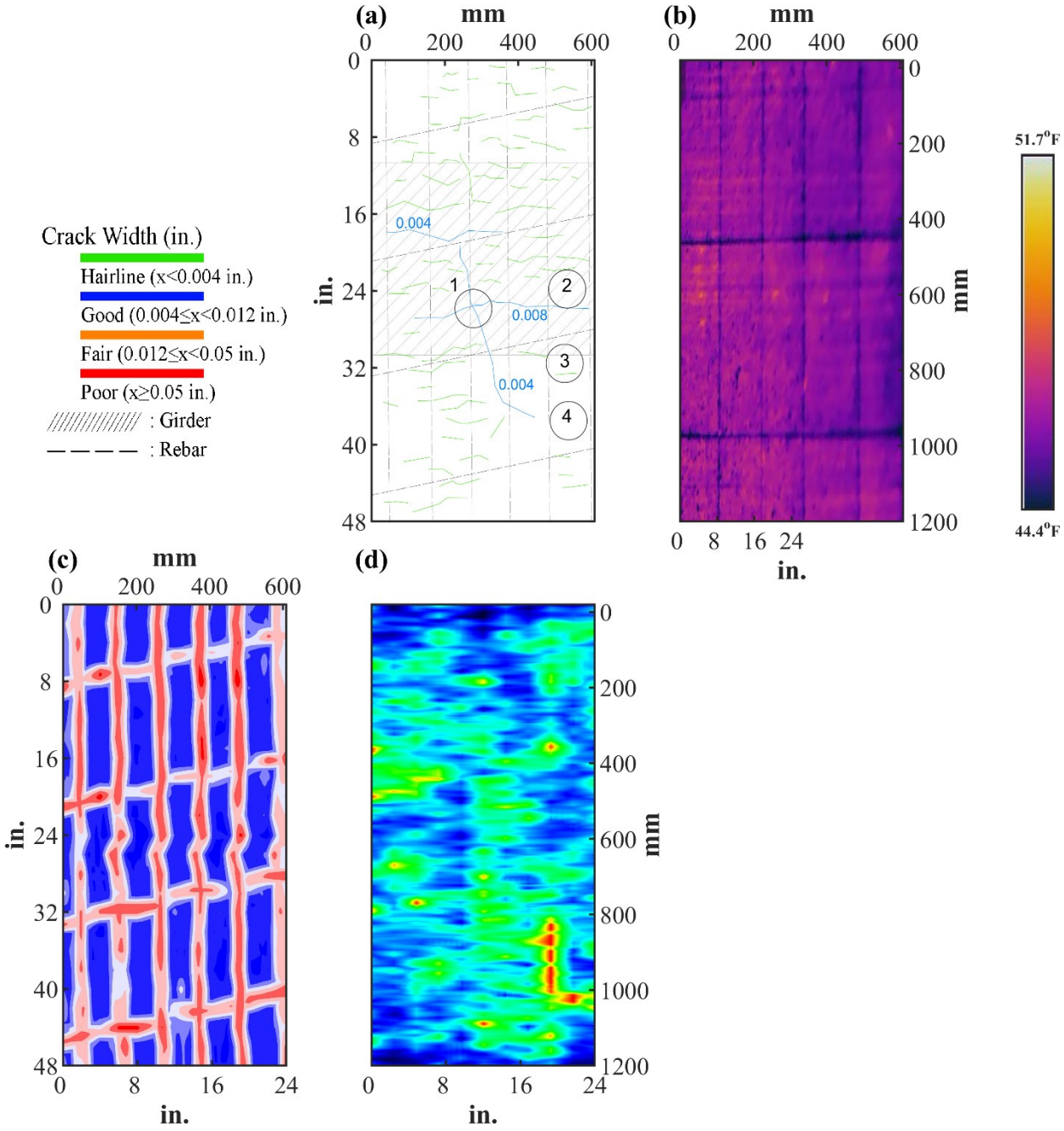

Figure 0.275. Crack Map and NDE Results of Grid 1: (a) Crack Map and Location of Cores; (b) Infrared Picture; (c) GPR C-scan at 2.0 in. to 3.2 in. Depth; (d) UST C-scan at 4.0 in. Depth

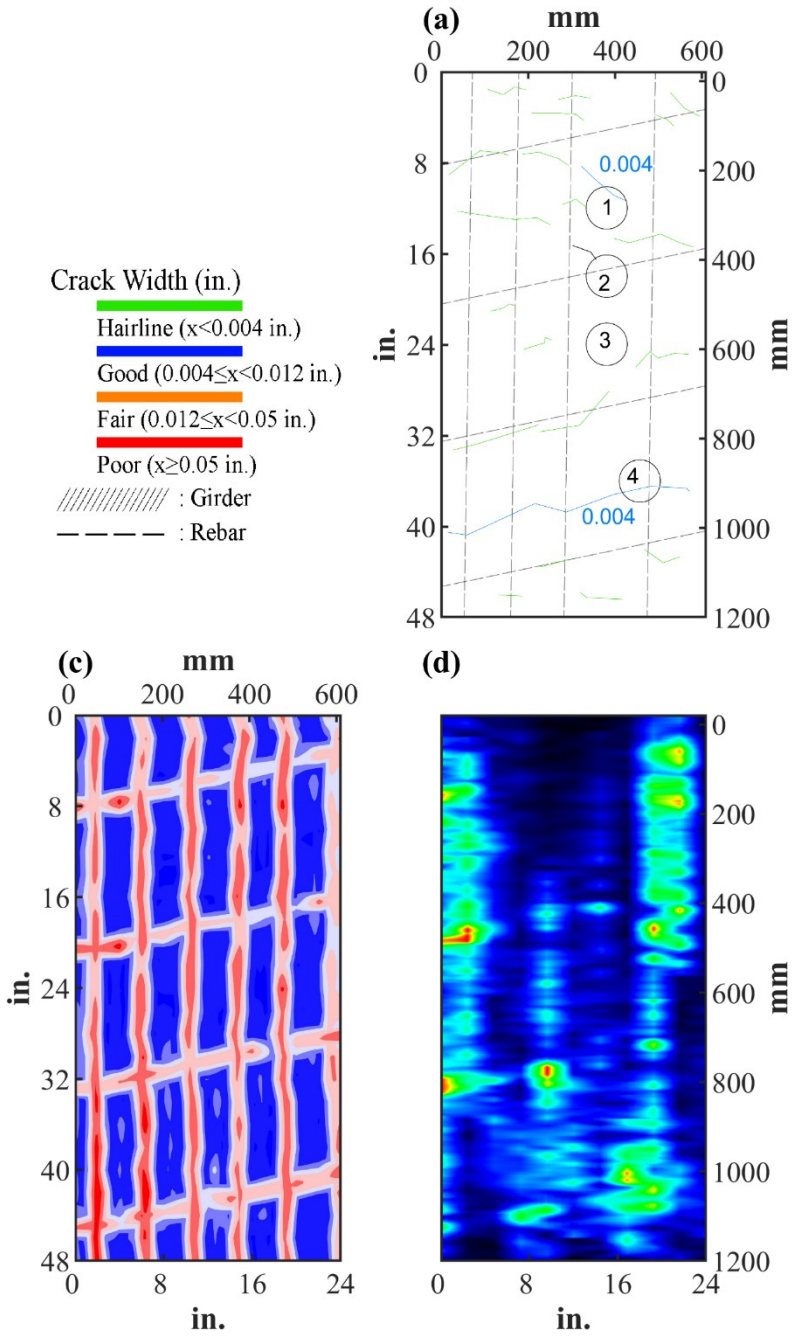

Figure 0.276. Crack Map and NDE Results of Grid 2: (a) Crack Map and Location of Cores; (c) GPR C-scan at 1.9 in. to 3.3 in. Depth; (d) UST C-scan at 4.0 in. Depth

B.38.3 Concrete Cores

Table B-135. Detail Information of concrete cores

Core	dia. x height (in.)	clear cover (in.)	Rebar size (#)	Epoxy (Y/N)	Crack type	Crack width (in)	Notes
1-1	3.75 x 5.2	2.2	5	Y	longitudinal; map	0.008; 0.004	-
1-2	3.75 x 5.1	-	-	-	-	-	-
1-3	3.75 x 5.0	2.2	5	Y	diagonal	HL	A void at 0.8 in. depth
1-4	3.75 x 5.1	-	-	-	-	-	-
2-1	3.75 x 5.9	-	-	-	diagonal	0.004	-
2-2	3.75 x 5.2	3.4	4	N	-	-	-
2-3	3.75 x 5.6	-	-	-	-	-	-
2-4	3.75 x 6.0	2.8	5	Y	-	-	-

Table B-136. Core Pictures

Core	Pictures of the Cores		
1-1			
1-2		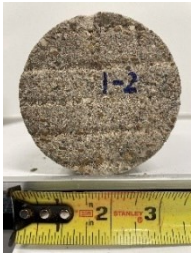	
1-3		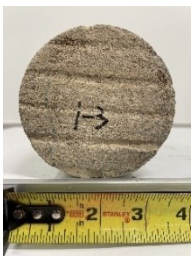	

1-4	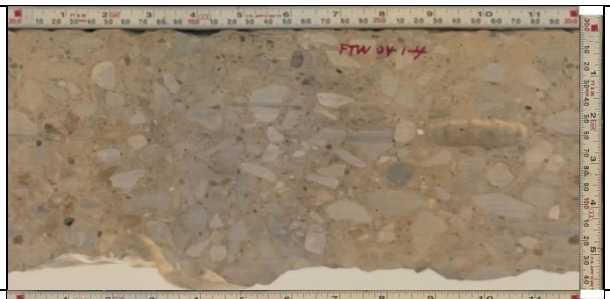		
2-1		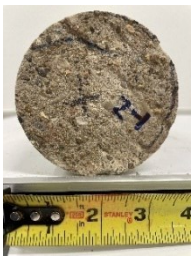	
2-2			
2-3			
2-4		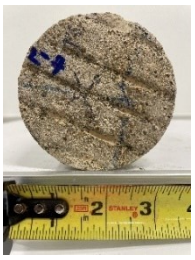	

B.38.4 Laboratory Experiment Results

B.38.4.1 Resistivity

Core Number	Surface Resistivity (kΩ·m)	Bulk Resistivity (kΩ·m)
1-2	43.5	9.4
1-4	46.8	-
2-1	39.5	-
2-3	41.5	9.5

B.38.4.2 Ultrasonic Pulse Velocity

Core Number	Ultrasonic Pulse Velocity (m/s)
1-2	4155
1-4	3982
2-1	4370
2-3	4243

B.38.4.3 Carbonation Depth

Core Number	Carbonation Depth (in.)
2-2	0.00

B.38.4.4 Acid-Soluble Chloride Content

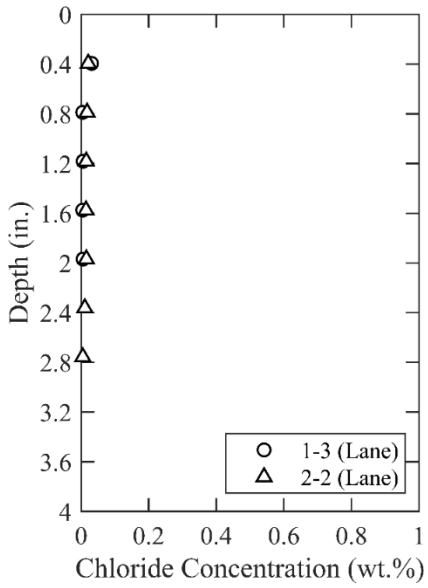

Figure 0.277. Chloride Content at Different Depth

B.38.4.5 Sorptivity

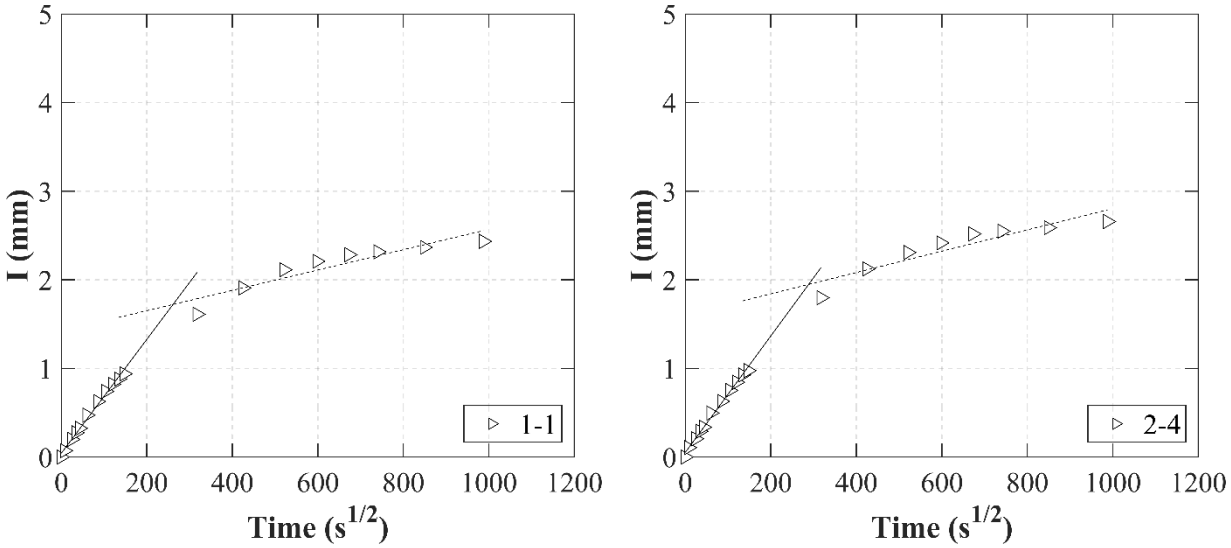

(a) Core 1–1 (b) Core 2–4

Figure 0.278. Absorption and Sorptivity of: (a) Core 1–1; (b) Core 2–4

Table B-137. Initial and Secondary Sorptivity Results

Core Number	Sorptivity	Results (mm/s$^{1/2}$)
Core 1–1	Initial Sorptivity	0.00643
	Secondary Sorptivity	0.00115
Core 2–4	Initial Sorptivity	0.00657
	Secondary Sorptivity	0.00120

B.38.4.6 Knife Test

Core Number	Score	Picture
2-2	8	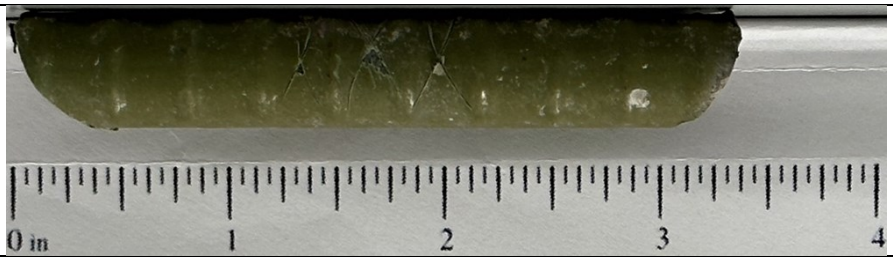

B.38.4.7 Electrochemical Impedance Spectroscopy

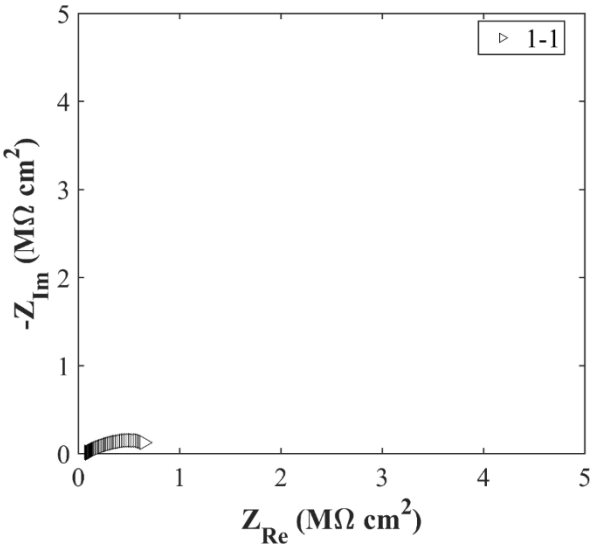

(a) Nyquist Diagram

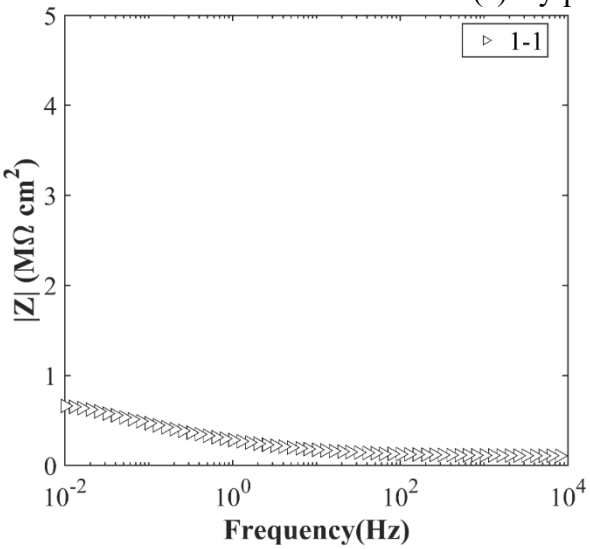

(b) Bode Plot of Impedance Modulus

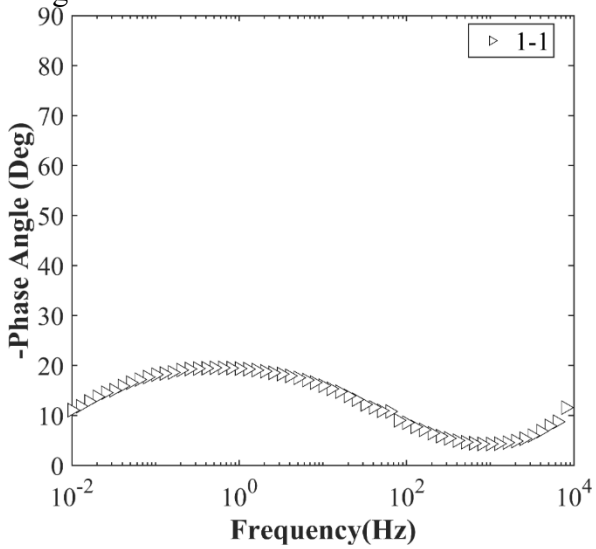

(c) Bode Plot of Impedance Phase

Figure 0.279. EIS Results: (a) Nyquist Diagram; (b) Bode Plot of Impedance Modulus; (c) Bode Plot of Impedance Phase

B.39 FTW-RC-05, FM 1938 OVER BIG BEAR CREEK

- Bridge ID: 22200197801004 (Tarrant County)
- Built in 1996
- Mitigation methods: Linseed oil, ECR
- Observed CIP depth: N/A
- Observed clear cover: 2.2 in.
- 3 spans, 12-concrete PS girder @ varying spacing with 3’ overhangs
- Inspected on June 28, 2021

Figure 0.280. Concrete Deck of the Bridge (source: google maps)

B.39.1 Observed Condition

Deck surface has transverse cracks. The main superstructure members are in good condition; however, abutment backwall has minor cracks and efflorescence as shown in Figure 0.281.

Figure 0.281. Crack and Efflorescence at the Abutment Wall

B.39.2 NDE Results

Both grid 1 and grid 2 were located on the SB lane of the span 1 of the bridge.

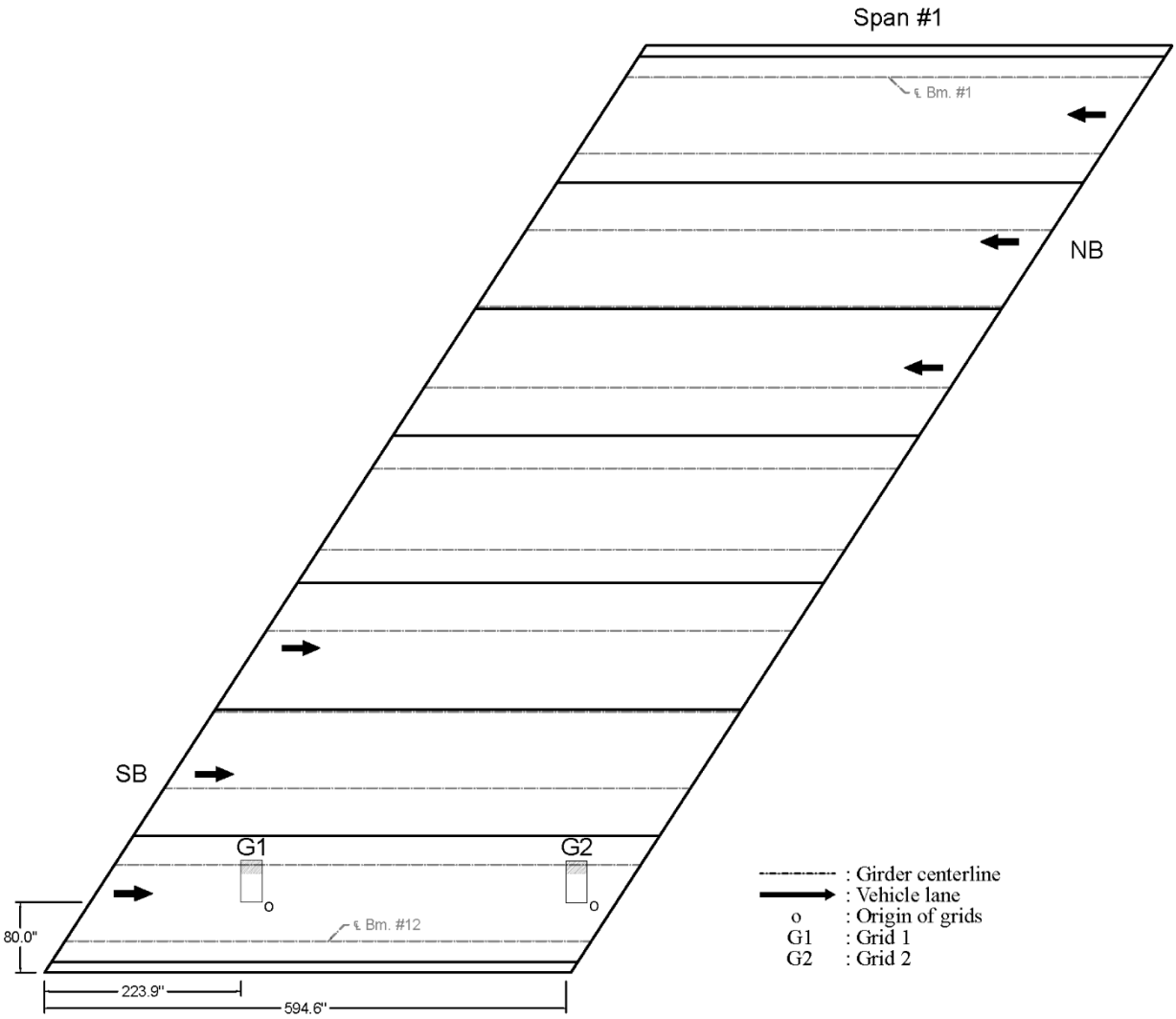

Figure 0.282. Plan View of the Bridge and Location of Grids

As shown in Figure 0.283 (a), there were widespread of hairline cracks and 0.004 in. wide cracks on top of a girder on grid 1. On grid 2, there were no cracks as shown in Figure 0.284 (a).

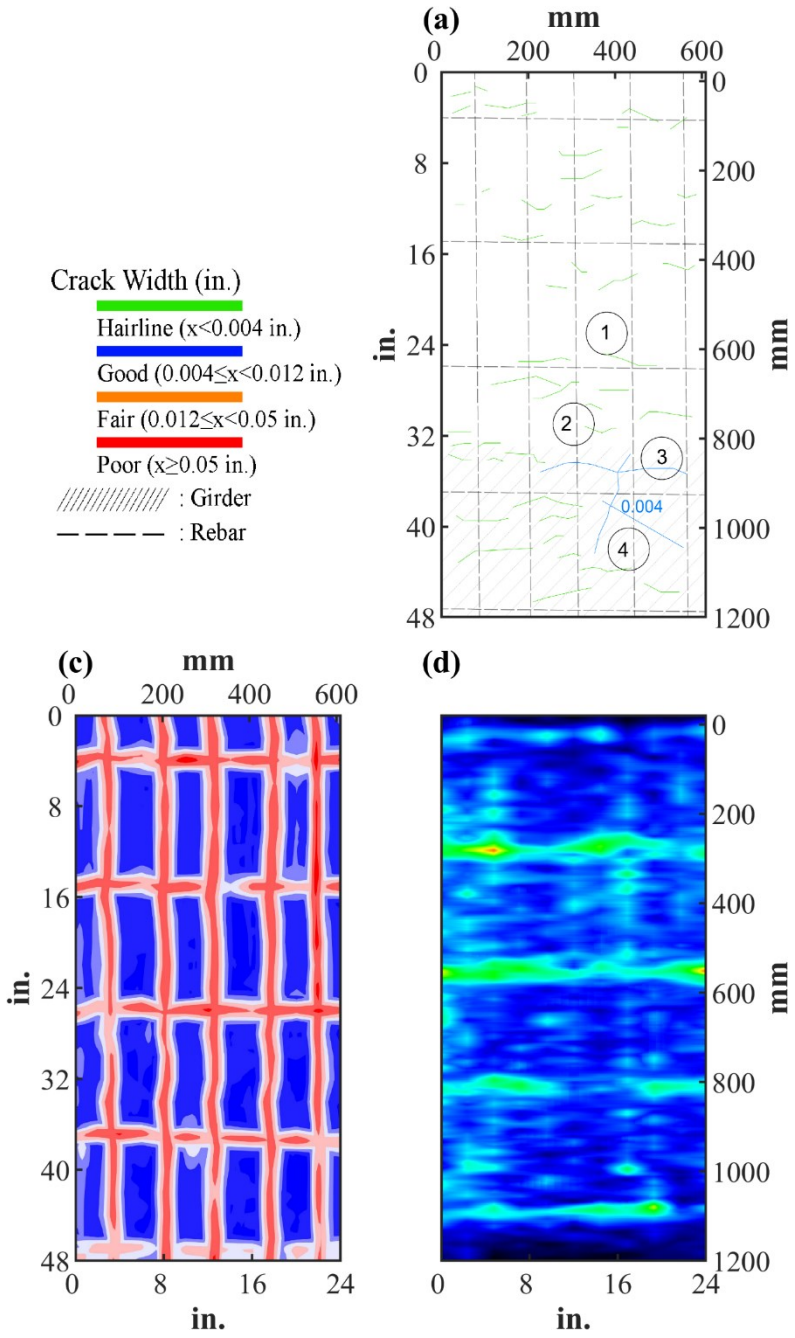

Figure 0.283. Crack Map and NDE Results of Grid 1: (a) Crack Map and Location of Cores; (c) GPR C-scan at 1.9 in. to 3.3 in. Depth; (d) UST C-scan at 4.0 in. Depth

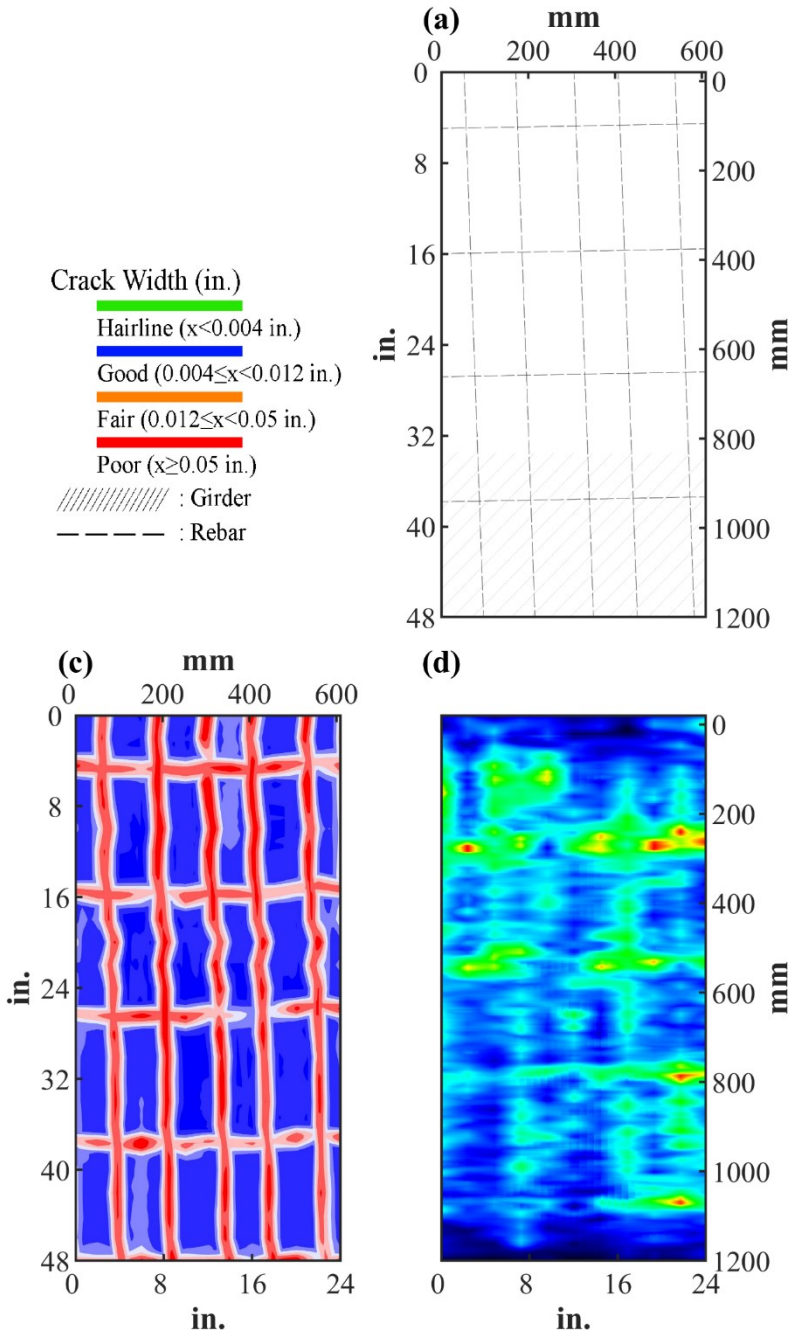

Figure 0.284. Crack Map and NDE Results of Grid 2: (a) Crack Map and Location of Cores; (c) GPR C-scan at 1.4 in. to 3.0 in. Depth; (d) UST C-scan at 3.1 in. Depth

B.39.3 Concrete Cores

Table B-138. Detail Information of concrete cores

Core	dia. x height (in.)	clear cover (in.)	Rebar size (#)	Epoxy (Y/N)	Crack type	Crack width (in)	Notes
1-1	3.75 x 6.1	-	-	-	-	-	-
1-2	3.75 x 5.9	2.2	5	Y	-	-	-
1-3	3.75 x 6.1	-	-	-	longitudinal	0.004	A void at 4.3 in. depth
1-4	3.75 x 5.7	2.2	5	Y	-	-	-

Table B-139. Core Pictures

Core	Pictures of the Cores		
1-1		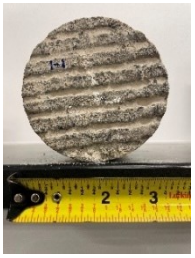	
1-2		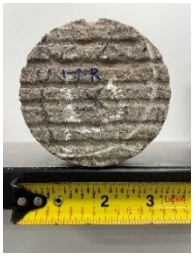	
1-3			

1-4		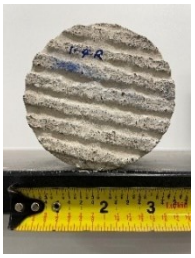	

B.39.4 Laboratory Experiment Results

B.39.4.1 Resistivity

Core Number	Surface Resistivity (kΩ·m)	Bulk Resistivity (kΩ·m)
1-1	22.6	5.1
1-3	19.4	-

B.39.4.2 Ultrasonic Pulse Velocity

Core Number	Ultrasonic Pulse Velocity (m/s)
1-1	3218
1-3	3768

B.39.4.3 Acid-Soluble Chloride Content

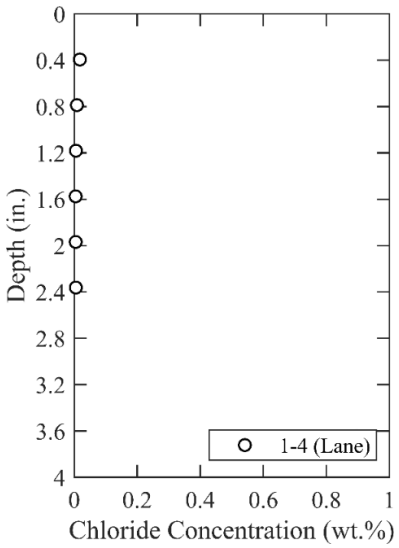

Figure 0.285. Chloride Content at Different Depth

B.39.4.4 Sorptivity

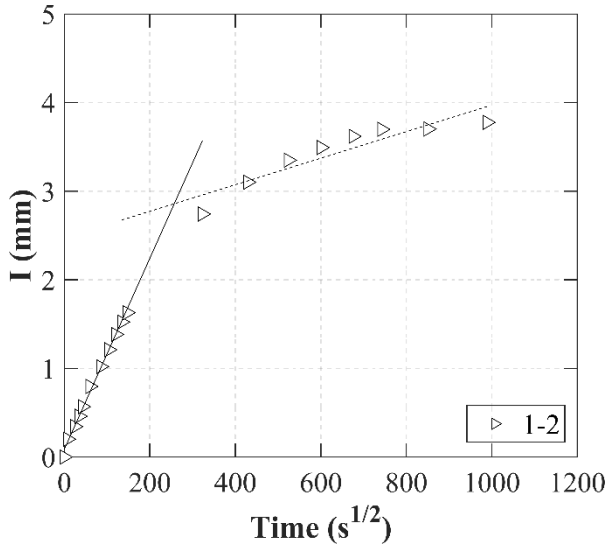

Figure 0.286. Absorption and Sorptivity of Core 1–2

Table B-140. Initial and Secondary Sorptivity Results

Core Number	Sorptivity	Results (mm/s$^{1/2}$)
Core 1–2	Initial Sorptivity	0.0108
	Secondary Sorptivity	0.00150

B.39.4.5 Knife Test

Core Number	Score	Picture
1-4	10	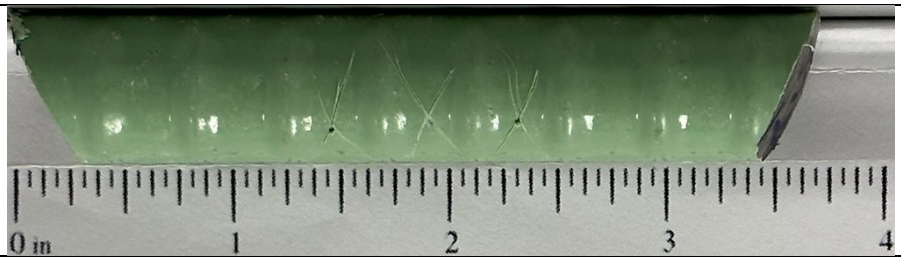

B.39.4.6 Electrochemical Impedance Spectroscopy

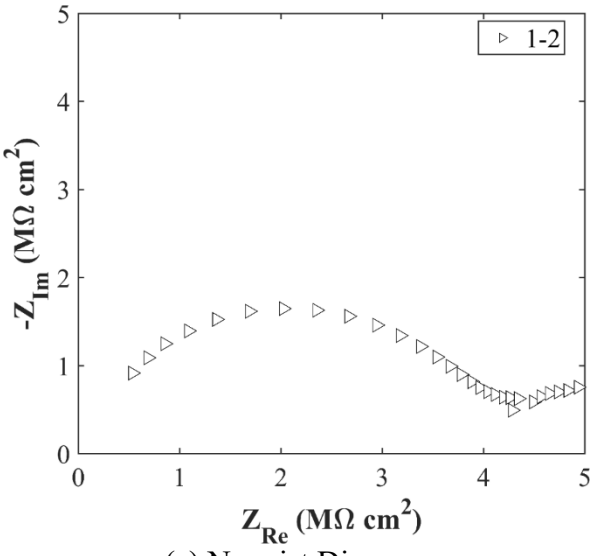

(a) Nyquist Diagram

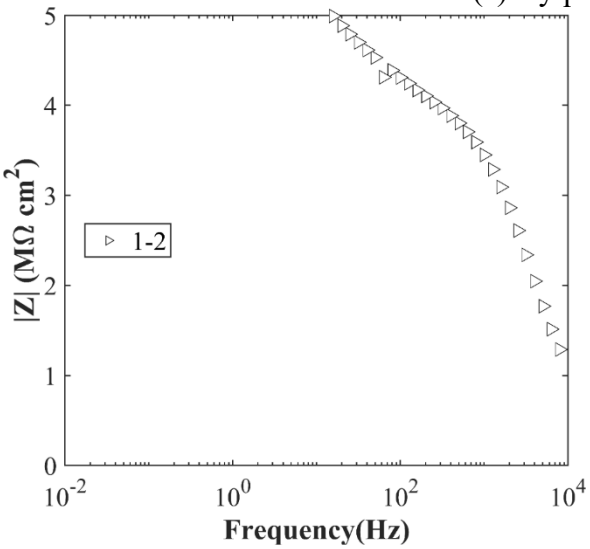

(b) Bode Plot of Impedance Modulus

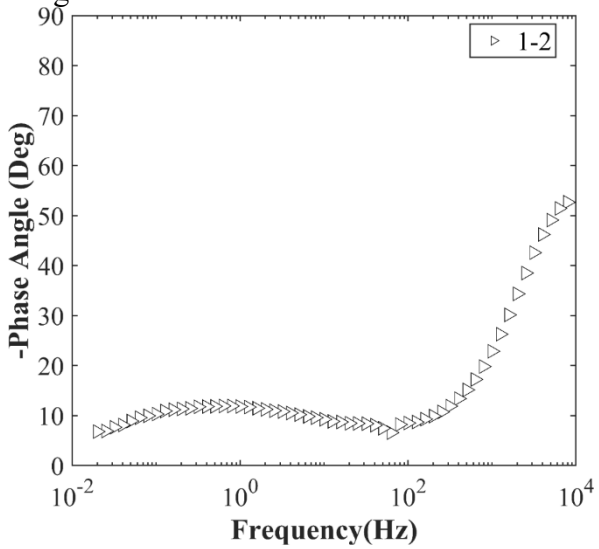

(c) Bode Plot of Impedance Phase

Figure 0.287. EIS Results: (a) Nyquist Diagram; (b) Bode Plot of Impedance Modulus; (c) Bode Plot of Impedance Phase

B.40 FTW-RC-06, COLLINS ST NB OVER IH 20

- Bridge ID: 22200237405495 (Tarrant County)
- Built in 2005
- Mitigation methods: Silane, ECR
- Observed CIP depth: N/A
- Observed clear cover: 2.9 in.
- 4 spans, 6-concrete PS girder @ varying spacing with 3’ overhangs
- Inspected on June 28, 2021

Figure 0.288. Concrete Deck of the Bridge (source: google maps)

B.40.1 Observed Condition

Deck surface has transverse cracks. The main superstructure members are in good condition; however, a vertical crack is found at the abutment wall as shown in Figure 0.289

Figure 0.289. Cracks at Abutment Wall

B.40.2 NDE Results

Grid 1 was located on the EB lane and grid 2 was located on the EB shoulder lane of the span 3 of the bridge.

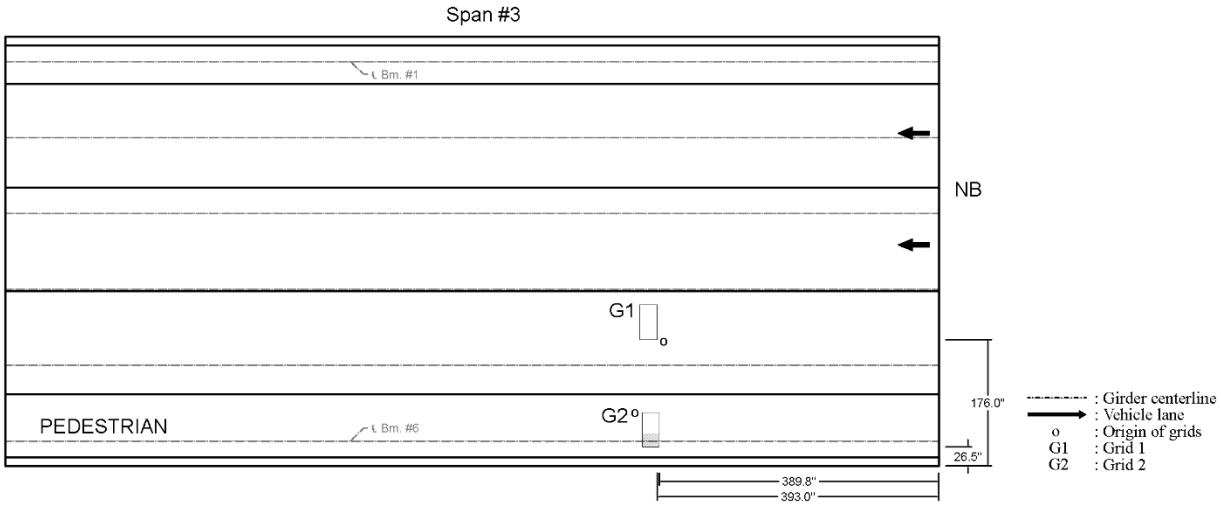

Figure 0.290. Plan View of the Bridge and Location of Grids

As shown in Figure 0.291 (a), there were widespread of hairline cracks and 0.004 in. wide transverse and longitudinal cracks on grid 1. On grid 2, there were only hairline cracks as shown in Figure 0.292 (a).

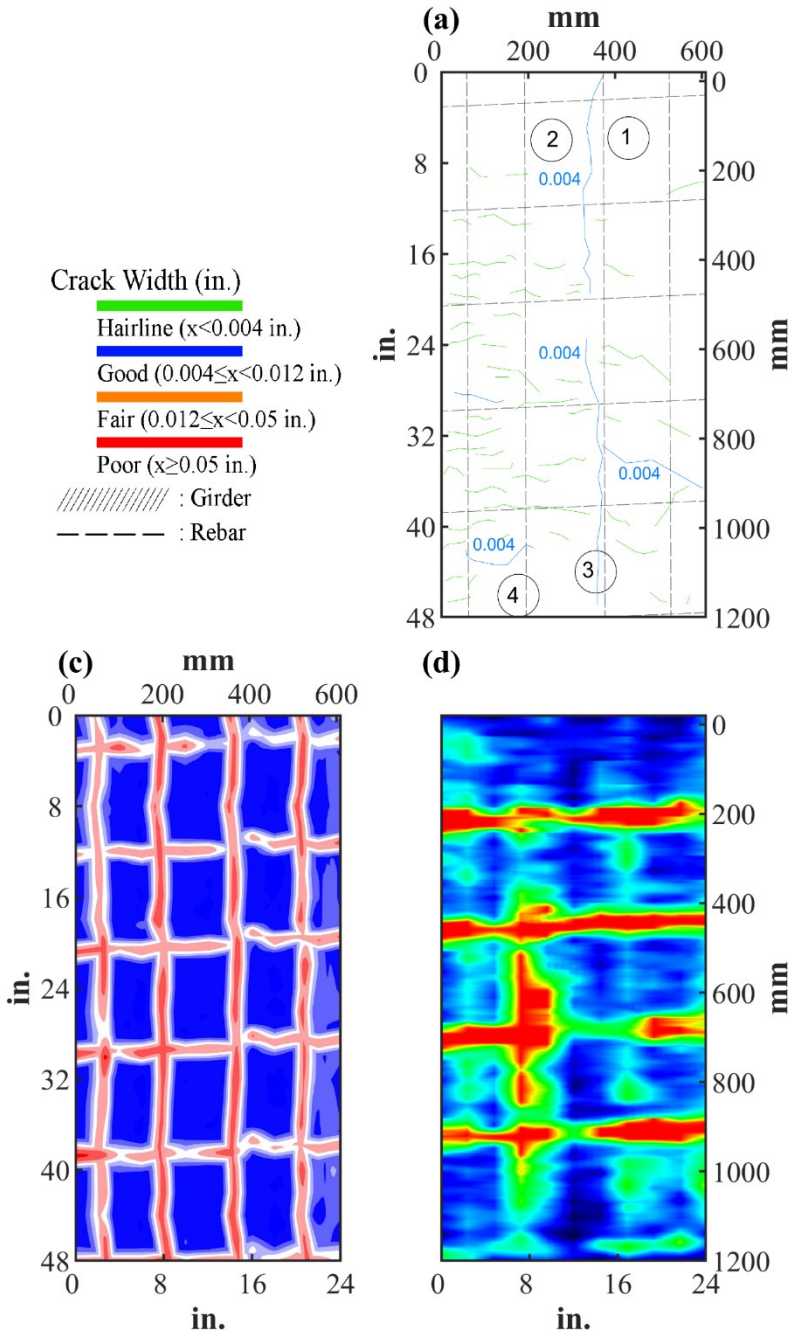

Figure 0.291. Crack Map and NDE Results of Grid 1: (a) Crack Map and Location of Cores; (c) GPR C-scan at 2.6 in. to 4.0 in. Depth; (d) UST C-scan at 4.9 in. Depth

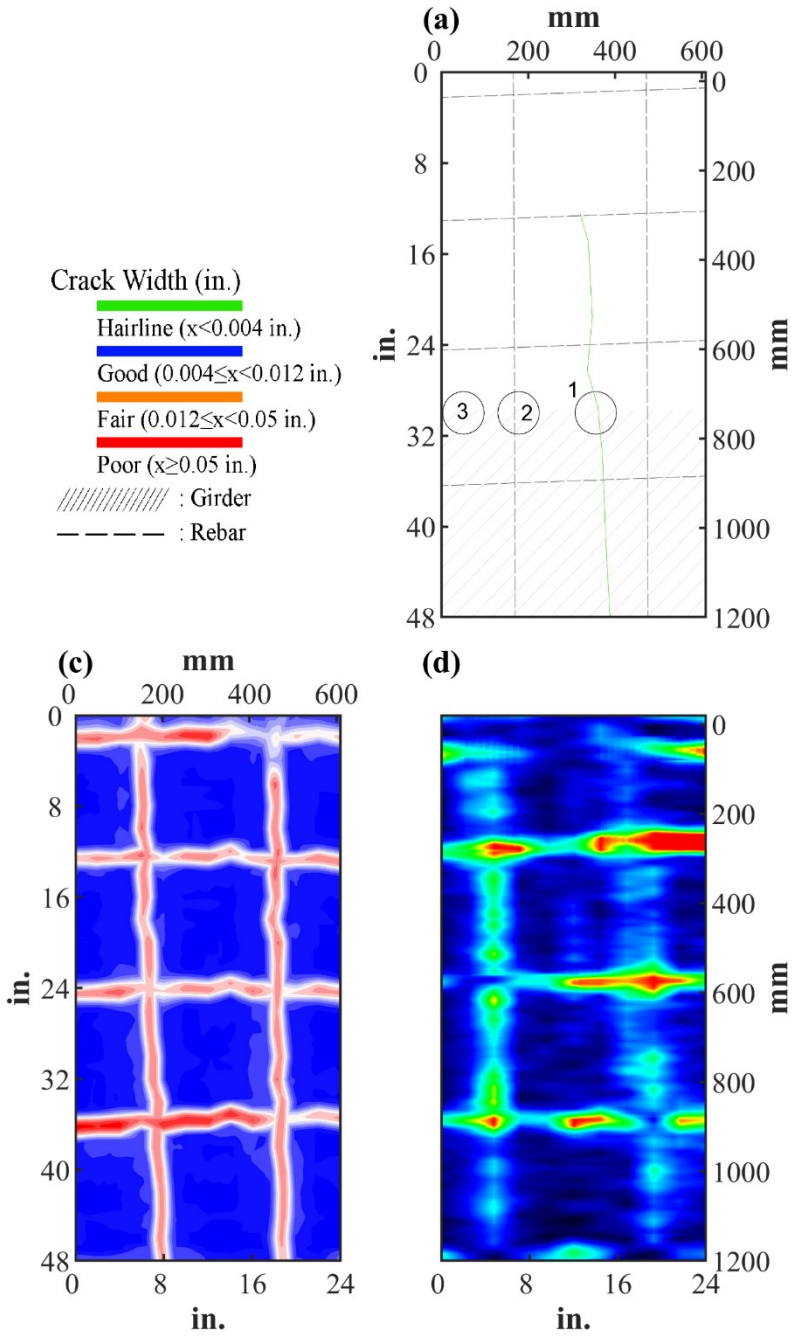

Figure 0.292. Crack Map and NDE Results of Grid 2: (a) Crack Map and Location of Cores; (c) GPR C-scan at 2.8 in. to 4.1 in. Depth; (d) UST C-scan at 4.3 in. Depth

B.40.3 Concrete Cores

Table B-141. Detail Information of concrete cores

Core	dia. x height (in.)	clear cover (in.)	Rebar size (#)	Epoxy (Y/N)	Crack type	Crack width (in)	Notes
1-1	3.75 x 5.9	-	-	-	-	-	-
1-2	3.75 x 6.1	-	-	-	-	-	-
1-3	3.75 x 5.0	2.9	5	Y	transverse	0.004	A crack propagates from panel joint
1-4	3.75 x 3.1	3.1	5	Y	-	-	-
2-1	3.75 x 7.1	-	-	-	-	-	-
2-2	3.75 x 9.6	3.2	4	Y	-	-	-
2-3	3.75 x 7.1	-	-	-	-	-	-

Table B-142. Core Pictures

Core	Pictures of the Cores		
1-1		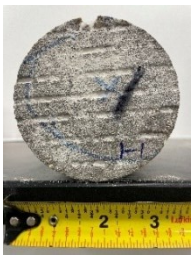	
1-2		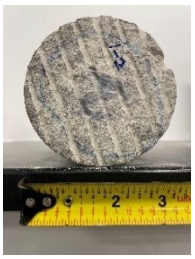	
1-3	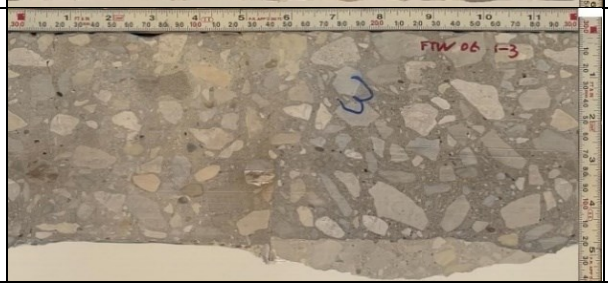		

1-4	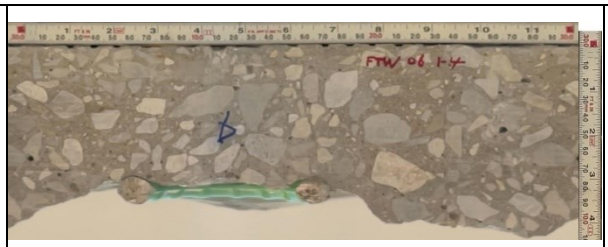	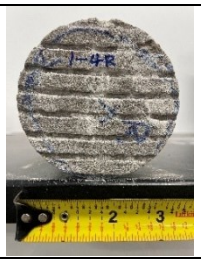	
2-1		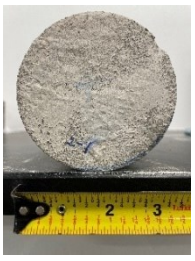	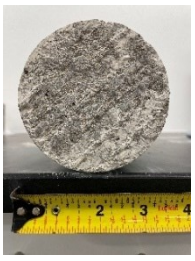
2-2		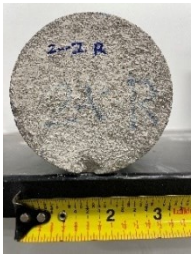	
2-3	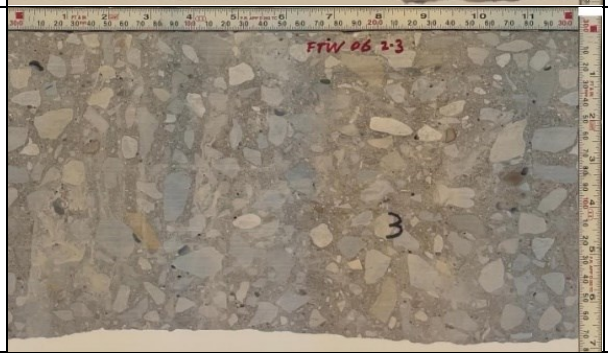	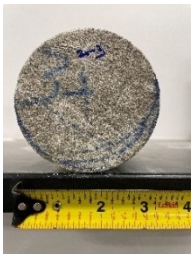	

B.40.4 Laboratory Experiment Results

B.40.4.1 Resistivity

Core Number	Surface Resistivity (kΩ·m)	Bulk Resistivity (kΩ·m)
1-1	33.8	-
1-2	39.2	10.0
2-1	39.9	9.6
2-3	48.2	-

B.40.4.2 Ultrasonic Pulse Velocity

Core Number	Ultrasonic Pulse Velocity (m/s)
1-1	4348
1-2	4328
2-1	4278
2-3	4455

B.40.4.3 Carbonation Depth

Core Number	Carbonation Depth (in.)
1-4	0.00
2-2	0.00

B.40.4.4 Acid-Soluble Chloride Content

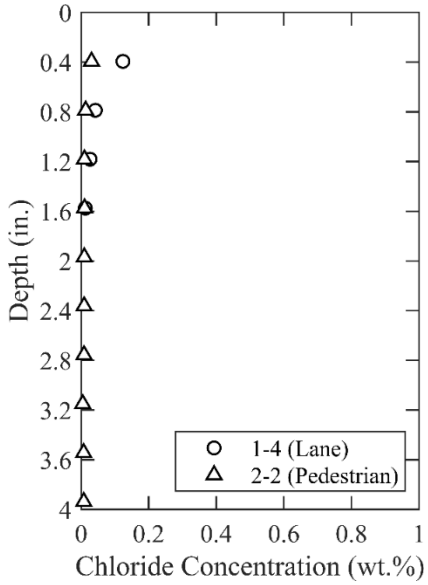

Figure 0.293. Chloride Content at Different Depth

B.40.4.5 Knife Test

Core Number	Score	Picture
1-4	10	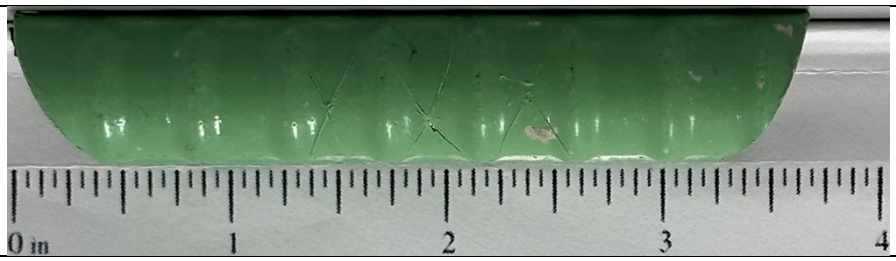

B.40.4.6 Electrochemical Impedance Spectroscopy

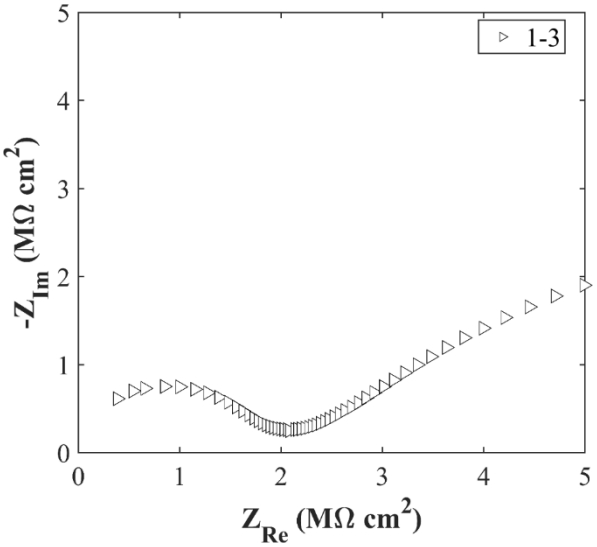

(a) Nyquist Diagram

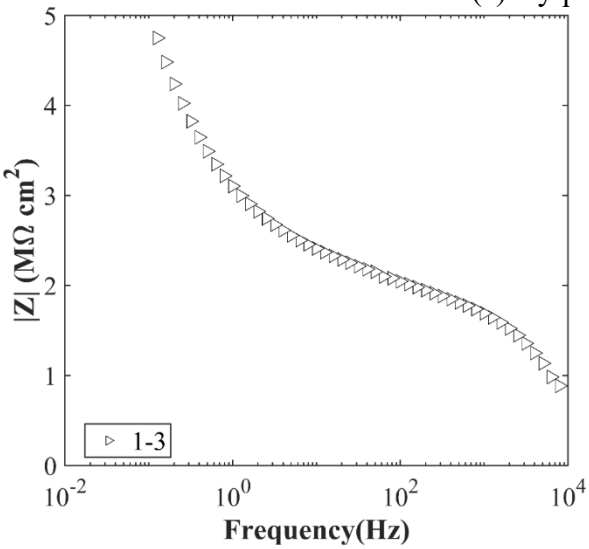

(b) Bode Plot of Impedance Modulus

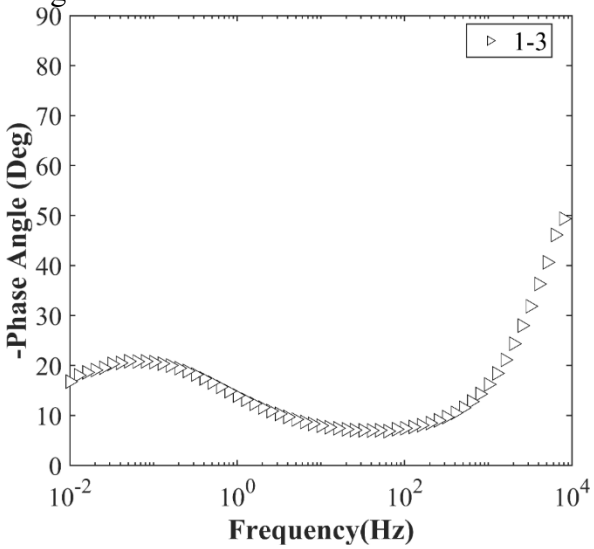

(c) Bode Plot of Impedance Phase

Figure 0.294. EIS Results: (a) Nyquist Diagram; (b) Bode Plot of Impedance Modulus; (c) Bode Plot of Impedance Phase

B.41 FTW-RC-07, FM 718 OVER TRINITY RELIEF

- Bridge ID: 22490109801007 (Wise County)
- Built in 2006
- Mitigation methods: Silane, ECR
- Observed CIP depth: 4.5 in.
- Observed clear cover: 2.6 in.
- 3 spans, 6-concrete PS girder @ varying spacing with 3’ overhangs
- Inspected on June 28, 2021

Figure 0.295. Concrete Deck of the Bridge (source: google maps)

B.41.1 Observed Condition

Deck surface has transverse cracks. The hairline vertical cracks are found on the concrete rails. The main superstructure members are in good condition.

B.41.2 NDE Results

Grid 1 was located on the SB shoulder and grid 2 was located on the SB lane of the span 2 of the bridge.

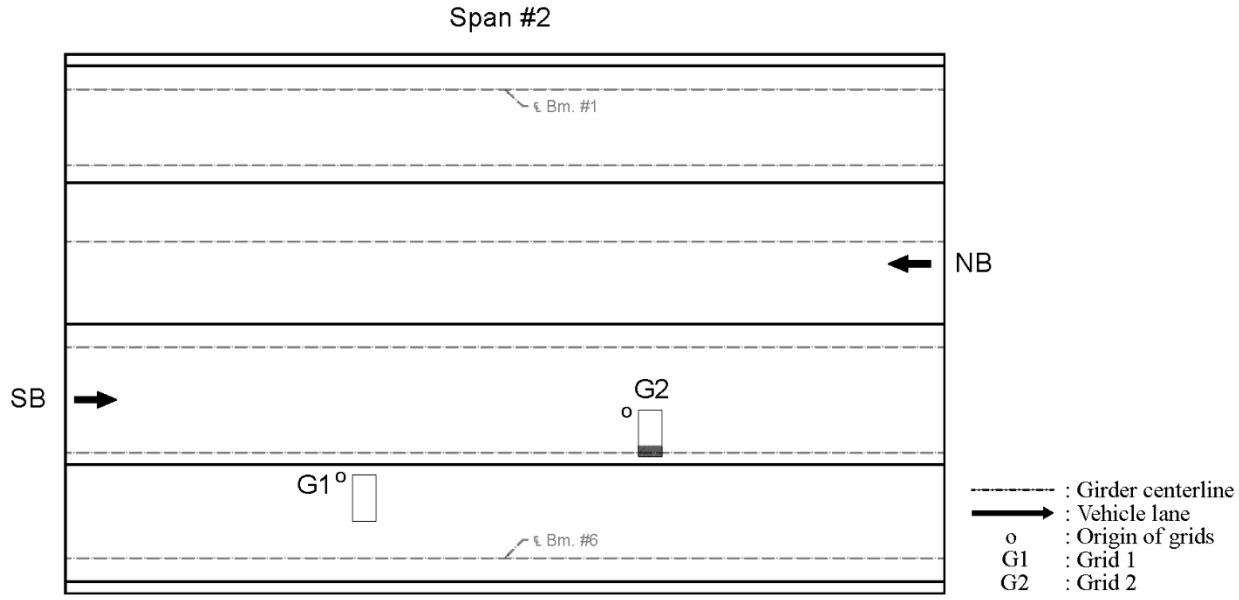

Figure 0.296. Plan View of the Bridge and Location of Grids

As shown in Figure 0.297 (a), 0.004 in. wide transverse cracks were propagating from a girder on grid 1. On grid 2, 0.004 in. wide longitudinal crack was on top of a girder and 0.004 in. wide transverse crack was propagating from a girder as shown in Figure 0.298 (a).

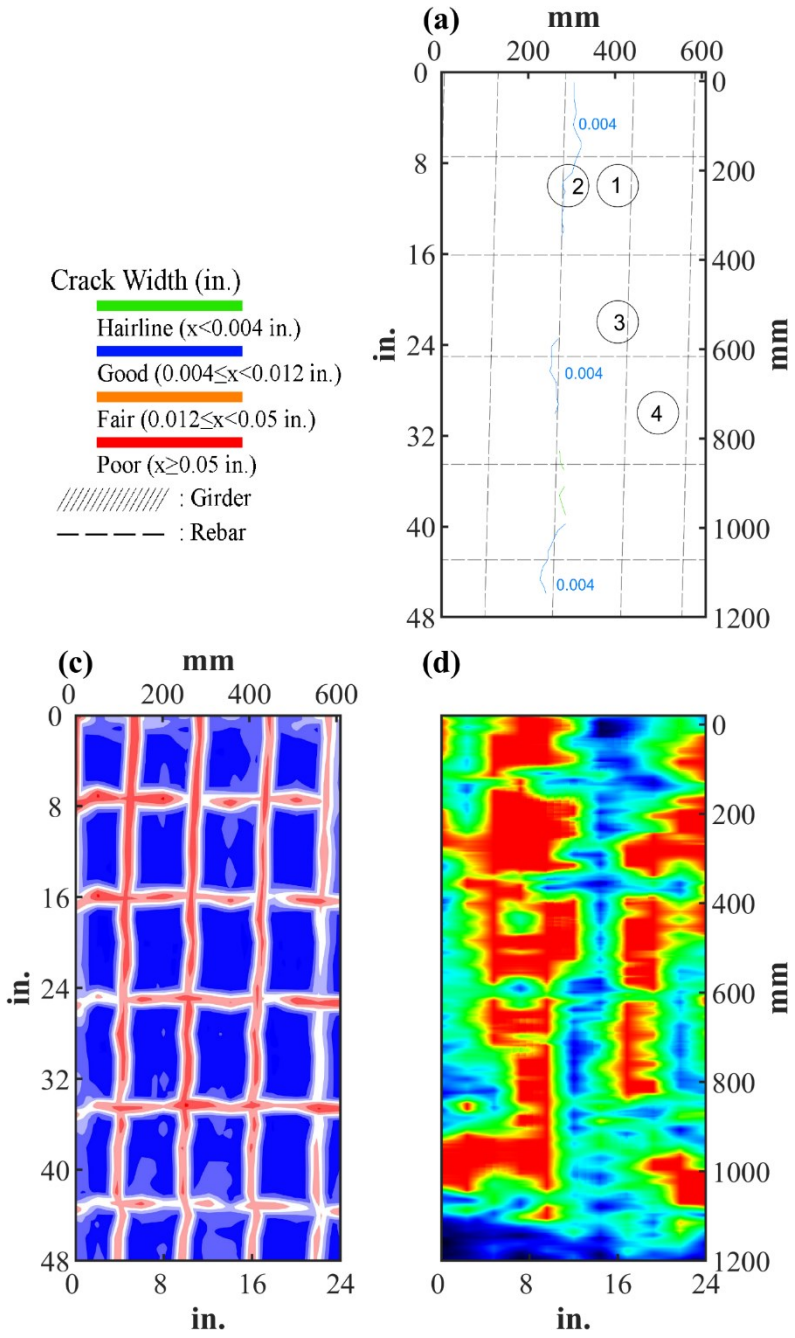

Figure 0.297. Crack Map and NDE Results of Grid 1: (a) Crack Map and Location of Cores; (c) GPR C-scan at 2.5 in. to 4.0 in. Depth; (d) UST C-scan at 4.0 in. Depth

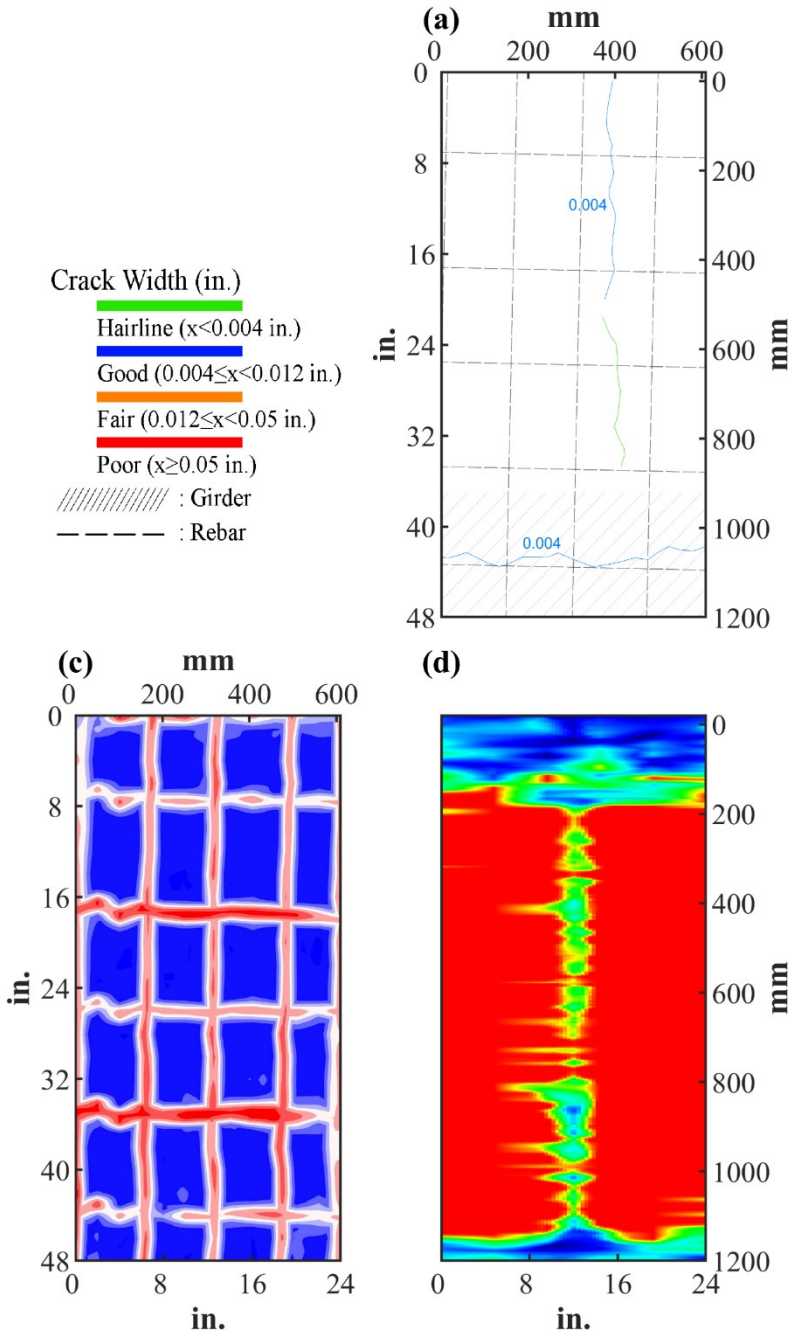

Figure 0.298. Crack Map and NDE Results of Grid 2: (a) Crack Map and Location of Cores; (b) Infrared Picture; (c) GPR C-scan at 2.6 in. to 3.9 in. Depth; (d) UST C-scan at 4.0 in. Depth

B.41.3 Concrete Cores

Table B-143. Detail Information of concrete cores

Core	dia. x height (in.)	clear cover (in.)	Rebar size (#)	Epoxy (Y/N)	Crack type	Crack width (in)	Notes
1-1	3.75 x 4.5	2.6	5	Y	-	-	Delamination between CIP and PCP
1-2	3.75 x 4.9	-	-	-	diagonal	0.004	Delamination between CIP and PCP
1-3	3.75 x 4.9	-	-	-	-	-	Delamination between CIP and PCP
1-4	3.75 x 5.0	2.7	5	Y	-	-	Delamination between CIP and PCP

Table B-144. Core Pictures

Core	Pictures of the Cores		
1-1			
1-2	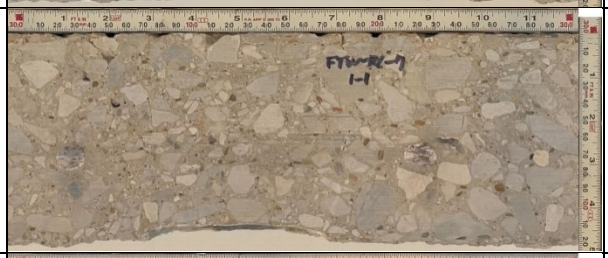		
1-3			
1-4			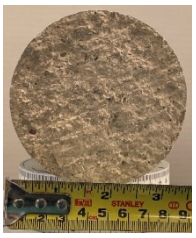

B.41.4 Laboratory Experiment Results

B.41.4.1 Resistivity

Core Number	Surface Resistivity (kΩ·m)	Bulk Resistivity (kΩ·m)
1-3	31.2	5.5

B.41.4.2 Ultrasonic Pulse Velocity

Core Number	Ultrasonic Pulse Velocity (m/s)
1-2	4325
1-3	3921

B.41.4.3 Carbonation Depth

Core Number	Carbonation Depth (in.)
1-1	0.08

B.41.4.4 Acid-Soluble Chloride Content

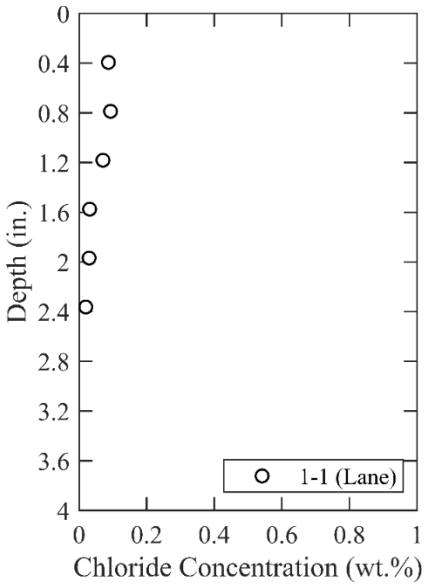

Figure 0.299. Chloride Content at Different Depth

B.41.4.5 Sorptivity

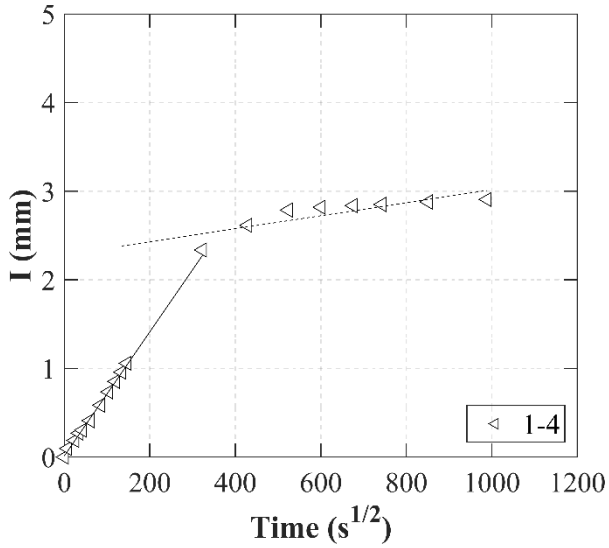

Figure 0.300. Absorption and Sorptivity of Core 1–4

Table B-145. Initial and Secondary Sorptivity Results

Core Number	Sorptivity	Results (mm/s$^{1/2}$)
Core 1–4	Initial Sorptivity	0.00700
	Secondary Sorptivity	0.00073

B.41.4.6 Knife Test

Core Number	Score	Picture
1-1	10	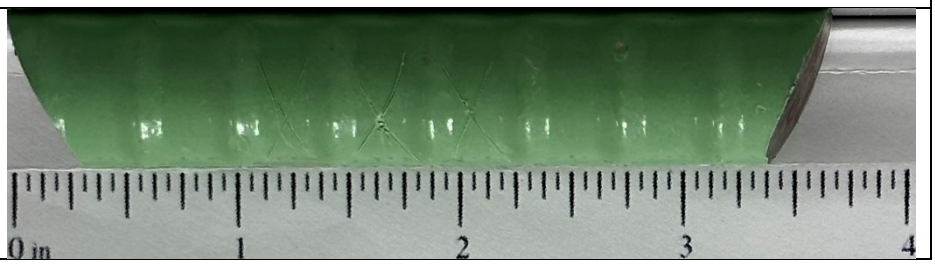

B.41.4.7 Electrochemical Impedance Spectroscopy

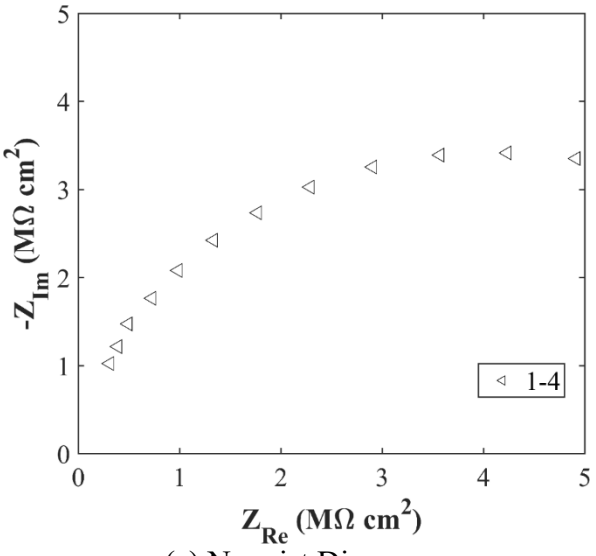

(a) Nyquist Diagram

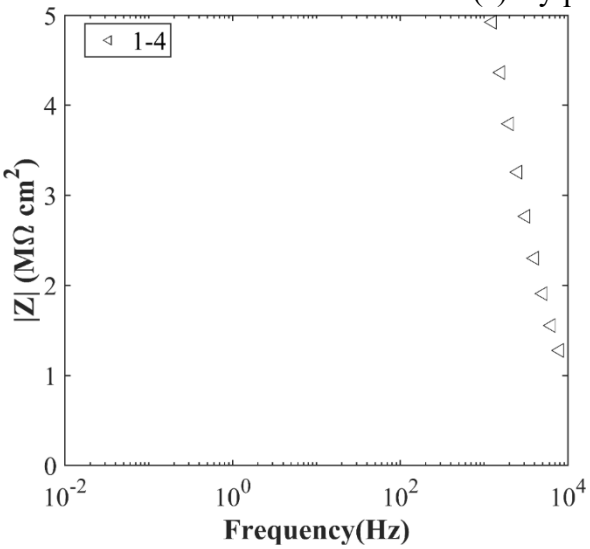

(b) Bode Plot of Impedance Modulus

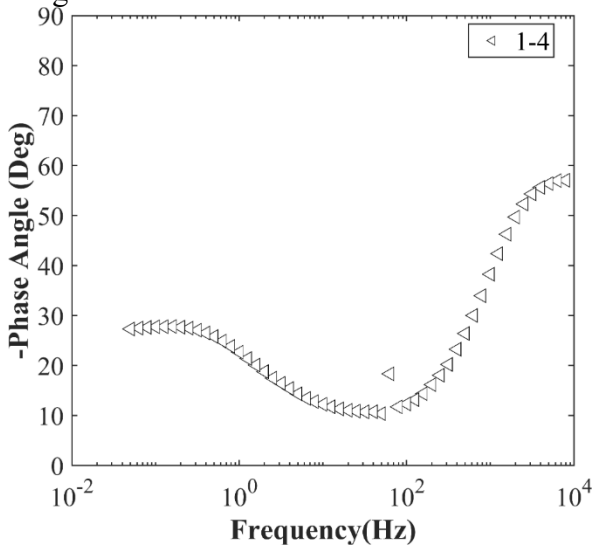

(c) Bode Plot of Impedance Phase

Figure 0.301. EIS Results: (a) Nyquist Diagram; (b) Bode Plot of Impedance Modulus; (c) Bode Plot of Impedance Phase

B.42 LBB-RC-01, US 84 WB OVER AT & SF RAILROAD

- Bridge ID: 50860005305092 (Garza County)
- Built in 1991
- Mitigation methods: Linseed oil, ECR
- Observed CIP depth: N/A
- Observed clear cover: 2.6 in.
- 3 spans, 10-concrete PS girder @ 8.5’ spacing with 3’ overhangs
- Inspected on July 22, 2021

Figure 0.302. Concrete Deck of the Bridge (source: google maps)

B.42.1 Observed Condition

The top surface of deck has spalling along joints and cracks. Diagonal cracks are propagating from PBJs, accentuated by the bridge's skew. Abutment 4’s SEJ exhibited an opening in the seal and a large patch beside it. On the backwall of Abutment 4, extensive cracking, including previously patched concrete, was observed. Rust staining was present on the bottom of the overhang and the girder haunch. On Abutment 1, a wide vertical crack (0.22 in.) was identified in the backwall. PMDF were present, including at the thickened ends and at the PBJ, where continuous rusting and staining under the PBJ crack was observed.

B.42.2 NDE Results

Grid 1 was located on the WB lane of the span 1 and grid 2 was located on the WB shoulder lane of the span 2 of the bridge.

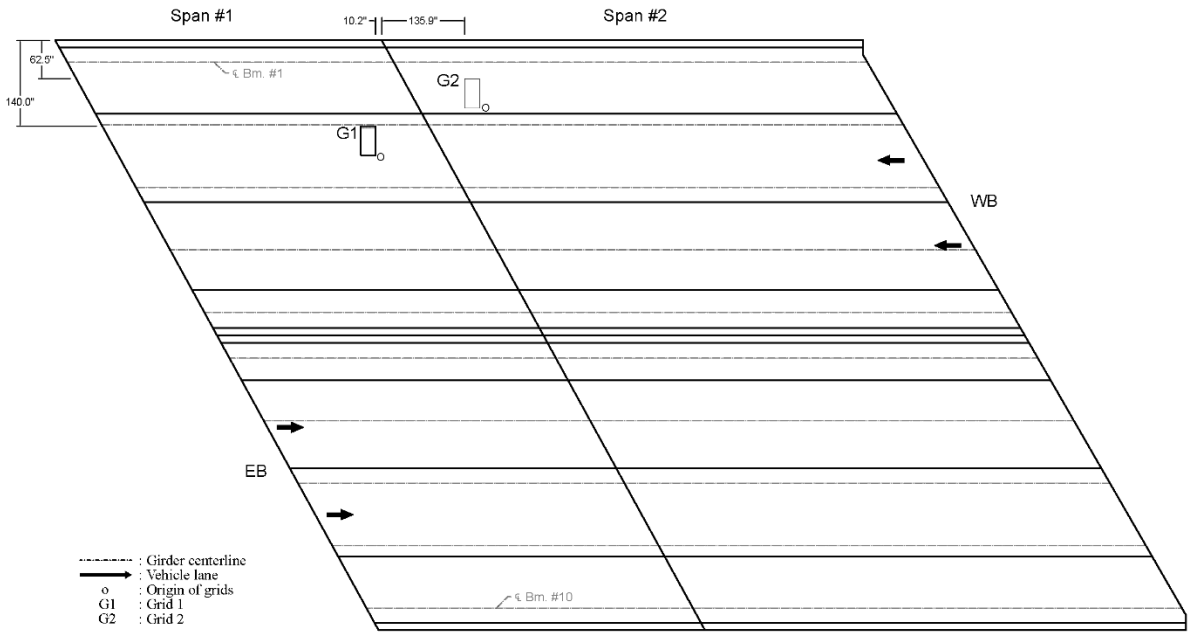

Figure 0.303 Plan View of the Bridge and Location of Grids

As shown in Figure 0.304 (a), widespread of hairline cracks and 0.004 in. wide cracks were observed on grid 1. Based on Figure A.1.3 (e), corrosion rate map shows low possibility of corrosion on grid 1. On grid 2, there were widespread of hairline cracks with a couple of cracks that were 0.004 in. wide in longitudinal and diagonal direction as shown in Figure 0.305 (a).

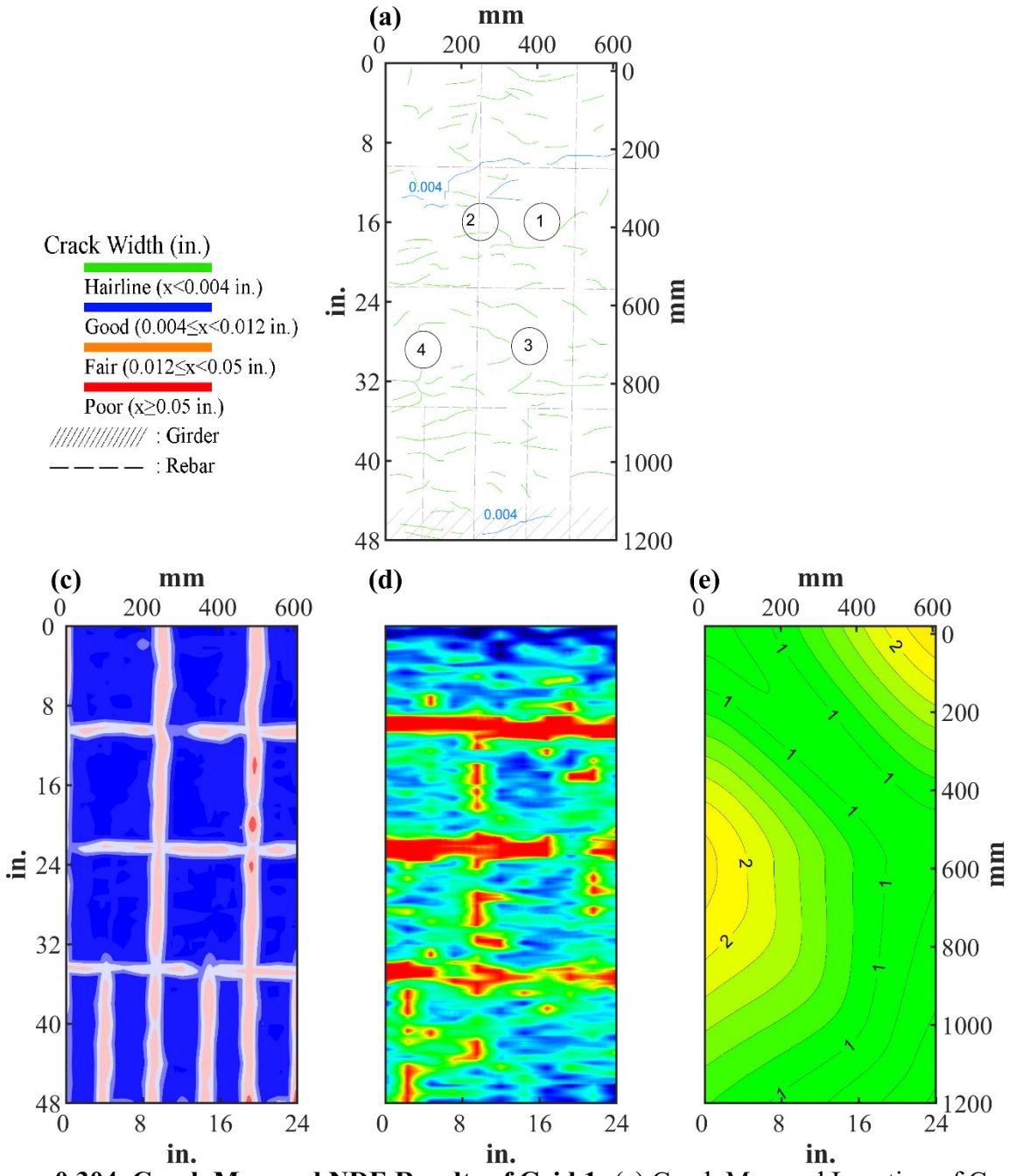

Figure 0.304. Crack Map and NDE Results of Grid 1: (a) Crack Map and Location of Cores; (c) GPR C-scan at 1.55 in. to 2.9 in. Depth; (d) UST C-scan; (e) Corrosion Rate Map

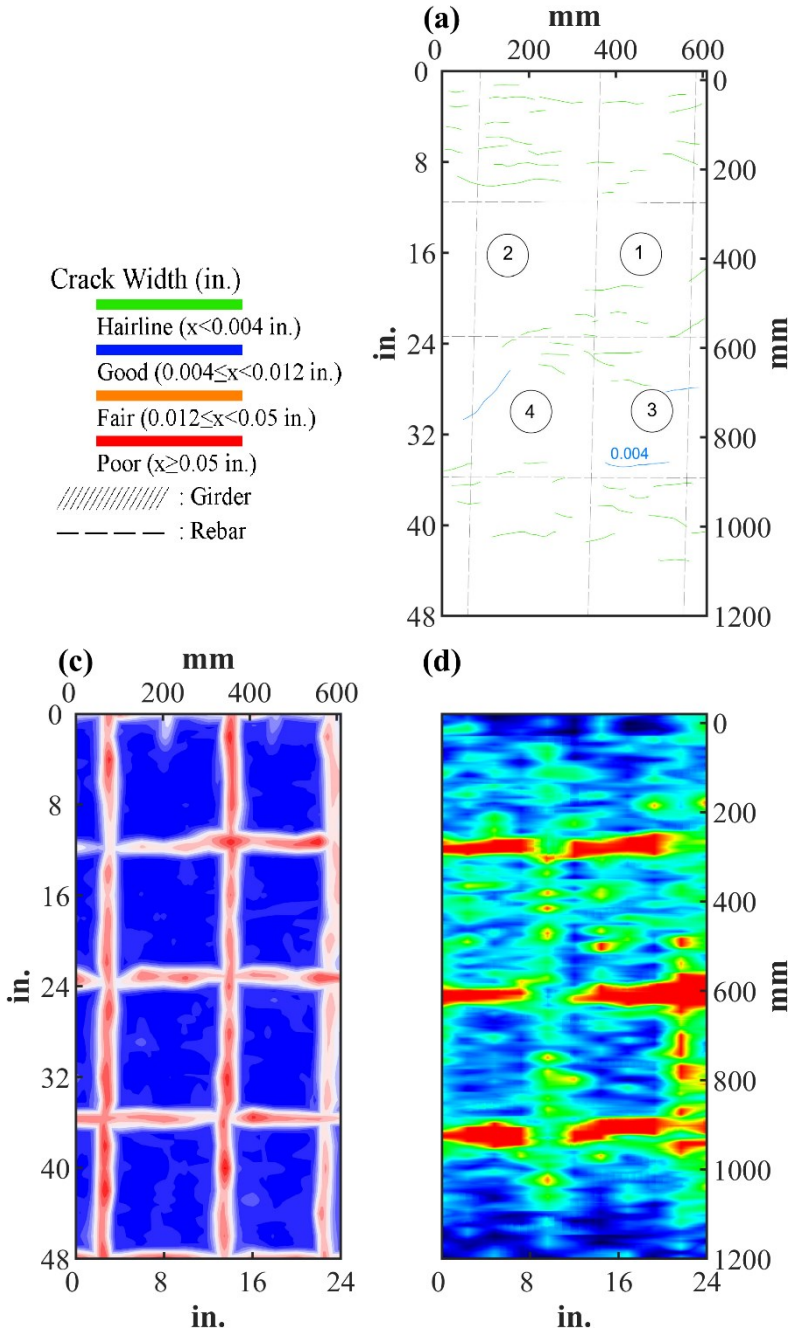

Figure 0.305. Crack Map and NDE Results of Grid 2: (a) Crack Map and Location of Cores; (c) GPR C-scan at 1.5 in. to 2.6 in. Depth; (d) UST C-scan

B.42.3 Concrete Cores

Table B-146. Detail Information of concrete cores

Core	dia. x height (in.)	Rebar depth (in.)	Rebar size (#)	Epoxy (Y/N)	Crack type	Crack width (in)	Notes
1-1	3.75 x 5.7	5.5	5	N	map	HL	
1-2	3.75 x 5.4	2.6; 5.3	5; 5	Y; N	transverse	HL	-
1-3	3.75 x 5.5	5.3	5	N	longitudinal	HL	-
1-4	3.75 x 5.0	-	-	-	-	-	-
2-1	3.75 x 5.1	-	-	-	-	-	-
2-2	3.75 x 5.1	-	-	-	diagonal	HL	-
2-3	3.75 x 6.1	5.5	5	N	-	-	-
2-4	3.75 x 5.9	5.4; 5.4	5; 5	N; N	-	-	-

Table B-147. Core Pictures

Core	Pictures of the Cores		
1-1			
1-2			

1-3			
1-4			
2-1			
2-2			
2-3			

2-4			

B.42.4 Laboratory Experiment Results

B.42.4.1 Resistivity

Core Number	Surface Resistivity (kΩ·m)	Bulk Resistivity (kΩ·m)
1-4	-	7.3
2-1	-	5.6

B.42.4.2 Ultrasonic Pulse Velocity

Core Number	Ultrasonic Pulse Velocity (m/s)
1-4	4198
2-1	4088
2-2	4157

B.42.4.3 Carbonation Depth

Core Number	Carbonation Depth (in.)
1-2	0.00
2-4	0.37

B.42.4.4 Acid-Soluble Chloride Content

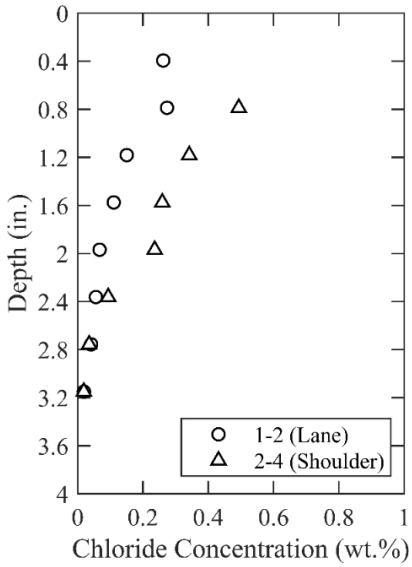

Figure 0.306. Chloride Content at Different Depth

B.42.4.5 Sorptivity

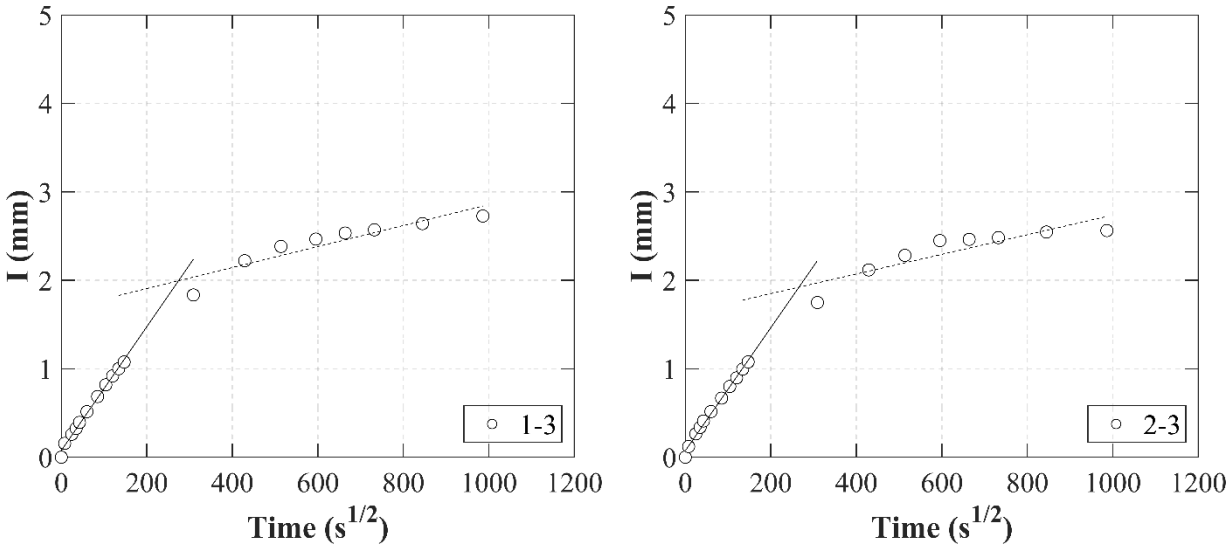

(a) Core 1–3 (b) Core 2–3

Figure 0.307. Absorption and Sorptivity of: (a) Core 1–3; (b) Core 2–3

Table B-148. Initial and Secondary Sorptivity Results

Core Number	Sorptivity	Results (mm/s$^{1/2}$)
Core 1–3	Initial Sorptivity	0.00700
	Secondary Sorptivity	0.00073
Core 2–3	Initial Sorptivity	0.00696
	Secondary Sorptivity	0.00111

B.42.4.6 Electrochemical Impedance Spectroscopy

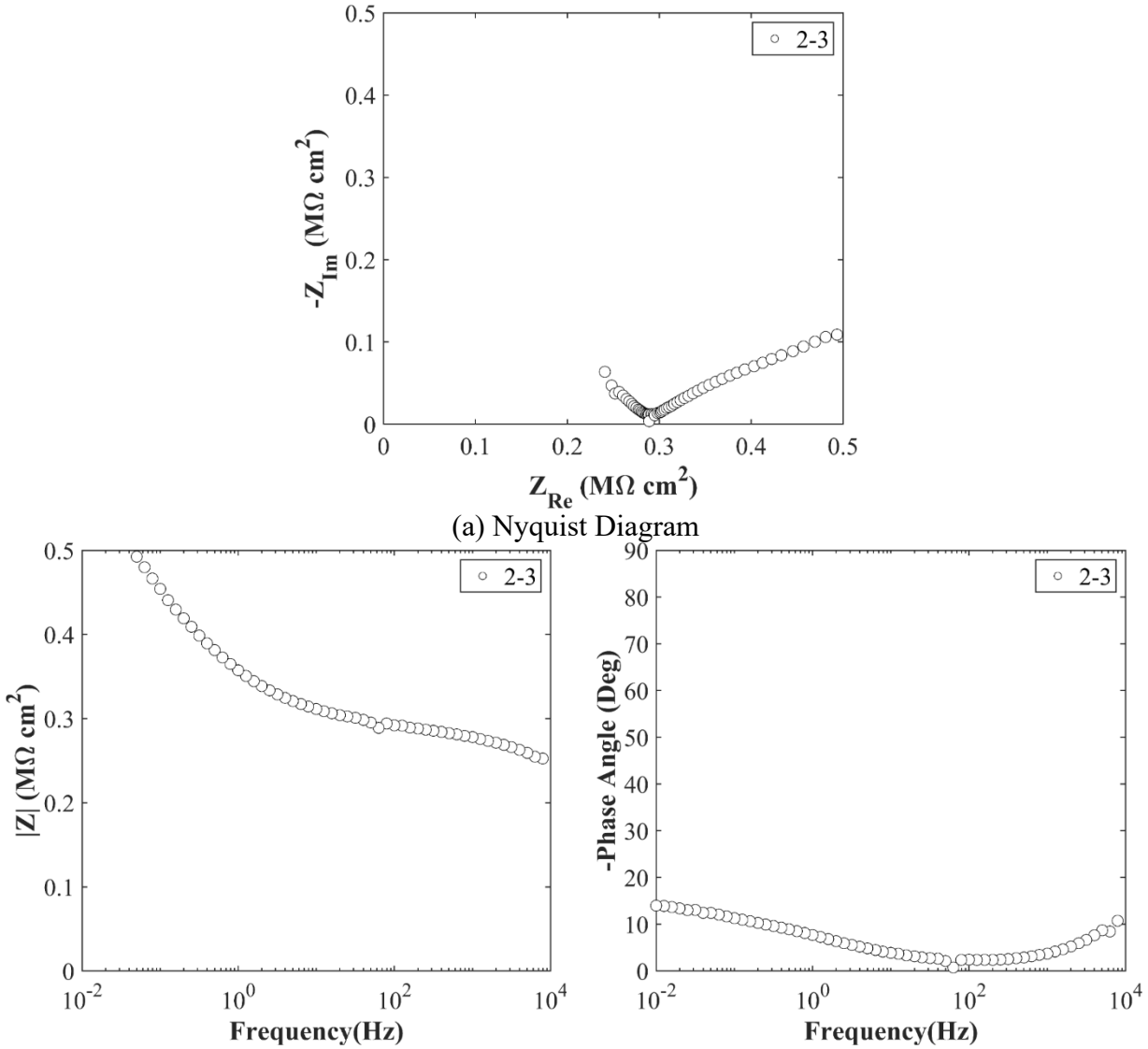

(a) Nyquist Diagram

(b) Bode Plot of Impedance Modulus

(c) Bode Plot of Impedance Phase

Figure 0.308. EIS Results: (a) Nyquist Diagram; (b) Bode Plot of Impedance Modulus; (c) Bode Plot of Impedance Phase

B.43 LBB-RC-02, FM 211 OVER BNSF RR

- Bridge ID: 50860249801001 (Garza Count)
- Built in 1962, Rehab in 2010
- Mitigation methods: HPC, Linseed oil, ECR
- Observed CIP depth: Unknown
- Observed clear cover: 1.5 in.
- 2 spans, 4 steel girder @ 6’8 in.spacing with 3’5 in. overhangs
- Inspected on July 22, 2021

Figure 0.309. Concrete Deck of the Bridge (source: google maps)

B.43.1 Observed Condition

The deck and rails were replaced at 2010. The steel beam 1 at span 1 has isolated moderate pitting corrosion in its web and bottom flange as shown in Figure 0.310. Transverse cracks were observed on the deck of the bridge, with a diagonal crack near the Abutment 1. Diagonal cracks were observed at the transition from a skew to a straight section on the overhang. The north side backwall of Abutment 1 has some water leaking through. In addition, some cracks (0.012 in.) were observed between girders.

Painted steel girders had dirt piled up in some areas on the bottom flanges at the ends (both interior and exterior), with small bits of rust showing about 3-4 feet from the end. The interior girders exhibited some rusting at the top flanges. The north column of the west bent had paint flaked off.

Figure 0.310. Pitting Corrosion on the Web and Bottom Flange

B.43.2 NDE Results

Both grids 1 and 2 were located on the WB of the span 1 of the bridge.

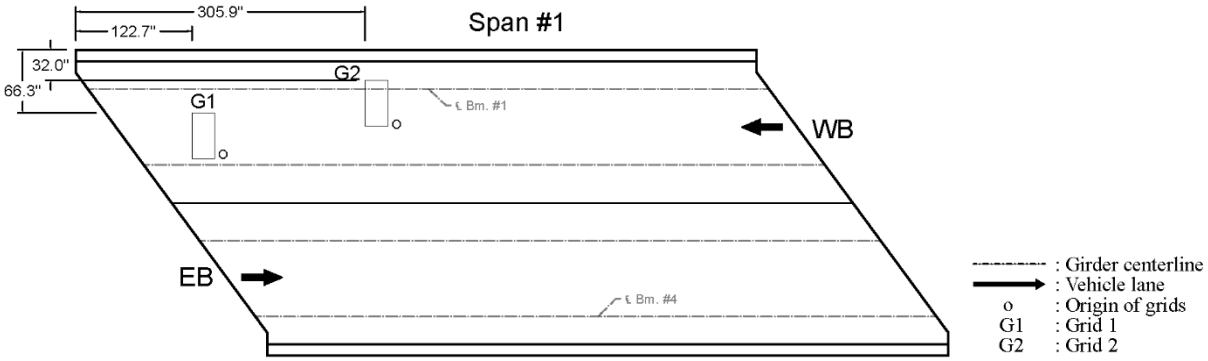

Figure 0.311. Plan View of the Bridge and Location of Grids

As shown in Figure 0.312 (a), there was 0.004 in. wide transverse crack which is possibly caused by panel joints on grid 1. Based on Figure A.2.4 (e), there is a small possibility of corrosion on grid 1. On grid 2, one diagonal 0.004 in. diagonal crack and 0.04 in. wide transverse crack propagating from a girder as shown in Figure 0.313 (a).

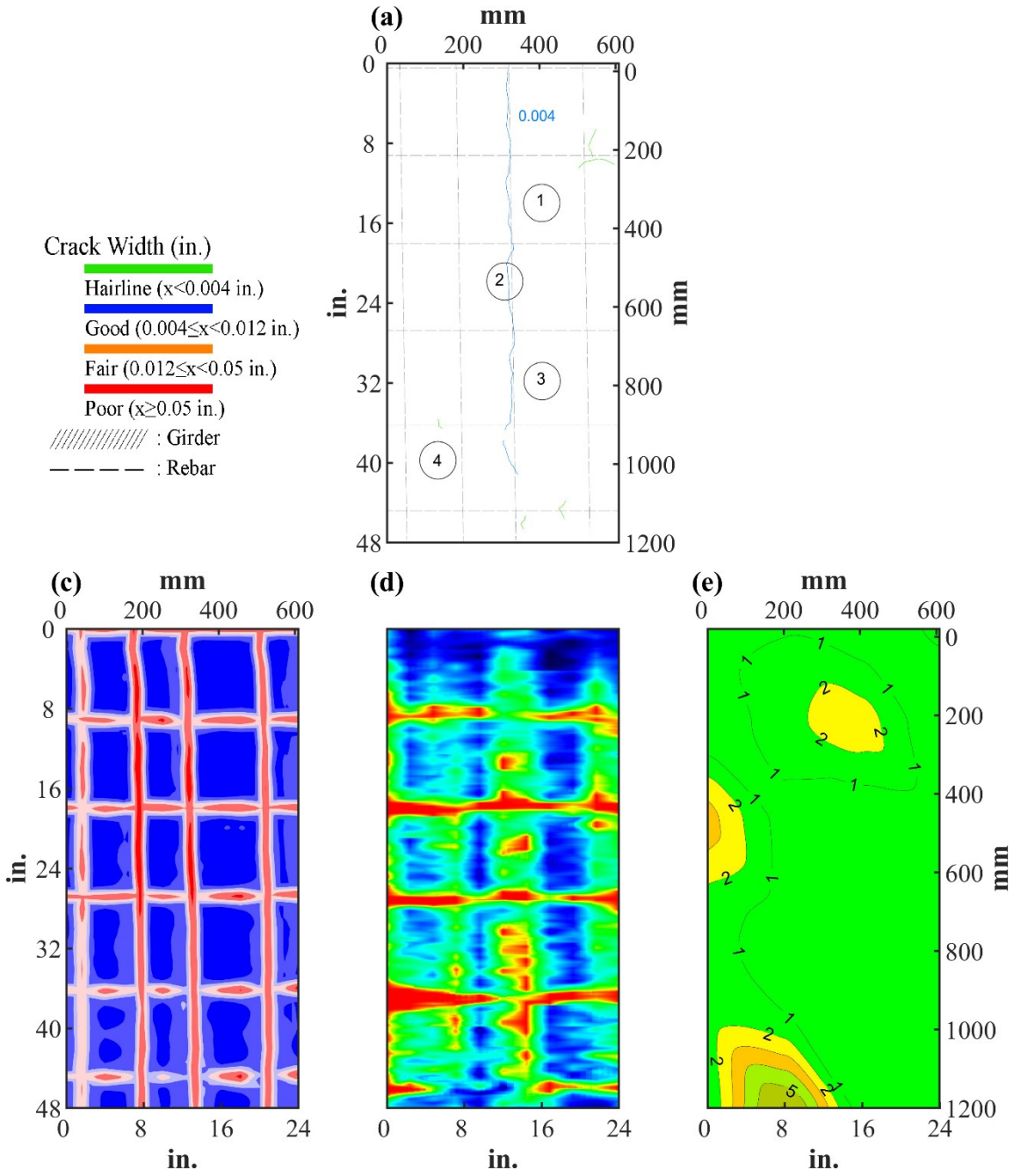

Figure 0.312. Crack Map and NDE Results of Grid 1: (a) Crack Map and Location of Cores; (c) GPR C-scan at 1.7 in. to 3.0 in. Depth; (d) UST C-scan; (e) Corrosion Rate Map

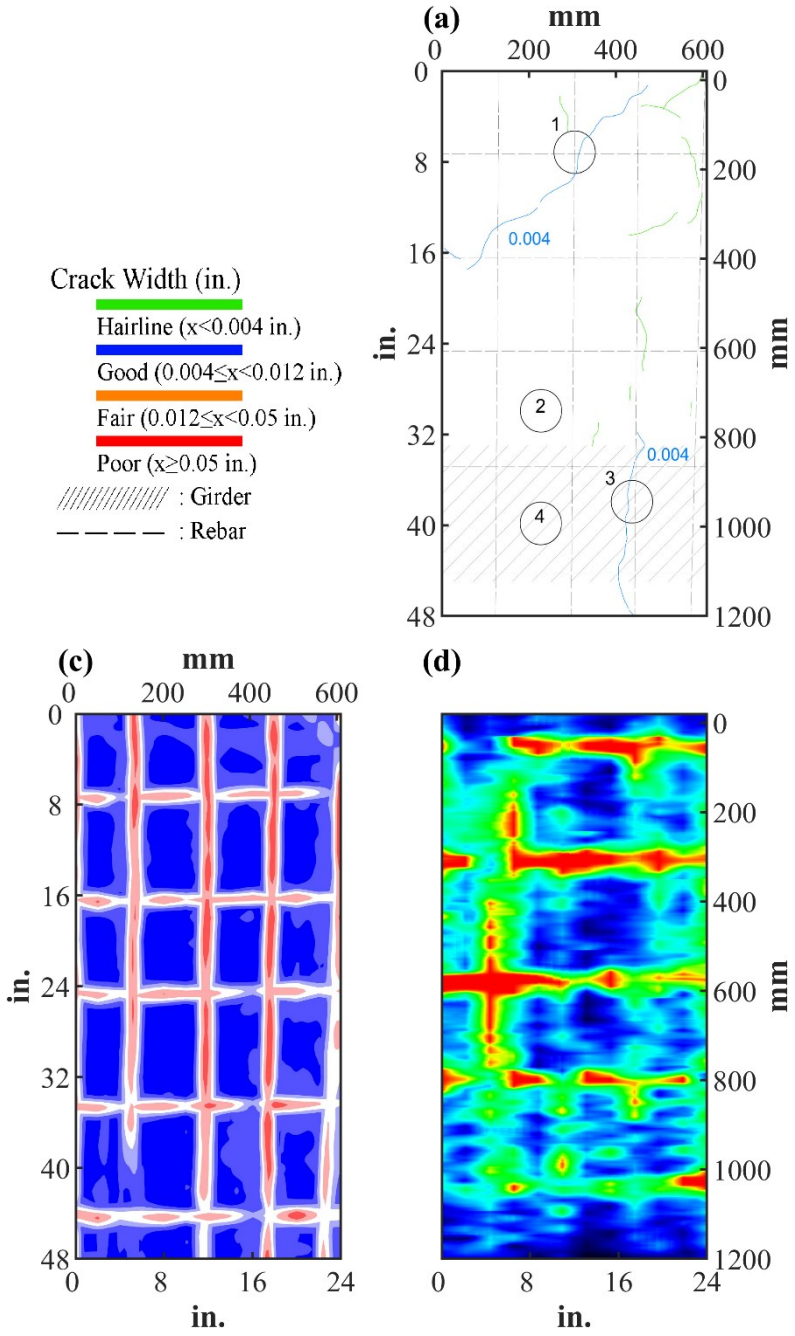

Figure 0.313. Crack Map and NDE Results of Grid 2: (a) Crack Map and Location of Cores; (c) GPR C-scan at 2.3 in. to 3.7 in. Depth; (d) UST C-scan

B.43.3 Concrete Cores

Table B-149. Detail Information of concrete cores

Core	dia. x height (in.)	Rebar depth (in.)	Rebar size (#)	Epoxy (Y/N)	Crack type	Crack width (in)	Notes
1-1	3.75 x 6.6	-	-	-	-	-	-
1-2	3.75 x 5.9	1.5; 5.8	5; 5	Y; Y; Y; Y; Y	transverse	0.004	A crack propagates from rebar
1-3	3.75 x 6.3	-	-	-	-	-	-
1-4	3.75 x 4.0	-	-	-	-	-	-
2-1	3.75 x 5.9	2.8; 3.3	5,4	Y; Y	diagonal	0.004	A crack propagates from rebar
2-2	3.75 x 5.9	-	-	-	-	-	-
2-3	3.75 x 5.5	2.2	5	Y	transverse	0.004	A crack propagates from rebar
2-4	3.75 x 6.4	-	-	-	-	-	-

Table B-150. Core Pictures

Core	Pictures of the Cores		
1-1			
1-2			

1-3			
1-4			
2-1			
2-2			
2-3			

2-4	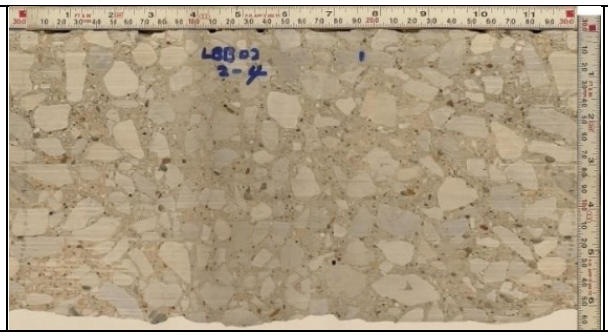		

B.43.4 Laboratory Experiment Results

B.43.4.1 Resistivity

Core Number	Surface Resistivity (kΩ·m)	Bulk Resistivity (kΩ·m)
1-1	-	24.5
2-2	-	12.4

B.43.4.2 Ultrasonic Pulse Velocity

Core Number	Ultrasonic Pulse Velocity (m/s)
1-1	4405
2-2	4315

B.43.4.3 Carbonation Depth

Core Number	Carbonation Depth (in.)
1-2	0.20
2-3	0.23

B.43.4.4 Acid-Soluble Chloride Content

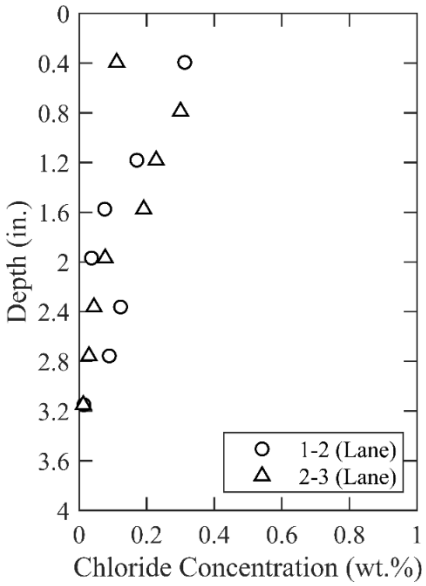

Figure 0.314. Chloride Content at Different Depth

B.43.4.5 Sorptivity

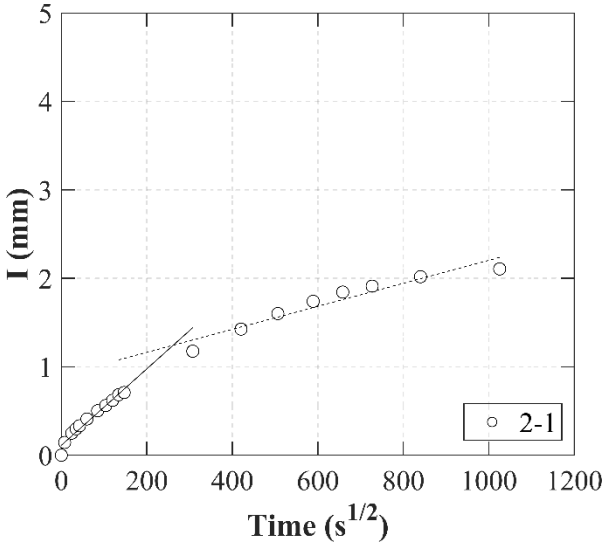

Figure 0.315. Absorption and Sorptivity of Core 2–1

Table B-151. Initial and Secondary Sorptivity Results

Core Number	Sorptivity	Results (mm/s$^{1/2}$)
Core 2–1	Initial Sorptivity	0.00432
	Secondary Sorptivity	0.00130

B.43.4.6 Electrochemical Impedance Spectroscopy

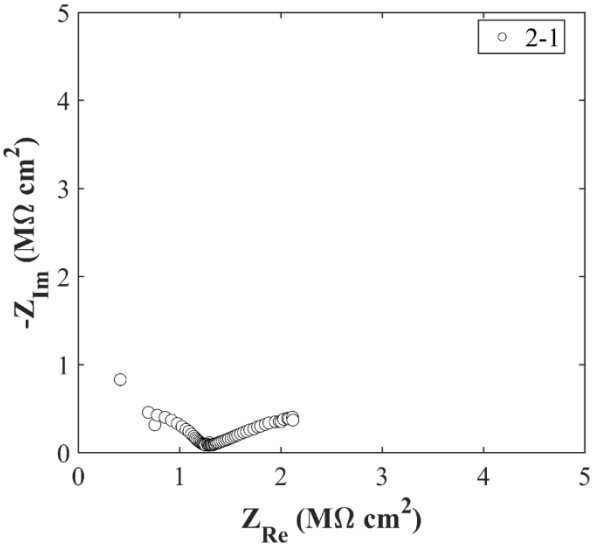

(a) Nyquist Diagram

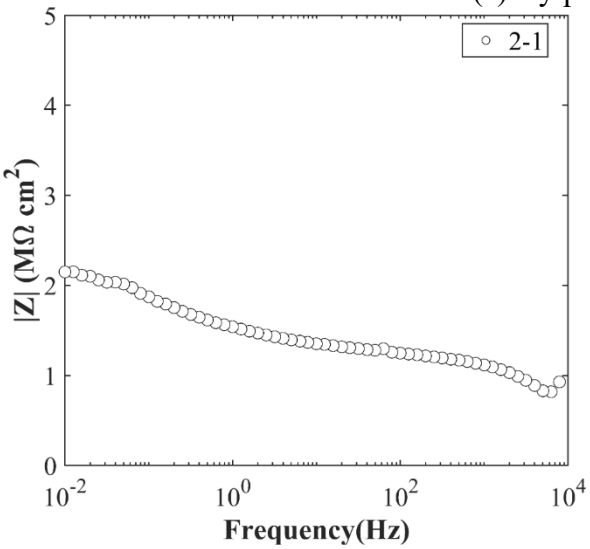

(b) Bode Plot of Impedance Modulus

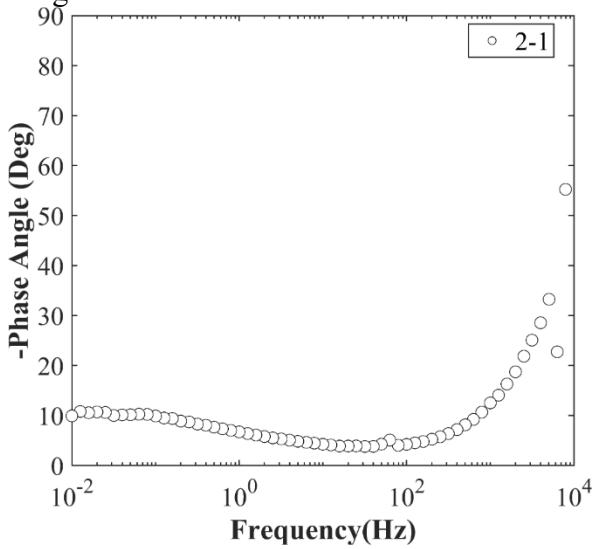

(c) Bode Plot of Impedance Phase

Figure 0.316. EIS Results: (a) Nyquist Diagram; (b) Bode Plot of Impedance Modulus; (c) Bode Plot of Impedance Phase

B.44 LBB-RC-03, IH 27 SB OVER 24TH ST.

- Bridge ID: 51520006711205 (Lubbock County)
- Built in 1992
- Mitigation methods: Linseed oil, ECR
- Observed CIP depth: Unknown
- Observed clear cover: 3.2 in.
- 2 spans, 13-concrete PS girder @ 8.5’ spacing with 3’ overhangs
- Inspected on June 17, 2021

Figure 0.317. Concrete Deck of the Bridge (source: google maps)

B.44.1 Observed Condition

The top surface of deck has longitudinal and transverse cracks.

B.44.2 NDE Results

Grid 1 was located on the NB lane and grid 2 was located on the NB shoulder lane of the span 1 of the bridge.

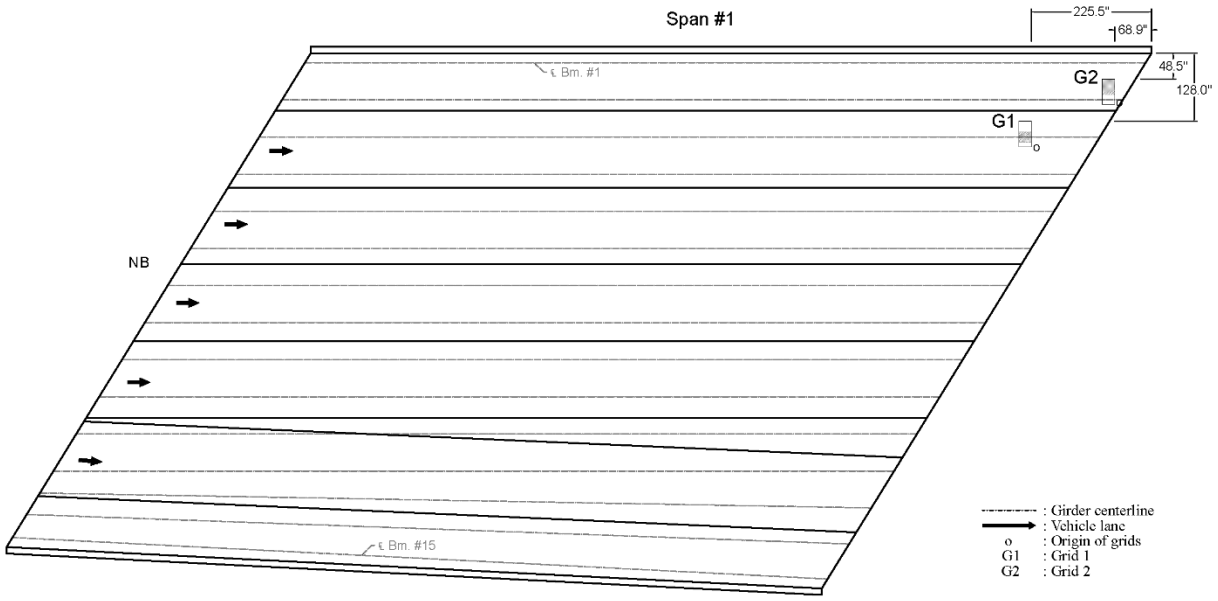

Figure 0.318. Plan View of the Bridge and Location of Grids

As shown in Figure 0.319 (a), a 0.004 in. wide transverse crack was observed on top of a girder on grid 1. Based on Figure A.3.3 (e), there is a high possibility of corrosion on grid 1 where the color is red. On grid 2, there were 0.006 in longitudinal crack and 0.008 in. wide transverse crack on top of a girder and propagating from a girder, respectively, as shown in Figure 0.320 (a).

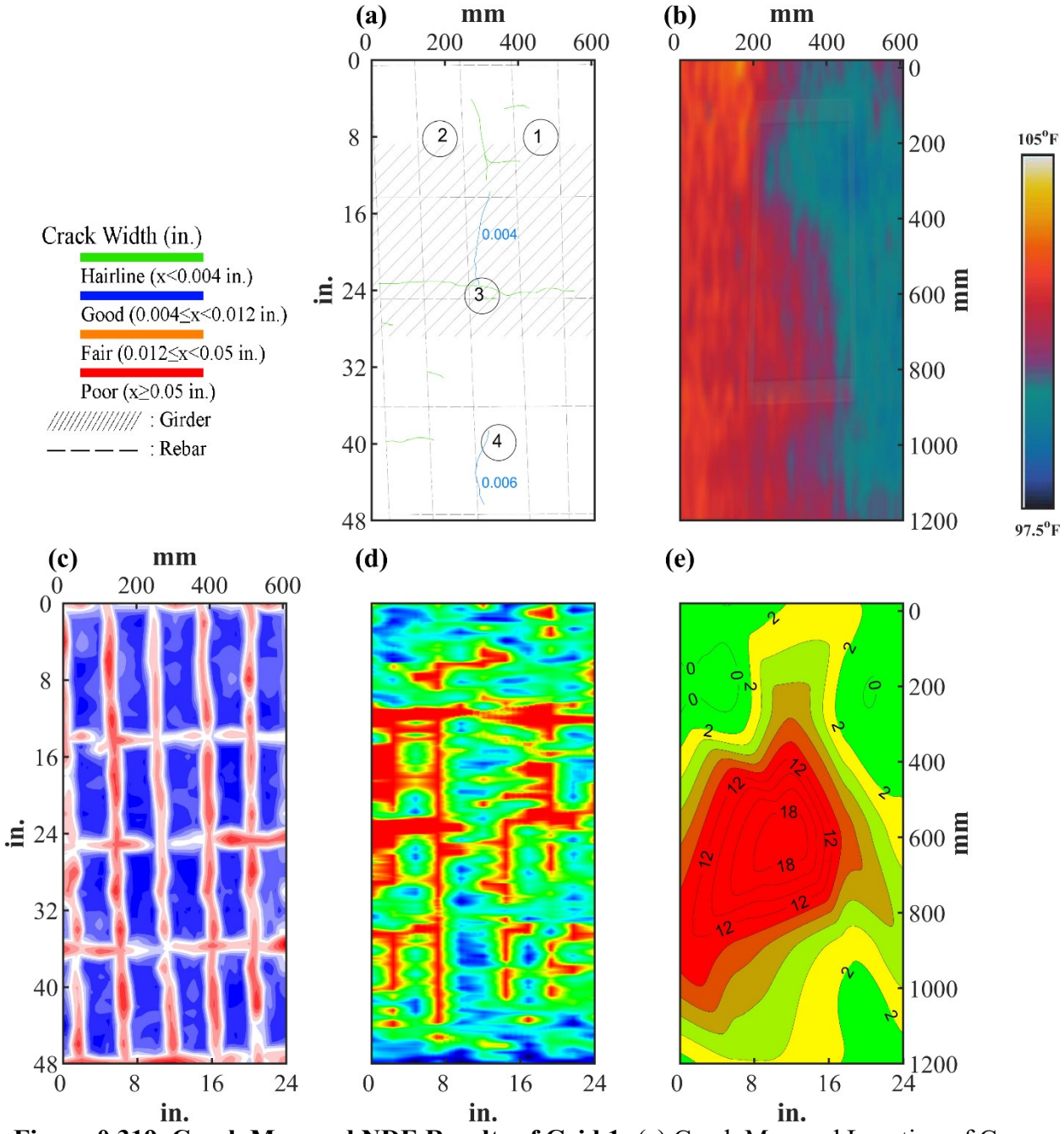

Figure 0.319. Crack Map and NDE Results of Grid 1: (a) Crack Map and Location of Cores; (b) Infrared Picture; (c) GPR C-scan at 3.0 in. to 4.1 in. Depth; (d) UST C-scan; (e) Corrosion Rate Map

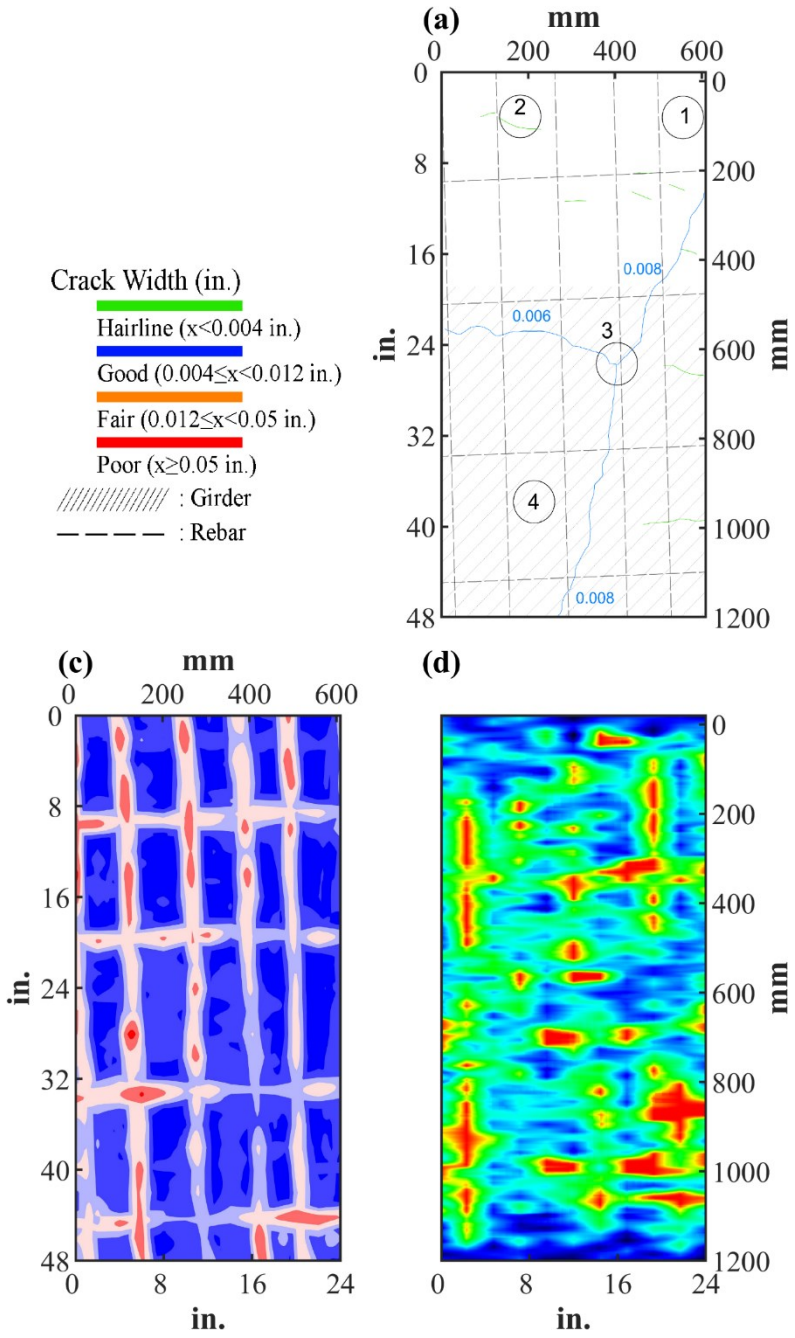

Figure 0.320. Crack Map and NDE Results of Grid 2: (a) Crack Map and Location of Cores; (c) GPR C-scan at 3.0 in. to 4.1 in. Depth; (d) UST C-scan

B.44.3 Concrete Cores

Table B-152. Detail Information of concrete cores

Core	dia. x height (in.)	Rebar depth (in.)	Rebar size (#)	Epoxy (Y/N)	Crack type	Crack width (in)	Notes
1-1	3.75 x 5.5	-	-	-	-	-	-
1-2	3.75 x 6.1	-	-	-	map	HL	-
1-3	3.75 x 3.9	3.2; 3.9	5; 4	Y; Y	map	HL	A void at 1.5 in. depth; a crack propagates from rebar through void
1-4	3.75 x 3.1	-	-	-	diagonal	0.006	A crack propagates along intersection of aggregates
2-1	3.75 x 5.5	-	-	-	-	-	-
2-2	3.75 x 5.7	-	-	-	-	-	-
2-3	3.75 x 5.9	3.4; 6.0	5; 5	Y; N	diagonal	0.006	A crack propagates from rebar
2-4	3.75 x 6.5	-	-	-	-	-	A void at 4.7 in. depth

Table B-153. Core Pictures

Core	Pictures of the Cores		
1-1			
1-2			

1-3			
1-4			
2-1			
2-2			
2-3			

2-4			

B.44.4 Laboratory Experiment Results

B.44.4.1 Resistivity

Core Number	Surface Resistivity (kΩ·m)	Bulk Resistivity (kΩ·m)
1-1	23.1	5.7
1-2	23.3	-
2-1	25.7	-
2-2	31.6	-
2-4	31.3	8.7

B.44.4.2 Ultrasonic Pulse Velocity

Core Number	Ultrasonic Pulse Velocity (m/s)
1-1	3468
1-2	3996
2-1	3469
2-2	3965
2-4	4233

B.44.4.3 Carbonation Depth

Core Number	Carbonation Depth (in.)
1-4	0.00
2-1	0.00

B.44.4.4 Acid-Soluble Chloride Content

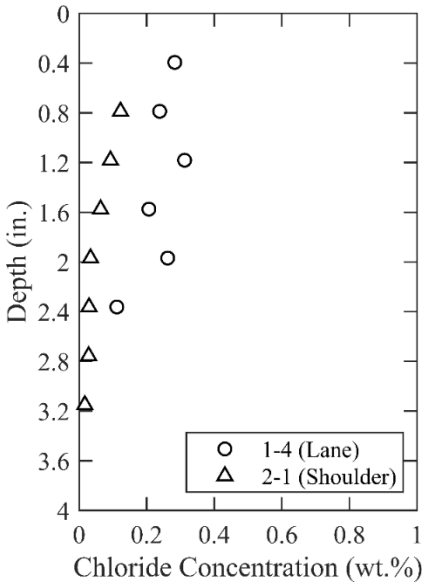

Figure 0.321. Chloride Content at Different Depth

B.44.4.5 Sorptivity

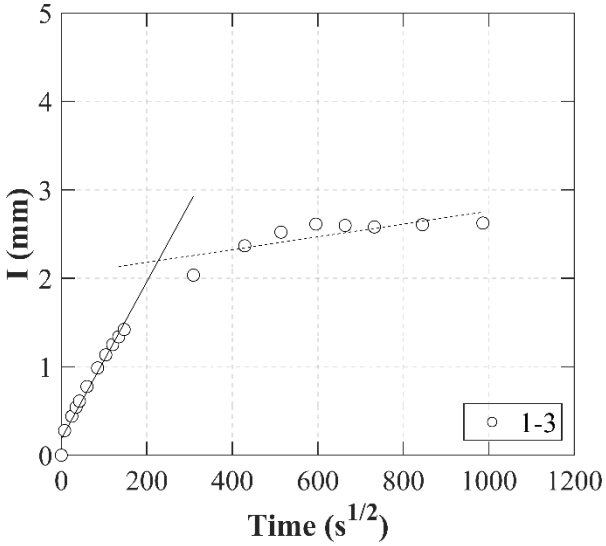

Figure 0.322. Absorption and Sorptivity of Core 1–3

Table B-154. Initial and Secondary Sorptivity Results

Core Number	Sorptivity	Results (mm/s$^{1/2}$)
Core 1–3	Initial Sorptivity	0.00888
	Secondary Sorptivity	0.00072

B.44.4.6 Knife Test

Core Number	Score	Picture
1-3	10	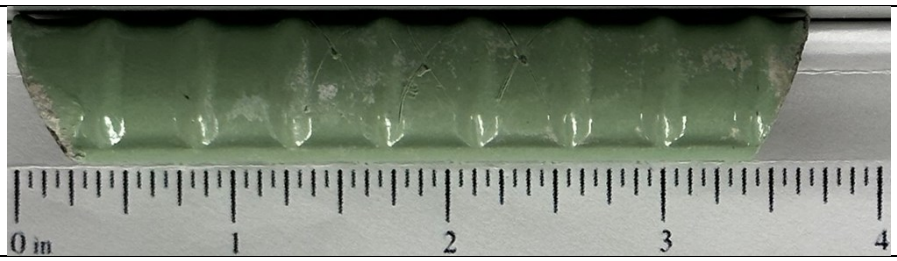

B.44.4.7 Electrochemical Impedance Spectroscopy

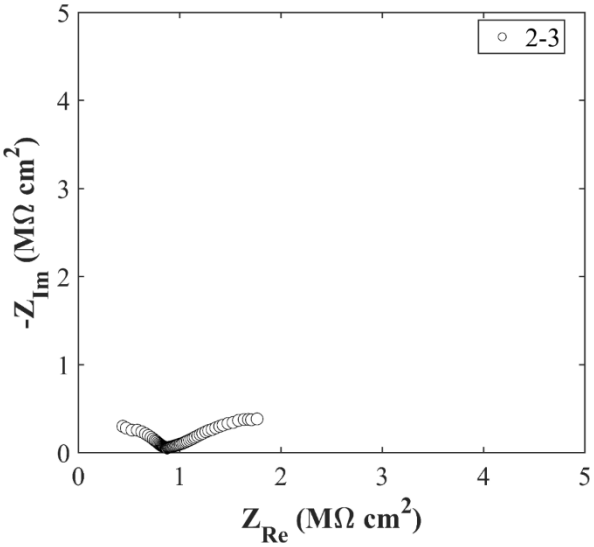

(a) Nyquist Diagram

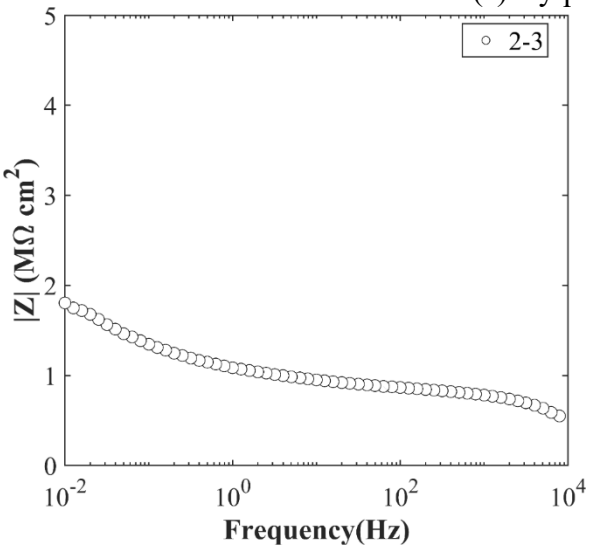

(b) Bode Plot of Impedance Modulus

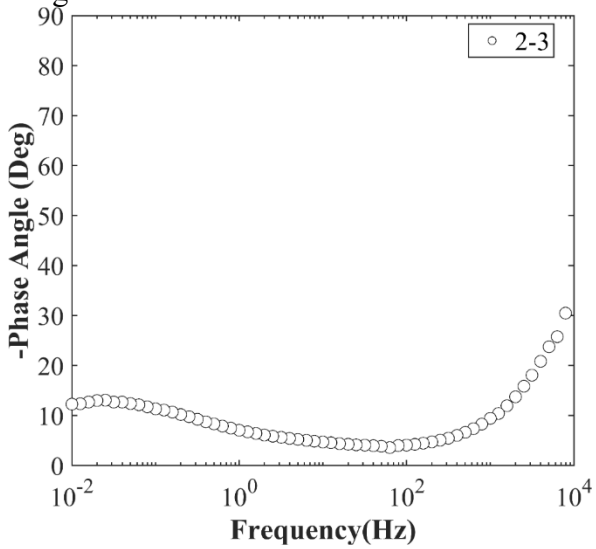

(c) Bode Plot of Impedance Phase

Figure 0.323. EIS Results: (a) Nyquist Diagram; (b) Bode Plot of Impedance Modulus; (c) Bode Plot of Impedance Phase

B.45 LBB-RC-04, S. LP 289 WB OVER IH 27

- Bridge ID: 51520006801085 (Lubbock County)
- Built 1988
- Mitigation methods: Linseed oil, ECR
- Observed CIP depth: N/A
- Observed clear cover: 2.6 in.
- 4 spans, 6-concrete PS girder @ 6.8’ with 3’ overhangs in span 1 and 4, 8-concrete PS girder @ 8.5’ with 3’ overhangs in span 2 and 3
- Inspected on June 17, 2021

Figure 0.324. Concrete Deck of the Bridge (source: google maps)

B.45.1 Observed Condition

The concrete deck has minor transverse cracks. There are several patches in span 1 deck. Concrete railing has minor horizontal cracks and impact scrapes. At the west end of the bridge, there are regions with asphalt patches, and some of these patches have exposed transverse rebar, with a spacing of 6 inches. At Abutment 1, between Beam 6 and Beam 5, there are signs of rusts on PMDF at several locations. Water stains are visible on the bottom of the bent cap ends and the bottom of the exterior girders.

B.45.2 NDE Results

Grid 1 was located on WB lane and grid 2 was located on WB shoulder lane of span 2 of the bridge.

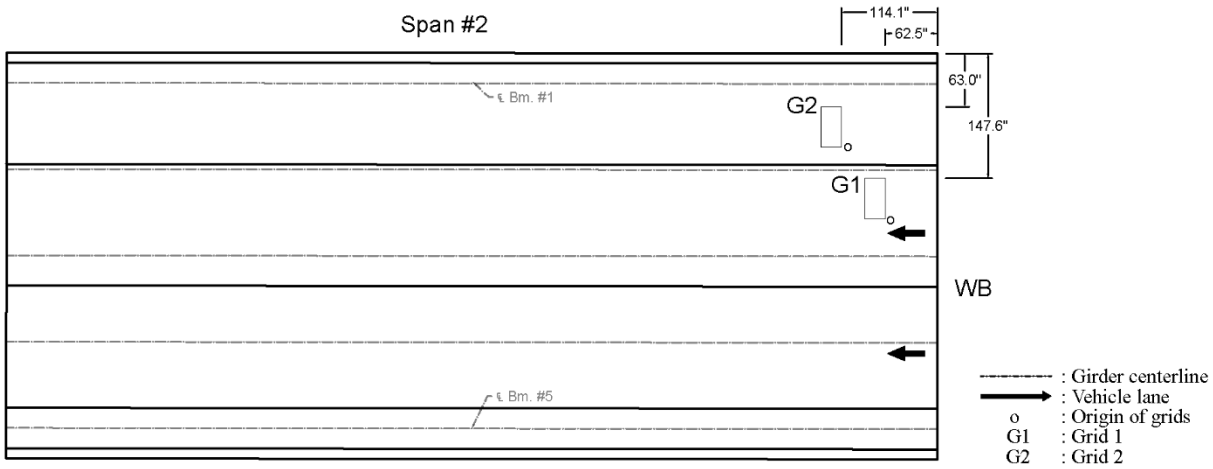

Figure 0.325. Plan View of the Bridge and Location of Grids

As shown in Figure 0.326 (a), 0.004 in. and 0.006 in. wide cracks were observed in grid 1 in longitudinal, transverse, and diagonal directions. Based on Figure A.4.3 (e), there is a low possibility of corrosion on grid 1. On grid 2, there was one 0.006 in. wide crack as shown in Figure 0.327 (a). It is possible that the crack is caused by panel joints.

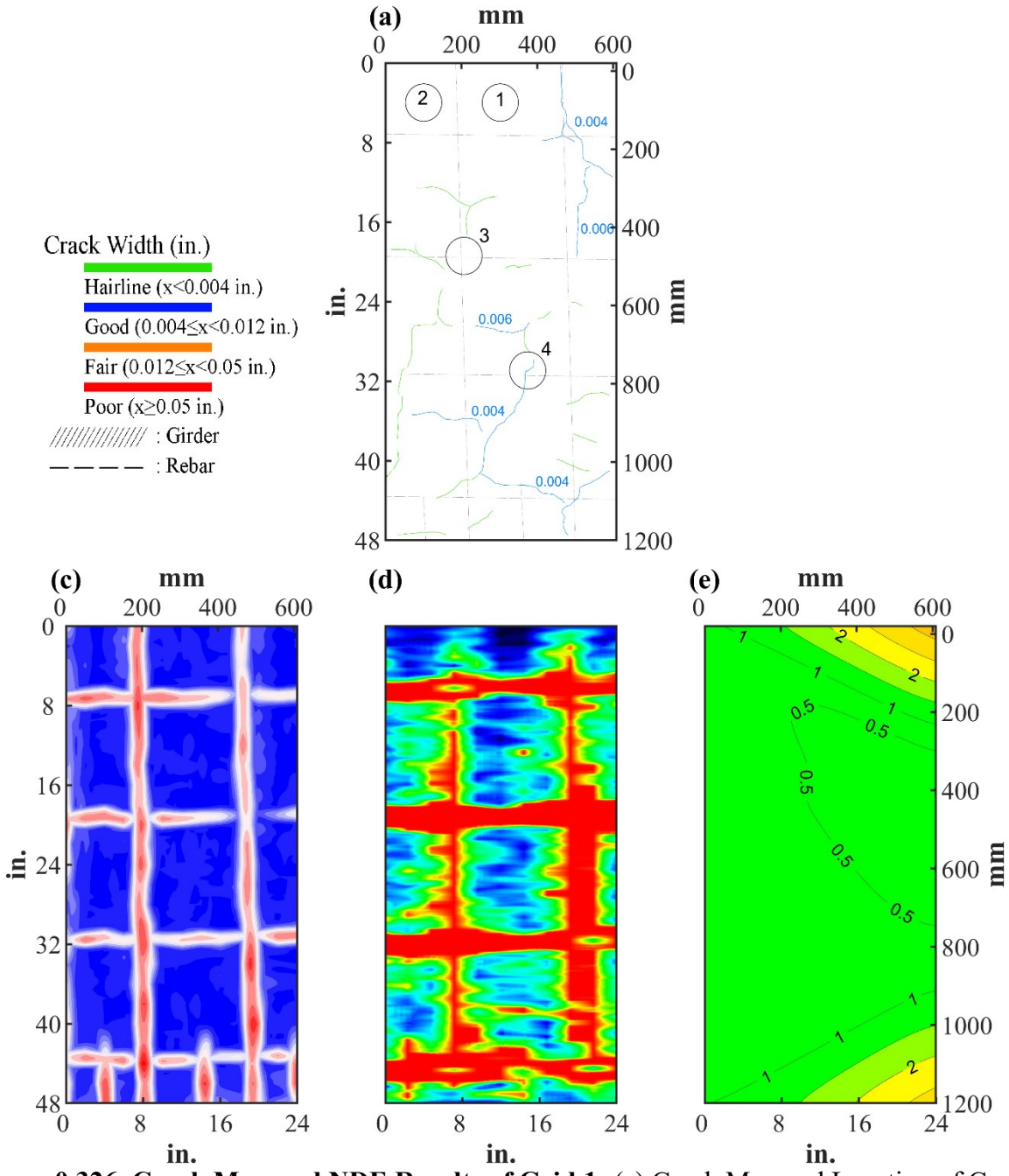

Figure 0.326. Crack Map and NDE Results of Grid 1: (a) Crack Map and Location of Cores; (c) GPR C-scan at 1.7 in. to 3.0 in. Depth; (d) UST C-scan; (e) Corrosion Rate Map

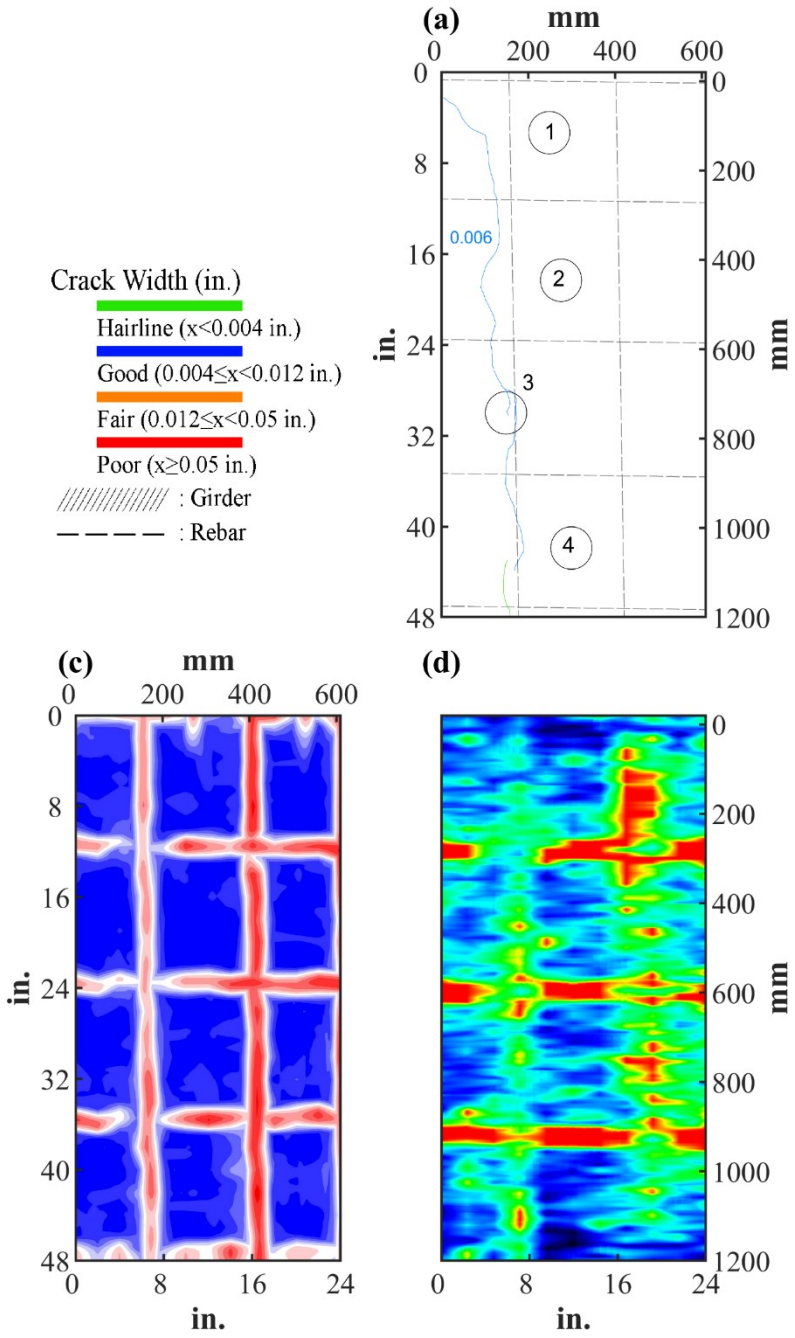

Figure 0.327. Crack Map and NDE Results of Grid 2: (a) Crack Map and Location of Cores; (c) GPR C-scan at 2.2 in. to 3.3 in. Depth; (d) UST C-scan

B.45.3 Concrete Cores

Table B-155. Detail Information of concrete cores

Core	dia. x height (in.)	Rebar depth (in.)	Rebar size (#)	Epoxy (Y/N)	Crack type	Crack width (in)	Notes
1-1	3.75 x 5.5	-	-	-	-	-	-
1-2	3.75 x 5.5	-	-	-	-	-	-
1-3	3.75 x 6.4	2.6; 3.3	5; 4	Y; Y	diagonal	HL	-
1-4	3.75 x 5.6	3.3	4	Y	transverse	0.004	-
2-1	3.75 x 5.1	5.3	5	Y	-	-	-
2-2	3.75 x 6.0	-	-	-	-	-	-
2-3	3.75 x 6.2	2.8; 5.7	5; 5	Y; Y	transverse	0.006	A crack propagates from rebar
2-4	3.75 x 5.6	-	-	-	-	-	-

Table B-156. Core Pictures

Core	Pictures of the Cores		
1-1			
1-2			

1-3			
1-4			
2-1			
2-2			
2-3			

2-4			

B.45.4 Laboratory Experiment Results

B.45.4.1 Resistivity

Core Number	Surface Resistivity (kΩ·m)	Bulk Resistivity (kΩ·m)
1-1	17.3	4.0
1-2	19.8	-
2-2	19.0	-
2-4	19.7	6.0

B.45.4.2 Ultrasonic Pulse Velocity

Core Number	Ultrasonic Pulse Velocity (m/s)
1-1	3248
1-2	3383
2-2	3863
2-4	3987

B.45.4.3 Carbonation Depth

Core Number	Carbonation Depth (in.)
1-3	0.00
2-1	0.20

B.45.4.4 Acid-Soluble Chloride Content

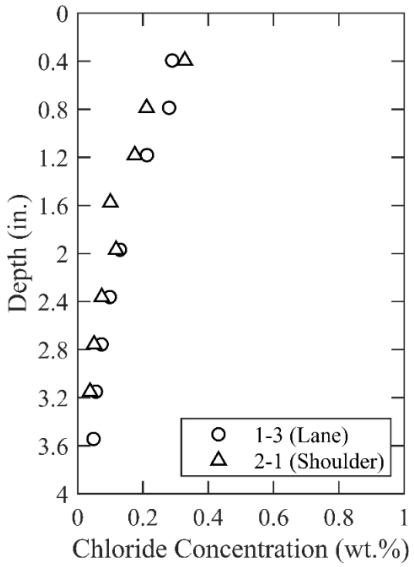

Figure 0.328. Chloride Content at Different Depth

B.45.4.5 Sorptivity

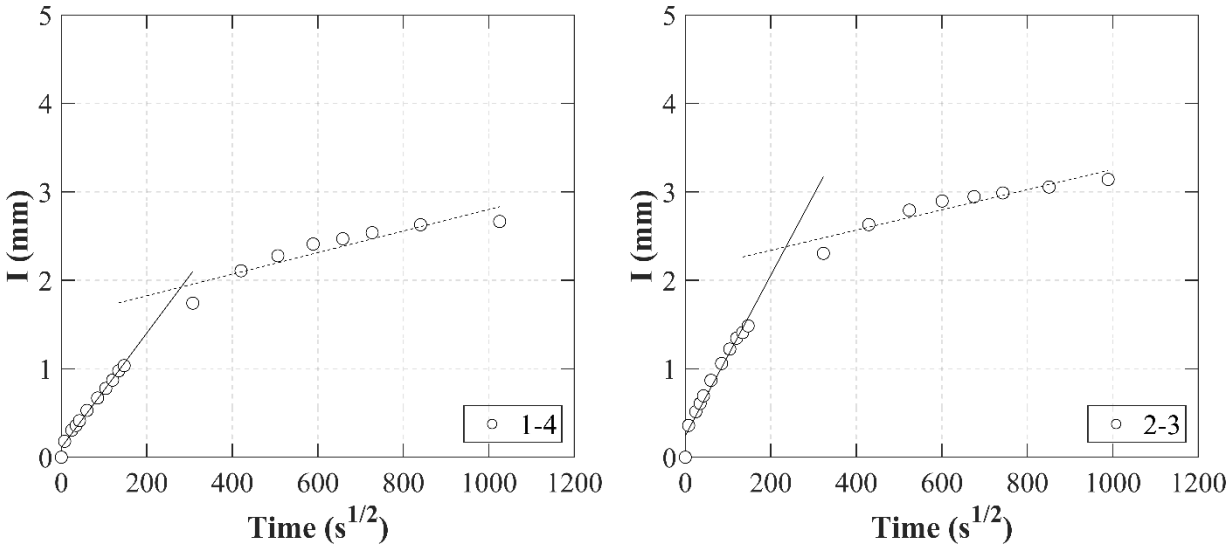

(a) Core 1–4 (b) Core 2–3

Figure 0.329. Absorption and Sorptivity of: (a) Core 1–4; (b) Core 2–3

Table B-157. Initial and Secondary Sorptivity Results

Core Number	Sorptivity	Results (mm/s$^{1/2}$)
Core 1–4	Initial Sorptivity	0.00647
	Secondary Sorptivity	0.00122
Core 2–3	Initial Sorptivity	0.00906
	Secondary Sorptivity	0.00114

B.45.4.6 Knife Test

Core Number	Score	Picture
2-3	4	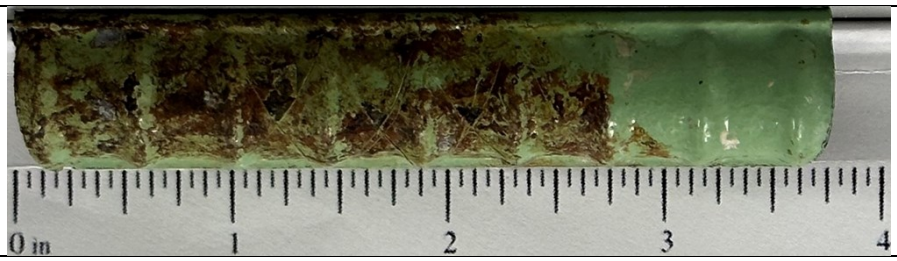

B.45.4.7 Electrochemical Impedance Spectroscopy

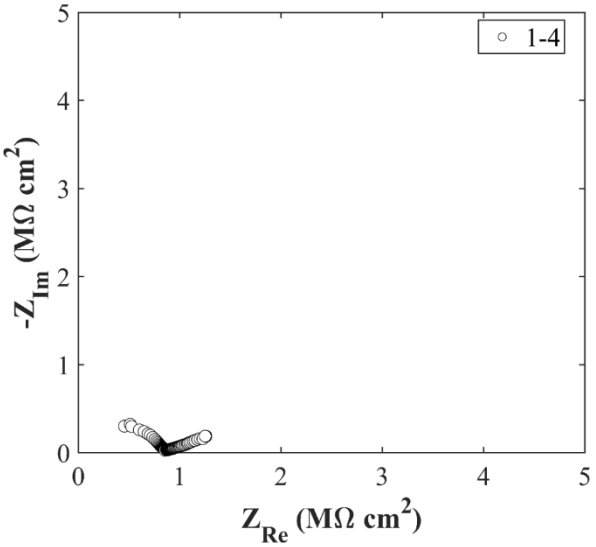

(a) Nyquist Diagram

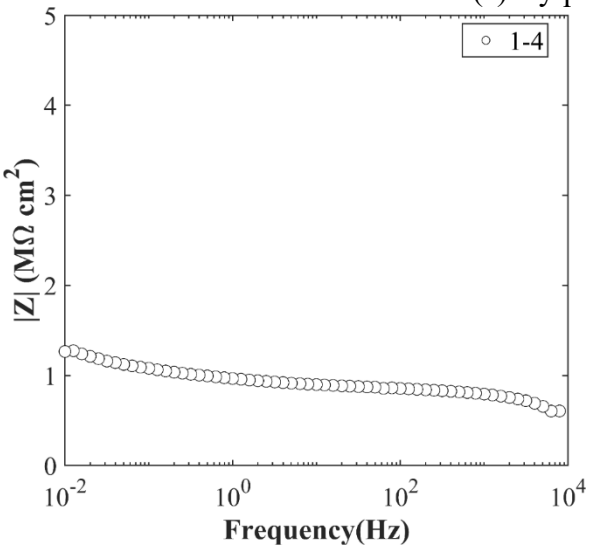

(b) Bode Plot of Impedance Modulus

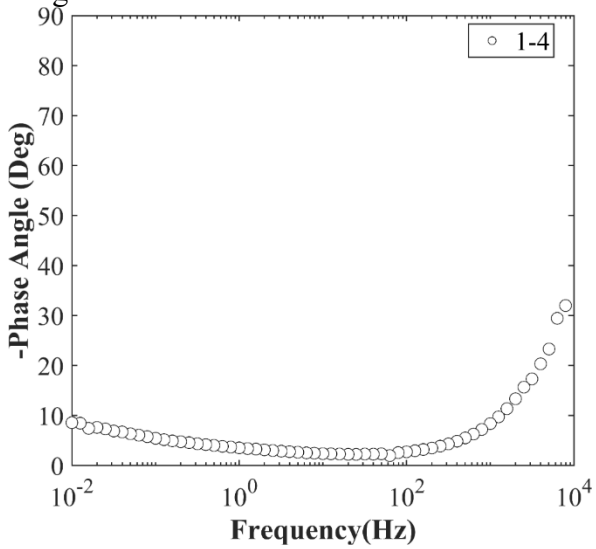

(c) Bode Plot of Impedance Phase

Figure 0.330. EIS Results: (a) Nyquist Diagram; (b) Bode Plot of Impedance Modulus; (c) Bode Plot of Impedance Phase

B.46 LBB-RC-05, LP 289 NB OVER SH 114

- Bridge ID: 51520013005208 (Lubbock County)
- Built in 2010
- Mitigation methods: HPC with macro fibers, ECR
- Observed CIP depth: N/A
- Observed clear cover: 2.6 in.
- 3 spans, 7-concrete PS girder @ 8.6’ with 3’ overhangs in span 1 and 3, 9-concrete PS girder @ 6.44’ with 3’ overhangs in span 2
- Inspected on June 18, 2021

Figure 0.331 Concrete Deck of the Bridge (source: google maps)

B.46.1 Observed Condition

There are isolated minor longitudinal and transverse cracks on the top surface of deck. The bridge has PCP with PMDF, featuring thickened end slabs. The overhang on the west side exhibited more cracks and efflorescence compared to the overhang on the east side of the structure.

B.46.2 NDE Results

Grid 1 was located on the NB lane and grid 2 was located on the NB shoulder lane of span 2 of the bridge.

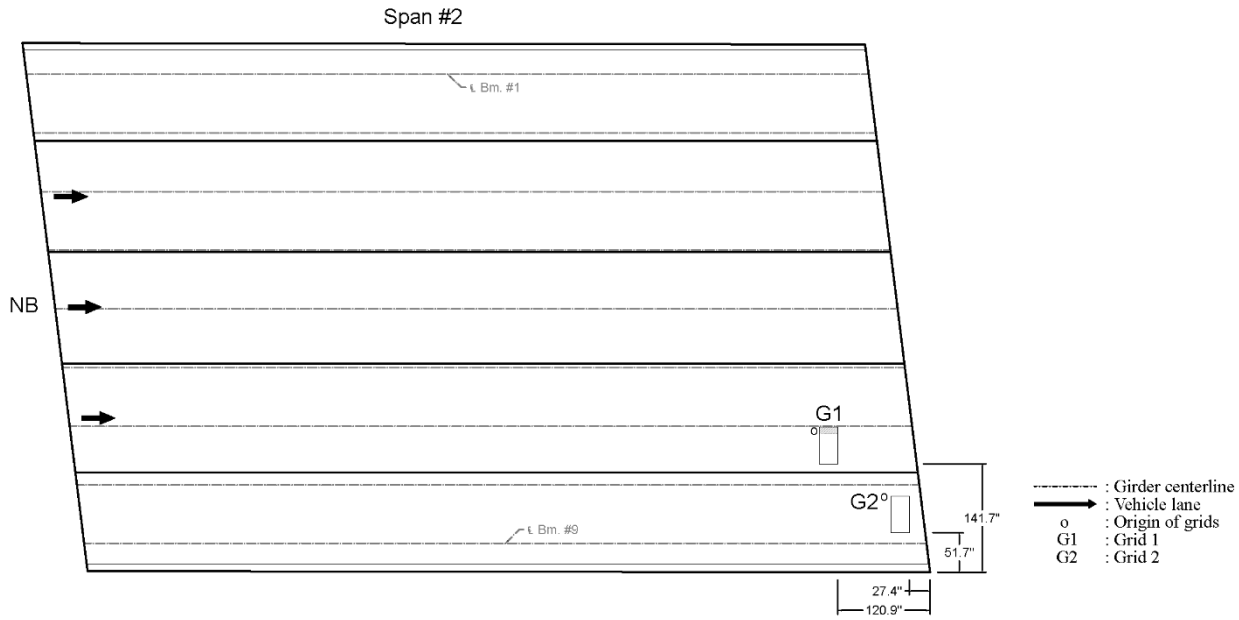

Figure 0.332. Plan View of the Bridge and Location of Grids

As shown in Figure 0.333 (a), a 0.008 in. wide longitudinal crack was located on top of a girder and 0.004 in., 0.01 in., and 0.024 in. cracks were propagating from a girder. Based on Figure A.5.3 (e), there is a low possibility of corrosion on grid 1. On grid 2, 0.004 in. wide cracks were in longitudinal and transverse direction, and 0.006 in. wide crack was in diagonal direction as shown in Figure 0.334 (a).

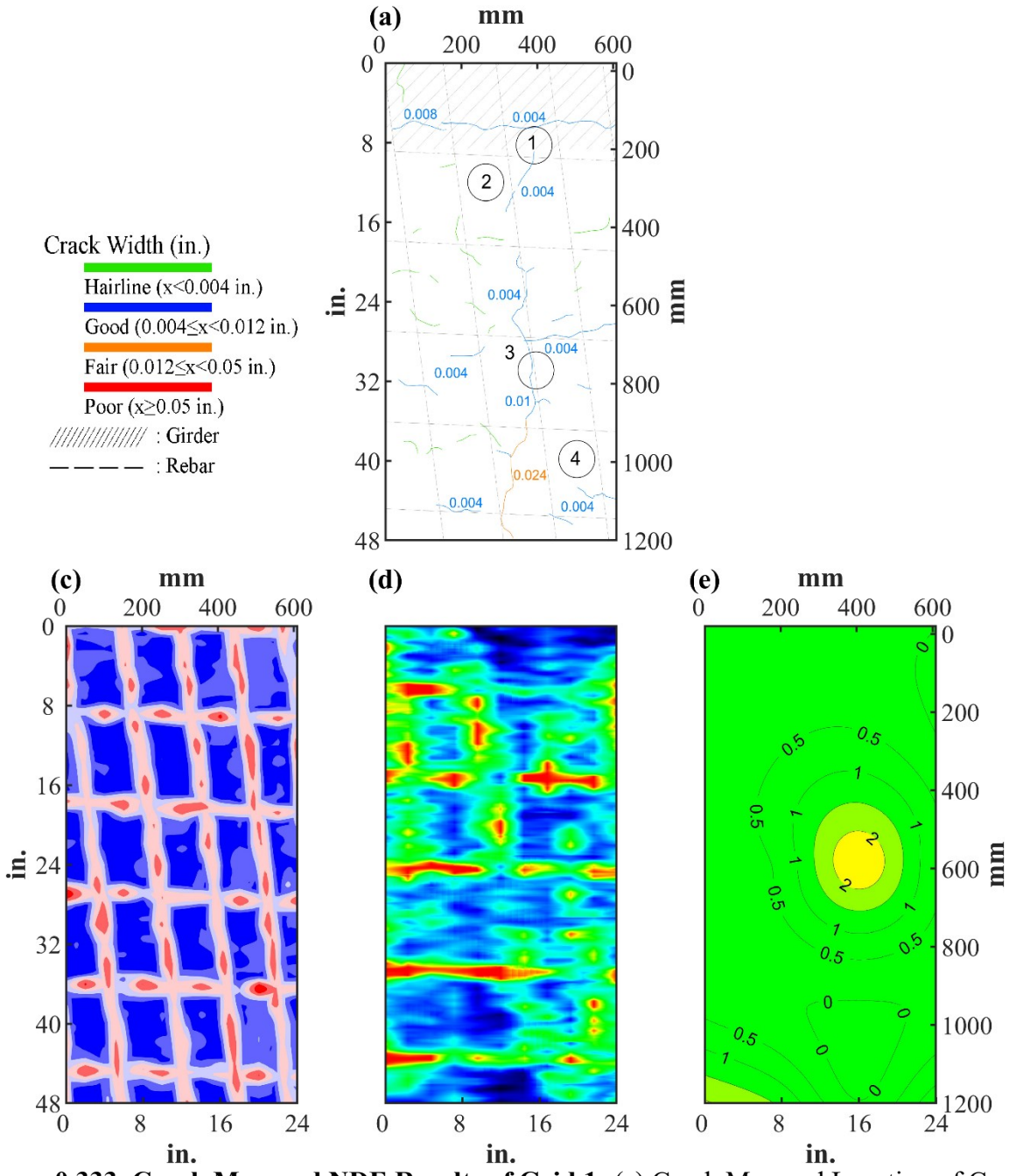

Figure 0.333. Crack Map and NDE Results of Grid 1: (a) Crack Map and Location of Cores; (c) GPR C-scan at 2.05 in. to 3.15 in. Depth; (d) UST C-scan; (e) Corrosion Rate Map

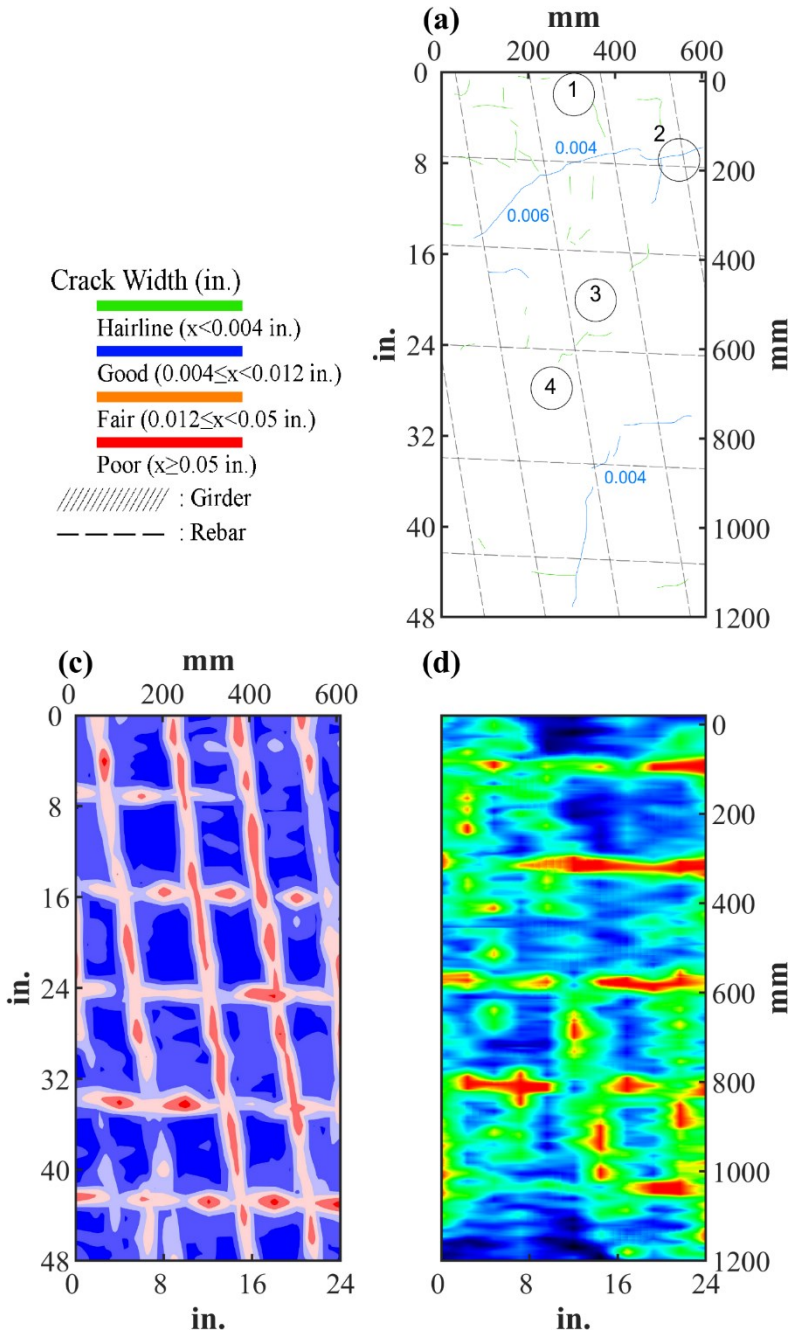

Figure 0.334. Crack Map and NDE Results of Grid 2: (a) Crack Map and Location of Cores; (c) GPR C-scan at 3.4 in. to 4.5 in. Depth; (d) UST C-scan

B.46.3 Concrete Cores

Table B-158. Detail Information of concrete cores

Core	dia. x height (in.)	Rebar depth (in.)	Rebar size (#)	Epoxy (Y/N)	Crack type	Crack width (in)	Notes
1-1	3.75 x 6.1	3.3	4	Y	transverse	0.1	A crack propagates from panel joint
1-2	3.75 x 5.7	-	-	-	-	-	-
1-3	3.75 x 5.5	2.6	5	Y	transverse	0.2	-
1-4	3.75 x 5.5	-	-	-	map	HL	-
2-1	3.75 x 5.9	-	-	-	-	-	-
2-2	3.75 x 6.2	4.0; 4.7	5; 4	Y; Y	longitudinal	0.25	-
2-3	3.75 x 5.2	-	-	-	-	-	-
2-4	3.75 x 6.0	-	-	-	-	-	-

Table B-159. Core Pictures

Core	Pictures of the Cores		
1-1			
1-2			

1-3			
1-4			
2-1			
2-2			
2-3	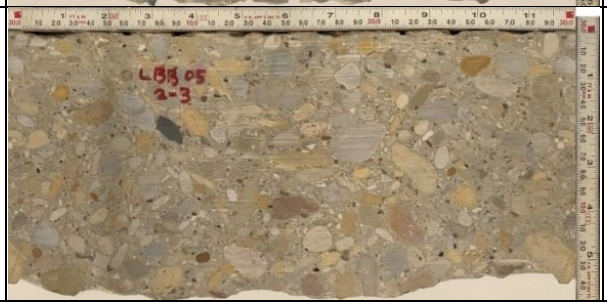		

2-4			

B.46.4 Laboratory Experiment Results

B.46.4.1 Resistivity

Core Number	Surface Resistivity (kΩ·m)	Bulk Resistivity (kΩ·m)
1-2	129.8	35.7
1-4	108.9	-
2-1	126.2	31.2
2-3	102.8	-
2-4	135.9	-

B.46.4.2 Ultrasonic Pulse Velocity

Core Number	Ultrasonic Pulse Velocity (m/s)
1-2	4290
1-4	4175
2-1	4179
2-3	4219
2-4	4214

B.46.4.3 Carbonation Depth

Core Number	Carbonation Depth (in.)
1-1	0.35
2-3	0.00

B.46.4.4 Acid-Soluble Chloride Content

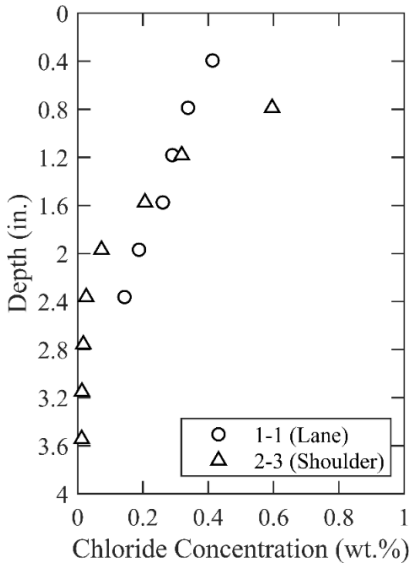

Figure 0.335. Chloride Content at Different Depth

B.46.4.5 Sorptivity

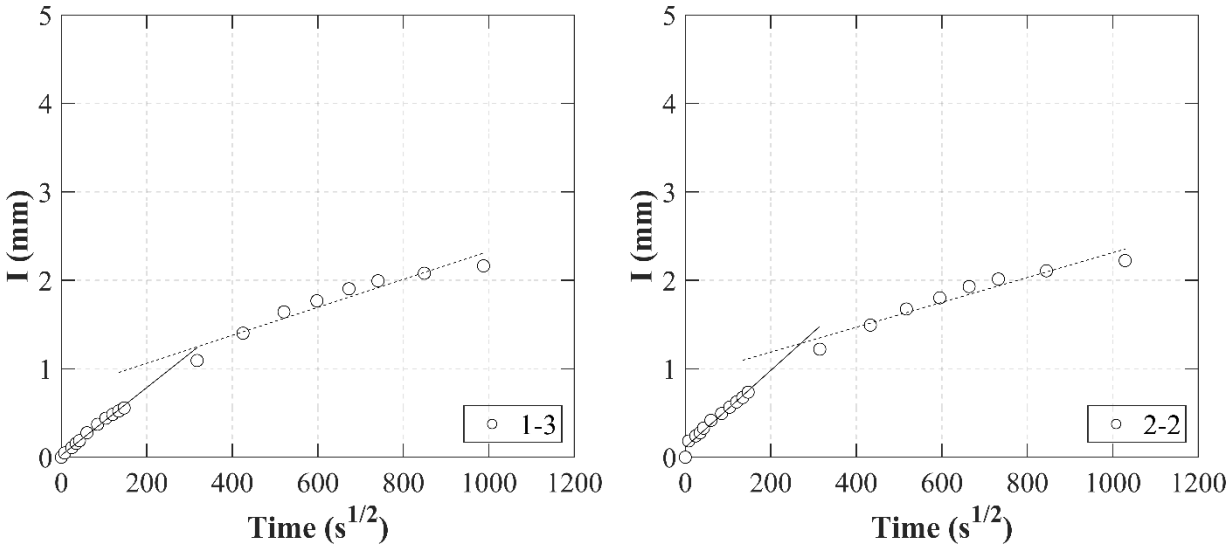

(a) Core 1–3 (b) Core 2–2

Figure 0.336. Absorption and Sorptivity of: (a) Core 1–3; (b) Core 2–2

Table B-160. Initial and Secondary Sorptivity Results

Core Number	Sorptivity	Results (mm/s$^{1/2}$)
Core 1–3	Initial Sorptivity	0.00383
	Secondary Sorptivity	0.00158
Core 2–2	Initial Sorptivity	0.00434
	Secondary Sorptivity	0.00141

B.46.4.6 Knife Test

Core Number	Score	Picture
2-2	2	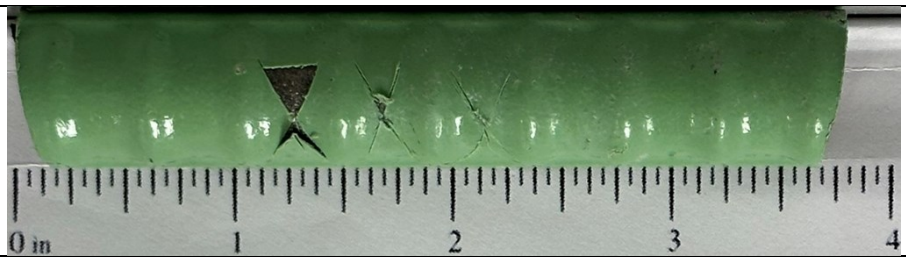

B.46.4.7 Electrochemical Impedance Spectroscopy

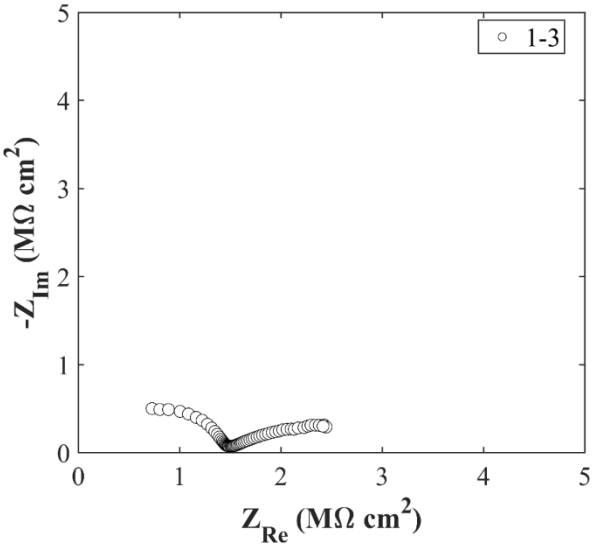

(a) Nyquist Diagram

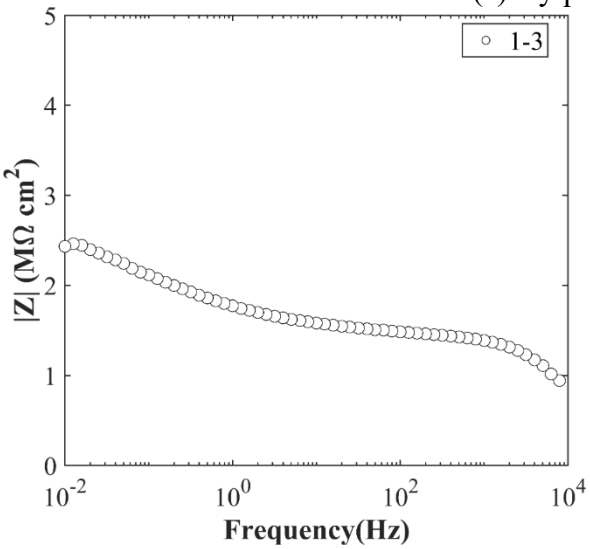

(b) Bode Plot of Impedance Modulus

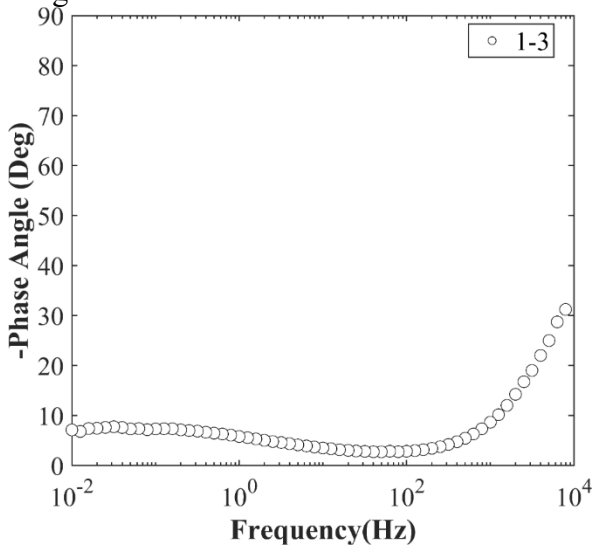

(c) Bode Plot of Impedance Phase

Figure 0.337. EIS Results: (a) Nyquist Diagram; (b) Bode Plot of Impedance Modulus; (c) Bode Plot of Impedance Phase

B.47 LBB-RC-06, US 62/82 EB OVER 82ND ST.

- Bridge ID: 51520038001016 (Lubbock County)
- Built in 1999
- Mitigation methods: HPC with macro fibers, ECR
- Observed CIP depth: Unknown
- Observed clear cover: 2.9 in.
- 3 spans, 8-concrete PS girder @ 5.143’ with 3’ overhangs
- Inspected on June 20, 2021

Figure 0.338. Concrete Deck of the Bridge (source: google maps)

B.47.1 Observed Condition

The top surface of deck has transverse, longitudinal, and diagonal cracks. There are minor hairline vertical, horizontal cracks, and impact scrapes at concrete railings. As shown in Figure 0.339 (a), spalling on the deck and corroded rebar was observed, and spalling on the girder end was also observed as shown in Figure 0.339 (b).

(a)

(b)

Figure 0.339. Deteriorations on the Bridge: (a) spalling on deck; (b) Exposed rebar on the girder end

B.47.2 NDE Results

Grid 1 was located on EB lane, and grid 2 was located on the EB shoulder of span 1 of the bridge.

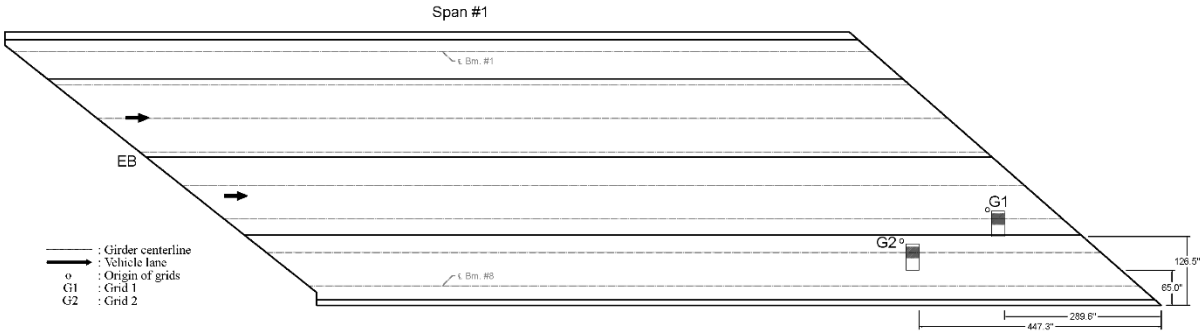

Figure 0.340. Plan View of the Bridge and Location of Grids

As shown in Figure 0.341 (a), there was a widespread of hairline cracks and narrow cracks ranging from 0.004 in. to 0.008 in. wide. Based on Figure A.6.3 (e), there was a high possibility of corrosion at the upper left corner of grid 1, but all other area had almost zero to no risk of corrosion. On grid 2, only hairline cracks were observed as shown in Figure 0.342 (a).

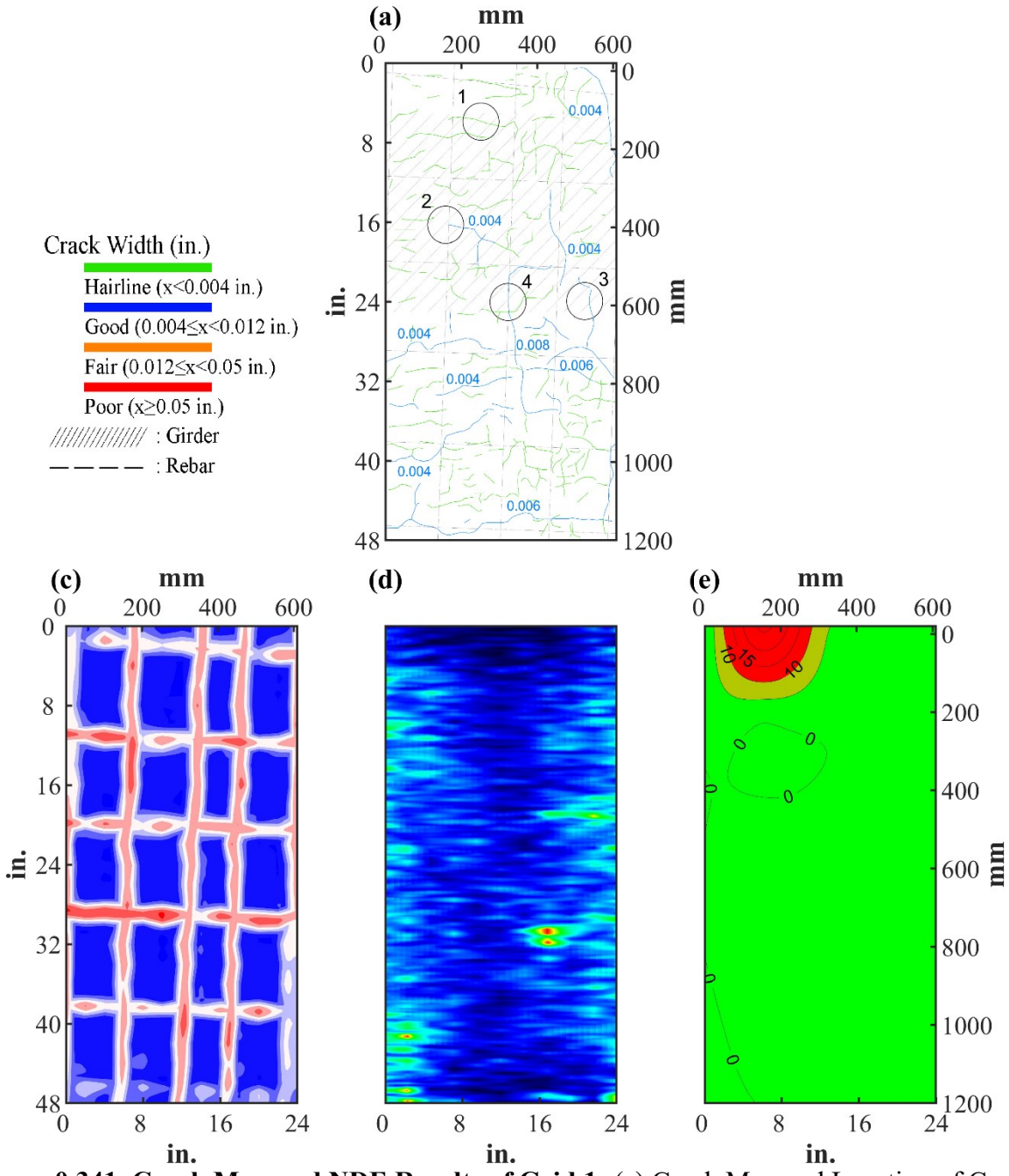

Figure 0.341. Crack Map and NDE Results of Grid 1: (a) Crack Map and Location of Cores; (c) GPR C-scan at 2.7 in. to 3.8 in. Depth; (d) UST C-scan; (e) Corrosion Rate Map

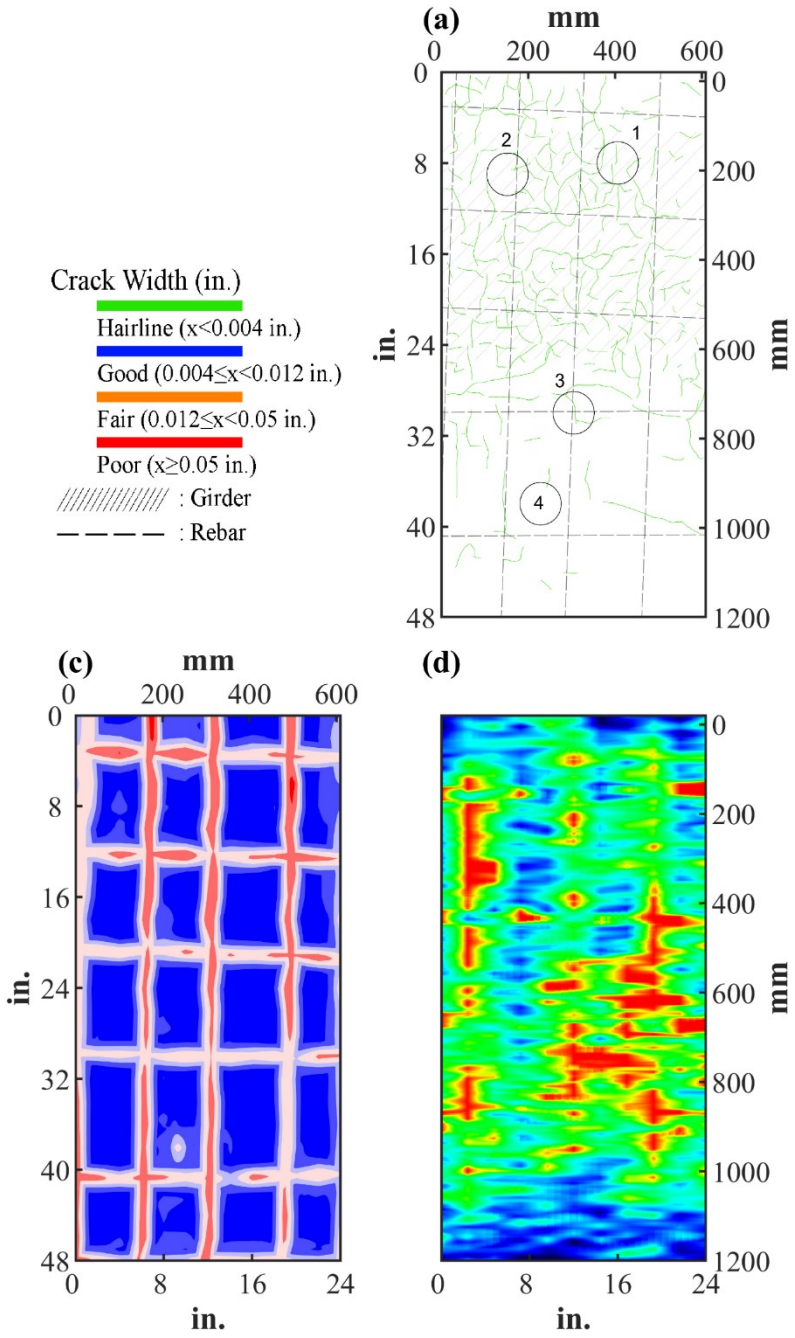

Figure 0.342. Crack Map and NDE Results of Grid 2: (a) Crack Map and Location of Cores; (c) GPR C-scan at 2.85 in. to 3.95 in. Depth; (d) UST C-scan

B.47.3 Concrete Cores

Table B-161. Detail Information of concrete cores

Core	dia. x height (in.)	Rebar depth (in.)	Rebar size (#)	Epoxy (Y/N)	Crack type	Crack width (in)	Notes
1-1	3.75 x 5.9	-	-	-	longitudinal	HL	-
1-2	3.75 x 5.9	2.9	5	Y	longitudinal	0.004	-
1-3	3.75 x 5.9	-	-	-	transverse	0.004	-
1-4	3.75 x 6.1	2.9	5	Y	transverse	0.008	-
2-1	3.75 x 6.5	-	-	-	diagonal	HL	Delamination between CIP and PCP
2-2	3.75 x 4.1	2.9	5	Y	diagonal	HL	Delamination between CIP and PCP
2-3	3.75 x 6.1	3.1; 3.7	5; 4	Y; Y	longitudinal	HL	-
2-4	3.75 x 6.0	-	-	-	-	-	Delamination between CIP and PCP

Table B-162. Core Pictures

Core	Pictures of the Cores		
1-1			
1-2			

1-3			
1-4			
2-1			
2-2			
2-3			
2-4			

B.47.4 Laboratory Experiment Results

B.47.4.1 Resistivity

Core Number	Surface Resistivity (kΩ·m)	Bulk Resistivity (kΩ·m)
1-1	19.0	-
1-3	13.3	3.7
2-1	20.5	-
2-4	-	3.4

B.47.4.2 Ultrasonic Pulse Velocity

Core Number	Ultrasonic Pulse Velocity (m/s)
1-1	3745
1-3	3306
2-1	3750
2-4	3437

B.47.4.3 Carbonation Depth

Core Number	Carbonation Depth (in.)
1-2	0.37
2-3	0.00

B.47.4.4 Acid-Soluble Chloride Content

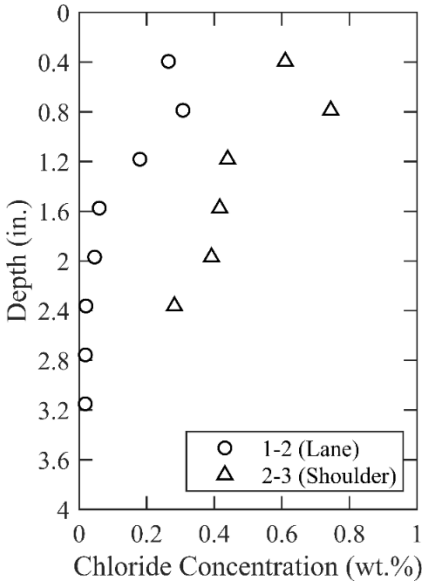

Figure 0.343. Chloride Content at Different Depth

B.47.4.5 Sorptivity

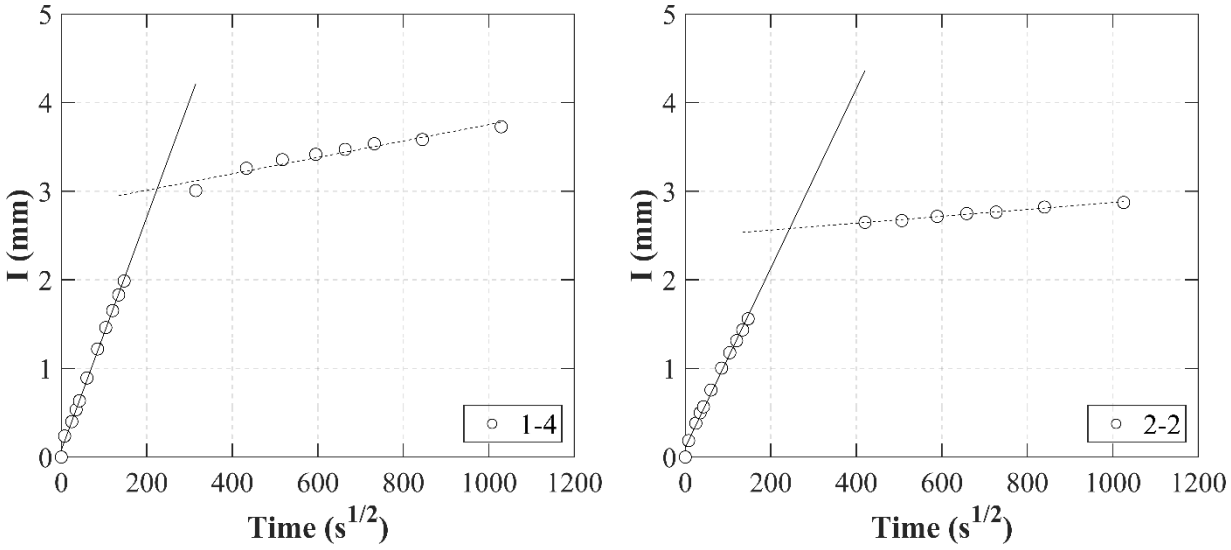

(a) Core 1–4 (b) Core 2–2

Figure 0.344. Absorption and Sorptivity of: (a) Core 1–4; (b) Core 2–2

Table B-163. Initial and Secondary Sorptivity Results

Core Number	Sorptivity	Results (mm/s$^{1/2}$)
Core 1–4	Initial Sorptivity	0.0131
	Secondary Sorptivity	0.00092
Core 2–2	Initial Sorptivity	0.0101
	Secondary Sorptivity	0.00039

B.47.4.6 Knife Test

Core Number	Score	Picture
1-4	10	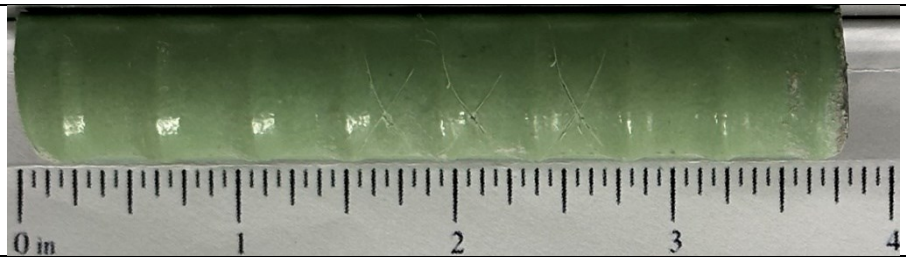

B.47.4.7 Electrochemical Impedance Spectroscopy

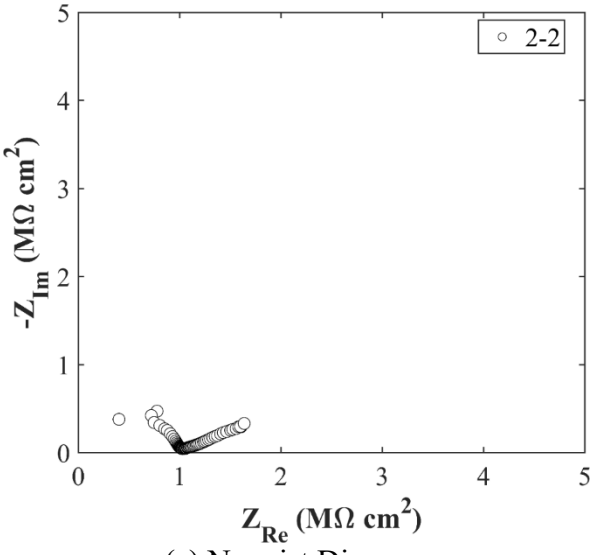

(a) Nyquist Diagram

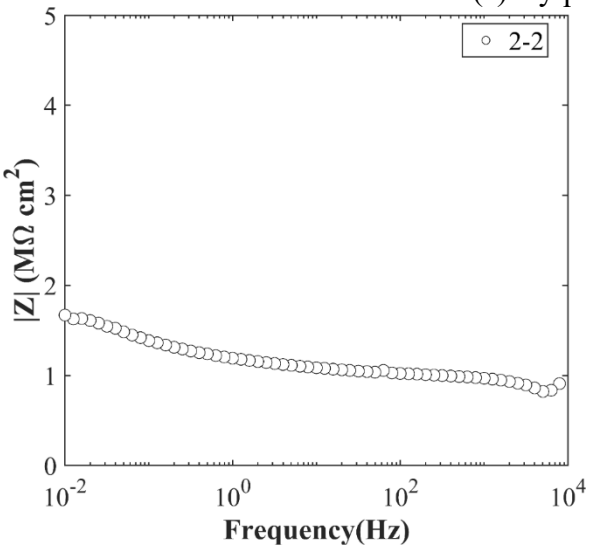

(b) Bode Plot of Impedance Modulus

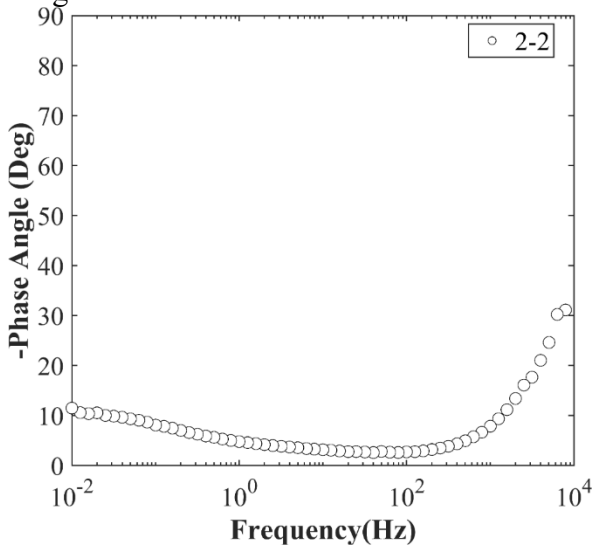

(c) Bode Plot of Impedance Phase

Figure 0.345. EIS Results: (a) Nyquist Diagram; (b) Bode Plot of Impedance Modulus; (c) Bode Plot of Impedance Phase

B.48 LBB-RC-07, W LP 289 SB OVER US 62/82 FR RD.

- Bridge ID: 51520038001096 (Lubbock County)
- Built 2006
- Mitigation methods: HPC with macro fibers, linseed oil, ECR
- Observed CIP depth: N/A
- Observed clear cover: 1.6 in.
- 7 spans, 10-concrete PS girder with varying spacing and 3’ overhangs
- Inspected on June 21, 2021

Figure 0.346. Concrete Deck of the Bridge (source: google maps)

B.48.1 Observed Condition

The west concrete railing has minor hairline vertical cracks. There is rust at the permanent metal deck. The deck displayed longitudinal cracks on the vehicle lane, and occasional transverse cracks. In some areas, there were more longitudinal cracks than in most places. The exterior backwall of Abutment 8 exhibits diagonal cracks (measuring 0.006 in.) and horizontal cracks at the top and bottom of the wall. The interior backwall also has diagonal cracks. PMDF is present. There are no apparent cracks in the overhang, but the paint is peeling on the exterior side. Between the girders, there is water stain at joints, and rust is evident, especially on the exterior side, where wide cracks were visible.

B.48.2 NDE Results

Grid 1 located on the SB lane and grid 2 was located on the SB shoulder lane of the span 7 of the bridge.

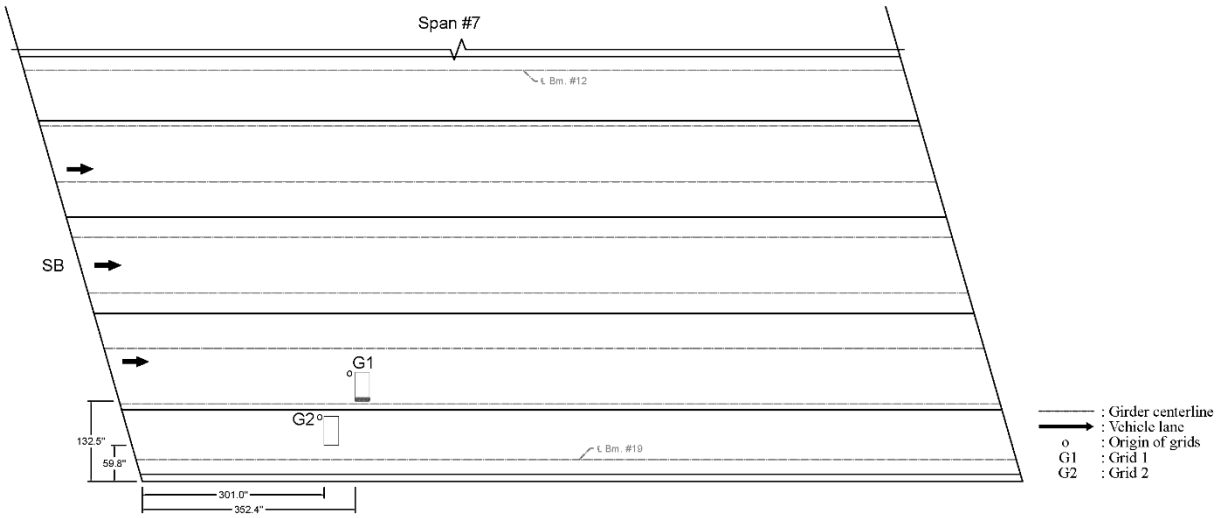

Figure 0.347. Plan View of the Bridge and Location of Grids

As shown in Figure 0.348 (a), hairline cracks were mostly observed from grid 1 with one 0.004 in. wide longitudinal crack along a girder. Based on Figure A.7.3 (e), there was low possibility of corrosion on grid 1. On grid 2, no cracks were observed as shown in Figure 0.349 (a).

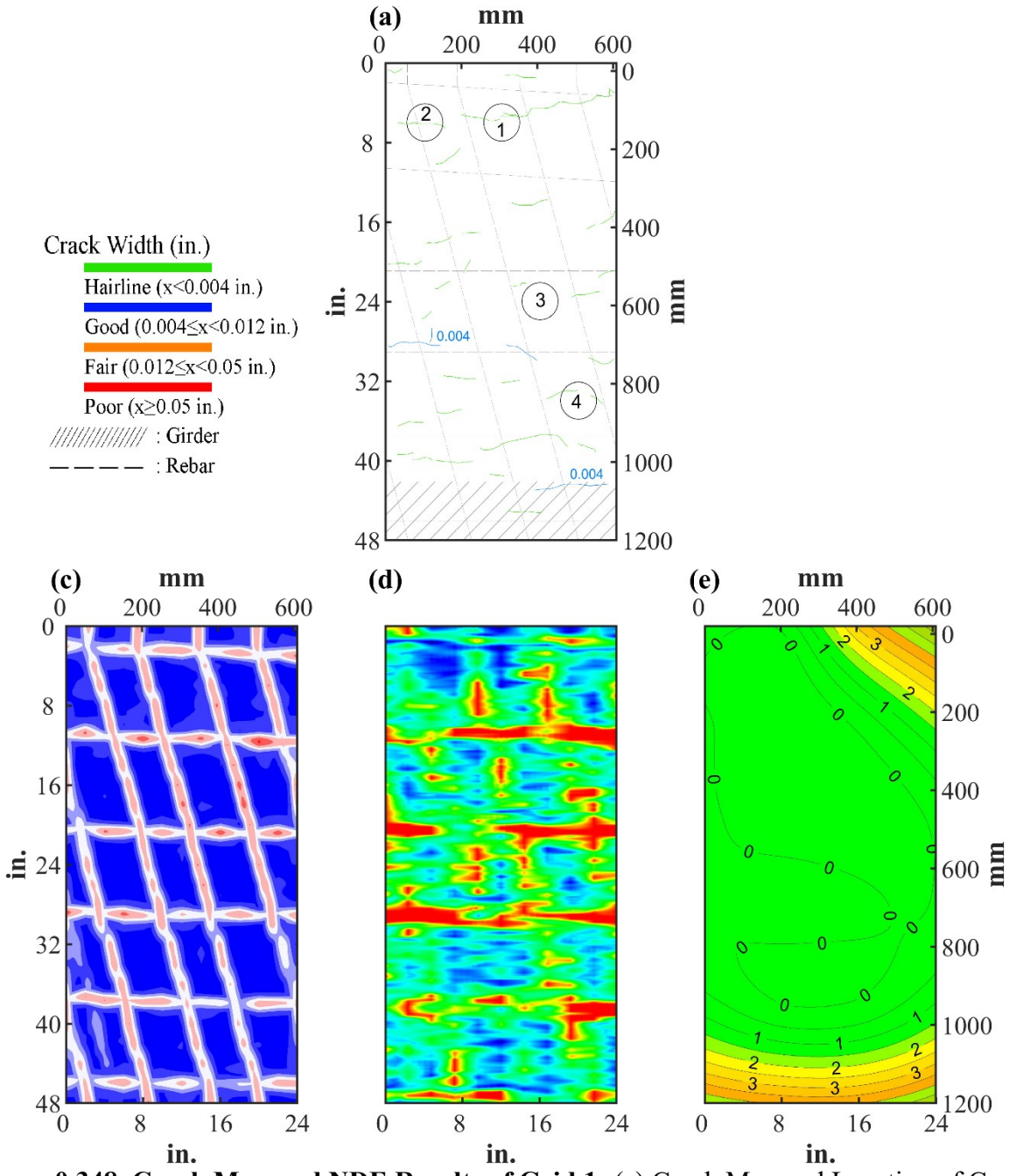

Figure 0.348. Crack Map and NDE Results of Grid 1: (a) Crack Map and Location of Cores; (c) GPR C-scan at 1.8 in. to 2.9 in. Depth; (d) UST C-scan; (e) Corrosion Rate Map

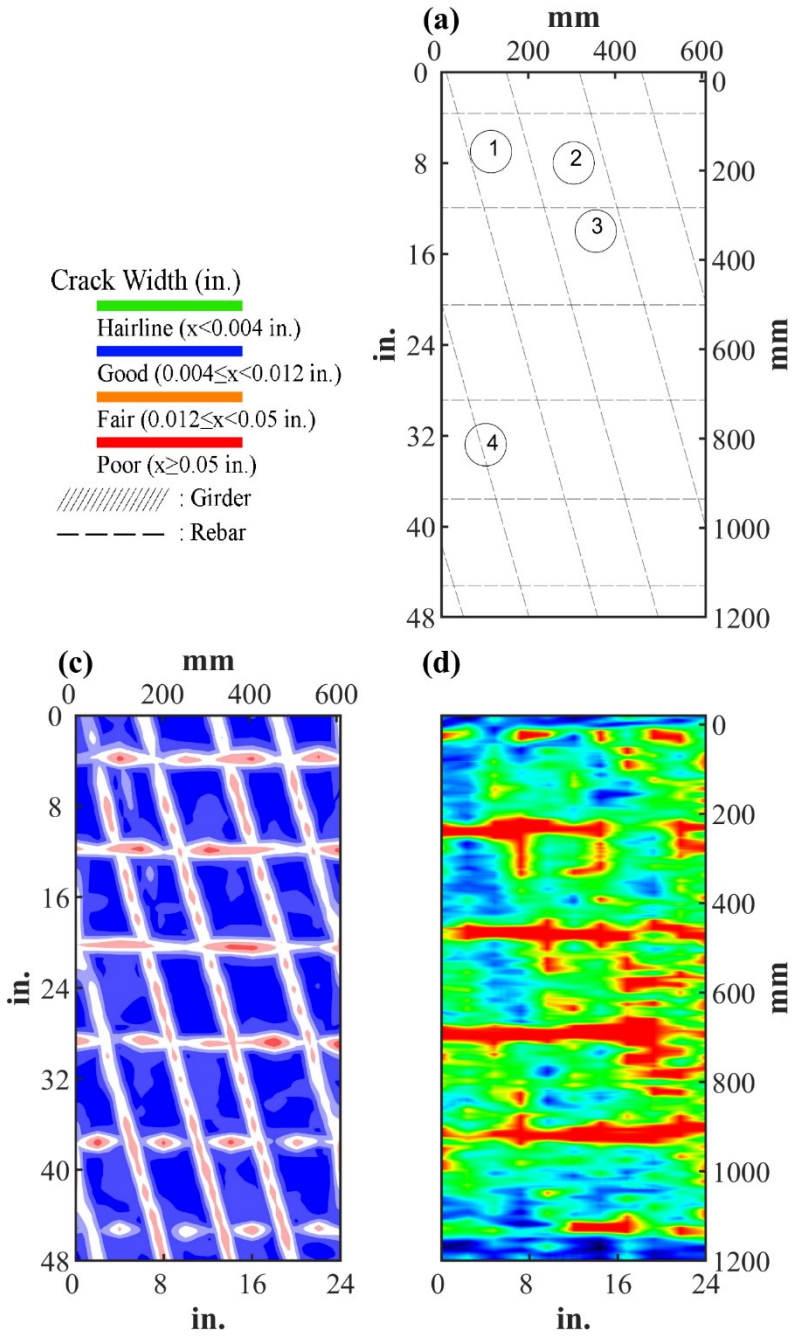

Figure 0.349. Crack Map and NDE Results of Grid 2: (a) Crack Map and Location of Cores; (c) GPR C-scan at 2.45 in. to 3.55 in. Depth; (d) UST C-scan

B.48.3 Concrete Cores

Table B-164. Detail Information of concrete cores

Core	dia. x height (in.)	Rebar depth (in.)	Rebar size (#)	Epoxy (Y/N)	Crack type	Crack width (in)	Notes
1-1	3.75 x 5.3	5.0	4	Y	longitudinal	HL	-
1-2	3.75 x 5.1	1.6; 4.9	5; 4	Y; Y	longitudinal	HL	-
1-3	3.75 x 2.0	-	-	-	-	-	-
1-4	3.75 x 5.8	-	-	-	diagonal	HL	-
2-1	3.75 x 6.3	3.6; 5.3; 5.4		Y; Y; Y	-	-	-
2-2	3.75 x 6.9	-	-	-	-	-	0.4 in. void at 2.8 in. depth
2-3	3.75 x 5.3	-	-	-	-	-	-
2-4	3.75 x 5.7	2.6	1.7	Y	-	-	-

Table B-165. Core Pictures

Core	Pictures of the Cores		
1-1			
1-2			

1-3	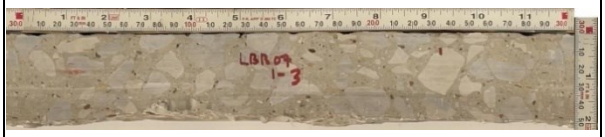		
1-4	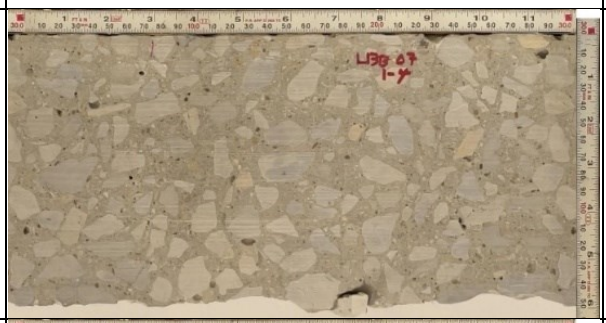		
2-1			
2-2			
2-3			

2-4			

B.48.4 Laboratory Experiment Results

B.48.4.1 Resistivity

Core Number	Surface Resistivity (kΩ·m)	Bulk Resistivity (kΩ·m)
1-4	112.2	22.2
2-2	99.5	-
2-3	81.2	13.9

B.48.4.2 Ultrasonic Pulse Velocity

Core Number	Ultrasonic Pulse Velocity (m/s)
1-3	3676
1-4	4290
2-2	4121
2-3	4297

B.48.4.3 Carbonation Depth

Core Number	Carbonation Depth (in.)
1-1	0.28
2-1	0.48

B.48.4.4 Acid-Soluble Chloride Content

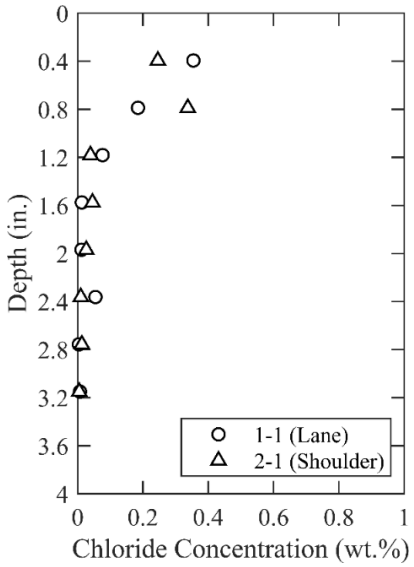

Figure 0.350. Chloride Content at Different Depth

B.48.4.5 Sorptivity

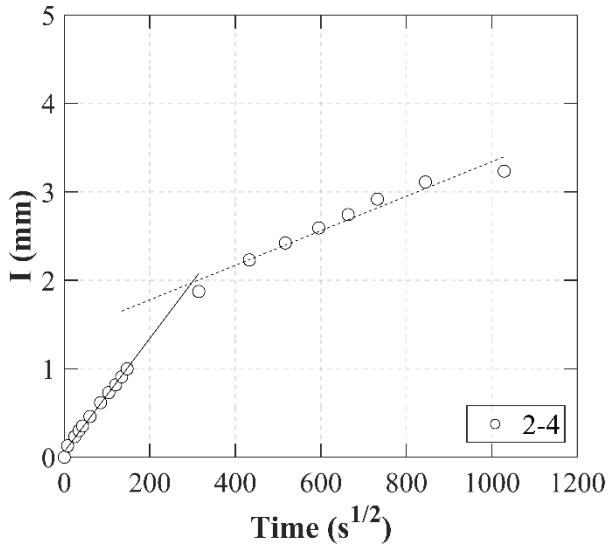

Figure 0.351. Absorption and Sorptivity of Core 2–4

Table B-166. Initial and Secondary Sorptivity Results

Core Number	Sorptivity	Results (mm/s$^{1/2}$)
Core 2–4	Initial Sorptivity	0.00640
	Secondary Sorptivity	0.00195

B.48.4.6 Knife Test

Core Number	Score	Picture
1-2	10	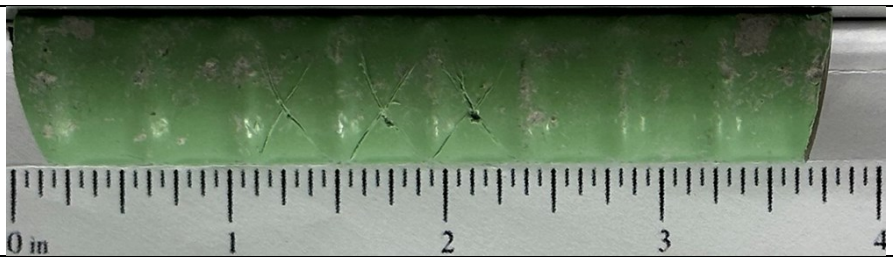

B.48.4.7 Electrochemical Impedance Spectroscopy

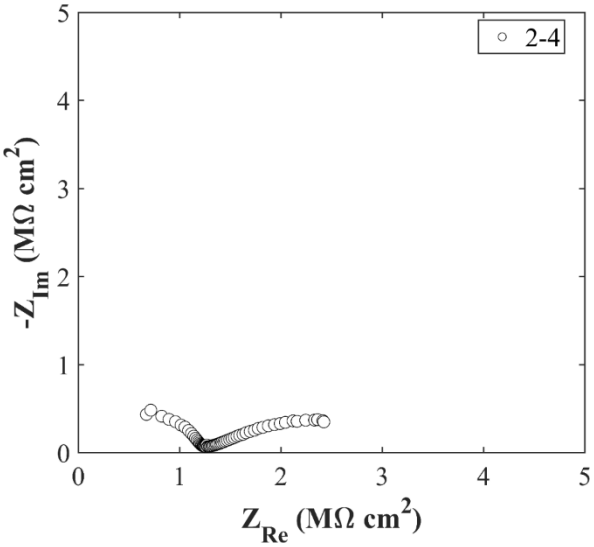

(a) Nyquist Diagram

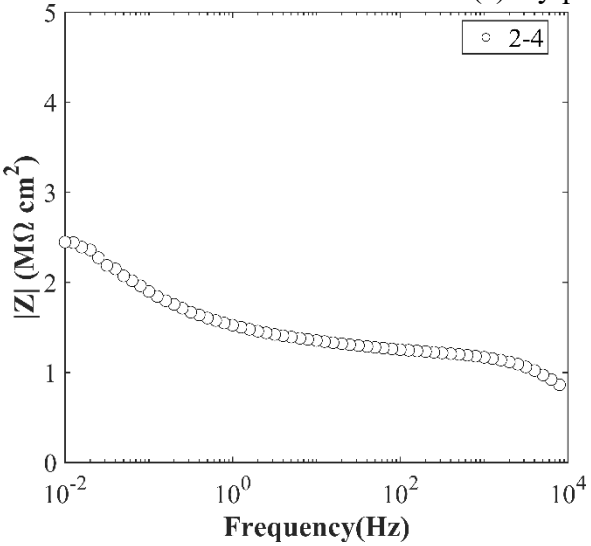

(b) Bode Plot of Impedance Modulus

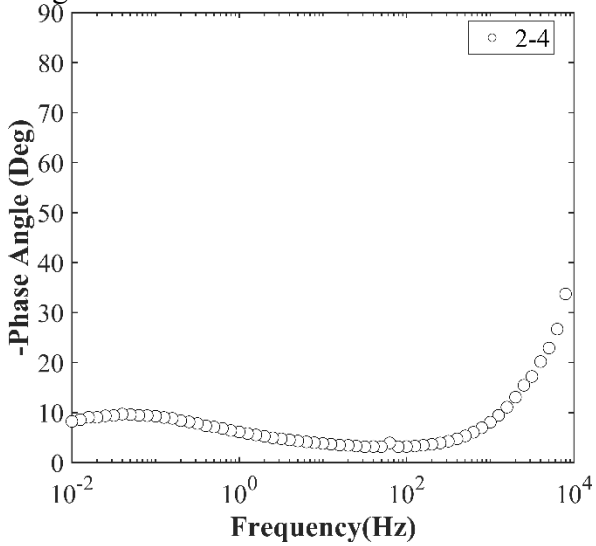

(c) Bode Plot of Impedance Phase

Figure 0.352. EIS Results: (a) Nyquist Diagram; (b) Bode Plot of Impedance Modulus; (c) Bode Plot of Impedance Phase

B.49 TYL-RC-01, IH 20 EB OVER RABBIT CREEK

- Bridge ID: 100930049507309 (Gregg County)
- Built 1988
- Mitigation methods: ECR
- Observed CIP depth: N/A
- Observed clear cover: N/A
- 5 spans, 6 concrete PS girder @ 8’ spacing with 3’ overhangs;
- Inspected on March 2, 2021

Figure 0.353. Concrete Deck of the Bridge (source: google maps)

B.49.1 Observed Condition

The top surface of deck has hairline to minor transverse cracks.

B.49.2 NDE Results

Grid 1 was located on the EB lane of the span 2 while grid 2 was on the shoulder lane.

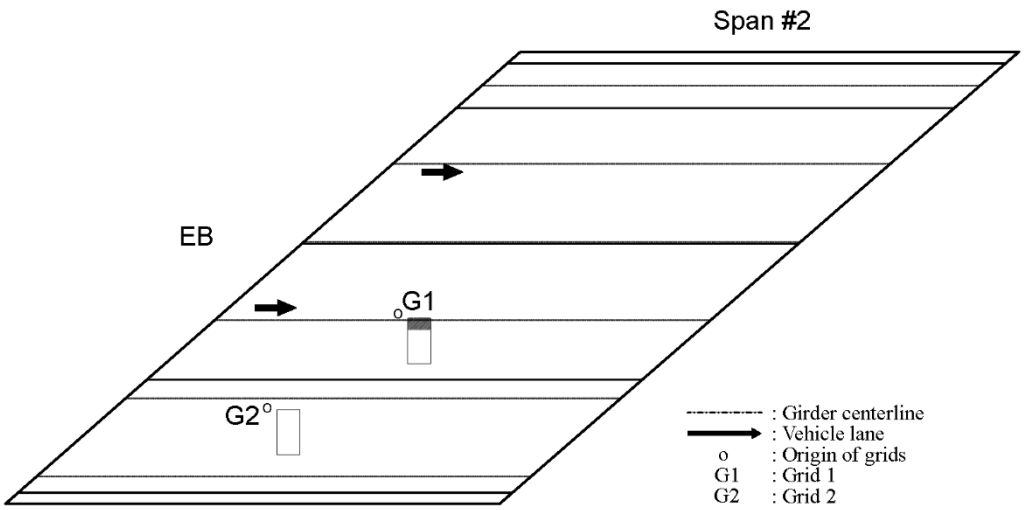

Figure 0.354. Plan View of the Bridge and Location of Grids

The deck was covered with asphalt overlay; therefore, there was no crack on the bridge as shown in Figure 0.355 (a) and Figure 0.356 (a)

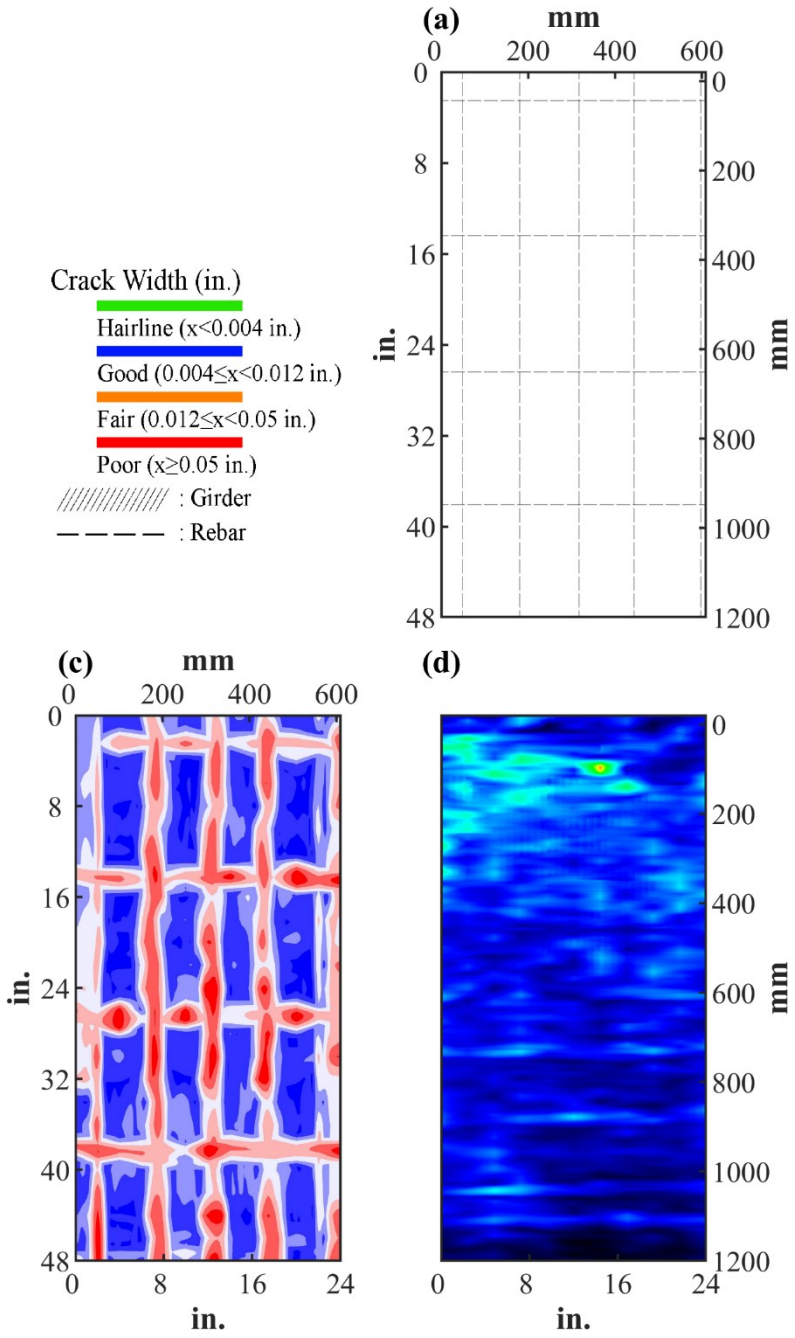

Figure 0.355. Crack Map and NDE Results of Grid 1: (a) Crack Map and Location of Cores; (c) GPR C-scan at 3.9 in. to 5.3 in. Depth; (d) UST C-scan

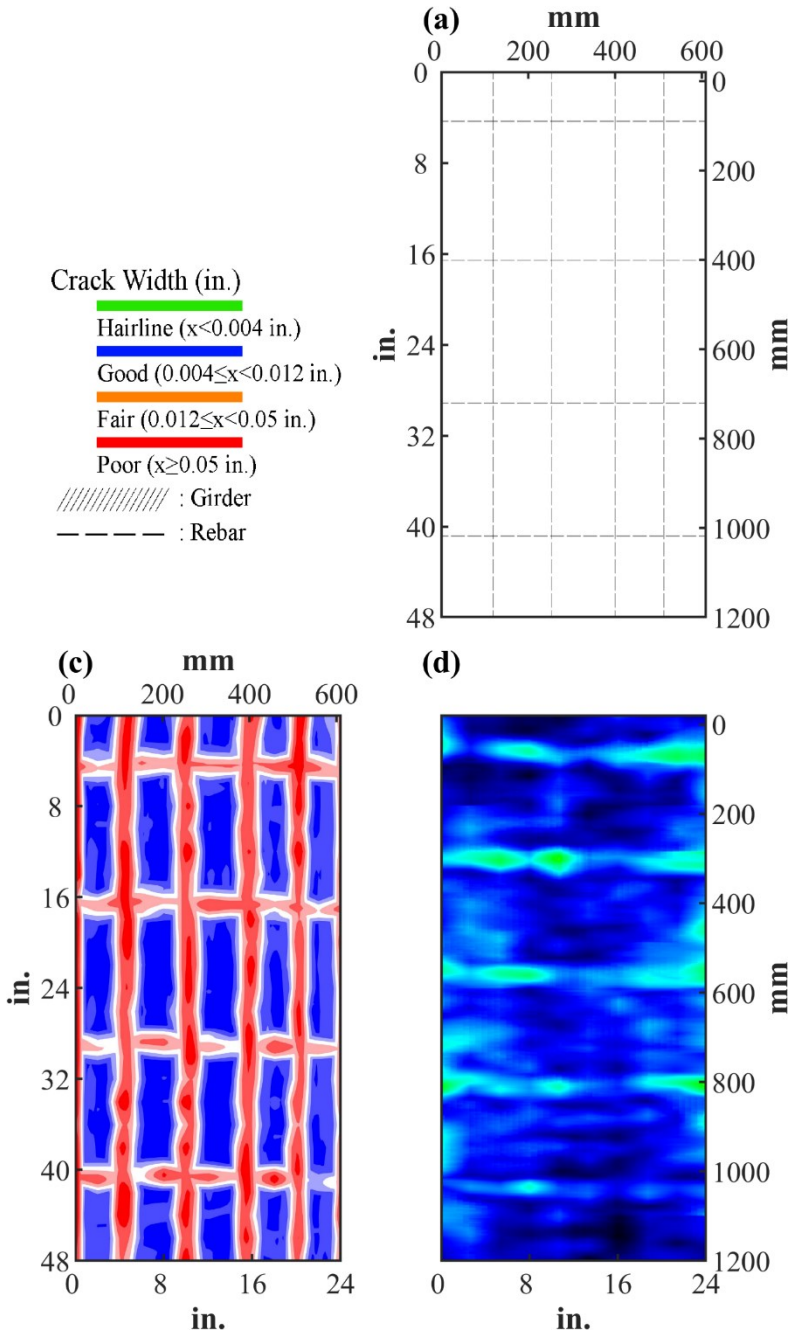

Figure 0.356. Crack Map and NDE Results of Grid 2: (a) Crack Map and Location of Cores; (c) GPR C-scan at 3.4 in. to 4.7 in. Depth; (d) UST C-scan

B.49.3 Concrete Cores

Because of asphalt overlay, cores could not be extracted.

B.50 TYL-RC-02, FM 2208 OVER SL 281

- Bridge ID; 100930264201104 (Gregg County)
- Built 2000
- Mitigation methods: None
- Observed CIP depth: 4.0 in.
- Observed clear cover: 1.7 in.
- 4 spans, 11 concrete PS girder @ 8.4’ spacing with 3’ overhangs
- Inspected on March 2, 2021

Figure 0.357. Concrete Deck of the Bridge (source: google maps)

B.50.1 Observed Condition

The top surface of deck has hairline to minor transverse cracks. The west railing has moderate spalling at its end. There is exposed and corroded at the exterior surface of abutment as shown in Figure 0.358 (a). The abutment cap between beam 7 and 8 has leakage issue as shown in Figure 0.358 (b).

(a) (b)

Figure 0.358. Deteriorations on the Bridge: (a) Exposed and Corroded Rebar at Abutment; (b) Leakage and cracks at abutment cap

B.50.2 NDE Results

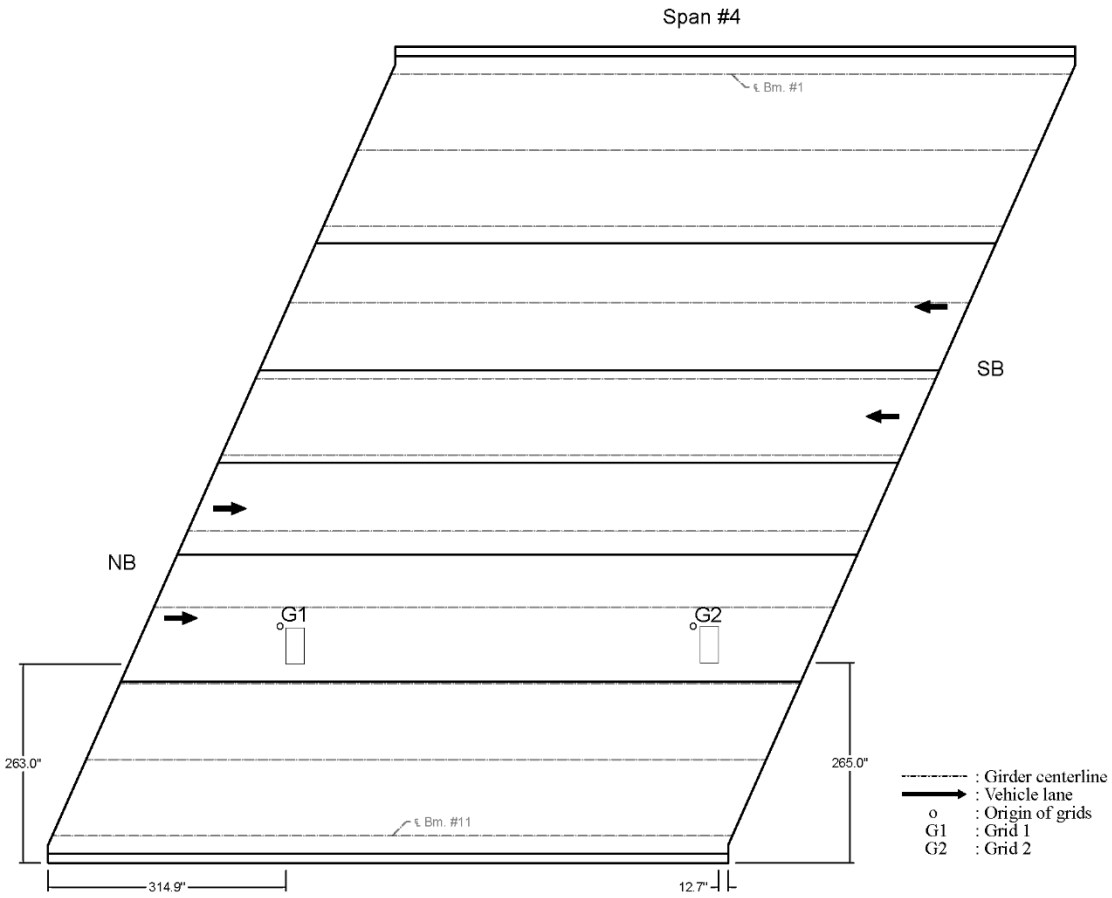

Figure 0.359. Plan View of the Bridge and Location of Grids

As shown in Figure 0.359 (a), grid 1 mostly had hairline cracks with 0.01 in. wide transverse crack that is possibly due to panel joint. And as shown in Figure A.2.4 (a), there was no crack on grid 2.

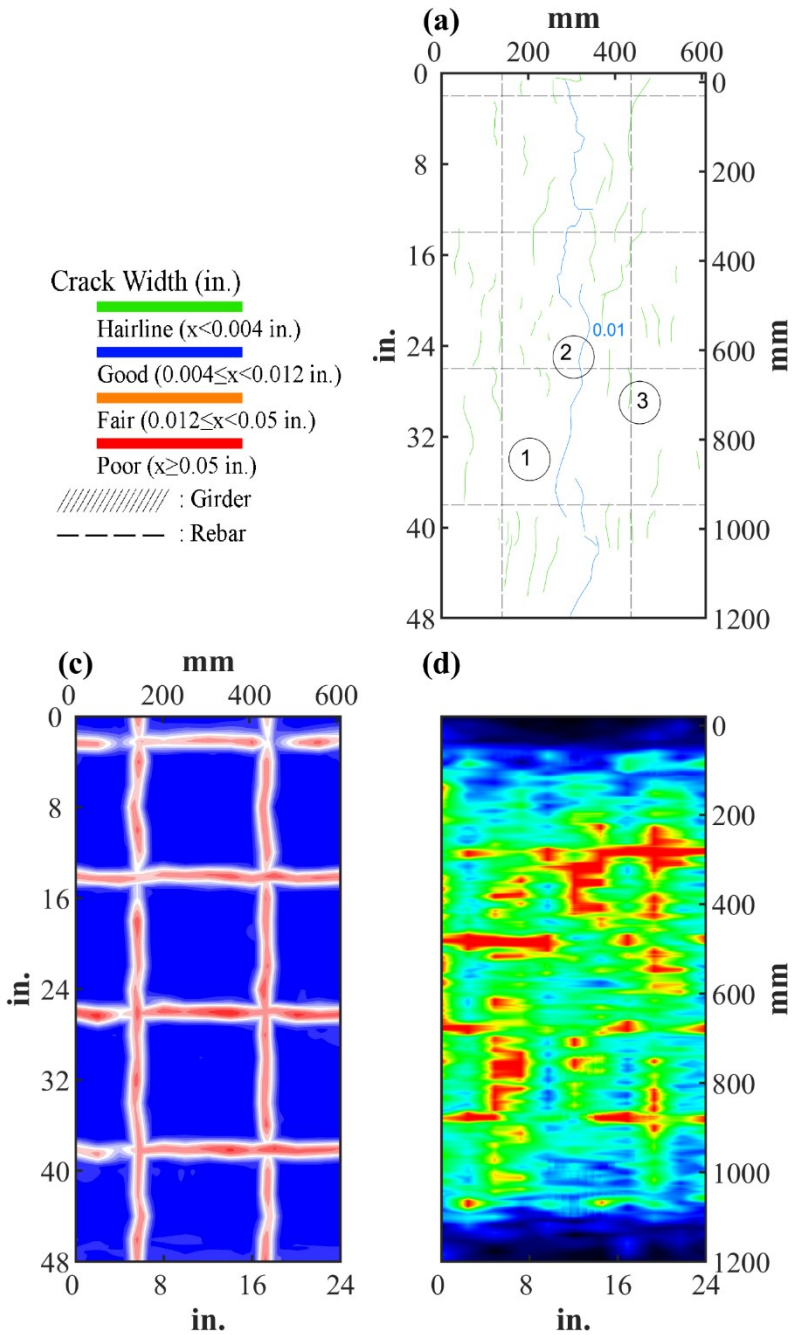

Figure 0.360. Crack Map and NDE Results of Grid 1: (a) Crack Map and Location of Cores; (c) GPR C-scan at 1.9 in. to 3.2 in. Depth; (d) UST C-scan

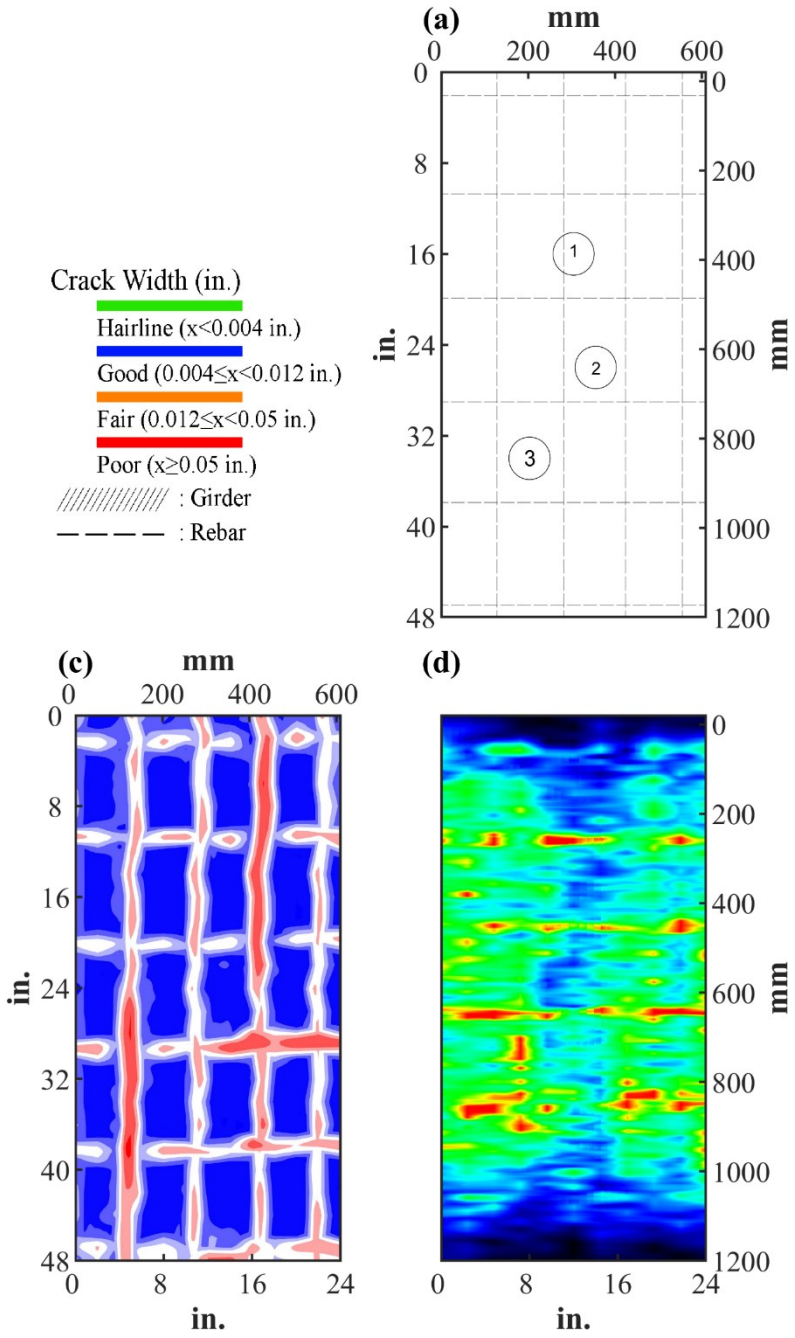

Figure 0.361. Crack Map and NDE Results of Grid 2: (a) Crack Map and Location of Cores; (b) Infrared Picture; (c) GPR C-scan 1.9 in. 3.3 in.; (d) UST C-scan; (e) Corrosion Rate Map

B.50.3 Concrete Cores

Table B-167. Detail Information of concrete cores

Core	dia. x height (in.)	Rebar depth (in.)	Rebar size (#)	Epoxy (Y/N)	Crack type	Crack width (in)	Notes
1-1	3.75 x 4.9	2.1	5	N	1. diagonal	0.01	A crack propagates from panel joint
1-2	3.75 x 5.1	-	-	-	-	-	-
1-3	3.75 x 4.2	2.1; 2.8	5; 4	N; N	longitudinal	HL	Delamination between CIP and PCP
2-1	3.75 x 5.5	1.8	5	N	longitudinal	0.3	A crack propagates from panel joint
2-2	3.75 x 4.1	-	-	-	longitudinal	0.2	A crack propagates from panel joint
2-3	3.75 x 4.7	1.7	5	N	longitudinal	HL	-

Table B-168. Core Pictures

Core	Pictures of the Cores		
1-1			
1-2			
1-3			

2-1			
2-2			
2-3			

B.50.4 Laboratory Experiment Results

B.50.4.1 Resistivity

Core Number	Surface Resistivity (kΩ·m)	Bulk Resistivity (kΩ·m)
1-1	85.9	-
1-2	99.9	7.5

B.50.4.2 Ultrasonic Pulse Velocity

Core Number	Ultrasonic Pulse Velocity (m/s)
1-1	4441
1-2	4510
2-3	4197

B.50.4.3 Carbonation Depth

Core Number	Carbonation Depth (in.)
1-3	0.00
2-3	0.00

B.50.4.4 Acid-Soluble Chloride Content

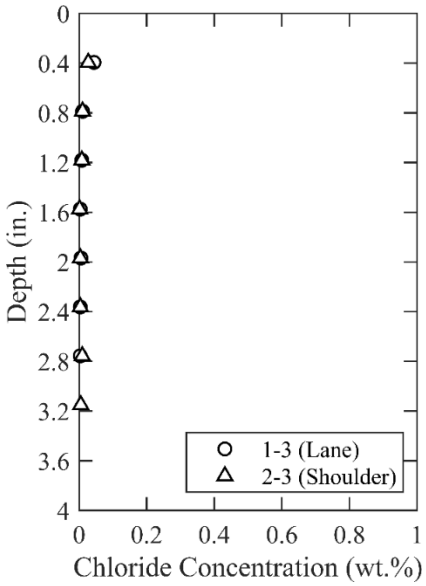

Figure 0.362. Chloride Content at Different Depth

B.50.4.5 Sorptivity

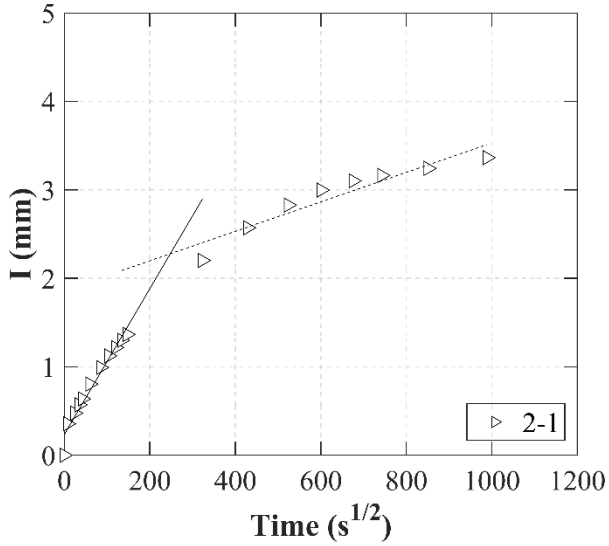

Figure 0.363. Absorption and Sorptivity of Core 2–1

Table B-169 Initial and Secondary Sorptivity Results

Core Number	Sorptivity	Results (mm/s$^{1/2}$)
Core 2–1	Initial Sorptivity	0.00824
	Secondary Sorptivity	0.00167

B.50.4.6 Electrochemical Impedance Spectroscopy

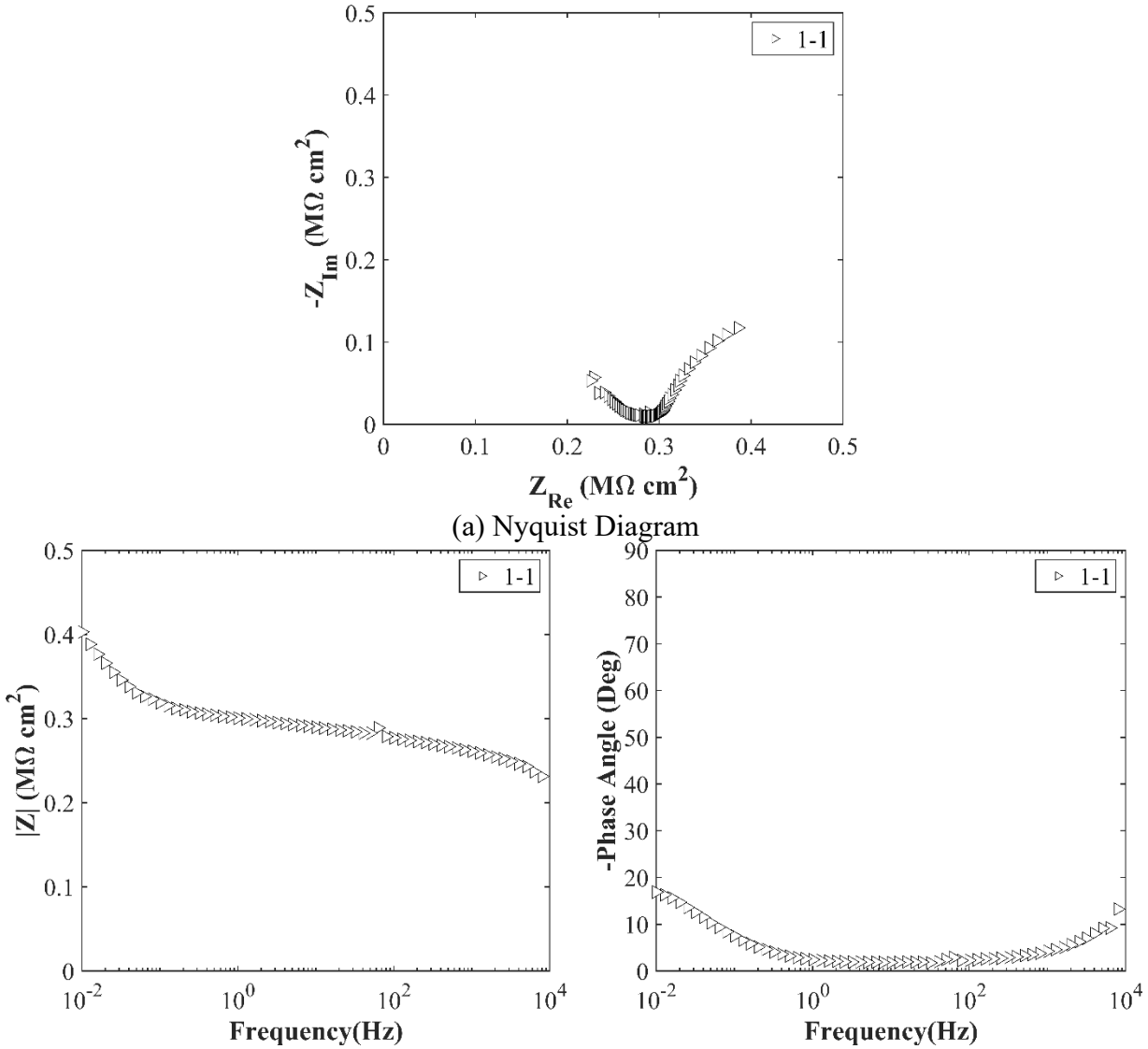

(a) Nyquist Diagram

(b) Bode Plot of Impedance Modulus

(c) Bode Plot of Impedance Phase

Figure 0.364. EIS Results: (a) Nyquist Diagram; (b) Bode Plot of Impedance Modulus; (c) Bode Plot of Impedance Phase

B.51 TYL-RC-03, SL 571 OVER SH 64

- Bridge ID: 102010024508039 (Rusk County)
- Built 2000
- Mitigation methods: Linseed oil, ECR
- Observed CIP depth: Unknown
- Observed clear cover: 1.6 in.
- 3 spans, 6 concrete PS girder @ 6.967’ spacing with 3’ overhangs;
- Inspected on February 1, 2021

Figure 0.365. Concrete Deck of the Bridge (source: google maps)

B.51.1 Observed Condition

There is a crack at the exterior abutment wall and a sign of corrosion is visible as shown in Figure 0.366 (a). In addition, As shown in Figure A.3.2 (b) and (c), there were spalling at abutment wall and concrete rail, respectively.

(a) (b) (c)

Figure 0.366. Deteriorations on the Bridge: (a) Crack at Abutment Wall; (b) Spalling at Abutment Wall; (c) Spalling at Concrete Rail

B.51.2 NDE Results

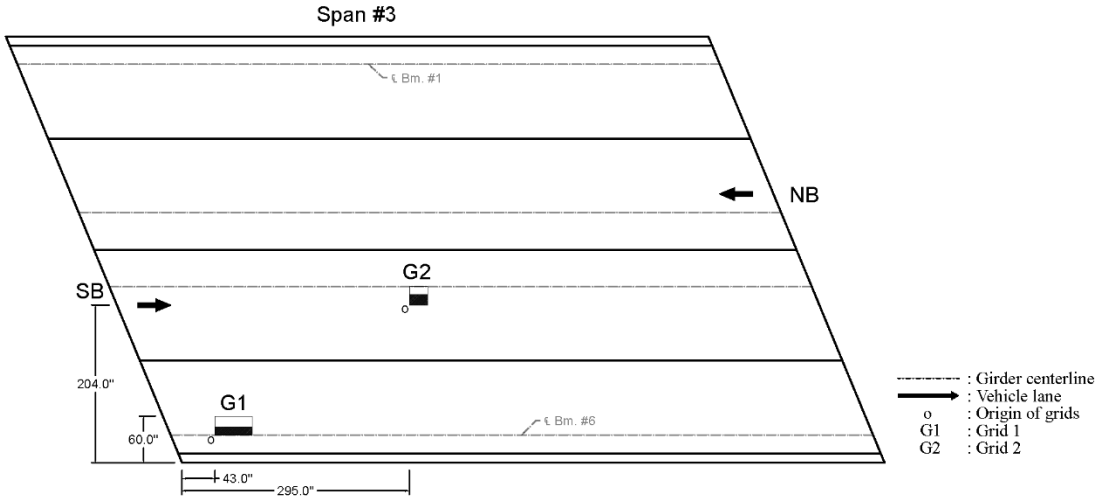

Figure 0.367. Plan View of the Bridge and Location of Grids

As shown in Figure 0.368 (a), there were no cracks on grid 1. On the other hand, grid 2 had a transverse crack that ranged from 0.004 in. to 0.007 in. wide. Based on its pattern, it is possible that the crack is due to panel joint.

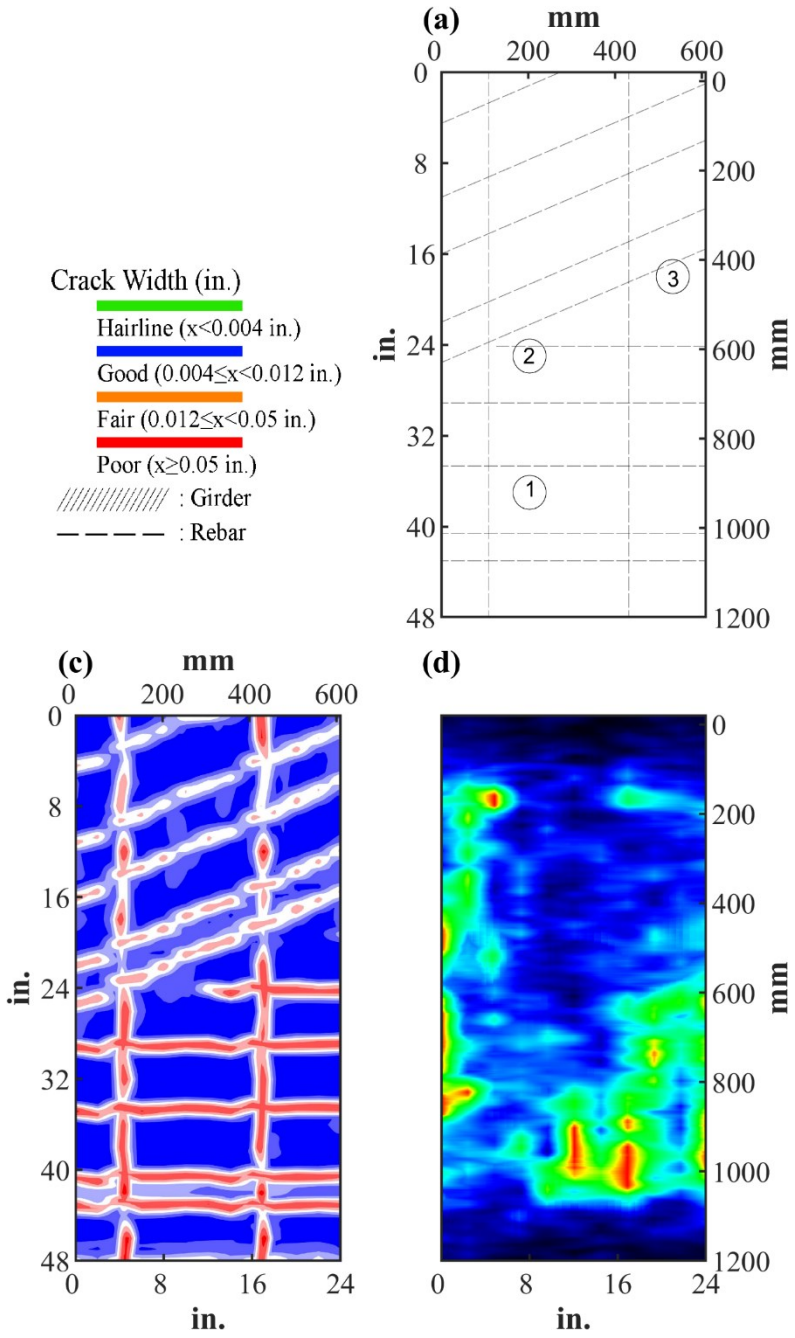

Figure 0.368. Crack Map and NDE Results of Grid 1: (a) Crack Map and Location of Cores; (c) GPR C-scan at 1.8 in. to 2.9 in. Depth; (d) UST C-scan

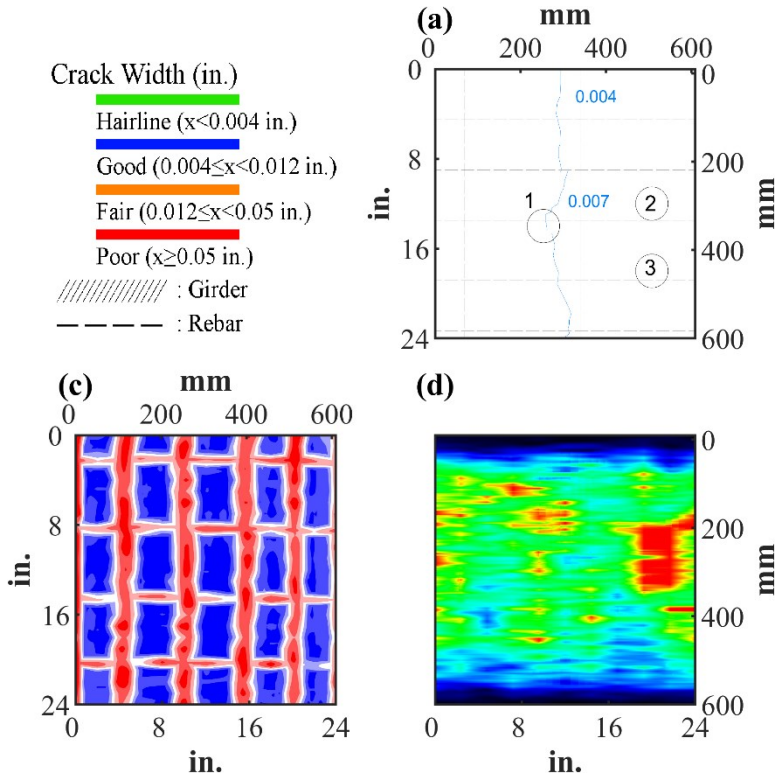

Figure 0.369. Crack Map and NDE Results of Grid 2: (a) Crack Map and Location of Cores; (c) GPR C-scan at 1.7 in. to 2.8 in. Depth; (d) UST C-scan

B.51.3 Concrete Cores

Table B-170. Detail Information of concrete cores

Core	dia. x height (in.)	Rebar depth (in.)	Rebar size (#)	Epoxy (Y/N)	Crack type	Crack width (in)	Notes
1-1	3.0 x 14.4	-	-	-	-	-	-
1-2	3.0 x 16.0	-	-	-	-	-	-
1-3	3.0 x 15.4	1.6	5	Y	longitudinal	0.008	A crack propagating from panel joint; Avoid around rebar
1-4	3.0 x 13.2	1.6	5	Y	-	-	-
1-5	3.0 x 13.2	1.6	5	Y	-	-	-
1-6	3.0 x 13.7	-	-	-	-	-	-

Table B-171. Core Pictures

Core	Pictures of the Cores		
1-1			
1-2			
1-3			
1-4			
1-5			

1-6			

B.51.4 Laboratory Experiment Results

B.51.4.1 Resistivity

Core Number	Surface Resistivity (kΩ·m)	Bulk Resistivity (kΩ·m)
1-2	44.3	-

B.51.4.2 Ultrasonic Pulse Velocity

Core Number	Ultrasonic Pulse Velocity (m/s)
1-2	4099

B.51.4.3 Carbonation Depth

Core Number	Carbonation Depth (in.)
1-3	0.98

B.51.4.4 Acid-Soluble Chloride Content

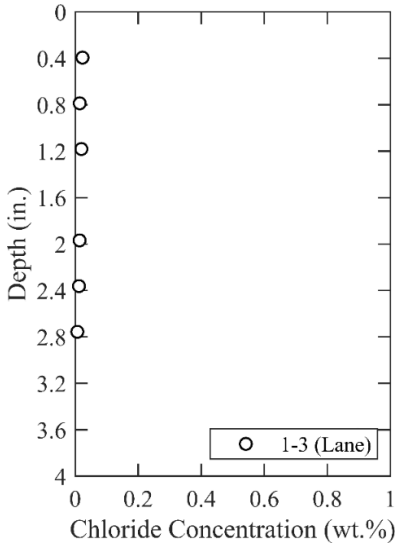

Figure 0.370. Chloride Content at Different Depth

B.51.4.5 Sorptivity

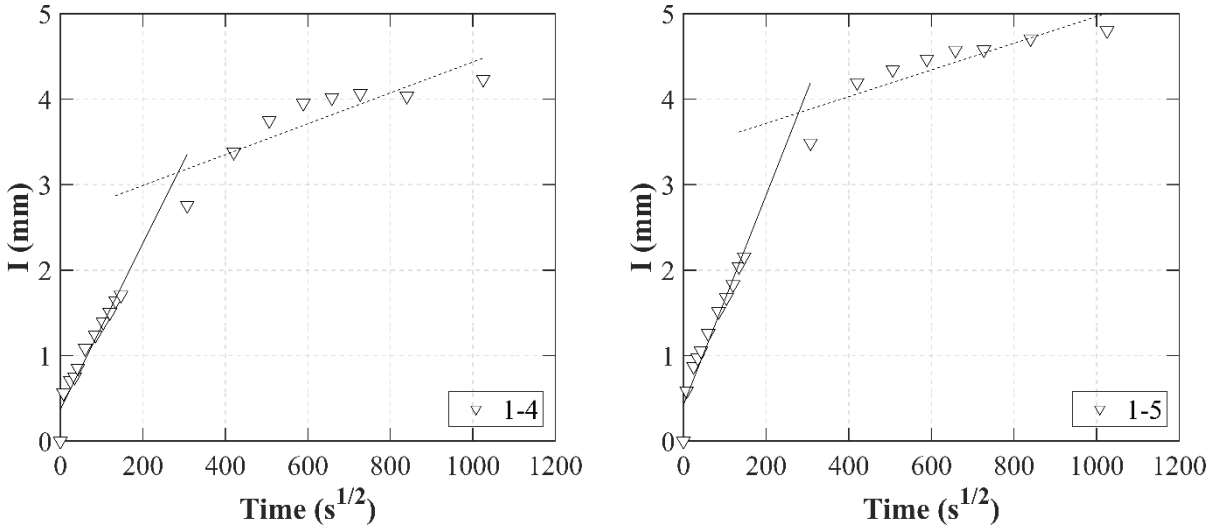

(a) Core 1–4 (b) Core 1–5

Figure 0.371. Absorption and Sorptivity of: (a) Core 1–1; (b) Core 2–2

Table B-172. Initial and Secondary Sorptivity Results

Core Number	Sorptivity	Results (mm/s$^{1/2}$)
Core 1–4	Initial Sorptivity	0.00971
	Secondary Sorptivity	0.00181
Core 1–5	Initial Sorptivity	0.0123
	Secondary Sorptivity	0.00156

B.51.4.6 Electrochemical Impedance Spectroscopy

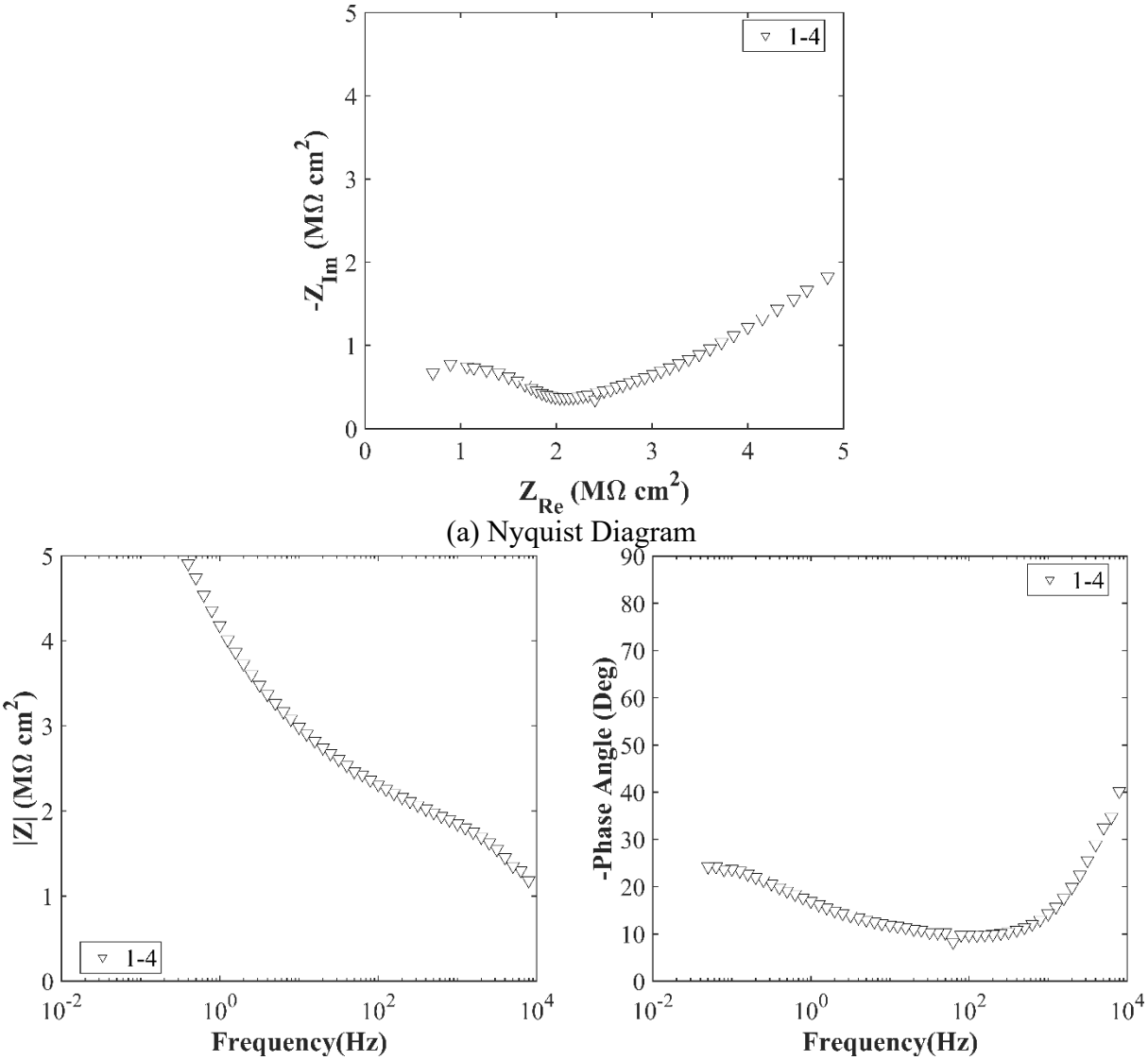

(a) Nyquist Diagram

(b) Bode Plot of Impedance Modulus

(c) Bode Plot of Impedance Phase

Figure 0.372. EIS Results: (a) Nyquist Diagram; (b) Bode Plot of Impedance Modulus; (c) Bode Plot of Impedance Phase

B.52 WFS-RC-01, IH 44 NB OVER 6TH STREET

- Bridge ID: 32430004309188 (Wichita County)
- Built in 2001
- Mitigation methods: HPC (20 to 25% Class F fly ash), CNI, linseed oil
- Observed CIP depth: 4.2 in.
- Observed clear cover: 2.3 in.
- 3 spans, 9-steel plate girder @ 9.37’ spacing with 3’ overhangs
- Inspected on June 1, 2021

Figure 0.373. Concrete Deck of the Bridge (source: google maps)

B.52.1 Observed Condition

Deck surface has minor diagonal, transverse, and longitudinal cracks. The bottom surface of deck flange is with efflorescence.

B.52.2 NDE Results

Grid 1 was located on the NB lane and grid 2 was located on the NB shoulder lane of the span 2 of the bridge.

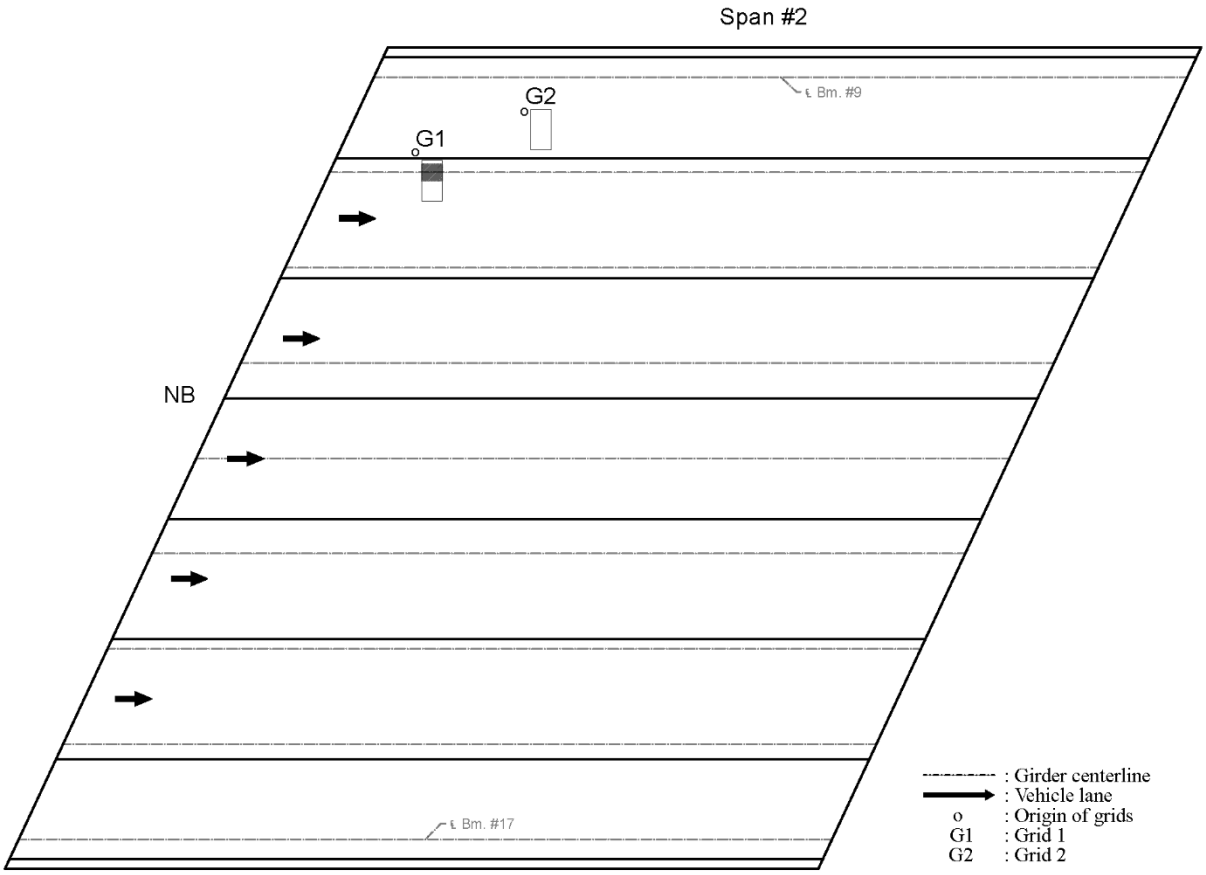

Figure 0.374. Plan View of the Bridge and Location of Grids

As shown in Figure 0.149 (a), there are widespread of hairline cracks and transverse cracks that range from 0.004 in. to 0.012 in. wide on grid 1. Transverse cracks were on top of a girder and propagated from it. On grid 2, hariline cracks and a 0.018 in. wide transverse crack were observed that was possibly caused by panel joints as shown in Figure 0.376 (a).

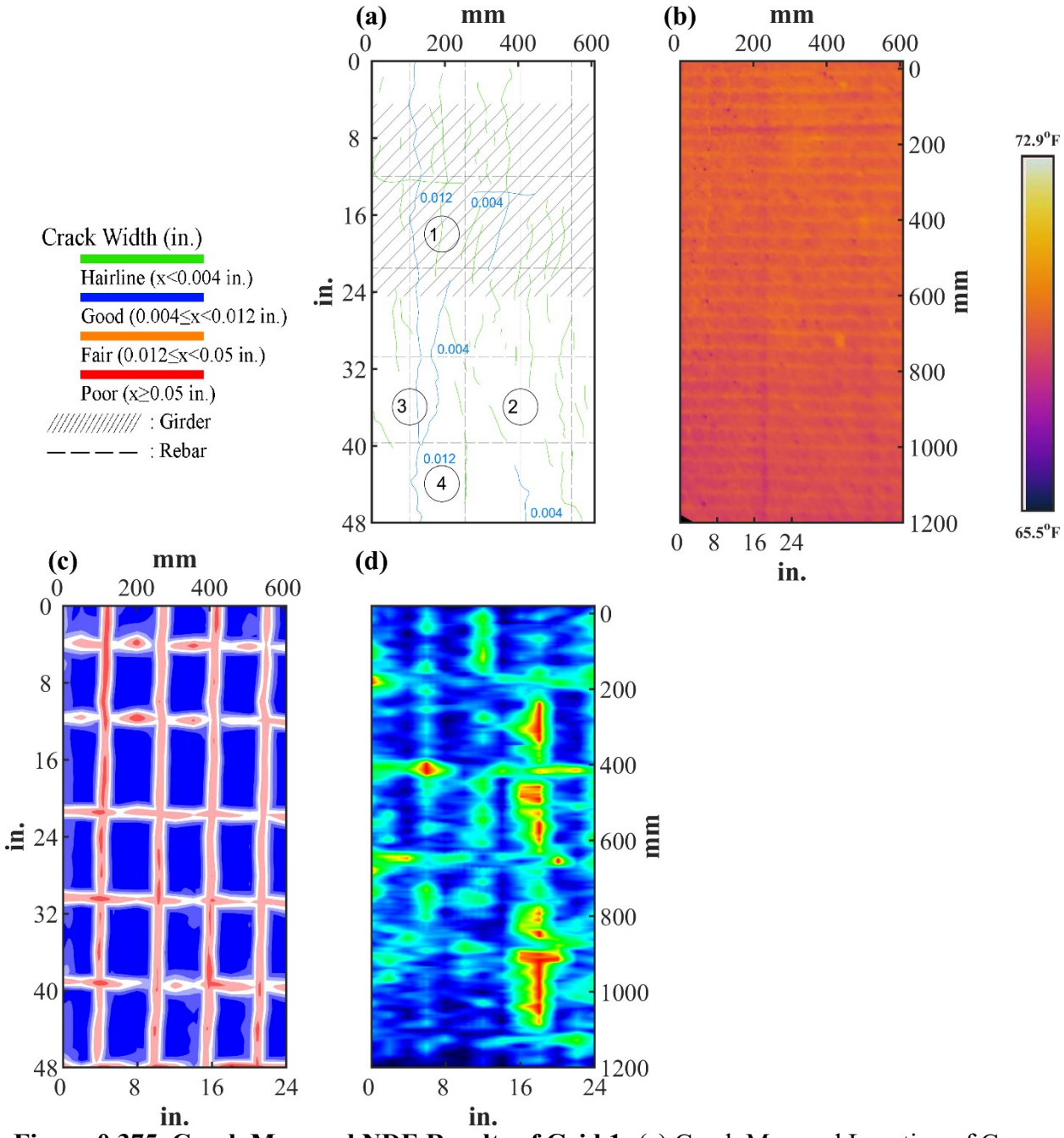

Figure 0.375. Crack Map and NDE Results of Grid 1: (a) Crack Map and Location of Cores; (b) Infrared Picture; (c) GPR C-scan at 1.9 in. to 3.3 in. Depth; (d) UST C-scan at 3.1 in. Depth

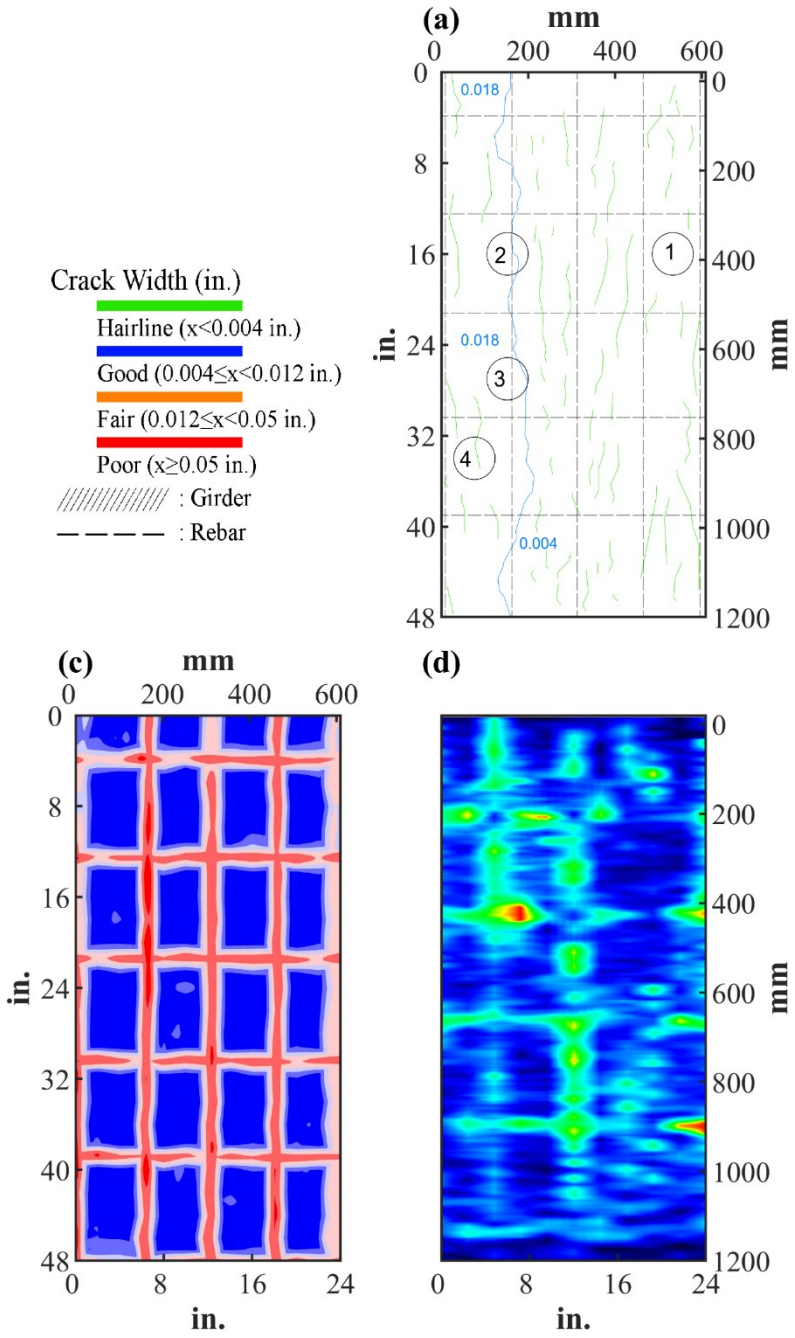

Figure 0.376. Crack Map and NDE Results of Grid 2: (a) Crack Map and Location of Cores; (c) GPR C-scan at 2.6 in. to 3.95 in. Depth; (d) UST C-scan at 3.5 in. Depth

B.52.3 Concrete Cores

Table B-173. Detail Information of concrete cores

Core	dia. x height (in.)	Rebar depth (in.)	Rebar size (#)	Epoxy (Y/N)	Crack type	Crack width (in)	Notes
1-1	3.75 x 5.9	-	-	-	-	-	-
1-2	3.75 x 4.2	2.3	5	N	-	-	Delamination between CIP and PCP
1-3	3.75 x 4.5	2.4	5	N	transverse	0.004	Delamination between CIP and PCP; a crack propagates from panel joint
1-4	3.75 x 6.1	-	-	-	-	-	
2-1	3.75 x 6.0	-	-	-	transverse	0.004	
2-2	3.75 x 4.2	2.6	5	N	transverse	0.004	A crack propagates from panel joint through rebar
2-3	3.75 x 5.5	2.6	5	N			A crack propagates from panel joint through rebar
2-4	3.75 x 6.1	-	-	-	-	-	

Table B-174. Core Pictures

Core	Pictures of the Cores		
1-1	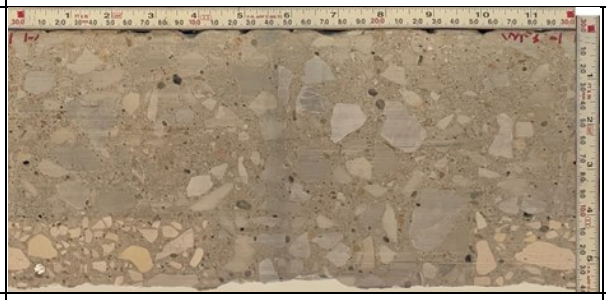		
1-2		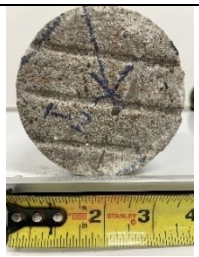	

1-3			
1-4			
2-1			
2-2			
2-3			
2-4			

B.52.4 Laboratory Experiment Results

B.52.4.1 Resistivity

Core Number	Surface Resistivity (kΩ·m)	Bulk Resistivity (kΩ·m)
1-1	86.7	18.3
2-1	111.2	-
2-4	122.1	18.3

B.52.4.2 Ultrasonic Pulse Velocity

Core Number	Ultrasonic Pulse Velocity (m/s)
1-1	4222
1-4	4248
2-1	4313
2-4	4444

B.52.4.3 Carbonation Depth

Core Number	Carbonation Depth (in.)
1-3	0.12
2-3	0.00

B.52.4.4 Acid-Soluble Chloride Content

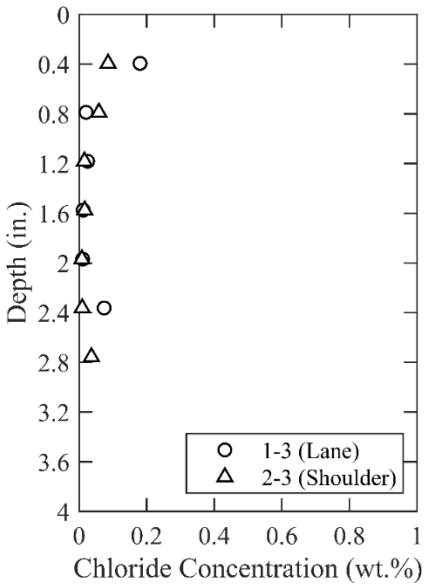

Figure 0.377. Chloride Content at Different Depth

B.52.4.5 Sorptivity

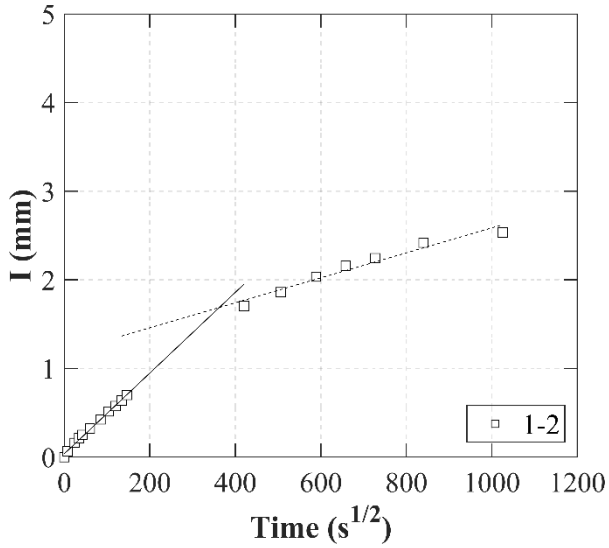

Figure 0.378. Absorption and Sorptivity of Core 1–2

Table B-175. Initial and Secondary Sorptivity Results

Core Number	Sorptivity	Results (mm/s$^{1/2}$)
Core 1–2	Initial Sorptivity	0.00455
	Secondary Sorptivity	0.00141

B.52.4.6 Electrochemical Impedance Spectroscopy

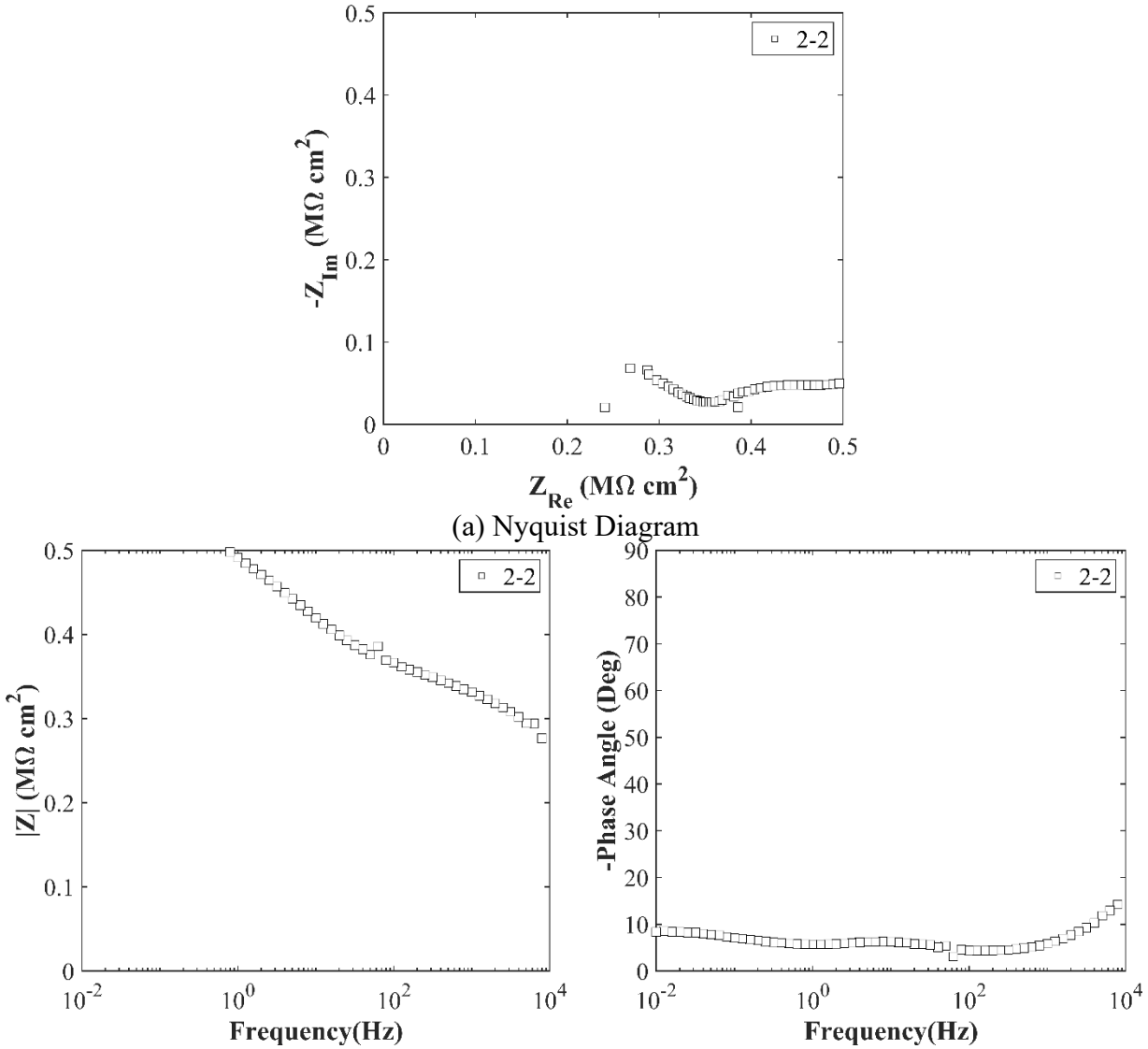

(a) Nyquist Diagram

(b) Bode Plot of Impedance Modulus

(c) Bode Plot of Impedance Phase

Figure 0.379. EIS Results: (a) Nyquist Diagram; (b) Bode Plot of Impedance Modulus; (c) Bode Plot of Impedance Phase

B.53 WFS-RC-02, IH 44 SB OVER WICHITA RIVER

- Bridge ID: 32430004309202 (Wichita County)
- Built in 2001
- Mitigation methods: HPC (20 to 25% Class F fly ash), CNI, linseed oil
- Observed CIP depth: Unknown
- Observed clear cover: 2.4 in.
- 3 spans, 9-steel plate girder @ varying spacing with max 3’ overhangs
- Inspected on June 3, 2021

Figure 0.380. Concrete Deck of the Bridge (source: google maps)

B.53.1 Observed Condition

Deck surface has transverse cracks. There are hairline vertical cracks on the north abutment cap.

B.53.2 NDE Results

Grid 1 was located on the SB lane and grid 2 was located on the SB shoulder lane of the span 4 of the bridge.

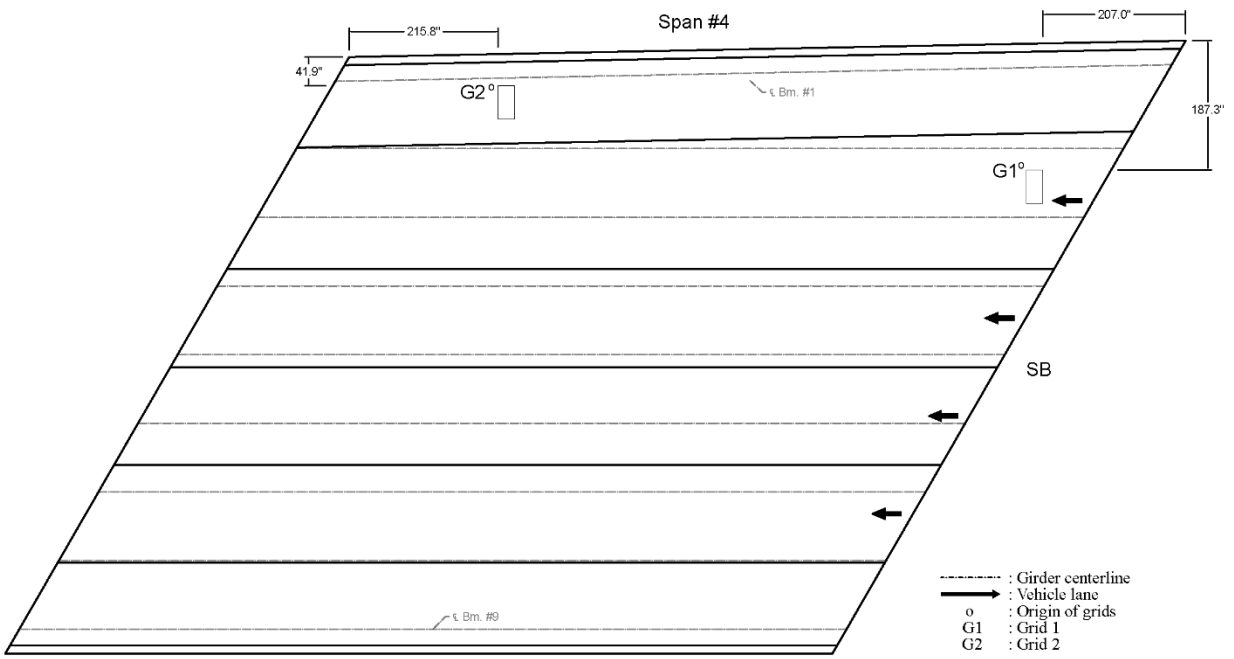

Figure 0.381. Plan View of the Bridge and Location of Grids

As shown in Figure 0.156 (a), there were widespread of transverse hairline cracks and 0.004 in. wide transverse cracks throughout grid 1. On grid 2, there was one 0.004 in. wide transverse crack that is possibly caused by panel joints as shown in Figure 0.157 (a).

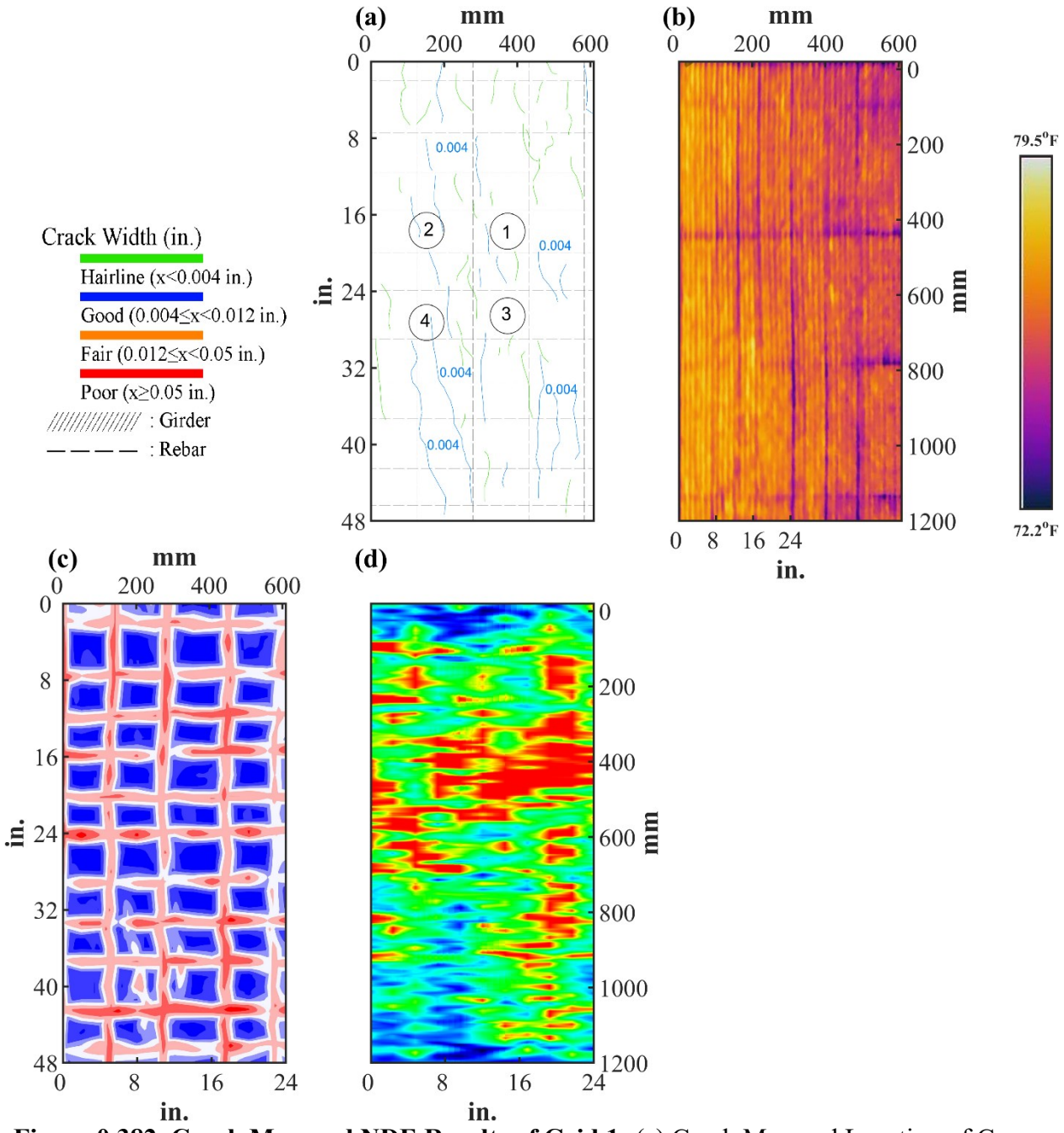

Figure 0.382. Crack Map and NDE Results of Grid 1: (a) Crack Map and Location of Cores; (b) Infrared Picture; (c) GPR C-scan at 1.9 in. to 3.3 in. Depth; (d) UST C-scan at 2.6 in. Depth

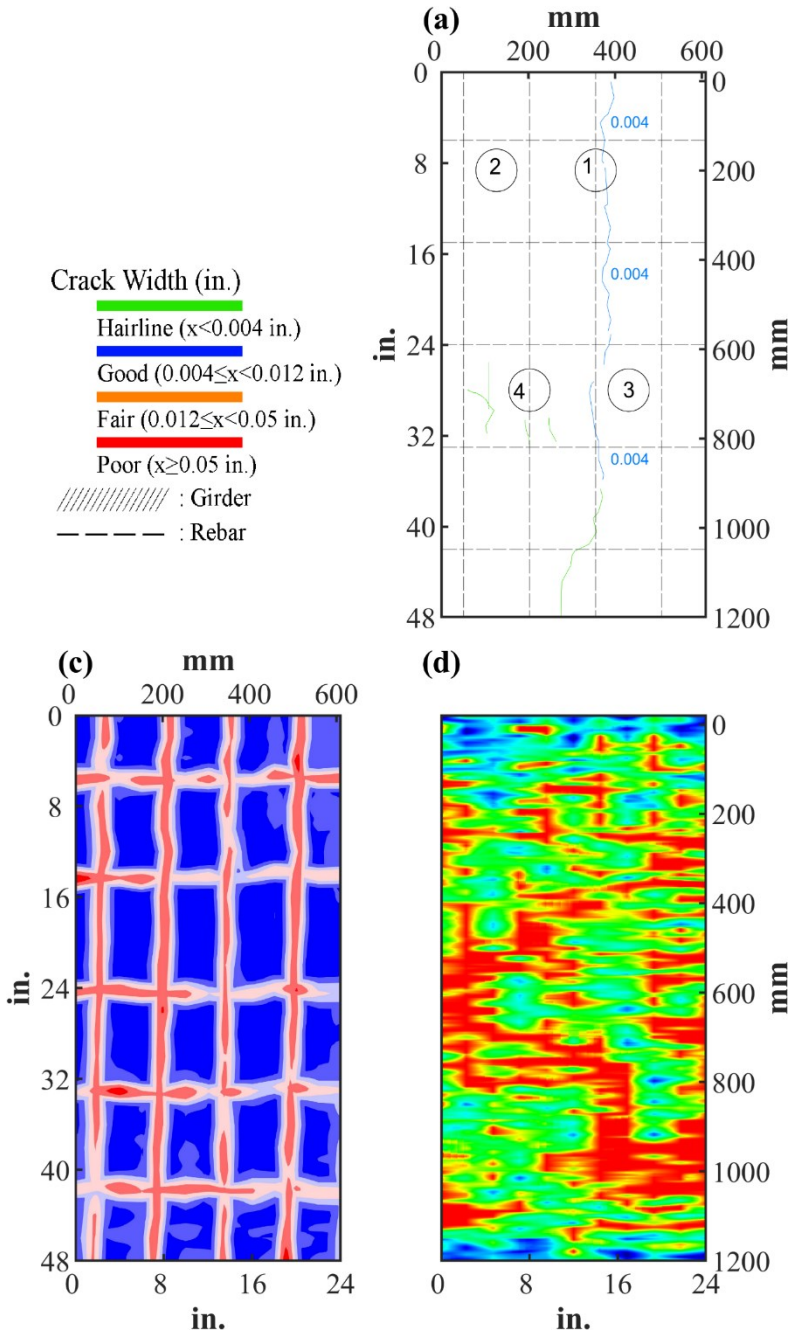

Figure 0.383. Crack Map and NDE Results of Grid 2: (a) Crack Map and Location of Cores; (c) GPR C-scan at 1.9 in. to 3.3 in. Depth; (d) UST C-scan at 2.4 in. Depth

B.53.3 Concrete Cores

Table B-176. Detail Information of concrete cores

Core	dia. x height (in.)	Rebar depth (in.)	Rebar size (#)	Epoxy (Y/N)	Crack type	Crack width (in)	Notes
1-1	3.75 x 5.9	-	-	-	-	-	-
1-2	3.75 x 5.5	2.4	5	N	transverse	0.004	-
1-3	3.75 x 5.5	-	-	-			-
1-4	3.75 x 5.9	2.4; 2.9	5; 4	N	transverse	0.004	-
2-1	3.75 x 6.3	2.7	5	N	transverse	0.004	-
2-2	3.75 x 6.3	-	-	-	-	-	-
2-3	3.75 x 6.5	5.7	5	N	-	-	-
2-4	3.75 x 6.3	2.7	5	N	-	-	-

Table B-177. Core Pictures

Core	Pictures of the Cores		
1-1			
1-2			

1-3			
1-4		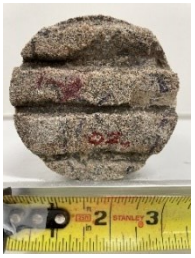	
2-1			
2-2			
2-3			

2-4			

B.53.4 Laboratory Experiment Results

B.53.4.1 Resistivity

Core Number	Surface Resistivity (kΩ·m)	Bulk Resistivity (kΩ·m)
1-1	70.4	12.8
1-3	61.5	-
2-2	57.6	12.8

B.53.4.2 Ultrasonic Pulse Velocity

Core Number	Ultrasonic Pulse Velocity (m/s)
1-1	4345
1-3	4343
2-2	4266

B.53.4.3 Carbonation Depth

Core Number	Carbonation Depth (in.)
1-4	0.31
2-3	0.00

B.53.4.4 Acid-Soluble Chloride Content

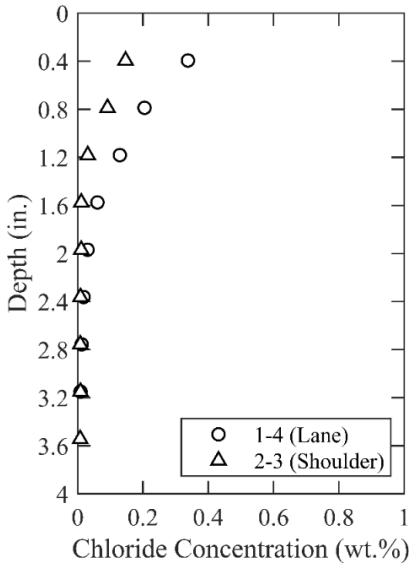

Figure 0.384. Chloride Content at Different Depth

B.53.4.5 Sorptivity

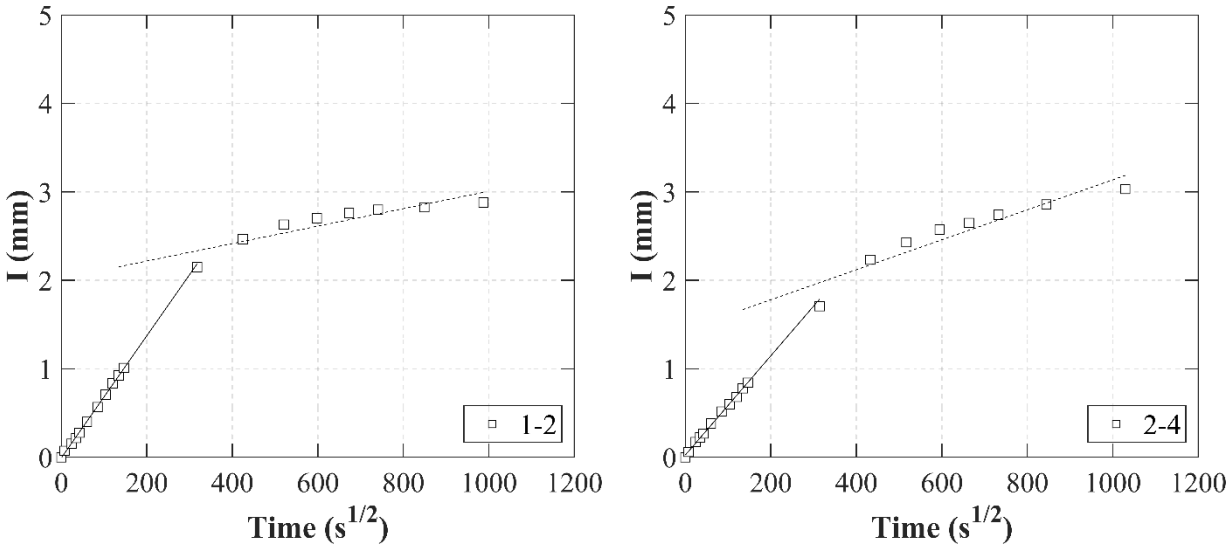

(a) Core 1–2 (b) Core 2–4

Figure 0.385. Absorption and Sorptivity of: (a) Core 1–1; (b) Core 2–2

Table B-178. Initial and Secondary Sorptivity Results

Core Number	Sorptivity	Results (mm/s$^{1/2}$)
Core 1–2	Initial Sorptivity	0.00691
	Secondary Sorptivity	0.00099
Core 2–4	Initial Sorptivity	0.00561
	Secondary Sorptivity	0.00169

B.53.4.6 Electrochemical Impedance Spectroscopy

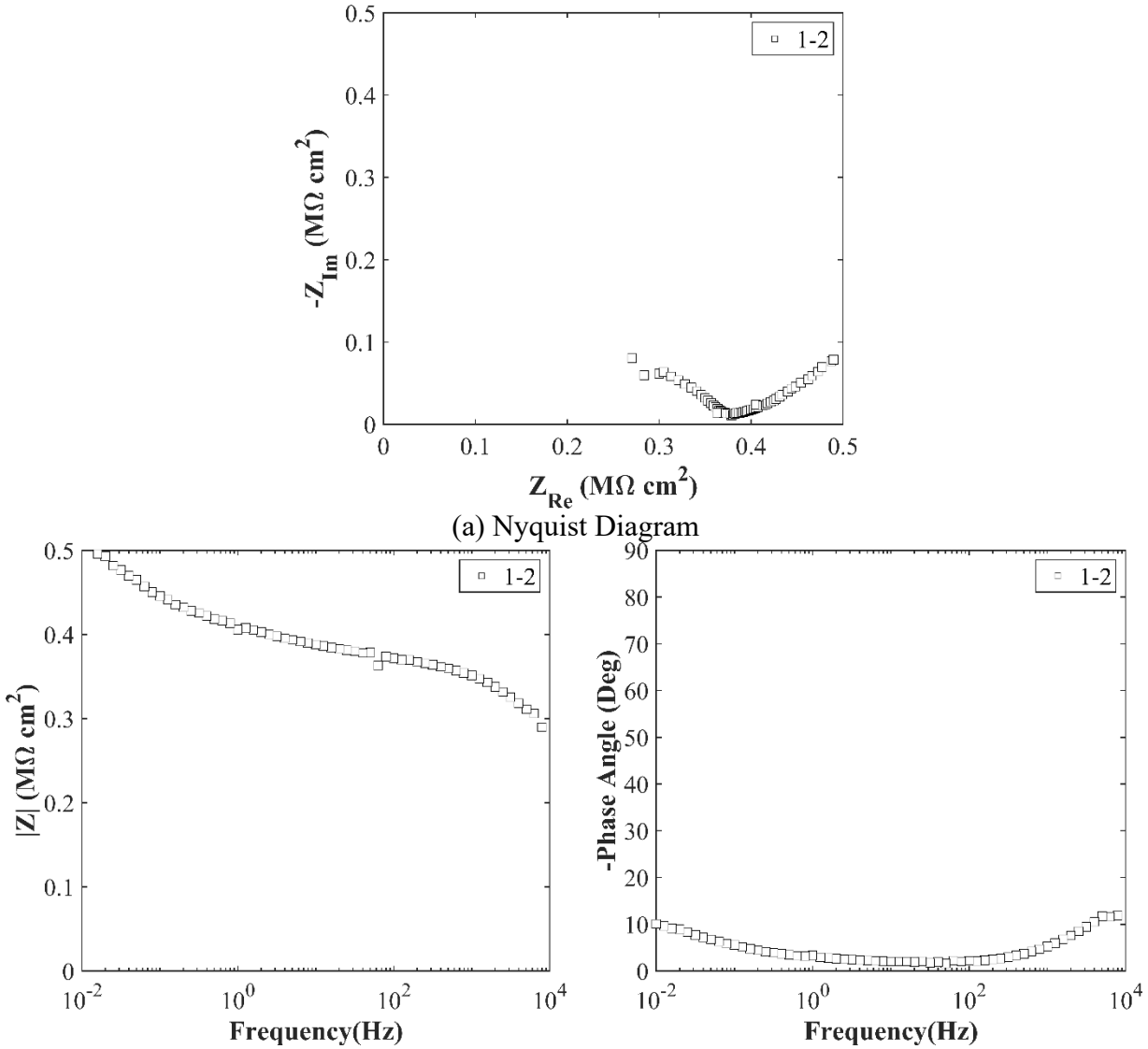

(a) Nyquist Diagram

(b) Bode Plot of Impedance Modulus

(c) Bode Plot of Impedance Phase

Figure 0.386. EIS Results: (a) Nyquist Diagram; (b) Bode Plot of Impedance Modulus; (c) Bode Plot of Impedance Phase

B.54 WFS-RC-03, BUS 287J (LP 370) OVER HOLLIDAY CREEK

- Bridge ID: 32430004410125 (Wichita County)
- Built in 1994
- Mitigation methods: HPC (30 to 35% Class F fly ash), ECR
- Observed CIP depth: N/A
- Observed clear cover: 2.0 in.
- 3 spans, 11-concrete PS girder @ 8’ with 3’ overhangs
- Inspected on June 2, 2021

Figure 0.387. Concrete Deck of the Bridge (source: google maps)

B.54.1 Observed Condition

Deck surface has transverse and longitudinal cracks. Concrete rail at north has spalling and exposed rebar at its west end as shown in Figure 0.388 (a). The abutment caps have vertical cracks with efflorescence as shown in Figure 0.388 (b).

(a) (b)

Figure 0.388. Deteriorations on the Bridge: (a) Exposed and Corroded Rebar at Concrete Railing; (b) Crack on the Abutment Wall

B.54.2 NDE Results

Grid 1 was located on the WB lane and grid 2 was not drawn due to a weather condition.

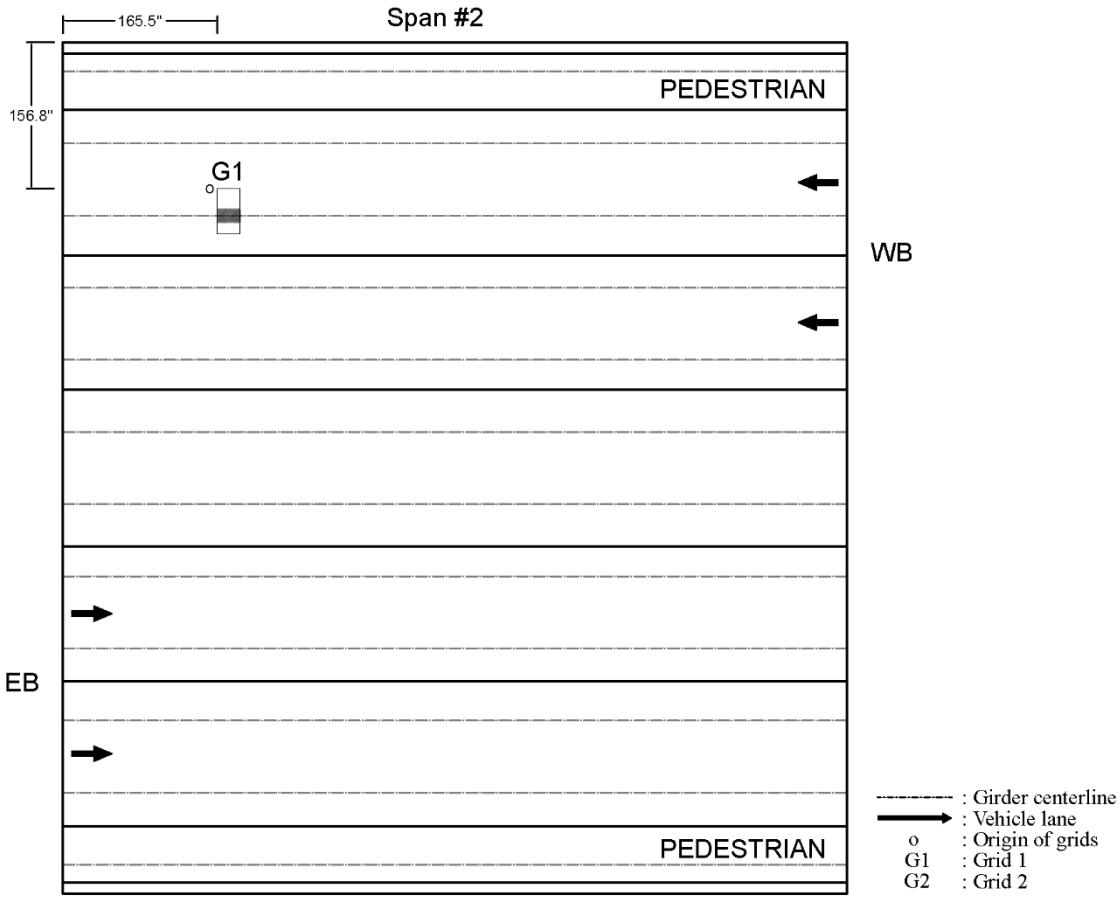

Figure 0.389. Plan View of the Bridge and Location of Grids

Due to a weather condition, crack map was not drawn for both grid 1 and grid 2, and GPR and UST of grid 2 was not measured.

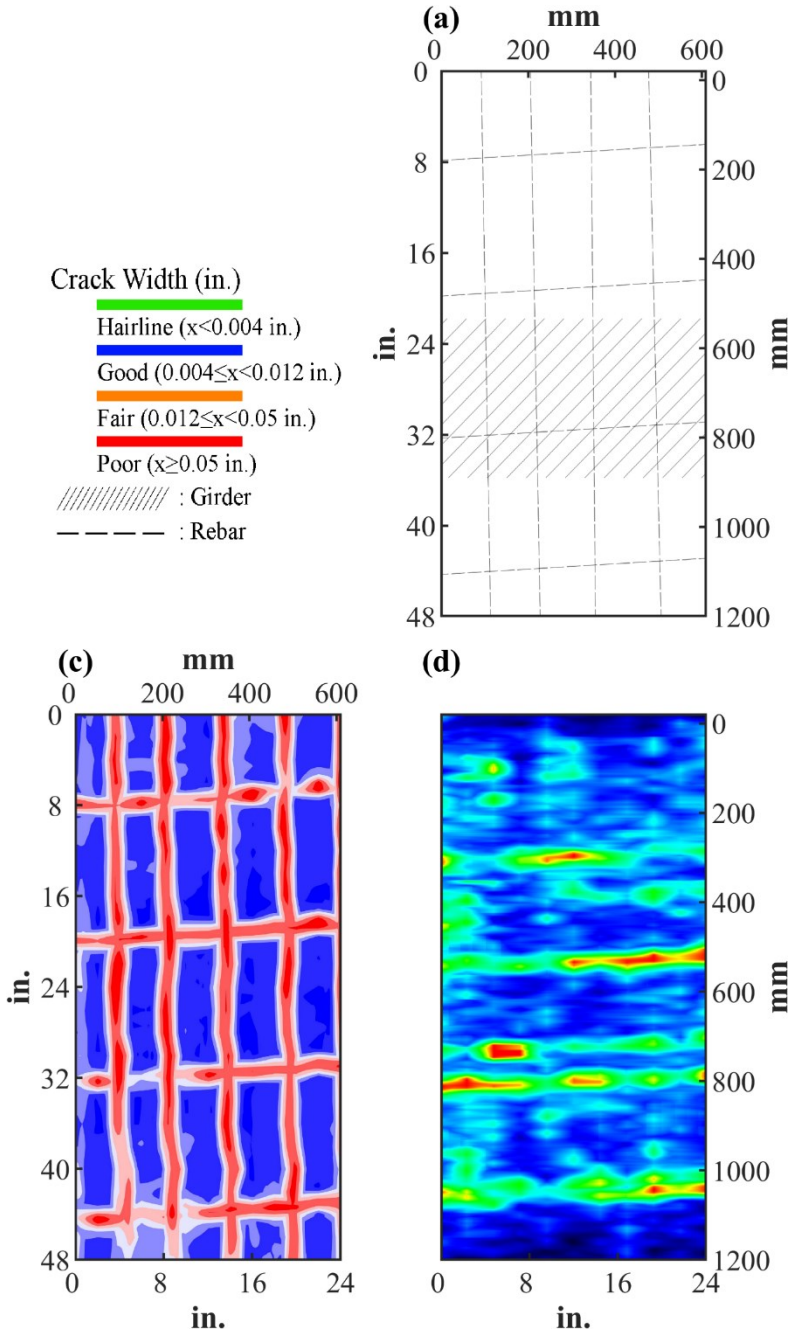

Figure 0.390. Crack Map and NDE Results of Grid 1: (c) GPR C-scan 2.5 in. to 3.8 in. Depth; (d) UST C-scan at 4.4 in. Depth

B.54.3 Concrete Cores

Table B-179. Detail Information of concrete cores

Core	dia. x height (in.)	Rebar depth (in.)	Rebar size (#)	Epoxy (Y/N)	Crack type	Crack width (in)	Notes
1-1	3.75 x 5.2	2.0; 2.8	5; 4	Y; Y	-	-	-
1-2	3.75 x 7.5	2.0	5	Y	-	-	-
1-3	3.75 x 6.3	2.1; 5.5	5; 5	Y; Y	-	-	-
1-4	3.75 x 5.6	2.8; 5.6	4; 5	Y; Y	-	-	-
1-5	3.75 x 7.0	2.7	4	Y	-	-	
1-6	3.75 x 7.2	-	-	-	-	-	-
1-7	3.75 x 6.7	2.0; 2.8	5; 4	Y; Y	-	-	-

Table B-180. Core Pictures

Core	Pictures of the Cores
1-1	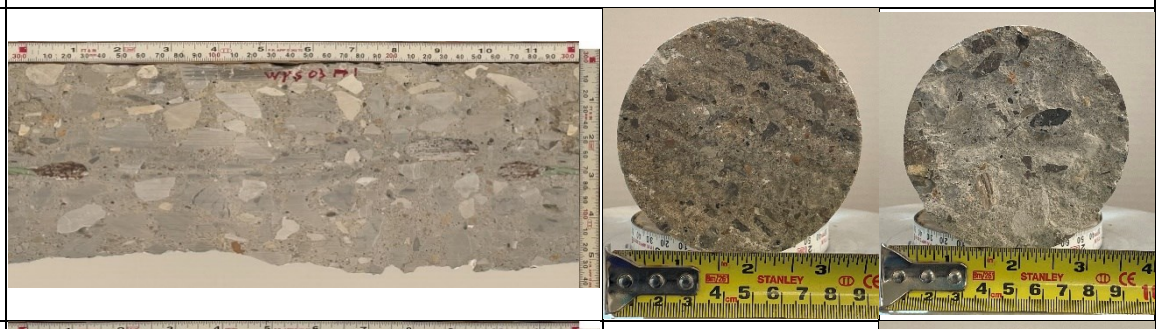
1-2	

1-3			
1-4			
1-5			
1-6			
1-7			

B.54.4 Laboratory Experiment Results

B.54.4.1 Resistivity

Core Number	Surface Resistivity (kΩ·m)	Bulk Resistivity (kΩ·m)
1-6	80.1	20.3

B.54.4.2 Ultrasonic Pulse Velocity

Core Number	Ultrasonic Pulse Velocity (m/s)
1-6	4400

B.54.4.3 Acid-Soluble Chloride Content

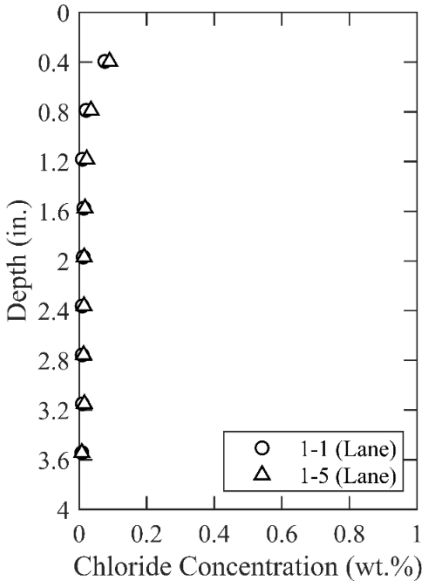

Figure 0.391. Chloride Content at Different Depth

B.54.4.4 Sorptivity

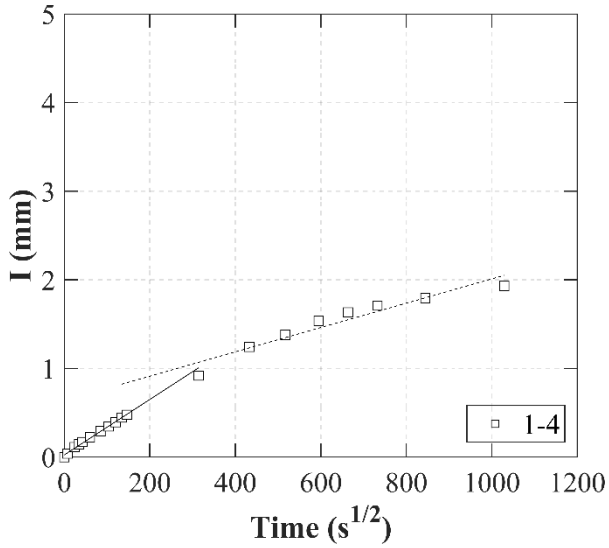

Figure 0.392. Absorption and Sorptivity of Core 1–4

Table B-181. Initial and Secondary Sorptivity Results

Core Number	Sorptivity	Results (mm/s$^{1/2}$)
Core 1–4	Initial Sorptivity	0.00313
	Secondary Sorptivity	0.00137

B.54.4.5 Electrochemical Impedance Spectroscopy

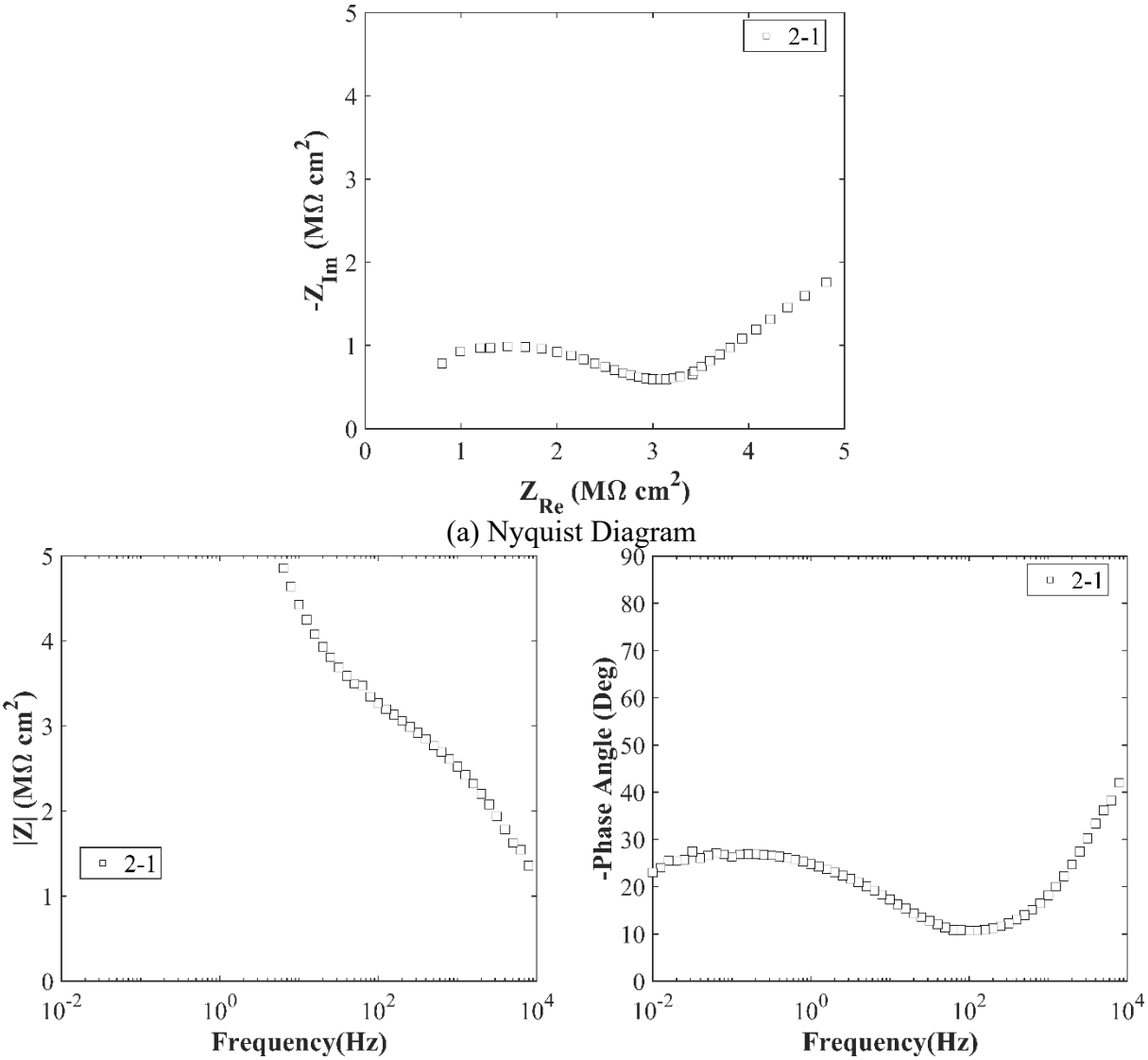

(a) Nyquist Diagram

(b) Bode Plot of Impedance Modulus

(c) Bode Plot of Impedance Phase

Figure 0.393. EIS Results: (a) Nyquist Diagram; (b) Bode Plot of Impedance Modulus; (c) Bode Plot of Impedance Phase

B.55 WFS-RC-04, US 82 WB OVER FM 369

- Bridge ID: 32430015604107 (Wichita County)
- Built in 2009
- Mitigation methods: HPC (25 to 30% Class F fly ash), ECR
- Observed CIP depth: 4.0 in.
- Observed clear cover: 2.5 in.
- 4 spans, 8-concrete PS-concrete girder @ 7.42’ with 3’ overhangs
- Inspected on June 2, 2021

Figure 0.394. Concrete Deck of the Bridge (source: google maps)

B.55.1 Observed Condition

Deck surface has hairline diagonal, transverse, and longitudinal cracks. Deck joints are partially filled with debris and dirt. Its metal arms has minor corrosion. The metal deck form at its end has corrosion rust as shown in Figure 0.395 (a). The columns have hairline cracks as shown in Figure 0.395 (b).

(a) (b)

Figure 0.395. Deteriorations on the Bridge: (a) Rust at Metal Deck Form; (b) Cracks on Column

B.55.2 NDE Results

Both grid 1 and grid 2 was located on the WB shoulder lane. Whereas grid 1 was located on span 2, grid 2 was located the joint of span 1 and span 2.

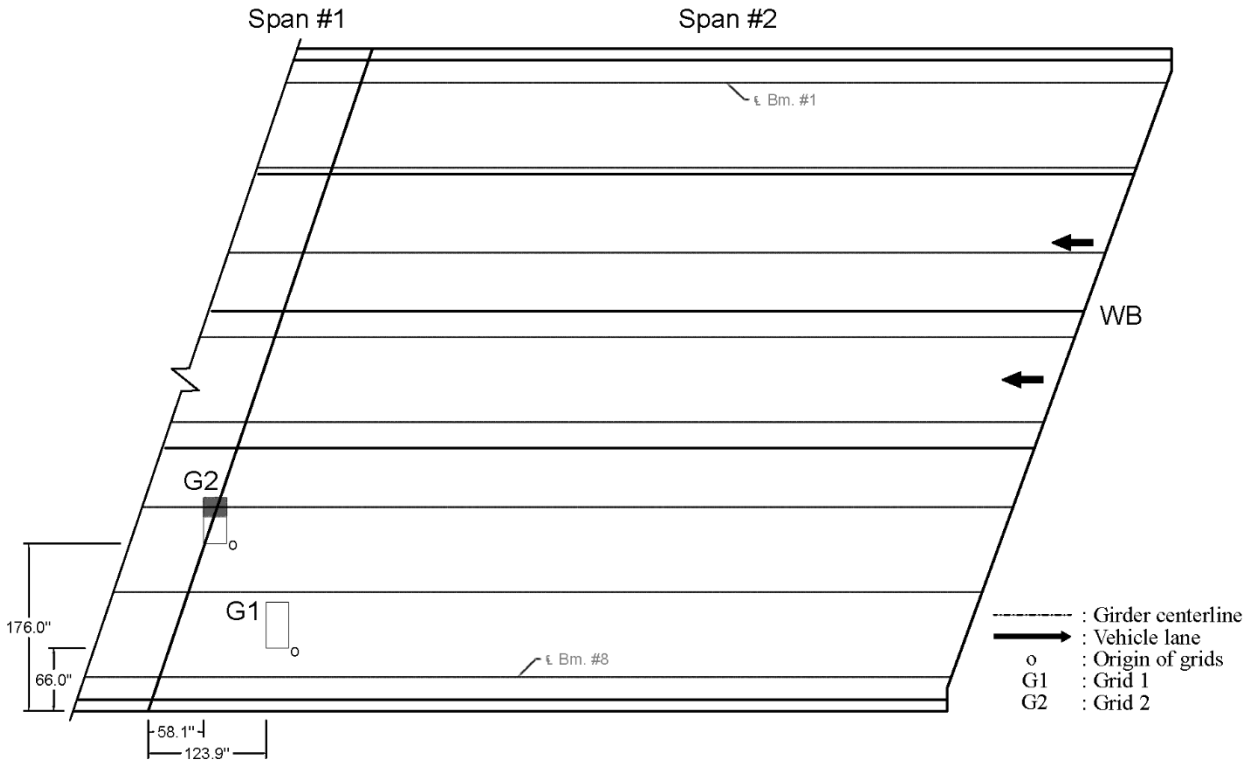

Figure 0.396. Plan View of the Bridge and Location of Grids

As shown in Figure 0.171 (a), there was one 0.008 in. wide transverse crack that might have been caused by panel joints on grid 1. Grid 2 was located on a joint and a 0.004 in. crack was propagating from the joint as shown in Figure 0.172 (a).

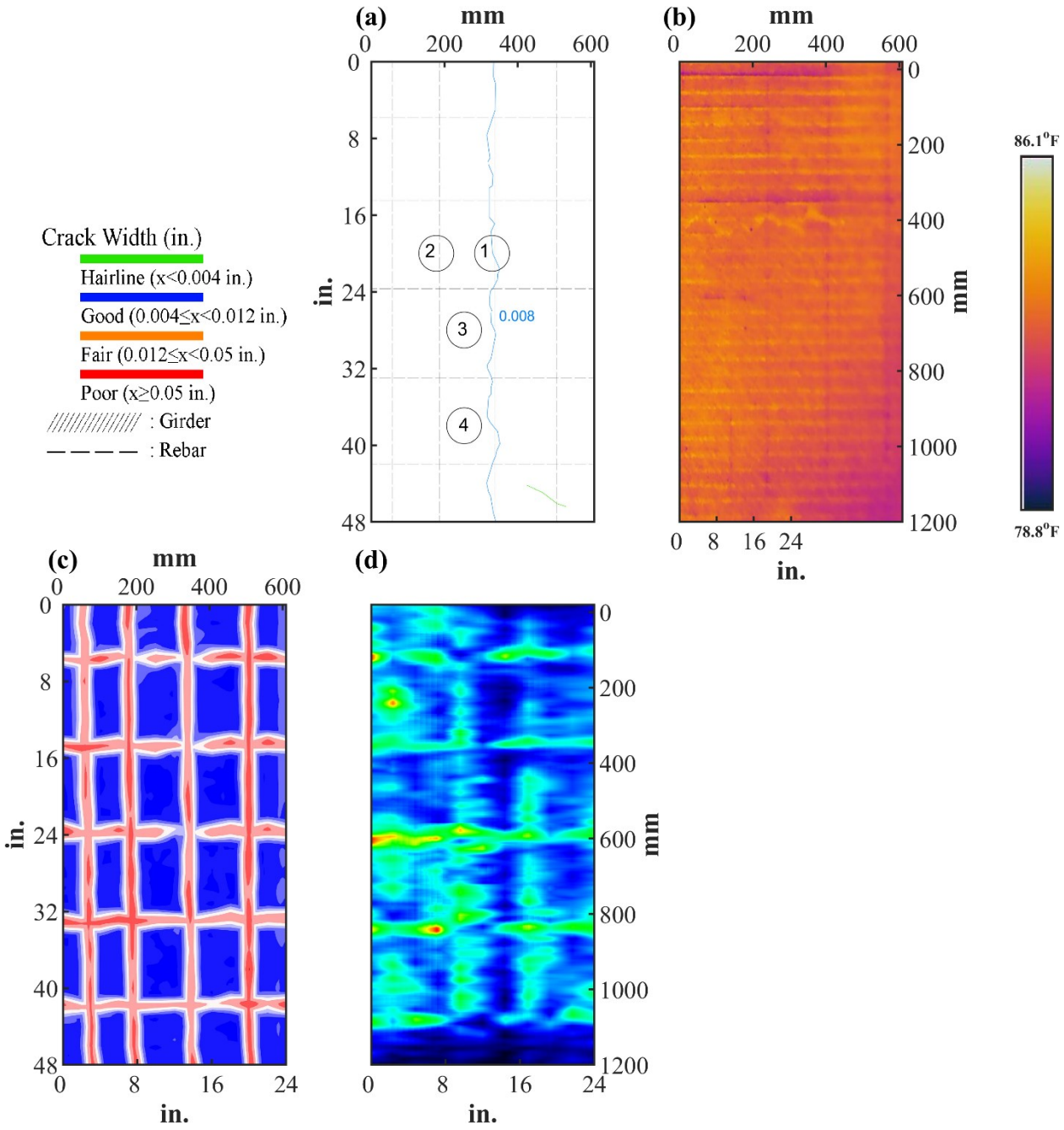

Figure 0.397. Crack Map and NDE Results of Grid 1: (a) Crack Map and Location of Cores; (b) Infrared Picture; (c) GPR C-scan at 1.9 in. to 3.3 in. Depth; (d) UST C-scan at 3.3 in. Depth

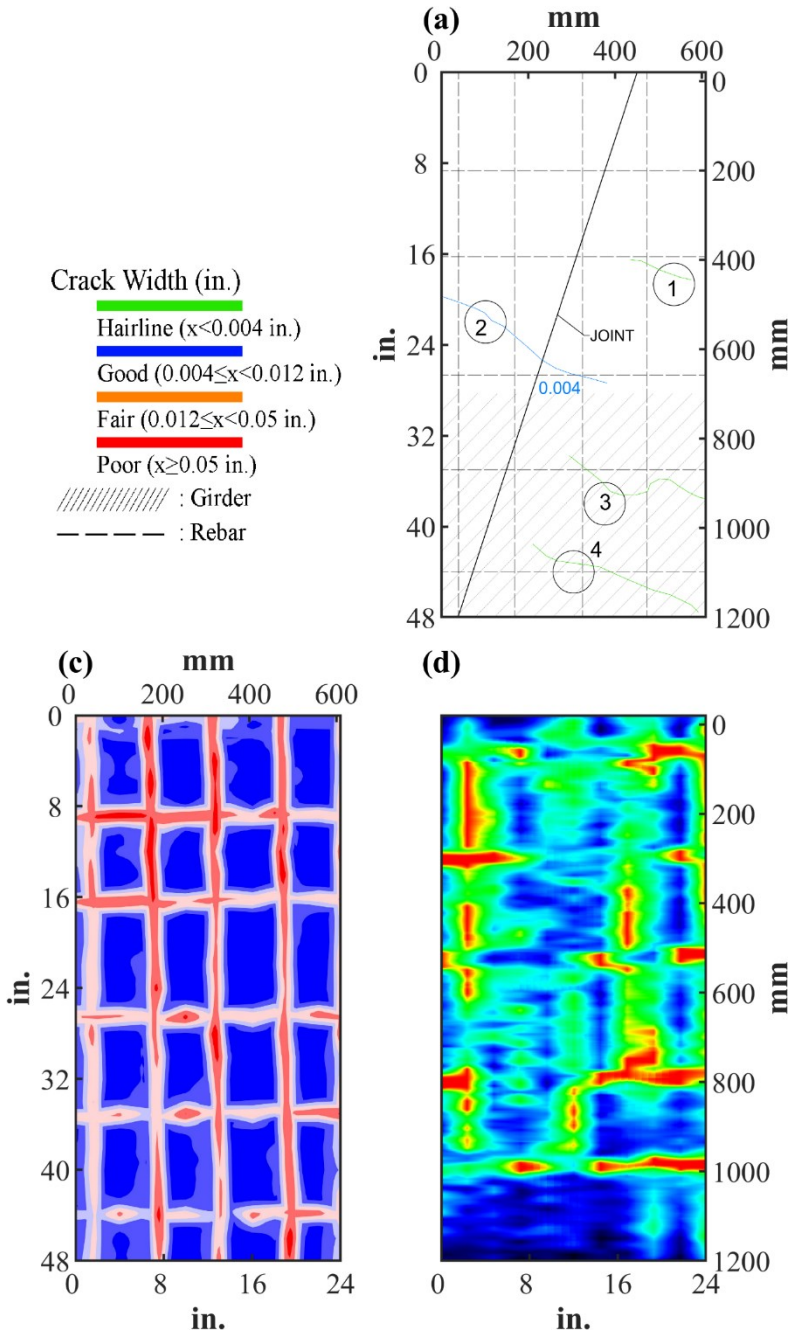

Figure 0.398. Crack Map and NDE Results of Grid 2: (a) Crack Map and Location of Cores; (c) GPR C-scan at 2.6 in. to 3.95 in. Depth; (d) UST C-scan at 3.5 in. Depth

B.55.3 Concrete Cores

Table B-182. Detail Information of concrete cores

Core	dia. x height (in.)	Rebar depth (in.)	Rebar size (#)	Epoxy (Y/N)	Crack type	Crack width (in)	Notes
1-1	3.75 x 4.4	2.6	5	Y	transverse	0.008	A crack propagates from panel joint
1-2	3.75 x 6.3	2.5	5	Y	-	-	-
1-3	3.75 x 6.3	-	-	-	-	-	-
1-4	3.75 x 5.9	-	-	-	-	-	-
2-1	3.75 x 3.5	-	-	-	longitudinal	HL	-
2-2	3.75 x 4.9	-	-	-	diagonal	0.004	-
2-3	3.75 x 4.3	3.1	5	Y	-	-	-
2-4	3.75 x 5.9	3.0; 3.6	5; 4	Y; Y	longitudinal	HL	-

Table B-183. Core Pictures

Core	Pictures of the Cores		
1-1			
1-2			

1-3		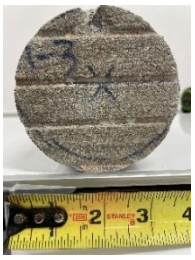	
1-4			
2-1			
2-2			
2-3	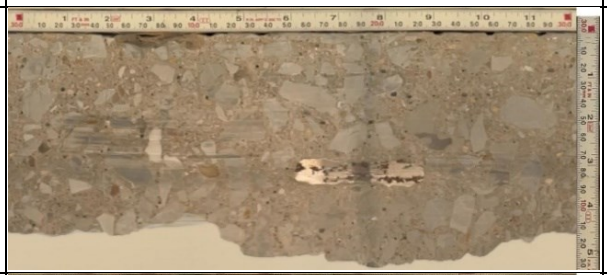		
2-4			

B.55.4 Laboratory Experiment Results

B.55.4.1 Resistivity

Core Number	Surface Resistivity (kΩ·m)	Bulk Resistivity (kΩ·m)
1-4	96.1	19.8

B.55.4.2 Ultrasonic Pulse Velocity

Core Number	Ultrasonic Pulse Velocity (m/s)
1-3	4246
1-4	4548
2-1	4079
2-2	4198

B.55.4.3 Carbonation Depth

Core Number	Carbonation Depth (in.)
1-1	0.12
2-3	0.00

B.55.4.4 Acid-Soluble Chloride Content

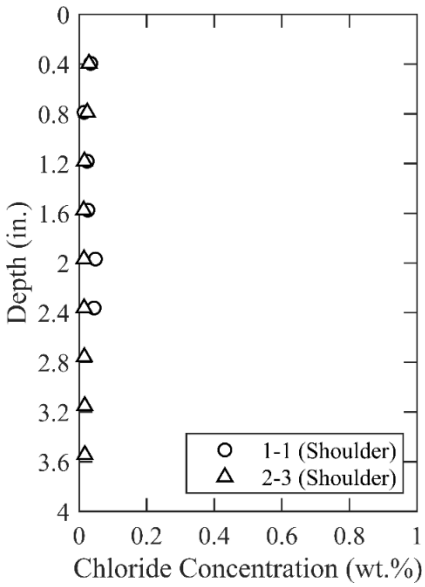

Figure 0.399. Chloride Content at Different Depth

B.55.4.5 Sorptivity

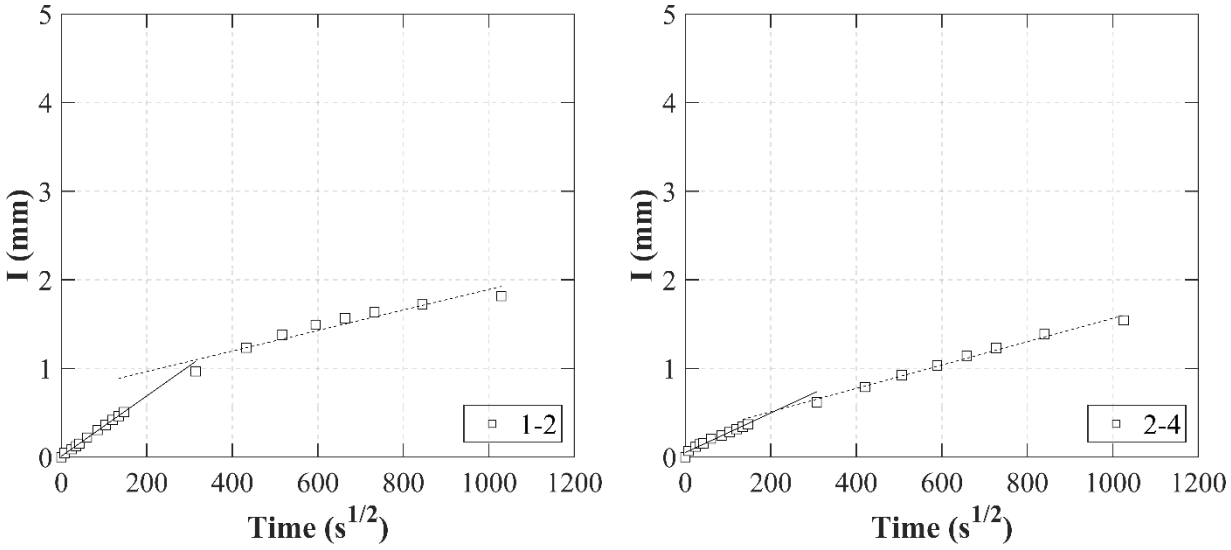

(a) Core 1–2 (b) Core 2–4

Figure 0.400. Absorption and Sorptivity of: (a) Core 1–1; (b) Core 2–2

Table B-184. Initial and Secondary Sorptivity Results

Core Number	Sorptivity	Results (mm/s$^{1/2}$)
Core 1–2	Initial Sorptivity	0.00341
	Secondary Sorptivity	0.00116
Core 2–4	Initial Sorptivity	0.00223
	Secondary Sorptivity	0.00132

B.55.4.6 Electrochemical Impedance Spectroscopy

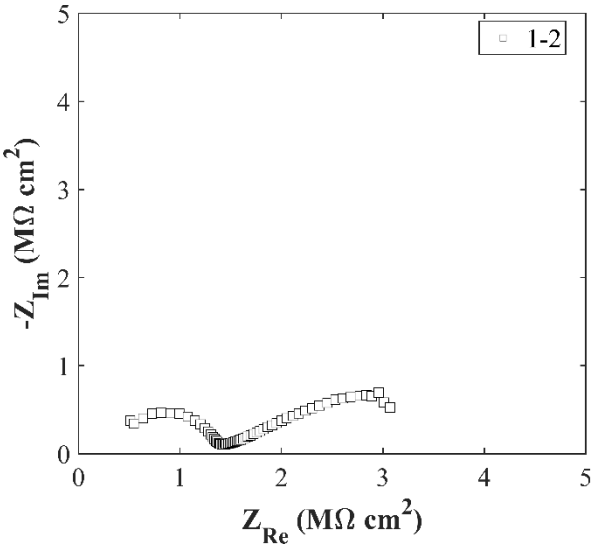

(a) Nyquist Diagram

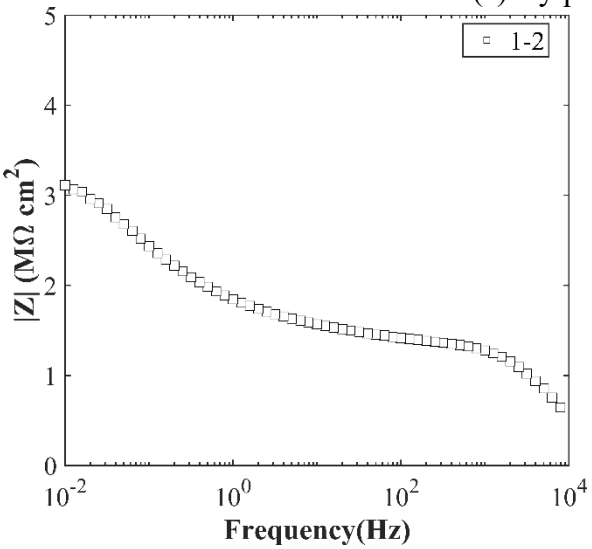

(b) Bode Plot of Impedance Modulus

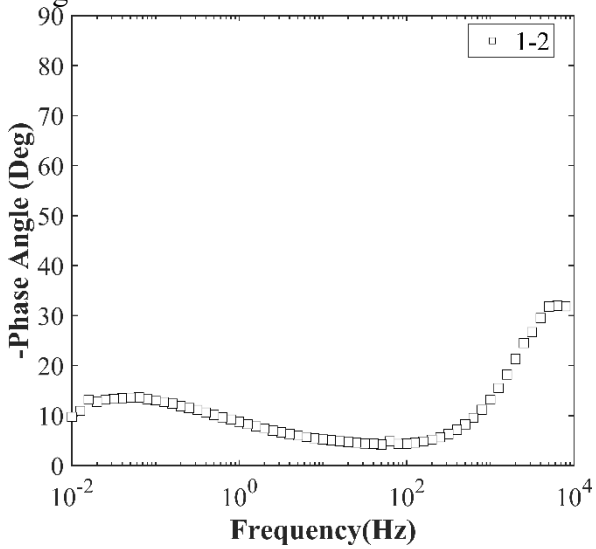

(c) Bode Plot of Impedance Phase

Figure 0.401. EIS Results: (a) Nyquist Diagram; (b) Bode Plot of Impedance Modulus; (c) Bode Plot of Impedance Phase

B.56 WFS-RC-05, FM 2380 OVER HOLLIDAY CREEK

- Bridge ID: 32430028301023 (Wichita County)
- Built in 1995
- Mitigation methods: ECR
- Observed CIP depth: Unknown
- Observed clear cover: 2.4 in.
- 3 spans, 3-concrete PS girder @ 8’ with 3’ overhangs
- Inspected on June 3, 2021

Figure 0.402. Concrete Deck of the Bridge (source: google maps)

B.56.1 Observed Condition

Deck surface has hairline transverse cracks. Abutment back wall has vertical and horizontal crack with efflorescence as shown in Figure 0.403 (a) and (b).

(a) (b)

Figure 0.403. Deteriorations on the Bridge: (a) Vertical Crack and Efflorescence at Abutment Wall; (b) Horizontal Crack and Efflorescence at Abutment Wall

B.56.2 NDE Results

Grid 1 was located on the NB lane of span 2 and grid 2 was located on the NB lane of the span 3 of the bridge.

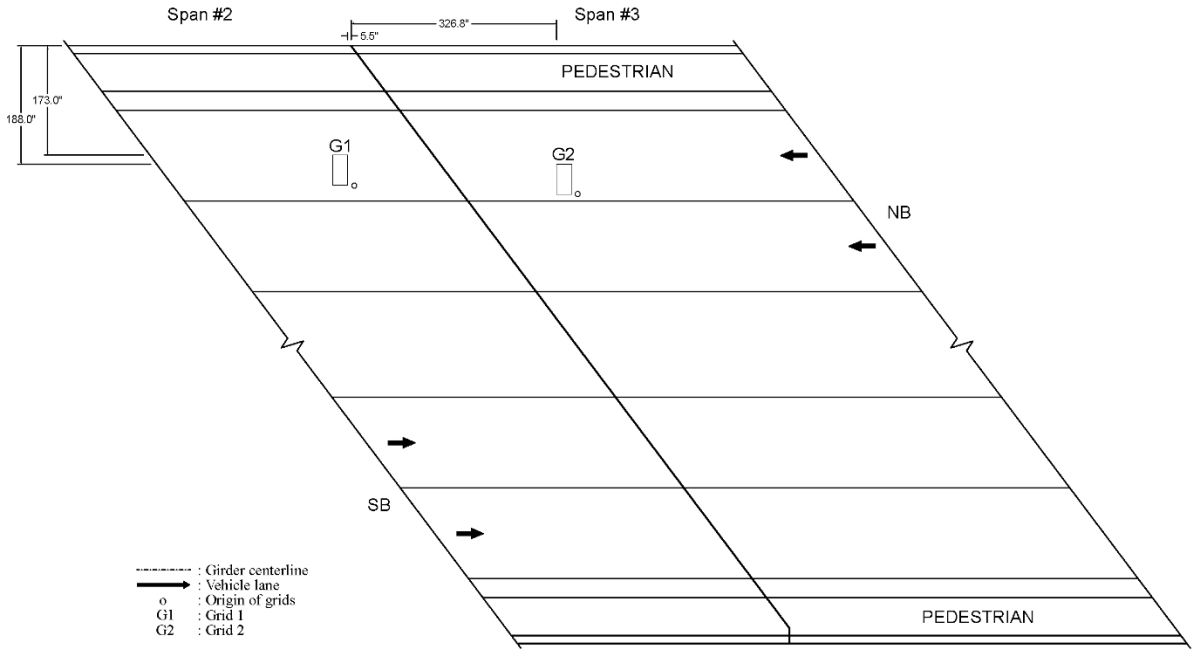

Figure 0.404. Plan View of the Bridge and Location of Grids

As shown in Figure 0.405 (a), there were 0.004 in. wide longitudinal cracks on grid 1. On grid 2, there were 0.004 in. longitudinal and diagonal cracks as shown in Figure 0.406 (a). Due to a weather condition, UST was not conducted on grid 2.

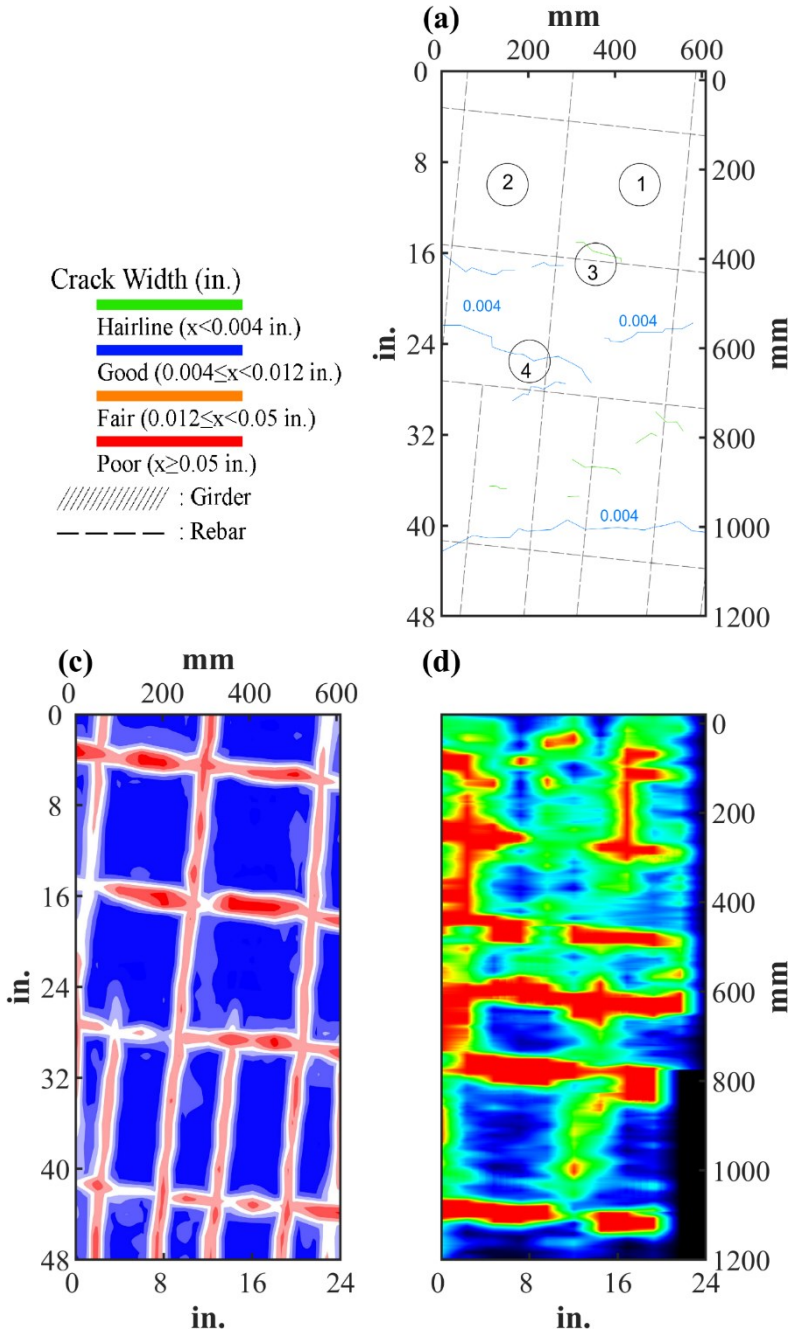

Figure 0.405. Crack Map and NDE Results of Grid 1: (a) Crack Map and Location of Cores; (c) GPR C-scan at 2.7 in. to 4.1 in. Depth; (d) UST C-scan at 4.4 in. Depth

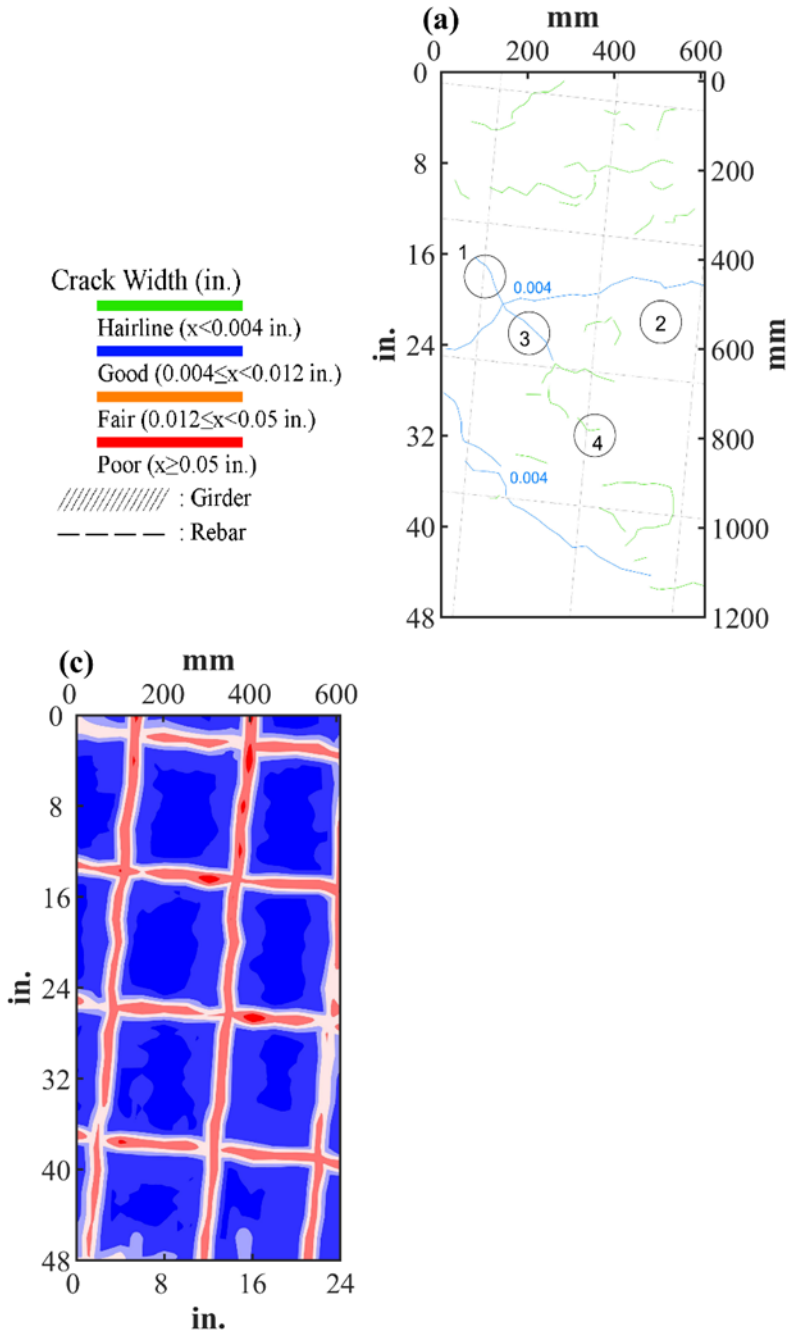

Figure 0.406. Crack Map and NDE Results of Grid 2: (a) Crack Map and Location of Cores; (c) GPR C-scan at 2.1 in. to 3.4 in. Depth

B.56.3 Concrete Cores

Table B-185. Detail Information of concrete cores

Core	dia. x height (in.)	Rebar depth (in.)	Rebar size (#)	Epoxy (Y/N)	Crack type	Crack width (in)	Notes
1-1	3.75 x 6.3	-	-	-	-	-	-
1-2	3.75 x 6.3	-	-	-	-	-	-
1-3	3.75 x 6.7	4.0; 4.1; 5.8; 5.9	5; 5; 5; 5	Y; Y; N; N	-	-	-
1-4	3.75 x 3.5	3.1	5	Y	-	-	Erosion at top surface of deck
2-1	3.75 x 7.5	2.8	5	Y	longitudinal	0.25	Erosion at top surface of deck
2-2	3.75 x 7.3	2.4; 5.0; 5.6		N; N; N	-	-	-
2-3	3.75 x 6.3	5.0; 5.6		N; Y	-	-	Erosion at top surface of deck
2-4	3.75 x 6.3	5.7	5	Y	-	-	-

Table B-186. Core Pictures

Core	Pictures of the Cores		
1-1			Bottom 
1-2			

1-3			
1-4			
2-1			
2-2			
2-3			

2-4			

B.56.4 Laboratory Experiment Results

B.56.4.1 Resistivity

Core Number	Surface Resistivity (kΩ·m)	Bulk Resistivity (kΩ·m)
1-1	40.0	9.9
1-2	36.5	-

B.56.4.2 Ultrasonic Pulse Velocity

Core Number	Ultrasonic Pulse Velocity (m/s)
1-1	3866
1-2	4561

B.56.4.3 Carbonation Depth

Core Number	Carbonation Depth (in.)
1-3	0.00
2-3	0.11

B.56.4.4 Acid-Soluble Chloride Content

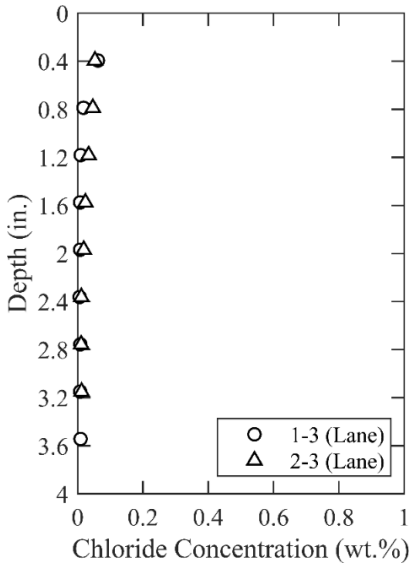

Figure 0.407. Chloride Content at Different Depth

B.56.4.5 Sorptivity

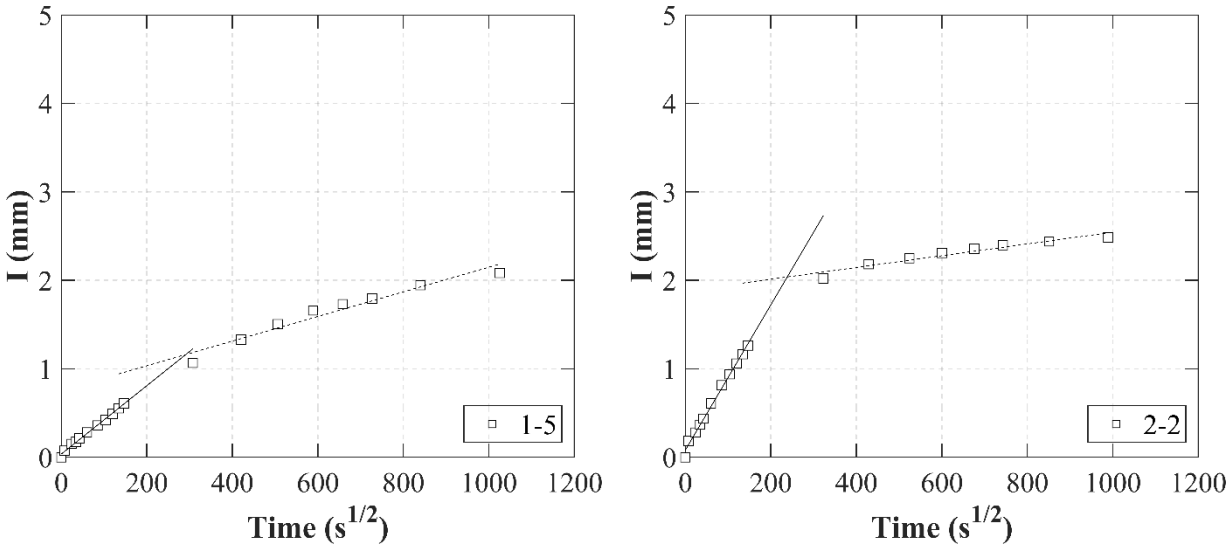

(a) Core 1–5 (b) Core 2–2

Figure 0.408. Absorption and Sorptivity of: (a) Core 1–1; (b) Core 2–2

Table B-187. Initial and Secondary Sorptivity Results

Core Number	Sorptivity	Results ($mm/s^{1/2}$)
Core 1–5	Initial Sorptivity	0.00386
	Secondary Sorptivity	0.00139
Core 2–2	Initial Sorptivity	0.00821
	Secondary Sorptivity	0.00066

B.56.4.6 Electrochemical Impedance Spectroscopy

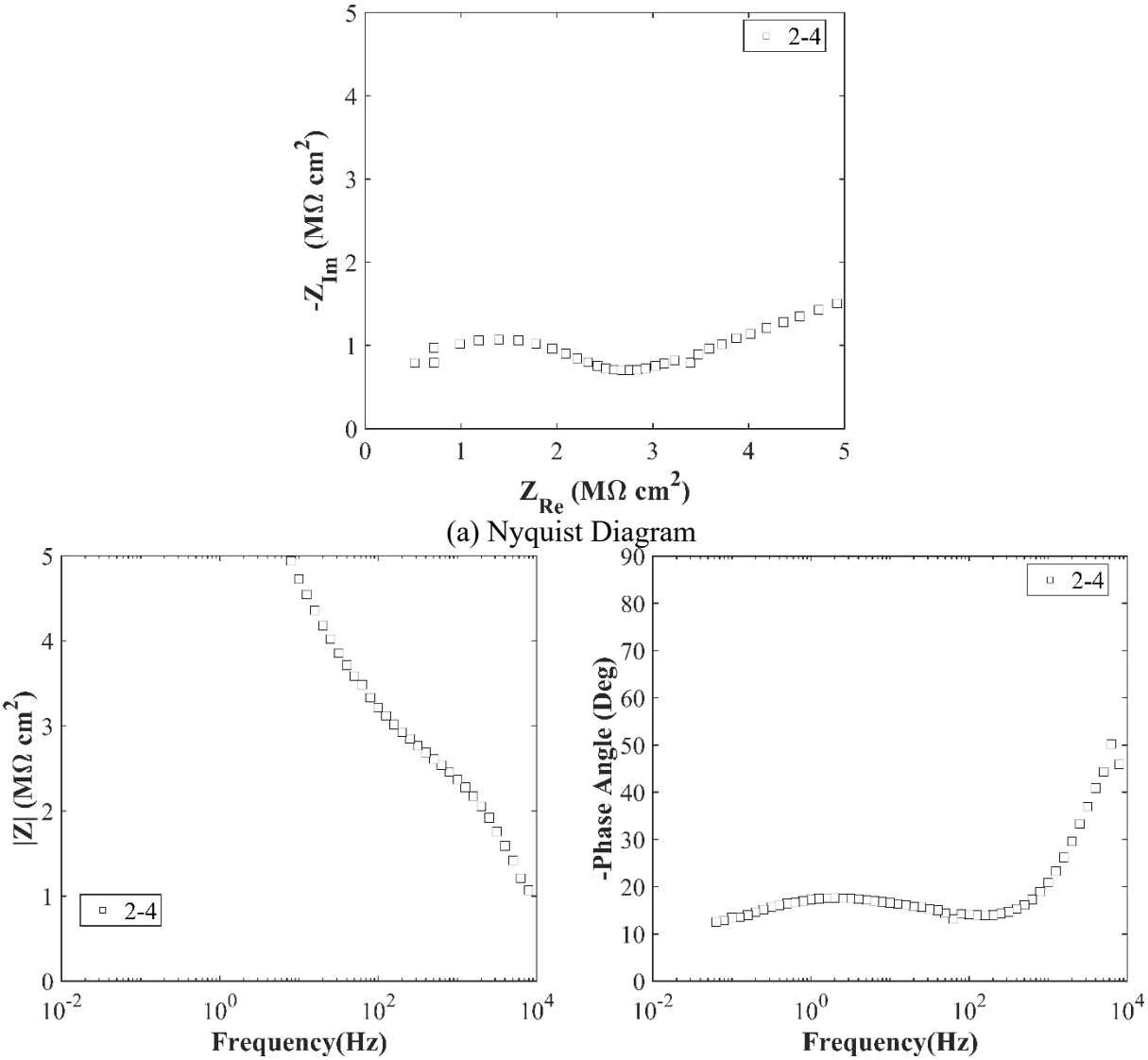

(a) Nyquist Diagram

(b) Bode Plot of Impedance Modulus

(c) Bode Plot of Impedance Phase

Figure 0.409. EIS Results: (a) Nyquist Diagram; (b) Bode Plot of Impedance Modulus; (c) Bode Plot of Impedance Phase

B.57 WFS-RC-06, US 70/287 NB OVER PARADISE CREEK

- Bridge ID: 32440004306186 (Wilbarger County)
- Built in 1995
- Mitigation methods: ECR
- Observed CIP depth: 3.0 in.
- Observed clear cover: 1.0 in.
- 3 spans, 8-concrete PS girder @ 5.143’ with 3’ overhangs
- Inspected on June 2, 2021

Figure 0.410. Concrete Deck of the Bridge (source: google maps)

B.57.1 Observed Condition

Deck surface has longitudinal cracks.

B.57.2 NDE Results

Grid 1 was located on the WB lane and grid 2 was located on the WB shoulder lane of the span 1 of the bridge.

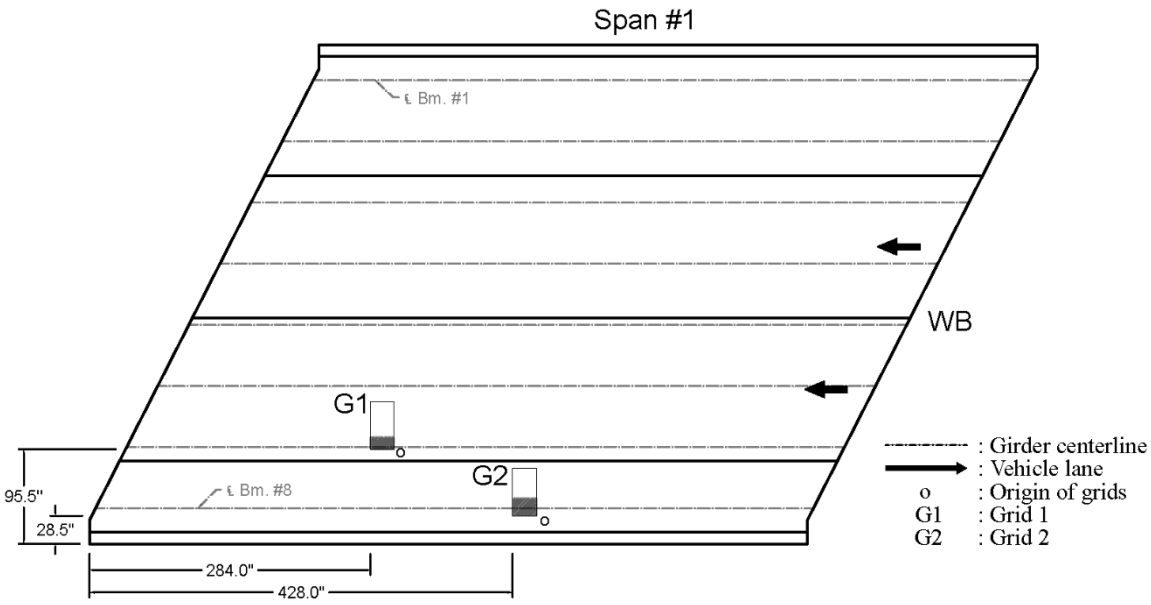

Figure 0.411. Plan View of the Bridge and Location of Grids

As shown in Figure 0.187 (a), there were longitudinal cracks that were 0.004 in. and 0.012 in. wide throughout the grid and along a girder on grid 1. On grid 2, there were two 0.004 in. wide longitudinal cracks and one of them were on top of a girder as shown in Figure 0.188 (a).

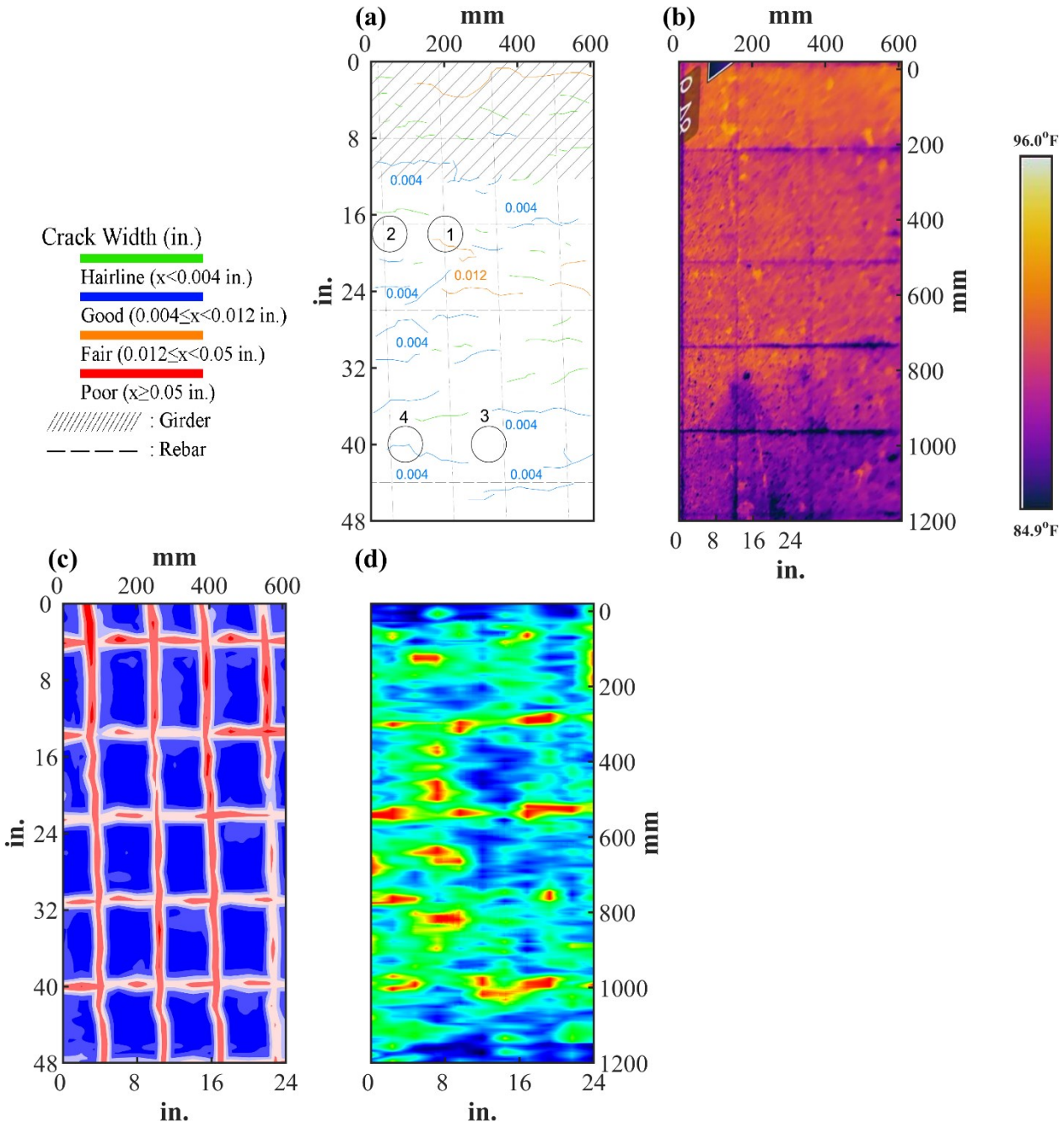

Figure 0.412. Crack Map and NDE Results of Grid 1: (a) Crack Map and Location of Cores; (b) Infrared Picture; (c) GPR C-scan at 1.55 in. to 2.9 in. Depth; (d) UST C-scan at 2.5 in. Depth

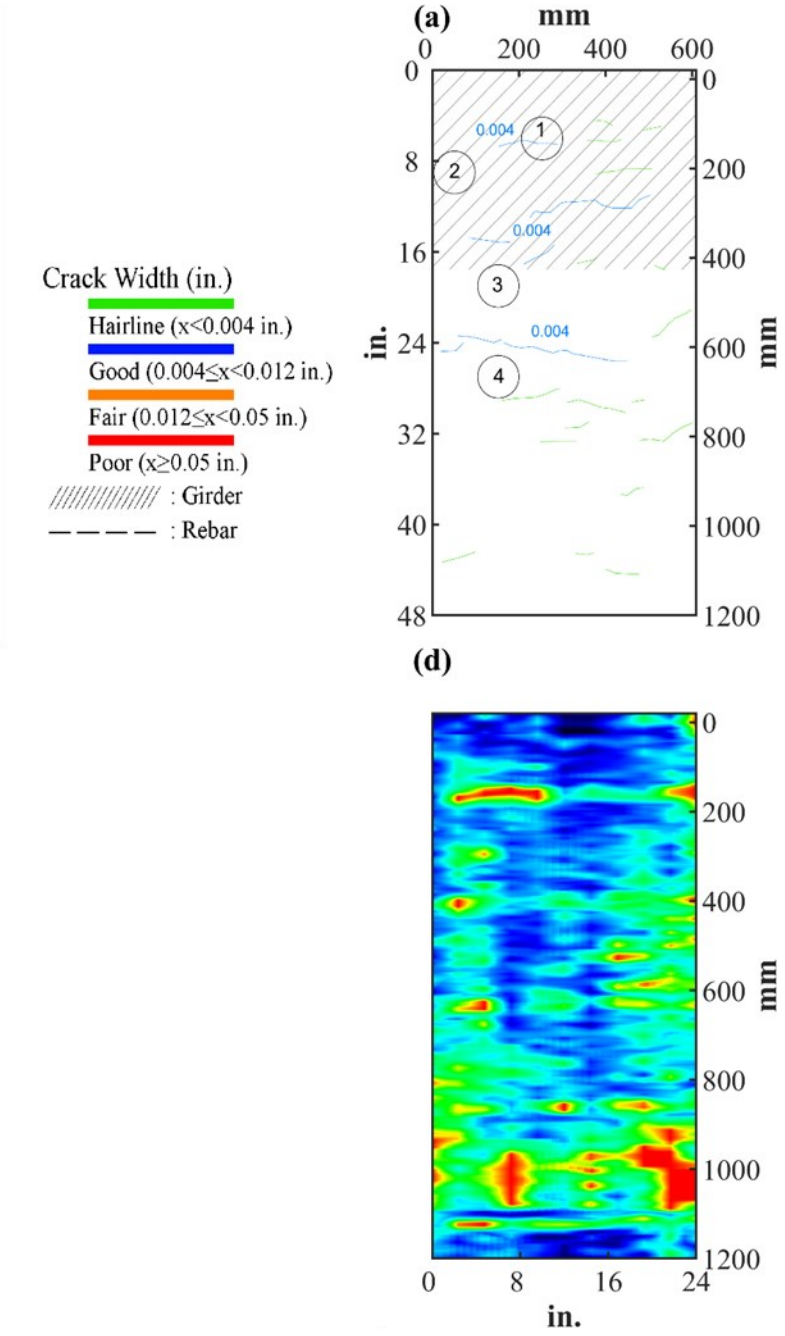

Figure 0.413. Crack Map and NDE Results of Grid 2: (a) Crack Map and Location of Cores; (d) UST C-scan at 3.0 in. Depth

B.57.3 Concrete Cores

Table B-188. Detail Information of concrete cores

Core	dia. x height (in.)	Rebar depth (in.)	Rebar size (#)	Epoxy (Y/N)	Crack type	Crack width (in)	Notes
1-1	3.75 x 6.9	1.2; 1.8	5,4	Y; Y	longitudinal	0.012	A crack propagates from rebar
1-2	3.75 x 7.0	1.0; 1.8	5,4	Y; Y	-	-	Delamination between CIP and PCP
1-3	3.75 x 6.7	1.2; 1.2	5	Y; Y	-	-	
1-4	3.75 x 6.8	1.2; 2.4; 2.6	5,4,4	Y; Y; Y	longitudinal	0.004	A crack propagates along intersection of aggregates
2-1	3.75 x 5.9	2.0; 2.6	5,5	Y; Y	longitudinal	0.004	A crack propagates along intersection of aggregates; panel joint
2-2	3.75 x 5.2	1.8	5	Y	-	-	-
2-3	3.75 x 4.9	-	-	-	-	-	A crack propagates along intersection of aggregates
2-4	3.75 x 4.9	-	-	-	-	-	-

Table B-189. Core Pictures

Core	Pictures of the Cores		
1-1			
1-2			

1-3			
1-4	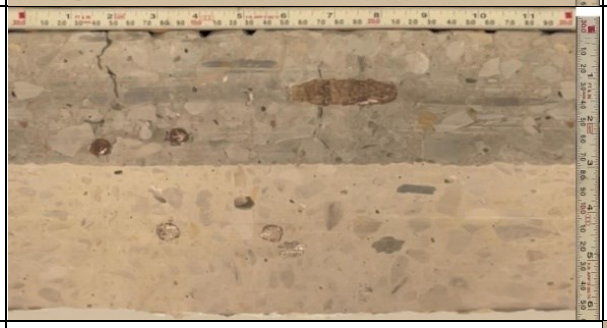		
2-1			
2-2			
2-3			

2-4	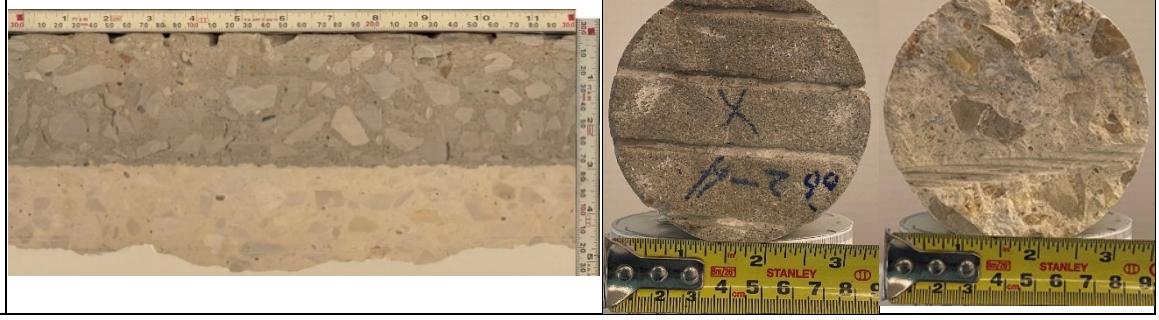

B.57.4 Laboratory Experiment Results

B.57.4.1 Resistivity

Core Number	Surface Resistivity (kΩ·m)	Bulk Resistivity (kΩ·m)
2-4	94.1	-

B.57.4.2 Ultrasonic Pulse Velocity

Core Number	Ultrasonic Pulse Velocity (m/s)
2-3	4534
2-4	4610

B.57.4.3 Carbonation Depth

Core Number	Carbonation Depth (in.)
1-2	0.00
2-1	0.09

B.57.4.4 Acid-Soluble Chloride Content

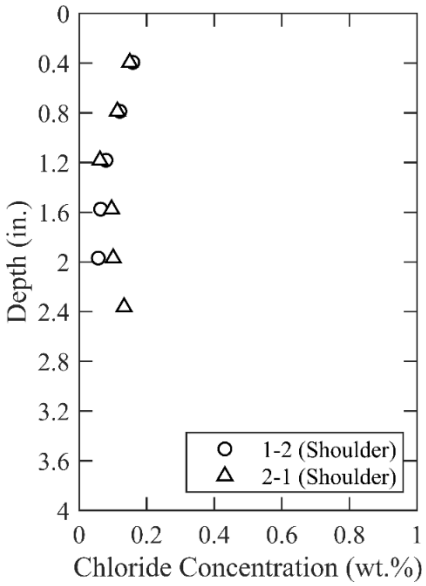

Figure 0.414. Chloride Content at Different Depth

B.57.4.5 Electrochemical Impedance Spectroscopy

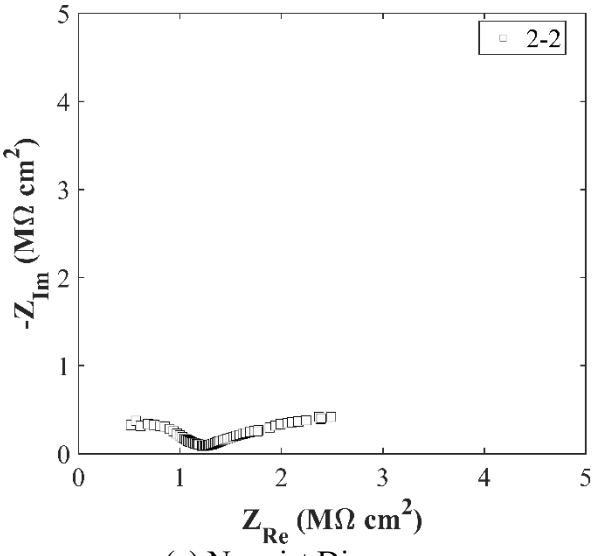

(a) Nyquist Diagram

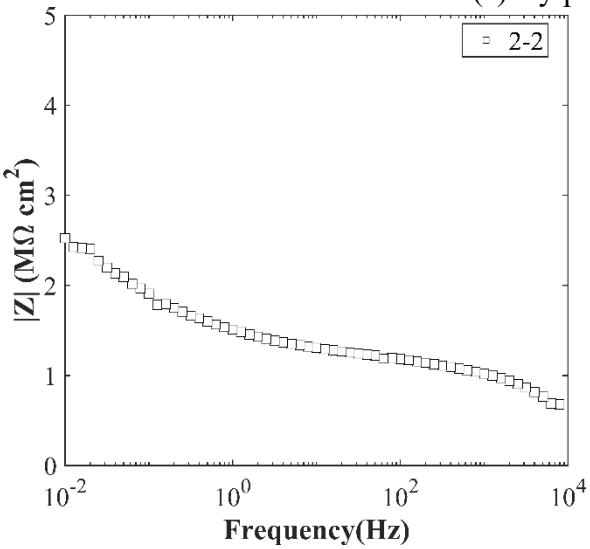

(b) Bode Plot of Impedance Modulus

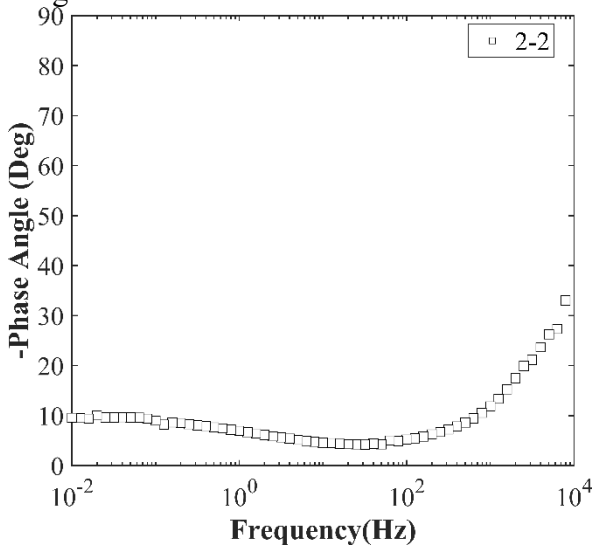

(c) Bode Plot of Impedance Phase

Figure 0.415. EIS Results: (a) Nyquist Diagram; (b) Bode Plot of Impedance Modulus; (c) Bode Plot of Impedance Phase

B.58 WFS-RC-07, LOOP 11 SB OVER US 287

- Bridge ID: 32430004309094 (Wichita County)
- Built in 1961
- Mitigation methods: None
- Observed CIP depth: Unknown in.
- Observed clear cover: 1.4 in.
- 4 spans, 5-concrete PS girder @ 6’-7 in. with 3’-2 in. overhangs
- Inspected on June 2, 2021

Figure 0.416. Concrete Deck of the Bridge (source: google maps)

B.58.1 Observed Condition

There are cracks on the top surface of deck. Crack is more widespread on span 2. There is a hole on a deck between beam 2 and 3 as shown in Figure 0.417 (a). Rebar had pitting corrosion as shown in Figure 0.417 (b). The joint is paved over by asphalt.

(a)

(b)

Figure 0.417. Deteriorations on the Bridge: (a) A Hole on Deck; (b) Pitting Corrosion on Exposed Rebar

B.58.2 NDE Results

As shown in Figure 0.418 (a), there was widespread of 0.004 in. wide cracks on grid 1, and a diagonal crack propagated along a rebar. It is possible that this crack might have been caused by panel joints.

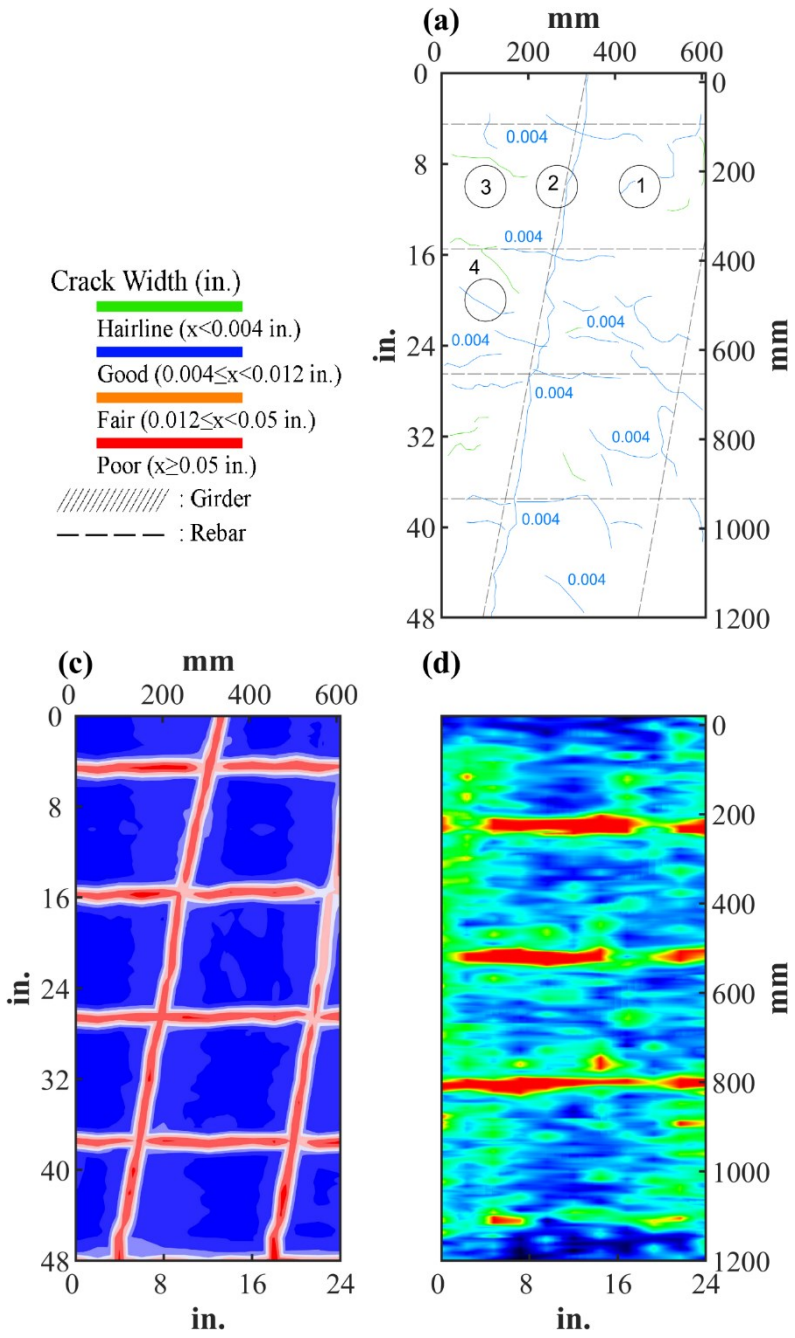

Figure 0.418. Crack Map and NDE Results of Grid 1: (a) Crack Map and Location of Cores; (c) GPR C-scan at 1.3 in. to 2.6 in. Depth; (d) UST C-scan at 2.4 in. Depth

B.58.3 Concrete Cores

Table B-190. Detail Information of concrete cores

Core	dia. x height (in.)	Rebar depth (in.)	Rebar size (#)	Epoxy (Y/N)	Crack type	Crack width (in)	Notes
1-1	3.75 x 10.6	-	-	-	longitudinal	0.004	-
1-2	3.75 x 8.4	1.4; 2.8	5; 6	N; N	transverse	0.004	A crack propagates from rebar
1-3	3.75 x 4.7	-	-	-	-	-	-
1-4	3.75 x 5.3	-	-	-	diagonal	0.004	-
1-7	3.75 x 10.3	-	-	-	diagonal	0.004	-

Table B-191. Core Pictures

Core	Pictures of the Cores		
1-1			
1-2		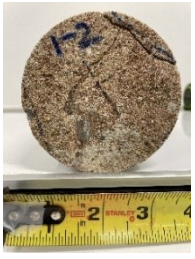	

1-3		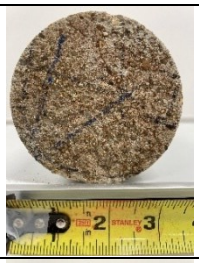	
1-4	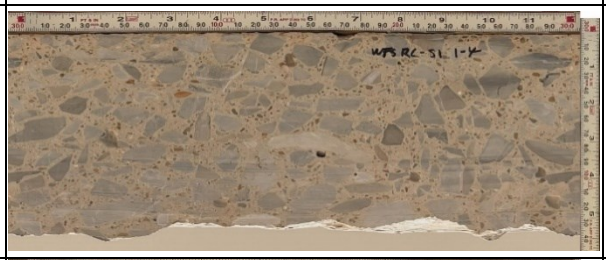		
Extra			

B.58.4 Laboratory Experiment Results

B.58.4.1 Resistivity

Core Number	Surface Resistivity (kΩ·m)	Bulk Resistivity (kΩ·m)
1-1	23.7	12.0
1-3	36.8	5.0
1-4	32.7	-

B.58.4.2 Ultrasonic Pulse Velocity

Core Number	Ultrasonic Pulse Velocity (m/s)
1-1	3682
1-3	4200
1-4	4291

B.58.4.3 Carbonation Depth

Core Number	Carbonation Depth (in.)
1-4	0.00

B.58.4.4 Acid-Soluble Chloride Content

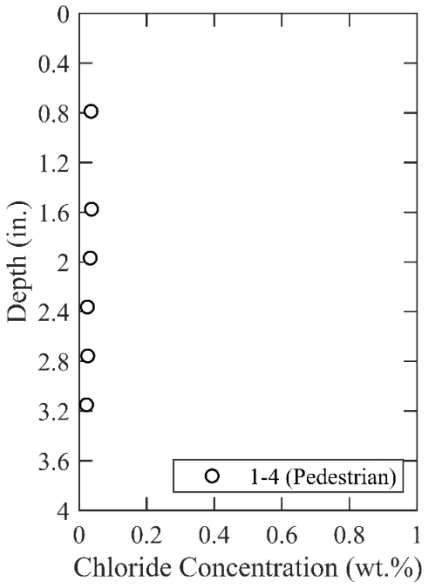

Figure 0.419. Chloride Content at Different Depth